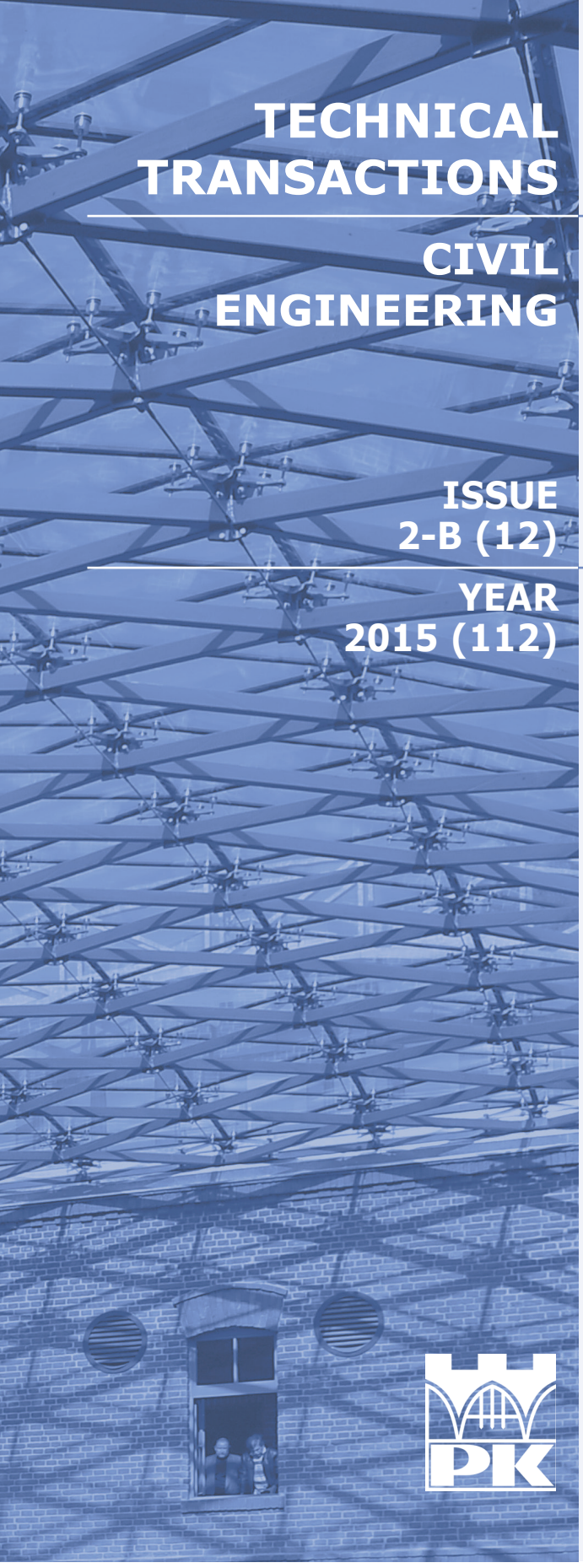

TECHNICAL TRANSACTIONS
CZASOPISMO TECHNICZNE

CIVIL ENGINEERING
BUDOWNICTWO

ISSUE 2-B (12) / ZESZYT 2-B (12)

YEAR 2015 (112) / ROK 2015 (112)

WYDAWNICTWO POLITECHNIKI KRAKOWSKIEJ

TECHNICAL TRANSACTIONS | CZASOPISMO TECHNICZNE

CIVIL ENGINEERING | BUDOWNICTWO

ISSUE 2-B (12) | ZESZYT 2-B (12)
YEAR 2015 (112) | ROK 2015 (112)

Basic version of each Technical Transactions magazine is its online version
Pierwotną wersją każdego zeszytu Czasopisma Technicznego jest jego wersja online
www.ejournals.eu/Czasopismo-Techniczne www.technicaltransactions.com www.czasopismotechniczne.pl

Civil Engineering Series
2-B/2015

PREFACE

The issues of environmental effects on buildings and people have an interdisciplinary character and comprise mainly the following branches of knowledge and science: physics of the Earth's atmosphere, meteorology, building aerodynamics, wind and snow engineering, structural mechanics, building physics, environmental actions on buildings and structures, environmental influences on building materials, measurement techniques, safety of buildings and structures, environmental acoustics, human comfort criteria at environmental actions and influences, etc.

The papers published in Technical Transactions 2-B/2015 deal primarily with the following topics:

- Environmental effects on buildings and structures (wind action, snow load, ice accretion and ice load, thermal action of climatic and technological origin, etc.);
- Combinations and interactions between environmental actions;
- Static and dynamic analysis of structures subjected to environmental actions;
- Wind power plants;
- Influence of wind on people in buildings and their surroundings;
- Environmental acoustics;
- Thermal influences on materials and structures;
- Effects of fire on buildings and structures;
- Ways of reduction of excessive environmental effects on people and buildings;
- Changes of mechanical and physical properties of building materials and structures caused by weather influences;
- Problems of standardization of environmental effects on buildings and people;
- New measuring techniques of environmental effects on buildings and people;
- Disasters caused by environmental actions;
- CFD applications in environmental actions.

These papers have been elaborated by persons working professionally in many different scientific and scientific-research institutions. The papers have been divided in the following three thematic groups:

- Aerodynamics of buildings and structures;
- Environmental effects on building materials, structures and people;
- Snow load and ice load.

We hope that papers presented in this issue of Technical Transactions will be interesting for all of the researchers, designers, building experts, consulting workers and students engaged in contemporary problems of environmental effects on buildings and people.

Ph.D. Eng. Tomasz Lipecki
Prof. Ph.D. D.Sc. Eng. Andrzej Flaga

AERODYNAMICS OF BUILDINGS AND STRUCTURES

AERODYNAMIKA BUDOWLI I KONSTRUKCJI

TECHNICAL TRANSACTIONS | CZASOPISMO TECHNICZNE
CIVIL ENGINEERING | BUDOWNICTWO
2-B/2015

GRZEGORZ BOSAK*

WIND TUNNEL TESTS OF WIND PRESSURE DISTRIBUTIONS OVER WALL AND ROOF SURFACES OF A UTILITY BUILDING WITH OPENWORK SIDE WALLS

BADANIA MODELOWE ROZKŁADÓW CIŚNIENIA WIATRU NA POWIERZCHNIACH ŚCIAN I DACHU HALI GOSPODARCZEJ Z AŻUROWYMI ŚCIANAMI BOCZNYMI

Abstract

This article presents results of model tests of pressure distributions over interior and exterior surfaces of a utility building model carried out in an boundary layer wind tunnel. The tests were carried out taking into consideration different variants of solidity ratio coefficient values of the structure's side walls. The main aim of the analyses was to determine the influence of the solidity ratio coefficient values of the side walls on the wind pressure distribution over the interior and exterior surfaces of the object. Four configuration variants of the side walls were taken into account for two directions of air flow – perpendicular to the gable wall and perpendicular to the side wall. The achieved results were analysed.

Keywords: *wind tunnel tests, wind action on buildings, wind pressure distributions on wall and roof surfaces of a building*

Streszczenie

W artykule przedstawiono rezultaty badań modelowych w tunelu aerodynamicznym z warstwą przyścienną rozkładów ciśnienia wiatru na powierzchniach wewnętrznych i zewnętrznych modelu budynku gospodarczego. Badania przeprowadzono w różnych wariantach wartości współczynnika wypełnienia ścian bocznych konstrukcji. Celem zasadniczym przeprowadzonych analiz było wyznaczenie wpływu wartości współczynnika wypełnienia ścian bocznych na rozkład ciśnienia wiatru na powierzchniach wewnętrznych i zewnętrznych obiektu. Rozpatrzono cztery warianty konfiguracji ścian bocznych przy dwóch kierunkach napływu powietrza: prostopadłym do ściany szczytowej i prostopadłym do ściany bocznej. Przeprowadzono analizę uzyskanych wyników.

Słowa kluczowe: *badania modelowe w tunelu aerodynamicznym, działanie wiatru na budynki, rozkłady ciśnienia wiatru na powierzchniach ścian i dachu budynku*

DOI: 10.4467/2353737XCT.15.121.4158

* Department of Structural Mechanics, Cracow University of Technology, Poland.

1. Introduction

In new utility buildings, it is now common to use technology in which ventilation systems are assembled in the form of permeable wind curtains on the side walls of halls and buildings mainly destined for use as storehouses, warehouses, driers, cow-houses, pigsties and horse breaking-in houses. Such a solution assures a continuous air exchange inside the object; moreover, it protects against sun exposure, insects, and limits dust getting in from the outside. The curtains are made of plastic of different parameters. An example of such a type of curtain in a utility building is shown in Fig. 1.

Fig. 1. A utility building with openwork side walls

The most commonly used solutions incorporate a two-layer system. Each layer is rolled and unrolled independently (vertically or horizontally), the outside layer always being an impenetrable fabric of permeability not exceeding 5%. The inside layer is a basic layer of determined net mesh dimensions. The state when the outside layer is fully unrolled is practically a state corresponding to a building made of solid walls. Situations with only the second layer, made of a permeable net, are realised. In the exploitation practice, situations may arise when the curtains can be wholly uplifted and then both side facades remain fully opened. The curtains can be steered manually or automatically – that is to say that the curtain draws when a given wind velocity is exceeded. Possible situations realised in practice are shown in Fig. 2.

From the design point of view, the curtain's permeability in reference to the wind pressure inside the object is of the greatest importance [1, 2]. In the designing process, additional load states occur which can change the values of wind action on particular structural elements – these are connected with various configurations of wind curtains realised on the side walls.

The aim of the tests carried out in an aerodynamic tunnel was to determine the influence of different configurations of wind curtains assembled on the side walls, on the wind pressure distribution over the surfaces of the structure. In order to carry out tests in a tunnel, a model

of utility building was built – this was based on typical solutions adopted in rural areas. Mean wind pressure was measured on external and internal surfaces of roof slopes and on the gable wall of the building model; mean wind pressure coefficients were then determined. Two wind directions were taken into account, one perpendicular to the gable wall, and one perpendicular to the side wall. Four variants of side walls which reflect actual cases realised in the exploitation practice of objects of this type were considered.

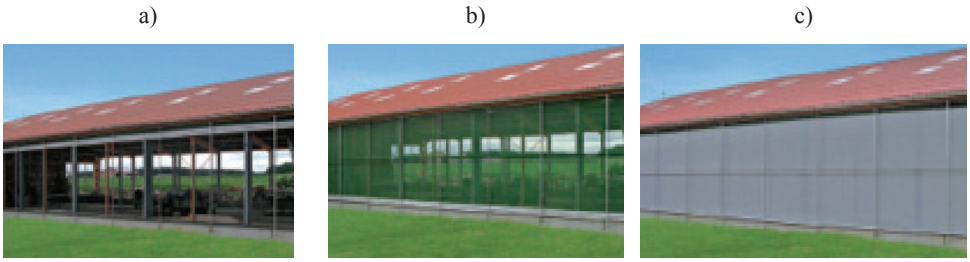

Fig. 2. A utility building with side air curtains: a) variant with uplifted curtains; b) variant with curtains permeable to wind; c) variant with curtains impermeable to wind

2. Description of the building model

The utility building model to be tested in an aerodynamic tunnel was made at a scale of 1:30 – this was dictated by the size of the measured space. The model consists of two longitudinal walls, two gable walls, two roof slopes and a base. The elements of the model were made of plywood. The roof is a symmetrical gable roof. Fig. 3 presents the scheme of the basic building elements.

Table 1 presents basic parameters of the building and the model

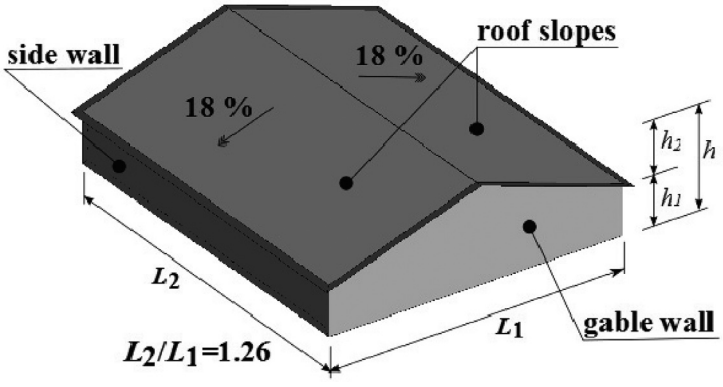

Fig. 3. Scheme of the utility building considered during wind tunnel tests

Table 1

Basic parameters of the building and the model

Parameter		Actual dimension [m]	Model dimension [mm]
Width	L_1	37.80	1260
Length	L_2	30.00	1000
Height at eaves	h_1	5.10	170
Height at roof ridge	h	10.20	340
Inclination angle of roof slope	α	18°	18°
Height of longitudinal walls plinth	-	0.50	20

The side walls of the model were built in four variants:

- variant I – the building had no side walls, the solidity ratio value φ = 0 was realised;
- variant II – side walls were made of a net of solidity ratio φ = 0.45;
- variant III – side walls were made of a net of solidity ratio φ = 0.6;
- variant IV side walls were made of plywood, thus a solidity ratio φ = 1.0 was realised.

Anti-wind curtain types applied in particular variants realised during model tests are shown in Fig. 4.

Features of nets applied during the tests on the producer's data are shown in table 2

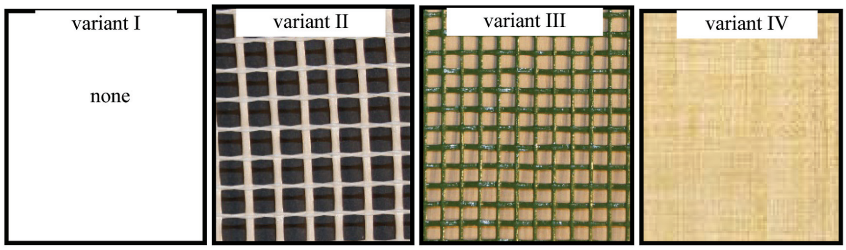

Fig. 4. Types of anti-wind curtains: a) none in variant I; b) a net with solidity ratio equal to 0.45 in variant II; c) a net with solidity ratio equal to 0.60 in variant III; d) impermeable to wind in variant IV

Table 2

Parameters of the anti-wind curtains

	Variant I	Variant II	Variant III	Variant IV
Designation	Open facade	WS-N 30.30	SG-S	Closed facade
Material	-	Polyester + PVC	Polyester + PVC	plywood
Mesh	-	10 mm x 10 mm	6 mm x 6 mm	-
Filling degree	φ = 0.00	φ = 0.45	φ = 0.60	φ = 1.00
Density	-	160 g/m^2	280 g/m^2	-

The applied nets are made of polyester combined with elastic PVC, as a result, the material has great mechanical strength and successfully takes over wind pressure. Furthermore, what is advantageous is that the nets are resistant to weather conditions such as snow, temperature and humidity. In model tests, the equality value of the solidity ratio of the side walls was accepted as the nets' aerodynamic similarity criterion, in the actual and the model scale.

3. Characterization of the wind tunnel tests

The tests were carried out in an aerodynamic tunnel with a boundary layer, making use of the building model at 1:30 scale. Two wind directions were considered: perpendicular to the gable wall, marked as 0°, perpendicular to the side wall of the structure, marked as 90° (see Fig. 5).

The building model in the test section of the wind tunnel together with a model configuration at two analysed wind directions is shown in Fig. 6.

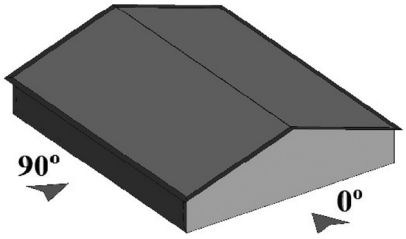

Fig. 5. The wind directions for which the wind pressure results were obtained

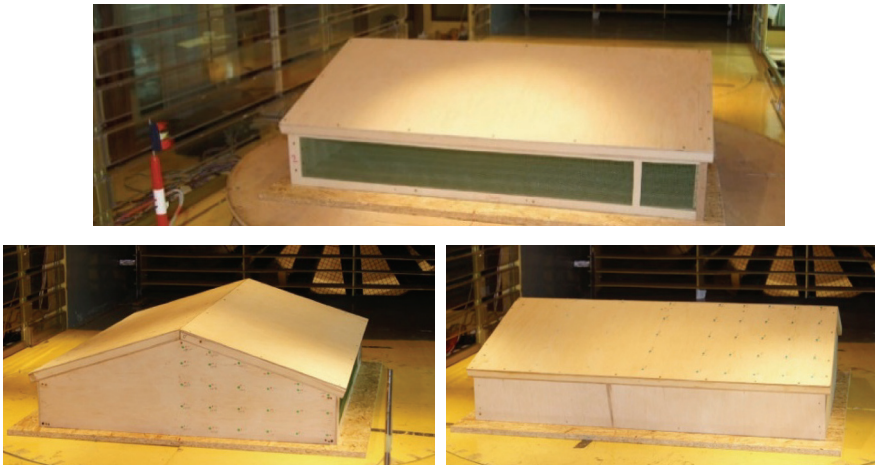

Fig. 6. The building model in the wind tunnel working section and the two analysed configurations of the wind direction during tests

The analysed model has two vertical symmetry planes; therefore, making use of this fact, detecting wind pressure taps were placed on the half of one gable wall and the half of one roof slope, as shown in Fig. 7.

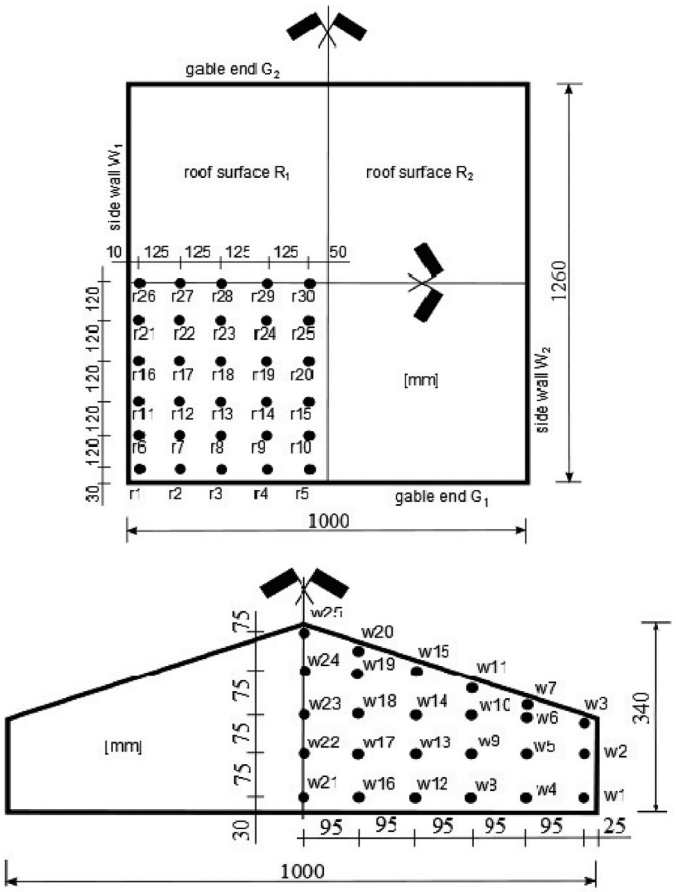

Fig. 7. Distributions of pressure taps on the gable wall and the roof slope

The distribution of pressure taps presented in Fig. 7 was the same on the internal and the external surface of the gable wall and the roof slope. On the roof slope, 30 points were assembled on the outside surface and 30 points on the internal surface in a regular manner. In the case of the gamble wall, there were 25 points on each side (external and internal). Making use of the system double symmetry and carrying out the tests at four wind directions (A, B, C, D), illustrated in Fig.8 allowed determining the wind pressure distribution coefficient over the whole area of the gable walls and over the roof slopes for two analysed wind directions dir = 0° i dir = 90° (see Fig. 5).

For each wind direction, the measurements were taken in four variants of side wall solidity ratio (see Fig. 9).

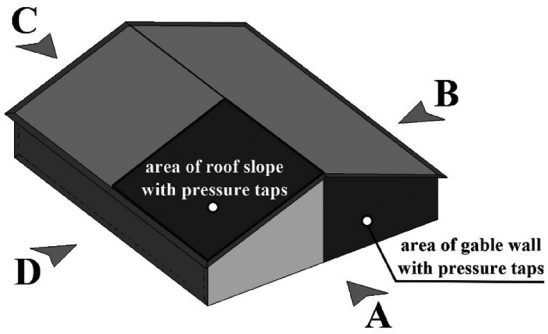

Fig. 8. The wind directions considered during wind tunnel tests

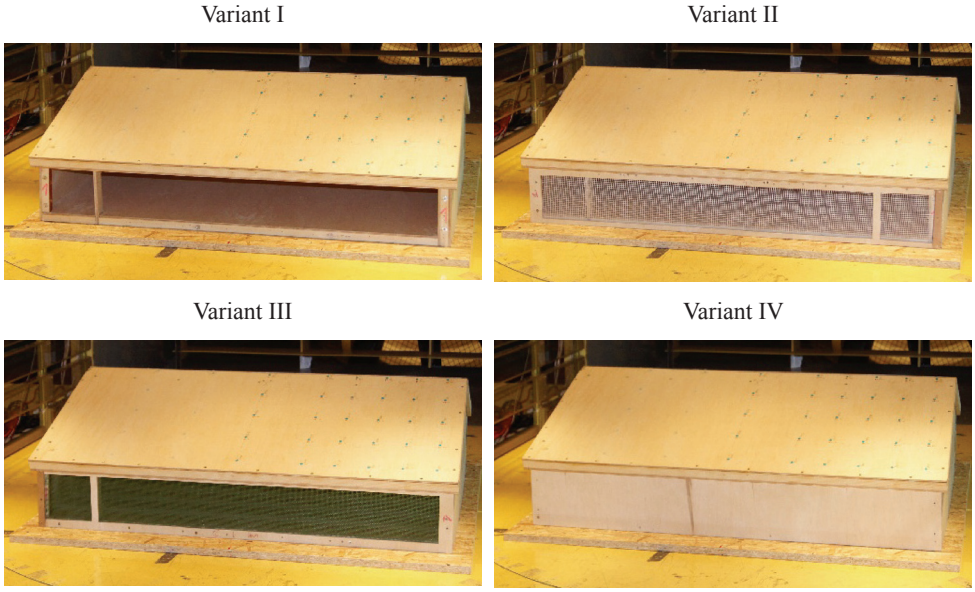

Fig. 9. Model of the utility building in the four variants of the side wall configuration in the wind tunnel working section

The experiments were performed with the following conditions: the mean wind velocity profile was constant; area-averaged turbulence intensity at the level of the building roof ridge was $I_v = 25\%$; the reference velocity at the height level of the roof model was $V_{ref} = 13.0$ m/s. The basic geometric dimensions of the working section of the tunnel were: width – 2.20 m; height – from 1.40 m at the beginning to 1.60 m at the end of the working section; length – 10 m. Formation of the mean wind velocity profile and atmospheric turbulence takes place in the first part of the working section at a length of 6 m by use of respective tubulisation networks, barriers, spires and blocks of respective geometry and a mechanically controlled height. Four characteristic segments each of 2.5 m long can be distinguished in the working

section. The side walls of the front segment are full (with windows) 2.20 m apart. The other segments have slotted side walls (with horizontal controlled slots aiming at diminution of the so called blockage effect) 2.20 m apart and full side walls with windows 3.40 m apart. In the third and fourth segment of the working section, there are two circular turntables 2 m in diameter, rotational by up to 180°. The first turntable is designed mainly for examination of the flow around phenomena, their visualization and for examination of wind environment climate. The other turntable is designed mainly for aerodynamic and aeroelastic investigations of buildings and structures. In the upper part of the working section, there is equipment for fixing all kinds of measurement probes and their controlled displacement for the whole working section in directions x, y, z. The roof of the working section may change its height; this permits control of the gradient of static pressure in the working section. Views from the side (a) and from the top (b) of the wind tunnel are presented in Fig. 10. All of the wind tunnel properties are optimized due to size of the model, its scale, external shape, roughness of the terrain – these properties are: configuration of adjustable ceiling; ejection of floor blocks; RPM of the fan; type of circulation; settings of barrier and spires. A profile pressure probe, a pressure electronic scanner – which allows measuring differential pressure in 64 taps simultaneously – and a hot-wire anemometer system were used during the experiments.

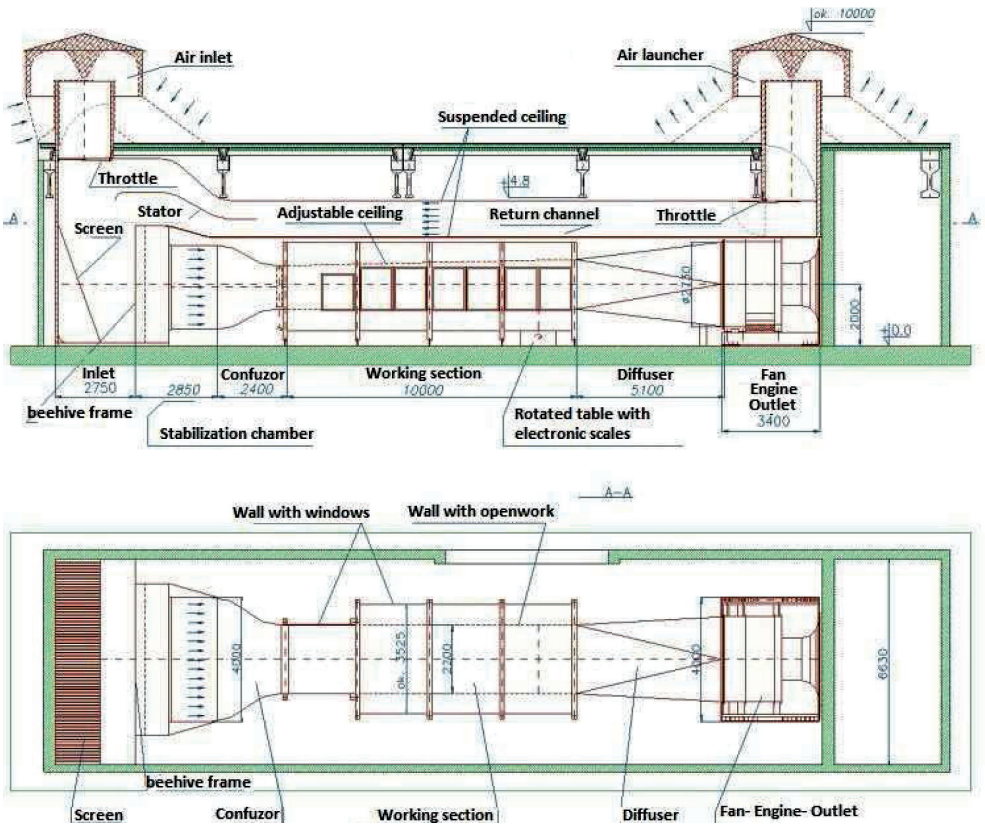

Fig. 10. Views from the side and from the top of the wind tunnel

4. Results of the wind tunnel tests

Wind pressure was measured on the external and internal surfaces of the roof slopes and the gable wall of the building model. Having determined the mean wind pressure value and having measured the reference pressure at the height of the roof edge of the building model, the values of wind pressure coefficients were calculated according to formulas 1 and 2:

$$C_{pe}(x,y,z,\mathrm{dir}) = \frac{p_e(x,y,z,\mathrm{dir})}{q_{ref}} \;\; ; \;\; C_{pi}(x,y,z,\mathrm{dir}) = \frac{p_i(x,y,z,\mathrm{dir})}{q_{\mathrm{ref}}} \tag{1}$$

$$C_{p,net}(x,y,z,\mathrm{dir}) = C_{pe}(x,y,z,\mathrm{dir}) - C_{pi}(x,y,z,\mathrm{dir}) \tag{2}$$

where: $p_e(x,y,z,\mathrm{dir})$ – wind pressure on the external surfaces of the building model; $p_i(x,y,z,\mathrm{dir})$ – wind pressure on the internal surfaces of the building model; $C_{pe}(x,y,z,\mathrm{dir})$ – the coefficient of the external wind pressure; $C_{pe}(x,y,z,\mathrm{dir})$ – the coefficient of the internal wind pressure; $C_{p,net}(x,y,z,\mathrm{dir})$ – the coefficient of the net wind pressure; dir – the wind direction (0° or 90°); x, y, z – coordinates in the global system; q_{ref} – the reference pressure on the level at the height of the top level of the model roof.

The manner of marking wind pressure values on the internal and external surfaces and differential pressure was assumed according to [2] and shown in Fig.11:

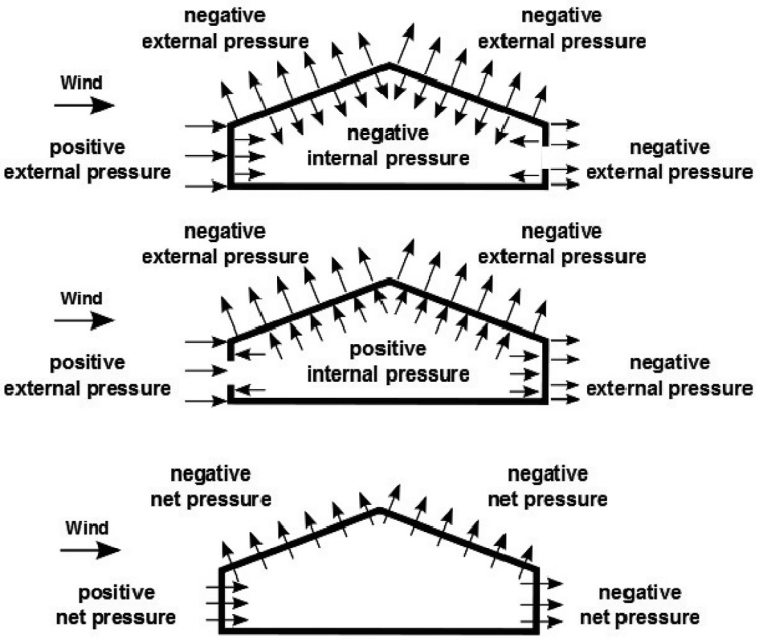

Fig. 11. Wind pressure on the building surfaces [2]

In the article, the results of measurements are presented for two wind directions in accordance with Fig. 12. In the figure, there are also names of the walls and roof slopes for which wind pressure distributions in particular cases were analysed.

Figures 13, 15 and 17 present the maps of wind pressure coefficients distributions on external C_{pe} and internal C_{pi} surfaces respectively and differential pressure $C_{p,net}$ at wind directions 0° and 90° for four analysed variants of side wall construction (I, II, III, IV).

Tables 3, 4, 5, placed below the figures, contain minimum and maximum values of the aerodynamic coefficients of wind pressure on particular surfaces of the model in the discussed measurement situations.

Figures 14, 16 and 18 present comparison of the measured wind pressure coefficient values with the values of coefficients determined on the basis of EN 1991-1-4 Eurocode 1: Actions on structures – Part 1-4: general actions – wind actions [4]. In the figures, the maximum values of measurements are marked with square markers while the minimum values with triangle markers. For reasons of comparison, coefficients provided in the standard were made use of in the following cases:

- vertical walls of rectangular plan buildings – Figure 7.5 and Table 7.1,
- duo pitch roofs – Figure 7.8, Table 7.4a and Table 7.4b,
- canopy roofs – Table 7.7,
- free-standing walls – Table 7.9,
- chapter 7.2.9 – internal pressure.

Maximum values determined on the basis of the standard are marked with a solid line. Minimum values determined on the basis of the standard are marked with a broken line. In some measurement situations determining, on the standard basis, of the maximum or minimum values was impossible because of the lack of data. In such cases, there are no adequate extreme lines referring to standard values. It has to be stressed that the accomplished comparison is approximate because standard situations in many cases do not fully reflect the conditions in the measurement configurations realized in an aerodynamic tunnel. Comparative analyses were carried out using the standard coefficients of external pressure $C_{pe,1}$.

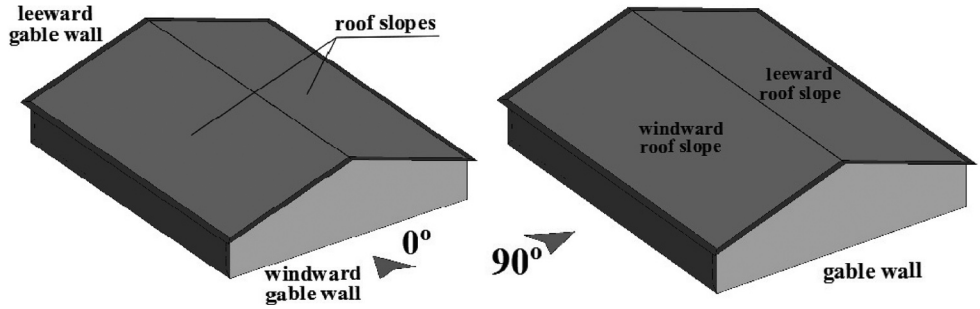

Fig. 12. The building surfaces for the analysed wind directions

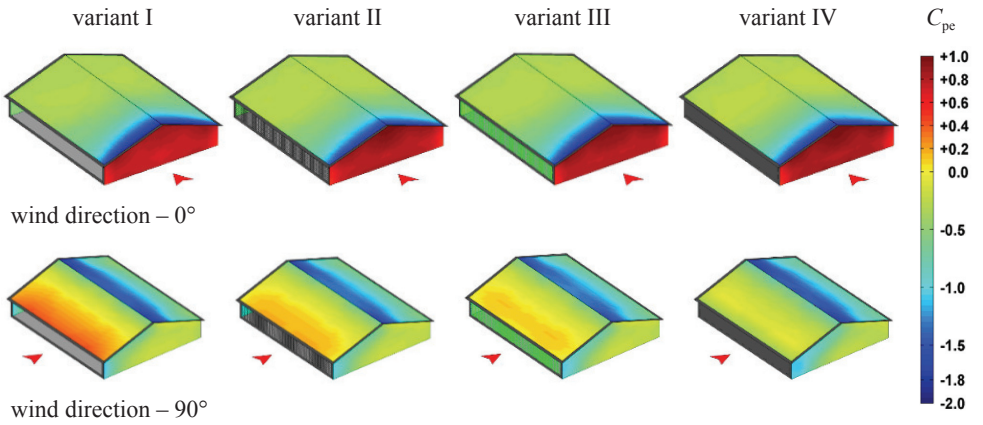

Fig. 13. Distributions of the wind pressure coefficient C_{pe} over external surfaces

Table 3

Extreme values of the wind pressure coefficient C_{pe} over external surfaces – wind tunnel tests results

the wind pressure coefficient C_{pe}									
variant →		I		II		III		IV	
wind direction	surface ↓	max	min	max	min	max	min	max	min
0°	windward gable wall	0.9	0.4	1.0	0.4	1.0	0.4	1.0	0.4
	leeward gable wall	-0.4	-0.6	-0.4	-0.5	-0.4	-0.5	-0.4	-0.5
	roof slopes	-0.3	-1.9	-0.3	-1.7	-0.3	-1.8	-0.3	-1.8
90°	windward roof slope	0.4	-0.7	0.2	-0.7	0.1	-0.7	-0.1	-0.9
	leeward roof slope	-0.4	-1.8	-0.5	-1.7	-0.5	-1.6	-0.6	-1.8
	gable walls	0.0	-1.2	0.0	-1.1	-0.1	-1.1	-0.1	-1.1

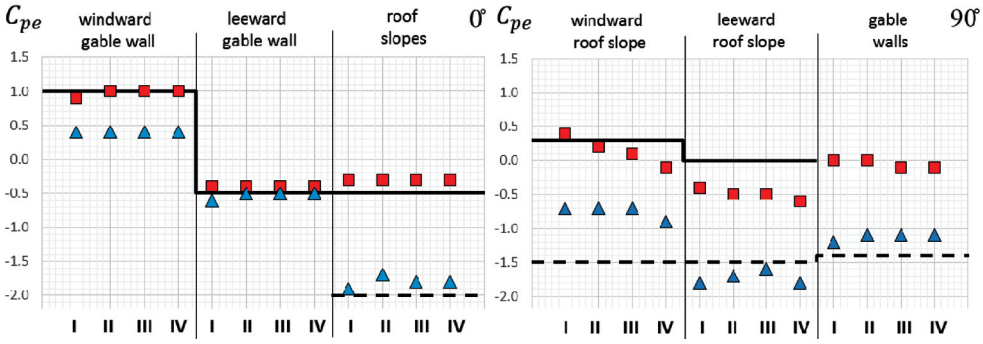

Fig. 14. Distributions of the wind pressure coefficient C_{pe} over external surfaces in comparison to the values obtained from the standard [4]

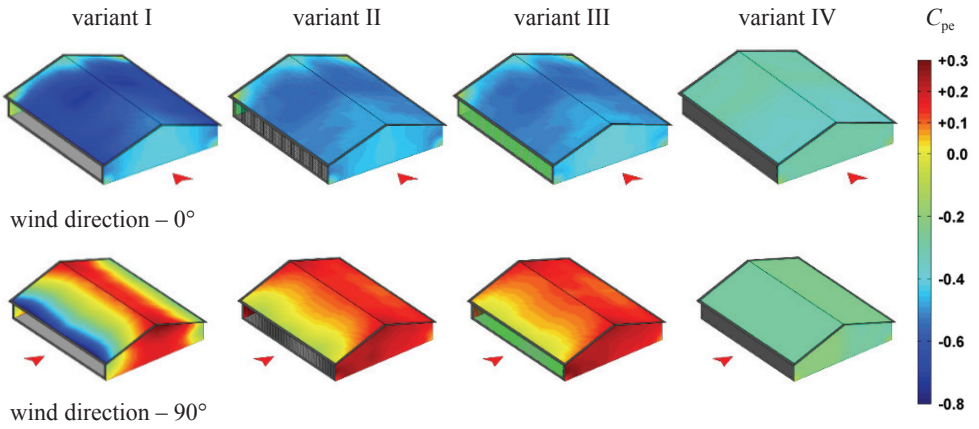

Fig. 15. Distributions of the wind pressure coefficient C_{pi} over internal surfaces

Table 4

Extreme values of the wind pressure coefficient C_{pi} over internal surfaces – wind tunnel test results

the wind pressure coefficient C_{pi}									
variant →		I		II		III		IV	
wind direction	surface ↓	max	min	max	min	max	min	max	min
0°	windward gable wall	-0.1	-0.5	-0.1	-0.5	-0.1	-0.5	-0.1	-0.3
	leeward gable wall	0.0	-0.4	0.0	-0.4	0.0	-0.4	-0.1	-0.3
	roof slopes	0.1	-0.7	0.1	-0.6	0.0	-0.6	-0.3	-0.4
90°	windward roof slope	0.2	-0.8	0.2	-0.2	0.2	-0.1	-0.3	-0.3
	leeward roof slope	0.2	-0.3	0.2	0.1	0.3	0.1	-0.2	-0.3
	gable walls	0.3	-0.3	0.3	0.0	0.3	0.0	0.0	-0.3

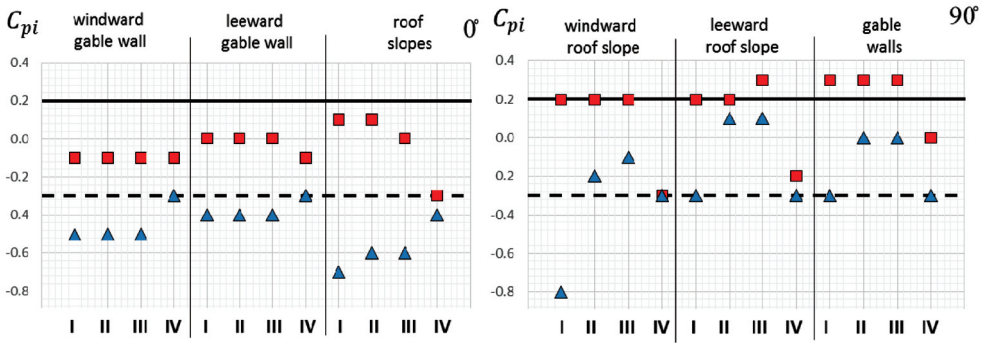

Fig. 16. Distributions of the wind pressure coefficient C_{pi} over internal surfaces in comparison to the values obtained from the standard [4]

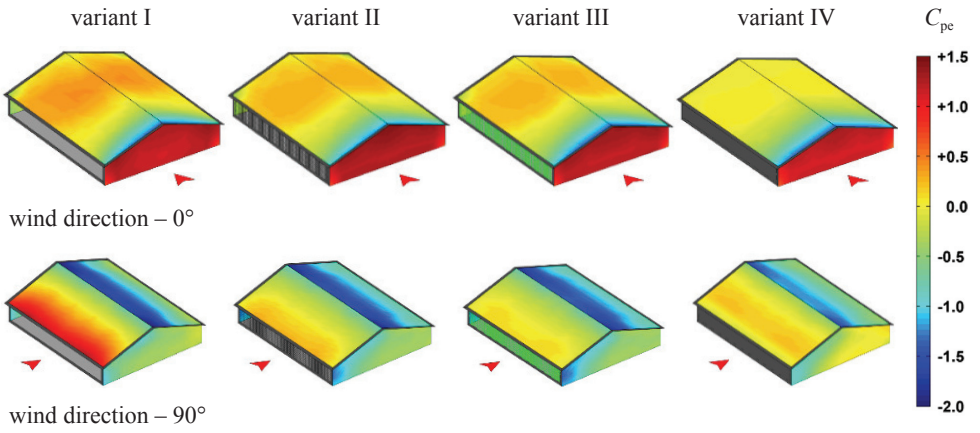

Fig. 17. Distributions of the differential wind pressure coefficient $C_{p,net}$

Table 5

Extreme values of the wind pressure coefficient $C_{p,net}$ – wind tunnel tests results

the wind pressure coefficient $C_{p,net}$									
variant →		I		II		III		IV	
wind direction	surface ↓	max	min	max	min	max	min	max	min
0°	windward gable wall	1.4	0.5	1.4	0.5	1.4	0.5	1.3	0.4
	leeward gable wall	-0.1	-0.5	-0.1	-0.4	0.0	-0.5	-0.1	-0.4
	roof slopes	0.4	-1.4	0.3	-1.2	0.3	-1.4	0.1	-1.4
90°	windward roof slope	1.1	-0.9	0.3	-0.9	0.1	-0.8	0.2	-0.6
	leeward roof slope	-0.2	-2.0	-0.7	-1.9	-0.7	-1.8	-0.4	-1.5
	gable walls	-0.1	-1.1	-0.3	-1.4	-0.3	-1.4	0.2	-1.0

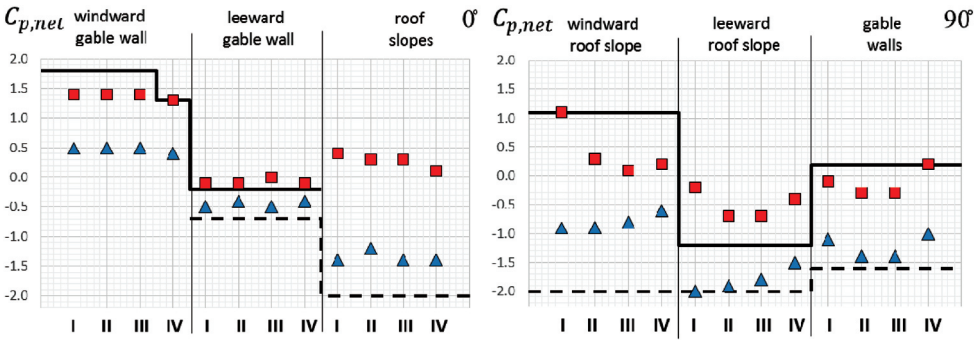

Fig. 18. Distributions of the differential wind pressure coefficient $C_{p,net}$ in comparison to the values obtained from the standard [4]

The following regularities can be stated from the performed measurement analysis and comparison:

- with reference to wind pressure distributions over external surfaces:
  - for wind direction perpendicular to the gable wall, pressure distribution over the analysed surfaces only slightly depends on the variant of the side wall solidity ratio; distributions measured in an aerodynamic tunnel are practically identical to those obtained from the standard for a closed building;
  - for wind direction perpendicular to the side wall, variation of the wind pressure, depending on the analysed configuration variant of the side wall, can be observed mainly for the positive pressure over the windward slope; the change refers to the lower windward slope and consists of a gradual decrease of pressure together with an increase of side wall solidity ratio coefficient – the values of negative wind pressure on particular external building surfaces only slightly depend on the discussed configuration variant of the side wall.
- with reference to wind pressure distributions over internal surfaces:
  - for wind direction perpendicular to the gable wall, the pressure distribution over the analysed surfaces in variants I to III shows inconsiderable variation – in variant IV (a closed building), the distribution measured in the aerodynamic tunnel is almost a constant value of the inner pressure at a coefficient level -0.3. In variants I – III, the value of inner partial pressure was measured at a level between -0.4 to -0.6 over particular surfaces. Over the roof slopes from the leeward direction, inner pressure coefficient values may reach -0.8 – this is an unfavourable effect, causing roof slope loading;
  - for wind direction perpendicular to the side wall, the character of the inner pressure coefficient distribution in variants I – III is quite different from the variant IV when the structure is closed. In variant IV, the value of inner partial pressure is practically the same as in the case of the direction perpendicular to the gable wall – the distribution is constant and described by a pressure coefficient value of -0.3. A very large variability of the internal pressure coefficient is observed on the windward slope, where its value changes from -0.8 at the eaves area to +0.2 at the roof edge area. In the case of assembling nets on the side walls (variant II and III), the character of pressure distribution changes on the windward slope remains unchanged, while at the same time, a significant reduction of negative pressure occurs at the eaves area up to a pressure coefficient value of -0.2. A characteristic feature of internal pressure distributions over the gable walls and the leeward slope is the occurrence of uniform positive pressure described by a coefficient value of +0.2.
- with reference to differential wind pressure distributions:
  - for wind direction perpendicular to the gable wall, the character of differential pressure coefficient in variants I – IV is similar, while the biggest loading of the roof slopes occurs in the area of leeward direction in variant I;
  - for wind direction perpendicular to the side wall, the character of differential pressure coefficient is similar to the external pressure coefficient distribution. Differential pressure distributions in the case of nets applied (variant II and III) are of a transitional character between pressure distributions typical of the open and closed building.

5. General conclusions

The results of the measurements which were carried out in the wind tunnel allow the formulation of the following general conclusions:

- the tests showed that using permeable wind nets on the utility building side walls does not cause load states more unfavourable than those resulting from the open building configuration and the closed building configuration. Net usage causes a transitional state between one configuration and the other;
- applying the current standard [4] in the case of an open building (canopy roof) and a closed building allows the estimation of wind actions on particular roof slopes and gable wall surfaces as envelope actions for cases where nets are applied on the side walls.

References

[1] Żurański J.A., *Obciążenia wiatrem budowli i konstrukcji*, Arkady, Warszawa 1978
[2] Koloušek V., Pirner M., Fischer O., Náprstek J., *Wind effects on civil engineering structures*, ACADEMIA/PRAHA, Praga 1983
[3] Cook N.J., *The designer's guide to wind loading of building structures*, Part II. Static Structures, Building Research Establishment, Butterworths, London 1990
[4] EN 1991-1-4: Actions on structures. Part 1-4: General actions- Wind actions

TECHNICAL TRANSACTIONS | CZASOPISMO TECHNICZNE
CIVIL ENGINEERING | BUDOWNICTWO
2-B/2015

GRZEGORZ BOSAK*, ANDRZEJ FLAGA*

ANALYSIS OF AERODYNAMIC INTERFERENCE BETWEEN A HIGH-RISE BUILDING AND ITS IMMEDIATE CITY SURROUNDINGS

ANALIZA INTERFERENCJI AERODYNAMICZNEJ POMIĘDZY BUDYNKIEM WYSOKIM A JEGO NAJBLIŻSZYM OTOCZENIEM

Abstract

This paper summarizes results of wind tunnel tests of a high-rise building placed in Warsaw city centre. Aerodynamic laboratory studies were accomplished in a boundary layer wind tunnel. The main objective of the research was to determine the distribution of the mean wind pressure coefficient over the building's external surfaces as affected by the aerodynamic interference between the structure and its immediate city surroundings. Interference coefficients of wind pressure and global wind forces acting upon the surfaces of the building walls and roof were calculated. The aerodynamic studies showed a significant influence of objects located nearby on the wind load that the high-rise building structure surfaces are subjected to.

Keywords: wind tunnel tests, aerodynamic interference, wind action on a building surfaces

Streszczenie

W artykule przedstawiono rezultaty badań modelowych w tunelu aerodynamicznym budynku wysokościowego położonego w centrum Warszawy. Badania zostały wykonane w tunelu aerodynamicznym z warstwą przyścienną. Podstawowym celem analiz było określenie rozkładu wartości współczynnika średniego ciśnienia wiatru na powierzchniach zewnętrznych budynku w warunkach występowania interferencji aerodynamicznej pomiędzy analizowaną konstrukcją a jej najbliższym miejskim otoczeniem. Wyznaczono współczynniki interferencji odnoszące się do ciśnienia wiatru oraz do sumarycznych sił działania wiatru na powierzchnie ścian i dachu budynku. Badania wykazały znaczący wpływ obiektów sąsiadujących na działanie wiatru na konstrukcję budynku wysokiego.

Słowa kluczowe: badania modelowe w tunelu aerodynamicznym, interferencja aerodynamiczna, działanie wiatru na powierzchnie budynku

DOI: 10.4467/2353737XCT.15.122.4159

* Department of Structural Mechanics, Cracow University of Technology, Poland.

1. Introduction

A high-rise building, the Echo Tower building, the height of which is equal to 155 m, is located in the center of Warsaw in the quarter bordered by Jan Paweł II Avenue, Grzybowska Street and Twarda Street. The distances between the buildings in the immediate surroundings of the Echo Tower building are very small. Along Grzybowska Street and on both sides of Jana Pawła II Avenue, there are 40 m high buildings. The Westin Hotel building, the TP SA Tower and the PZU SA building are all over 100 m tall – these predominate over the immediate surroundings. Additionally, during the wind tunnel tests, two high-rise buildings which are planned to be constructed nearby were taken into consideration. The Gmina Żydowska building is a structure of 170 m in height and will be located at a distance of 220 m from the analyzed building. The height of the Cosmopolitan Tower, the second planned building, is equal to 160 m and is going to be located a similar distance from the analyzed structure as the first planned building. Computer generated images of the Echo Tower building with its immediate surroundings are presented in Fig. 1.

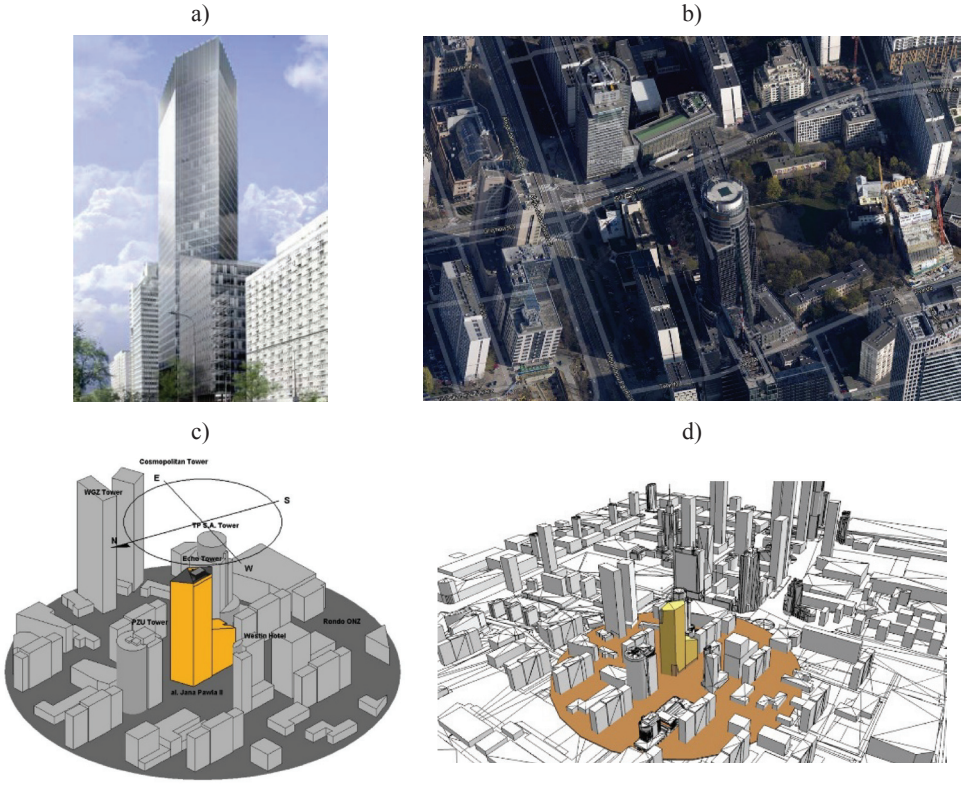

Fig. 1. Computer generated images: a) of the Echo Tower building; b) of the quarter limited by Jan Paweł II Avenue; Grzybowska Street and Twarda Street in Warsaw; c) of the interference configuration analysed during wind tunnel tests, d) of the immediate surroundings of the building on the architectural plan of Warsaw city centre

The subject of this article is to evaluate the influence of aerodynamic interference on the wind action on the building structure. The following circumstances are the reasons for the aerodynamic modelling of the building structure in a wind tunnel. Firstly, the shape of the building is non-standard and very complicated (see Fig. 1a). The building consists of two parts. The lower part, a podium, has a rectangular cross-section and consists of 17 levels. The second part of the building, the tower, has an irregular shape that various along the height a cross-section, narrowing towards the top of the building. The total height of the building is 155 m. The outer surface of the structure consists of 32 planes connected at corners and forming pointed edges. Secondly, the building is located in Warsaw city center where we can expect significant interference influences coming from the immediate surroundings. Even though the majority of buildings in the immediate surroundings have a height of about 40 m, there are 5 structures with a height of over 100 m. In addition, the distances between the highest buildings are very small, from 80 m to 220 m. All the above mentioned reasons motivated an aerodynamic wind tunnel investigation of the building model.

2. Characteristics of the wind tunnel tests

The wind tunnel tests were conducted, using a 1:250 scale model, in the wind tunnel of the wind engineering laboratory of Cracow University of Technology [1]. The building and its immediately surrounding area within a radius of 250 m were modelled.

a) b)

Fig. 2. Measuring configurations: a) a non-interference configuration; b) an interference configuration

The building model and the other model objects in the immediate surroundings were placed on a 200 cm diameter turn-table – this allowed for the simulation of any wind direction in the working section. The measurements were taken for 40 wind directions with increments of 10° each and additionally, for the four characteristic wind direction (45°, 135°, 225°, 315°). The model was instrumented with 219 pressure taps which allowed introducing the pressure taps

into all characteristic areas of the external building model surfaces with sufficient density. The mean wind pressure and the standard deviation of wind pressure fluctuations were measured at each tap. On the basis of the measured data, mean pressure coefficients were calculated based on the measured mean dynamic pressure of wind at a height equivalent to 150 m above the ground for the real construction. Two different measurement configurations were examined. In the first configuration, only the building model was placed in the tunnel working section; in the second configuration, the building model with the immediate surroundings was taken into consideration. The views of the tested model in the two different measurement configurations in the wind tunnel are presented in Fig. 2.

The experiments were performed for the following conditions: power law exponent of mean wind velocity profile $\alpha = 0.35$; area-averaged turbulence intensity $I_v = 12\%$ on the reference level (0.6 m in model scale equivalent to 150 m in full scale); reference velocity at a height level to the building roof model $V_{ref} = 15.6$ m/s. All of the wind tunnel properties such as the configuration of an adjustable ceiling, the ejection of floor blocks, the RPM of the fan, the type of circulation, the settings of barrier and spires was optimised due to the model size, its scale, external shape, and roughness of the terrain. The mean wind velocity profile obtained in the wind tunnel working section during the experiments is presented in Fig. 3.

A turbulence intensity profile obtained in the wind tunnel tests is given in Fig. 4.

A profile pressure probe, a pressure electronic scanner, which allows measuring wind pressure in 64 taps simultaneously, and a hot–wire anemometer system were used during the experiments.

A flow chart of the measuring system of wind pressure on the wall and roof surfaces of the building is presented in Fig. 5.

The comparison of the results, namely the values of the wind pressure coefficients and the components of the global wind forces acting on the building structure, was accomplished on the basis of the test results for the two analysed configurations.

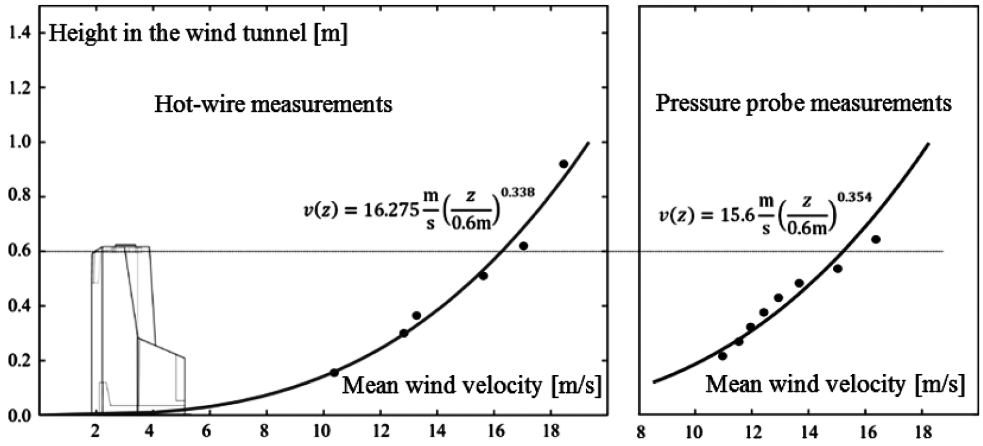

Fig. 3. Mean wind velocity profile obtained in the wind tunnel working section (the horizontal line marks the reference level)

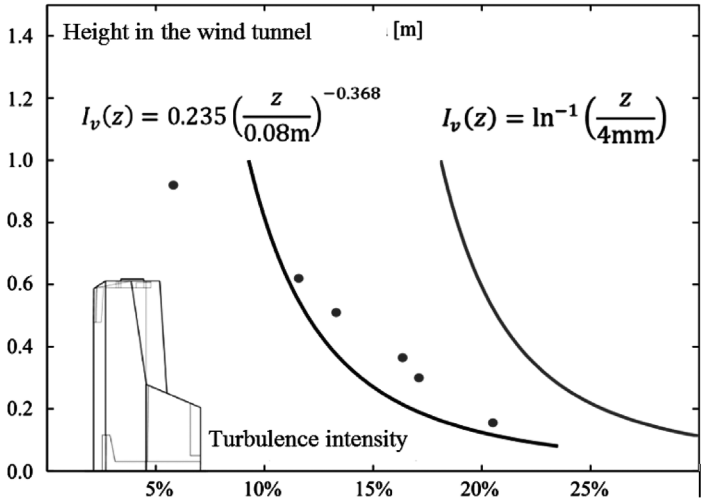

Fig. 4. Turbulence intensity profile obtained in the wind tunnel tests (the left curve) in comparison to the theoretical profile according to [3] (the right curve)

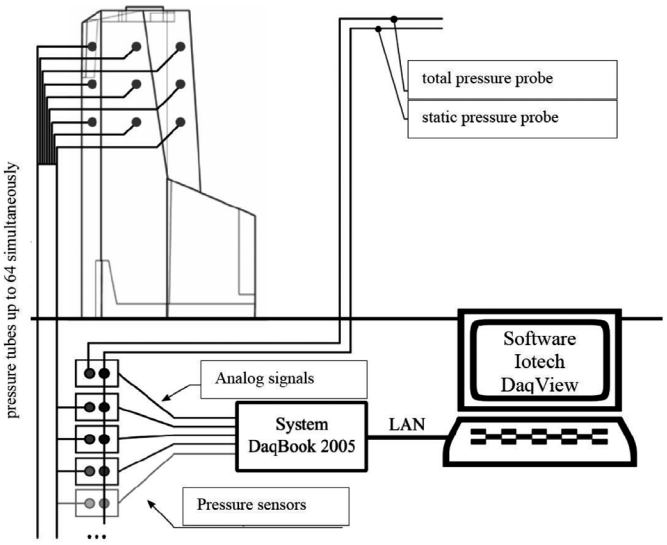

Fig. 5. Flow chart of the measuring system of differential wind pressure on the roof surface

3. Results of the wind tunnel tests

Firstly, the values of the C_{pe} coefficient were determined in the non-interference and the interference configurations according to the formula:

$$C_{pe}\left(x,y,z,\mathrm{dir}\right)=\frac{p_e\left(x,y,z,\mathrm{dir}\right)}{q_{\mathrm{ref}}\left(z_{\mathrm{ref}}\right)} \tag{1}$$

The reference level was at the height of the top level of the building model roof (equivalent to 150 m above the ground at full scale). Positive values of wind pressure act on the external surfaces in line with the inner unit vector perpendicular to the surface. Below, in Fig. 6, exemplary distributions of the C_{pe} coefficient in the non-interference and interference configuration for the chosen wind directions (30°, 70°) are presented. For these two wind directions, the largest changes of wind pressure distributions on the building surfaces are observed.

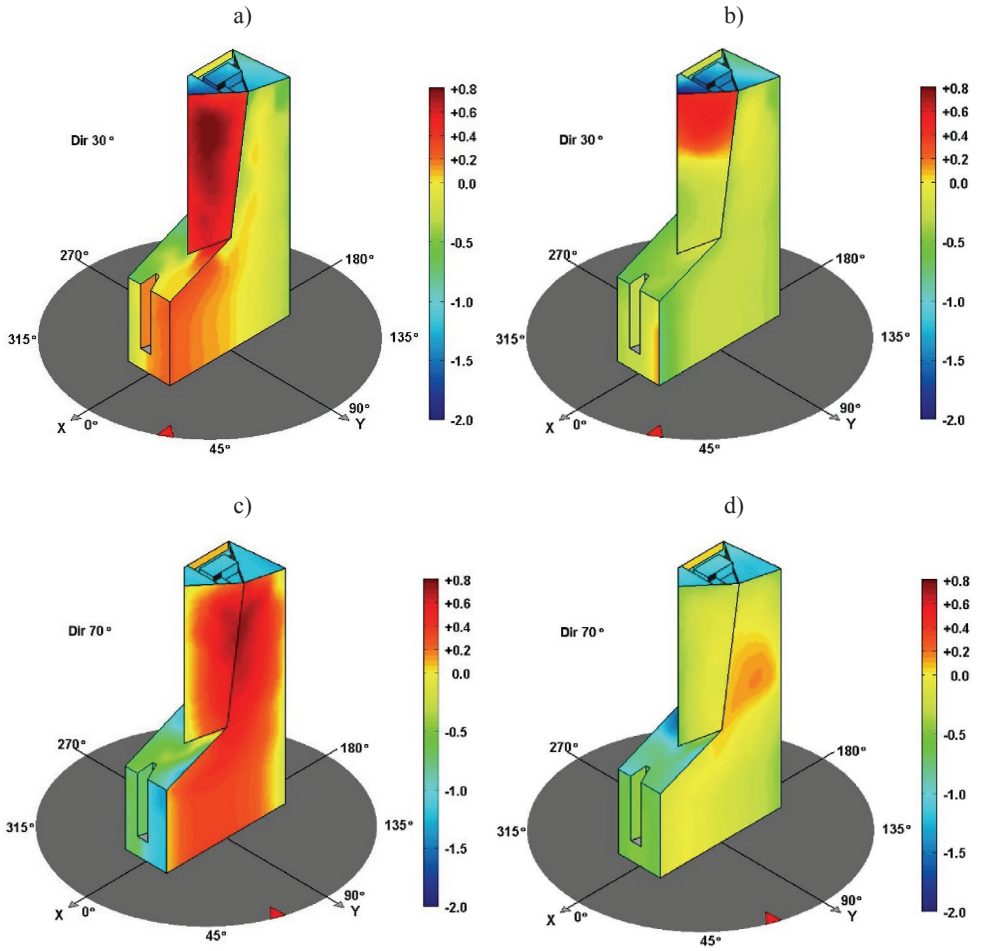

Fig. 6. Distributions of C_{pe} coefficient in the non-interference (a, c cases) and in the interference configurations (b, d cases) respectively for the 30° and 70° wind directions (red arrows indicate wind direction)

The values of the wind pressure coefficients are between +0.8 (positive pressure) and -2.0 (negative pressure [suction]) for both analysed configurations. It is observed that the leeward regions the lower sections of the building were sheltered by the neighbouring structures. This caused an aerodynamic effect which consisted of changing the positive wind pressure over these areas into negative values. At the same time, a negative aerodynamic effect was observed connected with the occurrence of an increase in the negative pressure values mainly over the areas at the edges of the building surfaces. The most significant factor relating to wind pressure distributions over the building surfaces was the existence of the highest structures located nearby. In cases where the building was in the leeward area behind the highest structures, which was the case for the 70°–80° wind directions, the pressure distribution changes occurred not only over the lower parts of the building but also over the rest of the building surfaces including the roof planes. An increase in the positive wind pressure on the building surfaces was not observed.

The significance of the aerodynamic interference for the changing of the wind pressure on the surfaces of the building was determined by the interference coefficient [2] obtained according to the formula:

$$I_c^p\left(x,y,z,\text{dir},\text{type},\text{area}\right)=\frac{\left|\left[C_{p,net}^{I}\left(x,y,z,\text{dir}\right)-C_{p,net}^{S}\left(x,y,z,\text{dir}\right)\right]_{\text{type}}\right|}{\max\left|C_{p,net}^{S}\left(x,y,z,\text{dir}\right)\right|_{\text{area}}} \tag{2}$$

where: dir – wind direction, *x,y,z* – point coordinates, *I* – interference configuration, *S* – non-interference configuration, type – the type of wind pressure variation on the surfaces according to Tab. 1., area – the wall or the roof area of the building.

Table 1

Types of wind pressure coefficients changing on the building surfaces

Type	Change type	Colour mark	$C^I_p(x,y,z,\text{dir})$	$C^S_p(x,y,z,\text{dir})$	$C^I_p(x,y,z,\text{dir}) - C^S_p(x,y,z,\text{dir})$
6	pos ↑		$C^I_p > 0$	$C^S_p \geq 0$	$C^I_p - C^S_p > 0$
5	pos ↓		$C^I_p \geq 0$	$C^S_p \geq 0$	$C^I_p - C^S_p \leq 0$
4	neg ↑ pos		$C^I_p \geq 0$	$C^S_p < 0$	$C^I_p - C^S_p > 0$
3	pos ↓ neg		$C^I_p \leq 0$	$C^S_p > 0$	$C^I_p - C^S_p < 0$
2	neg ↑		$C^I_p \leq 0$	$C^S_p < 0$	$C^I_p - C^S_p \geq 0$
1	neg ↓		$C^I_p < 0$	$C^S_p \leq 0$	$C^I_p - C^S_p < 0$

The most significant influence of the aerodynamic interference between the building and the objects in the immediate surroundings was observed for the wind directions of: 30°, 70°–80°, 280° and 340°. The situations for the 30°, 70° wind directions are presented in Fig. 7, where the building was sheltered by the highest structures located nearby (the building was located on the leeward side of the highest surrounding structures).

According to the wind tunnel tests, the largest influence of the aerodynamic interference connected with the existence of the neighbouring buildings, was observed for lower sections of

the building walls situated near the neighbouring structure. Mostly, the effect of aerodynamic interference consisted of sheltering these regions which resulted in the changing of positive pressure values to negative pressure (see Fig. 7).

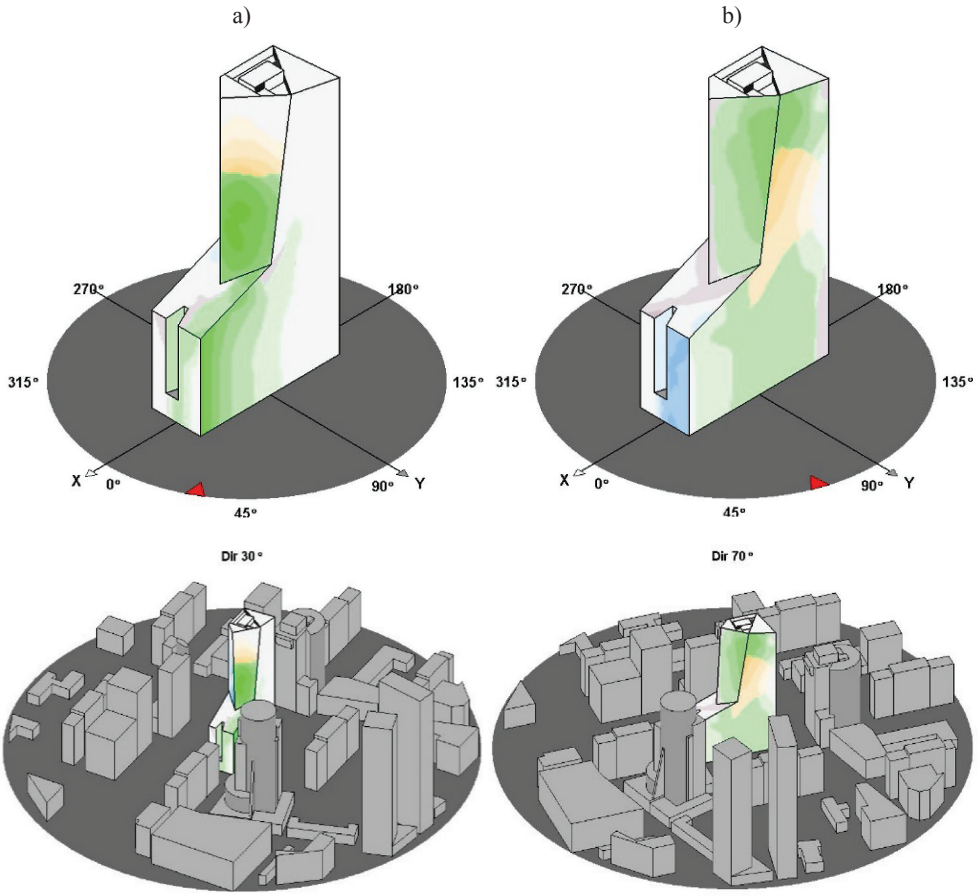

Fig. 7. Distribution of coefficient: a) for the 30° wind direction, b) for the 70° wind direction

At full scale, the global aerodynamic forces, F_k, for the building were separately calculated by using distributions of the C_{pe} coefficient obtained from the measurements according to the formula:

$$F_k(\mathrm{dir}) = q_p(z_{\mathrm{ref}}) \cdot \sum_{p=1}^{32} \sum_{A_p} C_{pe}(x, y, z, \mathrm{dir}) \cdot \Delta A_p(x, y, z) \cdot n_k(p) \tag{3}$$

where: dir – wind direction, $q_p(z_{\mathrm{ref}})$ – peak velocity pressure according to [3], k – coordinates x, y, z, p – the wall or the roof plane region (total number of planes was equal to 32), A_p – the

area of the particular plane region, ΔA – a part of the area of the wall or the roof surface, n_k – a coordinate of the unit vector, perpendicular to the surface,

The force components F_x, F_y of the horizontal global wind action acting on the building (at full scale) in the interference configuration (line with square markers) in comparison to the results obtained in the non-interference configuration (dashed line) is presented in Fig. 8. A coordinate system of the global aerodynamic forces for the building is also given in Fig. 8.

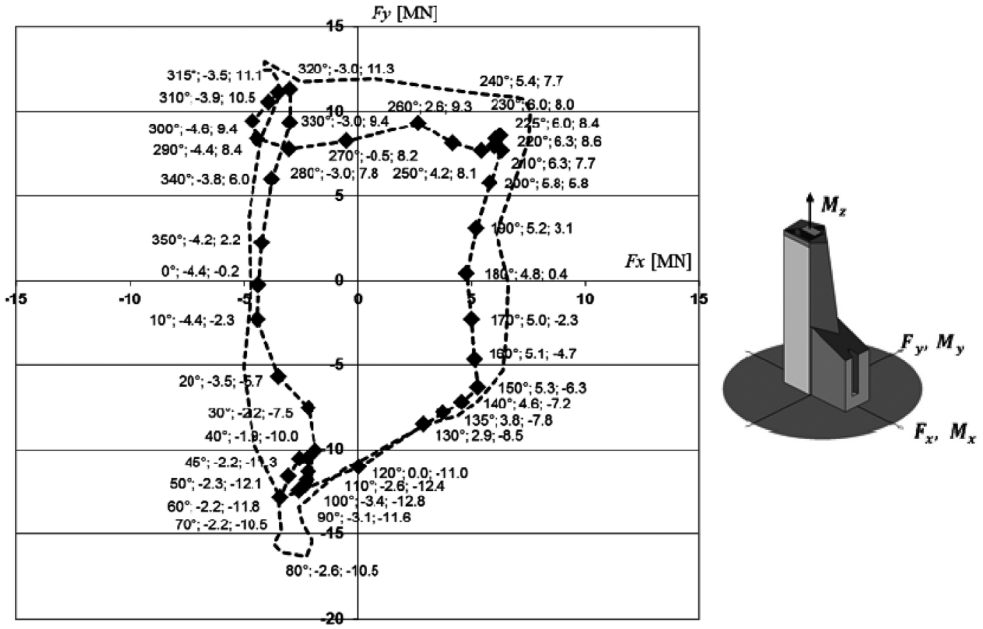

Fig. 8. The force components F_x, F_y of the horizontal global wind acting on the building (in full scale) in the interference configuration (line with square markers) in comparison to the results obtained in the non-interference configuration (dashed line)

A global force interference coefficient was assumed:

$$I_c^F(\mathrm{dir}) = \frac{F_H^I(\mathrm{dir}) - F_H^S(\mathrm{dir})}{\max\left|F_H^S(\mathrm{dir})\right|} \cdot 100\% \tag{4}$$

where: $F_H{}^S$, $F_H{}^I$ – absolute values of a vector of the horizontal global wind action force in the non-interference and in the interference configuration respectively.

A diagram of the interference coefficient as a function of the wind direction obtained using formula (4) is shown in Fig. 9.

The general conclusion referring to the total horizontal wind forces acting on the building structure is that the immediate surroundings play a positive, sheltering role. For all the wind directions, a decrease in the total horizontal wind force is observed.

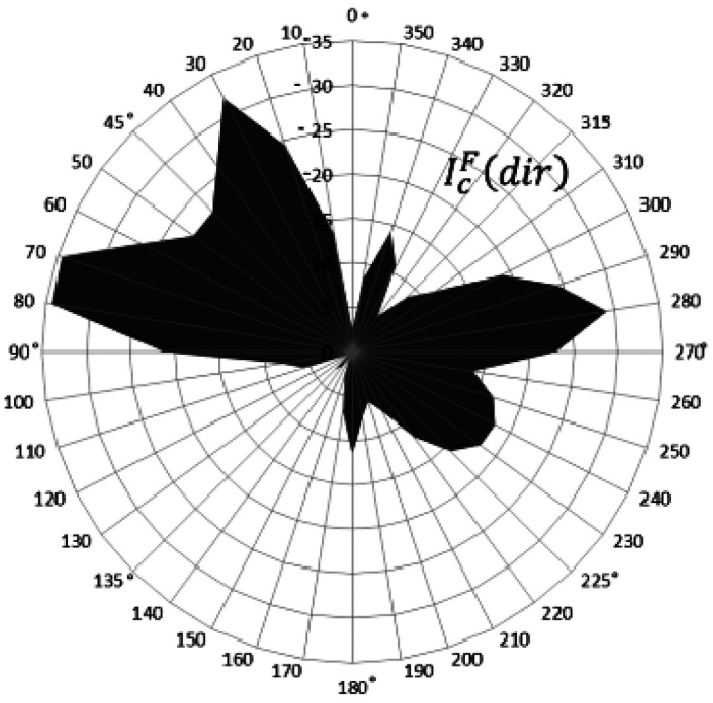

Fig. 9. Diagram of the force interference coefficient as a function of the wind direction

Local extremes, where the reduction of wind forces is significant, occurred for several wind directions. The global extreme took place for the 70°–80° wind directions where the reduction could be evaluated at a level of 35%. An important reduction of about 30% occurred for the 30° and 280° wind directions which was connected with the existence of the TP SA building (30°) and the Westin Hotel building (280°) located nearby.

4. Conclusions

The results of the measurements which were carried out in the wind tunnel allow for the formulation of the following conclusions:

- the building surroundings reduced the wind action on the building in relation to the horizontal global wind force;
- an increase in the positive wind pressure on the building surfaces was not observed;
- a noticeable rise of a suction (negative wind pressures) occurred mainly in areas located at the edges of the building surfaces.

The conclusions cannot be considered as general rules because of the single nature of the measurements. It is necessary to carry out such tests for different interference configurations [4, 5].

References

[1] Flaga A., Bosak G., Kłaput R., Flaga Ł., Kimbar G., *Wind tunnel tests and study analysis of the wind action on the high-rise building placed at the crossroads of Jana Pawła II Avenue and Grzybowska Street in Warsaw*, Research Report, Politechnika Krakowska, Kraków 2012 (in Polish).

[2] Bosak G., *Wind tunnel tests of aerodynamic interference of double-shell tanks*, Czasopismo Techniczne, 3-B/2012, Kraków, 3-19.

[3] PN-EN 1991-1-4: Actions on structures. Part 1-4: General actions- Wind actions.

[4] Khanduri A.C., Stathopoulos T., Bédart C., *Wind-induced interference effects on buildings – a review of the state-of-the-art,* Engineering Structures, Vol. 20(7), 1998, 617-630.

[5] Geurts C.P.W., *The use of wind tunnel experiments for wind loads on structures*, TNO Built Environment and Geosciences, Delft, The Netherlands.

TECHNICAL TRANSACTIONS | CZASOPISMO TECHNICZNE
CIVIL ENGINEERING | BUDOWNICTWO
2-B/2015

AGNIESZKA POROWSKA*, ANDRZEJ FLAGA*

WIND-TUNNEL MODELLING OF THE PHENOMENON OF RAILWAY WAGONS ROLLING OVER UNDER STRONG CROSSWIND ACTION

MODELOWANIE W TUNELU AERODYNAMICZNYM ZJAWISKA WYWRACANIA SIĘ WAGONÓW KOLEJOWYCH POD WPŁYWEM SILNEGO POPRZECZNEGO WIATRU

Abstract

This paper deals with the derivation of similarity criteria for the phenomenon of railway wagons rolling over when exposed to strong crosswinds. Utilizing these criteria, the authorial method for the determination of the aerodynamic coefficient of the rollover moment is also presented in the paper.

Keywords: railway vehicle, across strong wind, vehicle roll-over

Streszczenie

Artykuł przedstawia sposób wyprowadzenia kryteriów podobieństwa dla zjawiska wywracania się wagonów kolejowych pod wpływem silnego poprzecznego wiatru. Z użyciem tych kryteriów przedstawiono również autorską metodę wyznaczania współczynnika aerodynamicznego momentu obrotowego pojazdu szynowego.

Słowa kluczowe: pojazd szynowy, silny wiatr poprzeczny, wywracanie się pojazdów

DOI: 10.4467/2353737XCT.15.123.4160

* Faculty of Civil Engineering, Cracow University of Technology, Poland.

1. Introduction

Railway vehicles in general and especially empty freight wagons as well as empty containers transported on freight wagon platforms may roll over when subjected to strong winds that blow transversely to the direction of the train movement.

This problem is caused by a trend in which the weight of railway vehicles is being reduced and the operational speed is increasing. The reduction of running safety in the presence of crosswind must be considered. In particular, the running safety is strongly affected by crosswind through the interaction of the centrifugal force and the gravitational restoring force caused by cant when vehicles run on a curved track. This problem becomes larger if the wagon of the railway vehicle is empty. Figure 1 shows the number of vehicle roll-over accidents caused by strong crosswind action during the last 100 years. It can be seen that the frequency of this type of accident has grown over recent years [10, 16, 17, 22-26].

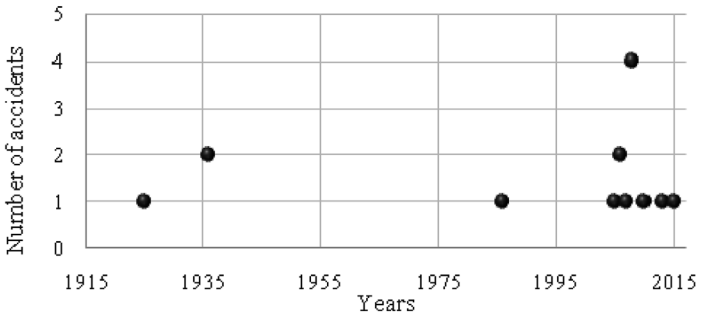

Fig. 1. Number of vehicle roll-over accidents caused by strong crosswind action during the last 100 years

During recent years, a lot of tests which concern this phenomenon have been performed [1–9, 11–13, 15]. The effect of crosswind action is still under investigations because up until now, there has not been enough data concerning this problem [18–21].

The paper presents methodology elaborated by the authors for determining the intrinsic roll-over wind speed V_W^{roll} for a freight railway vehicle, i.e. a wind speed which is just sufficient to cause a 100% unloading of the wheels on the windward side of the vehicle when the vehicle is running in its tare condition at its maximum designed operating speed on a straight track.

Using the calculation model based on the authorial procedure, examples of critical velocity V_W^{roll} calculations were made for entire railway vehicles (wagons with containers) in tare conditions. The same procedure can be used in the problem of roll over under strong crosswind action on a container placed on a wagon platform. But this case is not considered in this paper.

In wind tunnel testing of the roll-over phenomenon of railway vehicles, it is necessary to know the similarity criteria (conditions) for this situation. They may be derived, for example, on the basis of a dimensional analysis of relevant functional dependencies associated with the tested phenomenon. The method was also adopted in this paper.

Furthermore, using these criteria and their related functional dependencies, the authorial method for determining the roll-over aerodynamic moment coefficient of a railway vehicle, $C_{M_A,lee}$, is presented.

2. Sets of vehicle roll-over phenomenon parameters

2.1. Outline of dimensional analysis

In describing physical objects, events or phenomena quantitatively, one may refer to numerical values of base quantities and also introduce numbers derived by inserting these values into certain mathematical formulas, expressions, relationships, etc.

Each of the derived quantities can be written in a power-low form [8, 9, 14]

$$a_i = \breve{a}_i A_1^{\alpha_{i1}} \dots A_k^{\alpha_{ik}} \tag{1}$$

where: a_i – derived quantity; $\breve{a}_i$ – dimensionless quantity (number); $A_1 \dots A_k$ – dimensional base; α_{i1} – real number, whose values distinguish one type of derived quantity from another.

Hence, dimensionless quantity can be written as a quotient:

$$\breve{a}_i = \frac{a_i}{A_1^{\alpha_{i1}} \dots A_k^{\alpha_{ik}}} \tag{2}$$

where the dimensions of dimensional quantity a_i and the product of dimensions $A_1^{\alpha_{i1}} \dots A_k^{\alpha_{ik}}$ are the same.

Dimensionless quantities are the same regardless of the object scale:

$$\breve{a}_{iM} = \breve{a}_{iN} \tag{3}$$

where: M – model of the object, N – object at a 1:1 scale.

The above relationship can be written in another way:

$$\Pi_{iM} = \Pi_{iN} \tag{4}$$

Taking into account the presented relations, one can set the following relationship:

$$\frac{\left(\dfrac{a_i}{A_1^{\alpha_{i1}} \dots A_k^{\alpha_{ik}}}\right)_M}{\left(\dfrac{a_i}{A_1^{\alpha_{i1}} \dots A_k^{\alpha_{ik}}}\right)_N} = 1 \rightarrow \frac{(a_i)_M}{(a_i)_N} \frac{\left(A_1^{\alpha_{i1}} \dots A_k^{\alpha_{ik}}\right)_N}{(A_1^{\alpha_{i1}} \dots A_k^{\alpha_{ik}})_M} = 1 \tag{5}$$

$$\frac{k_{ai}}{k_{A1}^{\alpha_{i1}} \ldots k_{Ak}^{\alpha_{ik}}} = 1 \tag{6}$$

where:

$$k_{ai} = \frac{(a_i)_M}{(a_i)_N} \tag{7}$$

is the scale of derived quantities a_i

Finally, the relationship for the scales can be obtained:

$$k_{ai} = k_{A1}^{\alpha_{i1}} \ldots k_{Ak}^{\alpha_{ik}} = \frac{\left(A_1^{\alpha_{i1}} \ldots A_k^{\alpha_{ik}}\right)_N}{(A_1^{\alpha_{i1}} \ldots A_k^{\alpha_{ik}})_M}, \tag{8}$$

After this short introduction to dimensional analysis, one can now focus on the analyzed case of railway wagons.

2.2. Set of parameters characterizing inflowing air crosswind to the running train

The initial step in the dimensional analysis of the problem of overturning railway vehicles under strong crosswind is to determine sets of all quantities related to this phenomenon on the basis of knowledge and previous measurements [8, 9, 11, 14, 16].

The first set includes parameters describing inflowing air in a strong crosswind relative to the running train:

$$(W) = \left(\rho_a, \nu, V_W, V_R, \varphi, \beta, V_{ref}, V_b, I_v\right) \tag{9}$$

where: ρ_a – air mass density (1,225 kg/m^3); ν – kinematic viscosity of atmospheric air; V_W – peak (gust) wind velocity at the top of the vehicle; V_R – relative velocity of wind and train running at operating velocity V_T; φ – angle of wind attack; β – relative angle of wind attack; V_{ref} – mean wind velocity; V_b – basic wind velocity for the given localization according to PN-EN 1991-1-4; I_v – turbulence intensity.

Relationship between the wind angle and the relative wind angle and the three vectors of velocities is shown in Fig. 2.

2.3. Set of vehicle describing parameters treated as dimensionless

The next set of quantities concerns parameters which describe the vehicle and are treated as dimensionless. They identify the vehicle and its location in the convoy, together with adjacent vehicles. These are as follows:

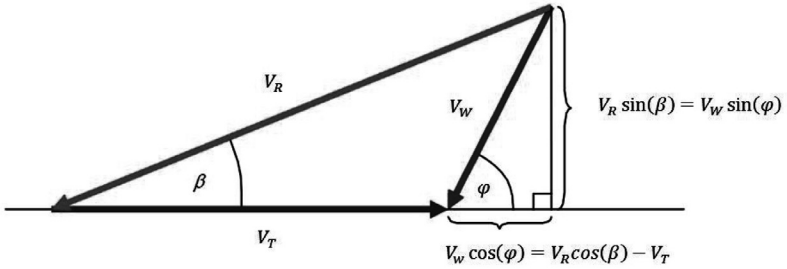

Fig. 2. Relationship between the wind angle φ and resultant (relative) wind angle β [10]

ID = vehicle type, level of corner rounding; aerodynamic character of vehicle geometry (streamlined, intermediate, non-streamlined), presence or not of adjacent vehicles in front of or behind the vehicle, etc.

2.4. Set of vehicle geometric parameters

Another set of quantities include parameters which allow describing features of vehicle geometry. Fig. 3 shows examples of these.

$$(G) = (A, H) \tag{10}$$

where: A – vehicle side area (reference area); H – mean longitudinal roof height above axle centerline (reference height).

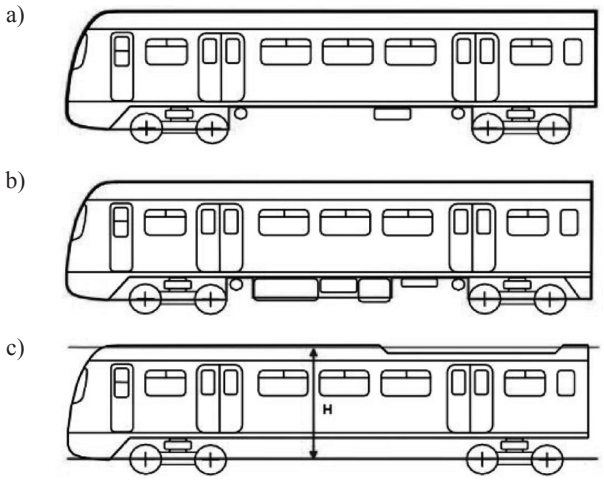

Fig. 3. Vehicle side area *A* and vehicle reference height *H* for different types of vehicles [19]

2.5. Set of aerodynamic and mechanical vehicle parameters

The last set which is presented in this paper includes parameters of aerodynamic and mechanical vehicle responses to strong crosswind action. These are as follows:

$$(O) = (F_{Ax}, F_{Az}, M_A, M_R, V_T) , \tag{11}$$

where: F_{Ax} – vehicle aerodynamic drag force; F_{Az} – vehicle aerodynamic lift force; M_A – vehicle aerodynamic rolling moment with respect to the resolution point O; M_R – vehicle restoring moment due to vehicle weight with respect to the top point of the leeward rail; V_T – operating speed of the running train.

Fig. 4 shows assumed coordinate system and positive components of aerodynamic actions, where the axis y is the horizontal mid-truck axis. The resolution point O of the aerodynamic forces F_{Ax}, F_{Az} and aerodynamic moment M_A are at the top of the rails at the mid-truck position, mid-way between the wheel-to-rail contact points.

Next to, or instead of, vehicle aerodynamic rolling moment at crosswind with respect to the resolution point O (M_A), one can also define the vehicle aerodynamic rolling moment at crosswind with respect to the another resolution point P ($M_{A,lee}$) which is the top point of the lee rail:

$$M_{A,lee} = M_A + F_{Az} \cdot \frac{B}{2} \tag{12}$$

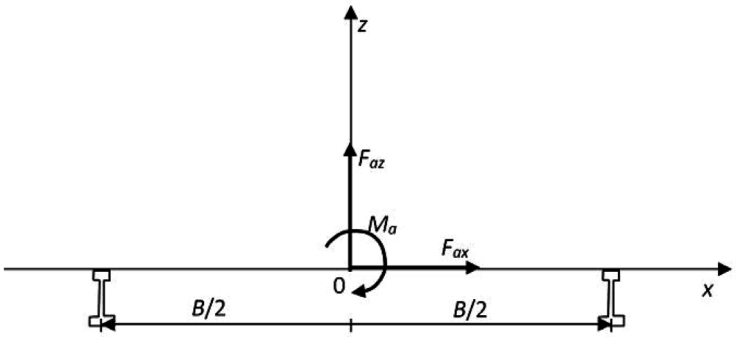

Fig.4. Assumed coordinate system and positive components of aerodynamic actions [8, 9]

Among the five parameters of the analyzed problem (V_R, V_T, V_W, β, φ) only two of them are independent. Relationships between these quantities determine formulae:

$$\beta = \tan^{-1}\left(\frac{V_W \sin(\varphi)}{V_T + V_W \cos(\varphi)}\right) \tag{13}$$

$$\varphi = \tan^{-1}\left(\frac{V_R \sin(\beta)}{V_R \cos(\beta) - V_T}\right) \tag{14}$$

$$V_W = \frac{V_R \sin(\beta)}{\sin(\varphi)} \tag{15}$$

3. The possible dimension and dimensionless functional relationships of the analyzed problem

3.1. Similarity criteria in case of problem I

Taking into account the above sets of parameters, one can determine possible dimension and dimensionless functional relationships of the analyzed problem, firstly in the case of the problem which concerns vehicle roll over aerodynamic moment coefficient. This problem will be referred to as problem I.

Vehicle roll over aerodynamic moment depends on several quantities:

$$M_{A,lee} = M_{A,lee}\left(\rho_a, \nu, V_R, \varphi, \beta, A, H; (ID)\right) \tag{16}$$

The next step of dimensional analysis is to determine the dimensional base. One can assume that the dimensional base constitutes: ρ_a – air mass density (1,225 kg/m^3), V_R – relative velocity of wind and train running at operating velocity V_T, H – reference height.

Taking into account this base and theorem Π [14] of dimensional analysis the previous relationship one can bring to dimensionless relationship in which appear the following quantities:

$$\breve{M}_{A,lee} = \breve{M}_{A,lee}\left(Re_R, \beta, \varphi, \lambda; (ID)\right), \tag{17}$$

where: $\breve{M}_{A,lee} = \dfrac{M_{A,lee}}{\rho_a V_R^2 H^3}$ – vehicle roll-over aerodynamic moment coefficient; $\mathrm{Re}_R = V_R H/\nu$ – vehicle Reynolds number; $\lambda = A/H^2$ – vehicle slenderness.

Instead of aerodynamic coefficient $\breve{M}_{A,lee}$, one can more frequently find this coefficient defined in another way:

$$C_{M_A,lee} = \frac{M_{A,lee}}{\frac{1}{2}\rho_a V_R^2 AH} \tag{18}$$

Finally, one can write the dimensionless relationship of problem I as follows:

$$C_{M_A,lee} = C_{M_A,lee}\left(Re_R, \beta, \varphi, \lambda; (ID)\right) \tag{19}$$

All dimensionless quantities appearing in this dimensionless functional relationship constitute determined similarity criteria in the case of problem I.

3.2. Similarity criteria in the case of problem II

The second problem in these considerations concerns dimensionless relative critical wind velocity. Firstly, the set of quantities related to intrinsic roll-over wind speed should be determined:

$$V_R^{roll} = V_R^{roll}\left(\rho_a, \nu, V_{ref}, V_b, I_v, \beta^{roll}, \varphi^{roll}, A, H, M_R; (ID)\right) \tag{20}$$

where: V_W^{roll} – intrinsic roll-over wind speed – the wind speed which is just sufficient to cause a 100% unloading of the wheels on the windward side of the vehicle when the vehicle is running in its tare condition at its maximum design operating speed on a straight track.

In general, one can investigate and analyze different cases of train speeds $V_T^* \in (0, V_T)$ where the case $V_T^* = 0$ refers to the stopped train.

In the limit (critical) situation, the vehicle roll-over aerodynamic moment $M_{A,lee}^{roll}$ caused by crosswind is balanced by the vehicle restoring moment M_R, resulting from gravitational forces acting on the vehicle.

Let us assume dimensional base in this case as: ρ_a – air mass density (1,225 kg/m^3), V_b – basic wind velocity for the given localization [18], H – reference height.
After this assumption, one can finally obtain the dimensionless relationship of problem II:

$$C_{V_R^{roll}} = C_{V_R^{roll}}\left(Re_b, \beta^{roll}, \varphi^{roll}, \lambda, C_{M_R}; (ID)\right) \tag{21}$$

where: $C_{V_R^{roll}} = \dfrac{V_R^{roll}}{V_b}$ – dimensionless relative critical wind velocity; $C_{M_R} = \dfrac{M_R}{\frac{1}{2}\rho_a V_b^2 AH}$ – dimensionless vehicle restoring moment coefficient (taking into account remarks as in the case of dimensionless vehicle roll-over aerodynamic moment coefficient $\breve{M}_{A,lee}$ and dimensionless roll-over aerodynamic moment coefficient $C_{M_A,lee}$); β^{roll}, φ^{roll}, λ – as before but in the limit (critical) situation.

All dimensionless quantities appearing in this dimensionless functional relationship constitute determined similarity criteria (numbers) in the case of problem II which should be fulfilled in model testing.

4. Problems of similarity criteria fulfillment in wind tunnel model tests and basic simplification assumptions in investigations

There are problems with the fulfilment of some of the similarity criteria in wind tunnel model tests. As a result, it is necessary to use simplification assumptions which are usually assumed in investigations.

There are following problems connected with wind tunnel tests in the case of railway vehicle roll over when subjected to strong crosswind:

- tests on the moving train,
- fulfillment of Reynolds number.

The first problem concerns the question of how to perform investigations on a scale model of the vehicle together with a part of a train which is moving with respect to the air stream in the working section of wind tunnel.

On the other hand, there is no problem with the realization of a suitable angle of wind attack on a model, this is because the tested model is placed on the rotating table of the wind tunnel working section.

It is common practice to simplify this problem by performing tests on motionless rigidly fixed models and assume that:

- inflowing air stream has the velocity: $V_W^{exp} = V_R$, $\left(V_W^{exp,roll} = V_R^{roll}\right)$;
- the angle of air stream attack is: $\varphi = \beta$, $\varphi^{roll} = \beta^{roll}$.

The second general problem of similarity criteria fulfillment in the wind tunnel model tests is the fulfillment of the Reynolds number. This number takes into consideration the influence of air viscous forces on aerodynamic actions caused by the wind blowing transversally on to a railway vehicle.

A simple example may be considered: if the geometric scale of model $k_H = 1/5$, then from the Reynolds criterion it results that the velocity scale $k_V = 5$. This means that in the wind tunnel, the velocity of air stream should be five times greater than in nature. This is very hard to make in practice.

However, in the case of weakly streamlined bodies – as is the case for railway vehicles in the draft of wagons – the dependence of aerodynamic coefficients on the Reynolds number, i.e. the flow-over crisis and connected with it, the different values of aerodynamic coefficients in subcritical, critical, supercritical and transcritical ranges of Reynolds number do not take place in practice.

It is commonly assumed that unfulfillment of this criterion in wind tunnel tests does not lead to essential mistakes in experimental results.

After these simplifications, instead of considering functions (19 and 21): $C_{M_A,lee} = C_{M_A,lee}\left(Re_R, \beta, \varphi, \lambda; (ID)\right)$ and $C_{V_R^{roll}} = C_{V_R^{roll}}(Re_b, \breve{V}_W^{roll}, \beta^{roll}, \varphi^{roll}, \lambda, C_{M_R}; (ID)$, the approximate functions evaluating the primary functions are considered:

$$C_{M_A,lee}^{exp} = C_{M_A,lee}^{exp}\left(\varphi, \lambda; (ID)\right) \tag{22}$$

and

$$C_{V_W^{exp,roll}} = C_{V_W^{exp,roll}}\left(\varphi^{roll}, \lambda, C_{M_R}; (ID)\right) \tag{23}$$

5. Examples of similarity criteria fulfillment for the case of railway wagons rolling over when subjected to strong crosswind action

5.1. Vehicle restoring moment

The restoring moment due to vehicle weight is calculated by taking into account the vehicle's mass and semi-span of the wheel-to-rail contact points. The roll-over moment M_R due to vehicle body, bogie and wheelset masses and their lateral and roll suspension displacements is given by the formula:

$$M_R = mgb - m_0 g y_0 - m_1 g y_1 - m_2 g y_2 \tag{24}$$

where: m – total tare mass of the vehicle; g – acceleration due to gravity (9.81 m/s2); b – semi-span of wheelset-to-rail contact points; m_0 – unsprung mass; y_0 – lateral displacement of unsprung mass; m_1 – primary sprung mass; y_1 – lateral displacement of primary sprung mass relative to track centerline; m_2 – secondary sprung mass; y_2 – lateral displacement of secondary sprung mass with any body center of gravity offset due to roll and/or weight asymmetry relative to the track centerline.

During the analysis of the considered case, one must first look at the scheme of vehicle construction and its reaction on transverse force action.

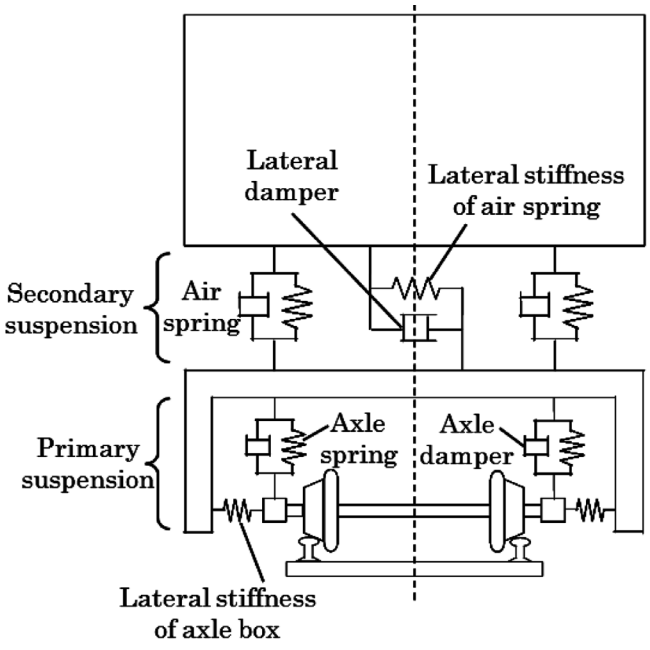

Fig. 5. Modeling of suspension [12]

The Fig. 5 shows the scheme of suspension in a railway wagon.

The wheelset constitutes the unsprung mass. Train wheels are based directly on the rails. The lateral displacement of the unsprung mass (y_0) is always considered to be zero as the roll-over moment is calculated about the point of contact of the wheelset itself on the rail head. The chassis of the wagon is mounted to the wheelset by horizontal and vertical springs which allow horizontal and vertical displacements. The chassis is the primary sprung mass. Other vehicle elements are attached to the chassis also by horizontal and vertical springs, which also allow horizontal and vertical displacements. The container with the other elements which are under the chassis are the secondary sprung mass.

The displacements of sprung masses are the effect of acting lateral force, i.e. wind action which is considered here. These displacements depend on the type of railway vehicle and the velocity of atmospheric air acting upon it.

The lateral displacements of the primary and secondary sprung masses (y_1 and y_2) can be taken as the maximum (metal to metal) displacements including the effects of roll at the height of the center of gravity.

Returning to define the railway restoring moment, its dimensional base should first be determined. In the event of the rolling over of railway wagons under strong crosswind action, the dimensional base will consist of the following quantities: ρ_a – density of atmospheric air; V_b – basic wind velocity; H – height of railway vehicle.

The next step of dimensional analysis is to set its dimensionless quantity on the basis of the assumed dimensional base:

$$\breve{M}_R = \frac{M_R}{\rho_a V_b^2 H^3} = \frac{mgb}{\rho_a V_b^2 H^3}\left(1 - \frac{m_0}{m}\frac{y_0}{b} - \frac{m_1}{m}\frac{y_1}{b} - \frac{m_2}{m}\frac{y_2}{b}\right) \tag{25}$$

where: $\rho_a V_b^2 H^3$ – the product quantities of the dimensional base defining the dimensions of railway restoring moment.

Particular components of the above equation are presented as dimensionless quantities: $\breve{M}_R^* = \frac{mgb}{\rho_a V^2 L^3}$ – dimensionless vehicle restoring moment; $\breve{m}_0 = m_0 / m$ – dimensionless unsprung mass; $\breve{m}_1 = m_1 / m$ – dimensionless primary sprung mass; $\breve{m}_2 = m_2 / m$ – dimensionless secondary sprung mass; $\breve{y}_0 = y_0 / b$ – dimensionless lateral displacement of unsprung mass; $\breve{y}_1 = y_1 / b$ – dimensionless lateral displacement of primary sprung mass; $\breve{y}_2 = y_2 / b$ – dimensionless lateral displacement of secondary sprung mass.

The relations listed above constitute similarity numbers, which should be fulfilled in wind tunnel model tests, so to be true the below relationship:

$$\breve{M}_{RM}^* = \breve{M}_{RN}^* \tag{26}$$

which implies the ratio of the railway restoring moment in the natural and model scale:

$$\frac{\breve{M}_{RM}^*}{\breve{M}_{RN}^*} = 1 \tag{27}$$

$$\frac{k_m k_g k_b}{k_{\rho_a} k_{V_b}^2 k_H^3} = 1 \rightarrow k_m k_b = k_{V_b}^2 k_H^3 \tag{28}$$

because:
$k_g = 1$ – gravitational scale is equal to one because gravitational force is the same in the model and natural scale (tests will be performed in normal gravitational conditions);
$k_{\rho_a} = 1$ – scale of density of atmospheric air is equal to one because density of atmospheric air is the same in the model and natural scale.

Finally, the similarity scales resulting from the above criteria can be written as follows:

$$k_m = k_{V_b}^2 \frac{k_H^3}{k_b} \rightarrow k_m = k_{V_b}^2 k_H^2 \tag{29}$$

where: k_m – scale of mass; k_{V_b} – scale of base wind velocity which acts on the railway vehicle; k_H, k_b – scale of railway vehicle geometry. $k_H = k_b$.

Scales of particular masses of railway vehicle: $k_{m_0} = k_m$; $k_{m_1} = k_m$; $k_{m_2} = k_m$.

Scales of geometry of particular railway vehicle elements displacements: $k_{y_0} = k_b$; $k_{y_1} = k_b$; $k_{y_2} = k_b$.

One can now consider two cases of the railway train model performing which will be tested in a wind tunnel and similarity criteria which should be fulfilled in each of them.

5.2. Examples of similarity criteria fulfillment

- **First case**

Assumption: the model is made of the same material as the real object.

The particular scales can be written as follows: $\rho_{mM} = \rho_{mN} \rightarrow k_{\rho_m} = 1$ – on the basis of assumption; $k_H = k_b$ – particular lengths are in relevant proportions – geometrical scale is the same for all of the dimensions of the model elements; $\frac{\Omega_M}{\Omega_N} = k_\Omega = k_H^3$ – volume scale; $m = \rho_m \Omega \rightarrow k_m = k_{\rho_m} k_\Omega$ – mass scale.

After substitution of the scale, the relation can be presented in such a form:

$$k_{\rho_m} k_\Omega = k_{V_b}^2 k_H^2 \rightarrow k_{V_b}^2 = k_H \rightarrow k_{V_b} = \sqrt{k_H} \tag{30}$$

where: k_H – geometrical scale of the model – assumed scale of the model; k_{V_b} – scale of the wind velocity, which acts on the model tested in wind tunnel, determined in accordance to the above relationship.

On the basis of relations determining dependence between the described two scales, a simple example can be shown:

Assumption: the model is performed at a geometric scale – 1:15, so $k_H = 1/15$.

Hence, one can easily determine velocity scale: $k_{V_b} = \sqrt{k_H} = \sqrt{\frac{1}{15}} \cong 0,258$.

Therefore, if the wind velocity in nature is: $V_{bN} = 22$ m/s (which refers to the basic wind velocity in the first zone of wind load in Poland according to PN-EN 1991-1-4), the velocity of inflowing air in the wind tunnel which is acting on the model must be: $V_{bM} \cong 5.68$ m/s

- **Second case**

  Assumption: the model is made of different material to the object in natural scale.

  Mass can be described by the following equation:

$$m = \int_{\Omega} \rho_m d\Omega = \rho_m \int_{\Omega} d\Omega = \rho_m \int_{\Omega} dxdydz = \rho_m \int_{S} ddS = \rho_m d \int_{S} dS \tag{31}$$

where: d – the wall thickness.

After writing this equation with using the scales can be obtained:

$$\rho_m d \int_{S} dS \rightarrow k_{\rho_m} k_d k_H^2 \tag{32}$$

As it was derived before, the scale of mass can also be written in a different way:

$$k_{\rho_m} k_d k_H^2 = k_{V_b}^2 k_H^2 \rightarrow k_{\rho_m} k_d = k_{V_b}^2 \rightarrow k_{V_b} = \sqrt{k_{\rho_m} k_d} = \sqrt{k_{\rho_m} k_H} \tag{33}$$

k_d – geometric scale of the model – assumed scale of the model ($k_d = k_H$); k_{ρ_m} – scale of material density – scale dependent on density of material used to perform the model; k_{V_b} – as before.

Similar to the first case, one can present a simple example but with such a difference that now three scales are taken into consideration.

Assumption: the model is performed at a geometric scale – 1:15, so $k_H = 1/15$; the model is performed of material with density 1.5 times smaller than the object at a 1:1 scale. Hence, there is: $\frac{\rho_{mM}}{\rho_{mN}} = \frac{1}{1,5} \rightarrow k_{\rho_m} \cong 0.67$.

On this basis, one can define the scale of wind velocity: $k_{V_b} = \sqrt{k_{\rho_m} k_H} = \sqrt{0.67 \cdot 0.067} \cong 0.211$.

Therefore, if the wind velocity in nature is: $V_{bN} = 22$ m/s , the velocity of inflowing air in wind tunnel which is acting on the model must be: $V_{bM} \cong 4.64$ m/s.

These two cases show the importance of adequate choice of similarity scales which should be satisfied by the model. Two different assumptions with respect to the similarity criteria fulfillment proceed to different ways of the model and test execution.

6. Authorial method of determination the vehicle roll-over aerodynamic moment coefficient under strong crosswind action

The vehicle roll-over aerodynamic moment coefficient $C_{M_A,lee}^{roll}$ can be determined on the basis of experimental results of the intrinisic roll-over wind velocity $V_W^{exp,roll}$ obtained in wind

tunnel model tests. In the limit case of the vehicle model roll-over phenomenon, one can write the following relationships:

$$C_{M_A,lee}^{roll} = \frac{M_{A,lee}^{roll}}{\frac{1}{2}\rho\left(V_R^{roll}\right)^2 AH} = \frac{\mathrm{M}_R}{\frac{1}{2}\rho\left(V_R^{roll}\right)^2 AH} = C_{M_R}\frac{\frac{1}{2}\rho\left(V_b\right)^2 AH}{\frac{1}{2}\rho\left(V_R^{roll}\right)^2 AH} = C_{M_R}\left(\frac{V_b}{V_R^{roll}}\right)^2$$

$$\cong C_{M_R}\left(\frac{V_b}{V_W^{exp,roll}}\right)^2 = \frac{C_{M_R}}{C_{V_W^{exp,roll}}^2\left(\varphi^{roll},\lambda,C_{M_R};(ID)\right)} \tag{34}$$

therefore:

$$C_{M_A,lee}^{roll} \cong \frac{C_{M_R}}{C_{V_W^{exp,roll}}^2\left(\varphi^{roll},\lambda,C_{M_R};(ID)\right)} \tag{35}$$

This relationship determines the way of conducting suitable experimental investigations in a wind tunnel. After fulfillment of the similarity number C_{M_R} at established values of the quantities φ^{roll} and λ, it is necessary to determine the respective value of the coefficient $C_{V_W^{exp,roll}} = V_W^{exp,roll}/V_b^{exp}$ from the wind tunnel model tests. Finally, one can obtained the value of the coefficient $C_{M_A,lee}^{roll}$ which is determined by the above equation.

7. Final remarks

The crucial thing in the problem of evaluation of intrinsic roll-over wind speed V_W^{roll} is knowing the adequate values of roll-over aerodynamic moment coefficient $C_{M,lee}(\beta)$. So far, there has not been enough data concerning this question obtained from wind tunnel tests.

It is worth pointing out that in technical specifications of interoperability (TSI), the effect of crosswind on the roll-over phenomena of railway vehicles is considered as an open point.

Due to this, such investigations for several arrangements of wagons in trains and for different types of wagons should be urgently performed in the near future.

References

[1] Baker C.J., *A framework for the consideration of the effects of crosswinds on trains,* Journal of Wind Engineering and Industrial Aerodynamics, Vol. 123, 2013, 130-142.

[2] Baker C.J., *The flow around high speed trains*, Journal of Wind Engineering and Industrial Aerodynamics, Vol. 98(6-7), 2010, 277-298.

[3] Baker C.J., *The simulation of unsteady aerodynamic crosswind forces on trains,* Journal of Wind Engineering and Industrial Aerodynamics, Vol. 98(2), 2010, 88-99.

[4] Bocciolone M., Cheli F., Corradi R., Muggiasca S., Tomasini G., *Crosswind action on rail vehicles: Wind tunnel experimental analyses*, Journal of Wind Engineering and Industrial Aerodynamics, Vol. 96(5), 2008, 584-610.
[5] Carrarini A., *Reliability based analysis of the crosswind stability of railway vehicles*, Journal of Wind Engineering and Industrial Aerodynamics, Vol. 95(7), 2007, 493-509.
[6] Cheli F., Giappino S., Tomasini G., Villani M., Zanetti G., *Aerodynamic loads on lightweight railway vehicles for the evaluation of rollover risk*, Proc. 2nd International Conference on Railway Technology: Research, Development and Maintenance, 2014.
[7] Deliancourt F., Sicot C., Aguinaga S., Boree J., Bouchet J-P., *Simulation of details in wind tunnel testing: application to railway trains*, Proc. 48th Applied Aerodynamics Symposium Saint-Louis, France, 25-27 March 2013.
[8] Flaga A., *Resistance of freight railway vehicles to roll-over in strong winds,* Cracow University of Technology, Cracow 2014.
[9] Flaga A., *Basic principles and theorems of dimensional analysis and theory of model similarity of physical phenomena*, Proc. 7th International Symposium on Environmental Effects on Buildings ad People: Actions, Influences, Interactions, Discomfort, Lublin-Kraków 2014.
[10] Flaga A., *Expert opinion on resistance of railway vehicles to roll-over in gales and on possibility of blowing off 20ft and 40ft freight containers from S04a FEA-B wagons running in the draft of wagons at maximum velocity 120 km/h*, Wagony Świdnica S.A., Świdnica 2013.
[11] Flaga A., Porowska A., *Charakterystyka zjawiska wywracania się wagonów przy silnym wietrze oraz metoda wyznaczania współczynnika aerodynamicznego momentu obrotowego pojazdu szynowego,* Inżynieria i Budownictwo, Vol. 12, 2014, 689-691.
[12] Shimada K., Tanifuji, K., *Influence of cross wind on the running safety of railway vehicle running on curve at low speed*, J-RAIL, 2008, 441-444.
[13] Proppe C., Wetzel C., *Overturning probability of railway vehicles under wind gust loads*, IUTAM Symposium on Dynamics and Control of Nonlinear Systems with Uncertainty, 2007, 23-32.
[14] Sonin A.A., *The physical basis of dimensional analysis,* Department of Mechanical Engineering MIT, Cambridge 2001.
[15] Suzuki M., Tanemoto K., Maeda T., *Aerodynamic characteristics of train/vehicles under cross winds*, Journal of Wind Engineering and Industrial Aerodynamics, Vol. 91(1-2), 2003, 209-218.
[16] Terry J., *Investigation of freight vehicle aerodynamic performance in accordance with GM/RT 2142 Resistance of Railway Vehicles to Roll-Over in Gales,* RSSB, 2012.
[17] RAIB, *Detachement of containers from freight wagons near Cheddington and Hardendale*, Department of Transport, 1 March 2008, Raport 12/2009 May 2009.
[18] PN-EN 1991-1-4 Eurocode 1 – Actions on structures. Part 1-4: General actions - Wind actions, 2008.
[19] GM/RT2142 Issue 3, Resistance of Railway Vehicles to Roll-Over in Gales, 2009;
[20] PN-EN 140-67-6:2010 Kolejnictwo – Aerodynamika – Część 6: Wymagania i procedury badań aerodynamicznych oddziaływania wiatru bocznego.
[21] 2008/232/WE Specyfikacje techniczne interoperacyjności podsystemu „Tabor" transeuropejskiego systemu kolei dużych prędkości (notyfikowana jako dokument nr C, 2008), 648.

[22] http://www.raib.gov.uk
[23] http://www.railwaysarchive.co.uk
[24] http://www.irsc2014.org
[25] http://www.intlrailsafety.com
[26] http://en.wikipedia.org/wiki/List_of_wind-related_railway_accidents

TECHNICAL TRANSACTIONS | CZASOPISMO TECHNICZNE
CIVIL ENGINEERING | BUDOWNICTWO
2-B/2015

OLIVIER FLAMAND*

SCALE QUESTIONS IN WIND ENGINEERING EXPERIMENTATION

ZAGADNIENIE SKALI W BADANIACH DOŚWIADCZALNYCH W INŻYNIERII WIATROWEJ

A b s t r a c t

Wind tunnel testing is sometimes achieved at reduced scale. Doing so, wind engineers must consider the similitude rules for giving results at full scale. These rules are deduced from the basic laws of Physics, for their theoretical part, and based on practical state of the art methods for wind tunnel application. A wide overview of this important part of wind engineering is given in this paper

Keywords: wind tunnel, reduced scale, similitude law

S t r e s z c z e n i e

Badania w tunelu aerodynamicznym czasami możliwe są do wykonania jedynie w skali zredukowanej. Należy wtedy wziąć pod uwagę kryteria podobieństwa dające wyniki, jak dla badań przeprowadzonych w pełnej skali. Kryteria te opierają się na podstawowych prawach fizyki, w części teoretycznej, oraz na praktycznym stanie wiedzy o stosowanych metodach – w części dotyczącej badań w tunelach aerodynamicznych. Szeroki przegląd tej ważnej części inżynierii wiatrowej przedstawiono w niniejszej pracy.

Słowa kluczowe: tunel aerodynamiczny, skala zredukowana, kryteria podobieństwa

DOI: 10.4467/2353737XCT.15.124.4161

* Centre Scientifique et Technique du Bâtiment, France.

1. Scaling in fluids mechanics

Wind engineering deals with man-made structures, works from structural engineers, architects and civil engineers that are mostly of large dimensions – this presents a problem for laboratory testing. Pioneers of fluid engineering have long faced this difficulty : how to reproduce natural phenomena on a smaller scale. Euler, in 1780, was probably the first to work seriously on scaling in engineering mechanics, this was followed by Fourier in the 1800s. In 1878, the French mathematician Joseph Bertrand was the first to demonstrate the theorem that was reused by Aimé Vaschy [1] and later popularized by Edgar Buckingham [2]. It is now known as the 'Vaschy-Buckingham' or 'Buckingham-Pi' theorem, giving the number of non-dimensional numbers necessary to describe a physical phenomenon. Because they are non-dimensional, these numbers opened the gate to dimensional analysis which gives the rules (Rayleigh's method) to be observed when transposing between a full-scale prototype and a reduced scale model.

In the 18th century, seven basic physical quantities were chosen as elementary elements, the combination of which can represent any physical quantity: length L, mass M, time or duration T, electric intensity I, thermodynamic temperature θ, number of molecules N and light intensity J.

Reynolds, Froude, Prantl, Scruton, Strouhal, Grashof, and Mach have all been immortalized by lending their names to one dimensionless quantity. Does this mean that everything has already been said concerning scale effects in wind tunnel simulations? Let's attempt to consider the practical rules and routines in scaling for wind tunnel studies.

2. Scaling practice in boundary layer wind tunnels

Boundary layer wind tunnels (BLWTs) have been used for more than 60 years for the reproduction of natural turbulent wind at a scale ranging from 1/200 to 1/3000. Prismatic blocks are placed upstream from the test area in order to generate this reduced-scale boundary layer with turbulence scales and spectra resembling the real situation as accurately as possible, using one time scale and one length scale.

It is clear that only part of the natural turbulence can be reproduced by these means, that corresponding to the input from kinetic energy, while the thermal part of the turbulence is neglected. It is commonly recognized that the BLWT [3] is efficient in reproducing a neutral atmosphere corresponding to most storm wind characteristics. It is therefore chiefly used to reproduce extreme loads due to wind on buildings and bridges etc, but it is not convenient for reproducing everyday types of wind, such as that which would be helpful in studying wind power harvesting and pollutant dispersion. Nevertheless, if the experiment is used to reproduce the local dispersion of flumes or the wake of one wind turbine impacting on a neighbouring one, all considered at a short distance, a boundary layer simulation can be very effective.

The first scale limit encountered in boundary layer wind tunnels is due to the Reynolds number. This balance of viscous forces to dynamic forces acting on flow particles is the main

parameter governing the reproduction of actual loads on a model. For a geometric scale of 1/200 in air, the wind speed should therefore be 200 times higher than in reality to maintain the same value of the Reynolds number, which is clearly impossible. As a consequence, wind engineers have developed many tricks to counterbalance the effects of the Reynolds number which is 100 to 1000 times lower than the full scale one.

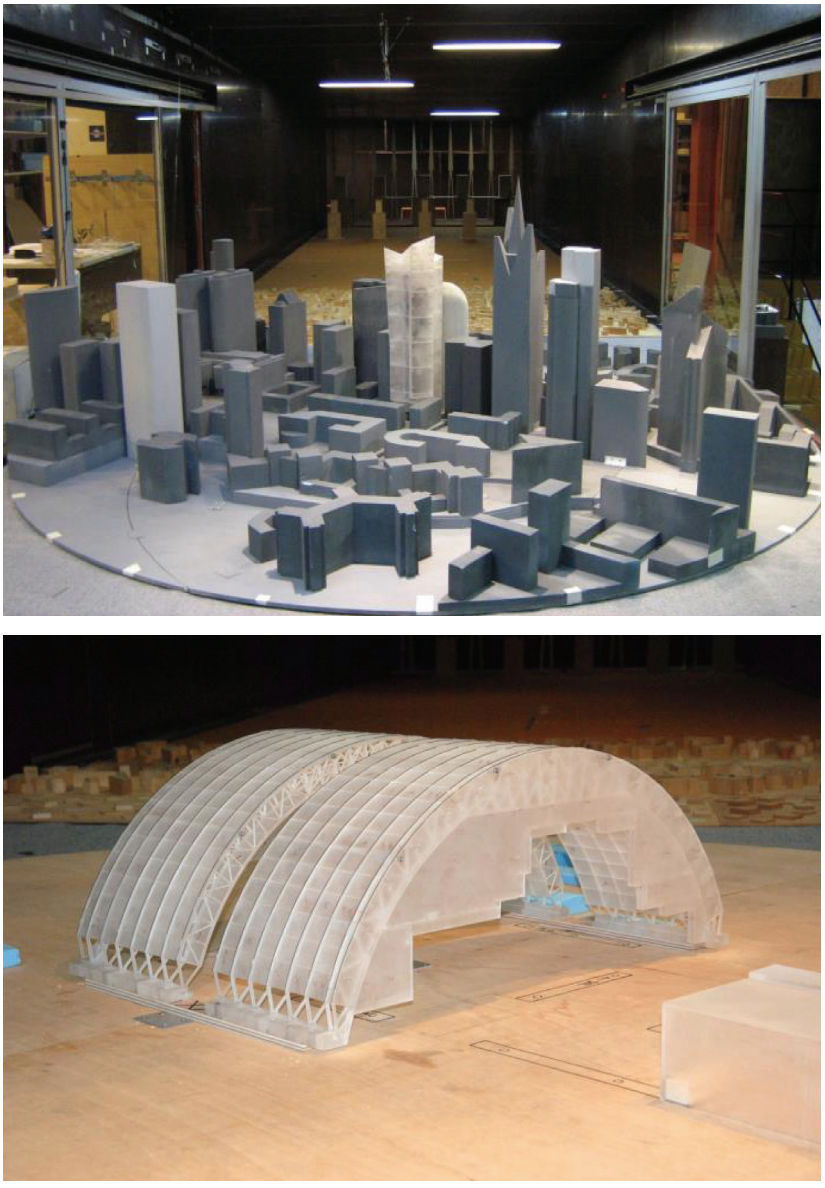

Fig. 1. A view of a BLWT operating at CSTB (top) and the case study of Novarka great arch with the Reynolds number effect on a round shape building and on a truss (bottom)

The first illustration of the Reynolds number scaling effects is given by the study of lattice structures. For elementary parts of the lattice with sharp edged profiles, it is commonly accepted that the drag force on each element does not change with a low Reynolds number. This assumption is based on drag coefficients measured on isolated squares, I, H and U-shaped beams, but is not fully verified when the lattice is so dense that it begins to behave as a mesh structure. Nevertheless, it is characteristic for rounded elements of a lattice structure that the drag force is highly dependent upon the flow regime. In such a case, there are two ways to change the lattice shape with the aim of better representing the wind loads on the model than via simply through the use of homothetic scaling. The first possibility lies in decreasing the diameter of the round bars of the lattice by the ratio of drag coefficient at full scale (say 0.6 for a given wind speed and a given roughness) to the drag coefficient at a reduced scale in the wind tunnel, (say 1.2). In practice, reducing the diameter of round bars by a factor of two is very common, and relies on the assumption of high wind speeds producing a drop in the drag force coefficient when overpassing the critical Reynolds number, usually called the drag crisis, at full scale[4]. The second possibility is to replace round bars by square bars, the thickness of which being calculated with the same ration of drag coefficient of the square compared to the drag coefficient of the circular cylinder at a given Reynolds number at full scale.

The second limit encountered in downscaling is the blockage effect in the wind tunnel itself, especially when it is a closed loop circuit with solid walls. When the wind 'hits' a building at full scale, stream lines are deflected around the bluff body with no constraint in the vertical direction, and sometimes none in the lateral direction. In a wind tunnel, it is clear that the ceiling and lateral walls represent a first physical limit to the expansion of the deflected streamlines. Even if correction methods have been applied, especially in aeronautics on streamlined two dimension bodies and for the sake of measuring mean loads, these cannot be effective in boundary layer wind tunnels. The main reason is that not only is the means flow deflected here but additionally, the large eddies composing the low frequency part of the atmospheric turbulence cannot 'develop' vertically and laterally. Therefore, it is difficult to establish a universal limit as the effect of walls depends on the size of eddies and the shape of the structure reproduced, but a 5% to 10% blockage ratio is often taken as a maximum.

A third limit is linked with surface state characteristics and machining precision. At a scale of 1/200, a mistake of 0.1 mm on a building model corresponds to 20 cm at full scale. This means models should be machined with a precision of $1/100^{th}$ mm – this is costly and in real life, often impossible to attain on complex shaped models made of easily machined materials. The best commonly available precision delivered today in 3D printing and classical machining is close to 100 microns – this limits the downscaling to 1 to 10 for a very good geometrical precision and 1 to 100 for moderately good precision. 1 to 1000 is often considered as 'coarse' and may be unable to deliver accurate results. The second aspect when downscaling is the surface roughness. The painted surface of a steel structure has a characteristic roughness of 10^{-6} to 10^{-7} compared to its overall size. Reproducing the same roughness in a wind tunnel on a model downscaled 1 to 100 would mean making surface state of less than 1 μm, which is the surface state of a mirror. Once again, it is at the same time very difficult and costly (if not totally impossible) to achieve such precision. In actuality, the wind engineer may find an interest in reproducing rougher surfaces in the small scale model. With respect to the aforementioned drag crisis phenomenon on circular cylinders, this can

be triggered at lower wind speeds, i.e. lower Reynolds numbers, by increasing the roughness of the surface; various kinds of artificial roughening are used in the wind tunnel. These can include glued sand, added strips or ligneous material such as wood or dots. Whatever the method and it's efficiency, the aim is to counterbalance the lack of inertial forces compared to viscous forces by forcing separation to occur at a given point on the boundary layer at the skin of the model. This strategy is commonly named the 'increase of the apparent Reynolds number' and can be easily calibrated by making models of the same structure at different scales and comparing the surface pressure patterns and aerodynamic loads measured in the wind tunnel. This approach requires the use of a large wind tunnel that has the capability of testing models of the same shape with a scale ratio close to 10 without blockage effects.

As a matter of synthesis, downscaling effects are complex and cannot be restrained to simple recipes that would work in all cases. The scaling effect in wind tunnel experiment should be studied first, for instance by repeating the experiment at various Reynolds numbers. Attention must be paid to each aerodynamic phenomenon involved in a complex study: it is common that in the same study in the wind tunnel, two phenomena acting jointly will not have the same downscaling process.

3. Some examples of scaling studies in the wind tunnel

3.1. Scaling the drag of cylindrical buildings

The first need for such a scaling study appeared in the 1990s for a high rise tower in Paris, the shape of which was close to a cylinder. This tower, designed by famous architect Jean Nouvel, was named 'la Tour Sans Fins', which means 'the endless tower', because its summit was to vanish in the sky, with no clear limit, with its outer skin becoming more and more porous with altitude. The same concept is now widely seen in recent tower designs. Because the shape was not a perfect cylinder and with the aim of a 1/300 scaled model in BLWT, it was decided to make a first model 10 times the diameter of the tower model but without the same diameter to height ratio, and carefully measure the pressure pattern around it in the large, high-speed Jules Verne wind tunnel [5]. With a diameter of 0.8m and a flow speed of 80 m/s, the corresponding Reynolds number of 4.0 E^6 was reached – this was considered high enough to be representative of the full scale value of 7.0 E^7. Bearing this reference pressure pattern in mind, the 1 to 300 scale model was built and tested with the same kind of flow at wind speeds corresponding to the BLWT test and with various arrangements of added roughness on the model surface. It was found that meridional strips with a thickness of 0.6 mm and a step of 15° provided the best artificial surface roughening in this case. The same question was addressed some years later for the European Launcher Ariane 4, then Ariane 5, with models at a scale of 1 to 100. Similar tests were conducted, first in a high Reynolds number condition in a large wind tunnel, then at lower wind speed in the boundary layer wind tunnel with calibration of the relevant roughening. It must be pointed out that in both cases, longitudinal strips proved to be the only efficient manner to reach the required apparent Reynolds number, while sand roughness was not rough enough.

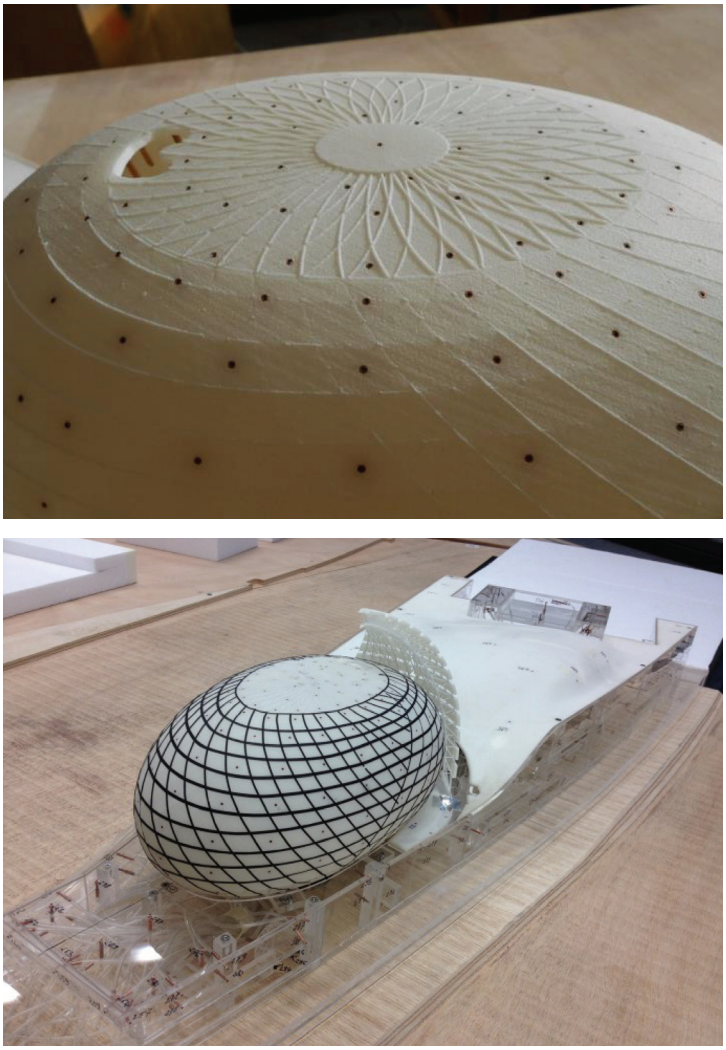

Fig. 2. Extra trips on a powder sintered model for reaching the right roughness in BLWT

3.2. Scaling the porosity of cladding elements

There are a series of recent cases of high-rise buildings incorporating sun shades for the reduction of solar energy input in summer time. Architects also try to use these external structures to give the building a unique appearance, changing the shape and size of these elements across the façade, requiring the design engineer to carefully design them. Due to their exposure at the façade, they are subject to high wind loads, sometimes in accelerated flow areas.

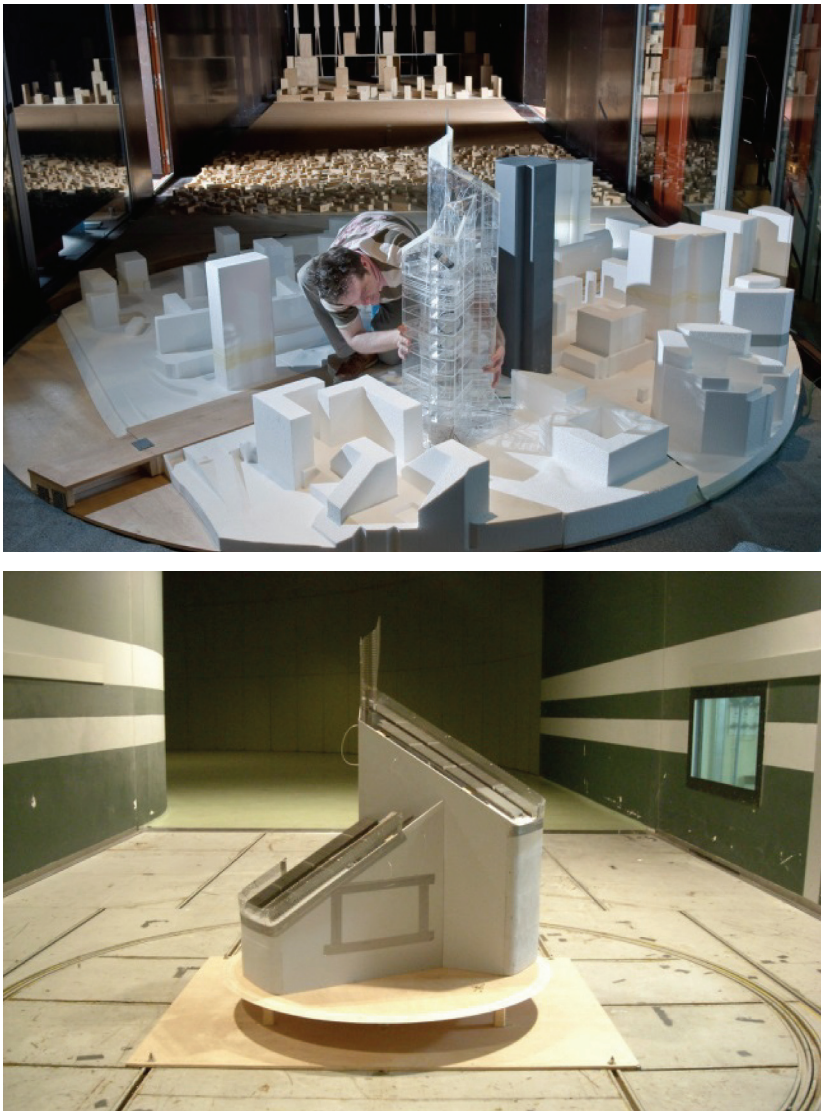

Fig. 3. High rise building scaled 1/200 in BLWT (top) and model of the top of the same tower at a 1/50 scale in a high-speed wind tunnel (bottom) for measurements at a high Reynolds number

At the usual scale of buildings in BLWT; typically from 1/200 to 1/500, it is rather difficult to reproduce the detailed shape and porosity of the shades. The porosity of these screens is especially poorly represented at a very reduced scale because the viscous part in the Reynolds number is considerably increased. Therefore, the classical BLWT model is used to determine global wind forces and flow fields around the building in its environment and a second model of the façade is usually built, at a larger scale, say 1/50, for the fine modelling of wind loads on the shading structures.

3.3. Scaling snow in climatic wind tunnel

There are many questions raised by the researchers involved in the investigation of snow loads. Failures induced by snow ingress in systems, snow accretions on structures and vehicles are efficiently studied by full scale approaches either outdoor or in laboratory environment. On the other hand, questions dealing with large environments, typically interaction between various structures and their surroundings can only be studied with reduced scale models. Snow accumulation around buildings belongs to this category. Reliable experimental modelling in the wind tunnel depends on geometric, dynamic and kinetic criteria: snow particles (shape, density, velocity, drag, lift, liquid water ratio) and wind (temperature, speed, turbulence) must be modeled. Experiments are commonly based on theoretical approaches first introduced by Kind [6] and Iversen [7].

Since a thorough examination of similitude criteria reveals incompatibilities, choices have to be made according to their relevance. Snow particles are usually modelled using sand, sawdust or glass balls which do not reproduce all inter-particle forces. However, it is advisable to use a model particle which reproduces the shapes and stacking up of actual snow particles. From this point of view, artificial snow, although scarcely used as a model particle in the wind tunnel, is the most appropriate choice.

Table 1

Similitude parameters for particles transport and accumulation with D_p particle diameter, L reference length, g gravity, ρ fluid density, ρ_p particle density, u_t^* threshold friction velocity, u^* friction velocity, u reference wind velocity

D_p/L	Geometric ratio particle length/building
$u_t^{*2}/D_p g\left(\rho/(\rho_p-\rho)\right)$	Froude number for particle friction threshold
$u_t^{*2}/Lg\left(\rho/(\rho_p-\rho)\right)$	Froude number for friction on the building
u^*/u_t^*	Threshold speed/friction speed ratio
u^*/u	Friction/fluid speed ratio
$u^2/D_p g\left(\rho/(\rho_p-\rho)\right)$	Froude number for particle transport
u^2/Lg	Conventional Froude number
ρ_p/ρ	Particle/fluid density ratio

A noticeable disagreement of the prototype and model Froude number, based on the threshold friction velocity weighted by the particle/fluid density ratio, indicates that the

trajectory of the model particle is different from that of the natural snow particle. According to Kind [6], if the Froude number is not conserved, it is particularly important to verify that the saltation length, which represents 10 times the saltation height, is shorter than the model reference length and the typical size of snow drifts. In practice, this may be verified with moderately reduced scale models.

In the same way, the forces on particles are better modeled if the Reynolds number based on the saltation height is greater than 30.

Regarding the suspended particles, the particulate Froude number, weighted by the density ratio, is the parameter which allows assessment of the similarity of the transport mechanism, globally around the building or locally which drives the accumulation process. Finally, a choice has to be made between the saltation mechanism (close to the ground surface) or long distance transport processes.

In practice, the wind engineer settles simple rules for common applications, essentially considering the simulation of the drifting volume v_0. The basic similitude parameter is v_0/L^3, where L is the reference length of the structure, which leads to the simple criteria

$$\left(1-\frac{u^*}{u}\right)\left(\frac{u^2}{Lg}\right)_p = \left(1-\frac{u^*}{u}\right)\left(\frac{u^2}{Lg}\right)_m \tag{1}$$

where indexes p and m stand respectively for the prototype and the model. This relationship does not imply any constraint regarding particle density and size. Hence, the model particle scale does not interfere with the drifting volume simulation.

The experiment duration, which is a main parameter of reduced scale simulation, can be calculated according to several dimensionless time numbers. Various expressions can be found in literature. Each of the dimensionless times of Table 2 leads to a different snowstorm duration and there is no real agreement about what criteria should be used.

Table 2

Dimensionless time used to assess the equivalent snow event duration

ut/L
$\rho/\rho_p . ut/L$
$1/2\,\rho/\rho_p\, u^2/gL\left[1-u_0/u\right]ut/L$
$tQ\eta/\rho_p L^2$

Therefore, it is quite advisable to rely on the measurement of a real outdoor accumulation if available – this can be compared to its wind tunnel counterpart.

Fig. 4. Testing snow accumulation in the climatic wind tunnel at full scale (top) and reduced scale (bottom)

4. Conclusion

It was exposed in this keynote lecture that downscaling in wind tunnel always leads to making choices. Because every part of aerodynamic forces cannot be faithfully reproduced, the wind engineer must in practice give advantage to the main phenomenon with respect to the final need. Because scale effects are mostly complex, it proved useful in many cases to calibrate the scaled simulation by comparison with a full-scale reference. In practice, such a strategy is highly recommended.

References

[1] Vaschy A., *Sur les lois de similitude en physique*, Annales Télégraphiques, Vol. 19, 1892, 25-28.

[2] Buckingham E., *On physically similar systems. Illustrations of the use of dimensional equations,* Physical Review, Vol. 4, 1914, 345-376.

[3] Davenport A.G., Vickery B.J., Holmes W.H., *The structural and environmental effects of wind on buildings and structures*, Post graduate course of the University of Sidney, School of Civil Engineering, Sydney 1975.

[4] Roulle C., *Reproduction du régime hypercritique sur formes rondes en soufflerie à couche limite atmosphérique*, CSTB report n°EN-ADIM 80-20L, 1980.

[5] Lemoult B. et al., *Caractérisation des efforts aérodynamiques développés sur un cylindre en régime supercritique, simulation en soufflerie*, CSTB report n°EN-SC 90.11-C, 1990.

[6] Kind R.J. *A critical examination of the requirements for model simulation of wind induced erosion deposition phenomena such as snow drifting*, Atmospheric Environment, Vol. 10(3), 1976, 219-227.

[7] Iversen J.D., *Drifting snow similitude*, Proc. ASCE, Journal of Hydraulics Division, Vol. 105, 1979, 737-753.

[8] Delpech P. et al., *Snowdrifting simulation around antarctic buildings*, Journal of Wind Engineering and Industrial Aerodynamics, Vol. 74-76, 1988, 567-576.

TECHNICAL TRANSACTIONS | CZASOPISMO TECHNICZNE
CIVIL ENGINEERING | BUDOWNICTWO
2-B/2015

RICHARD G.J. FLAY*

MODEL TESTS OF WIND TURBINES IN WIND TUNNELS

BADANIA MODELOWE TURBIN WIATROWYCH W TUNELACH AERODYNAMICZNYCH

Abstract

This paper describes methods for testing model wind turbines in wind tunnels based on published data and the experience gained by the author through having tested many different wind turbines in wind tunnels at the University of Auckland. Wind tunnels can be used to determine the performance of small wind turbines at full scale, or larger wind turbines at reduced scale. Such experiments need to be done with care as one needs to be aware of issues regarding blockage, the effect of Reynolds number, and being able to control the speed of the turbine so that is power coefficient can be obtained over a suitable range of tip speed ratios. With rotating machinery, it is also important to have a regard to safety, so the models have to be made with care and a stress analysis carried out to ensure that the material properties are not exceeded during the testing. It is found that wind tunnel testing is a useful way of determining experimentally the performance of wind turbines in order to predict the power output, and for obtaining data to validate theoretical or numerical model predictions.

Keywords: wind engineering, wind energy, wind tunnel test, blade aerodynamics, renewable energy, blockage correction

Streszczenie

W poniższym artykule opisano metody testowania modeli turbin wiatrowych w tunelach aerodynamicznych na podstawie opublikowanych danych oraz doświadczenia autora uzyskanego w wyniku badań wielu turbin wiatrowych przeprowadzonych w tunelach aerodynamicznych Uniwersytetu w Auckland. Tunele aerodynamiczne mogą być wykorzystywane do wyznaczania wydajności małych turbin wiatrowych w pełnej skali, albo większych turbin w skali zredukowanej. Takie doświadczenia muszą być przeprowadzane bardzo starannie, ze zwróceniem uwagi na takie problemy, jak efekt blokady, efekt liczby Reynoldsa. Trzeba także mieć możliwość kontrolowania prędkości turbiny, tak aby współczynnik mocy mógł być uzyskany w odpowiednim zakresie współczynnika szybkobieżności. W przypadku maszyn wirnikowych ważne jest zapewnienie bezpieczeństwa, tak aby modele były wykonane z należytą starannością na podstawie przeprowadzonej wcześniej analizy wytrzymałościowej, co pozwala upewnić się, że odpowiednie charakterystyki materiałowe nie zostaną przekroczone w trakcie badań. Stwierdzono, że badania w tunelu aerodynamicznym to użyteczna metoda doświadczalnego wyznaczania wydajności turbin wiatrowych. Pozwalają one przewidzieć moc wyjściową oraz inne dane umożliwiające walidację modeli teoretycznych i numerycznych.

Słowa kluczowe: inżynieria wiatrowa, energia wiatrowa, badania w tunelu aerodynamicznym, aerodynamika łopat turbin, energia odnawialna, korekcja efektu blokady

DOI: 10.4467/2353737XCT.15.125.4162

* Department of Mechanical Engineering, University of Auckland, New Zealand.

1. Introduction

As the population of Earth grows, so does its use of energy. Fossil fuels have provided energy for mankind for centuries, but the remaining coal and oil is harder to extract and thus more expensive. Coupled with this is our knowledge that burning fossil fuels releases carbon dioxide into the atmosphere and this can contribute to global warming, a serious issue that mankind has to face. This background has increased the focus on renewable energies like wind. Wind energy is abundant, free, environmentally friendly and inexhaustible. Consequently it has been one of the largest sources of new electricity generation in many parts of the world in recent times. Further details on wind energy can be found in the World Wind Energy Association reports [28].

Recent rapid growth in wind energy has been driven by advances in turbine technology, which have allowed wind turbine sizes to be increased from 15 m in diameter in the 1980s, to over 150 m today. Turbine capacity has grown from 55 kW to 5 MW, with turbines having diameters of 100 m or more. The world's largest wind turbine called the Sea Titan has a diameter of 190 m, a rotational speed of 10 rpm, and a rated power of 10 MW. It is interesting that its tip speed ratio, $V_t = (10/60)(2\pi)(190/2) = 99.5$ m/s, which is approximately one third of the speed of sound and so the air can be assumed to be incompressible.

Clearly with such a large investment in wind energy there is a need for considerable research on wind turbine performance. The aerodynamics can be explored using theoretical methods, numerical computations, full-scale monitoring as well as wind tunnel testing. It is usual to attack such problems using more than one approach in order to validate and check predictions of performance, loads, dynamics etc. Wind tunnel testing is one of these options and is described in detail in the present paper.

2. Literature Review

The University of Auckland has had a longstanding interest in wind energy, beginning at the time of the rapid increase in the price of oil in the 1970s. Two Darrius wind turbines were built and tested at the Universities of Auckland and Canterbury [5]. At the same time, research was being undertaken by Lindley et al. [18] to measure wind structure at levels relevant to wind turbines. In more recent times, there has been considerable research undertaken at the University of Auckland where the wind tunnel has been an important tool in determining the performance of non-conventional wind turbines, namely a diffuser augmented wind turbine (e.g. [20]), and wind turbine blades with extendable [16].

A perusal of the recent literature on wind tunnel testing of wind turbines shows that it is an active area and that wind tunnel tests are being carried out all over the world to investigate various aspects of wind turbine performance. For example Bottasso et al. [4] describe testing in a very large wind tunnel, which is aeroelastically scaled, and features active individual blade pitch and torque control. The flow simulation took place in a boundary layer wind tunnel.

Wind tunnel testing of wind turbine models to investigate aerodynamics have been reported by, for example, Oku et al. [19], Hand et al. [12], Vermeer et al. [26], Snel et al. [24]

and Schepers and Snel [23]. These and similar studies have produced valuable information and measurements regarding the performance of rotors and the behaviour of airfoils, blades and wakes, which has helped the understanding of the aerodynamics, and has also provided valuable information for validation and calibration of mathematical models.

3. Wind tunnel calibration

It is important when undertaking any measurement in a wind tunnel to measure the reference quantities precisely in order to be able to determine the appropriate coefficients. One of the most important measurements is that of the reference dynamic pressure at the vicinity of the test model. From the dynamic pressure the velocity can be determined. In the case of testing wind turbines, the plane where the model blade plane is to be located should be surveyed with a Pitot-static or other high quality probe, such as a Cobra probe [6, 13] in order to determine the uniformity of the flow field. The average dynamic pressure over this plane can then be related to the reference pressure measuring system using the procedure outlined below.

The reference dynamic pressure is usually measured with a high quality pressure transducer connected either to pressure taps in the wind tunnel contraction, or to a reference Pitot-static probe located well upstream and away from the test model, so that it is not influenced by the pressure field generated by the model itself. In this example, I will assume that the reference pressure is being measured by contraction pressure taps, as shown in Fig. 1. Sometimes the reference pressure taps at the contraction inlet and outlet are manifolded together from taps on the top, bottom, far and near sides, but this is probably not necessary. The most important thing is that they are installed in a careful and professional manner so that there are no burrs and that the taps are flush with the surface and normal to it.

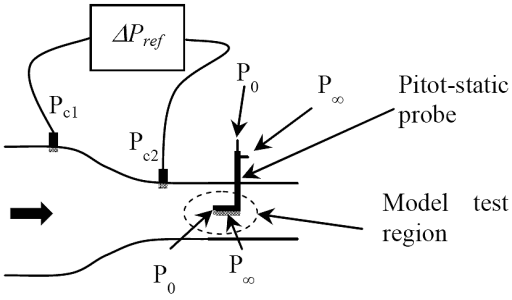

Fig. 1. Schematic diagram of a wind tunnel contraction with pressure taps, and a Pitot-static probe located at the centre of the test region

An empty wind tunnel calibration is done prior to putting the model in the wind tunnel. It is assumed that all pressure differences in the wind tunnel are proportional to each other. The wind tunnel fan is then turned on and the speed varied over the range that will be used for the

testing. At the same time, the pressure differences P_{c1} - P_{c2}, P_∞ - P_{c2} and P_0 - P_∞ are measured simultaneously. The pressure differences P_0 - P_∞ and P_∞ - P_{c2} are then plotted against P_{c1} - P_{c2} as shown in Fig. 2 in order to obtain the slopes, $k_{q\infty}$ and $k_{p\infty}$ of straight lines fitted to the data points.

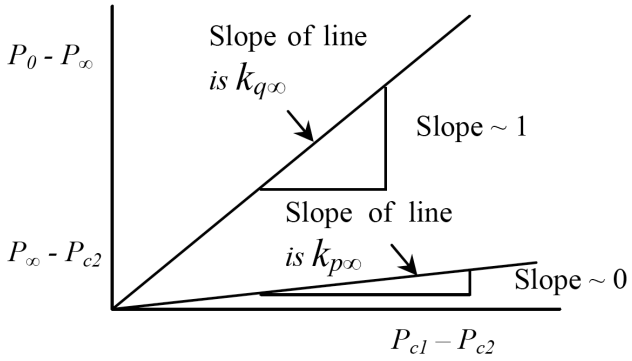

Fig. 2. Plot of wind tunnel pressure measurement data to derive test section calibration data

Referring to Fig. 2, it is evident that

$$k_{q\infty} = \frac{P_0 - P_\infty}{P_{c1} - P_{c2}} \tag{1}$$

and that

$$k_{p\infty} = \frac{P_\infty - P_{c2}}{P_{c1} - P_{c2}} \tag{2}$$

During an actual test a model will be located in the wind tunnel at the location of the Pitot-static probe shown in Fig. 1. However, the dynamic pressure there may be determined by measuring the contraction pressure drop and using Eqn. (1), viz,

$$q_\infty = P_0 - P_\infty = k_{q\infty}\left(P_{c1} - P_{c2}\right) \tag{3}$$

The static pressure at the model location can be determined by rearranging Eqn. (4).

$$P_\infty = P_{c2} + k_{p\infty}\left(P_{c1} - P_{c2}\right) \tag{4}$$

Force coefficients, e.g. thrust on the wind turbine can now be determined from the dynamic pressure resulting from Eqn. (3). For example if the force measured is T, then the coefficient is given by Eqn. (5).

$$C_T = \frac{T}{A_{ref} q_\infty} \tag{5}$$

where A_{ref} is a reference area for coefficients.

Pressure coefficients, e.g. on a wind turbine blade at position "x", may also be determined. An approximate "raw" coefficient may be determined using Eqn. (6).

$$Cp_x^* = \frac{P_x - P_{c2}}{P_{c1} - P_{c2}} \tag{6}$$

A corrected pressure coefficient may be determined using Eqn. (7).

$$Cp_x = \frac{P_x - P_\infty}{P_0 - P_\infty} = \frac{P_x - \left(P_{c2} + k_{p\infty}\left(P_{c1} - P_{c2}\right)\right)}{k_{q\infty}\left(P_{c1} - P_{c2}\right)} \tag{7}$$

Now by expanding Eqn. (7), it can be written in terms of Cp_x^* and the calibration values, as shown below in Eqn. (8).

$$Cp_x = \frac{P_x - P_{c2}}{k_{q\infty}\left(P_{c1} - P_{c2}\right)} - \frac{k_{p\infty}\left(P_{c1} - P_{c2}\right)}{k_{q\infty}\left(P_{c1} - P_{c2}\right)} = \frac{Cp_x^*}{k_{q\infty}} - \frac{k_{p\infty}}{k_{q\infty}} \tag{8}$$

The author has sometimes seen pressure distributions on aerofoils which appear to be shifted on the ordinate. This may have occurred because the reference pressure for the coefficients was offset slightly from the actual pressure P_∞ that existed there.

4. Similarity requirements

The relevant dimensionless quantities for wind turbine testing are considered in this section.

Probably the most important dimensionless quantity is the so-called tip speed ratio, often given the symbol λ, $\lambda = \omega R / V_\infty$ where $\omega R = u_{\text{tip}}$ the blade tip speed, ω is the rotational speed in radians per second, R is the blade radius and is the free-stream wind speed. λ is often around 5-8 for horizontal axis wind turbines. It is important in wind tunnel testing to keep this parameter the same as in full-scale, as it controls the direction of the flow onto the blade.

The Mach number for a wind turbine can be defined by $M = u_{\text{tip}}/a$, where $u_{\text{tip}} = \omega R$, a is the speed of sound, and is typically around 340 m/s. As noted in the introduction, the blade tip speed is typically up to around 100 m/s. At this speed M = 0.3, which is low enough for compressibility to be neglected.

The Reynolds number, $\text{Re} = VL/\nu$, where V is reference speed, L is a reference length and ν is the kinematic viscosity of the fluid. In the present case, we may write $V = u_{tip} = \omega R$, and $L = c$, the reference blade chord, which is proportional to R for a geometrically similar blade.

Hence for wind turbine testing the Reynolds number can be written $\mathrm{Re} = \omega R^2/\nu$. For testing in air, the kinematic viscosity is unchanged. The model is reduced in size by the scale factor. Hence if the wind tunnel speed is the same as the full scale speed, the product ωR will also be the same in order keep the same tip speed ratio, and so Re will be lower by approximately the model scale factor.

The model scale factor for a 100 m diameter rotor would be of the order of 50 in order to have a 2 m diameter model, and so Re will reduce by a factor of 50 or so. The full scale Reynolds number will be of the order of $\mathrm{Re} = \omega R^2/\nu = 100 \cdot 3/(15 \cdot 10^{-6}) = 20 \cdot 10^6$ (which is a very high Reynolds number) whereas the model scale Reynolds number would be around 2 to $4 \cdot 10^5$. Since the model scale Reynolds number will be substantially lower than the prototype wind turbine, it is important that during the design of the model for the wind tunnel tests that the lift and drag characteristics as a function of Reynolds number are researched to check that there is no substantial difference in performance at the reduced Reynolds numbers. If it is found that the blade profile is rather sensitive to Re, then perhaps a different profile could be used for the wind turbine model. One would select a profile with properties that are relatively insensitive to Re for the range of values that are anticipated in the tests.

These dimensionless groups are the most important and lead onto the next section, corrections for wind tunnel blockage.

5. Correction for wind tunnel blockage

It is very well known that when a model is placed in a solid wall wind tunnel that an error in the resulting force or other measurements will occur due to the acceleration of the air in the gap between the wall and the model itself. This increase in the dynamic pressure in the gap causes a larger pressure drop than would occur in the "free air", and so the model base pressure drops, thereby causing an increase in the pressure difference between front and rear, and thus an increase in the drag. This phenomenon does not occur from tests in a free jet with a constant pressure boundary condition at the jet boundaries, as the flow is free to expand away from the model and generally the force is underestimated, and the error is of order half or less that which would occur in a solid wall wind tunnel with the same blockage.

Other errors can occur, e.g. for long models in a wind tunnel with a longitudinal static pressure gradient a "buoyancy" correction must be applied. Further details of these and other corrections can be found in Barlow et al [3]. Blockage corrections are also discussed by Wilson et al [27] and by Chen and Liou [7] who carried out an experimental investigation on the effects of blockage.

An elegant theory for the effect of blockage on testing airscrews (propellers) in wind tunnels was worked out by Glauert [11]. This has been illustrated for wind turbine testing in the present paper.

Consider a wind turbine rotor placed in a circular cross-section wind tunnel of area C. Assume that the drag is uniformly distributed over the whole of the swept area and that the axial velocity of the air has a constant value over this disc and over a cross-section of the wake well downstream. This situation is shown schematically in Fig. 3. The stream-tube enveloping the blade-plane expands in area both upstream and behind the blade plane, as the

air experiences the resistance of the disc. The air approaches the blade plane at speed V_∞. u is the axial velocity at the blade plane, u_1 is the velocity within the stream-tube well downstream and u_2 is the axial velocity outside the stream-tube well downstream. A_∞ is the upstream area of the stream-tube enveloping the blade-plane, which increases to area A at the blade-plane and increases further to area A_1 well downstream. P_∞ is the static pressure in the wind tunnel well upstream of the blade-plane, and P_1 is the static pressure well downstream.

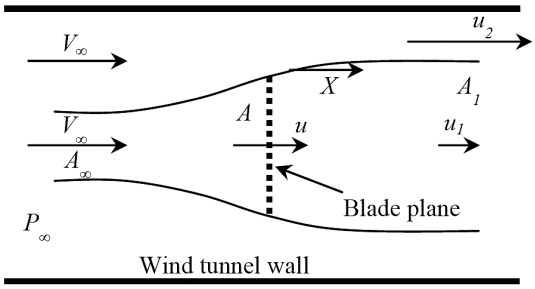

Fig. 3. Schematic diagram of a stream-tube enveloping a wind turbine rotor located centrally in a circular section wind tunnel

Then from the continuity equation, it follows that

$$u_1 A_1 = uA \tag{9}$$

$$u_2 \left(C - A_1\right) = V_\infty C - uA \tag{10}$$

The total pressure of the fluid stream (H_∞) remains constant outside the stream-tube, whereas the total pressure inside the stream-tube reduces to H_1 due to the drag which is applied by the turbine disc.

$$H_\infty = P_\infty + \frac{1}{2}\rho V_\infty^2 = P_1 + \frac{1}{2}\rho u_2^2 \tag{11}$$

$$H_1 = P_1 + \frac{1}{2}\rho u_1^2 \tag{12}$$

Hence from Eqns. (11) and (12) the reduction in total pressure is

$$H_\infty - H_1 = \frac{1}{2}\rho\left(u_2^2 - u_1^2\right) \tag{13}$$

This reduction in total pressure is equal to the static pressure drop across the blade plane, and hence the drag force (T) on the blades is given by Eqn. (14).

$$T = A\frac{1}{2}\rho\left(u_2^2 - u_1^2\right) \tag{14}$$

The momentum equation is now applied to the flow both inside and outside the stream tube, and enables the reduction in pressure in the far wake to be determined.

$$\left(P_\infty - P_1\right)C - T = A_1\rho u_1\left(u_1 - V_\infty\right) + \left(C - A_1\right)\rho u_2\left(u_2 - V_\infty\right) \tag{15}$$

From Eqn. (13), the reduction in pressure in the wake is given by Eqn. (16).

$$P_\infty - P_1 = \frac{1}{2}\rho\left(u_2^2 - V_\infty^2\right) \tag{16}$$

The drag coefficient of the disc is now defined as

$$C_T = \frac{T}{A\frac{1}{2}\rho V_\infty^2} \tag{17}$$

Some rather non-trivial algebraic manipulation is then required to simplify the equations into a form that can be used to assess the effects of blockage ratio on the results. The required manipulation has been carried out by Glauert [11] in his development to assess the effect of blockage on propeller testing. For this testing, an "equivalent free air speed V'" has been defined, as the speed which corresponds to the same values of the thrust T and of the axial velocity u as obtained in the wind tunnel with an upstream speed of V. For the case of propellers being tested in a solid wall wind tunnel, Glauert's correction can be plotted as in Fig. 4. Note here that Glauert's thrust coefficient τ, is based on double the reference wind tunnel upstream dynamic pressure, i.e. $\tau = T/(A\rho V^2)$. A/C is the ratio of the propeller swept area to the wind tunnel area.

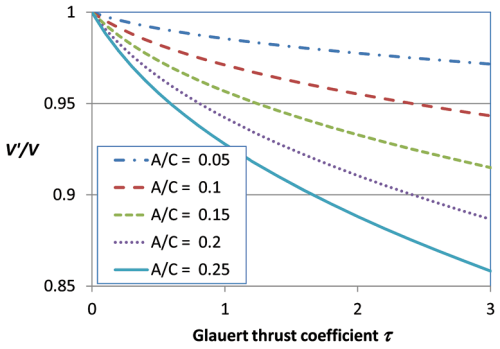

Fig. 4. Ratio of equivalent air speed to reference wind tunnel speed as a function of area blockage and thrust coefficient, for a propeller test

Glauert notes that typical tests are done at blockage ratios of 0.15.

The blockage correction for testing wind turbines in wind tunnels is discussed by Wilson et al [27]. They use the method developed by Glauert and give the resulting correction in a figure which is reproduced here as Fig. 5. The measured coefficient of thrust in Figure 5 is determined using Eqn (17), and then the power coefficient (C_p) correction is applied using the measured ratio of wind tunnel area to wind turbine blade-plane (swept) area.

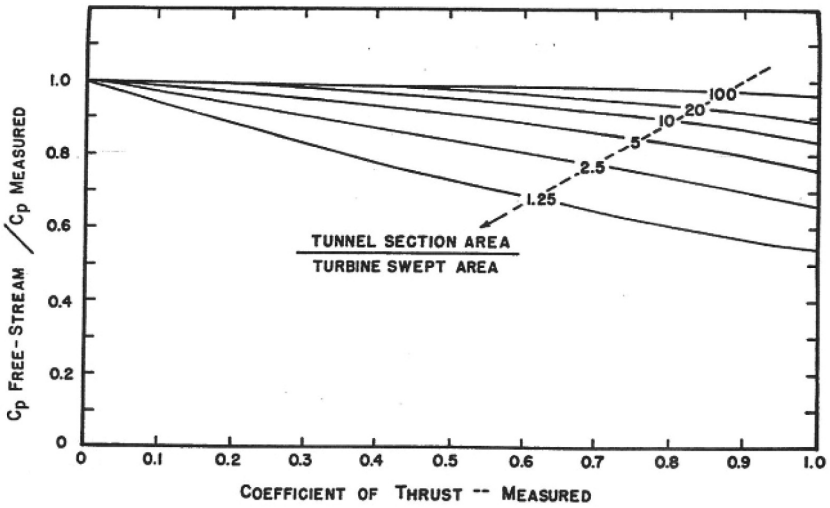

Fig. 5. Blockage correction for wind turbine testing [27]

From the Betz actuator disc theory, it can be shown that the ideal thrust coefficient is 8/9. For this thrust coefficient and for 20% blockage, the ratio of free-stream to measured power coefficient is 0.8, meaning a 25% overestimate, which is quite significant. If the blockage is reduced to 10%, then the overestimate on power coefficient is reduced to 15%.

Testing in an air jet has significant advantages for both propeller and wind turbines. Whereas a solid-wall test section constrains the flow in such a way that the streamlines adjacent to the wall must travel along the wall, the boundary condition for a free jet is a constant pressure. Hence the jet can expand due to the pressure field imposed by a wind turbine rotor. In this case the power coefficient determined in a wind tunnel test can be expected to be smaller than in free air, as the jet will expand more than it should. However, this effect is much smaller that the overestimate provided by a solid wall boundary. Glauret [11] states that in testing propellers with diameter ratios up to about 0.7 (49% area blockage) in a free jet gave interference free results. Hence most of the early testing of propellers at Farnborough was done in open jet wind tunnels.

Some wind tunnel designers have therefore tried to design test sections that are a combination of solid and open walls in order to have a zero blockage effect. This is sometimes called a blockage tolerant test section. A simple example of such a test section is shown in Fig. 6, which is a photograph of a wind tunnel (1.5 m x 1.5 m cross-section) and diffuser augmented wind turbine model at the University of Auckland.

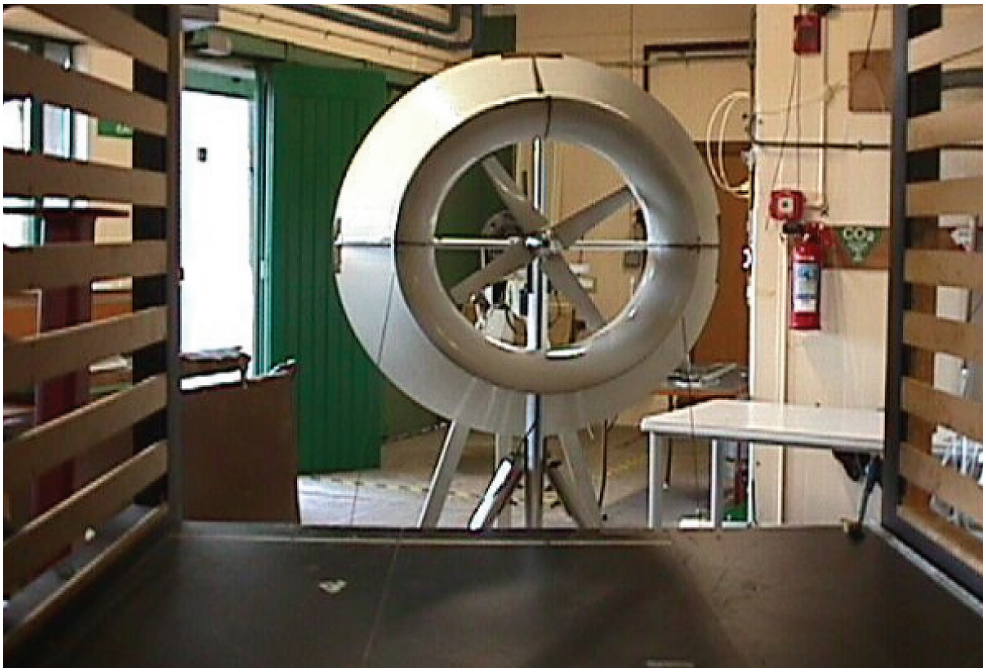

Fig. 6. Photograph of wind turbine model positioned downstream of a slotted wall wind tunnel designed to reduce blockage corrections

6. Examples of wind tunnel tests

Some recommendations on how to carry out wind tunnel tests on model wind turbines are now discussed and are based on testing that has been carried out in the writer's laboratory.

6.1. Wind tunnel testing diffuser augmented wind turbines

The author was asked to assist a company that had begun to build a diffuser augmented wind turbine, based on work done by researchers at Grumman [10]. A 7 m diameter prototype was built near Auckland, and is shown in Fig. 7.

The performance of the wind turbine was less than predicted and so a programme of work was carried out to try to ascertain why this was the case. A PhD student was recruited to work on the project. Investigations took place using CFD and wind tunnel experiments, as well as measurements on site using pressure transducers with self-orientating Pitot-static tubes, as well as other instrumentation. Several of the following figures were used from the thesis that resulted from this research [21].

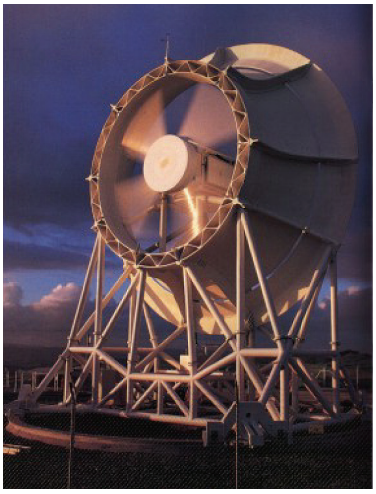

Fig. 7. The Vortec 7 diffuser augmented wind turbine at Waikaretu, New Zealand

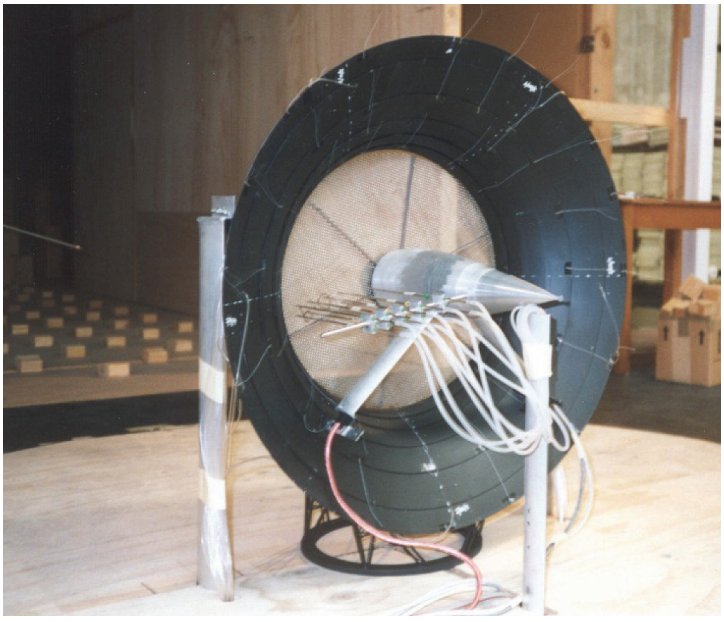

Fig. 8. Wind tunnel model of a diffuser augmented wind turbine with a wire mesh screen to simulate the blades, and with a rack of Pitot tubes to measure the pressure drop and flow speed through the blade-plane

In order to find out if the blade loading was matched to the diffuser, a model scale Vortec 7 wind turbine was constructed and then tested in the University of Auckland's large 7 m x 3.5 m wind tunnel. Fig. 8 shows the model in the wind tunnel. The blades have

been replaced by wire mesh screens of suitable pressure drop coefficient. Screens are very convenient to use for testing and can give a good indication of potential output of wind turbines. In the present design, it is important to match the resistance at the blade plane to the diffuser area ratio. An estimate of the power output can be made by measuring both the flow speed through the mesh, u, as well as the pressure drop, ΔP. Then the power is

$$\dot{W} = Au\Delta P \tag{17}$$

where the pressure drop is

$$\Delta P = k_s \frac{1}{2}\rho u^2 \tag{18}$$

Hence,

$$\dot{W} = Ak_s \frac{1}{2}\rho u^3 \tag{19}$$

It is much more challenging to build model wind turbines with small blades. Notwithstanding the lack of Reynolds number similarity, it is difficult practically to build small blades. However, this was necessary in the Vortec project and after the optimum pressure drop was determined from tests using a range of screen pressure drop coefficients in preliminary tests, blades were designed in such a way that their pressure drop (or drag) coefficient was the required value.

A wind tunnel model equipped with blades can be seen in Fig. 9.

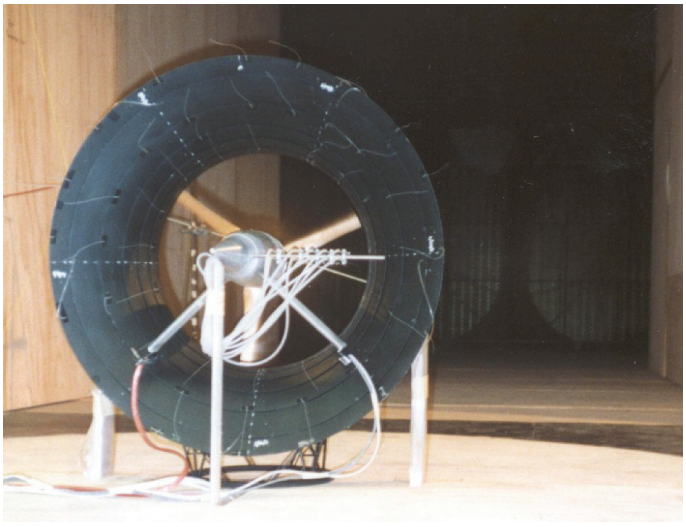

Fig. 9. Wind tunnel model equipped with blades and a Pitot tube rack to measure pressures and speeds

Typical results from wind tunnel test with screens and blades can be seen in Fig. 10.

Fig. 10 shows a range of results from the blade tests for different blade loadings. The axial drag from the blades was altered by changing the pitch angle as well as the tip speed. The screen loading was changed by using screens of differing porosities. The results from the blade tests are rather impressive and were obtained by using a special hub, which measured the thrust and torque to a motor/generator whose rotational speed could be set remotely. Thus by changing the motor speed, the required tip speed ratios for an individual test could essentially be dialled up. This is also illustrated in Fig. 11. The excellent spread of results illustrates that this feature is powerful in carrying out such wind tunnel tests. It should be noted that the augmentation is larger when the blades are used instead of the wire mesh screens. It is believed that this is because of the turbulence and swirl that is generated by the blades that travels downstream and makes the diffuser perform more efficiently.

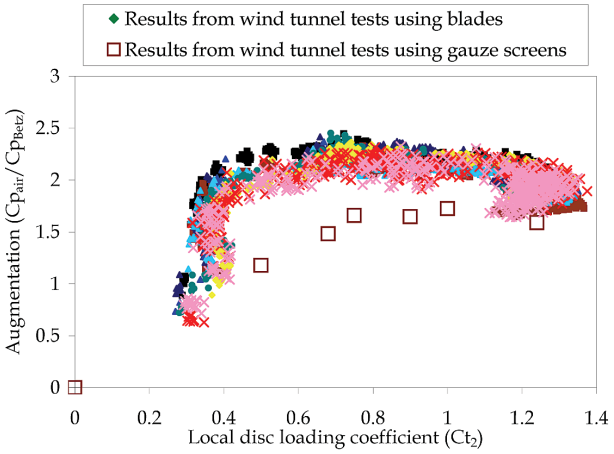

Fig. 10. Typical results from the wind tunnel comparing performance with a screen with that of blades

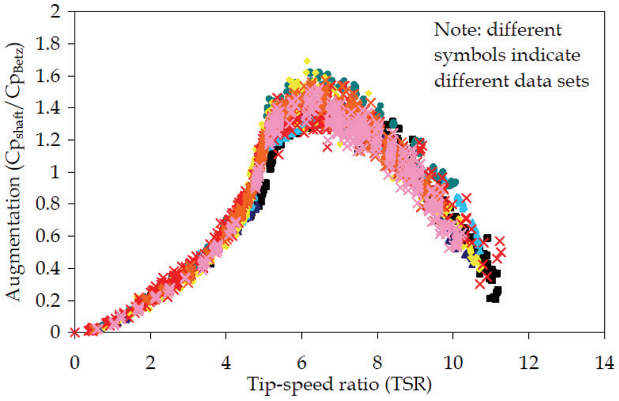

Fig. 11. Augmentation of wind turbine for a wide range of tip speed ratios that could be set by the motor/generator wind turbine load

6.2. Wind tunnel tests of telescoping blade wind turbine

Another interesting study on wind turbines was carried out by a former PhD student, Imraan [14], and concerned increasing the output of wind turbines by using telescoping blades. Further details on this research project can be found in Imraan et al. [15].

A significant aspect of this research resulted from careful wind tunnel tests using various blades. The same instrumented hub was used for this research as for the earlier work by Phillips [21]. The hub and rotor with three blades attached is shown in Fig. 12. Note its streamlined shape. A close-up photograph of the hub is shown in Fig. 13. As explained above, the hub contains a variable speed motor/generator. Although it is not very clear in Fig. 13, the motor/generator system is attached to ground via strain-gauged links that enable both the torque and thrust to be measured. A small l.e.d. is evident at the top of Fig. 13. This led is used to measure the rotational speed.

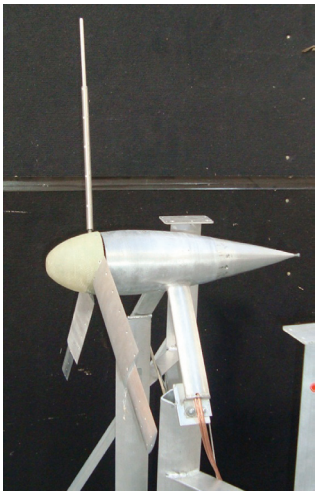

Fig. 12. Photograph of wind turbine model with stepped blades mounted on the instrumented hub

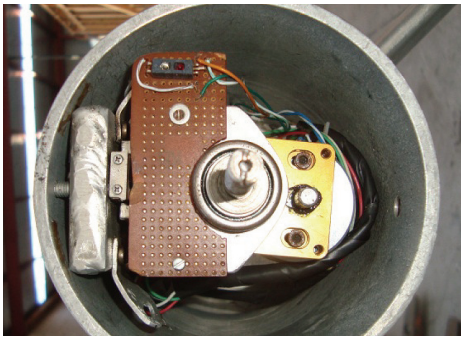

Fig. 13. Close up front view of the instrumented hub

The step in the blades mounted on the hub is clearly evident in Fig. 12. However, here the blades are rather small and thus the Reynolds number was low. It is often useful to know more about the details of the loading in wind turbine investigations, and in this case a larger pressure tapped stepped blade was built for test, and is shown in Fig. 14. The black marks on the blade at the numbering for the pressure taps. These pressure taps were connected to a multi-channel pressure system that can sample up to 1000 Hz. It can be seen in Fig. 15.

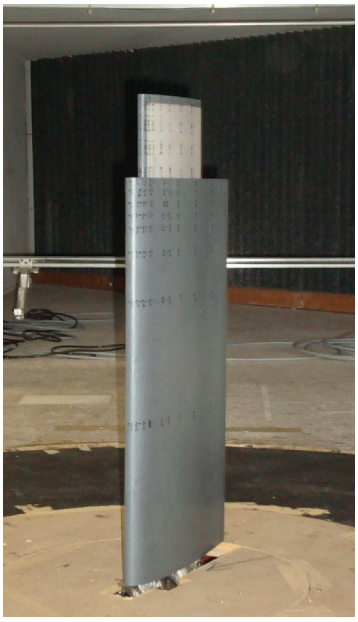

Fig. 14. Photograph of larger pressure tapped model stepped blade in the wind tunnel

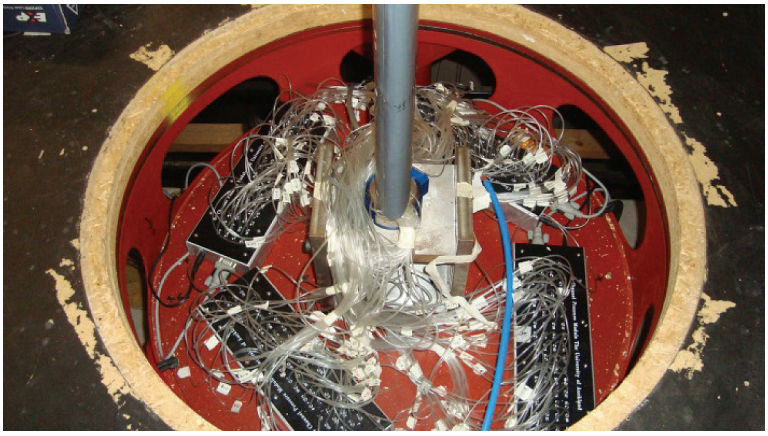

Fig. 15. Photograph of wing mounted on turntable. Tubing from pressure taps leaves the wing at the base and connects to the multi-channel pressure transducer boxes

6.3. Wind tunnel tests on a vertical axis wind turbine

It has been found at The University of Auckland that it is very practical to use an open jet wind tunnel of large size, where the models can be placed on the floor either in a location with side walls, or further downstream without sidewalls. A recent study carried out by an undergraduate student, which is now continuing into a master's project, concerned a vertical axis wind turbine [8]. This wind turbine was fitted with a Voith-Schneider linkage system which enabled the blades to be rotated to different angles of attack with respect to the circumferential direction. The model wind turbine is shown in Fig. 16. The important point of this modelling is that to conveniently build the Voith Schneider linkage, the model could not be too small. The model shown in Fig. 16 has blades that are 1.5 m long and the diameter of the wind turbine was 2 m. The wind tunnel outlet is 3.5 m x 3.5 m in cross-section. At this large size, the linkage mechanism was relatively straightforward to build.

In order to assess the performance of this wind turbine, the reference wind tunnel air speed, the wind turbine rotational speed, and the generator power were measured for a range of settings of the Voith Schneider system. This required the use of a computer based measuring system which sampled the data at 1000 Hz.

Fig. 16. Vertical axis wind turbine set up in open circuit wind tunnel

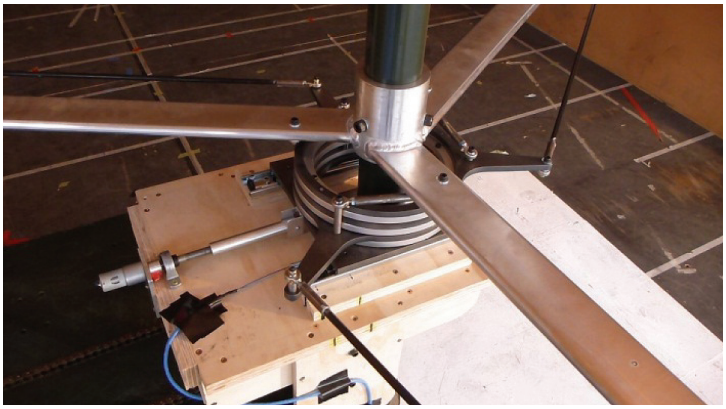

Fig. 17. Voith Schneider linkage system used to alter the angle of attack of the blades during each rotation

7. Conclusions

The paper has shown that in order to undertake successful measurements of wind turbine models in wind tunnels, it is necessary to have an excellent instrumentation setup that can measure the reference quantities of barometric pressure, temperature and pressure accurately. It is also important that the wind tunnel is calibrated so that the dynamic and static pressures measured by the reference measuring system can be transferred to the location of the model.

The paper has discussed blockage corrections and reproduced a procedure originally put forward by Wilson et al [27] who based it on work of Glauert [11], which can be used to correct wind turbine power coefficient measurement from the interference of the walls. It has also been pointed out that much higher blockage ratios can be tolerated in an open jet test, which may be preferable in cases where the available wind tunnels are small, and there is a desire to build as large a model as possible.

Some lessons learnt from testing at the University of Auckland have been discussed by referring to previous research on wind turbines. It has been pointed out that it may be possible to undertake initial testing using porous mesh screens to simulate the pressure drop of rotating blades, which can be hard to manufacture at a small size, and will always operate at a Reynolds number that is at least the model scale ratio lower than full scale Reynolds number.

A suitably equipped hub is needed in order to measure the output from the model wind turbine. The outputs normally needed are thrust, torque and rotational speed. Power produced is also useful but not essential. The load from the motor/generator in the hub should be able to be controlled remotely to enable it to be set to suitable values to enable data to be acquired for the desired range of tip speed ratios. Such a system can be built by mounting the motor/generator with strain-gauged supports.

Additional information on the performance of wind turbines, such as the effect of step changes in the blade can be found by pressure-tapping the blade in the region of interest and testing a larger non-rotating model in a wind tunnel.

For some tests, particularly where there are complicated mechanisms to be built, it is wise to build the model as large as possible to simplify the manufacturing process.

Overall, it is clearly evident that wind tunnel testing is an important tool to make progress in research on wind turbine performance, and the aerodynamics of wind turbine blades.

The writer acknowledges the contributions from his colleagues and from former PhD students Dr Derek Phillips and Dr Mustahib Imraan, and from current student Mr Simon Corkery, whose results are used for some of the examples in this paper.

References

[1] Blocken B., Carmeliet J., Stathopoulos T., *CFD evaluation of wind speed conditions in passages between parallel buildings - effect of wall-function roughness modifications for the atmospheric boundary layer flow*. Journal of Wind Engineering and Industrial Aerodynamics, Vol. 95(9-11), 2007, 941-962.

[2] Builtjes P.J.H., Milborrow D.J., *Modelling of wind turbine arrays*. Proc. 3rd International Symposium Wind Energy Systems, Denmark, Copenhagen 1980.

[3] Barlow J.B., Rae W.J., Pope A., *Low speed wind tunnel testing*, Wiley-Interscience, John Wiley and Sons, USA 1999.

[4] Bottasso C.L., Campagnolo F., Petrovi V., *Wind tunnel testing of scaled wind turbine models: Beyond aerodynamics*, Journal of Wind Engineering and Industrial Aerodynamics, Vol. 127, 2014, 11-28.

[5] Chasteau V.A.L., *Operational experience with a 5 m Darrieus wind turbine*, Proc. 6th Australasian Hydraulics and Fluid Mechanics Conference, Australia, Adelaide, 5-9 December 1977.

[6] Chen J., Fletcher D.F., Haynes B.S., *Validation of the cobra probe using turbulence measurements in a fully developed pipe flow*. Proc. 13th Australasian Fluid Mechanics Conference, 13-18 Dec, eds. M. C. Thompson & K. Hourigan, Monash University, Melbourne, Australia, 1998, Vol. 1, 385-388.

[7] Chen T.Y., Liou L.R., *Blockage corrections in wind tunnel tests of small horizontal-axis wind turbines*. Experimental Thermal and Fluid Science, Vol. 35(3), 2011, 565-569.

[8] Corkery S., *Vertical axis wind turbine with new variable pitch blades*, Project Report 2013-ME18, October 2013.

[9] Fitzgerald R., *Wind tunnel blockage corrections for propellers*, Master Thesis, University of Maryland, 2007.

[10] Gilbert B.L., Foreman K.M., *Experimental demonstration of the diffuser-augmented wind turbine concept*, Journal of Energy, Vol. 3(4), 1979, 235-240.

[11] Glauert H., Durand W.F. (Ed.), *Aerodynamic theory*, "*Airplane propellers*", Vol. IV, Division I, Chapter VII, Section 4, Julius Springer, Berlin 1935, 169-360.

[12] Hand M.M., Simms D.A., Fingersh L.J., Jager D.W., Cotrell J.R., Schreck S., Larwood S.M., *Unsteady aerodynamics experiment phase VI: wind tunnel test configurations and available data campaigns*, Technical Report NREL/TP-500-29955, NREL National Renewable Energy Laboratory, USA 2001.

[13] Hooper J.D., Musgrove A.R., *Multi-hole pressure probes for the determination of the total velocity vector in turbulent single-phase flow*, Proc. 4th International Symposium on Transport Phenomena in Heat and Mass Transfer, ed. J. A. Reizes, Pacific Centre of Thermal-Fluids Engineering, Sydney, Australia 1991, Vol. 4, 1364.

[14] Imraan M. *Aerodynamic analysis of a wind turbine with telescopic blades*, PhD thesis, Mechanical Engineering Department, The University of Auckland, New Zealand, 2013.

[15] Imraan M., Sharma R.N., Flay R.G.J., *Wind tunnel testing of a wind turbine with telescopic blades: The influence of blade extension*, Energy, Vol. 53, 2013, 22-32.

[16] Imraan M, Sharma, R.N., Flay, R.G.J. *Wind tunnel testing of a wind turbine with telescopic blades*, Proc. 13th International Conference on Wind Engineering, Amsterdam, The Netherlands, July 10-15, 2011.

[17] Sorensen J.N., Wen Zhong Shen, Mikkelsen R., *Wall correction model for wind tunnels with open test section*, AIAA Journal, Vol. 44(8), 2006, 1890-1894.

[18] Lindley D., Flay R.G.J., Bowen A.J., *Field measurements of the characteristics of a rural boundary-layer near the ground: Part I; The measured data*, Proc. 6th Australasian Conference on Hydraulics and Fluid Mechanics, Adelaide, Australia, Vol. 1, 1977, 182-185.

[19] Whale J., Papadopoulos K.H., Anderson C.G., Helmis C.G., Skyner D.J., *A study of the near wake structure of a wind turbine comparing measurements from laboratory and full-scale experiments*, Solar Energy, Vol. 56, 1996, 621-633.

[20] Phillips D.G., Richards P.J., Flay R.G.J., *CFD Modelling and the development of the diffuser augmented wind turbine*, Wind and Structures, Vol. 5(2-4), 2002, 267-276.

[21] Phillips D.G., *An investigation on diffuser augmented wind turbine design*, PhD thesis, School of Engineering, The University of Auckland, New Zealand 2003.

[21] Ross I.J., *Wind tunnel blockage corrections: an application to vertical-axis wind turbines*. MSc Thesis, University of Dayton, Dayton, Ohio, May 2010.

[22] Ross I.J., Altman A., *Wind tunnel blockage corrections: Review and application to Savonius vertical-axis wind turbines*, Journal of Wind Engineering and Industrial Aerodynamics, Vol. 99, 2011, 523-538.

[23] Schepers J.G., Snel H., *Model experiments in controlled conditions – final report*. Technical Report, ECN-E-07-042, ECN Wind Energy, The Netherlands 2007.

[24] Snel H., Schepers J.G., Montgomerie B., *The MEXICO projec (Model EXperiments In Controlled cOnditions): the data base and first results of data processing and interpretation*, Journal of Physics: Conference Series, Vol. 75, 2007.

[25] Tamura Y., Kareem A. (Eds.), *Advanced structural wind engineering*, Springer, Japan 2013.

[26] Vermeer L.J., Sørensen J.N., Crespo A., *Wind turbine wake aerodynamics*, Progress in Aerospace Sciences, Vol. 39, 2003, 467-510.

[27] Wilson R.E., Lissaman P.B.S., Walker S.N., *Aerodynamic performance of wind turbines – Final report*, Report ERDA/NSF/04014-76/1, Department of Mechanical Engineering, Oregon State University, Corvallis, Oregon. Available from NTIS, U.S. Department of Commerce, Springfield, Virginia 22161, USA.

[28] World Wind Energy Association, WWEA., World Wind Energy Half Year Report, 2014, http://www.wwindea.org/home/index.php 2014.

TECHNICAL TRANSACTIONS | CZASOPISMO TECHNICZNE
CIVIL ENGINEERING | BUDOWNICTWO
2-B/2015

ROMAN I. KINASH*, JAROSLAV S. HUK**

GEOGRAPHICAL ALTITUDE COEFFICIENT UTILISATION FOR WIND GUST LOADING DETERMINATION IN THE MOUNTAINOUS TERRAIN OF THE TRANSCARPATHIAN REGION

WYKORZYSTANIE WSPÓŁCZYNNIKA WYSOKOŚCI GEOGRAFICZNEJ DO OBLICZANIA ODDZIAŁYWANIA WIATRU NA TERENACH GÓRSKICH REGIONU ZAKARPACIA

Abstract

This paper presents the method and results of a geographical altitude factor calculation to determine wind loading C_{alt} at 9 meteorological stations in the Transcarpathian region. According to state building standards B.1.2-2:2006, the coefficient of geographical altitude is used to calculate wind pressure while positioning the building site at an altitude of up to 0.5 km it equals 1, at altitudes higher than 0.5 km, it is determined using the formula $C_{alt} = 4H–1$. With the help of the suggested method, according to 23 directions and high wind coefficients, as well as data of meteorological observations from 1955–2005, the coefficients of geographical altitude were calculated to determine wind loading in July and January for each residential site, the peaks and mountain passes for the Transcarpathian region of Ukrainian Carpathians.

Keywords: wind load, geographical altitude factor, building construction, Transcarpathian region, meteorological station, mountainous terrain

Streszczenie

W artykule przedstawiono metodykę i wyniki określenia współczynnika wysokości geograficznej do obliczeń oddziaływania wiatru C_{alt} wg danych pomiarów z 9 stacji meteorologicznych Zakarpacia. Według DBN B.1.2-2:2006 współczynnik wysokości geograficznej jest wykorzystywany do obliczania parcia wiatru przy lokalizacji obiektu budowlanego: na wysokości do 500 m jest równy 1,0, a na wysokości ponad 500 m – obliczany wg wzoru $C_{alt} = 4H$-1. Z proponowanej metody dla 23 kierunków i współczynników wiatrowo-wysokościowych oraz danych meteorologicznych z lat 1955–2005 obliczono współczynniki wysokości geograficznej do określenia oddziaływania wiatru w lipcu i styczniu dla każdej miejscowości, szczytów oraz przełęczy Ukraińskich Karpat dla Obwodu Zakarpatskiego.

Słowa kluczowe: obciążenie wiatrem, współczynnik wysokości geograficznej, obiekt budowlany, region Zakarpacia, stacja meteorologiczna, tereny górskie

DOI: 10.4467/2353737XCT.15.126.4163

* AGH University of Science and Technology, Krakow, Poland; Lviv Polytechnic National University, Ukraine.
** Uzhgorod National University, Ukraine.

1. Introduction

Wind impact, which is considered in the calculations of building construction, is determined on the basis of a wide range of interdependent values such as: wind speed, depending on climatic conditions, as well as the type of area and the altitude above it; the external shape of the building, specific architectural and constructive solutions; dynamic properties [1, 2]. Each of the described values is variable and random, and depends on a wide range of factors. Characterising and calculating loads depends on adopting liability criteria of the building units [9, 10].

Wind load is the main type of impact which is impossible to avoid compared with other types of wind impact such as disturbance vortices, flatter or galloping which can be predicted. All of these are shown in the way of one of the general correlations of characteristic value, for example, as a load which acts at a unity of surface [3].

The region of the Ukrainian Carpathians comprises almost 4% of the Ukrainian territory. It is situated almost within the geographical center of Europe. However, the construction in the Carpathian region as well as in mountainous regions overall, has its own peculiarity related to the higher levels of seismic, wind and snow loads, the possibility of floods, sills, geological landslips, avalanches etc.

Therefore, the necessity of scrutinised research and precise determination of wind load parameters for the Transcarpathian region has arisen. It is wise to mention that up to 80% of this region is comprised of mountainous areas which will be sensible to investigate with the help of the direction method using altitude, altitude and logarithmical, latitude and longitude factors and by checking the results using the method of barometric leveling [6–8].

2. Method to determine the geographical altitude factor

According to state building standards DBN B.1.2-2:2006 [4], exploitation-calculating value of the wind load, W_e, is determined with the help of the following formula:

$$W_e = \gamma_{fe} \cdot W_o \cdot C \tag{1}$$

where γ_{fe} – liability factor due to exploitation-calculating value of the wind load; W_o – characteristic value of wind pressure, Pa; C – general factor determined by:

$$C = C_{\text{aer}} \cdot C_h \cdot C_{\text{alt}} \cdot C_{\text{rel}} \cdot C_{\text{dir}} \cdot C_d \tag{2}$$

where C_{aer} – aerodynamic coefficient; C_h – coefficient of construction height; C_{alt} – coefficient of geographical altitude; C_{rel} – relief coefficient; C_{dir} – direction coefficient; C_d – coefficient of dynamics.

The characteristic value of wind pressure W_o equals the average (static) component of wind pressure at a height of 10 m above the Earth's surface which can be exceeded once every 50 years.

The characteristic value of wind pressure W_o is determined depending on the wind region on the map or due to details in appendix E [4].

Where necessary, it is acceptable to determine W_o by means of statistical processing of the results of temporary measurements of wind speed.

The geographical altitude factor of wind pressure, C_{alt}, considers the height H (km) above Baltic sea level of the positioning of the construction unit and is calculated by the following formulas:

$$C_{alt} = 4H - 1 \quad (H > 0.5 \text{ km}) \tag{3}$$

$$C_{alt} = 1 \quad (H < 0.5 \text{ km}) \tag{4}$$

Formulas (3) and (4) are used for units situated in mountainous areas and provide approximate values for liability purposes. Having the results of meteorological observations, the characteristic value of wind load is calculated by means of statistic processing of the results of temporary measurements of wind speed and adopting that C_{alt} is accepted as equal to 1.

Calculations of C_{alt} were performed for 9 meteorological stations of Transcarpathian region [1–3] utilising the base meteorological station Berehovo, situated at the lowest level of the Baltic sea (altitude – 113 m).

To estimate actual values of the coefficient $C_{alt,}$ the maximum wind loads in July and January were calculated according to the observations from 1955 to 2005 at the meteorological stations and the following formula was used:

$$C_{alt} = \frac{W_{o,st.X}}{W_{o,st.\text{Berehovo}}} \tag{5}$$

where $W_{o,st.X}$ – calculated maximum wind loads in July and January at the meteorological stations X, Pa; $W_{o,st.\text{ Berehovo}}$ – calculated maximum wind loads in July and January at the basic and the lowest altitude above the Baltic sea level at the weather station situated at Berehovo, Pa.

According to formula (4) for six meteorological stations: V. Bereznyi, Mizhgir'ya, N. Vorota, Rakhiv, Yzhgorod Hust, which are situated higher than weather station Berehovo and not more than 0.5 km, coefficient C_{alt} = 1. Due to formula (5) coefficient, C_{alt} for meteorological station Plai equals 4.08, for meteorological station N. Studeniy – 1.008, accordingly ΔH_{Plai}= 1.27 km, $\Delta H_{\text{N.Studeniy}}$ = 0.502 km.

3. The calculation results of the geographical altitude factor and wind load

Calculation results of the geographical altitude factor, C_{alt}, due to state building standards DBN B.1.2-2:2006 [4] and observational data of wind loads from 1955 to 2005 at the 9 meteorological stations of the Transcarpathian region are provided in Table 1.

Table 1

Calculation results of the geographical altitude factor, C_{alt}, due to [4] and observational data of wind loads from 1955 to 2005 at the 9 meteorological stations of the Transcarpathian region

No.	Name of weather station	Altitude above Baltic sea level	Altitude difference between Berehovo station and other weather stations	C_{alt} eqs. (3) (4)	Observations maximum wind load		C_{alt} eqs. (5)	
					July	January	July	January
		[m]	[m]		[Pa]	[Pa]		
1.	Berehovo	113	–	1	350	240	1	1
2.	V.Bereznyi	209	96	1	380	240	1.08	1
3.	Mizhgir'ya	456	343	1	740	320	2.11	1.33
4.	N.Studenyi	615	502	1.008	200	320	0.57	1.33
5.	N.Vorota	500	387	1	270	240	0.77	1
6.	Rakhiv	438	325	1	550	240	1.57	1
7.	Yzhgorod	114.6	1.6	1	410	320	1.17	1
8.	Khust	166	53	1	240	240	0.68	1
9.	Plai	1330	1270	4.08	970	970	2.77	4.04

The plots of the geographic altitude factor change C_{alt} which was calculated by formulae (3) and (4) according to [4] and formula (5) calculated according to the maximum wind loads at the meteorological stations for the observations made from 1955 to 2005 are shown in the Fig 1.

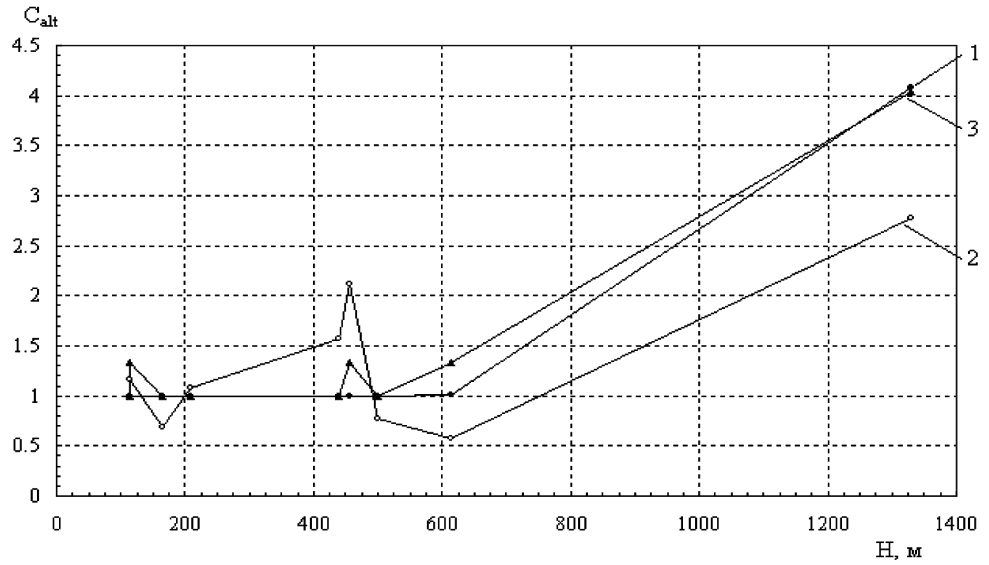

Fig. 1. Correlation between the change of geographic altitude factor C_{alt} and position of meteorological stations in the Transcarpathian region above Baltic sea level, 1 – according to eqs. (3) and (4) according to [4]; 2 – according to the results of observations in July due to formula (5); 3 – according to the results of observations in January due to formula (5)

The comparison of the values of average compound of wind pressure W_o, calculated according to the observations made from 1955 to 2005 at the 9 meteorological stations of the Transcarpathian region with the standards of building norms and rules SNiP 2.01.07-85 [5] and the state building standards DBN B.1.2-2:2006 [4] are shown in Table 2.

Table 2

Comparison of the values of average compound of wind pressure W_o

No.	Name of weather station	Altitude above Baltic sea level	Average compound of maximum wind pressure, W_o				Calculated differences between W_o, according to the observations and standard data			
			[5]	[4]	observations		[5] (summer)	[5] (winter)	[4] (summer)	[4] (winter)
					summer	winter				
		[m]	[Pa]	[Pa]	[Pa]	[Pa]	[Pa] / [%]	[Pa] / [%]	[Pa] / [%]	[Pa] / [%]
1.	Berehovo	113	480	400	350	240	-130 / -27.1	-240 /-50.0	-50 / -12.5	-160 / -40.0
2.	V.Bereznyi	209	480	450	380	240	-100 / -20.8	-240 / -50.0	-70 / -15.6	-210 / -46.7
3.	Mizhgir'ya	456	480	450	740	320	+260 / +54.2	-160 / -33.3	+290 / +64.4	-130 / -28.9
4.	N.Studenyi	615	480	450	200	320	-280 / -58.33	-160 / -33.3	-250 / -55.6	-130 / -28.9
5.	N.Vorota	500	480	450	270	240	-210 / -43.7	-240 / -50.0	-180 / -40.0	-210 / -46.7
6.	Rakhiv	438	480	450	550	240	+70 / +14.6	-240 / -50.0	+100 / +22.2	-210 / -46.7
7.	Yzhgorod	114.6	480	400	410	320	-70 / -14.6	-160 / -33.3	+10 / +2.5	-80 / -20.0
8.	Khust	166	480	400	240	240	-240 / -50.0	-240 / -50.0	-160 / -40.0	-160 / -40.0
9.	Plai	1330	480	450	970	970	+490 / +102.1	+490 / +102.1	+520 / +115.0	+520 / +115.0

Fig. 2 concludes of the change of average compound of wind pressure, W_o, due to the observations during the years from 1955 to 2005 and standards [4] and [5] depending on the altitude above Baltic sea level of 9 meteorological stations of the Transcarpathian region.

The characteristic value of wind pressure, W_o, standardised by [5] for the Transcarpathian region is 480 Pa. In comparison to the calculated statistical data at the 9 meteorological stations, according to the observations made from 1955 to 2005 in July, for six meteorological stations the actual values of maximum wind pressure W_o are raised too high within the limits of 14.6% to 58.3%; for three weather stations, W_o values are set too low within the limits of 14.6% to 102.1%; in January, for 8 meteorological stations, W_o values are raised too high within the limits of 33.3% to 50.0%; for the weather station Plai, W_o values are set too low at 102.1%.

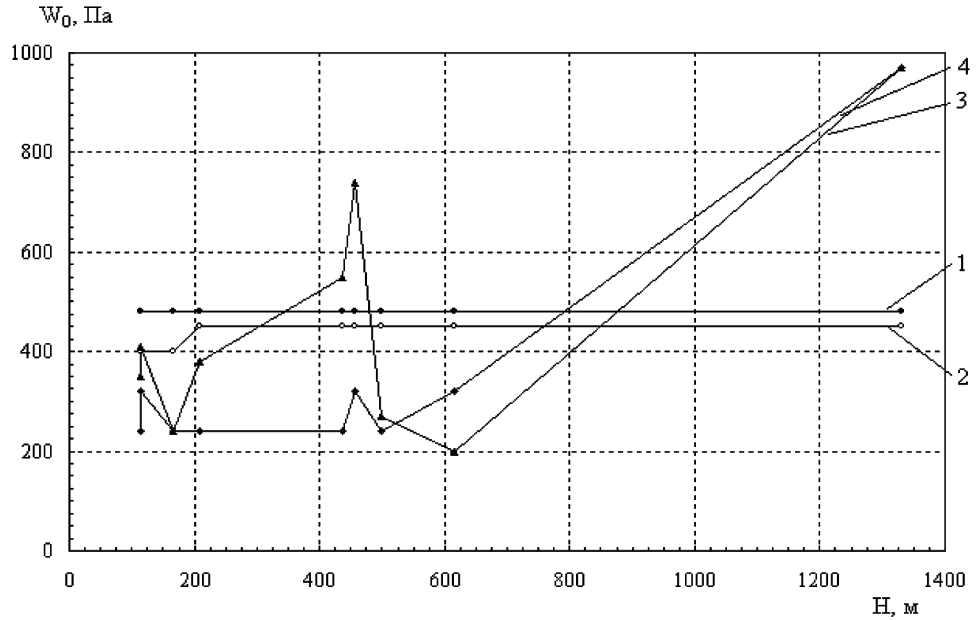

Fig. 2. Change of average compound of maximum wind pressure, W_o, due to [4] and [5] and data of the observations made from 1955 to 2005 at 9 meteorological stations: 1 – due to [5]; 2 – due to [4]; 3 – due to the observations at the meteorological stations made from 1955 to 2005 (summer); 4 – due to the observations at the meteorological stations made from 1955 to 2005 (winter)

The characteristic values of wind pressure, W_o, standardised by [4] for the lowlands of the Transcarpathian region comprises 400 Pa (first region), for mountainous regions 450 Pa (second region). In comparison to the received statistical data at the 9 meteorological stations of Transcarpathian region according to the observations made from 1955 to 2005 in July:

- for 5 meteorological stations, the actual values of maximum wind pressure W_o are raised too high within the limits of 12.5% to 55.6%;
- for 4 meteorological stations, the W_o values are set too low within the limits of 2.5% to 115%;

in January:

- for 8 meteorological stations, the actual values of W_o are set too high within the limits of 20% to 46.7%;
- for meteorological station Plai, the actual values of W_o are set too low up to 115%.

4. Conclusions

1. The geographical altitude coefficient C_{alt} in the Transcarpathian region calculated according to [4] is not always correlated with the actual values received on the basis of investigations of the data of meteorological observations made from 1955 to 2005 at 9 meteorological stations.

2. The value of the coefficient C_{alt} given in [4] correlates with the value received according to the data of meteorological observations in January at 5 meteorological stations; for 3 meteorological stations, it is set too low; for meteorological station Plai, it is less than standard for 0.04; and in comparison with the summer period at 3 weather stations, it is higher than 1.0.
3. Using the method explained in [1, 2], according to 23 directions and altitude wind coefficients as well as data of meteorological observations made from 1955 to 2005, the geographical altitude coefficients for determination of wind loads in July and January for each residential area, peak and mountain pass for the Transcarpathian region of the Ukrainian Carpathians were calculated.
4. For precise determination of wind loads in mountainous regions, it is necessary to use data from many years of observations of wind speed at the weather stations of that particular region.

The thesis was done within the frames of regulation researches of AGH Scientific Technical University in Krakow, Poland nr 11.11.100.197.

References

[1] Kinash R.I., Huck J.S., *The method of calculation of wind parameters for settlements Transcarpathian region, peaks and passes of the Carpathians*, Metalevì konstrukcìï, Makiivka, Vol. 3. 2006, 209-216 (in Ukrainian).
[2] Kinash R.I., Huck J.S., *Technique of definition of parameters building of climatology for settlements, tops and passes of the Zakarpatye region*, Lviv: Problems of the Technical Meteorology, 22-26 may, 2006, 50-56 (in Ukrainian).
[3] Kinash R., *Technique of Determination the Parameters of snowloads for Towns, peaks and Passes of Carnation region*, [in:] Kinash R.I., Huck J.S., Snow Engineering VI, June 1-5, Canada 2008, 121-128.
[4] State Building Standards DBN B.1.2-2:2006 Lodes and impacts, Kijiv, 2006, 78p (in Ukrainian).
[5] Building Norms and Rules SNiP 2.01.07-85. Lodes and impacts, Gosstroj USSR, Moscov 1985, 36p (in Russian).
[6] Kinash R.I., Huck J.S., *Research options climatic loads and impacts to mountain regions Transcarpathia Ukraine*, Metalevì konstrukcìï, Makiivka. Vol. 17(4), 2008, 36-42 (in Ukrainian).
[7] Kinasz R.I., Burnajev O.M., *Wind load and wind power resources in Ukraine,* Lviv, Publishers of scientific – technical literature, 2006, 1152p (in Ukrainian).
[8] Kinash R.I, Huk J.S., *Application of factor geographically heights for determining snow loads in the mountainous district Transcarpathian region*, Metalevì konstrukcìï, Makiivka, Vol. 18(4), 2012, 219-226 (in Ukrainian).
[9] Flaga A., *Inżynieria wiatrowa: podstawy i zastosowania*, Arkady, Warszawa 2008.
[10] Żurański J.A.*, Oddziaływanie wiatru na konstrukcje budowlane w ujęciu PN-EN 1991-1-4:2008*, Inżynieria i Budownictwo, nr 7/2010.

TECHNICAL TRANSACTIONS | CZASOPISMO TECHNICZNE
CIVIL ENGINEERING | BUDOWNICTWO
2-B/2015

TOMASZ LIPECKI*

THE RELATIONSHIP BETWEEN WIND PRESSURE ON THE SURFACE OF RECTANGULAR PRISMS AND ATMOSPHERIC BOUNDARY LAYER PARAMETERS

ZALEŻNOŚĆ MIĘDZY CIŚNIENIEM WIATRU NA POWIERZCHNI OBIEKTÓW PROSTOPADŁOŚCIENNYCH A PARAMETRAMI WARSTWY PRZYŚCIENNEJ

Abstract

This paper considers the dependence of pressure fields on surfaces of rectangular prisms obtained from wind tunnel experiments on boundary layer characteristics. Six different variants of boundary layer flows were simulated in the wind tunnel. The qualitative coefficients of correlation R_s between the wind pressure coefficient C_p or its standard deviation σ_p and parameters describing boundary layer flows (wind speed profile, turbulence intensity profile, power spectral density) were estimated in order to determine how wind parameters influence surface pressure. Five rectangular prisms were placed in the wind tunnel. The following ratios of prism dimensions were adopted: $D/B/H$ = 1:2:20 (R5); 1:2:10 (R3); 1:2:5 (R1); 1:4:20 (R4); 1:4:10 (R2).

Keywords: wind action, wind tunnel, pressure coefficient, Spearman correlation coefficient

Streszczenie

W artykule przedstawiono analizę zależności ciśnienia zmierzonego na powierzchniach obiektów prostopadłościennych w trakcie badań wykonanych w tunelu aerodynamicznym od parametrów opisujących strukturę wiatru w warstwie przyściennej. W pomiarach przyjęto sześć różnych wariantów struktury wiatru. Wyznaczono jakościowy współczynnik korelacji R_s między współczynnikiem średniego ciśnienia C_p lub jego odchylenia standardowego σ_p na powierzchni modeli, a parametrami określającymi strukturę wiatru w warstwie przyściennej (pionowym profilem średniej prędkości wiatru, pionowym profilem intensywności turbulencji, funkcją gęstości widmowej mocy). Celem analiz było określenie wpływu poszczególnych parametrów wiatru na ciśnienie powierzchniowe. Pomiary wykonano na pięciu modelach prostopadłościanów o następujących stosunkach wymiarów: $D/B/H$ = 1:2:20 (R5), 1:2:10 (R3), 1:2:5 (R1), 1:4:20 (R4), 1:4:10 (R2).

Słowa kluczowe: oddziaływanie wiatru, tunel aerodynamiczny, współczynnik ciśnienia, współczynnik korelacji Spearmana

DOI: 10.4467/2353737XCT.15.127.4164

* Department of Structural Mechanics, Lublin University of Technology, Poland.

1. Introduction

Investigations of the pressure structure on the surfaces of prisms placed in the wind tunnel have been reported several times. The majority of experiments concerned 2D flows with constant wind speed and turbulence intensity and were related to square [1–5] and to rectangular cross-sections [4–7] mainly elongated along the mean wind speed. Some papers also refer to 3D flows, where prisms were placed vertically in the atmospheric boundary layer (ABL). Such measurements were mainly conducted on models with square cross-section [8–10] and seldom on rectangular cross-sections [11–13]. When 2D models and flows are taken into consideration, the determination of dependencies between surface pressure and wind parameters is rather simple. On the other hand, when prisms in the ABL are considered, the problem becomes more complicated. A detailed description of the ABL structure in the wind tunnel was reported in [14–28]. Generally, wind structure should be described by the following parameters: vertical profile of the wind speed v; vertical profile of the turbulence intensity I_v; length scale of turbulence L_v; power spectral density function of the wind speed (PSD). In more recent studies, the above parameters are related to three components of the wind speed vector (longitudinal, transverse and vertical).

There is an attempt to numerically describe the dependencies between surface pressure and several wind structure parameters in this paper. In order to investigate these dependencies, the qualitative coefficient of correlation (Spearman coefficient) R_s were calculated. Six different variants of the ABL structure were adopted in the wind tunnel simulations. Measurements of pressure were taken on the surfaces of five models with rectangular cross-sections. The ratio of the cross-section dimensions D/B was 2 for three models and 4 for two of them. The ratios of all dimensions were: $D/B/H$ = 1:2:20 (R5); 1:2:10 (R3); 1:2:5 (R1); 1:4:20 (R4); 1:4:10 (R2).

2. Description of wind tunnel measurements

All experiments were conducted in the boundary layer wind tunnel of Cracow University of Technology. Details of the wind tunnel specification and equipment can be found in [29].

Pressure on all faces of the rectangular prisms were measured during wind tunnel experiments. Different prisms of side ratio D/B = 1:2 (3 models) and D/B = 1:4 (2 models) were placed vertically on the rotational table in the measuring section of the wind tunnel. Dimensions of all models are presented in Table 1. Every prism was equipped with pressure taps at 16 levels along the height and around circumference (Fig. 1a). The angle of the wind attack was set at 15° increments from 0° to 90°. In the initial position (0°), the longer side of the prism was placed perpendicularly to the mean wind speed (Fig. 1b). The recorded dynamic pressure was averaged and normalized by the reference pressure measured at the front of the prism at a height of 70 cm. Detailed description of pressure measurements can be found in [30–32].

Six different cases of ABL flows were simulated in the wind tunnel. These correspond to consecutive terrain categories, and varied significantly in vertical profiles of the mean

wind speed, turbulence intensity, and power spectral density functions (PSD). A detailed description of ABL parameters is presented in [33]. Vertical profiles of the wind speed and turbulence are presented in Fig. 2.

Table 1

Geometric characteristics of prisms

Model	*H*	*B*	*D*	*H*/*D*	*B*/*D*
	[cm]	[cm]	[cm]	[-]	[-]
R1	100	40	20	5	2
R2	100	40	10	10	4
R3	100	20	10	10	2
R4	100	20	5	20	4
R5	100	10	5	20	2

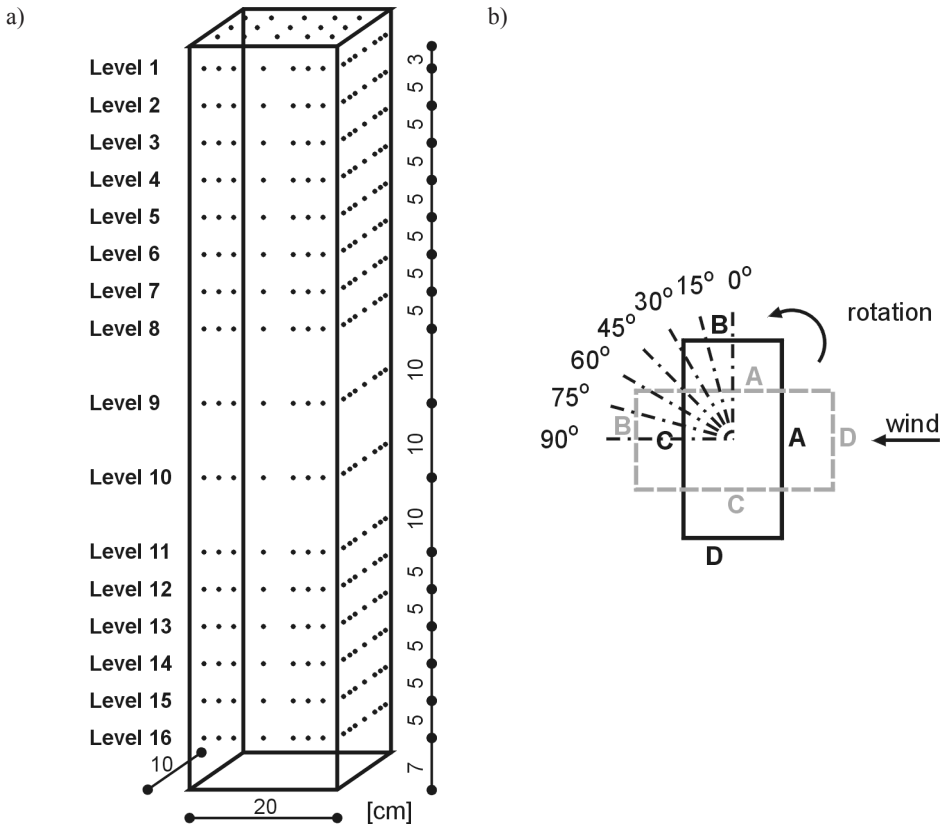

Fig. 1. a) Pressure taps locations on model R3, b) denotations of walls and angles of wind attack α_w

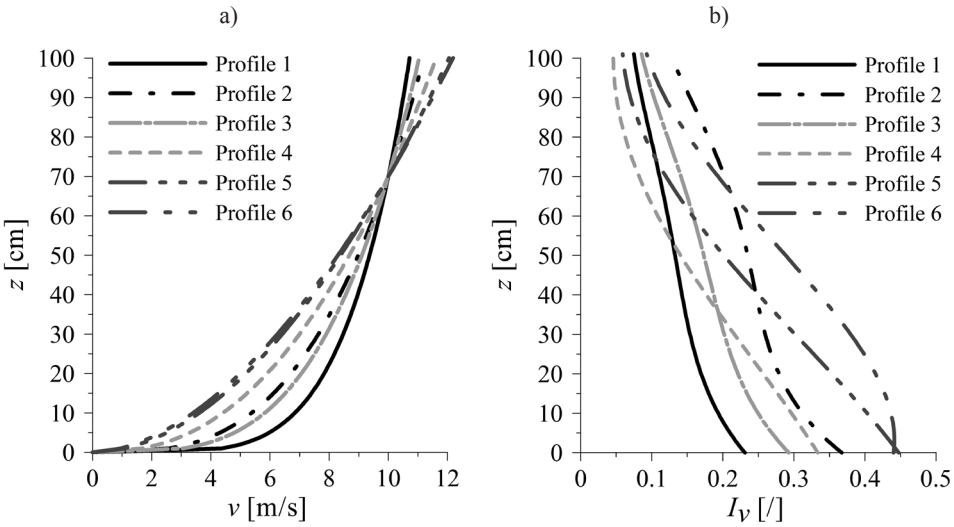

Fig. 2. a) Vertical profile of the mean wind speed v, b) vertical profile of turbulence intensity I_v

3. Spearman rank correlation

Qualitative correlation was calculated in order to estimate the dependence of surface pressure on ABL parameters. The Spearman rank correlation coefficient was chosen as a statistical instrument which allows the determination of such a relationship.

The coefficient describes qualitative dependence between wind structure parameters and pressure coefficients or its standard deviation. It can be used in cases where two variables are non-measurable and are of a qualitative nature, and their empirical values can be described by respective features of assumed ranks. Moreover, the data set has to be small. In the considered case, the data set is small, equal to 6 wind variants, and both wind parameters as well as pressure coefficients are treated as non-measurable values of respective ranks. Spearman coefficient can be calculated from the simple formula:

$$R_s = 1 - \frac{6\sum_{i=1}^{n} d_i^2}{n\left(n^2 - 1\right)} \tag{2}$$

where: n – number of probes, in that case is a number of wind structure variants, $n = 6$, d_i – difference between variables ranks.

Assignment of ranks is based on the consecutive numbering of features of two variables in ascending or descending sequence (from 1 to n). The limiting values for R_s are -1 and 1. $R_s = 0$ means independent variables, R_s in the range 0–0.3 means a lack of correlation, whereas in the range 0.9–1, a very strong correlation, finally $R_s = 1$ describes a full correlation between variables. Negative values can be interpreted in the same way.

In this paper, Spearman's coefficient was applied to investigate the dependence between the sequence of respective wind characteristics and the sequence of pressure coefficient C_p or its standard deviation σ_p on particular measurement levels. Wind structure variants were numbered from 1 to 6, according to Fig. 2. Every feature of the wind structure variants were then set from the highest value to the lowest on respective levels according to assumed numbers. To such segregated values, the appropriate ranks from 1 to 6 were applied. Rank 1 relates to the maximum value, rank 6 to the minimum value. Therefore, if the wind velocity on 97 cm for wind variant no 1 is the lowest then it will receive rank 6, whereas if the velocity for variant 6 is the highest, then it will receive rank 1 (Tables 2 and 3). Values of C_p or σ_p on the surfaces of particular walls and levels were arranged in the same way. For example, if C_p on 97 cm for the variant no. 2 of the wind structure is the highest, then it will receive a rank of 1, whereas on the same level, if C_p is minimum for variant no. 1, then the rank will be 6.

As dependent variables, the following features of wind structure simulated in the wind tunnel were assumed: 1) mean wind speed profile of longitudinal component, v; 2) turbulence intensity profile of longitudinal component of wind speed, I_v; 3) maximum of PSD function of longitudinal wind speed component, max *PSD*. Their correlations with dependent variables on the surfaces of prisms: 1) mean wind pressure coefficient C_p; 2) its standard deviation σ_p were calculated.

Due to the fact that in some cases the sequence of values of C_p and σ_p changed along the width of the wall at the same level, the average sequence was assumed.

Spearman's rank correlation coefficient R_s was calculated for all walls (A, B, C and D), at every measuring level (16 levels) and for all considered angles of wind attack (0°–90°), according to denotations presented in Fig. 1. Values above 0 indicate the consistency between the sequence of C_p or σ_p and respective wind characteristics. If R_s value is closer to 1 then consistency will be higher. This means that if respective wind characteristic values decrease, then respective values on the prism surface will also decrease. R_s below 0 mean that the decrease in wind characteristic values is connected to the increase of C_p or σ_p on the surfaces of models.

The example of the approach in single case (model R1, angle of wind attack 0°, measuring level 1, windward wall of the prism) is presented in Table 2, whereas ranks describing v, I_v. max *PSD* at particular heights are collected in Tables 3–5 (rank 1 – maximum value, rank 6 – minimum value). Ranks in Tables 3–5 are independent of the angle of wind attack and are related to wind parameters.

Table 2

Ranks of dependent variables, model R1, angle 0°, level 1 (97 cm), windward wall

Flow variant	$v(z)$	$I_v(z)$	Max *PSD*	C_p	σ_p
profile 1	6	4	5	6	5
profile 2	4	1	1	1	1
profile 3	5	3	3	4	3
profile 4	3	6	6	5	6
profile 5	2	5	4	3	4
profile 6	1	2	2	2	2

Table 3

Ranks of values of the mean wind speed, *v*, on respective measurement levels

H [cm]	97	92	87	82	77	72	67	62	52	42	32	27	22	17	12	7
profile 1	6	6	6	6	6	6	1	1	1	1	1	1	1	1	1	1
profile 2	4	4	4	4	4	4	3	3	3	3	3	3	3	3	3	3
profile 3	5	5	5	5	5	5	2	2	2	2	2	2	2	2	2	2
profile 4	3	3	3	3	3	3	4	4	4	4	4	4	4	4	4	4
profile 5	2	2	2	2	2	2	5	5	5	5	5	5	5	5	5	5
profile 6	1	1	1	1	1	1	6	6	6	6	6	6	6	6	6	6

Table 4

Ranks of values of the turbulence intensity, I_v, on respective measurement levels

H [cm]	97	92	87	82	77	72	67	62	52	42	32	27	22	17	12	7
profile 1	4	4	4	4	4	5	5	5	6	6	6	6	6	6	6	6
profile 2	1	1	1	1	1	1	1	2	2	2	3	3	3	3	3	3
profile 3	3	3	3	3	3	3	3	3	4	4	5	5	5	5	5	5
profile 4	6	6	6	6	6	6	6	6	5	5	4	4	4	4	4	4
profile 5	5	5	5	5	5	4	4	4	3	3	2	2	2	2	2	2
profile 6	2	2	2	2	2	2	2	1	1	1	1	1	1	1	1	1

Table 5

Ranks of values of the maximum of PSD function, *max* PSD, on respective measurement levels

H [cm]	97	92	87	82	77	72	67	62	52	42	32	27	22	17	12	7
profile 1	5	4	5	5	5	5	5	5	5	5	6	6	6	6	6	5
profile 2	1	1	1	1	1	1	1	2	2	2	3	4	2	1	1	1
profile 3	3	3	3	3	3	3	3	4	4	4	4	5	5	5	3	2
profile 4	6	6	6	6	6	6	6	6	6	6	5	3	4	4	5	6
profile 5	4	5	4	4	4	4	4	3	3	3	1	1	1	3	2	4
profile 6	2	2	2	2	2	2	2	1	1	1	2	2	3	2	4	3

4. Results and discussion

4.1. The relationship between pressure parameters and mean wind speed

Results which illustrate the correlation coefficient R_s between the order of C_p or σ_p values and the order of mean wind speed, v, values along the height of models are presented in

Figs 3–4, for two exemplary angles of wind attack $\alpha_w = 0°$ and $\alpha_w = 90°$, on consecutive walls of the prisms (A,B,C and D), and for all models (R1–R5).

On the windward wall (A, $\alpha_w = 0°–45°$ and D, $\alpha_w = 60°–90°$), R_s coefficient is above 0 (Fig. 3). Unexpectedly, the correlation is quite low with a maximum of about +0.6 on windward walls A and D on levels above 70 cm (at that height, the wind speeds in every ABL variant are equal). Values of R_s for different models are similar. Higher correlation is visible below 45 cm, but values differ significantly between models.

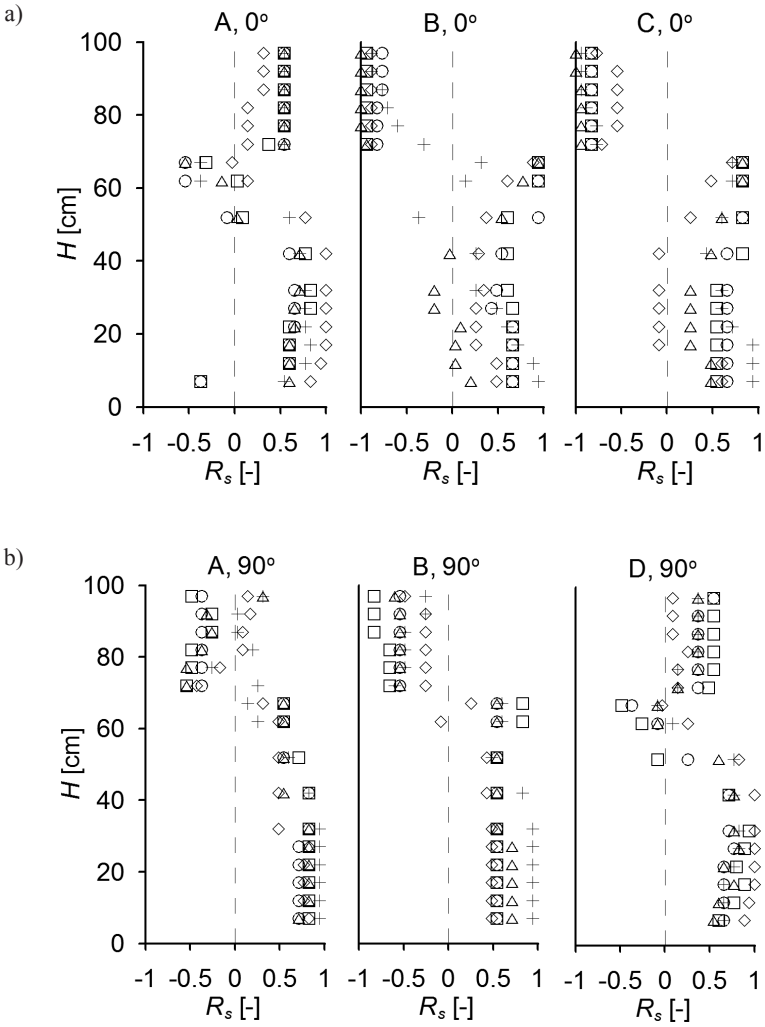

Fig. 3. Correlation coefficient R_s between the order of C_p and the order of the mean wind speed values: a) $\alpha_w = 0°$ A – windward wall, B (D – symmetric) – side wall, C – leeward wall; b) $\alpha_w = 90°$, A (C – symmetric) – side wall, B – leeward wall, D – windward wall, □ – model R1, ○ – model R2, ◇ – model R3, △ – model R4, + – model R5

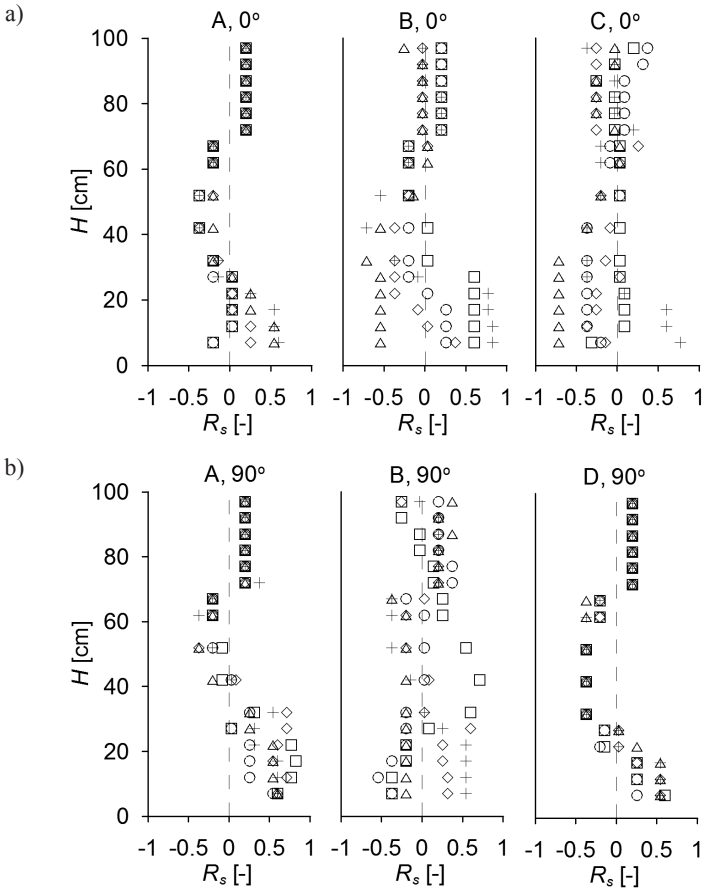

Fig. 4. Correlation coefficient R_s between the order of σ_p and the order of the mean wind speed values: a) $\alpha_w = 0°$; b) $\alpha_w = 90°$. Notations are as in Fig. 3

On side and leeward walls where the suction is, for all angles of wind attack, the values of R_s above 70 cm are close between models and are equal to a maximum of -1, so their correlation is very high (Fig. 3a – B, C and Fig. 3b – A, B). This means that when the speed increases (between ABL variants), the suction coefficient on walls will decrease (above 70 cm). For example, the wind speed in profile 6 is the highest at the top levels and this gives the lowest values of C_p on the leeward wall. Such a tendency to a lesser extent appears at $\alpha_w = 75°–90°$ for which R_s is lower and differences between models are high. Below a level of 70 cm, correlation coefficient changes its sign to +, and large discrepancies between models exist. Only for $\alpha_w = 90°$, the correlation coefficients are closer between models and their values approach +1. Positive values of R_s mean that when wind speed increases (between ABL variants) suction on walls will also increase (below 70 cm).

When considering the correlation between σ_p and wind speed, it can be noticed that R_s values are close to each other on walls with positive pressure, but correlation is very weak (about +0.2) on levels above 70 cm (Fig. 4a – A, Fig. 4b – D). On heights below that level,

the correlation coefficient changes its sign to '-', maximum to -0.5, and for heights around 30 cm again changes the sign to "+" and correlation slightly increases, maximum to +0.7, but the scatter of results between models also increases. On walls where the suction is, differences of R_s values between models are high. R_s values are lower above 70 cm and at that height, correlation is very weak or there is no correlation at all. Even a larger scatter of R_s appears below 70 cm, but values of R_s are higher and in the majority of cases, are negative, maximum to -0.7 (Fig. 4a – B, C, Fig. 4b – A, B)

4.2. The relationship between pressure parameters and turbulence intensity

Correlation coefficients R_s between pressure coefficient C_p or standard deviation σ_p and intensity of turbulence I_v, for $\alpha_w = 0°$ and $\alpha_w = 90°$ are presented in Figs 5–6.

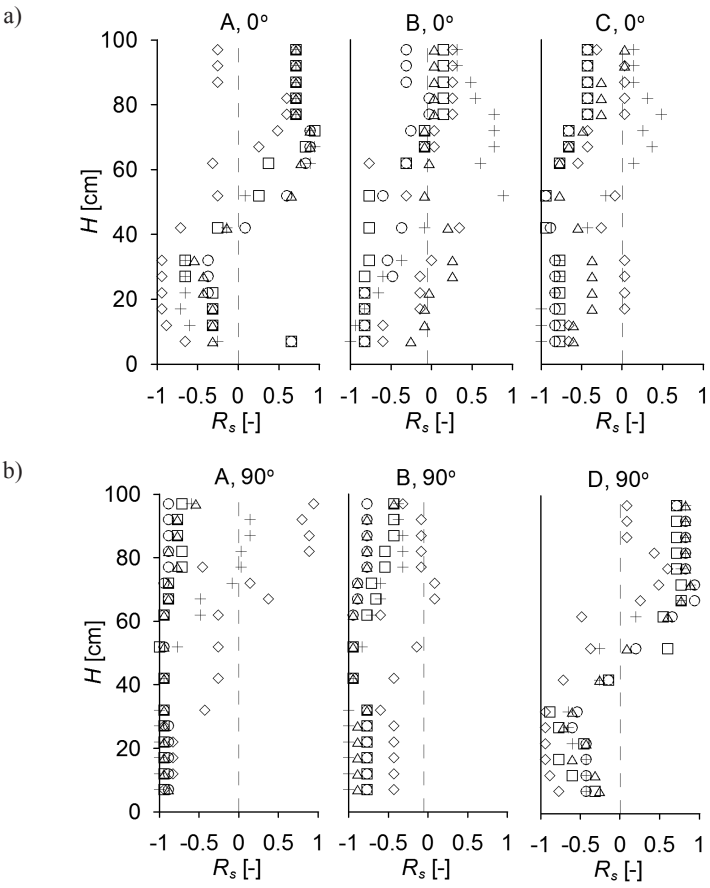

Fig. 5. Correlation coefficient R_s between the order of C_p and the order of the turbulence intensity values I_v. a) $\alpha_w = 0°$, b) $\alpha_w = 90°$. Notations are as in Fig. 3

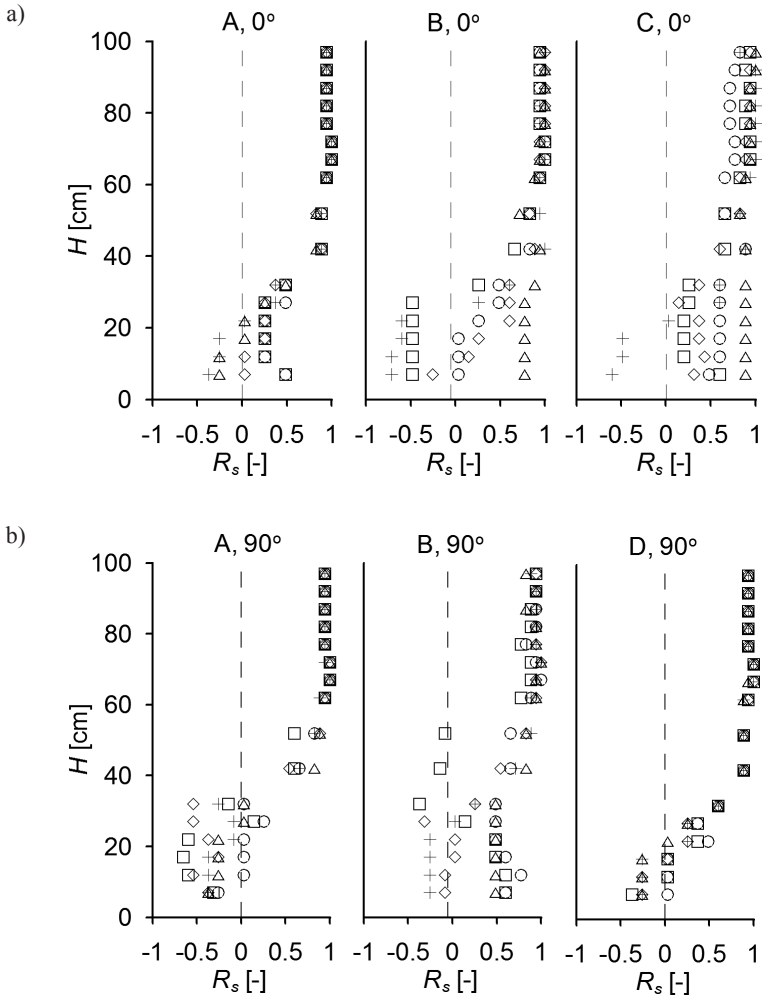

Fig. 6. Correlation coefficient R_s between the order of σ_p and the order or the turbulence intensity values I_v. a) $\alpha_w = 0°$, b) $\alpha_w = 90°$. Notations are like in Fig. 3

The correlation coefficient is positive, equal to +0.7–+0.8 above 70 cm on walls with positive pressure (Fig. 5a – A, Fig. 5b – D). Beneath 70 cm, the coefficient R_s is less than 0 and the scatter of results is larger, between -0.4 and -1. Correlation on walls with suction is low, with a different sign, and increases in direction to the support, where the sign is "-" (Fig. 5a – B, C). The scatter of results between models is considerable. For angles $\alpha_w = 75°–90°$ differences between models decrease and R_s is closer to -1 (Fig. 5b – A, B).

Coefficient R_s between σ_p and I_v above 40 cm is very high, close to +1 on every wall and for all angles of wind attack (Fig. 6a, b). Differences between models are negligible. Beneath 40 cm, correlation decreases and for angles $\alpha_w = 0°$ and $\alpha_w = 75°–90°$ achieves negative values with maximum of about -0.5 close to the support. The scatter of results is large.

4.3. The relationship between pressure parameters and maximum of PSD

Correlation coefficient R_s between C_p or σ_p and maximum of PSD function values (max *PSD*) for $\alpha_w = 0°$ and $\alpha_w = 90°$ are presented in Figs 7–8.

The R_s coefficient is positive, high or very high about +0.9 on walls with positive pressure above 70 cm (Fig. 7a – A, Fig. 7b – D). Differences between models are rather small. Beneath 70 cm, correlation decreases, changes sign, reaches a maximum of -0.9–-1 at 30 cm, then again changes sign and increases to about +0.9 at supports. When suction is on the walls, the negative correlation prevails on higher levels, but in some cases, also positive values appear (Fig. 7a – B, C, Fig. 7b – A, B). Generally, correlation is rather weak with maximum of about -0.7, with the exception of $\alpha_w = 75°–90°$ where it reaches -0.9. For all angles of wind attack, the highest correlation is at 40–50 cm and its maximum value is -1 ($\alpha_w = 75°–90°$). The R_s decreases in the direction to the base. There is considerable scatter between models for the whole height of all walls.

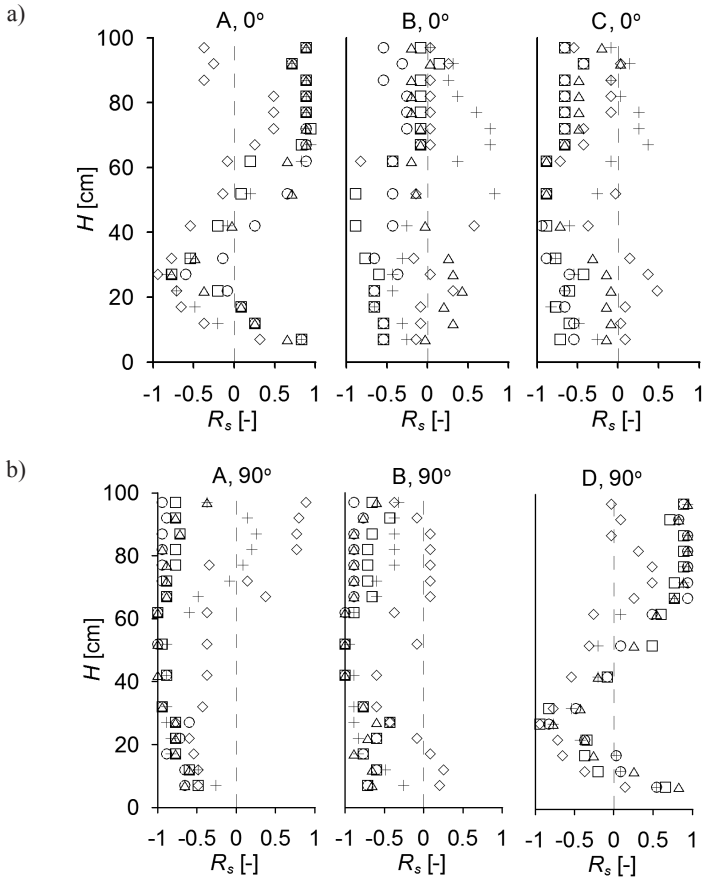

Fig. 7. Correlation coefficient R_s between the order of C_p and the order of the maximum values of PSD function, max *PSD*, a) $\alpha_w = 0°$, b) $\alpha_w = 90°$. Notations are as in Fig. 3

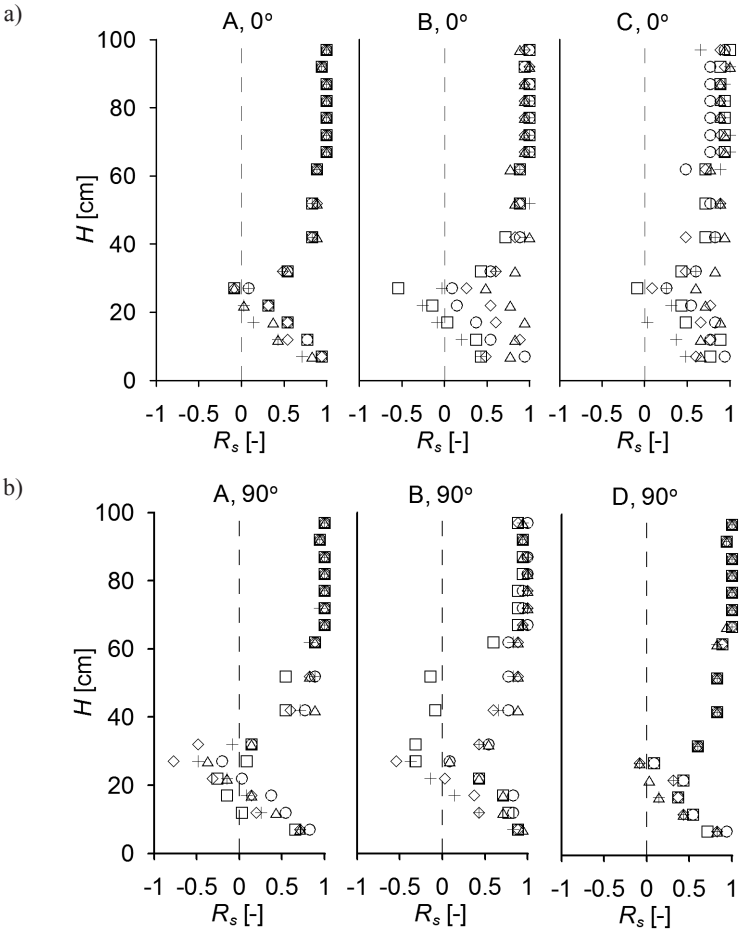

Fig. 8. Correlation coefficient R_s between the order of σ_p and the order of the maximum values of PSD function, max *PSD*, a) $\alpha_w = 0°$, b) $\alpha_w = 90°$. Notations are as in Fig. 3

A very high R_s, in the majority of cases equal to +1, is noticeable above about 60 cm when analyzing the correlation between max *PSD* and σ_p (Fig. 8a, b). Values between models are very close to each other. The coefficient decreases to a height of 25–30 cm where it is equal to 0 or changes sign. Below that height, R_s increases to 1 at the floor. The scatter of results also increases but is smaller on walls with positive pressure.

5. Conclusions

The attempt to numerically estimate the dependence between ABL parameters and rectangular prisms surface pressure parameters was undertaken in this paper. Two variables

of surface pressure were considered – the coefficient of the mean pressure C_p and its standard deviation σ_p. Three parameters of ABL were taken into account: vertical profile of the mean wind speed, v; turbulence intensity, I_v; the maximum value of PSD function, max *PSD*. Each group of parameters was treated as non-measurable values. The order of their values at respective levels was considered. The Spearman rank correlation coefficient was assumed and calculated as a measure which allows describing that dependence. In general, surprisingly, it seems that the higher correlation is between σ_p and flow characteristics than between C_p and respective flow characteristics. A more clear dependence is for σ_p. When considering the correlation between C_p and wind parameters, the scatter of results along the height is considerable. In the upper parts of the models, closer to their free ends, correlation coefficients are higher and generally better ordered; moreover, the values are closer to each other than at bottom levels.

References

[1] Vickery B.J., *Fluctuating lift and drag on a long cylinder of square cross-section in a smooth and in a turbulent stream*, Journal of Fluid Mechanics, Vol. 25(3), 1966, 481-491.

[2] Saathoff P., Melbourne W.H., *Effects of free stream turbulence on streamwise pressure measured on a square-section cylinder*, Journal of Wind Engineering and Industrial Aerodynamics, Vol. 79, 1999, 61-78.

[3] Lee B.E., *The effect of turbulence on the surface pressure field of a square prism*, Journal of Fluid Mechanics, Vol. 69(2), 1975, 263-282.

[4] Miyata T., Miyazaki M., *Turbulence effects on aerodynamic response of rectangular bluff cylinders,* Cermak J.E. (Ed.), *Wind Engineering*, Proc. 5th International Conference on Wind Engineering, Fort Collins, Colorado, USA, July 1979, 631-642.

[5] Noda H., Nakayama A., *Free-stream turbulence effects on the instantaneous pressure and forces on cylinders of rectangular cross section*, Experiments in Fluids, Vol. 34, 2003, 332-344.

[6] Li Q.S., Melbourne W.H., *Effects of turbulence on surface pressures of the flat plate and rectangular cylinders in separated and reattaching flows*, Proc. 9th International Conference on Wind Engineering, New Delhi, India, 1995, 165-176.

[7] Li Q.S., Melbourne W.H., *The effects of large scale turbulence on pressure fluctuations in separated and reattaching flows*, Journal of Wind Engineering and Industrial Aerodynamics, Vol. 83, 1999, 159-169.

[8] Kareem A., Cermak J.E., *Pressure fluctuations on a square building model in boundary-layer flows,* Journal of Wind Engineering and Industrial Aerodynamics, Vol. 16, 1984, 17-41.

[9] Sitheeq M.M., Iyengar A.K.S., Farell C., *Effect of turbulence and its scales on the pressure field on the surface of a three-dimensional square prism*, Journal of Wind Engineering and Industrial Aerodynamics, Vol. 69-71, 1997, 461-47l.

[10] Butler K., Cao S., Kareem A., Tamura Y., Ozono S., *Surface pressure and wind load characteristics on prisms immersed in a simulated transient gust front flow field*, Journal of Wind Engineering and Industrial Aerodynamics, Vol. 98, 2010, 299-316.

[11] Kareem A., *Measurements of pressure and force fields on building models in simulated atmospheric flows*, Journal of Wind Engineering and Industrial Aerodynamics, Vol. 36, 1990, 589-599.
[12] Cheng C.M., Tsai M.S., *Along wind design wind load for tall buildings (I) Results of wind tunnel tests*, Proc. 5th International Advanced School on wind Engineering, The GCOE Program at Tokyo Polytechnic University, Poland, Opole 2009.
[13] Rosa L., Tomasini G., Zasso A., Aly A.M., *Wind-induced dynamics and loads in a prismatic slender building: A modal approach based on unsteady pressure measurements*, Journal of Wind Engineering and Industrial Aerodynamics, Vol. 107-108, 2012, 118-130.
[14] Counihan J., *Simulation of an adiabatic urban boundary layer in the wind tunnel*, Atmospheric Environment, Vol. 7, 1973, 673-689.
[15] Robins A.G., *The development and structure of simulated neutrally stable atmospheric boundary layers*, Journal of Wind Engineering and Industrial Aerodynamics, Vol. 4, 1979, 71-100.
[16] Farell C., Iyengar A.K.S., *Experiments on the wind tunnel simulation of atmospheric boundary layers*, Journal of Wind Engineering and Industrial Aerodynamics, Vol. 79, 1999, 11-35.
[17] Witter A.R., Möller S.V., *Characteristics of the low-speed wind tunnel of the UNNE*, Journal of Wind Engineering and Industrial Aerodynamics, Vol. 84, 2000, 307-320.
[18] Iyengar A.K.S., Farell C., *Experimental issues in atmospheric boundary layer simulations: roughness length and integral length scale determination*, Journal of Wind Engineering and Industrial Aerodynamics, Vol. 89, 2001, 1059-1080.
[19] Balendra, T., Shah, D.A., Tey, K.L., Kong, S.K., *Evaluation of flow characteristics in the NUS-HDB Wind Tunnel*, Journal of Wind Engineering and Industrial Aerodynamics, Vol. 90, 2002, 675-688.
[20] De Bortoli M.E., Natalini B., Paluch M.J., Natalini M.B., *Part-depth wind tunnel simulations of the atmospheric boundary layer*, Journal of Wind Engineering and Industrial Aerodynamics, Vol. 90, 2002, 281-291.
[21] Chen K., Jin X.Y., Zhao J.D., *Design and characteristics of a large boundary layer wind tunnel with two test sections*, Proc. 7th Asia-Pacific Conference on Wind Engineering, Taipei, Taiwan, 2009, CD.
[22] Kozmar H., *Scale effects in wind tunnel modeling of an urban atmospheric boundary layer*, Theoretical and Applied Climatology, Vol. 100(1-2), 2010, 153-162.
[23] Kozmar H., *An alternative approach to experimental simulation of wind characteristics in urban environments*, Procedia Environmental Sciences, Vol. 4, 2011, 43-50.
[24] Kozmar H., *Truncated vortex generators for part-depth wind-tunnel simulations of the atmospheric boundary layer flow*, Journal of Wind Engineering and Industrial Aerodynamics, Vol. 99, 2011, 130-136.
[25] Kozmar H., *Characteristics of natural wind simulations in the TUM boundary layer wind tunnel*, Theoretical and Applied Climatology, Vol. 106, 2011, 95-104.
[26] Kozmar H., *Physical modeling of complex airflows developing above rural terrains*, Environmental Fluid Mechanics, Vol. 12, 2012, 209-225.
[27] Varshney K., Poddar K., *Experiments on integral length scale control in atmospheric boundary layer wind tunnel*, Theoretical and Applied Climatology, Vol. 106, 2011, 127-137.

[28] Varshney K., *Tailoring wind properties by various passive roughness elements in a boundary-layer wind tunnel*, International Journal of Physical Sciences, Vol. 7(8), 2012, 1182-1186.

[29] Flaga A. Lipecki T. (eds.), *Environmental effects on buildings, structures, materials and people*, Lublin 2007.

[30] Lipecki T., Bęc J., Błazik-Borowa E., *Surface pressures on rectangular cylinders – the dependence on aspect ratio, wind structure and angle of wind attack*, Proc. 7th Symposium on Bluff Body Aerodynamics and Applications, China, Shanghai 2012.

[31] Lipecki T., Jamińska P., *Analysis of wind pressure distribution on the surface of 2:1 rectangular cylinder*, Proc. XX Fluid Mechanics Conference, Poland, Gliwice 2012.

[32] Lipecki T., *Oddziaływanie wiatru na budynki wysokie w świetle badań własnych i ujęć normowych*, Budownictwo i Architektura, Vol. 12(2), 2013, 143-150.

[33] Bęc J., Lipecki T, Błazik-Borowa E., *Research on wind structure in the wind tunnel of Wind Engineering Laboratory of Cracow University of Technology*, Journal of Physics: Conference Series 318, 072003, doi: 10.1088/1742-6596/318/7/072003, 2011.

TECHNICAL TRANSACTIONS | CZASOPISMO TECHNICZNE
CIVIL ENGINEERING | BUDOWNICTWO
2-B/2015

TOMASZ LIPECKI*, JAROSŁAW BĘC*, PAULINA JAMIŃSKA*

A COMPARATIVE STUDY OF ALONG-WIND AND CROSSWIND RESPONSES OF STEEL CHIMNEYS ACCORDING TO POLISH AND EUROCODE STANDARDS

STUDIA PORÓWNAWCZE PODŁUŻNEJ I POPRZECZNEJ ODPOWIEDZI KOMINÓW STALOWYCH NA ODDZIAŁYWANIE WIATRU PRZYJĘTE WEDŁUG NORM POLSKICH I EUROKODU

Abstract

An analysis of the response of steel chimneys to wind action is presented in this paper. The approaches presented in the Polish standards and in Eurocode 1 referring to steel chimneys and wind action are shown here. Comparisons of along-wind and crosswind action according to these procedures are made. Responses to the wind action, i.e. displacements of the top of each chimney, are compared. Real chimneys were analyzed. In almost every case, significant vibrations due to vortex excitation was observed. Structural data was obtained from the literature. All chimneys and wind actions were modelled in FEM system – Autodesk Mechanical Simulation 2013. Very significant differences of the crosswind response were observed when analyzing two approaches proposed by Eurocode. Lateral displacements were larger than longitudinal displacements in many analyzed cases.

Keywords: steel chimneys, wind action, vortex excitation, wind standards

Streszczenie

Przedmiotem analiz przedstawionych w niniejszym artykule jest odpowiedź kominów stalowych na oddziaływanie wiatru, którą wyznaczono na podstawie wytycznych zawartych w Normach Polskich oraz w Eurokodzie 1. Analizowano dwa rodzaje odpowiedzi: wzdłuż średniego kierunku wiatru oraz w kierunku prostopadłym. Odpowiedź konstrukcji wyrażono za pomocą przemieszczenia wierzchołka, któro dla różnych kominów ze sobą porównano. Analizom poddano rzeczywiste kominy stalowe, dla których na przestrzeni lat zaobserwowano znaczące wzbudzenie wirowe. Dane konstrukcyjne określono na podstawie literatury. Wszystkie konstrukcje oraz oddziaływanie wiatru zostały zamodelowane w programie MES – Autodesk Mechanical Simulation 2013. Otrzymano znaczne różnice odpowiedzi poprzecznej kominów, gdy obciążenie przyjmowano zgodnie z dwoma procedurami Eurokodu. Przemieszczenia poprzeczne są w wielu przypadkach większe niż podłużne.

Słowa kluczowe: kominy stalowe, oddziaływanie wiatru, wzbudzenie wirowe, normy wiatrowe

DOI: 10.4467/2353737XCT.15.128.4165

* Department of Structural Mechanics, Lublin University of Technology, Poland.

1. Introduction

When analyzing wind action on steel chimneys, two directions should be considered: along-wind action and crosswind action. Crosswind action is generated by Benard-Kármán vortices. Estimation of the first one in almost all standards over the world is based on the mathematical model elaborated by Alan Davenport in the 1960s, [1–2]. Eurocode 1 [3] allows determination on the basis of the peak values of wind speed, while Polish standards, PN-93/B-03201 [4] and PN-77/B-02011 [5], are based on 10-minute mean wind speeds. Crosswind action, according to Eurocode 1 [3], can be calculated with the use of two alternative procedures originally based on the Ruscheweyh model – procedure 1, [6–9] and Vickery-Clark model – procedure 2, [10–13]. These procedures lead to considerably different results. In Polish standard PN-93/B-03201 [4] the simplified model proposed by Ruscheweyh was introduced. A vortex excitation phenomenon, lateral vibrations, lock-in effect as well as analyses of different standard approaches describing vibrations of industrial chimneys which are generated with vortices have been widely presented in literature [12–15] and more recently in [16–41].

In this paper, along-wind action and crosswind action are separately analyzed for three types of steel chimneys: type 1 – of constant outer diameter; type 2 – with tapered lower part; type 3 – tapered for the whole height of the structure. Finite element models of each chimney structure were made on the basis of the data obtained from literature. The objective of this paper is a comparative study of the along-wind and crosswind responses of three groups of steel chimneys according to approaches presented in Polish and Eurocode standards.

2. Wind action according to Polish and Eurocode standards

2.1. Along-wind action

In Polish standards, PN-93/B-03201 [4] and PN-77/B-02011 [5] the static along-wind action equivalent to the dynamic one is calculated in pressure units according to the formula:

$$p_x = q_k C_e C_x C_{te} \beta \tag{1}$$

where: q_k – characteristic wind speed pressure, C_e – exposure factor, C_x – aerodynamic drag coefficient, C_{te} – coefficient regarding expected service time, β – dynamic wind gust coefficient.

According to Eurocode 1 [3] wind force acting on the structure is calculated from:

$$F_w = c_s c_d \cdot c_f \cdot q_p \left(z_e\right) A_{ref} \tag{2}$$

where: $c_s c_d$ – structural factor, calculated for the reference height $z_s = 0.6H$ and being the product of c_s – size factor reducing wind action as the result of a lower correlation due to large

structure dimensions and c_d – dynamic factor increasing wind action regarding gusts, c_f – aerodynamic drag coefficient, $q_p(z_e)$ – peak wind speed pressure at the height of the analyzed structure section, A_{ref} – reference area exposed to wind action.

2.2. Crosswind action

Polish standard, PN-93/B-03201 [4] gives two procedures: simplified with wind action treated as static equivalent to the real dynamic one, and detailed procedure with dynamic wind action as a harmonic one in accordance with the natural frequency of the structure. In both procedures, wind action should be applied in the area of extreme structure deflections, at a correlation length of $0.25H$, not less than $6D$ (H – structure height, D – diameter). Simplified procedures may only be applied for the first natural frequency, when the slenderness $H/D < 30$, Scruton number $Sc < 15$, and expected service time is less than 20 years. The load is expressed in [kN/m] and calculated with the formula:

$$p_y = \frac{0,05\rho}{T_1^2 \delta_s} c_{lat} D^3 \tag{3}$$

where: ρ – air density, T_1 – first period of natural vibrations, δ_s – logarithmic decrement of structural damping, c_{lat} – aerodynamic lift force coefficient.

According to the detailed procedure, dynamic wind action referring to the i-th mode shape is calculated with the use of the following formula:

$$p_{y,i} = \frac{\rho v_{kr,i}^2}{2} D c_{lat,i} \sin\left(\omega_i t\right) \tag{4}$$

where: ω_i – i-th circular frequency of natural vibrations, $v_{kr,i}$ – i-th critical wind speed, $v_{kr,i} = f_i \cdot D/\mathrm{St}$, f_i – i-th natural frequency, St – Strouhal number.

Eurocode 1 [3] allows the application of two procedures for calculation of crosswind action. Both of them are based on the evaluation of the maximum deflections generated by vortex excitation. Wind action considering internal forces is applied in accordance with the mode shape and is calculated for j-th node of the structure according to the formula:

$$F_{i,j} = m_j \left(2\pi n_i\right)^2 \Phi_{i,y,j}\left(z\right) \max y_F \tag{5}$$

where: m_j – the vibrating mass at the node j, n_i – natural frequency referring to the i-th mode shape, $\Phi_{i,y,j}(z)$ – normalized i-th mode shape in the crosswind direction, $\max y_F$ – maximum displacement caused by vortex excitation.

The first of the procedures has been elaborated by Ruscheweyh [6–9] and takes resonant vortex excitation into account. The basics of the second procedure have been proposed by Vickery [10–11], then modified by Dyrbye and Hansen [12–13] by introducing the influence

of turbulence and in this form introduced into Eurocode 1 [3]. The basis of both procedures is the determination of maximum displacements caused by vortex excitation (max y_F).

In Ruscheweyh's procedure, the effective vortex excitation is assumed as uniformly distributed along the effective correlation length L_j. The increase in crosswind action caused by lock-in phenomenon is taken into account by feedback between correlation length L_j and amplitude of lateral vibrations y_F. The ratio of correlation length to outer diameter of the chimney L_j/D depends on the ratio of the vibration amplitude to the outer diameter in the following way: when $y_F/D < 0.1$ then $L_j/D = 6.0$, when $0.1 < y_F/D < 0.6$ then $L_j/D = 4.8 + 12y_F/D$, when $y_F/D > 0.6$ then $L_j/D = 12$. The maximum vibrations amplitude is calculated from the equation:

$$\frac{\max y_F}{D} = K_W K c_{lat} \frac{1}{\mathrm{St}^2} \frac{1}{\mathrm{Sc}} \tag{6}$$

where: D – outer diameter of the chimney, K_w – coefficient of effective correlation length, K – coefficient of the mode shape, c_{lat} – coefficient of aerodynamic lift, St – Strouhal number, Sc – Scruton number.

Maximum amplitude max y_F must be calculated with use of iterative procedure. One should assume the initial displacement y_f, then calculate L_j, then c_{lat} and K_w (which also depends on L_j) and K, finally, estimate max y_F according to the equation (6). If max y_F is different from initial value the procedure must be repeated.

Maximum displacement in the second procedure is calculated from the equation:

$$y_{\max} = \sigma_y \cdot k_p \tag{7}$$

where: σ_y – standard deviation of displacements at the location of maximum deflection, k_p – peak factor.

Standard deviation and peak factor are described by the following equations:

$$\frac{\sigma_y}{D} = \frac{1}{\mathrm{St}^2} \cdot \frac{C_c}{\sqrt{\frac{\mathrm{Sc}}{4\pi} - K_a \cdot \left[1 - \left(\frac{\sigma_y}{D a_L}\right)^2\right]}} \cdot \sqrt{\frac{\rho D^2}{m_e}} \cdot \sqrt{\frac{D}{H}} \tag{8}$$

$$k_p = \sqrt{2}\left\{1 + 1.2 \arctan\left[0.75\left(\frac{\mathrm{Sc}}{4\pi K_a}\right)^4\right]\right\} \tag{9}$$

where: C_c, K_a – aerodynamic parameters which are dependent on turbulence intensity, Reynolds number, mode shape, mean wind speed and outer diameter changing along the height, a_L – limited amplitude obtained at very low damping, m_e – equivalent mass per unit length.

Value of the peak factor is usually between 3.5 and 4 for low vibration amplitudes and equals to $2^{1/2}$ for high amplitudes.

Crosswind load may not be taken into consideration when: critical wind speed v_{kr} is larger than the 10-minutes mean wind speed at a height of 10 m reduced by time of chimney exploitation or Sc > 15 or this is a guyed chimney or there are dampers on the chimney [4]. According to Eurocode 1 [3], vortex excitation must not be analyzed when critical wind speed is larger than 1.25 of the mean wind speed at respective height.

3. Analyzed steel chimneys

Three groups of chimneys were analyzed: 35 chimneys of a constant diameter (type 1); 38 chimneys with a tapered lower part and a constant diameter on the top section (type 2); 9 chimneys tapered on the whole height of the structure (type 3) – detailed data is taken from literature [8–9, 12–15, 18, 23, 29, 33]. Finite element models were prepared for each of the chimneys and modal analysis was performed as the first stage of the study. Structural data are presented for every chimney in Tables 1–3. The basic denotations are presented in Figure 1. Moreover, the following denotations are introduced: m_e – equivalent mass of the chimney; δ_s – logarithmic decrement of structural damping; f_1 – first frequency of natural vibrations; $\lambda = H/D$ ($\lambda = H/D_T$) – chimney slenderness; m_{e_calc}, $\mathrm{Sc_{calc}}$, f_{1calc} $V_{kr,1}$ – equivalent mass; Scruton number; the first frequency; the first critical wind speed obtained by FEM calculations. Exact total mass of the structure is represented in the FEM models, however, natural frequencies obtained in calculations differ from the ones presented in the data in some cases (as is noted in Tables 1–3). This is caused by the lack of sufficiently detailed information about stiffness and mass distribution throughout the height of the structures as well as the service time when frequencies were measured. Taking this into account, an applied numerical approach seems reasonable. Moreover, in some cases, frequencies of vibrations were only very roughly estimated in in-situ conditions with no special equipment.

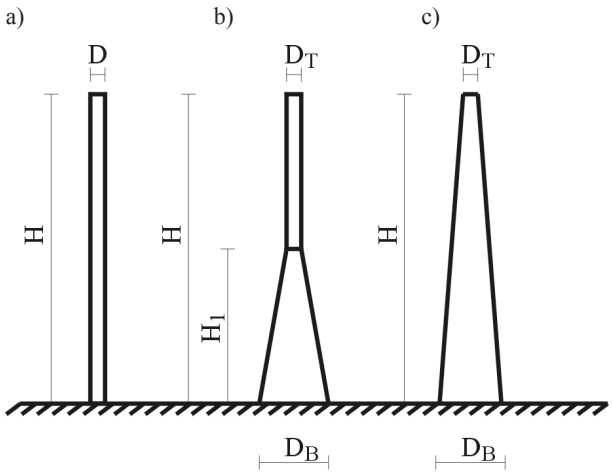

Fig. 1. Denotations of the steel chimneys: a) type 1; b) type 2; c) type 3

Table 1

Structural data, dynamic and damping parameters for chimneys of type 1

Lp	H	D	m_e	δ_s	f_1	λ	m_{e_calc}	Sc_{calc}	f_{1calc}	$V_{kr;1}$
	[m]	[m]	[kg/m]	[-]	[Hz]	[-]	[kg/m]	[-]	[Hz]	[m/s]
1	17	0.6	95	0.025	2	28.33	95.3	10.6	2.227	6.7
2(1)	23	1.5	510	0.038		15.33	511.2	13.8	2.271	17.0
3	25.5	1.8	360	0.031		14.17	359.7	5.5	2.898	26.1(3)
4	25.5	0.71	199	0.025	0.72	35.92	199.1	15.8	1.102	3.9
5	26	1.25	199.2	0.030	1.88	20.80	199.6	6.1	1.991	12.4
6	28	0.914	88.8	0.015	1.72	30.63	88.8	2.6	1.872	8.6
7	29	1.4	216	0.019		20.71	216.9	3.4	1.687	11.8
8	30	0.816	135.7	0.020	1.06	36.76	135.5	6.5	1.094	4.5
9	30	0.711	157	0.025	0.7	42.19	157.0	12.4	0.848	3.0
10	31	1.5	240	0.031	1.5	20.67	242.1	5.3	1.796	13.5
11	31	1.35	215	0.031	1.6	22.96	217.5	5.9	1.619	10.9
12	34	0.813	159	0.025	0.76	41.82	159.1	9.6	0.761	3.1
13	35	1.8	280	0.019		19.44	276.2	2.6	1.763	15.9
14	35	0.813	201.6	0.015	0.61	43.05	201.8	7.3	0.751	3.1
15(1)	38	3.3	1080	0.031		11.52	1085.5	4.9	1.888	31.1(3)(4)
16	38	1.016	231	0.030	0.68	37.40	231.4	10.8	0.847	4.3
17	40.45	1.65	22(2)	0.025	0.81	24.52	461.1	6.8	1.169	9.6
18	40.7	1.42	29(2)	0.025	0.68	28.66	639.8	12.7	0.937	6.7
19(1)	41	3.04	1166	0.038		13.49	1170.1	7.7	1.362	20.7
20	45	1.12	182	0.025	0.62	40.18	182.6	5.8	0.753	4.2
21(1)	46	3.2	3280	0.038		14.38	3281.7	19.5	0.910	14.6
22	46	1.8	447	0.025	0.9	25.56	448.0	5.5	1.012	9.1
23	48.7	1.62	181	0.025	0.72	30.06	181.5	2.8	0.952	7.7
24	54	3.9	61(2)	0.031	1.1	13.85	894.7	2.9	1.604	31.3(3)
25	55	2.04	49(2)	0.031	1.09	26.96	652.1	7.8	0.866	8.8
26	58.8	2.4	63(2)	0.031	0.68	24.50	879.4	7.6	0.620	7.4
27	60	1.575	233	0.031	0.5	38.10	232.5	4.6	0.532	4.2
28	60	2	315	0.013	0.8	30.00	314.6	1.6	0.696	7.0
29	60	2	345	0.125	0.77	30.00	345.2	17.3	0.665	6.7
30	61	3.35	620	0.038	0.97	18.21	619.6	3.4	1.026	17.2
31(1)	61	3.35	2040	0.057	0.71	18.21	2039.5	16.6	0.556	9.3
32	65	1.91	58(2)	0.031	0.71	34.03	648.8	8.8	0.589	5.6
33	80	3.96	5096.5	0.020	0.53	20.20	5093.7	10.4	0.483	9.6
34	90	2.3	661	0.040	0.29	39.13	660.8	8.0	0.303	3.5
35	90	2.3	661	0.070	0.29	39.13	660.8	14.0	1.000	11.5

(1) there is chimney insulation, (2) total mass of the chimney in tonnes (3) vortex excitation does not need to be calculated according to Polish standard, (4) vortex excitation does not need to be calculated according to Eurocode.

Table 2

Structural data, dynamic and damping parameters for chimneys of type 2

Lp,	H	H_1	D_T	D_B	m_e	δ_s	f_1	λ	m_{e_calc}	Sc_{calc}	f_{1calc}	$V_{kr,1}$
	[m]	[m]	[m]	[m]	[kg/m]	[-]	[Hz]	[-]	[kg/m]	[-]	[Hz]	[m/s]
1	28	6.16	1.6	2.304	255	0.031		17.50	255.1	4.9	2.774	22.2(3)
2	30.5	7.625	1.4	2.45	275	0.025		21.79	274.6	5.6	2.016	14.1
3	30.5	7.625	1.4	2.45	330	0.025	1.6	21.79	331.3	6.8	2.251	15.8
4	36	0.72	1.5	2.325	230	0.025	1.04	24.00	230.2	4.1	1.180	8.9
5	36	12.96	0.4	0.904	85	0.019	0.4	90.00	84.9	16.1	0.537	1.1
6	40	12	1.45	2.32	214	0.038		27.59	214.8	6.2	1.801	13.1
7(1)	43	12.9	1.8	3.294	895	0.031		23.89	894.4	13.7	0.908	8.2
8	43	12.9	1.8	3.294	300	0.019	1	23.89	299.8	2.8	1.578	14.2
9	43.5	15.225	1.68	3.024	330	0.025	0.95	25.89	331.4	4.7	1.330	11.2
10(1)	44	11	1.450	2.596	490	0.031		30.34	491.5	11.6	0.705	5.1
11	44.7	12.069	2.54	3.581	500	0.019	1.2	17.60	499.6	2.4	1.626	20.7
12(1)	44.7	12.069	2.54	3.581	950	0.031	0.91	17.60	950.4	7.3	1.178	15.0
13	45	13.5	1.83	2.928	270	0.038		24.59	270.7	4.9	1.512	13.8
14	45.7	11.882	1.22	3.05	190	0.025	0.92	37.46	188.4	5.1	1.193	7.3
15(1)	45.7	10.511	2.2	3.036	735	0.031		20.77	734.2	7.5	0.913	10.0
16	46	18.4	1.7	3.74	262	0.025	-	27.06	261.1	3.6	1.535	13.0
17(1)	46	18.4	1.7	3.74	650	0.038	-	27.06	649.5	13.7	0.966	8.2
18(1)	46	13.34	1.4	2.8	450	0.038		32.86	449.8	14.0	0.702	4.9
19(1)	46	11.04	2.2	3.432	745	0.031		20.91	744.8	7.6	0.928	10.2
20(1)	47.5	15.2	2	2.66	755	0.044	0.9	23.75	755.0	13.3	0.753	7.5
21(1)	49	15.19	2.9	5.22	955	0.038		16.90	955.6	6.9	1.080	15.7
22	55	17.05	2.14	3.681	323	0.025	1.1	25.70	322.1	2.8	1.308	14.0
23	56	3.92	2.4	3.768	780	0.031	0.83	23.33	779.6	6.7	0.817	9.8
24	60	36	1	1.6	148	0.031	0.6	60.00	148.6	7.4	0.754	3.8
25	61	15.25	2.1	3.675	410	0.025	0.66	29.05	408.8	3.7	0.861	9.0
26	68.5	27.4	3.45	5.693	680	0.025	1.12	19.86	682.9	2.3	1.234	21.3
27(1)	68.5	27.4	3.45	5.693	1470	0.038	0.82	19.86	1469.6	7.5	0.836	14.4
28	72	23.76	2.5	4.225	470	0.025		28.80	469.3	3.0	0.876	11.0
29(1)	72	23.76	2.5	4.225	980	0.038	0.8	28.80	979.9	9.5	0.601	7.5
30(1)	74	18.5	3.5	5.25	1640	0.038		21.14	1642.2	8.2	0.589	10.3
31	74	24.42	3	4.5	595	0.019	0.66	24.67	595.6	2.0	1.060	15.9
32(1)	76	28.88	4.9	8.33	2175	0.05	1.05	15.51	2174.3	7.2	1.010	24.7(3)
33	76	23.56	2.75	6.105	450	0.025		27.64	453.5	2.4	0.940	12.9
34(1)	76	19.76	2.9	4.35	1270	0.031	0.68	26.21	1270.1	7.5	0.553	8.0
35(1)	76.2	15.24	2.62	3.563	970	0.038	0.6	29.08	971.4	8.6	0.387	5.1
36	90	23.4	4.5	5.49	1098	0.025		20.00	1098.2	2.2	0.811	18.2
37	91.5	29.28	4.88	8.247	765	0.031	1	18.75	765.1	1.6	1.118	27.3(3)
38	145	34.8	6	10.08	1950	0.025	0.48	24.17	1943.5	2.2	0.456	13.7

Table 3

Structural data, dynamic and damping parameters for chimneys of type 3

Lp	H	D_T	D_B	m_e	δ_s	f_1	λ	m_{e_calc}	Sc_{calc}	f_{1calc}	$V_{kr,1}$
	[m]	[m]	[m]	[kg/m]	[-]	[Hz]	[-]	[kg/m]	[-]	[Hz]	[m/s]
1	37	2.45	3.68	450	0.038		15.10	452.4	4.6	3.221	39.5(3)(4)
2(1)	49	0.85	2.32	245	0.038		57.65	245.6	20.7	1.043	4.4
3(1)	67	3.85	9.16	3510	0.038	0.84	17.40	3510.5	14.4	1.646	31.7(3)
4(1)	73	5.1	7.91	4100	0.038	0.64	14.31	4097.4	9.6	1.191	30.4(3)
5	75	0.96	3.17	140	0.031	1.25 (0.8)	78.13	140.0	7.5	0.875	4.2
6	77	3.2	5.54	1360	0.031	0.69	24.06	1361.4	6.6	1.050	16.8
7	83	3.2	6.4	1360	0.038	1.15 (1.2)	25.94	1360.2	8.1	1.073	17.2
8	90	4.5	7.2	2090	0.031	0.75 (0.8)	20.00	2088.6	5.1	0.978	22.0
9(1)	91.5	4.38	6.92	2010	0.025	0.68 (0.8)	20.89	2010.2	4.2	0.851	18.6

4. Results and discussion of chimney response

4.1. Along-wind response

When analyzing along-wind action, open terrain (category A according to Polish standards or its closest equivalent in Eurocode – category 2) is introduced in calculations. Two Eurocode procedures of the structural coefficient $c_s c_d$ calculations were used. In most cases, a good accordance of both methods has been obtained. The differences of the results obtained with these two procedures are less than 5% – this is consistent with Eurocode information and may confirm the accuracy of the FEM models.

In each case, higher values have been obtained with use of the second procedure. However, static FEM analyses have been performed with the use of the values of the structural coefficient from the first procedure, as more probable ones. In the presented calculations, the mode shapes of natural vibrations were obtained in FEM modal analyses and they slightly differ from those assumed in Eurocode recommendations. This could be a reason for small discrepancies in values of $c_s c_d$, as coefficients used in Eurocode are related to functions proposed by the standard.

There are comparisons of $c_s c_d$ values according to both procedures in Fig. 2.

It should be mentioned that the values of $c_s c_d$, and subsequently, wind load values are very sensitive to the choice of the terrain roughness and to the logarithmic decrement of structural damping δ_s for the analyzed chimney. Along-wind loads were calculated as static values according to respective standards and then applied to nodes of the FEM model as concentrated forces.

The normalized maximum top displacements x/D in the function of chimney slenderness λ and Scruton number Sc are presented respectively in Figs 3 and 4.

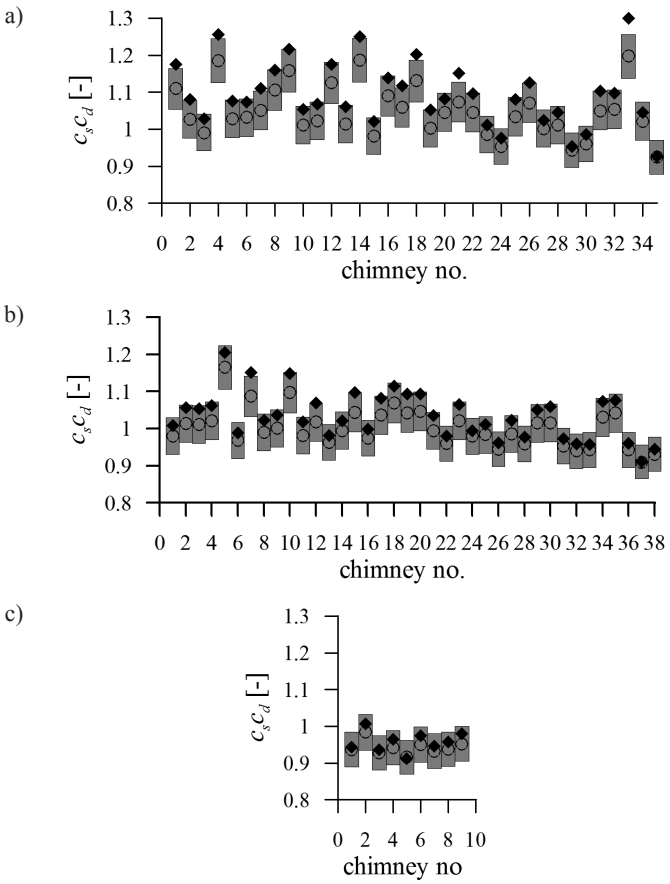

Fig. 2. Comparison of structural coefficient $c_s c_d$ for a) type 1, b) type 2, c) type 3, O – procedure 1, ◆ – procedure 2, grey range – procedure 1 ± 5%

Displacements calculated according to Polish standards and Eurocode are similar to each other but slightly higher for Polish standards. The first procedure of $c_s c_d$ calculations has been used. The application of the second procedure increases top displacements about 5%. Relative differences calculated as $(x_{\max,PN} - x_{\max,Eurocode})/x_{\max,PN} \cdot 100\%$ between top displacements are in the ranges:

- 22.3%–30.8% for type 1,
- 0.6%–14.4% for type 2,
- 2%–15.4% for type 3.

The largest displacements have been obtained for chimneys of type 1. For all types values are higher for larger λ, whereas no distinct dependence on Sc have been noticed. The highest values of top displacements in Fig. 4a,b,c are related to chimneys with relatively small diameter and high slenderness. The probable reason for differences between codes is that Polish standards distinguish 3 terrain categories whereas Eurocode – five. The transition between categories is always questionable.

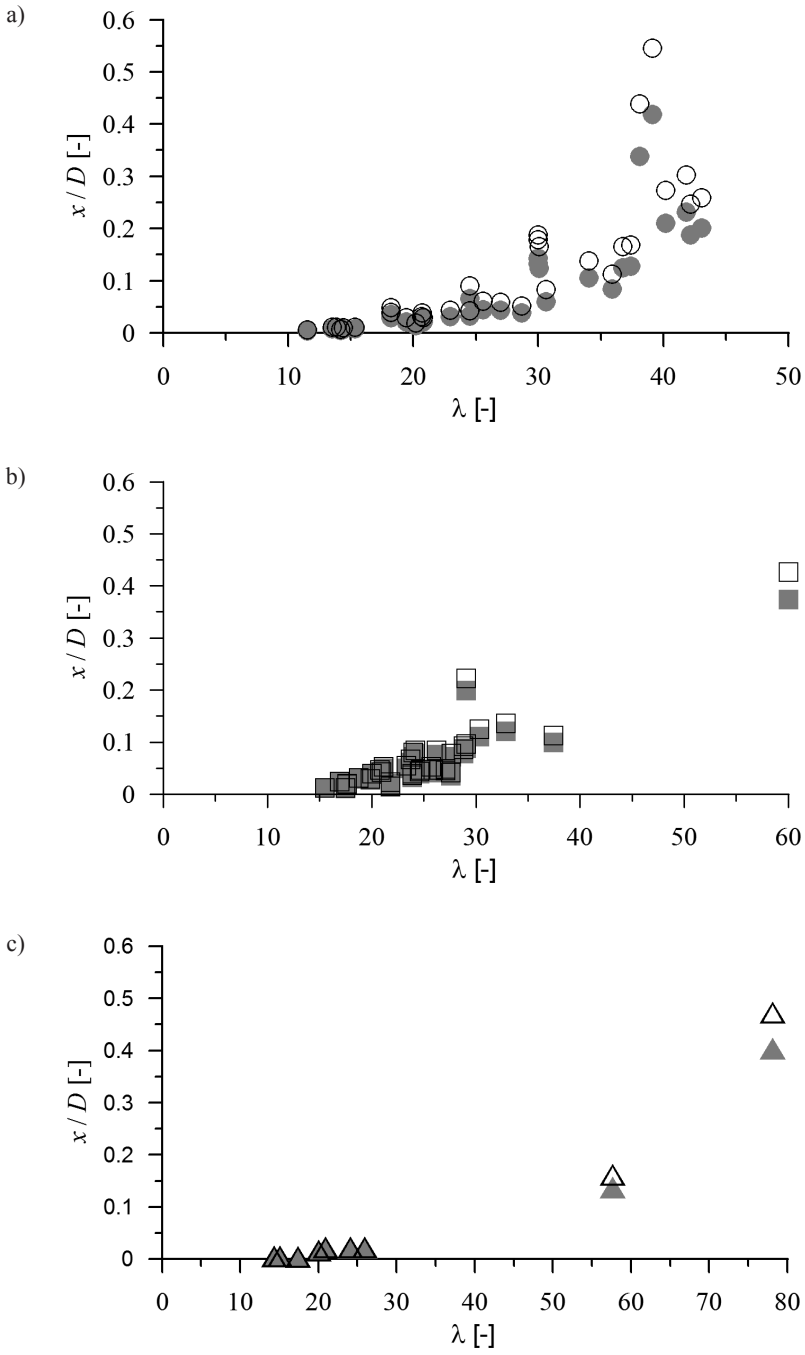

Fig. 3. Normalized top displacements in along-wind direction in dependence on slenderness λ for a) type 1, ○ – Polish standards, ● – Eurocode, b) type 2, □ – Polish standards, ■ – Eurocode, c) type 3, △ – Polish standards, ▲ – Eurocode

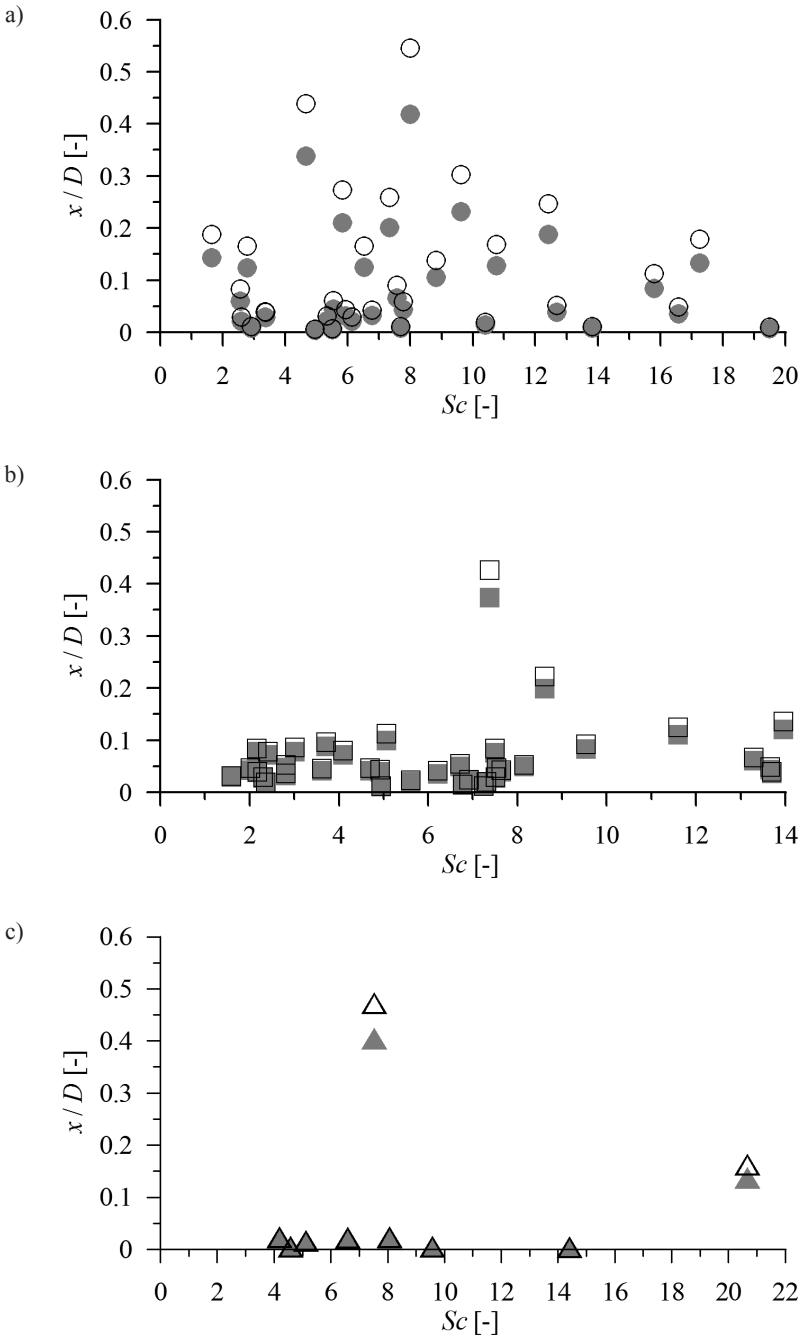

Fig. 4. Normalized top displacements in along-wind direction in dependence on Scruton number Sc for a) type 1, ○ – Polish standards, ● – Eurocode, b) type 2, □ – Polish standards, ■ – Eurocode, c) type 3, △ – Polish standards, ▲ – Eurocode

4.2. Crosswind response

Crosswind load caused by vortex excitation has been analyzed according to three approaches: one recommended by Polish standards and two recommended by Eurocode. All parameters describing respective loads have been assumed according to code's rules. There are dependencies between maximum normalized top displacements and λ, Sc and f_1 shown in Figs 5–7. The use of normalized displacements y/D on vertical axis shows in some cases characteristics trends which are not visible when only y is used. In case of Eurocode procedures No. 1 and No. 2 top displacements caused by vortex shedding have been calculated in the first step (eqs 6, 7) and then static inertia forces (eq. 5) have been applied to nodes of the FEM models. Final displacements obtained in static analyses are very similar to the ones caused by vortices only.

Displacements calculated with Polish standards are in accordance with those calculated with procedure 1 from Eurocode and are slightly higher. A similar model is adopted in both methods but the Polish standard assumes constant correlation length independent from lock-in effect and, in the majority of cases, it is longer than that determined from the iterative procedure in Eurocode. (Fig. 8). Another reason for small discrepancies is the Strouhal number value which is equal to 0.2 (Polish standard) and 0.18 (Eurocode). This leads to different critical wind speeds. The recommended structural logarithmic decrement of damping also differs between both codes. In the paper, the same level of damping based on measurements has been assumed; therefore, it does not influence the results.

On the other hand, displacements obtained according to procedure 2 from Eurocode are significantly higher. Top displacements according to procedure 2 are higher than those obtained with procedure 1, on average:

- type 1 – 4.17 times (in two cases displacements are lower, in two cases displacements are much higher, these results have not been averaged);
- type 2 – 4.8 times (in two cases displacements are lower, these results have not been averaged);
- type 3 – 5.3 times (in one case displacements are lower, in one case much higher, these results have not been averaged). Moreover, the representative number of chimneys of type 3 is quite low.

Considering procedure 2, it must be underlined that lower displacements have been obtained for high Scruton number values which means that damping forces are high when compared to inertia forces. When the Scruton number is high, the standard deviation of displacements σ_y (eq. 8) and y_{max} (eq. 7) is very small.

There is a clear dependence between the maximum normalized top displacements and Scruton number. Obviously, values of y/D decrease with an increase of Sc – almost linearly in the case of procedure 2 and according to exponential function in the case of Polish standard and procedure 1. Such a tendency is clearly visible mainly for chimneys of type 2.

There is no clear dependence between y/D and slenderness λ and values obtained from procedure 2 are higher for all ranges of λ.

There is either no clear dependence between y/D and f_1. The range of first frequencies for the analyzed chimneys is 0.303–3.221 Hz. A higher f_1 means a higher critical wind speed but on the other hand, it also means a higher stiffness of the structure.

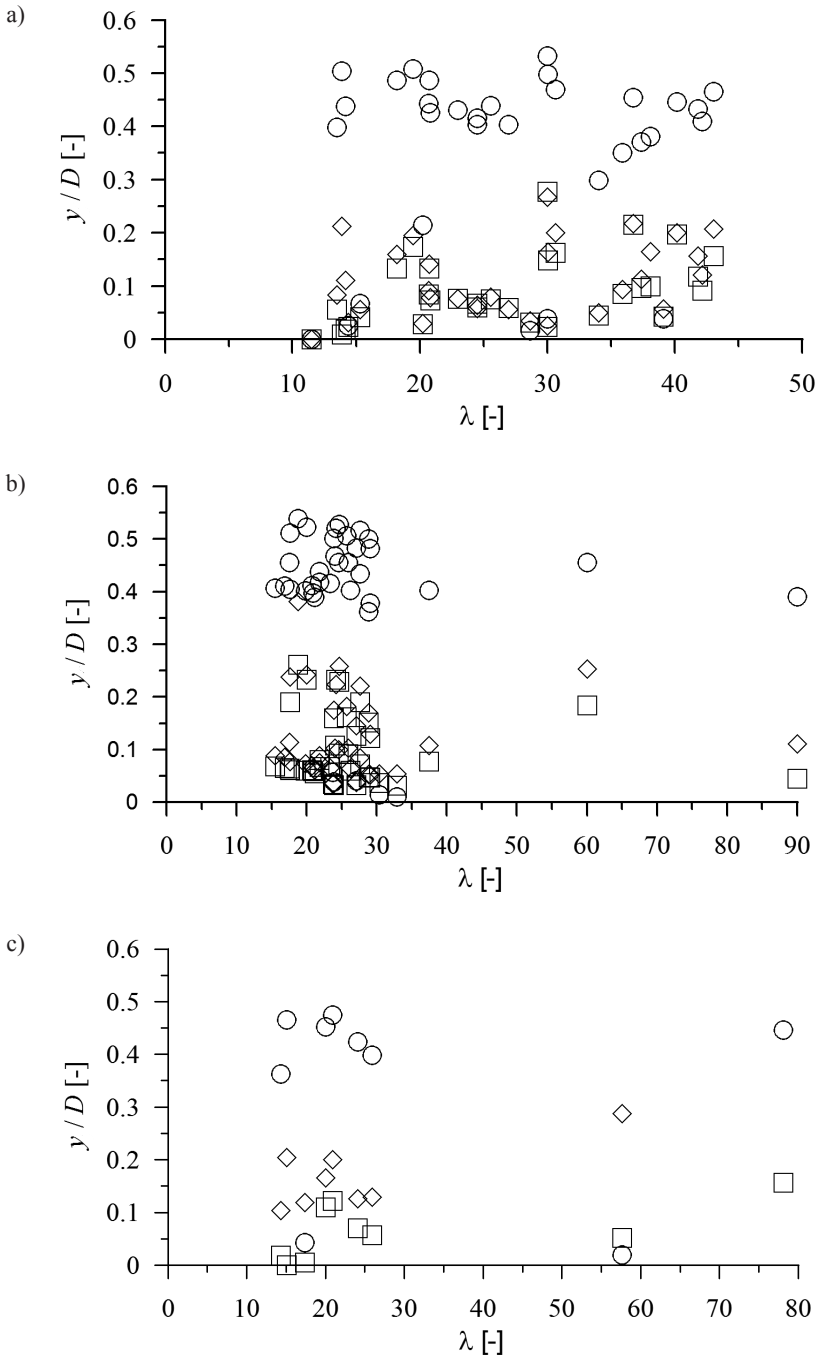

Fig. 5. Normalized top displacements in crosswind direction in dependence on slenderness λ, a) type 1, b) type 2, c) type 3, ◇ – Polish standard, □ – Eurocode, procedure 1, ○ – Eurocode, procedure 2

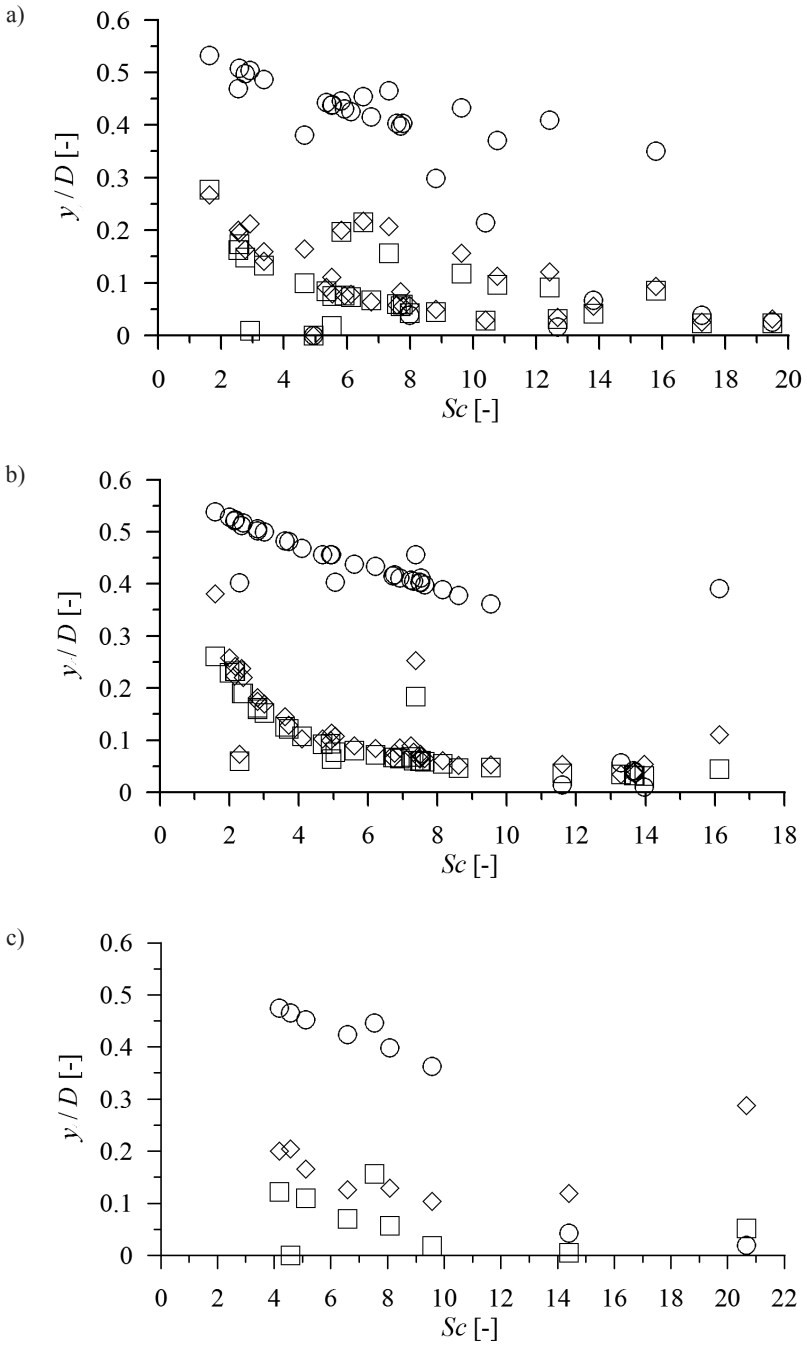

Fig. 6. Normalized top displacements in crosswind direction in dependence on Scruton number Sc, a) type 1, b) type 2, c) type 3, ◇ – Polish standard, □ – Eurocode, procedure 1, ○ – Eurocode, procedure 2

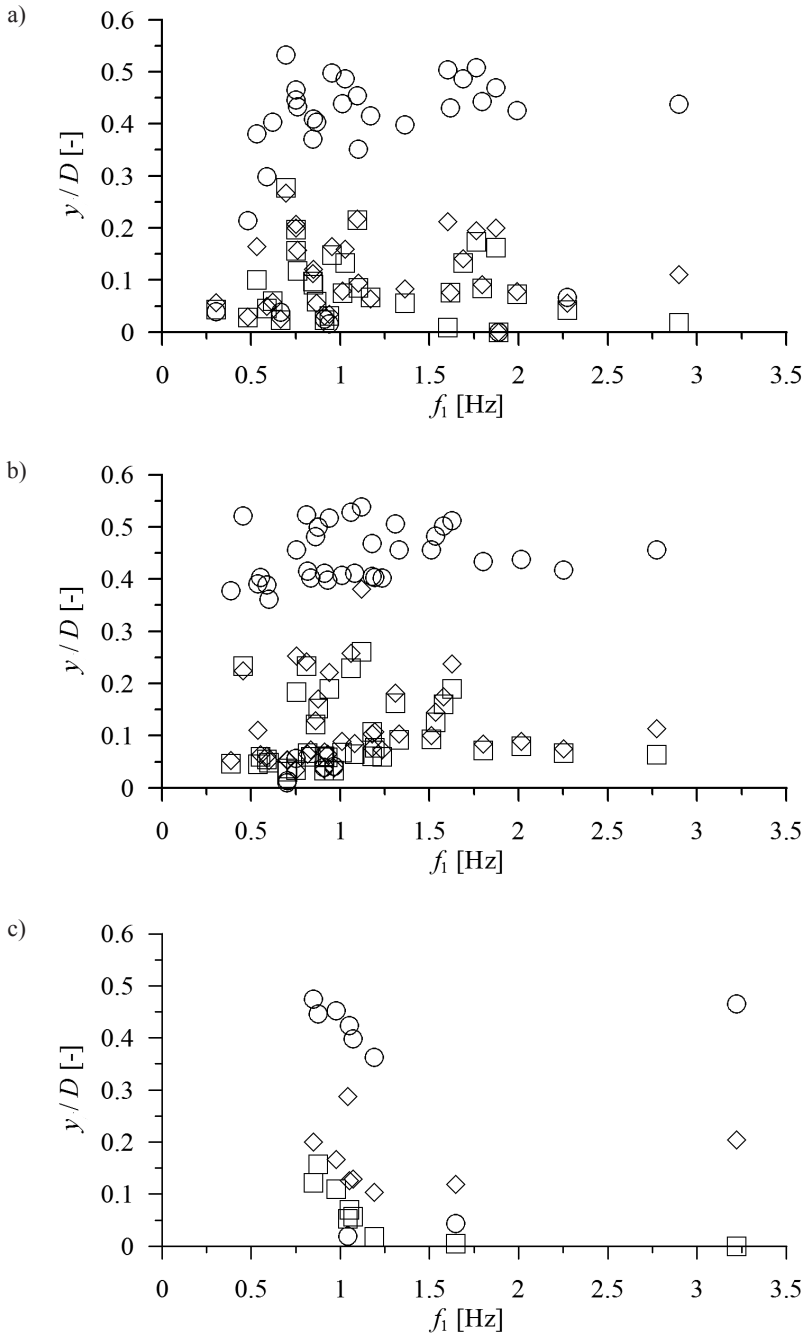

Fig. 7. Normalized top displacements in crosswind direction in dependence on the first natural frequency f_1, a) type 1, b) type 2, c) type 3, ◇ – Polish standard, □ – Eurocode, procedure 1, ○ – Eurocode, procedure 2

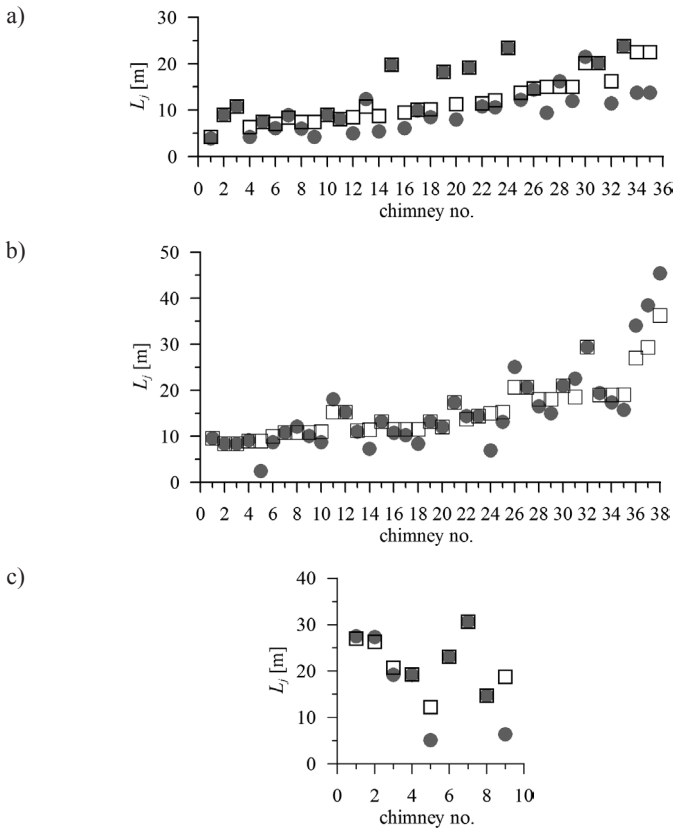

Fig. 8. Correlation length: a) type 1, b) type 2, c) type 3, □ – polish standard, ● – Eurocode

4.3. Comparison of displacements in along-wind and crosswind responses

There are comparisons of normalized top displacements obtained in along-wind and crosswind load analyses presented in Fig. 9. As can be seen, in almost all cases the crosswind load causes larger displacements.

5. Conclusions

Deflections at the top of the chimneys in the case of along-wind action calculated with each of the standards are similar. One of the main factors influencing discrepancies is the definition of terrain roughness in different standards. Additional discrepancies are produced with different assumed values of structural damping or the procedure of the structural coefficient calculation that has been used.

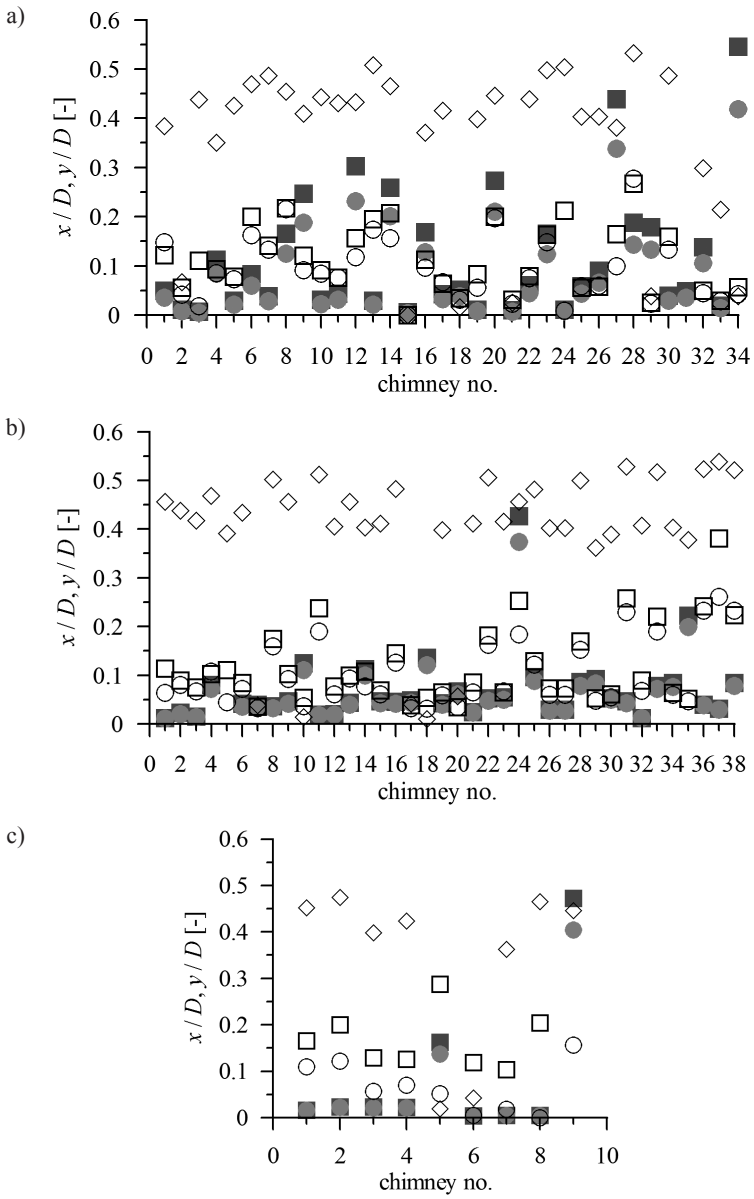

Fig. 9. Normalized top displacements in along-wind and crosswind directions for a) type 1, b) type 2, c) type 3, ■ – along-wind, Polish standard, ● – along-wind, Eurocode, □ – crosswind, Polish standard, ○ – crosswind, Eurocode, procedure 1, ◇ – crosswind, Eurocode, procedure 2

Significant differences are noticeable when crosswind action is considered. In the case of lower Sc numbers, the obtained values of deflections are higher for each type of chimney and such conclusion is in force for all natural frequencies. There is no significant relation of

deflections to the slenderness of the structure λ as well as to natural frequency f_1. The main factors influencing the results are: assumed value of St number; structural damping; assumed area of vortex excitation; and most of all, the choice of analytical procedure. Results obtained due to the Polish standard and Eurocode 1, procedure 1 are quite similar, whereas procedure 2 gives top displacements that are a few times higher.

Generally, the calculated deflections generated by the along-wind action are a few times smaller than the ones generated by the crosswind action.

The coauthor Paulina Jamińska participates in the project „Kwalifikacje dla rynku pracy – Politechnika Lubelska przyjazna pracodawcy" co-financed by the European Union under the European Social Funding.

References

[1] Davenport A.G., *The spectrum of horizontal gustiness near the ground in high winds*, Quaterly Journal of the Royal Meteorological Society, Vol. 87, 1961, 194-211.

[2] Davenport A.G., *The relationship of wind structure to wind loading*, Proc. 1st Conference on Wind Effects on Building and Structures, Teddington, England 1965.

[3] PN-EN 1991-1-4, Eurocode 1: Actions on structures – General actions – Part 1-4: Wind actions. PKN, 2008.

[4] PN-93/B-03201, Steel structures. Chimneys. Design rules, PKN, 1993 (in Polish).

[5] PN-77/B-02011, Loads in static calculations. Wind loads, PKN, 1977 (in Polish).

[6] Ruscheweyh H., *Codification of vortex excited* vibrations, [In:] *Recent advances in wind engineering*, Proc. 2nd Asia-Pacific *Symposium* on Wind Engineering, Beijing, China, Pergamon Press, Vol. 1, 1989, 362-72.

[7] Ruscheweyh H., *Windlastannahmen für turmartige Bauwerke*, DIN-Mitt, Vol. 71(11), 1992, 644-47.

[8] Galemann T., Ruscheweyh H., *Measurements of wind induced vibrations of a full-scale steel chimney*, Journal of Wind Engineering and Industrial Aerodynamics, Vol. 41-44, 1999, 241-252.

[9] Ruscheweyh H., Galemann T., *Full-scale measurements of wind-induced oscillations of chimneys*, Journal of Wind Engineering and Industrial Aerodynamics, Vol. 65, 1996, 55-62.

[10] Vickery B.J., Clark A.W., *Lift or acrosswind response of tapered stacks*, ASCE Journal of Structural Division, Vol. 98(1), 1972, 1-20.

[11] Vickery B.J., Basu R.I., *Acrosswind vibrations of structures of circular cross-section. Part I & Part II*, Journal of Wind Engineering and Industrial Aerodynamics, Vol. 12, 1983, 49-73 and 75-97.

[12] Dyrbye C., Hansen S.O., *Wind loads on structures*, Wiley, New York 1997.

[13] Hansen S.O., *Vortex-induced vibrations of line-like structures*, CICIND Report, Vol. 15(1), 1999, 15-23.

[14] Van Koten H., *Wind induced vibrations of chimneys: the rules of the CICIND code for steel chimneys*, Engineering Structures, Vol. 6, 1984, 350-356.

[15] Pritchard B.N., *Steel chimney oscillations: A comparative study of their reported performance versus predictions using existing techniques*, Engineering Structures, Vol. 6, 1984, 315-323.
[16] Ciesielski R., Gaczek M., Kawecki J., *Observation of crosswind response of towers and steel chimneys*, Journal of Wind Engineering and Industrial Aerodynamics, Vol. 41-44, 1992, 2205-2211.
[17] Arunachalam S., Govindaraju S.P., Lakshmanan N., Appa Rao T.V.S.R., *Acrosswind aerodynamic parameters of tall chimneys with circular cross section - a new empirical model*, Engineering Structures, Vol. 23, 2001, 502-520.
[18] Tranvik P., Alpsten G., *Dynamic behaviour under wind loading of a 90m steel chimney*, Alstom Power Sweden AB, Report S-01041/9647-3, 2002.
[19] Włodarczyk W., *O niektórych problemach projektowania kominów stalowych*, Inżynieria i Budownictwo, Vol. 11, 2004, 591-596 (in polish).
[20] Chmielewski T., Górski P., Beirow B., Kretzschmar J., *Theoretical and experimental free vibrations of tall industrial chimney with flexibility of soil*, Engineering Structures, Vol. 27, 2005, 25-34.
[21] Włodarczyk W., *Wzbudzenie wirowe drgań według Eurokodu 1 jako oddziaływanie wiatru na kominy stalowe*, Inżynieria i Budownictwo, Vol. 10, 2006, 530-533 (in polish).
[22] Kalabińska J., *Analiza podatności kominów stalowych na wzbudzenie wirowe według ujęć normowych*, Inżynieria i Budownictwo, Vol. 3, 2007, 199-202 (in polish).
[23] Kawecki J., Żurański J.A., *Crosswind vibrations of steel chimneys – A new case history*, Journal of Wind Engineering and Industrial Aerodynamics, Vol. 95, 2007, 1166-1175.
[24] Górski P., Chmielewski T., *A comparative study of long and crosswind responses of tall chimney with and without flexibility of soil*, Wind and Structures, Vol. 11(2), 2008, 121-135.
[25] Black C.J.M., Barrios H.H., López A.L., *A comparison of crosswind response evaluation for chimneys following different international codes*, Proc. 11th Americas Conference on Wind Engineering, Puerto Rico, San Juan 2009.
[26] Górski P., *Some aspects of the dynamic crosswind response of tall industrial chimney*, Wind and Structures, Vol. 12(3), 2009, 259-279.
[27] Chmielewski T., Breuer P., Górski P., Konopka E., *Monitoring of tall slender structures by GPS measurements*, Wind and Structures, Vol. 12(5), 2009, 401-412.
[28] Flaga A., Lipecki T., *Code approaches to vortex shedding and own model*, Engineering Structures, Vol. 32(6), 2010, 1530-1536.
[29] Verboom G.K., van Koten H., *Vortex excitation: Three design rules tested on 13 industrial chimneys*, Journal of Wind Engineering and Industrial Aerodynamics, Vol. 98, 2010, 145-154.
[30] Wichtowski B., Żurański J.A., *Pewne przypadki rezonansu wiatrowego kominów stalowych*, Inżynieria i Budownictwo, Vol. 3, 2011, 154-156 (in polish).
[31] Flaga A., Lipecki T., *Vortex excitation of steel chimneys with corrosion*, Proceedings of the ICE – Engineering and Computational Mechanics, Vol. 164(4), 2011, 233-243.
[32] Żurański J.A., Gaczek M., *Oddziaływania klimatyczne na konstrukcje budowlane według Eurokodu 1, Komentarze z przykładami obliczeń*, ITB, Warszawa 2011 (in polish).

[33] Clobes M., Willecke A., Peil U., *Vortex excitation of steel chimneys: Two ultimate limit states*, Proc. 13th International Conference on Wind Engineering, Amsterdam 2011.

[34] Repetto M.P., *Neutral and non-neutral atmosphere: Probabilistic characterization and wind-induced response of structures*, Journal of Wind Engineering and Industrial Aerodynamics, Vol. 99, 2011, 969-978.

[35] Arunachalam S., *Studies on acrosswind load and response of a circular chimney including lock-in effects*, Proc. 13th International Conference on Wind Engineering, Amsterdam 2011.

[36] Arunachalam S., *Studies on acrosswind load and response of a circular chimney including lock-in effects -part 2*, Proc. 13th International Conference on Wind Engineering, Amsterdam 2011.

[37] Włodarczyk W., *Wzbudzenie wirowe drgań w projektowaniu kominów stalowych według PN-EN 1991-1-4 i PN-EN 1993-3-2*, Inżynieria i Budownictwo, Vol. 11, 2012, 576-579 (in polish).

[38] Belver A.V., Iban A.L., Martin C.E.F., *Coupling between structural and fluid dynamic problems applied to vortex shedding in a 90 m steel chimney*, Journal of Wind Engineering and Industrial Aerodynamics, Vol. 100, 2012, 30-37.

[39] Lipecki T., Flaga A., *Vortex excitation model. Part I. mathematical description and numerical implementation*, Wind and Structures, Vol. 16(5), 2013, 457-476.

[40] Lipecki T., Flaga A., *Vortex excitation model. Part II.* application to real s*tructures and validation*, Wind and Structures, Vol. 16(5), 2013, 477-490.

[41] Górski P., *Investigation of dynamic characteristics of tall industrial chimney based on GPS measurements using Random Decrement Method*, Engineering Structures, Vol. 83, 2015, 30-49.

TECHNICAL TRANSACTIONS | CZASOPISMO TECHNICZNE
CIVIL ENGINEERING | BUDOWNICTWO
2-B/2015

TOMASZ NOWICKI*

THE DISCRETE VORTEX METHOD FOR ESTIMATING HOW SURFACE ROUGHNESS AFFECTS AERODYNAMIC DRAG ACTING ON A LONG CYLINDER EXPOSED TO WIND

OSZACOWANIE WPŁYWU CHROPOWATOŚCI POWIERZCHNI NA SIŁĘ OPORU AERODYNAMICZNEGO DZIAŁAJĄCEGO NA DŁUGI WALEC ZA POMOCĄ METODY WIRÓW DYSKRETNYCH

Abstract

This paper focuses on the aerodynamic drag force that acts on a long cylinder standing up to aerodynamic wind in the critical regime of the fluid flow. The core problem addressed here is how surface roughness of a high level and further increase of that level affects the drag. The research is based on computer simulations using the Discrete Vortex Method. A meshless version of the method was applied in order to let the boundary layer form freely in the way of a direct computer simulation. Fundamental ideas behind the Discrete Vortex Method, the original research program and the obtained results are presented. The main conclusion is that a small level of surface roughness may be neglected in engineering estimations.

Keywords: *wind engineering, discrete vortex method, surface roughness, aerodynamic force, aerodynamic drag*

Streszczenie

W pracy skupiono się na sile oporu aerodynamicznego działającej na nieskończenie długi walec poddany działaniu wiatru w zakresie krytycznym przepływu. Centralnym zagadnieniem badań było określenie wpływu dużej chropowatości walca na wartość tej siły oraz określenie związku pomiędzy zmianą parametru chropowatości a jej wartością. W ramach badań wykonano serię symulacji komputerowych przy użyciu metody wirów dyskretnych. Została zastosowana bezsiarkowa implementacja metody w celu osiągnięcia efektu swobodnego formowania się warstwy brzegowej. Praca przestawia podstawy teoretyczne metody wirów dyskretnych, założenia programu badań autorskich oraz uzyskane wyniki. Głównym wnioskiem postawionym w pracy jest określenie poziomu chropowatości poniżej którego może ona być zaniedbana w oszacowaniach inżynierskich.

Słowa kluczowe: inżynieria wiatrowa, metoda wirów dyskretnych, chropowatość, opór aerodynamiczny

DOI: 10.4467/2353737XCT.15.129.4166

* Department of Structural Mechanics, Lublin University of Technology, Poland.

1. Introduction

The knowledge of how surfaces roughness affects the aerodynamic response of solid bodies during exposure to wind is very important for a wide spectrum of technical problems. The ability of determining the level below which the roughness may be neglected is very useful from an engineering point of view. The upper limit of surface roughness is similarly very important. The upper limit of surface roughness is defined here as its size that is not yet the change in shape of the original body. The presented paper fits in long lasting interest in flows past circular cylinders. The flows are not only theoretical problems but also are very important from a practical point of view in relation to engineering structures. It is well known that the flow past a circular cylinder can be categorised according to the Reynolds number as subcritical, critical, supercritical or transcritical. In the critical regime ($Re \approx 1 \cdot 10^5 – 5 \cdot 10^5$) the phenomenon combines flow separation, turbulence transition, reattachment and turbulent separation of a boundary layer. The transition causes delaying of the separation point, which results in a reduction of the resultant drag force acting on the cylinder. On the other hand, high level surface roughness of the cylinder strongly effects the turbulent boundary layer making the process much more complicated.

This work aims at finding out how surface roughness changes the resultant aerodynamic drag force (expressed here as a drag force coefficient) under conditions of complex physics. For this purpose, Discrete Vortex Method (DVM) computer simulations were carried out. This method was chosen due to its meshless nature, which lets the turbulence (including boundary layer) form freely in the way of direct computer simulation. The main asset of DVM compared to a mesh-based method (e.g. the finite volume method) is the lack of artificial models of turbulence like RANS, LES or k-ε. Computer simulations were carried out at Reynolds number values of $0.7 \cdot 10^5$, $1.3 \cdot 10^5$, $2.0 \cdot 10^5$, $2.7 \cdot 10^5$ for 5 different levels of surface roughness. It would not be a surprise that increasing roughness poses a growing challenge due to increases in the complexity of the phenomena to be modelled. Three parameters describing surface roughness have been introduced. Finally, the obtained results allowed determining the levels of surface at which a) it can be neglected in engineering estimations, b) it means a change in the shape of the original object.

2. Problem description

The inspiration for the presented research comes from engineering practice. Real objects such as cables, pipes, or circular chimneys are never with a completely smooth surface. It is always a decision for an engineer whether the roughness can or cannot be neglected when the object is studied in a wind tunnel or numerically modelled. This work is intended to be an aid during the decision making process.

The object of study is a circular cylinder (Fig. 1a) long enough in order to treat the air flow around it as a 2D case. The cylinder is subjected to an air stream at speed u_{AIR}, which results in the appearance of aerodynamic forces: F_X – drag, F_Y – lift, M – moment. This research focuses on the drag force. The cross-section of the cylinder has been designed to be cogwheel

shaped (Figs. 1b, 2b), which simulates surface roughness. Each cogwheel is composed of 18 cogs in the shape of equilateral triangles uniformly distributed around the mean diameter D_{MEAN}=0.2m. The mean diameter, that is also the outline of the cylinder with surface of zero roughness, crosses each of the cogs in the middle of its depth, which is illustrated in Fig. 3. The number of cogs is a compromise between the complexity of the numerical models and the requirement of similarity to real surface roughness and has been found by way of preliminary study. Five levels of roughness have been taken into consideration (Fig. 2). In order to describe the level of roughness, three dimensionless parameters have been introduced. The first one f_1 is a ratio of cavity depth (h = 0.000 m, 0.005 m, 0.010 m, 0.020 m, 0.030 m) to the mean diameter of the cylinder D_{MEAN} (Fig. 3):

$$f_1 = h / D_{MEAN} \tag{1}$$

The parameter does not consider the total volume of cavity in the cylinder surface. On the contrary the second parameter of roughness (Fig. 4):

$$f_2 = A_{CLOSE} / A_{OUT} \tag{2}$$

where A_{CLOSE} is the total area of the cavity in the cross-section plane, $A_{OUT} = \pi \cdot D_{OUT}^2/4$ is the area of the circle enclosing the outline of the cross-section – this does not include any direct information on roughness depth. The parameter f_2 applied to the 3D object refers to volumetric size of the cavity on the surface. The third parameter of roughness (Fig. 5):

$$f_3 = \left(L_{COG} - L_{MEAN}\right) / L_{MEAN} \tag{3}$$

where $L_{MEAN} = \pi \cdot D_{MEAN}$ is a circumference of the original cylinder while L_{COG} indicates the perimeter of the real shape, describe the increment in surface area when applied to 3D object. This indirectly contains information about the size and the amount of surface cavity. For the studied case when the surface roughness is generated as regular geometry, all the parameters are of course geometrically correlated but for real uniformly distributed roughness, the correlation would not be so simple and this is the reason for introducing the parameters independently. Table 1 lists values of the defined parameters of roughness for the cross-sections used in the numerical experiment.

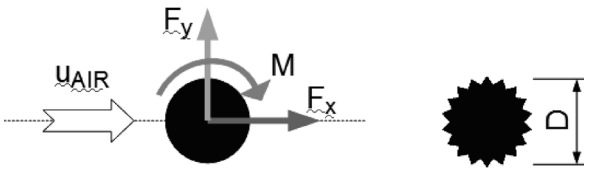

Fig. 1. The object of study: a) circular cylinder in an air stream at speed u_{AIR} with resulting aerodynamic forces: F_X – drag, F_Y – lift, M – moment; b) structure of surfaces roughness of the cylinder D = 0.20 m – mean diameter

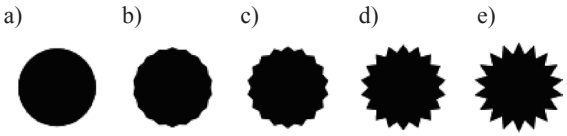

Fig. 2. View of the cross-section of the cylinder under study introduced according to growing roughness of its surface

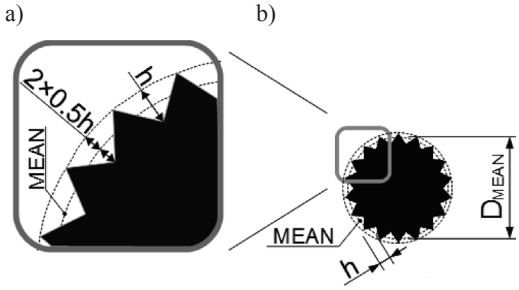

Fig. 3. View of geometrical structure of the roughness being generated on surface of the cylinder under study: a) close-up, b) general view. The uniform cog-wheel shape with depth of h is evenly distributed about the contour of the original cylinder with diameter D_{MEAN}

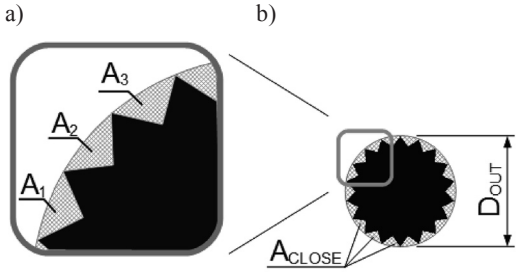

Fig. 4. View of a closing area ($A_{CLOSE} = A_1+A_2+A_3+...$) that is needed to smoothed the rough surface of the cylinder: a) close-up, b) general view, D_{OUT} – diameter of resulting cylinder

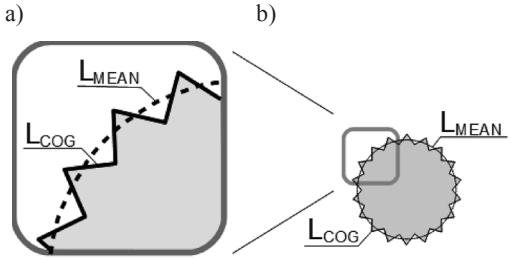

Fig. 5. View of a real perimeter of the cog-wheel shape L_{COG} compared to circumference of original shape L_{MEAN}: a) close-up, b) general view

Table 1

Values of parameters of roughness for the cross-sections used in the study

	a) 	b) 	c) 	d) 	e) 
h [m]	0.000	0.005	0.010	0.020	0.030
f_1 [%]	0.0	2.5	5.0	10.0	15.0
f_2 [%]	0.0	5.3	10.0	18.5	26.5
f_3 [%]	0.0	3.9	15.0	51.7	98.2

The consecutive cross-sections of the cylinder simulate growing roughness of its surface. It can be seen clearly that the choice of parameter determines the quantitative description of the roughness. Moreover, it is not the absolute values that is the most important in the description but their increments between the next levels of roughness. This characteristic determines which of them would be the most useful in a specific engineering problem.

3. Discrete Vortex Method

3.1. Theoretical background of DVM

Discrete Vortex Method (DVM) is a numerical method developed for solving the Navier–Stokes equation (N-S) based on the Lagrangian model of a particle tracing. In DVM, the equation is solved by the direct computer simulation of a physical phenomena. A finite mesh known from finite element and finite volume methods is not applied in DVM. Artificial models of turbulence such as LES or k-ε are also not used.

Considering 2D areas of fluid flow and assuming a homogeneous dry air with a constant density, the following form of the N–S equation can be used to describe the phenomenon under interest [1]:

$$\frac{\partial \mathbf{u}}{\partial t} + (\mathbf{u} \cdot \nabla)\,\mathbf{u} = -\frac{1}{\rho}\nabla p + \nu \Delta \mathbf{u} \tag{4}$$

where: $\mathbf{u}$ – velocity field, p – pressure field, ρ – density, t – time, ν – kinematic viscosity. The part $(\mathbf{u} \cdot \nabla)$ is an operator.

Eq. (5) is decomposed by calculating the rotation of the vector $\mathbf{u}$, which gives the so–called vorticity transport equation:

$$\frac{\partial \boldsymbol{\omega}}{\partial t} + (\mathbf{u} \cdot \nabla)\,\boldsymbol{\omega} = \nu \Delta \boldsymbol{\omega} \tag{5}$$

where $\boldsymbol{\omega} = \nabla \times \mathbf{u}$ is a vorticity field of the flow. The last equation (5) is composed of two components: advection (6) and diffusion (7):

$$\frac{\partial \boldsymbol{\omega}}{\partial t} + (\mathbf{u} \cdot \nabla)\, \boldsymbol{\omega} = 0 \tag{6}$$

$$\frac{\partial \boldsymbol{\omega}}{\partial t} = \nu \Delta \boldsymbol{\omega} \tag{7}$$

The separation lets us treat the fluid flow as two simultaneous and independent phenomena – advection and diffusion – and is known as a split algorithm. In DVM, it is not the velocity field that is being directly simulated but its vorticity equivalent. The vorticity field is represented in a discrete form, which for the 2D case reduces to a set of particles to a so-called vortex cloud. Each vortex particle contributes to the total cloud velocity field of flow that it co-represents, under the aerodynamic Bio–Savart law. Assembly of the cloud velocity field and potential velocity field not included in (5) but present in (4) gives the final velocity field in which the vortex cloud is drifted. The process is described by the advection formula (6). While the diffusion (7) is implemented as the vortex cloud erosion caused by the viscosity of the fluid medium.

The source of vorticity in the flow is a solid body immersed in it. Saying precisely the solid-fluid border. Because fluid velocity at the border is zero, there is a need to cover the body with a vortex sheet that reduces the influence of the environment outside the body. The sheet is created and shed at every simulation step. Vortex particles that have been shed become members of the vortex cloud.

The vortex sheet also determines pressure distribution on the solid body. After completing advection and diffusion simulation steps, the N–S Eq. (5) reduces to:

$$\frac{\partial \mathbf{u}}{\partial t} = -\frac{1}{\rho} \nabla p \tag{8}$$

which is the base to find the distributions under interest and finally resulting forces F_x, F_y, M acting on the cylinder.

3.2. DVM applications in wind engineering

The origin of DVM dates back to the 1930s. However, fast developments in vortex methods started in the 1980s, preceded by the progress in computer technology. Since then, DVM has been successfully applied to many scientific and engineering problems. Many of them have entered the canon of research literature.

The first example [2] concerns a real building included in the Texas Tech University campus The building was equipped with measuring utilities allowing monitoring parameters of wind flow over it. It was localized in a flat open area far from other buildings. The wind

flow had an angle-of-attack of 90° with respect to the longest wall of the building. In the computer DVM simulations, the problem was simplified to a 2D flow case. The numerical simulation was performed for the Reynolds number $Re = 2.3 \cdot 10^6$. Numerical results were compared with experimental data. Selected results are presented in Fig. 6. The example shows good conformity between numerical simulation results and experimental data. The most important achievement is the shape of the line obtained from computer simulations. This shows that DVM algorithms are able to model the phenomena of turbulence that occurs near corners. The discrepancy between the experiment and the calculations comes from the fact that the building was not long enough (the length to depth ratio was equal to 1.5) to treat the flow as two dimensional and the influences of walls parallel to the flow should not have been neglected and three dimensional analysis of the flow would have been more proper in this case. However, the differences are small and do not disqualify the results from a civil engineer's point of view.

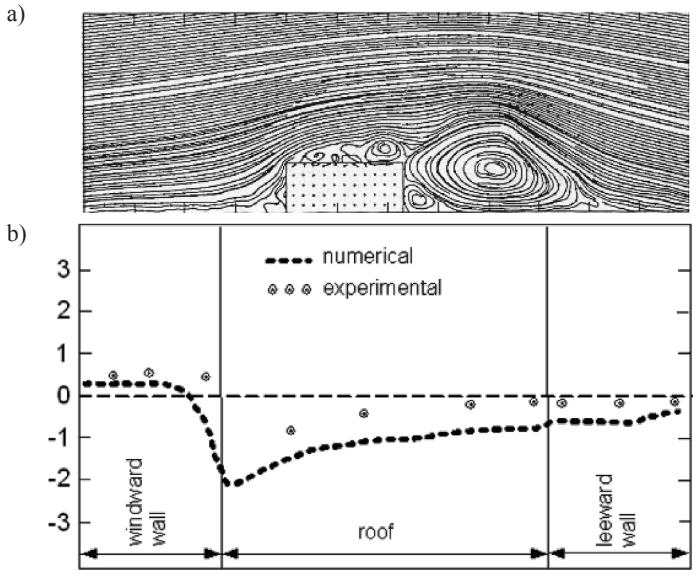

Fig. 6. Wind flow over a Texas Tech building [2]: a) streamlines obtained from computer simulations, b) mean pressure coefficients numerical and experimental

The second problem [3] concerned finding coefficients of aerodynamic resistance: drag, lift and moment, by way of DVM computer simulations. Square and rectangular sections were analyzed against wind action with a different angle of incidence. The shape ratio varied form 1/4 to 3 and the angle of incidence evolved from 45 to 90 degrees. Two-dimensional flow was assumed. During the simulations, the Reynolds number came to $2 \cdot 10^4$. Numerical results were confronted with experimental data. The conclusion was that DVM analysis may be successfully used for determining aerodynamic coefficients for engineering practice.

Undeniable superiority to other CFD methods DVM presents in analysis including aeroelastic interaction. An example of such a simulation one can find at [4], where the authors

presented their results of the dynamic response of a bridge glider placed in a turbulent wind flow. They used DVM to examine the aero-elastic stability of Tacoma Narrow Bridge and compared the results with historical experimental data. Numerical simulations concerned only the deck of the bridge. Because flutter occurred in the center area of the bridge and the bridge span was a few dozen times longer than its width, simplification to 2D analysis was justified and did not introduce big errors.

Computer calculations reconstructed the catastrophe that happened in 1940. Numerical experiments conducted for wind speed in a range from 5 to 20 m/s. They confirmed that the critical speed for flutter was 19 m/s, which was consistent with historical data.

3.3. DVM implementation – in home solver

Computer simulations presented in this paper were carried out using an original computer program Ventus2D developed by the author [5]. The computer program implements algorithms of DVM and, at its present stage of development, it is able to simulate fluid flow around a solid body of random shape by way of direct numerical calculations (Fig. 7). The solid body immersed in fluid can be stationary (i.e. fixed) or elastically suspended (with or without damping). In both cases, a boundary layer phenomenon, turbulence effects (e.g. vortex street) and interaction between a solid body and fluid are effects of 'intelligent' DVM algorithms. The DVM solver does not use any mesh. All vortexes are free to move in the calculation domain.

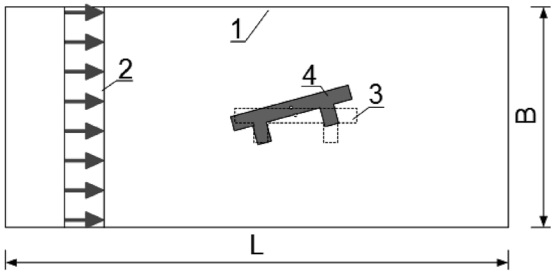

Fig. 7. Diagram of an aeroelastic problem solved by Ventus2D i.e. solid body suspended in a fluid stream: 1 – rectangular calculation domain, 2 – uniform fluid stream, 3 – initial position of a solid body suspended in the stream, 4 – the body in motion and interacting with the fluid

The main idea behind DVM simulation is a vortex cloud and its mechanics executed in accordance with Eq. 6 and Eq. 7. In a general 3D case, the vortex cloud is a set of vorticity filaments that are, on the grounds of Helmholtz's laws, closed or start and end on a solid body surface. For the case of 2D flows, all the filaments are straight lines perpendicular to the plane of analysis, therefore, they are illustrated as points on following figures and are just called discrete vortexes. The solid body immersed in the stream is covered with panels (Fig. 8). The panels are able to generate discrete vortexes on them. Each vortex induces

a velocity field according to the Biot-Savart law. The vorticity layer on the solid body is needed to cancel the velocity field inside the body because there is no fluid flow inside the body. Subsequently, the discrete vortexes generated on the panels are shed into the stream. Consequently, the velocity field of the fluid flow changes (free vortexes in the stream generate their velocity field) and new discrete vortexes on the panels have to be generated to cancel the velocity field inside the body. Free discrete vortexes are drifted and diffused in the stream according to Eq. 6 and Eq. 7 respectively. The resultant velocity field is a superposition of the oncoming homogeneous stream with velocity u_{AIR} and turbulent field generated by all discrete vortexes. The simulation job is a repetition of generating, shedding and propagating discrete vortexes in the stream. The structure of turbulence and macroscopic phenomena like resultant aerodynamic forces are the results of a direct simulation. The fundamental outcomes of the Ventus2D program are values and positions of discrete vortexes at every step of the computer simulation. Subsequently, the data enables finding velocity and pressure fields of the flow and calculates resultant aerodynamic forces acting on the solid body according to Eq. 8.

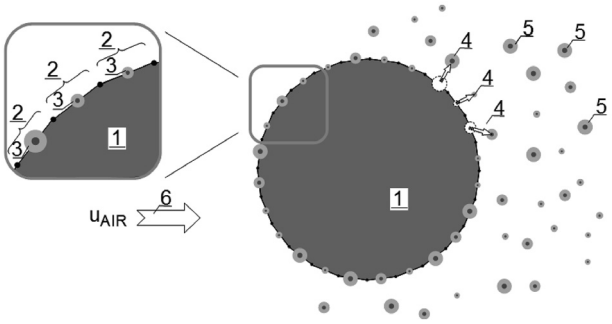

Fig. 8. Solid body in a stream as a source of vorticity: 1 – solid body, 2 – panels, 3 – discrete vortexes generated on the panels, 4 – discrete vortexes shed into the stream, 5 – discrete vortexes drifted in the stream

4. The influence of surface roughness on the cross-flow around a circular cylinder (Review of literature)

The influence of surface roughness on the cross-flow around a circular cylinder has long been the subject of intense attention both from academic and practical points of view. Achnebach [6] described a wind tunnel experiment carried out in a range of Reynolds number $1 \cdot 10^5 < \mathrm{Re} < 3 \cdot 10^6$. The object of the study was a cylinder with a diameter of 0.15 m. The levels of roughness examined were k_s/D = 0, $110 \cdot 10^{-5}$, $450 \cdot 10^{-5}$ and $900 \cdot 10^{-5}$ according to original notation, which gives f_1 = 0%, 0.11%, 0.45% and 0.90%. Results clearly showed that a small degree of surface roughness did not change the course of the phenomena. There were still four characteristic regimes: subcritical, critical, supercritical and transcritical. Small surface roughness, e.g. $f_1 < 1\%$, seems to have no effect on aerodynamic drag force coefficient in the subcritical level but increases the coefficient in the supercritical level. However, the

values reported did not exceeded 1.3. Taking into consideration the critical and supercritical ranges, it was depicted that surface roughness changes the critical Reynolds number where the minimum of the coefficients is achieved. The minimum value still depends on the level of roughness and grows with increasing roughness and the values are equal to 0.4, 0.5, 0.72 and 0.72 respectively for the different levels of roughness.

Similar results are presented by Nakamura and Tomonari [7]. The range of Reynolds numbers covered here was $4.0 \cdot 10^4 < \mathrm{Re} < 1.7 \cdot 10^6$. The diameter of the cylinder used in the experiment was 0.62m and the levels of surface roughness were r/D = 0, $6.5 \cdot 10^{-5}$, $9.4 \cdot 10^{-5}$, $18.5 \cdot 10^{-5}$, $90 \cdot 10^{-5}$, $226 \cdot 10^{-5}$, $516 \cdot 10^{-5}$ and $1000 \cdot 10^{-5}$ according to original notation or recalculated to f_1 = 0%, 0.007%, 0.009%, 0.019%, 0.09%, 0.226%, 0.516% and 1% respectively. The experiment did not cover the subcritical regime. In the transcritical regime, the roughness again lost importance on the value of the drag force. The reported coefficient took the value of approximately 1. Transition from the critical to supercritical regime depends on the level of roughness, but the differences mainly concerned the critical Reynolds number and the minimum values were similar.

[8] considered bridge cables with a pattern-intended surface with a diameter of 140mm. The relative surface roughness defined by the depth of the indentations was 1%. The experiment intended to find aerodynamic forces carried out for the Reynolds number from $0.3 \cdot 10^5$ to $2.7 \cdot 10^5$. The cable exhibited a very early transition into the supercritical region due to the level of surface roughness. The early flow transition agreed well with what was observed for circular cylinders with uniform roughness. The drag force coefficient at the lowest Re number was equal to 1.2 and decreased with increases to the number. Finally, it reached a value of 0.6 for $\mathrm{Re} > 1 \cdot 10^5$.

5. Own research

All computer simulations were carried out in the same way. They were performed in a calculation domain with a size of 2 m × 10 m divided into 10×50 = 500 cells (Fig. 9) used only as containers for free vortex particles. A cylinder with a 0.2 m in diameter and graded surface roughness (Fig. 2) was placed on the horizontal axis of symmetry at a distance of 1m from its start. This distance is sufficient for the boundary layer to form and propagate into the stream, which can be seen in Figs 10–14. The width of the domain was able to house the von Karman vortex street. Most of the discrete vortexes left the domain through the rear (right) side. In the computer simulations, the air stream has started abruptly from 0 do u_{AIR} (Fig. 15). For this reason, the first second of the outcome was rejected as being not real. After the first second, the process stabilised and the results could be used for macroscopic estimations. Every simulation consisted of 500 computational steps of constant length of Δt = 0.005 s, which gave 2.5 s of the total process but only the last 1.5 s were valuable. However, the period of time of 1.5 s was long enough to determine the aerodynamic drag and extending it would only result in extra hours of computer work. The cross-section of the cylinder under study was covered with DVM panels numbering from 109 to 253 depending of the level of roughness with length ΔL from 0.0045 m to 0.0058 m (see Table 2). The simulations were designed in order to keep the dimensionless parameter of the simulation step:

$$S = \frac{\Delta t \cdot u_{\mathrm{AIR}}}{\Delta L} \tag{9}$$

in the range of 1 to 25.

The oncoming fluid steam was dry air with a uniform value in the calculation domain (Fig. 9). The velocity of the stream u_{AIR} took values of 5 m/s, 10 m/s, 15 m/s, 20 m/s, which gave Reynolds number values of $0.7 \cdot 10^5$, $1.3 \cdot 10^5$, $2.0 \cdot 10^5$, $2.7 \cdot 10^5$ respectively at a kinematic viscosity of $1.5 \cdot 10^{-5}$ m^2/s. Finally, 20 computer simulations were carried out, which took about 72 hours of computational time on 32-bit PC computer with CPU 2×2.10 GHz and 2 GB RAM.

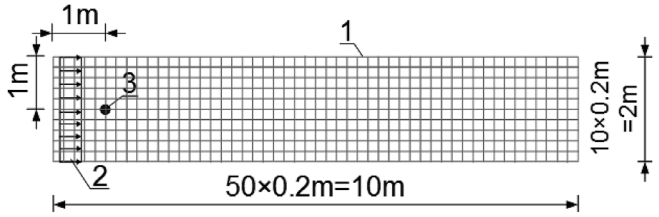

Fig. 9. The cylinder under study in a calculation domain: 1 – calculation domain divided in 500 square cells, 2 – uniform fluid stream, 3 – stationary cylinder

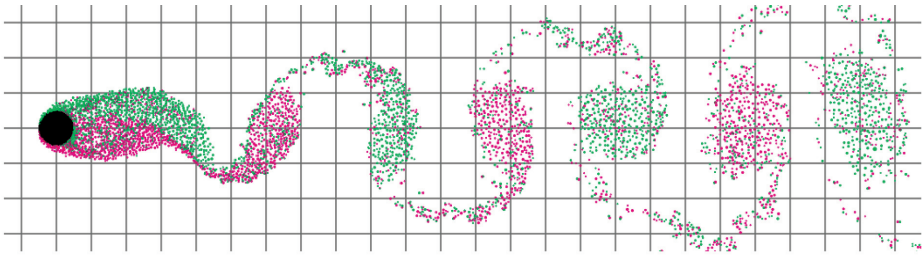

Fig. 10. Snapshot of DVM simulation for u_{AIR}=10 m/s, roughness level: a (Fig. 2), simulation step 500

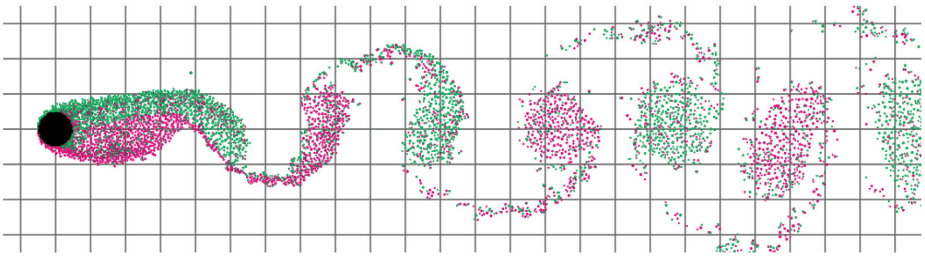

Fig. 11. Snapshot of DVM simulation for u_{AIR}=10 m/s, roughness level: b (Fig. 2), simulation step 500

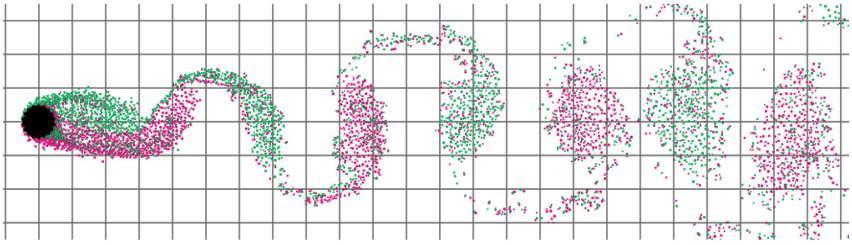

Fig. 12. Snapshot of DVM simulation for u_{AIR}=10 m/s, roughness level: c (Fig. 2), simulation step 500

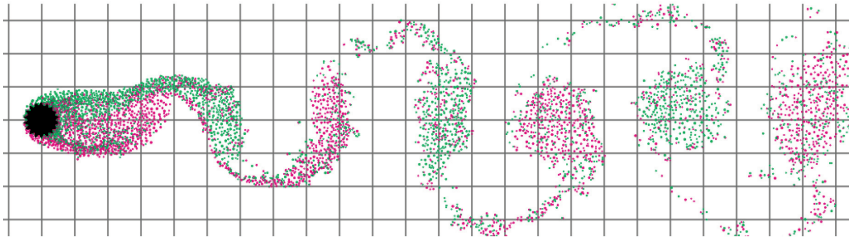

Fig. 13. Snapshot of DVM simulation for u_{AIR}=10 m/s, roughness level: d (Fig. 2), simulation step 500

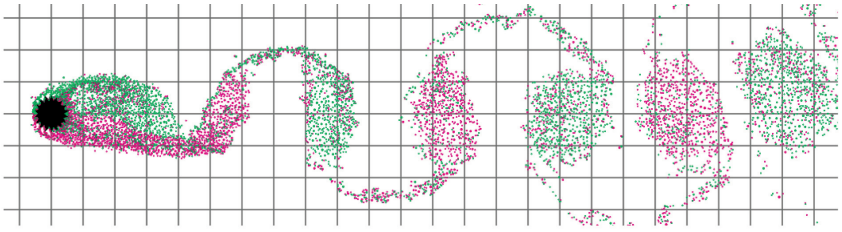

Fig. 14. Snapshot of DVM simulation for u_{AIR}=10 m/s, roughness level: e (Fig. 2), simulation step 500

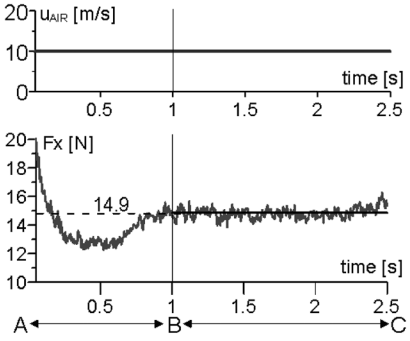

Fig. 15. Stabilization of the calculation process for abruptly started stream velocity u_{AIR} (a) by the example of aerodynamic drag force F_X (b). The range A-B was rejected and the mean aerodynamic force was calculated in the range B-C. Diagram for case: u_{AIR}=10m/s, roughness level: d acc. to Fig. 2

Table 2

Comparison of DVM models and the dimensionless parameter of a simulation step

Level of roughness	DVM panels		$S = \Delta t \cdot u_{AIR} / \Delta L$
	Total numbers	Length ΔL [m]	
a) 	109	0.0058	4.3 ÷ 17.2
b) 	145	0.0045	5.5 ÷ 22.1
c) 	145	0.0050	5.0 ÷ 19.9
d) 	181	0.0053	4.7 ÷ 18.9
e) 	253	0.0049	5.1 ÷ 20.2

6. Results

The output of computer simulations was the records of 20 air flows around the cylinder. Each record consists of 500 snapshots. Every snapshot is a trace of the discrete vorticity field, sample of which are presented on figures from 10 to 14, where the colour green indicates vortexes of a clockwise circulation. Positions and values of discrete vortexes enable finding the velocity and pressure field of the flow and finally, finding the resultant aerodynamic forces such as aerodynamic drag. The values and dimensionless coefficients corresponding to them are presented in Table 3. The drag coefficient has been calculated using formula:

$$C_X = \frac{F_X}{q \cdot D_{MEAN}} \tag{10}$$

where F_X is a drag force for a unit length of the cylinder [N/m], q = 1/2·1.21 kg/m^3·u_{AIR}^2 is stream pressure and is equal to 15.1 Pa, 60.5 Pa, 136.1 Pa, 242.0 Pa for u_{AIR}= 5 m/s, 10 m/s, 15 m/s, 20 m/s respectively, D_{MEAN} – mean diameter of the cylinder. Using a mean diameter instead of a closing diameter is justified by the method by which the surface roughness in treated. The roughness is not a change in shape but perturbation of the original surface. The shape and dimensions of the original surface do not change. This is a very convenient approach to the problem from an engineering point of view.

The change in the coefficient against increasing roughness is depicted on figures from 20 to 22. At this point, the starting value of C_X which is less than 1.2, needs a note. DVM computer simulations do not cover the whole spectrum of solid–fluid interaction. Such simulations neglect i.a. turbulence of oncoming air stream, effects of the 3D nature of the flow, impact of surrounding walls and of course the results incorporate many other physical simplifications. Finally, the values obtained from DVM 2D computer simulations are usually lower than experimental results [3, 5].

Table 3

Aerodynamic drag force F_X [N/m] acting on the cylinder and corresponding drag coefficient C_X [-] corresponding to air stream velocity u_{AIR} [m/s] for five different levels of surface roughness

	u_{AIR} = 5; Re = 0.7·10^5			u_{AIR} = 10; Re = 1.3·10^5			u_{AIR} = 15; Re = 2.0·10^5			u_{AIR} = 20; Re = 2.7·10^5		
	F_X	C_X		F_X	C_X		F_X	C_X		F_X	C_X	
a)	3.31	1.09	100%	12.89	1.07	100%	29.31	1.08	100%	52.00	1.07	100%
b)	3.36	1.11	102%	13.03	1.08	105%	29.10	1.07	99%	51.82	1.07	100%
c)	3.60	1.19	109%	13.94	1.15	112%	30.02	1.10	102%	51.90	1.07	100%
d)	4.47	1.48	135%	14.88	1.23	120%	33.28	1.22	114%	59.66	1.23	115%
e)	4.67	1.54	141%	18.04	1.49	145%	39.73	1.46	136%	74.28	1.53	143%

Looking at the columns in Table 3, we can state that increases in roughness result in increases in aerodynamic force and its coefficient for the same air stream velocity. This is in line with intuition and is therefore unsurprising. Owing to the critical regime of the flow, one should expect a decrease in the aerodynamic force caused by the increase of stream velocity for a given level of surface roughness. Comparing values in rows in Table 3, we can observe the effect for the levels of roughness indicated by 'b', 'c', and 'd'. For the level marked by 'e', the value first decreases and then grows. For the first level named 'a', the effect does not occur and the value does not change much. The last column in Table 3 shows that at higher air stream speed, the modest roughness of surface does not affect the aerodynamic drag.

The resulting drag force is related to a turbulent boundary layer which is formed by the surface of the solid body. Undoubtedly, roughness of the surface affects the layer. Figures from 16 to 19 depict boundary layers developed in DVM computer simulations. It can be easily discovered that the boundary layer stays similar for the 3 first levels of surface roughness, i.e. 'a', 'b', 'c', and is apparently different for the last level (e). The last boundary layer is thicker and does not cover the body with a uniform film. The level marked by d may be considered as a transition stage. This observation corresponds with diagrams of C_x presented in figures 20, 21 and 22. The last value of the coefficient differs significantly from the first three, which have similar values.

Taking into account all the observations, it is possible to state that small surface roughness is covered with a turbulent boundary layer and does not change the aerodynamic drag much. One can say that the roughness is hidden in the layer. Table 3 and diagrams of C_X (Figs 20, 21, 22) clearly show that the influence of the roughness strongly depends on the air stream. For u_{AIR} = 15 m/s and 20 m/s, the roughness of level 'c' is still small but it is significant at u_{AIR} = 5 and 10 m/s. This can be explained by the fact that along with increasing stream velocity, the importance of viscous forces decreases. In other words, the Reynolds number grows. Therefore, the limit level of roughness, below which the roughness can be omitted, should be related to the Reynolds number. Such an approach seems to be appropriate but is of little use for objects that have to stay to wind of broad spectrum of speed. Taking into consideration the last, the limit must be set up to be safe in all cases. Assuming that a 5% error is acceptable in engineering estimations of aerodynamic drag force, the two first levels

of roughness can be neglected. Using the parameters of roughness introduced earlier, the rule may be expressed quantitatively. The surface roughness can be neglected in engineering estimations of C_X if $f_1 < 3\%$, $f_2 < 5\%$, $f_3 < 4\%$. The values have been rounded to the nearest whole numbers.

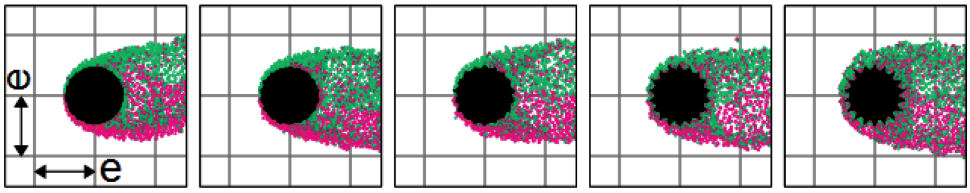

Fig. 16. Visualisation of discrete boundary layer formed at an air stream velocity of $u_{AIR} = 5$ m/s for all the levels of roughness from a to e. Reference dimension $e = 0.2$ m

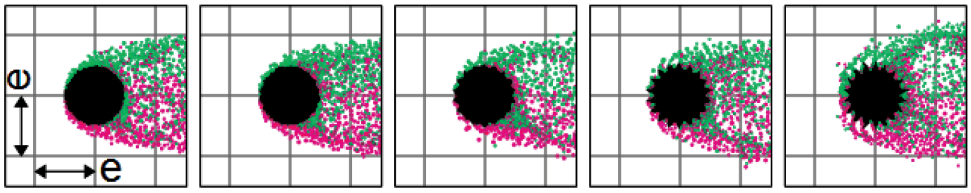

Fig. 17. Visualisation of discrete boundary layer formed at an air stream velocity of $u_{AIR} = 10$ m/s for all the levels of roughness from a to e. Reference dimension $e = 0.2$ m

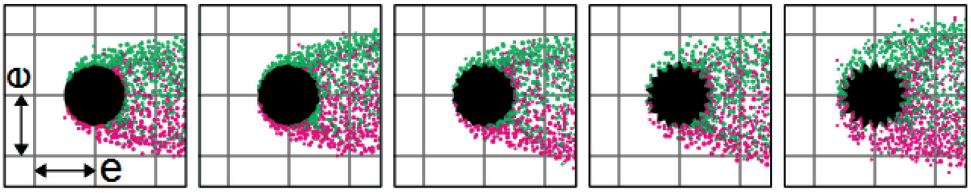

Fig. 18. Visualisation of discrete boundary layer formed at an air stream velocity of $u_{AIR} = 15$ m/s for all the levels of roughness from a to e. Reference dimension $e = 0.2$ m

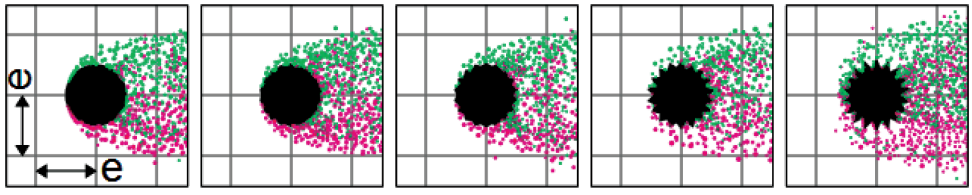

Fig. 19. Visualisation of discrete boundary layer formed at an air stream velocity of $u_{AIR} = 20$ m/s for all the levels of roughness from a to e. Reference dimension $e = 0.2$ m

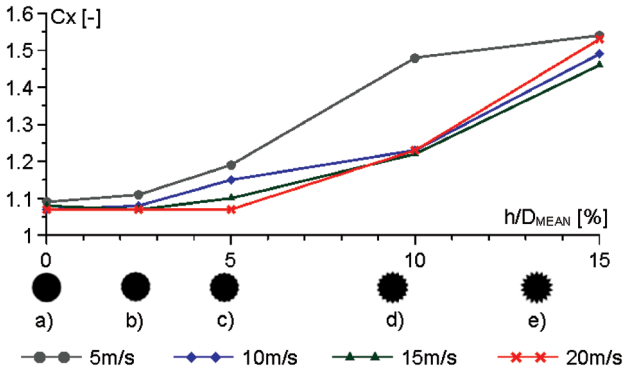

Fig. 20. Diagram of aerodynamic drag coefficient C_X against growing surface roughness described by parameter $f_1 = h/D_{MEAN}$ for different air stream velocity

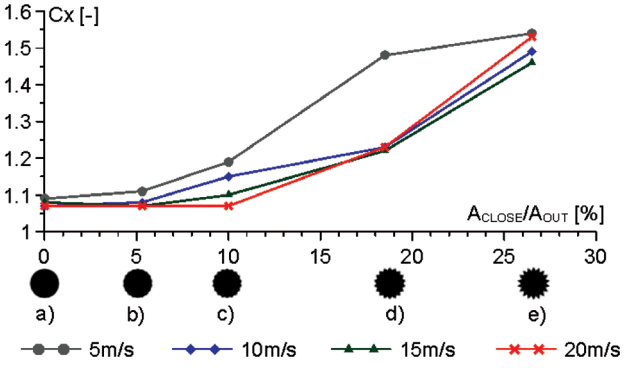

Fig. 21. Diagram of aerodynamic drag coefficient C_X against growing surface roughness described by parameter $f_2 = A_{CLOSE}/D_{OUT}$ for different air stream velocity

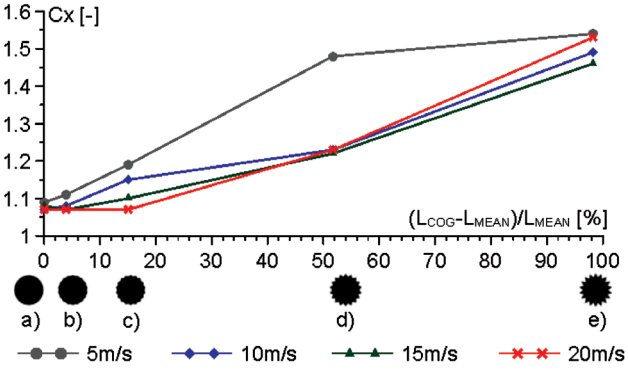

Fig. 22. Diagram of aerodynamic drag coefficient C_X against growing surface roughness described by parameter $f_1 = (L_{COG}\text{-}L_{MEAN})/L_{MEAN}$ for different air stream velocity

Another question was regarding when the level of roughness should be treated as a change in the original shape. The criterion here can be changed in the structure of boundary layer. Any perturbation in the smooth surface can be treated as roughness for as long as the form of the boundary layer remains the same. Figures from 16 to 19 show that the three first levels of roughness (i.e. 'a', 'b', and 'c') generate a very similar boundary layer form but the last one (f) varies considerably. The next to the last case (d) seems to be the transitional stage and can be treated as the roughness limit. Using the parameters of roughness, the limit should be set to $f_1 < 10\%$ $f_2 < 20\%$ $f_3 < 50\%$. The values have been rounded to the nearest ten due to estimation that is not precise.

Finally, there is the possibility to determine the range of surface perturbation that cannot be neglected and that is still regarded as roughness of the original shape and not a change in shape. Using the parameters, the range is: $3\% < f_1 < 10\%$, $5\% < f_2 < 20\%$, $4\% < f_3 < 50\%$. In the range, the influence of surface roughness is significant and should be counted while estimating aerodynamic drag. The data collected in the research is, alas, not adequate to find such correction factors. The factors seem to be related to the wind speed or the Reynolds number and will be the subject of further research. The parameter of surface roughness also may be significant. The parameters f_3 vs. f_1 and f_2 narrow the range of negligible surface roughness and stretch the range of significant roughness (see Figs 20, 21 and 22).

7. Conclusions

Computer simulations of air flow around a cylinder with a surface with a high level of roughness were carried out in order to find the relationship between surface roughness and drag coefficient. The analyses were limited to the critical region of the flow. The critical region arose due to the Reynolds number range covered in the simulations and the roughness that generated the turbulent boundary layer. Despite the high level of roughness, the phenomena proceeded as expected for a smooth cylinder. Since in many engineering estimations of aerodynamic drag force coefficient only the upper limits are important, it was possible to assess the level of roughness at which the roughness became important and the limit when the roughness should be treated as a change in shape.

References

[1] Lewis R.I., *Vortex element methods for fluid dynamic analysis of engineering systems*, Cambridge University Press, 2005.

[2] Turkiyyah G., Reed D., Yang J., *Fast vortex methods for predicting wind – induced pressures on buildings*, Journal of Wind Engineering and Industrial Aerodynamics, Vol. 58, 1995.

[3] Taylor I., Vezza M., *Predition of unsteady flow around square and rectangular section cylinder using a discrete vortex method*, Journal of Wind Engineering and Industrial Aerodynamics, Vol. 82, 1999, 247-269.

[4] Larsen A., Walther J.H., *Aeroelastic analysis of bridge girder sections based on discrete vortex simulation*, Journal of Wind Engineering and Industrial Aerodynamics, Vol. 67-68, 1997.

[5] Nowicki T., *Influence of boundary condition implementation in discrete vortex method on aeroelastic response of bridge decks*, Monografie – Politechnika Lubelska, Lublin 2012 (in Polish).

[6] Achnebach E., *Influence of surface roughness on the cross-flow around a circular cylinder*, Journal of Fluid Mechanics, Vol. 46(2), 1970, 321-335.

[7] Nakamura Y., Tomonari Y., T*he effects of surface roughness on the flow past circular cylinder at high Reynolds numbers*, Journal of Fluid Mechanics, Vol. 123, 1981, 363-378.

[8] Kleissl K., Georgakis C.T., *Comparison of the aerodynamics of bridge cables with helical fillets and a pattern-indented surface*, Journal of Wind Engineering and Industrial Aerodynamics, Vol. 104-106, 2012, 166-175.

TECHNICAL TRANSACTIONS | CZASOPISMO TECHNICZNE
CIVIL ENGINEERING | BUDOWNICTWO
2-B/2015

JOHN S. OWEN*

WINDBORNE DEBRIS IN THE URBAN ENVIRONMENT

ODŁAMKI KONSTRUKCJI UTWORZONE PRZEZ DZIAŁANIE WIATRU W ŚRODOWISKU MIEJSKIM

Abstract

This paper presents a comprehensive review of the research into windborne debris using. It introduces the components of the typical debris risk model - wind field model, debris generation model, debris trajectory model and debris impact model - and reviews the research that has been done in each of these constituent areas. The majority of this research has focussed on understanding the fundamental physics of debris flight, using both experimental and computational approaches to derive analytical and empirical models. This fundamental physics must be viewed, however, within a probabilistic framework that allows the risk to be assessed in a relevant manner. Much of the research relates to hurricane hazard in the USA, however windborne debris is clearly a threat to the urban environment during European wind storms. The way that FEMA's HAZUS®MH hazard assessment tool has brought natural hazard modelling into the engineering context is viewed as an approach that could be adapted for both mitigation and design in a European context.

Keywords: wind engineering, damage, windborne debris, CFD, hazard

Streszczenie

Niniejsza praca przedstawia kompleksowy przegląd badań dotyczących szczątków konstrukcji utworzonych i niesionych przez wiatr. Artykuł wprowadza elementy modelu ryzyka dla typowych odłamków – model pola wiatru, model tworzenia się odłamków, model trajektorii ruchu odłamków i model uderzenia odłamków – oraz przegląd badań, które zostały wykonane w obszarze tych zagadnień. Większość badań skupia się na zrozumieniu podstaw fizyki lotu odłamków, przy użyciu zarówno metod doświadczalnych jak i obliczeniowych, co pozwoliło na stworzenie modeli analitycznych i empirycznych. Należy rozpatrzyć podstawy fizyczne zjawiska, jednak w ramach zagadnień probabilistycznych, które pozwalają na odpowiednie oszacowanie ryzyka. Duża część badań odnosi się do zagrożenia huraganami w USA, jednak odłamki utworzone i niesione przez wiatr stanowią też istotne zagrożenie dla środowiska miejskiego w czasie burz występujących w Europie. Sposób, w jaki narzędzia do oceny ryzyka, utworzone przez FEMA i HAZUS®MH, pozwoliły na modelowanie ryzyka w ramach inżynierii, można postrzegać jako podejście, które może być dostosowane do ograniczania zjawiska i projektowania w kontekście europejskim

Słowa kluczowe: inżynieria wiatrowa, uszkodzenia, odłamki konstrukcji utworzone przez działanie wiatru, CFD, ryzyko

DOI: 10.4467/2353737XCT.15.130.4167

* Faculty of Engineering, University of Nottingham, UK.

1. Introduction

Reviews of damage caused to buildings and structures during strong winds have shown that windborne debris contributes greatly to the quantity and cost of damage [31, 32, 39]. Although the problem is most significant during the strongest winds associated with tropical storms and tornadoes, windborne debris also occurs in extra-tropical cyclonic storms such as those that occur in Northern Europe. The Federal Emergency Management Agency (FEMA) in the USA has published a number of reports on hurricane damage [2–4], which illustrate both the source of windborne debris and the damage caused by that debris. Examples of typical damage caused by windborne debris are shown in Fig. 1.

a)

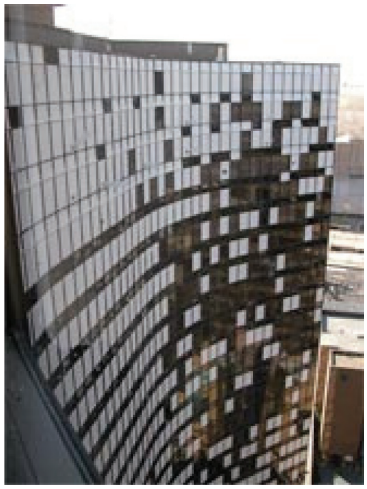

b)

c)

Fig. 1. Examples of damage caused by windborne debris, a) north façade of Hyatt Hotel, New Orleans damage by pea gravel from neighbouring roof (photo by K. Porter for MCEER), b) example of hazard due to missiles generated by failed structures (photo by T. Reinhold, AAWE gallery), c) example of cladding damage due to windborne missiles (photo by T. Reinhold, AAWE gallery)

Windborne debris arises from a variety of sources including building components where tiles, shingles or cladding sheets are torn from roofs. Items attached to buildings, such as signage or HVAC equipment, or loose construction material e.g. shingle and gravel on built up roof (BUR) structures, can also be torn free during high winds and become windborne debris. Other sources of debris include materials stored in the open at ground level, street furniture and tree branches. However, it is generally roofing materials that pose the greatest risk because their height and exposure make them more vulnerable to wind and more likely to fly further and faster.

Debris picked up by the wind can rapidly accelerate to reach and even exceed the background wind speed. The debris can travel significant distances (ranges of over one hundred metres have been reported) and can have significant momentum when it impacts the ground or downwind buildings. Clearly, in an urban environment, the risk of damaging impact with other structures is much higher and there are also risks associated with cars and pedestrians in the streets. Several fatalities have been reported in the media with people or vehicles struck by debris.

Typical debris impact damage involves the penetration of the building envelope, usually through broken windows, though cladding can also be damaged. However, it is important to note that the damage is not usually limited to the building envelope. Once the building envelope is compromised water is able to enter the building, which could lead to damage to the contents. Furthermore, the subsequent internal pressurisation of the damaged building can also cause internal damage and makes it more likely that the building will suffer further structural damage, such as roof loss. This in turn produces more debris, including structural members, which can cause damage to property further downwind. This is the so-called debris damage chain Fig. 2 [43].

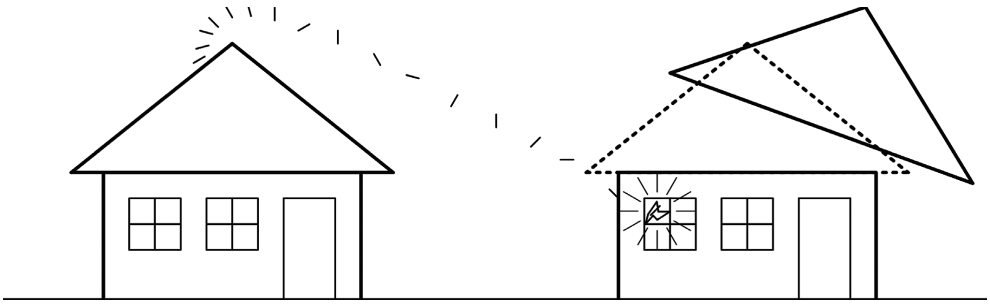

Fig. 2. The windborne debris damage chain (after [43]) Debris shed from the upwind building penetrates the downstream building causing internal pressurisation and subsequent major damage

Windborne debris is clearly a significant hazard and the associated risk is considerable. Design against windborne debris focuses on preventing debris generation by following guidance on appropriate fixings and fastenings and on dealing with the consequences of debris damage, such as internal pressurisation. However, field reconnaissance has shown that the generation of wind borne debris is not usually the result of poor design. When component failure generates debris, it is usually the result of the failure of the fasteners, either due to

poor installation or to corrosion. Therefore, much of the responsibility for managing the risk of windborne debris lies with government authorities and building owners. Hence, in hurricane prone regions of the US, building codes such as the Florida Building Code provide guidance on the protection of vulnerable building envelopes using shutters etc. Inevitably, though, many of the losses fall on the insurance and re-insurance industries and it is these sectors that have driven the production of appropriate hazard loss models.

This paper will present a comprehensive review of the research into windborne debris using the general structure of the debris risk models as a template. It will introduce the components of the typical debris risk model and then review the research that has been done in each of the constituent areas. Although much of the research relates to hurricane hazard in the USA, windborne debris is clearly a threat to the urban environment during European wind storms. An aim of the paper is to highlight the progress made in US hazard modelling and hence identify future research opportunities in the European context.

2. Debris risk models

In his review paper, Holmes [10] identifies the four core components of a windborne debris damage model:

- Wind field model
- Debris generation model
- Debris trajectory model
- Debris impact model

There have been several models created with this outline structure. An early attempt to model damage caused by windborne debris [49] identified the maximum debris flight speed as a key parameter for predicting damage, which was assumed proportional to the debris kinetic energy. Three types of debris were defined in that study – compact, sheet and rod (Tab. 1). For a number of specimens of each type comparisons were made between wind tunnel test data and the predictions of flight speed, which was defined as the wind speed necessary to initiate flight. Although the comparisons were good, the model itself was very simple and limited in scope; the work's significant contribution being the debris classification.

A more detailed and comprehensive debris risk model has been incorporated into FEMA's HAZUS®MH hazard assessment tool. HAZUS®MH is a nationally applicable standardized methodology that contains models for estimating potential losses from earthquakes, floods and hurricanes [38]. The hurricane model of HAZUS®MH [44] includes not only the detailed wind field model, but also two separate windborne debris models: debris from residential buildings and roof top gravel debris. The former consist of shingles, tiles, roof-sheets etc. (sheet debris) and small roof timbers (rod debris). The latter are compact type debris and represent debris that has caused significant damage in historic hurricanes, such as Katrina (Fig. 1 and [3]). The model considers failure of individual component fixings under wind pressure and then predicts the subsequent debris trajectories. The trajectories are used to obtain energy and momentum risk curves that then form the input for a damage and loss estimation model [45] which is shown schematically in Figs. 3. and 4.

Table 1

Classification of debris types according to [49] with examples

Compact			
Sheet			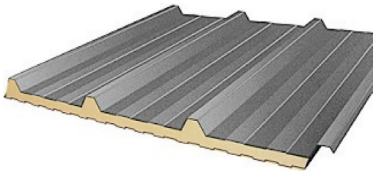
Rod			

The output from the HAZUS®MH hurricane model is a probabilistic estimate of the loss ratio, which compares well with insurance loss data for historic hurricanes. The purpose of the HAZUS®MH model is to allow users to quantify the cost effectiveness of mitigation techniques in different locations. It is therefore not a design tool as traditionally used in wind engineering, but a tool to be used by government bodies and building owners to estimate and then mitigate risk.

A later debris risk assessment model [24] uses Poisson random measure theory to predict damage during a hurricane due to debris from building sources. The approach includes a probabilistic model of debris trajectories that are used to predict impact and damage locations on neighbouring structures. Predictions of simulated debris transport distance and velocity are compared with field observations [25] and the model used to assess the vulnerability of residential developments using a Monte Carlo simulation [26, 50].

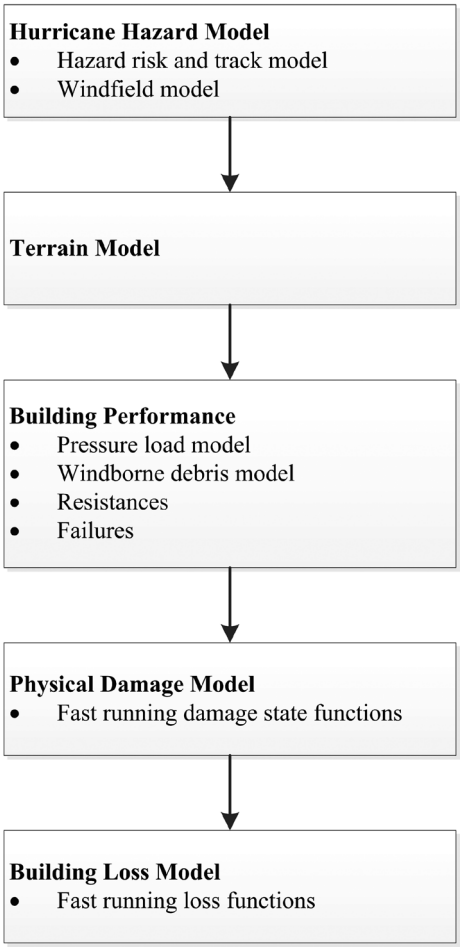

Fig. 3. HAZUS overview of damage and loss function calculation approach [45]

3. Wind field models

The purpose of the wind field model is to estimate the likely occurrence of damaging winds at a given location and to relate wind storm parameters to local mean and gust wind speeds at, say, rooftop height. These can then be used in conjunction with the debris generation model to predict the likely occurrence of wind borne debris.

The hurricane model in HAZUS®MH is based on an extensive study [46, 47] that considered historical hurricane data, including hurricane tracks, to create a model that could be used to generate simulations of future hurricanes. The simulations compared well with historical data in terms of both wind speed and central pressure. The model also includes a terrain model so that the simulation data can be used to predict wind speed and pressure

data for specific locations. Similar studies on historic storms in North West Europe have been performed, but these have been in the context of catastrophe modelling for the insurance industry or meteorology; there is, as yet, not effective transfer into the engineering context. How and whether the traditional wind speed data from design codes such as EC1 can be applied to analysis of the risk from windborne debris has also still to be fully addressed.

One important aspect of the wind field model that requires further development is the local flow around buildings. It is known that the gust wind speed is most critical for debris generation. However, within the urban environment, this is likely to be determined by large scale turbulence and flow separation around buildings. These flow features will also have a significant influence on the debris trajectory and hence the risk of impact. It is therefore important that the local wind features are properly considered in the wind field model, both for the analysis of the debris generation process and modelling debris flight.

4. Debris generation model

The purpose of the debris generation model is to predict the type and source location of debris during a wind storm and the likelihood that the debris will take off. Field observations on typical debris indicate that residential roofing materials (e.g. tiles, shingles and roof sheets) are the most common components. Debris from roofs is particularly significant because it will be subject to higher wind speeds and so is more likely to be torn off. It is also likely to fly further because it is launched from height and is of the sheet type.

Damage surveys report that failure of roofing elements is most likely to result from failure of the fasteners, either because of poor installation practices or through mechanical failure of inadequate or corroded fasteners. These factors have been the focus of full scale investigations of residential buildings [16, 40]. Although local failure of roof coverings is important, in some cases the underlying roof structure can also become the source of debris. This usually occurs because the structural design did not take into account the consequences of internal pressurisation following perforation of the building envelope.

Future research to refine the debris generation model is limited by the wide variability of debris form and fixing capacity. It must therefore focus on an appropriate probabilistic representation of these factors based on historical damage surveys.

5. Debris trajectory model

The purpose of the debris trajectory model is to predict the flight path of wind borne debris, and in particular to determine the distance and direction travelled and the impact speed. The former is required to assess the likelihood of impact on surrounding buildings and assets. The latter is required to assess the likelihood of damage being caused by that impact. The debris trajectory model must take account of the uncertainty of the processes involved including aerodynamics, flow field and launch conditions. Hence, the debris damage loss models outlined above include a probabilistic approach to modelling debris flight.

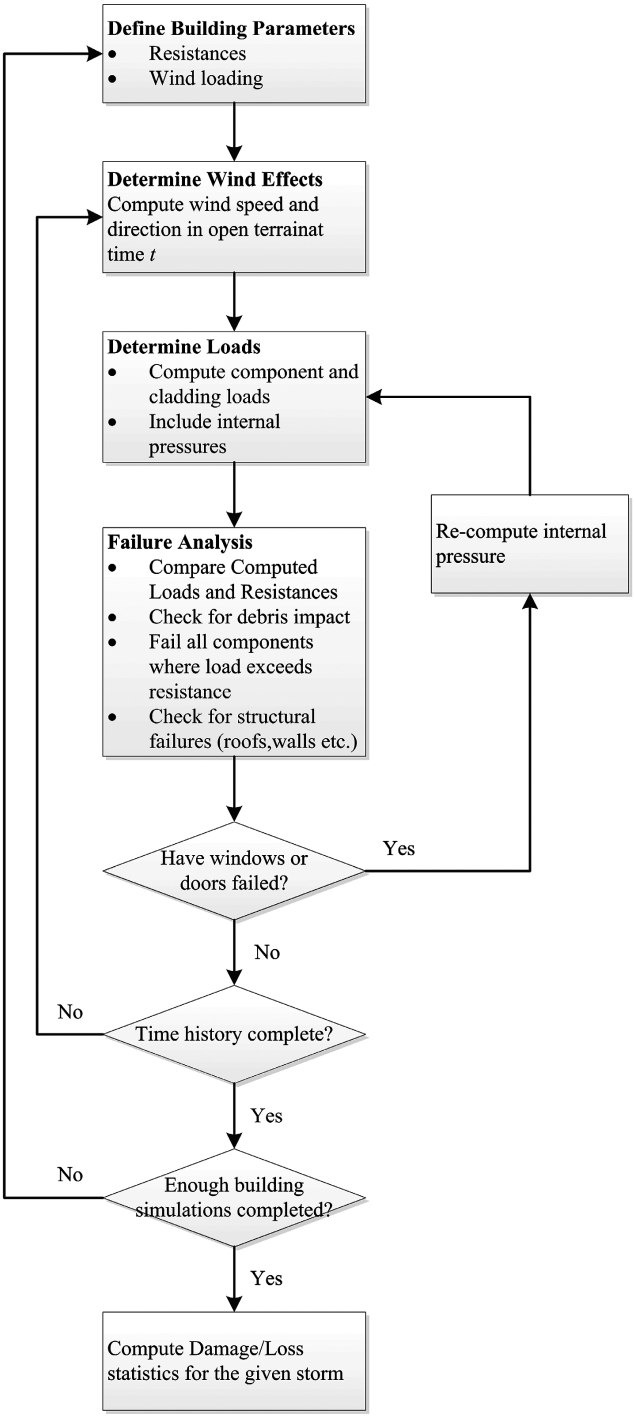

Fig. 4. HAZUS hurricane damage estimation methodology (after [45])

The ground breaking work on debris flight was carried out by Professor Tachikawa, who studied the flight of plate like debris in the wind tunnel [41] and subsequently developed a first debris trajectory model [42]. The wind tunnel studies revealed a number of different "flight modes" including translation, flutter and auto-rotation. As different flight modes have different aerodynamic characteristics this increases the spread in simulation results. The flight model included the effect of auto-rotation on the aerodynamic forces, which are analogous to the Magnus effect and generate additional aerodynamic lift and moment. These in turn influence the flight trajectory. The contribution of Professor Tachikawa to the development of the field by identifying the fundamental parameters affecting the flight of plate like debris was recognised by the designation of the Tachikawa number to describe the key non-dimensional ratio between aerodynamic and gravity forces [11].

5.1. Analytical Models

A very simple model of debris flight is included within [49]. Although this does not attempt to predict trajectories, it does propose a condition for debris launch in terms of the ratio of aerodynamic to gravity and restraining forces. The resultant debris flight speed is described as a proportion of the mean wind speed and comparisons made between predicted and wind tunnel results for the three debris types (compact, sheet and rod). A more detailed model for compact debris was developed by Holmes [9] who considered the 2D equation of motion ignoring rotational effects. The influence of atmospheric turbulence on the debris trajectories was investigated by modulating the background wind speed. The model was used to predict flight distances and velocities at impact for two spheres with different diameters and materials (8mm stone and 80mm wood).

Baker [1] presented a more complete version of the 2D debris flight equations, which included the rotation of the particle and the aerodynamic forces associated with autorotation. Baker proposed a different non-dimensionalisation of the equations to Tachikawa, but identified the same non-dimensional ratio of aerodynamic to gravity forces as the governing parameter. He presented solutions for both compact and plate-like debris including the effects of turbulence, and compared his predictions with the wind tunnel results presented by Wills [49]. An interesting result from this model was that, for auto-rotating flight modes, sheet like debris could achieve a flight speed greater than the mean wind speed because of the influence of the auto-rotational force coefficients. This indicates that accurate prediction of the flight of wind borne plate like debris requires an accurate model of the auto-rotational behaviour of the debris. This is fundamental to predicting the correct flight mode and determining the correct aerodynamic forces. A subsequent re-working of Baker's analysis using an improved definition of auto-rotational force coefficients illustrates the effects [17]. This later work was subsequently extended to a full three dimensional quasi steady model for plate like debris flight [18], which was evaluated by comparison with wind tunnel data. The results compared well when there is a dominant wind (as in debris flight). A further comparison of the models developed by Baker [1] and Holmes [12] is presented by Scarabino [37], who considers the stability of sheet type debris flight and the asymptotic solution of the debris flight equations.

A full six degree of freedom, 3D model of wind-borne debris trajectories was presented in [6]. Here, a Monte Carlo simulation approach is taken to address some of the uncertainties

in the initial conditions and wind regime. The results are predicted probability distributions of debris impact locations and impact velocities, which match data from small scale wind tunnel tests.

5.2. Wind Tunnel Studies

Wind tunnel tests for debris trajectory models can loosely be classified into two different types. The first are aimed at understanding the aerodynamic performance of individual items of debris, usually in terms of measuring the aerodynamic and auto rotational force coefficients needed for the analytical models described above. The second are aimed at measuring debris trajectories to provide data for the validation of simulate trajectories predicted by those analytical models. These studies also consider the effect of local flow conditions (e.g. flow round buildings) on debris launch and flight.

The earlier models of debris trajectory made use of standard data sources such as ESDU to obtain aerodynamic parameters, although these sources don't provide the full range of angles needed. The first debris specific tests [36] measured static force coefficients on plates and rods, while varying both the angle of attack and the angle of tilt. However, direct measurements of the important auto-rotational behaviour were not made, instead values of force coefficients were modified using an approximation to dynamic stall and apparent camber to account for auto-rotation.

A subsequent series of tests did measure pressures and forces on auto-rotating square plates in the wind tunnel [27]. Two different plate sizes were considered, 1m by 1m and 0.3m by 0.3m, with the plates restrained to rotate about a horizontal axis. In this case the situation was effectively 2D and the plates did exhibit stable auto-rotation for certain wind speeds. The values of lift, moment and drag coefficients measured during these tests were then compared with the values used in the analytical models described above [1, 12, 36]. Further processing of the experimental data was then performed to compare the tip speed ratio during auto-rotation with theoretical models [29] and to investigate the fluctuating pressure fields [28].

Apart from the pioneering work of Tachikawa [41], one of the earliest wind tunnel tests to validate debris trajectory models is presented by Wills [49] for cube and plate type debris. Measurements were made of initial flight speeds, i.e. the mean wind speed at which the debris first launched, which was then use to calibrate their model for the debris launch criterion. A more comprehensive wind tunnel study of plate like debris is presented in [23]. Here, wind speed, angle of attack, debris size and debris density are studied to determine the influence of each on the trajectory. The debris is held on a launch mechanism by an electro-magnet, which is turned off to trigger release (hence, failure of fixing components is not considered at debris launch) and then the debris flight tracked by camera. The results of the wind tunnel study are used to propose an empirical formula for non-dimensional trajectories in terms of the Tachikawa number, which is then compared with the results in a 2D analytical model [12]. The authors later extended their work to include rod and compact debris types [22]. Their empirical trajectory models for different types of debris are compared in Fig. 5, which shows sheet type debris achieving the highest speed, yet not reaching the background wind speed.

a)

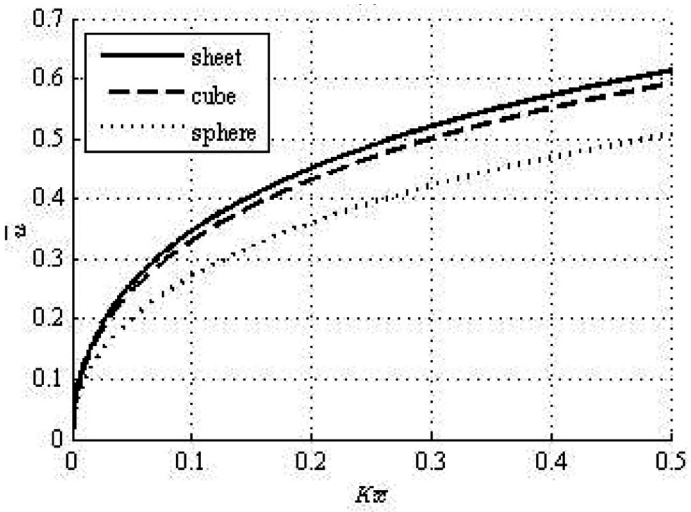

b)

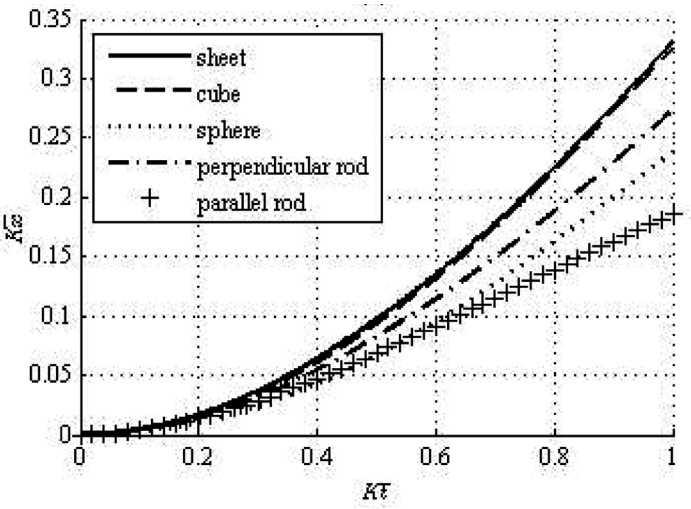

Fig. 5. Comparison of empirical trajectories for different debris types in terms of Tachikawa number (K) and non-dimensional time ($\bar{t}$) and distance ($\bar{x}$)

More recent wind tunnel studies have considered the performance of roof sheets on a 1:20 scale model of a typical house structure. In the first of these studies [48] the experimental design is described including the scaling of the fastener failure load, which is used to determine the hold down force for the electro-magnets. Only winds normal to the ridge line of the house were considered and the roof sheet was located immediately downwind of the ridge. The tests produced a probability distribution for the wind speed at panel failure and a set of trajectories that were recorded using high speed cameras. Significantly, both translational and auto-rotational flight modes were observed. Later tests on the same model considered the influence of wind direction [20] and panel location [19] on the debris flight.

Wind direction and the location of the panel on the roof both had an effect on the failure wind speed, the range of debris flight and the spread of debris. Another important observation was the influence of surrounding buildings. The presence of neighbouring buildings made a significant difference to the range and spread of debris, providing further evidence that the detailed local wind field is very important.

5.3. Numerical Simulations

Computational wind engineering is a rapidly developing field and recent work has applied Computational Fluid Dynamics (CFD) to the solution of the wind borne debris problem. As with wind tunnel testing, in the simplest cases CFD is just used to predict the aerodynamic and auto-rotational force coefficients for use in an analytic model. Measurements of auto-rotational force coefficients in the wind tunnel are especially sensitive to the experimental conditions including mass distribution, bearing friction and boundary effects. These factors can be identified and quantified by comparing the experimental results to computational simulations. A further advantage of the numerical simulations when studying the force coefficients is that they provide more details of the flow field and pressure distributions across the debris than can be obtained from wind tunnel testing. This in turn improves the conceptual understanding of the flow regime and flight dynamics.

The real advantages of using CFD, though, are seen when it is applied to the simulation of the debris flight itself. In this case, flight trajectories can be obtained for debris without the need to obtain force coefficients. Hence, irregular and non-standard debris can be simulated. Furthermore, the simulation of debris flight is effectively embedded within a simulation of the local flow field. It is therefore possible to study the effects of debris origin, local flow separation, building interference etc. on the debris trajectories. In effect simulations of debris trajectory are then not dependent on an assumed flow field as inherent in an analytical model, but on a simulated flow field that captures the key features of the flow.

However, the complexity of the physical problem means that the simulations are not trivial. First, it is necessary to simulate the local flow field around the debris. Because the debris is translating and rotating through the fluid, this has to be considered as a fluid structure interaction problem using an ALE formulation. The debris motion is calculated using a six degree of freedom rigid body solver in response to the flow induced forces. Motion of the debris then imposes a displacement on the mesh around the debris, which must be accounted for in the fluid solution. Second, unlike many FSI problems, the debris is in effect also translating through the domain, requiring regular re-meshing to avoid mesh distortions. Finally, the flow fields around buildings are notoriously difficult to simulate and so the mesh required may be very large and demand significant resource to solve it.

The first detailed presentation of the CFD simulation of plate like debris is given in [15] where the simulations are compared with experimental data obtained from the wind tunnel [27]. The propriety CFD code, ANSYS FLUENT, was used to simulate the flow field using an unsteady RANS approach with the realisable k-ε turbulence model. An inner spherical region of mesh was defined around the plate like debris, which translated and rotated with the plate without deforming. This spherical region was then allowed to translate through an outer region which was re-meshed on every time step, Fig. 6. Comparison of force coefficients for

static and fixed axis rotating plates with values from the literature and wind tunnel gave good agreement. Importantly, discrepancies with the wind tunnel data identified problems with the experiment including mass eccentricity and bearing friction. Predictions of the debris flight also compared well, with different flight modes being predicted.

This model was later refined by adopting a singularity free rigid body solver to avoid the complications of gimbal lock and by improving the outer domain by using an unstructured mesh, Fig. 7, [13]. Using this model, different debris flight modes (flutter, transitional and auto-rotational) were observed that corresponded to those seen in wind tunnel tests. Fig. 8 shows a comparison of simulated trajectories using CFD with an empirical model obtained from wind tunnel testing [23]. The simulations predict that in the auto-rotational flight mode sheet type debris can exceed the background wind speed. This agrees with the results of analytical models, but wasn't observed in the wind tunnel.

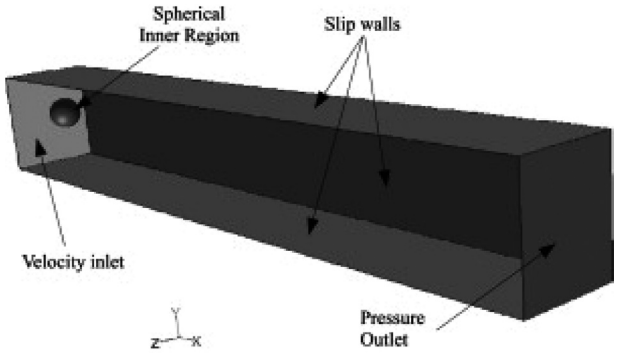

Fig. 6. Computational domain and boundaries for free-flight simulation of debris [13]

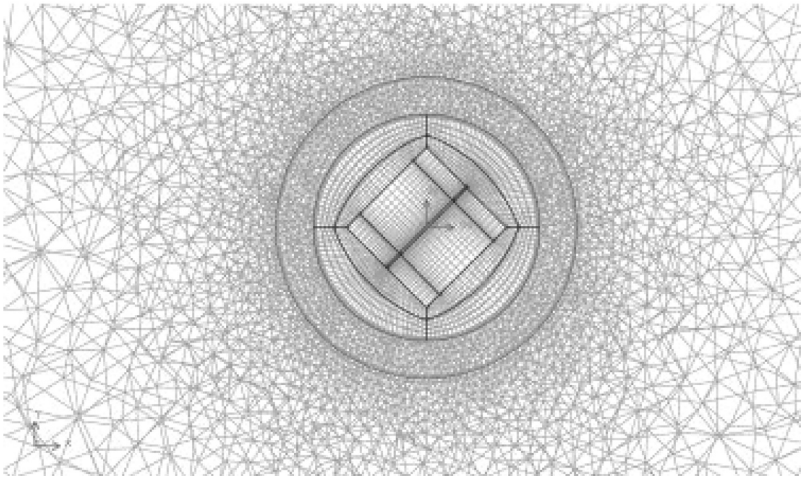

Fig. 7. Section through computational grid showing structured hexahedral mesh in the moving inner region surrounding the plate, together with an unstructured tetrahedral outer mesh that is re-meshed at each time step (after [13])

a)

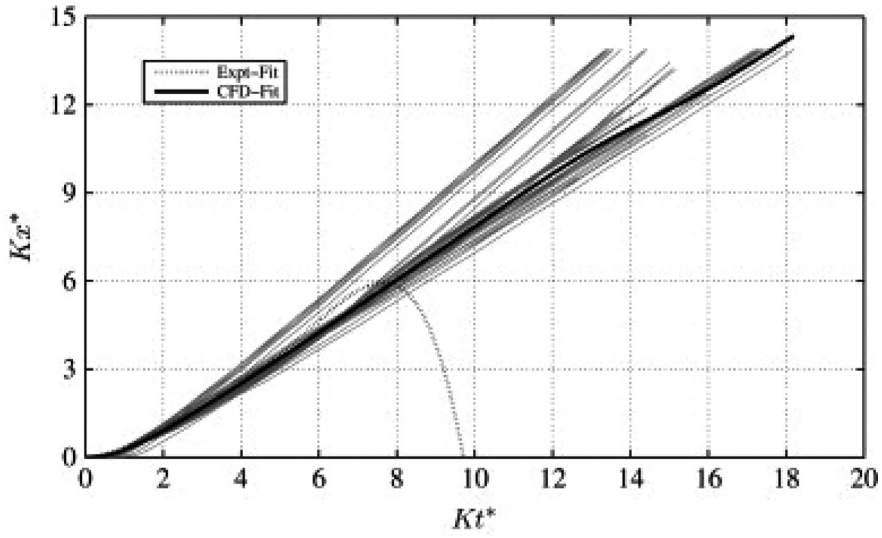

b)

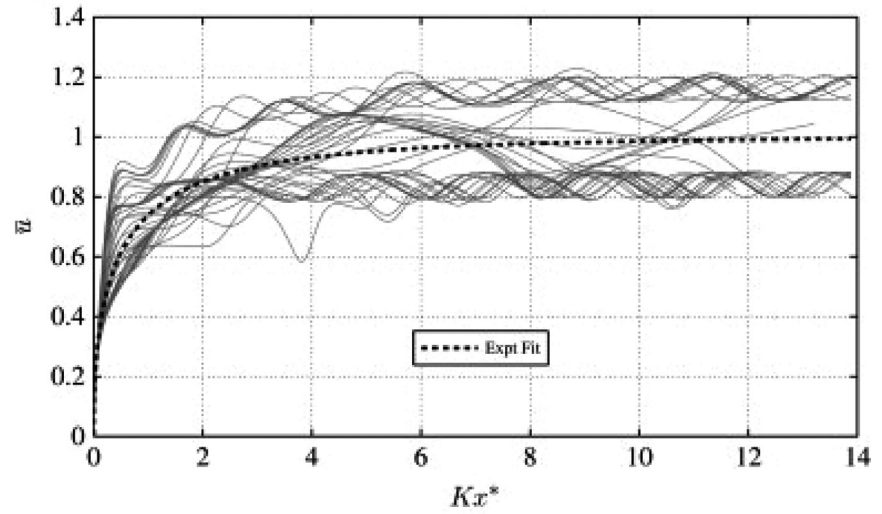

Fig. 8. CFD–RBD predicted trajectories for initial angles of attack of $-85° \leq \alpha \leq 90°$, showing (a) experimental (Lin et al., 2006) and CFD–RBD based fit expressions for non-dimensionalised horizontal distance, $K\bar{x}$, and (b) CFD–RBD predictions for non-dimensionalised horizontal speed (after [13]).

Figs. 9 and 10 present typical trajectories for different flight modes. Fluttering plates oscillate about an axis, but never rotate. Transitional plates oscillate at first, before developing stable auto-rotational behaviour. The auto-rotational plates enter stable autorotation from launch. For auto-rotating plates, the final flight speed depends on the direction of rotation. The key factor in determining the flight mode was the launch angle.

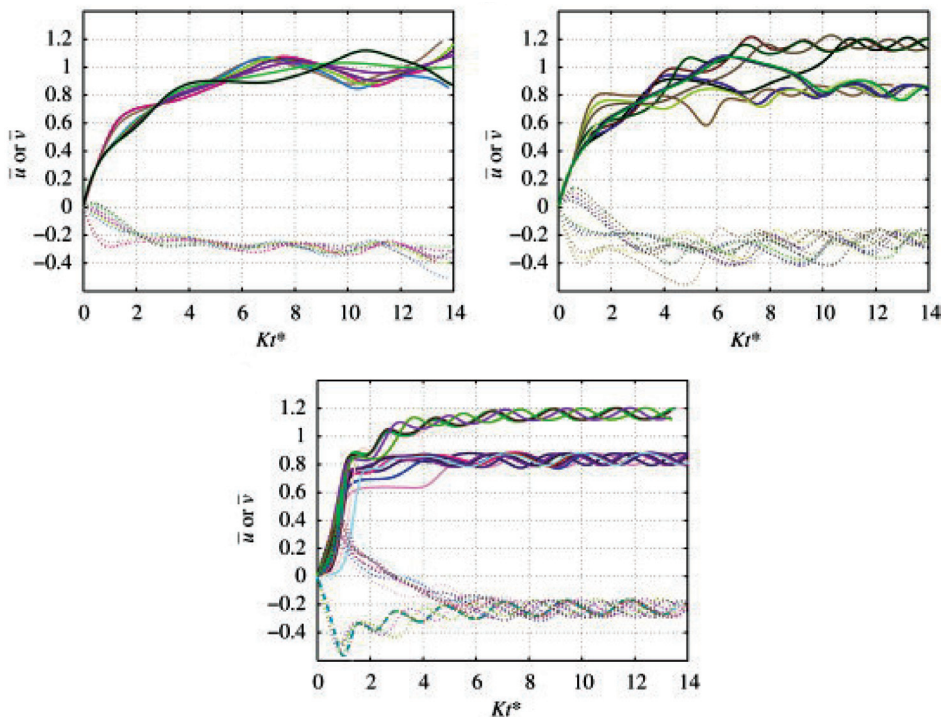

Fig. 9. Non-dimensionalised time-series of vertical (dashed lines) and horizontal (solid lines) plate speed for (a) flutter, (b) transitional and (c) auto-rotational flight modes (after [14])

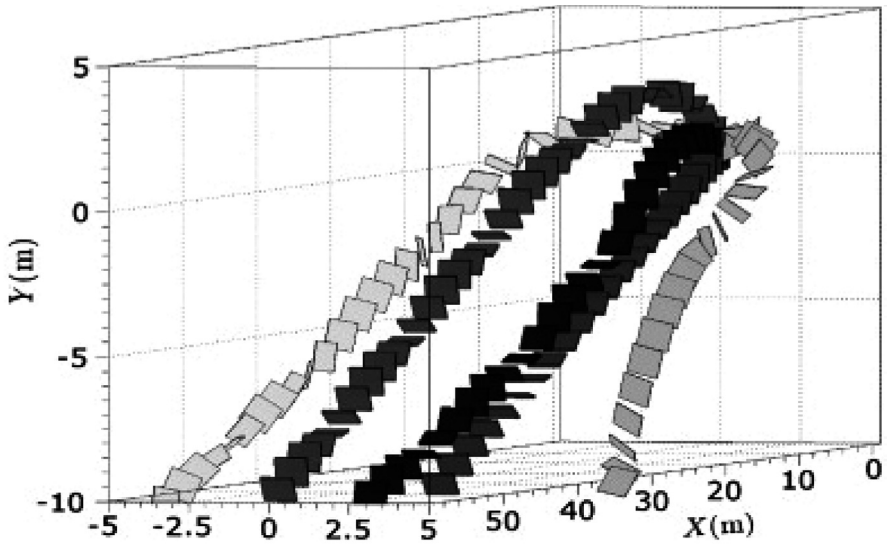

Fig. 10. Instantaneous orientations of plates in flutter (red), transitional (blue), autorotational (red) and complex 3D spinning (yellow and brown) modes of flight (after [14])

The CFD simulation was also used to propose equivalent empirical formulae for drag, moment and lift as a function of rotational speed. Trajectories for debris were predicted for a number of different debris types with different Tachikawa numbers and plate properties.

The influence of local environment was considered by including a representative building in the simulation; Fig. 11 presents typical and trajectories for roof debris [14]. The benefits of the CFD approach in terms of the improved understanding or the auto-rotation phenomenon is also clear [8].

The major limitation of the computational model described here is that it is deterministic, predicting the flight of specific debris in specific wind fields. Future work must address this by introducing an appropriate stochastic representation for both debris and wind field.

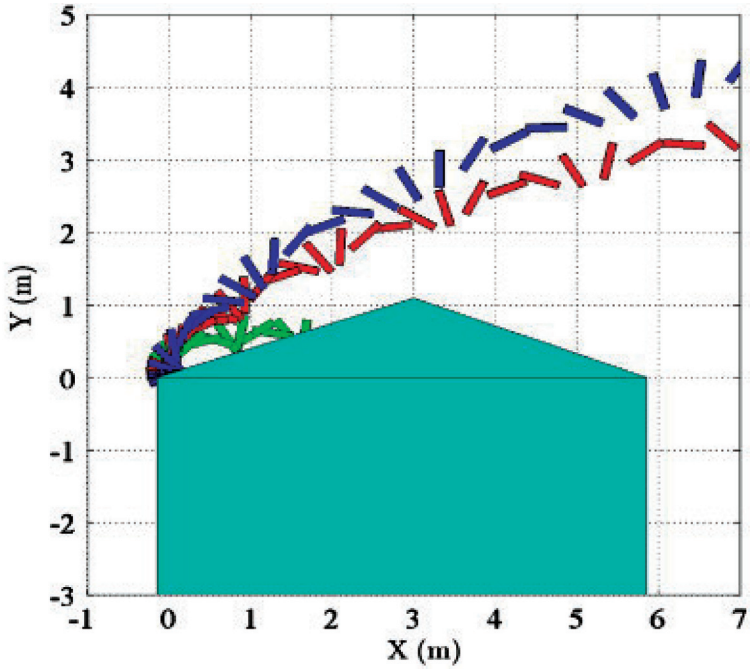

Fig. 11. Instantaneous snapshots of plate position and orientation during flight above the building for the 1 kg plate (blue), the 6.35 kg plate (red) and the 12 kg plate (green) (after [14])

6. Debris impact model

The purpose of the debris impact model is to predict the likelihood of damage due to debris impact during a storm. It therefore needs to consider the likely impact location and velocity of a debris particle, both of which can be obtained from the debris trajectory model. Typically a Monte Carlo analysis would be performed using the trajectory model to account for the uncertainties in the system; this highlights the benefits of having an efficient trajectory

model. The debris impact model must also consider the likely damage caused by an impact, i.e. it needs to relate the kinetic energy and momentum of the debris at impact to the strength of the asset hit.

The earliest debris damage model [49] simply used the debris flight speed to provide an estimate of the energy at impact, assuming that this correlated with damage. Although simple, this damage function was able to provide helpful insight when used to compare the damage caused by Typhoon York in Hong Kong (Lee & Wills, 2002). The conclusions drawn are necessarily limited, but they do identify the debris damage chain seen in the field.

A more recent study considering the vulnerability of the facades on a representative tall building to wind-borne debris has taken the CAARC building as an example with a typical distribution of glazing (Moghim & Caracoglia, 2012a). A deterministic trajectory model was calibrated against the empirical equations given in [21] and then used to perform Monte-Carlo simulations in 2D and 3D. The influence of debris type (cubes and spheres) was considered together with the effect of the height and distance from the building of the debris source. 2D simulations showed a greater likelihood of damage, and should therefore be considered conservative or inaccurate.

When a simulation of a vertical gust is included [34] there is a noted increase in the likelihood of damage as the debris trajectory is longer. The vertical gust is a quite simplistic model in this context, but using a stochastic model to generate a turbulent wind field is more refined and has a marked influence on the debris flight and hence likelihood of damage [35]. Although both the turbulence and gust models require further validation, the results emphasise the importance of the local wind environment on the predictions of damage.

Grayson [7] has proposed an assessment framework for predicting building envelope failure during the passage of hurricane. The framework includes all the key elements of a debris damage model, including a generation model that reflects failure of fasteners under the action of wind pressure. The debris impact aspect of this model calculates both momentum and kinetic energy at impact and also considers the consequences of internal pressurisation on the integrity of the structure once the envelope has failed.

Considering the vulnerability of the building envelope to debris impact, ASTM specifies standard procedures for testing the impact resistance of cladding, glazing and hurricane shutters, but considers only spherical and rod like debris. Novel testing procedures have therefore been developed to determine the vulnerability of windows to lightweight sheet type debris such as shingles [30]. A range of mechanisms were used to project the debris, including an air cannon, catapult (shingles) and drop tests (rods) and tests considered different flight modes and impact angles. The vulnerability of the glazing was expressed in terms of the impact momentum of the projectile. A second study considered the vulnerability of hurricane shutters to impact from roof tiles [5]. In this case an air cannon was used to launch the projectiles whose flight was recorded using high speed video to determine impact speed and orientation.

7. Discussion and concluding comments

The literature reviewed in this paper has addressed an issue of real importance in the built environment; windborne debris does cause significant damage and considerable economic

loss on an annual basis. It is also clear from the papers reviewed that a new and effective strategy has been proposed in the USA for mitigating this, and other natural hazards, and their associated risks. The HAZUS®MH model has provided an overarching framework within which detailed engineering research has contributed to the development of a workable model. It is important to note that through this framework engineering research has produced an impact that is accessible to a wider audience than the engineering community. Whereas previous research might have resulted in codes of practice for engineers, the HAZUS®MH model equips government agencies, property owners and insurance companies as well as engineers.

Although the direct outcome of this paper is to inform a specific audience about a specific hazard, the more valuable outcome is to ask questions about the overall methodology for managing natural hazards. FEMA has invested in a major programme of work, where is the equivalent in Europe? There is a significant body of research on wind hazard in Europe, but this is principally within the domain of meteorologists and catastrophe modellers in the insurance industry. It is on the periphery of engineering research.

The HAZUS®MH model is not a design tool, but the underlying concepts are core to the implementation of performance based design. Is there a need for a performance based design approach within wind engineering? Moreover, FEMA uses this tool to address other natural hazards: flooding and earthquake. However, the basic methodology could be adapted to address hazards relating environmental effects on buildings and people: pedestrian comfort and safety, pollution, heating and ventilation, fire, and terrorist actions such as dirty bombs.

Within such a model, there is also a need to identify the best protocol for simulating the risk. All the models reviewed here have relied on a deterministic analytical model of debris flight that is used as the basis of a Monte Carlo simulation to predict the likely trajectories. However, work has also been reviewed that presents an alternative computational framework. This approach has been shown to replicate work done in the wind tunnel, both to simulate trajectories and to determine aerodynamic and auto-rotational coefficients. There is great potential for developing CFD simulations of the urban built environment to provide not just more informed predictions of debris flight, but also better understanding of wind effects on the users of that environment.

I would like to thank the organising committee of the 7th International Symposium on Environmental Effects on Buildings and People: Actions, Influences, Interactions, Discomfort for inviting me to submit this paper. I would also like to acknowledge the very significant contributions of Dr David Hargreaves and Dr Bruce Kakimpa to this paper.

References

[1] Baker C.J., *The debris flight equations*, Journal of Wind Engineering and Industrial Aerodynamics, Vol. 95(5), 2007, 329-353.

[2] FEMA488, *Mitigation Assessment Team Report: Hurricane Charley in Florida*, 2005.

[3] FEMA489, *Hurricane Ivan in Alabama and Florida: Observations, Recommendations and Technical Guidance*, 2005.

[4] FEMA549, *Hurricane Katrina in the Gulf Coast: Mitigation Assessment Team Report, Building Performance Observations, Recommendations, and Technical Guidance*, 2006.

[5] Fernandez G., Masters F.J., Gurley K.R., *Performance of hurricane shutters under impact by roof tiles*, Engineering Structures, Vol. 32(10), 2010, 3384-3393.

[6] Grayson M.J., Pang W., Schiff S., *Three-dimensional probabilistic wind-borne debris trajectory model for building envelope impact risk assessment*, Journal of Wind Engineering and Industrial Aerodynamics, Vol. 102, 2012, 22-35.

[7] Grayson M.J., Pang W., Schiff S., *Building envelope failure assessment framework for residential communities subjected to hurricanes*, Engineering Structures, Vol. 51, 2013, 245-258.

[8] Hargreaves D.M., Kakimpa B., Owen J.S., T*he computational fluid dynamics modelling of the autorotation of square, flat plates*, Journal of Fluids and Structures, Vol. 46, 2014, 111-133.

[9] Holmes J.D., *Trajectories of spheres in strong winds with application to wind-borne debris*, Journal of Wind Engineering and Industrial Aerodynamics, Vol. 92(1), 2004, 9-22.

[10] Holmes J.D., *Windborne debris and damage risk models: A* review, Wind and Structures, An International Journal, Vol. 13(2), 2010, 95-108.

[11] Holmes J.D., Baker C.J., Tamura Y., T*achikawa number: A proposal*, *J*ournal of Wind Engineering and Industrial Aerodynamics, Vol. 94(1), 2006, 41-47.

[12] Holmes J.D., Letchford C.W., Lin N., I*nvestigations of plate-type windborne debris. Part II: Computed trajectories*, Journal of Wind Engineering and Industrial Aerodynamics, Vol. 94(1), 2006, 21-39.

[13] Kakimpa B., Hargreaves D.M., Owen J.S., *An investigation of plate-type windborne debris flight using coupled CFD-RBD models. Part I: Model development and validation*, Journal of Wind Engineering and Industrial Aerodynamics, Vol. 111, 2012a, 95-103.

[14] Kakimpa B., Hargreaves D.M., Owen J.S., *An investigation of plate-type windborne debris flight using coupled CFD-RBD models. Part II: Free and constrained flight*, Journal of Wind Engineering and Industrial Aerodynamics, Vol. 111, 2012b, 104-116.

[15] Kakimpa B., Hargreaves D.M., Owen J.S., Martinez-Vazquez P., Bakers C.J., Sterling M., Quinn A.D., *CFD modelling of free-flight and auto-rotation of plate type debris*, Wind and Structures, An International Journal, 13(2), 2010, 169-189.

[16] Kopp G.A., Morrison M.J., Gavanski E., Henderson D. J., Hong H.P., *"Three Little Pigs" project: Hurricane risk mitigation by integrated wind tunnel and full-scale laboratory tests*, Natural Hazards Review, Vol. 11(4), 2010, 151-161.

[17] Kordi B., Kopp G.A., *"The debris flight equations" by C.J. Baker*, Journal of Wind Engineering and Industrial Aerodynamics, Vol. 97(3-4), 2009a, 151-154.

[18] Kordi B., Kopp G.A., *Evaluation of quasi-steady theory applied to windborne flat plates in uniform flow*, Journal of Engineering Mechanics, Vol. 135(7), 2009b, 657-668.

[19] Kordi B., Kopp G.A., *Effects of initial conditions on the flight of windborne plate debris*, Journal of Wind Engineering and Industrial Aerodynamics, Vol. 99(5), 2011, 601-614.

[20] Kordi B., Traczuk G., Kopp G.A., *Effects of wind direction on the flight trajectories of roof sheathing panels under high winds*, Wind and Structures, An International Journal, Vol. 13(2), 2010, 145-167.

[21] Lee B.E., Wills J., *Vulnerability of fully glazed high-rise buildings in tropical cyclones*, Paper presented at the Enhancing the Performance of Building Systems in High Wind Regions, 2002.

[22] Lin N., Holmes J.D., Letchford C.W., *Trajectories of wind-borne debris in horizontal winds and applications to impact testing*, Journal of Structural Engineering, Vol. 133(2), 2007, 274-282.

[23] Lin N., Letchford C., Holmes J., *Investigation of plate-type windborne debris. Part I. Experiments in wind tunnel and full scale*, Journal of Wind Engineering and Industrial Aerodynamics, 94(2), 2006, 51-76.

[24] Lin N., Vanmarcke E., *Windborne debris risk assessment*, Probabilistic Engineering Mechanics, 23(4), 2008, 523-530.

[25] Lin N., Vanmarcke E., *Windborne debris risk analysis. Part I. Introduction and methodology*, Wind and Structures, An International Journal, Vol. 13(2), 2010, 191-206.

[26] Lin N., Vanmarcke E., Yau S.-C., *Windborne debris risk analysis. Part II. Application to structural vulnerability modeling*, Wind and Structures, An International Journal, Vol. 13(2), 2010, 207-220.

[27] Martinez-Vazquez P., Baker C.J., Sterling M., Quinn A., Richards P.J., A*erodynamic forces on fixed and rotating plates*, Wind and Structures, An International Journal, Vol. 13(2), 2010, 127-144.

[28] Martinez-Vazquez P., Kakimpa B., Sterling M., Baker C.J., Quinn A.D., Richards P.J., Owen J.S., P*ressure field of a rotating square plate with application to windborne debris*, Wind and Structures, An International Journal, Vol. 15(6), 2012, 509-529.

[29] Martinez-Vazquez P., Sterling M., Baker C.J., Quinn A.D., Richards P.J., A*utorotation of square plates, with application to windborne debris*, Wind and Structures, An International Journal, Vol. 14(2), 2011, 167-186.

[30] Masters F.J., Gurley K.R., Shah N., Fernandez G., T*he vulnerability of residential window glass to lightweight windborne debris*, Engineering Structures, Vol. 32(4), 2010, 911-921.

[31] Minor J. E., *Windborne debris and the building envelope*, Journal of Wind Engineering and Industrial Aerodynamics, Vol. 53(1-2), 1994, 207-227.

[32] Minor J.E., Mehta K.C., *Wind damage observations and implications*, Vol. 105(11), 1979, 2279-2291.

[33] Moghim F., Caracoglia L., A *numerical model for wind-borne compact debris trajectory estimation: Part 1: Probabilistic analysis of trajectory in the proximity of tall buildings*, *E*ngineering Structures, Vol. 38, 2012a, 153-162.

[34] Moghim F., Caracoglia L., *A numerical model for wind-borne compact debris trajectory estimation: Part 2 - Simulated vertical gust effects on trajectory and mass momentum*, Engineering Structures, Vol. 38, 2012b, 163-170.

[35] Moghim F., Caracoglia L., *Effect of computer-generated turbulent wind field on trajectory of compact debris: A probabilistic analysis approach*, Engineering Structures, Vol. 59, 2014, 195-209.

[36] Richards P.J., Williams N., Laing B., McCarty M., Pond M., *Numerical calculation of the three-dimensional motion of wind-borne debris*, Journal of Wind Engineering and Industrial Aerodynamics, Vol. 96(10-11), 2008, 2188-2202.
[37] Scarabino A., Giacopinelli P., *Analysis of the two dimensional sheet debris flight equations: Initial and final state*, Wind and Structures, An International Journal, Vol. 13(2), 2010, 109-125.
[38] Schneider P.J., Schauer B.A., *HAZUS – its development and its future*, Natural Hazards Review, Vol. 7(2), 2006, 40-44.
[39] Sparks P.R., Schiff S.D., Reinhold T.A., *Wind damage to envelopes of houses and consequent insurance losses*, Journal of Wind Engineering and Industrial Aerodynamics, Vol. 53(1-2), 1994, 145-155.
[40] Surry D., Kopp G.A., Bartlett F.M., *Wind load testing of low buildings to failure at model and full scale*, Natural Hazards Review, Vol. 6(3), 2005, 121-128.
[41] Tachikawa M., T*rajectories of flat plates in uniform flow with application to wind-generated missiles*, Journal of Wind Engineering and Industrial Aerodynamics, Vol. 14(1-3), 1983, 443-453.
[42] Tachikawa M., Me*thod for estimating the distribution range of trajectories of wind-borne missiles*, Journal of Wind Engineering and Industrial Aerodynamics, Vol. 29 pt 2(1-3), 1988, 175-184.
[43] Tamura Y., *Wind-induced damage to buildings and disaster risk reduction*, Paper presented at the 7th Asia-Pacific Conference on Wind Engineering, APCWE-VII, November 2009, Taipei, Taiwan.
[44] Vickery P.J., Lin J., Skerlj P.F., Twisdale Jr L.A., Huang K., *HAZUS – MH hurricane model methodology. I: Hurricane hazard, terrain, and wind load modeling*, Natural Hazards Review, Vol. 7(2), 2006, 82-93.
[45] Vickery P.J., Skerlj P.F., Lin J., Twisdale L.A., Young M.A., Lavelle F.M., *HAZUS-MH hurricane model methodology. II: Damage and loss estimation*, Natural Hazards Review, Vol. 7(2), 2006, 94-103.
[46] Vickery P J., Skerlj P.F., Steckley A.C., Twisdale L.A., *Hurricane wind field model for use in hurricane simulations*, Journal of Structural Engineering New York, N.Y., Vol. 126(10), 2000, 1203-1221.
[47] Vickery P.J., Skerlj P.F., Twisdale L.A., *Simulation of hurricane risk in the U.S. using empirical track model*, Journal of Structural Engineering New York, N.Y., Vol. 126(10), 2000, 1222-1237.
[48] Visscher B.T., Kopp G. A., *Trajectories of roof sheathing panels under high winds*, Journal of Wind Engineering and Industrial Aerodynamics, Vol. 95(8), 2007, 697-713.
[49] Wills J A.B., Lee B.E., Wyatt T.A., *A model of wind-borne debris damage*, Journal of Wind Engineering and Industrial Aerodynamics, Vol. 90(4-5), 2002, 555-565.
[50] Yau S., Lin N., Vanmarcke E., *Hurricane damage and loss estimation using an integrated vulnerability model*, Natural Hazards Review, Vol. 12(4), 2011, 184-189.

TECHNICAL TRANSACTIONS | CZASOPISMO TECHNICZNE
CIVIL ENGINEERING | BUDOWNICTWO
2-B/2015

FUMIYOSHI TAKEDA*, TATSUYA YOSHINO*, YASUSHI UEMATSU**

DESIGN WIND FORCE COEFFICIENTS FOR FREE-STANDING CANOPY ROOFS OF MEMBRANE STRUCTURES

WSPÓŁCZYNNIKI PROJEKTOWE OBCIĄŻENIA WIATREM DLA WOLNOSTOJĄCEGO DACHU WYKONANEGO Z MEMBRANY

Abstract

The present study examines the wind-induced behaviour of free-standing membrane canopy roofs with various types of roof-supporting systems and presents wind force coefficients for designing such roofs. The effects of roof deformation and choice of roof-supporting system on wind force coefficients are investigated. The characteristics of wind-induced responses of the roofs are taken into account for improving the wind force coefficients that we previously proposed based on the results of wind tunnel experiment with rigid roof models.

Keywords: *design wind force coefficients, membrane structure, structural analysis, computational fluid dynamics (CFD)*

Streszczenie

W przedstawionych badaniach analizowane jest zachowanie wolnostojącego dachu membranowego, z różnymi systemami podparcia, poddanego oddziaływaniu wiatru. Zaprezentowano współczynniki użyteczne podczas projektowania takich dachów. Zbadano wpływ deformacji dachu oraz zastosowania różnych systemów wsporczych na współczynniki obciążenia wiatrem. W celu uzyskania poprawy współczynników sił pochodzących od wiatru, wcześniej zaproponowanych w oparciu o wyniki uzyskane eksperymentalnie w tunelu aerodynamicznym dla modelu ze sztywnym poszyciem dachu, uwzględniono charakterystyki odpowiedzi dachów na oddziaływanie wiatru.

Słowa kluczowe: *współczynniki projektowe obciążenia wiatrem, konstrukcja membranowa, analiza konstrukcji, komputerowa mechanika płynów (CFD)*

DOI: 10.4467/2353737XCT.15.131.4168

* Technical Research Center, Taiyo Kogyo Corporation, 3-20, Syodai-Tajika, Hirakatashi, Osaka, Japan.
** Department of Architecture and Building Science, Tohoku University, Sendai, Japan.

1. Introduction

Many free-standing canopy roofs of membrane structures are constructed to provide shade and weather protection in public spaces. Because they are lightweight and flexible, wind resistance is critical to their structural design. Regarding the wind loads on free-standing membrane canopy roofs, some studies have been carried out. For example, Pun and Letchford [5] analysed the response of an HP-shaped tension membrane roof subjected to fluctuating wind loads. Recently, Michalski et al. [1, 2] have shown an application of computational fluid dynamics (CFD) to the fluid-structure interaction (FSI) for a flexible umbrella structure. Nagai et al. [3] investigated the wind loads on a horn-shaped membrane structure. However, the number of studies on the design wind force coefficients of free-standing membrane canopy roofs is quite limited.

The authors proposed wind force coefficients for designing free-standing canopy roofs of various shapes based on wind tunnel experiments with rigid roof models [9, 10]. Assuming that four corner columns support the roof and that the roof deformation can be neglected, focus is on the axial forces induced in the columns. In practice, however, the roof deforms under wind loading, and roof-supporting systems other than four corner columns are also used. Takeda et al. [7, 8] showed that, in some cases, wind forces acting on the roof were significantly affected by the roof deformation and roof-supporting system. In this study, we propose design wind force coefficients for membrane roofs considering these two factors. Among the many roof configurations, we focus on mono-sloped and hyperbolic paraboloid (HP)-shaped roofs (Fig. 1).

Firstly, a brief explanation of the design wind force coefficients based on the wind tunnel experiments with rigid roofs is given. Then, the effects of roof deformation and type of roof-supporting system on the wind-induced responses are discussed. Finally, the design wind force coefficients for flexible membrane roofs are proposed.

Fig. 1. Free-standing canopy roofs of membrane structures, a) mono-sloped, b) HP-shaped

2. Definition of wind force and moment coefficients

2.1. Roof configurations

Figs. 2a and 3a show the tested roof configurations, where the mean roof height (H) of the mono-sloped roof and HP-shaped roofs are 6 m and 8 m, respectively.

2.2. Definition of wind force and moment coefficients

The definitions of the aerodynamic forces (D and L) and moments (M_x and M_y) are shown in Figs. 2b and 3b. The values of D, L, M_x and M_y for the mono-sloped and HP-shaped roofs are normalized using Eqns. (1) to (4) for mono-sloped roofs and Eqns. (5) to (8) for HP-shaped roofs, respectively,

$$C_D = \frac{D}{q_H\left(b^* l \sin\beta\right)} \qquad C_L = \frac{L}{q_H\left(bl\right)} \tag{1) (2)}$$

$$C_{Mx} = \frac{M_x}{q_H\left(bl^2\right)} \qquad C_{My} = \frac{M_y}{q_H\left(b^{*2} l\right)} \tag{3) (4)}$$

$$C_D = \frac{D}{q_H ha} \qquad C_L = \frac{L}{q_H S} \tag{5) (6)}$$

$$C_{Mx} = \frac{M_x}{q_H Sa} \qquad C_{My} = \frac{M_y}{q_H Sa} \tag{7) (8)}$$

where q_H is the reference velocity pressure at mean roof height H. For the mono-sloped roofs, b represents the horizontal (projection) width of the roof, while b^* (= l) represents the actual width of the roof (Fig. 2). For the HP-shaped roofs, h represents the difference in height of the roof, a represents the horizontal (projection) width of the roof, and S represents the projection area of the roof.

For simplicity, the design wind force coefficients on the roof are specified by two uniformly distributed values (C_{NW} and C_{NL}) over the windward and leeward halves, which are defined in terms of the velocity pressure q_H at the mean roof height.

The wind force coefficients are

$$C_{NW} = \frac{N_W}{q_H\left(b^* l/2\right)} \qquad C_{NL} = \frac{N_L}{q_H\left(b^* l/2\right)} \tag{9) (10)}$$

for the mono-sloped roof and

$$C_{NW} = \frac{N_W}{q_H (S/2)} \qquad C_{NL} = \frac{N_L}{q_H (S/2)} \tag{11) (12}$$

where N_W and N_L respectively represent the normal positive downward wind forces, on the windward and leeward halves. The coefficients C_{NW} and C_{NL} are given by Eqns. (13) and (14) for mono-sloped roof and by Eqns. (15) and (16) for HP-shaped roofs.

$$C_{NW} = -C_L - 4C_{My} \qquad C_{NL} = -C_L + 4C_{My} \tag{13) (14}$$

$$C_{NW} = -C_L - 3\sqrt{2}C_{My} \qquad C_{NL} = -C_L + 3\sqrt{2}C_{My} \tag{15) (16}$$

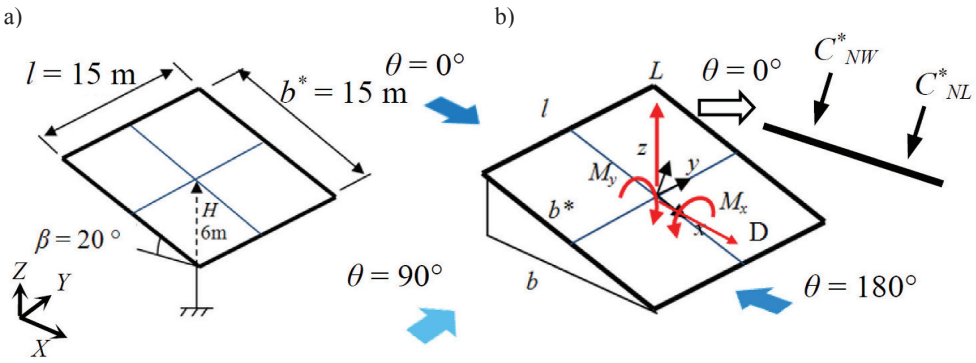

Fig. 2. Mono-sloped free roof, a) configuration, b) definitions

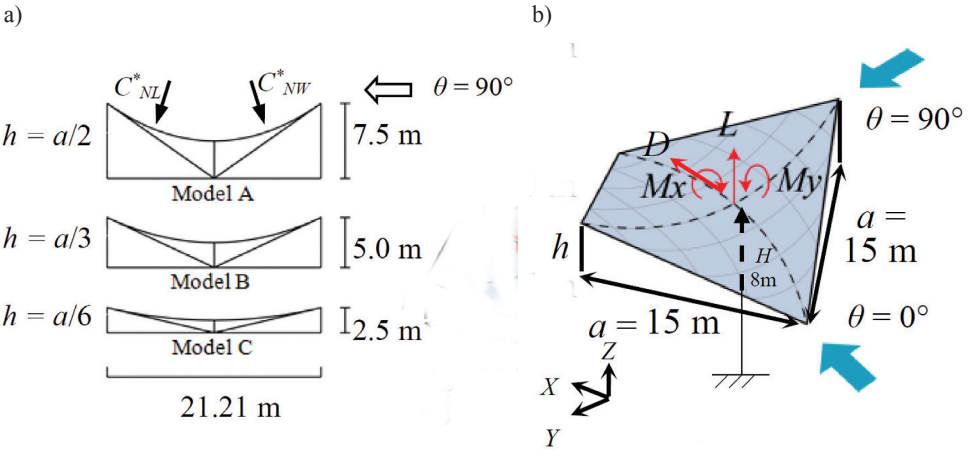

Fig. 3. Hyperbolic paraboloid-shaped free roofs, a) configuration, b) definitions

3. Design wind force coefficients for rigid free roofs

In a previous study [10], the design wind force coefficients C^*_{NW} and C^*_{NL} for mono-sloped and HP-shaped rigid roofs were specified by Eqns. (17) and (18),

$$C^*_{NW} = \frac{\gamma C_{NW0}}{G_f} \qquad C^*_{NL} = \frac{\gamma C_{NL0}}{G_f} \tag{17) (18}$$

where C_{NW0} and C_{NL0} represent the basic values of C_{NW} and C_{NL} for θ = 0° and 180° in the mono-sloped roof case and for θ = 0° and 90° in the HP-shaped roof case. They are computed by using a combination of C_L and C_{My} (or C_{Mx}) at an apex of the hexagon as shown in Fig. 4, which approximates the envelope of the C_L–C_{My} (or C_L–C_{Mx}) trajectory obtained from the wind tunnel experiments (see Fig. 5). A gust effect factor (G_f) of 2.0 based on the load effect is used. A correction factor (γ) is used for considering the effect of wind direction. Two sets of C_{NW0} and C_{NL0} values are selected from the six sets corresponding to the apexes, which produce the maximum tension and compression in the columns.

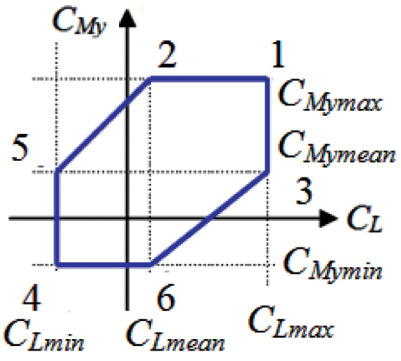

Fig. 4. Model of the envelope of the C_L and C_{My}

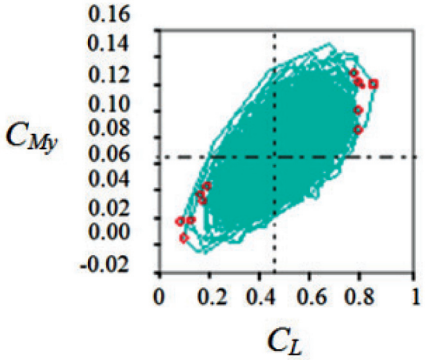

Fig. 5. Time history of the C_L–C_{My} trajectory

4. Roof-supporting systems of membrane structures

4.1. Analytical models

Structural analysis was performed by using a finite-element method (FEM) to investigate how the roof-supporting system of membrane roofs affected the load effects. Figs. 6a–6c and 7a–7c show analytical models for mono-sloped roof of β = 20° and HP-shaped roof of $h = a/2$ with different roof-supporting systems, respectively. Frame and suspension types are often used in membrane structures. The F1 and F2 models in Figs. 6 and 7 represent

frame types, whereas the S1 model represents a suspension type. In the F1 model, the roof structure consists of perimeter girders and binding beams. The roof frame is covered with a pre-tensioned membrane. The F2 model consists of perimeter girders and pre-tensioned membrane (Figs. 6b and 7b). In the F1 and F2 models, four corner columns support the roof girders. The S1 model consists of curved perimeter cables and pre-tensioned membrane. The roof is supported by posts and guy cables at the four corners. The column bases of the F1 and F2 models are fixed, whereas the posts of the S1 models are pin-supported. The roof area of the S1 model is approximately 82% of that of the frame models because of the curved perimeter. The S1 model is the most flexible of the three, which causes the roof to deform the most under wind loading. On the other hand, the F1 model is relatively rigid. Moreover, the roof membrane slightly deforms in the downward direction owing to its weight. Therefore, the initial shapes of these three roofs slightly differ from each other because of the difference in the supporting system. The pre-stress is 4 kN/m in the warp and fill (weft) directions of the membrane. The self-weight of the membrane is 12 N/m^2.

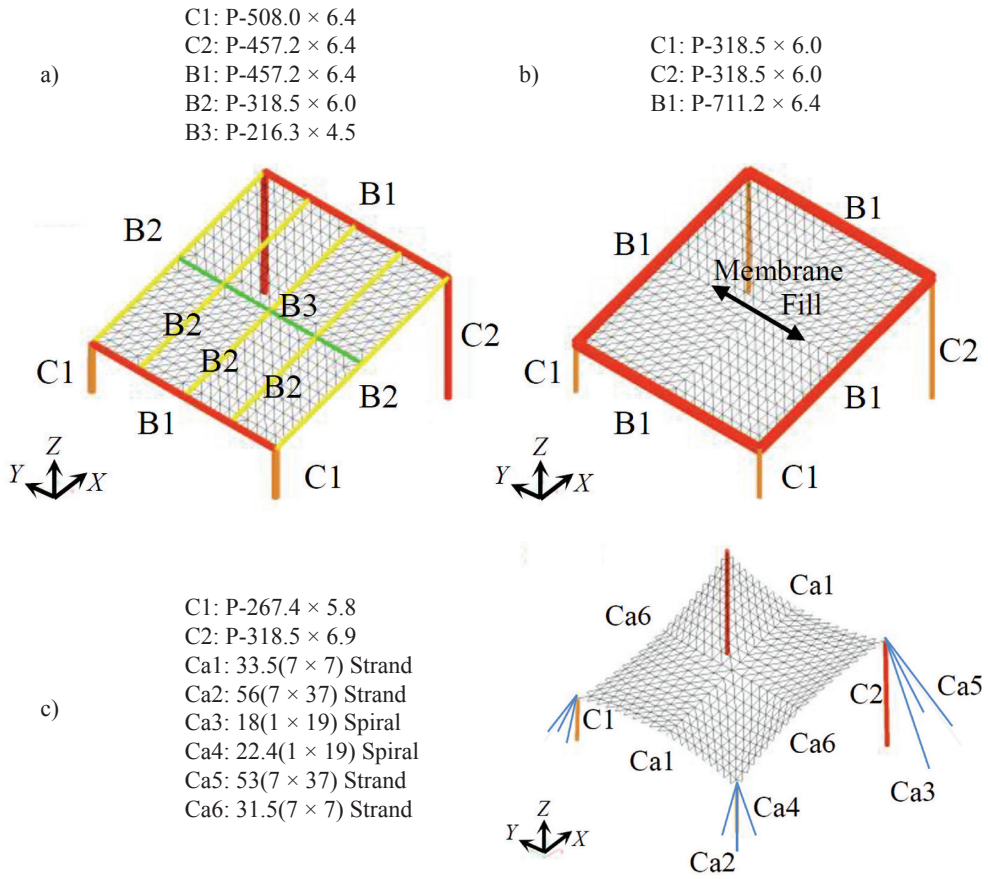

Fig. 6. Mono-sloped roof structural models, a) frame type 1 (F1), b) frame type 2 (F2), c) suspension type (S1)

a)
C1: P-558.8 × 6.4
C2: P-406.4 × 6.4
B1: P-318.5 × 6.9
B2: P-216.3 × 5.8
B3: P-165.2 × 3.7

b)
C1: P-406.4 × 6.4
C2: P-406.4 × 6.4
B1: P-558.8 × 6.4

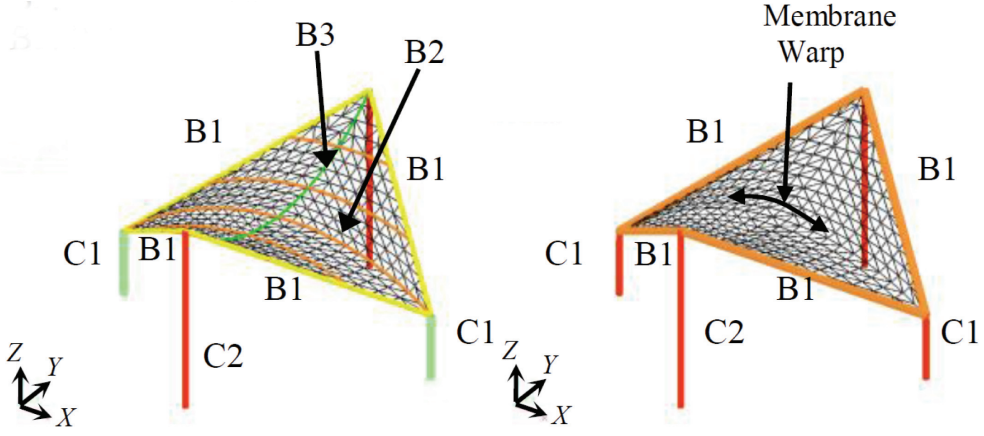

c)
C1: P-406.4 × 6.4
C2: P-216.3 × 4.5
Ca1: 30(7 × 19) Strand
Ca2: 42.5(1 × 61) Spiral
Ca3: 14(1 × 19) Spiral
Ca4: 18(1 × 19) Spiral
Ca5: 45(1 × 91) Spiral

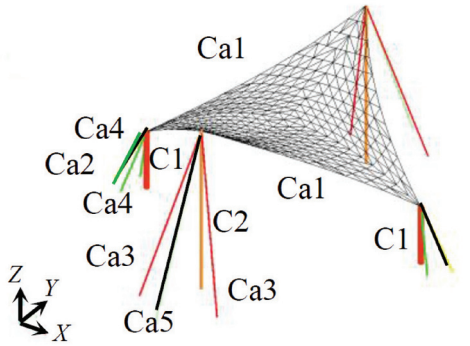

Fig. 7. HP-shaped roof structural models, a) frame type 1 (F1), b) frame type 2 (F2), c) suspension type (S1)

4.2. Structural analysis

Structural analysis was carried out by using the in-house Taiyo Kogyo Corporation MAGESTIC software. The program is based on FEM, in which the geometrical non-linearity and the Newton–Raphson method are taken into account. The membrane material is assumed to be orthotropic and elastic. Furthermore, we assume that the membrane only carries tension; in other words, it does not resist compression and bending moment. The design wind speed is 31.5 m/s and the corresponding velocity pressure is 605 N/m^2. Wind force coefficients based on wind tunnel experiments with rigid models were used for computing the wind loads, which are the six sets of C_L and C_{My} corresponding to the apexes of the hexagon shown in Fig. 4.

Tables 1 and 2 summarize the wind force coefficients for the mono-sloped and HP-shaped roofs, respectively. We have adopted the correction factor $\gamma = 1.0$ because the maximum tension and compression are induced when $\theta = 0°$ and $\theta = 180°$ for the mono-sloped roof and when $\theta = 0°$ and $\theta = 90°$ for the HP-shaped roof. We take the gust effect factor $G_f = 2.0$ for evaluating the design wind force coefficients.

Table 1

Wind force coefficients for the mono-sloped roofs

Apex	Combination of C_L and C_{My}	Wind direction $\theta = 0°$		Wind direction $\theta = 180°$	
		C_{NW0}	C_{NL0}	C_{NW0}	C_{NL0}
1	$C_{Lmax} + C_{Mymax}$	−2.45	−0.19	0.19	0.50
2	$C_{Lmean} + C_{Mymax}$	−1.96	0.30	0.65	0.96
3	$C_{Lmax} + C_{Mymean}$	−1.93	−0.71	−0.13	0.83
4	$C_{Lmin} + C_{Mymin}$	−0.51	−0.20	0.59	2.76
5	$C_{Lmin} + C_{Mymean}$	−0.96	0.25	1.20	2.16
6	$C_{Lmean} + C_{Mymin}$	−0.99	−0.68	−0.28	1.89

Table 2

Wind force coefficients for the HP-shaped roofs

Apex	Combination of C_L and C_{My}	Wind direction $\theta = 0°$		Wind direction $\theta = 90°$	
		C_{NW0}	C_{NL0}	C_{NW0}	C_{NL0}
1	$C_{Lmax} + C_{Mymax}$	−0.65	−0.72	−0.37	0.11
2	$C_{Lmean} + C_{Mymax}$	−0.31	−0.38	0.02	0.50
3	$C_{Lmax} + C_{Mymean}$	−0.40	−0.97	−0.89	0.63
4	$C_{Lmin} + C_{Mymin}$	0.80	−0.67	−0.56	2.31
5	$C_{Lmin} + C_{Mymean}$	0.35	−0.22	0.12	1.63
6	$C_{Lmean} + C_{Mymin}$	0.39	−1.08	−1.17	1.70

Table 3

Membrane (*t*: thickness)

Tensional stiffness	$E_w \times t = 1284.67$ kN/m (Warp) $E_f \times t = 861.024$ kN/m (Fill)
Poisson's ratio	$\nu_w = 0.85$ (Warp) $\nu_f = 0.57$ (Fill)
Shear modulus	$G \times t = 57$ kN/m

Note: Measured by 'MSAJ/M-02 1995' and 'MSAJ/M-01 1993' in the Standards of the Membrane Structures Association of Japan.

Table 4

Cable

Elastic modulus	$E = 1.37 \times 10^8$ kN/m^2 (Strand) $E = 1.57 \times 10^8$ kN/m^2 (Spiral)

Table 5

Beam and Post

Elastic modulus	$E = 2.05 \times 10^8$ kN/m^2
Poisson's ratio	$\nu = 0.3$

In the structural analysis, the stresses involved in the members are calculated based on the Building Standard Law of Japan and the design standard for steel structures. For the membranes and cables, tensile stresses are calculated from the tensile forces; for the beams and columns, the extreme fibre stresses are calculated by combining the axial force and bending moment; the axial stresses involved in the posts of the S1 model are calculated from the axial forces. The allowable stresses and material constants are also determined based on the Building Standard Law. Tables 3–5 summarize the material constants. Moreover, the ratio of the computed stress to the allowable stress is calculated and we call it the 'stress ratio'. Each member size is determined so that the stress ratios become less than 1.0.

4.3. Load effect

The design wind force coefficients C^*_{NW} and C^*_{NL} were proposed assuming that the roof was rigid and supported by four corner columns, focussing on the column axial forces as the load effect. The wind force coefficients provide the maximum tension and compression on the columns, which correspond to the wind loads at the two apexes of the hexagon shown in Fig. 4. For the rigid mono-sloped roofs, apexes 1 and 4 provide the maximum load effects, whereas apexes 3 and 6 are applicable to the rigid HP-shaped roofs. However, in the case of membrane structures, the roof is so flexible that it cannot be considered rigid. Furthermore, the roof-supporting system may differ from that assumed in the previous study. Wind forces acting on the roof are first transferred to the peripheral members (beams or cables) via the membrane tension and thereafter, they are transferred to the columns or the post and guy cables. Therefore, load effects other than the column axial forces should also be considered for such structures. This subject is discussed below based on the structural analysis.

Figs. 8–10 and 11–13 show the results of the structural analysis for the F1, F2 and S1 models of the mono-sloped and HP-shaped roofs, respectively. In these figures, the maximum stress ratios for the members, i.e. membrane (Mem), cable, column, beam and post, are shown for the six apexes of the hexagon in Fig. 4. The maximum stress ratios are given at one of the two apexes providing the design wind force coefficients obtained from wind tunnel experiments with rigid models. However, these combinations are not sufficient for providing the maximum stress ratio. Tables 6 and 7 summarize such cases.

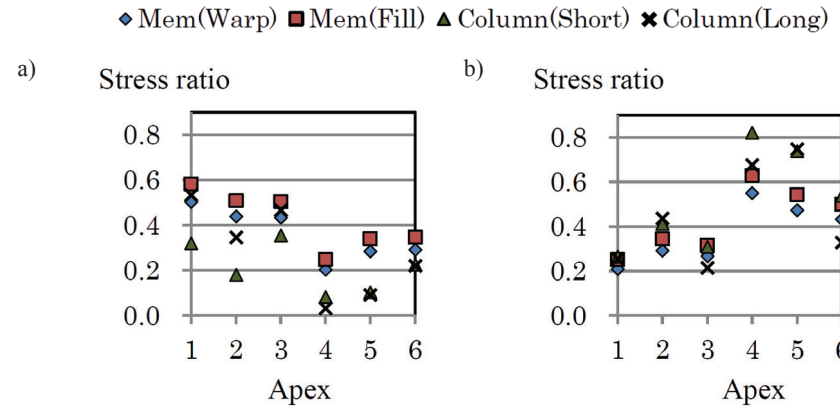

Fig. 8. Stress ratio for the F1 model of the mono-sloped roof, wind direction a) θ = 0°, b) θ = 180°

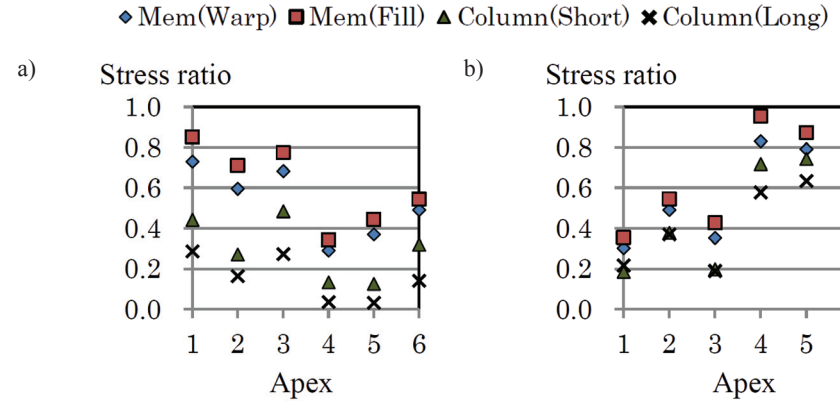

Fig. 9. Stress ratio for the F2 model of the mono-sloped roof, wind direction a) θ = 0°, b) θ = 180°

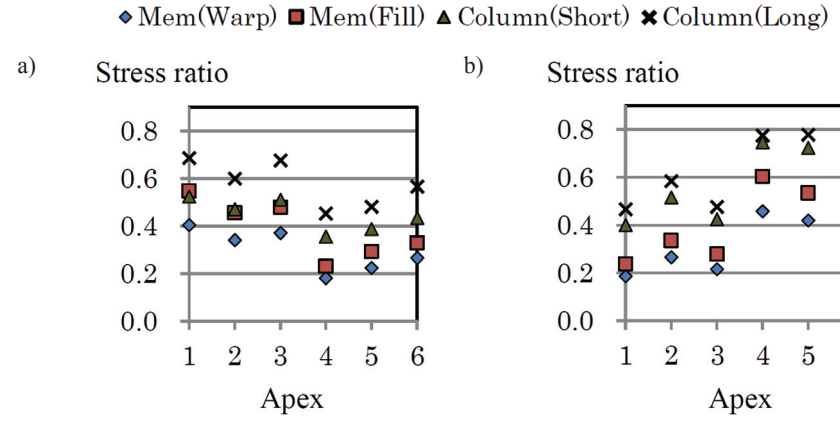

Fig. 10. Stress ratio for the S1 model of the mono-sloped roof, wind direction a) θ = 0°, b) θ = 180°

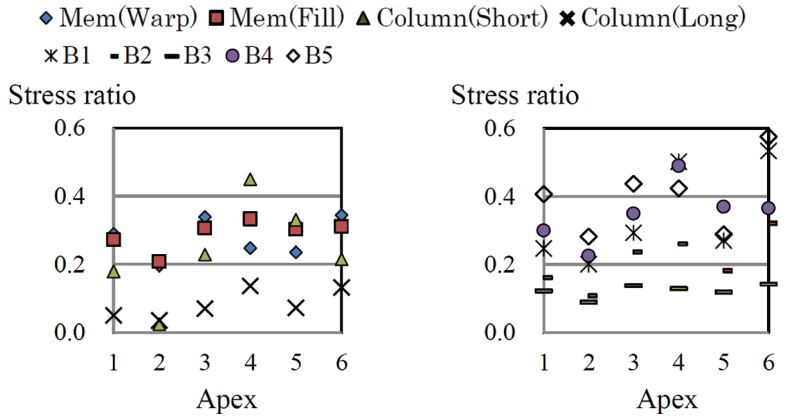

Fig. 11. Stress ratio for the F1 model of the HP-shaped roof, wind direction θ = 0°

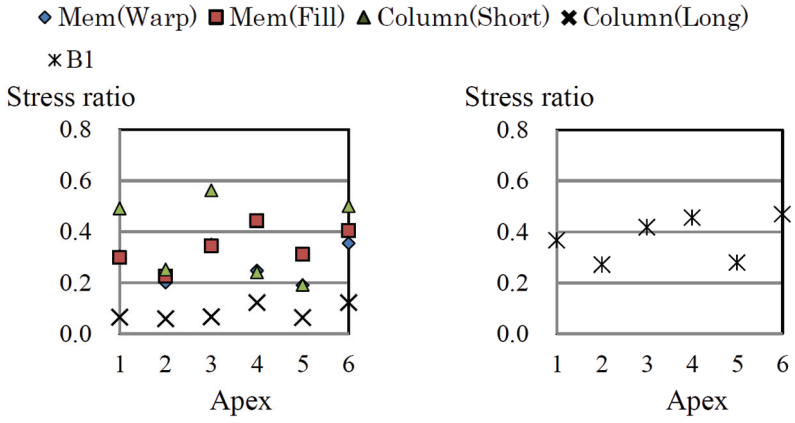

Fig. 12. Stress ratio for the F1 model of the HP-shaped roof, wind direction θ = 0°

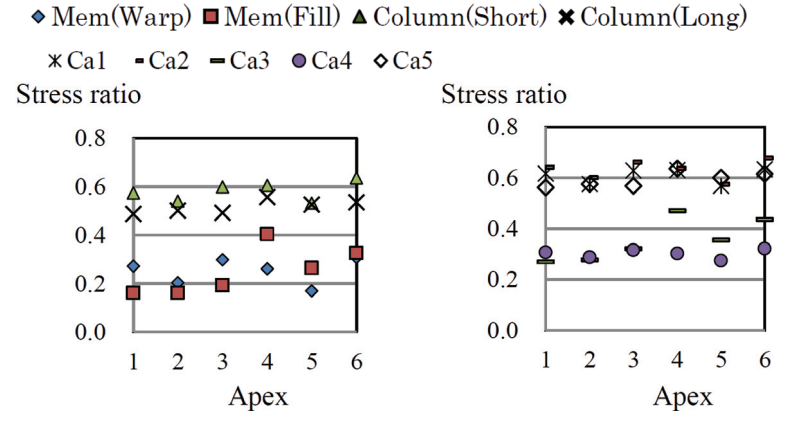

Fig. 13. Stress ratio for the S1 model of the HP-shaped roof, wind direction θ = 0°

Table 6

Stress ratios for the mono-sloped roof

a) Wind direction θ = 0°

	Member	Stress ratio			Ratio of Apex 3 to 1 or 4
		Apex 1	Apex 4	Apex 3	
F1	C1	0.32	0.08	0.35	1.11
F2	C1	0.44	0.13	0.49	1.10
S1	Ca3 Ca4	0.58 0.50	0.46 0.36	0.61 0.54	1.06 1.07

b) Wind direction $\theta = 180^{\circ}$

	Member	Stress ratio			Ratio of Apex 5 to 1 or 4
		Apex 1	Apex 4	Apex 5	
F1	C2	0.25	0.68	0.75	1.11
F2	C1 C2	0.19 0.22	0.72 0.58	0.74 0.64	1.03 1.10
S1	C2	0.47	0.77	0.78	1.01

Table 7

Stress ratios for the HP-shaped roof

Wind direction θ = 0°

	Member	Stress ratio			Ratio of Apex 6 to 3 or 4
		Apex 3	Apex 4	Apex 6	
F1	Mem (Warp) B2 B3	0.34 0.29 0.44	0.25 0.50 0.42	0.34 0.53 0.58	1.02 1.06 1.32
F2	Mem (Warp) B1	0.35 0.42	0.25 0.46	0.35 0.47	1.01 1.03
S1	Mem (Warp) Ca1 Ca2 Ca4 C1	0.30 0.63 0.66 0.32 0.60	0.26 0.63 0.64 0.30 0.60	0.31 0.63 0.68 0.32 0.64	1.03 1.01 1.06 1.03 1.02

4.4. Combination of lift and aerodynamic moment coefficients providing the maximum values for various load effects

It was shown in the previous section that the two apexes corresponding to the design wind force coefficients for rigid roofs do not always give the maximum stress ratio. This cause may

be related to (i) the bending moment, (ii) the roof-supporting system and (iii) the direction of wind resultant force vector induced by the roof deformation.

Firstly, we consider the effect of the bending moment. Fig. 14 shows the maximum stress ratios for the axial force, bending moment and their combination that are induced in the C1 columns of the F2 model with mono-sloped roof. The figure shows that the stress ratio for the bending moment dominates the maximum stress ratios. This is also observed in the HP-shaped roofs. Therefore, the bending moment may affect the proposed design wind force coefficients because the maximum stress ratio is provided by the combination of the extreme fibre stress of bending moment and the axial stress. This feature implies that not only the column axial forces but also other load effects, such as the bending moment, should be considered when discussing the design wind force coefficients for membrane roof structures.

Secondly, we consider the roof-supporting system. There are various roof-supporting systems for membrane roofs. Figs. 15a–15c show examples of roof-supporting systems for mono-sloped roofs. In these figures, the arrows show the flow of the wind load (i.e. load pass) from the roof to the ground. The type-1 model is obtained by removing the B3 member from the F1 model (Fig. 6a); therefore, the structure and load pass of type-1 are similar to those of F1. Wind loads acting on the roof of type-1 are transferred from the roof to the ground via the gate-shaped frames with the horizontal beam. On the other hand, in type-3 model, the roof girders are disposed in a direction perpendicular to those of the type-1; therefore, the load pass is different as shown in Fig. 15c. The type-2 model is a combination of type-1 and type-3; the wind loads flow to the perimeter girders. Fig. 16a shows the roof girders for the type-1 model, in which the wind load distributed along the girder for $\theta = 0°$ is also shown. Vertical reactions are induced at the edges of the girders by the wind loads. These reactions act on the gate-shaped frames in the opposite direction, as shown in Fig. 16b. Figs. 17a and 17b show the wind force coefficients corresponding to the apex 1 (AP1) and apex 3 (AP3), respectively. The wind load corresponding to AP1 provides the design wind force coefficients proposed by Uematsu et al. (2008). However, the maximum load effects are attributed to the wind load corresponding to AP3 (see Table 6a) because of the difference in the vertical reaction at the edge B of the girder between AP1 and AP3. The value of reaction at the edge point B for AP3 is about 1.35 times greater than that for AP1. As a result, the bending moment for AP3 is greater than that for AP1 (Fig. 16c). Therefore, the wind load corresponding to AP3 produces the maximum load effects.

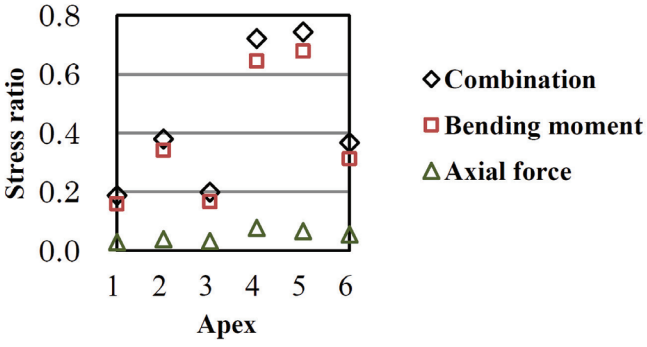

Fig. 14. Stress ratios for the bending moment, axial force and combinations

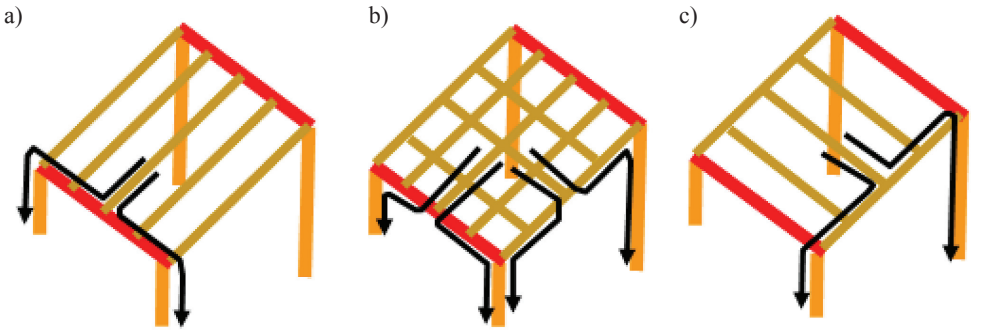

Fig. 15. Various roof-supporting systems for the mono-sloped roof and load flows, a) type-1, b) type-2, c) type-3

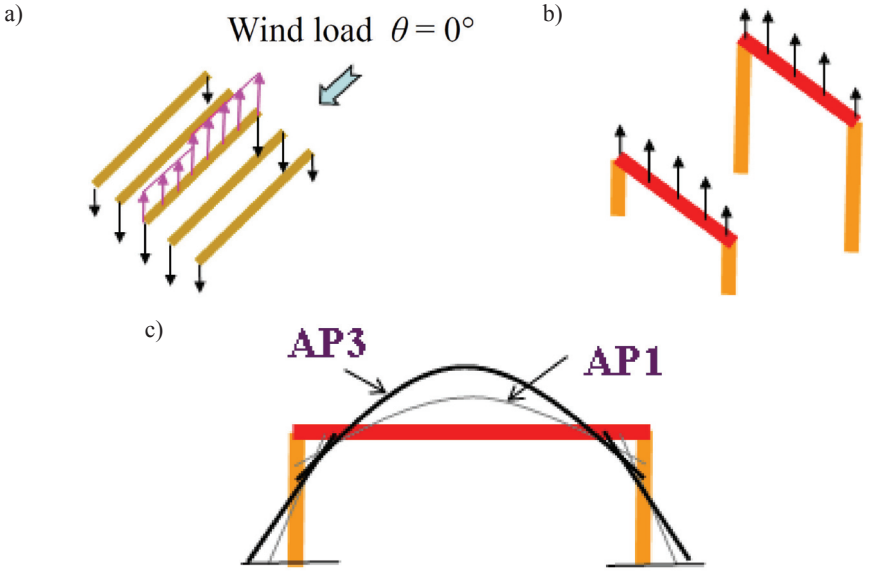

Fig. 16. Load flows and resultant bending moments, a) wind load applied to roof girders, b) wind load applied to gate-shaped frame, c) bending moments

Thirdly, we consider the roof deformation. The membrane roofs are composed of triangular elements in the FEM analysis. The wind pressure is uniform in each triangular element. The wind force vector is obtained by integrating the distributed wind load, as shown in Fig. 18a. This vector is perpendicular to the surface of the triangle. The resultant force vector for the wind load is obtained by adding the wind force vectors of the triangular element of the roof. Figs. 18b and 18c show the deformed roof shapes of the F2 model for the mono-sloped roof that correspond to the wind loads corresponding to AP1 and AP3, respectively. The resultant force vectors are also shown in the figures. The absolute values of the *X*, *Y* and *Z* components for the resultant force vector can be found from the total value of each reaction force at the

supporting point of the columns, because it is necessary to balance the total reaction forces and the total external force (i.e. the wind force). Table 8 shows the *X* and *Z* components of the total reaction forces of the F1 and F2 models at AP1 and AP3 when wind direction is θ = 0°. Comparing the reaction forces *X* (i.e. horizontal force) for AP1 and AP3 with each other, we can find that the value for AP3 is greater than that for AP1; i.e. the resultant force vector of the wind load for AP3 is more inclined to the ground compared with that for AP1, as shown in Fig. 18c. The greater horizontal force for AP3 induces additional bending moment by multiplying the horizontal force by the distance between the acting point of the vector and the ground. As a result, the wind load corresponding to AP3 is responsible for the maximum load effects. From the above discussion, we should improve the proposed design wind force coefficients for rigid roofs.

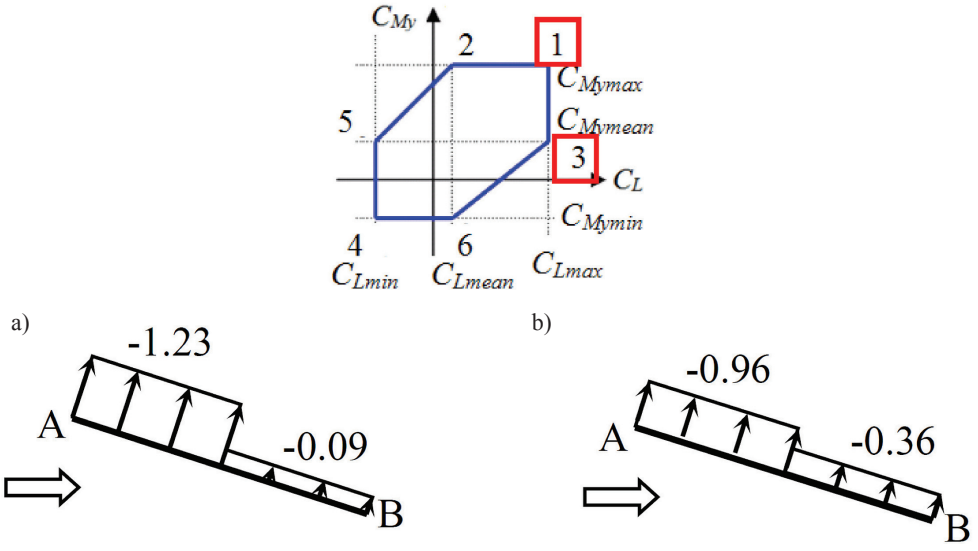

Fig. 17. Differences in the distribution of wind force coefficients between AP1 and AP3, wind direction θ = 0°, a) AP 1, b) AP3

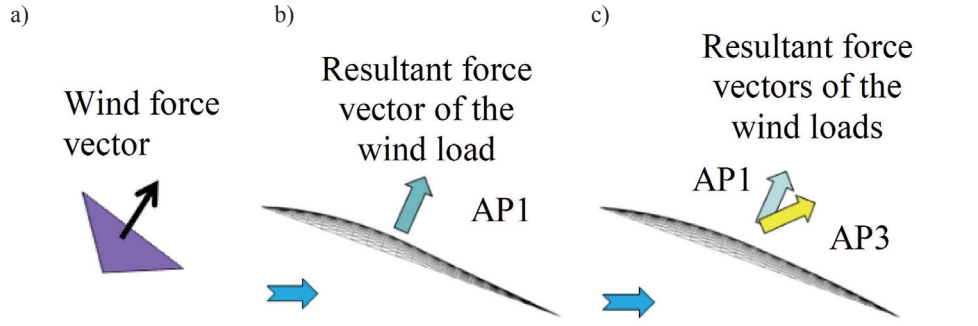

Fig. 18. Comparison of the total load vectors between AP1 and AP3, wind direction θ = 0°, F2 model of the mono-slope roof, a) triangle element in FEM, b) AP1, c) AP3

Table 8

Comparison of the total reaction forces between AP1 and AP3 of the mono-sloped roof

		Wind direction $\theta = 0^{\circ}$	
		AP1	AP3
F1	Reaction force X (kN)	−61	−61
	Reaction force Z (kN)	−169	−169
	Moment Y (kNm)	−322	−332
F2	Reaction force X (kN)	−52	−56
	Reaction force Z (kN)	−171	−170
	Moment Y (kNm)	−133	−142

5. Effect of roof deformation on wind forces

5.1. Analytical method

Because the membrane canopy roof structures are generally flexible, they may deform significantly under wind loading. The deformation may affect the flow pattern around the roof structure and change the wind loads on it, which in turn will cause additional deformation of the roof structure. The present paper focuses on the effect of static deformation on the time-averaged wind forces. In fact, the dynamic fluid-structure interaction (FSI), represented as aerodynamic damping and stiffness, may affect the response of the roof significantly in some cases. This will be the subject of a future study.

The effect of the roof deformation of flexible roofs on the wind force coefficients was investigated by computational fluid dynamics (CFD) and structural analysis [7, 8]. We focussed only on the time-averaged values of the wind forces and structural responses. The procedure that we followed consisted of the following steps. Firstly, the wind force coefficients acting on the rigid roof were obtained by CFD analysis using the Reynolds averaged Navier–Stokes model (Step 1). Secondly, using the wind force coefficients obtained at Step 1, we computed the roof deformation (Step 2). Thirdly, we computed the wind force coefficients acting on the deformed roof (Step 3). Finally, we used the wind force coefficients obtained at Step 3 to compute the roof deformation (Step 4). This procedure was repeated until the load effects converged to constant values (Fig. 19). Here, we used $G_f = 1.0$ because the focus was only on the time-averaged values. In practice, membrane roofs vibrate under dynamic wind loads; however, the effects are not considered in the present analysis. Referring to the Japanese design standard for steel structures, the criterion for convergence is based on the variation of the deformed roof shape,

$$\frac{\delta_n - \delta_{n-1}}{a} \leq \frac{1}{300} \tag{19}$$

where δ_n and δ_{n-1} represent the maximum displacement at the n and $n-1$ step, respectively.

We used the open-source code named OpenFOAM, version 1.5, released in 2008. The wind tunnel experiments were simulated. The computational domain for the mono-sloped roof was 1.0 m wide, 1.0 m high and 3.0 m long and for the HP roofs, it was 1.0 m wide, 1.4 m high and 3.0 m long. The roof models were placed at the same configuration as that used in the wind tunnel experiments. Fig. 20 shows the numerical model of the mono-sloped roof with the initial shape. The computation is based on the finite-volume method, in which the semi-implicit method for pressure-linked equations (SIMPLE) algorithm and the renormalization group k-ε (RNG k-ε) model are used. The boundary conditions are summarized in Tab. 9. The turbulence intensity I_u for the analysis was determined based on the wind tunnel experiment (Fig. 21).

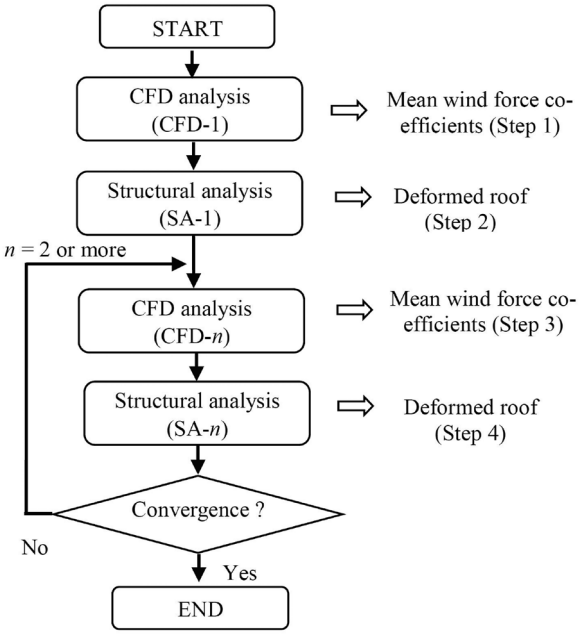

Fig. 19. Procedure for investigating the effect of roof deformation due to mean wind load

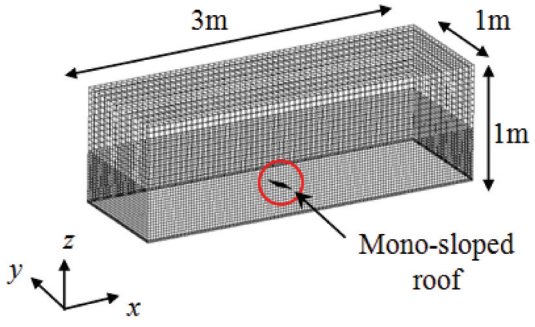

Fig. 20. Numerical model for the mono-sloped roof

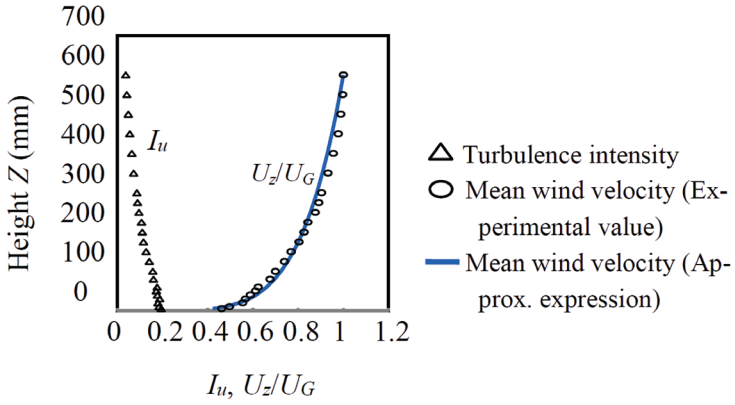

Fig. 21. Profiles of turbulence intensity I_u and mean wind velocity normalized by the value at a height of Z_G = 600 mm, U_G – mean wind velocity at the reference height of Z_G = 600 mm

Table 9

Boundary conditions in the simulated wind tunnel

Surface at X_{min} (Inlet)	<Power law > $U_Z = U_G \left\{ \frac{Z}{Z_G} \right\}^{\alpha}$ Reference height: Z_G = 0.6 m Wind velocity at the reference height: U_G = 8 m/s Power law index: α = 0.18 Turbulence intensity: experimental values (Fig. 21)
Surface at X_{max} (Outlet)	Surface pressure at outlet: 0 Pa
Surface at Y_{min}, Y_{max} and Z_{max}	Free-slip wall
Surface at Z_{min}	No-slip wall
HP surface	No-slip wall

5.2. Roof deformation and mean wind forces

Figs. 22a–22c and 23a–23c show the roof deformations at Step 4 for the mono-sloped and HP-shaped roofs, respectively. Figs. 24a–24d and 25a–25d show the ratio of stress at Step 4 to that at Step 2 for the mono-sloped and HP- shaped roofs, respectively. As might be expected, the ratio is generally small for the F1 model because the roof deformation is relatively small. In contrast, the ratios for the F2 and S1 models are generally larger than that for the F1 model; the largest value is approximately 1.2 for the F2 model (Fig. 24a). This feature may be related to the stiffness and arrangement of the members. Moreover, the difference in the

structural system between frame and suspension types may cause a difference in the stress ration between models. These results suggest that previously proposed design wind force coefficients cannot be applied to flexible roofs.

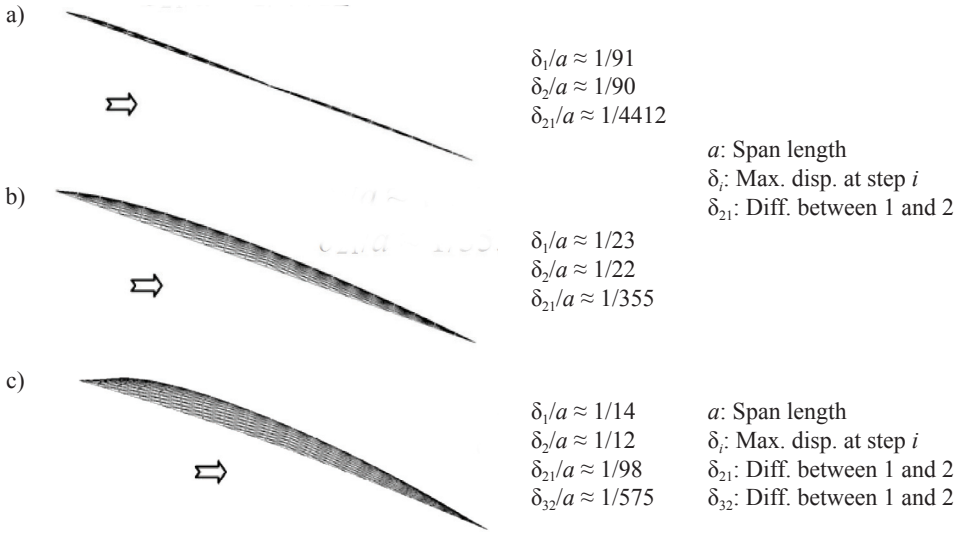

Fig. 22. Deformation of the mono-sloped models (wind direction θ = 0°). Scale factor for displacement: one time. a) F1 model, b) F2 model, c) S1 model

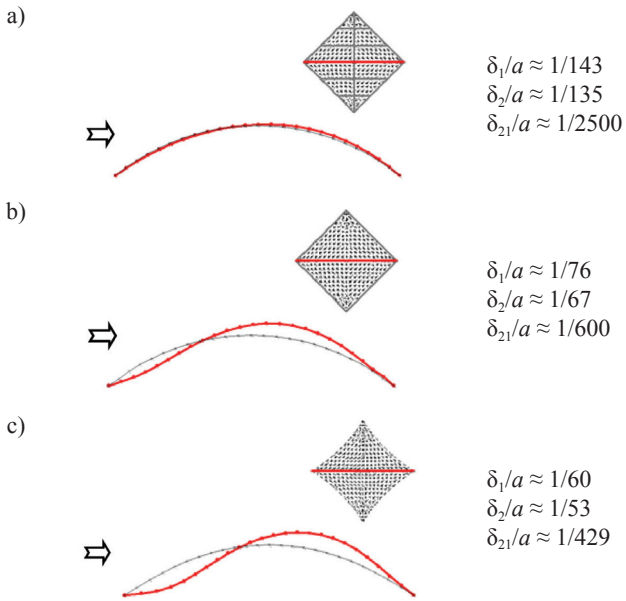

Fig. 23. Deformation of the HP-shaped models (wind direction θ = 0°). Scale factor for displacement: five times. a) F1 model, b) F2 model, c) S1 model

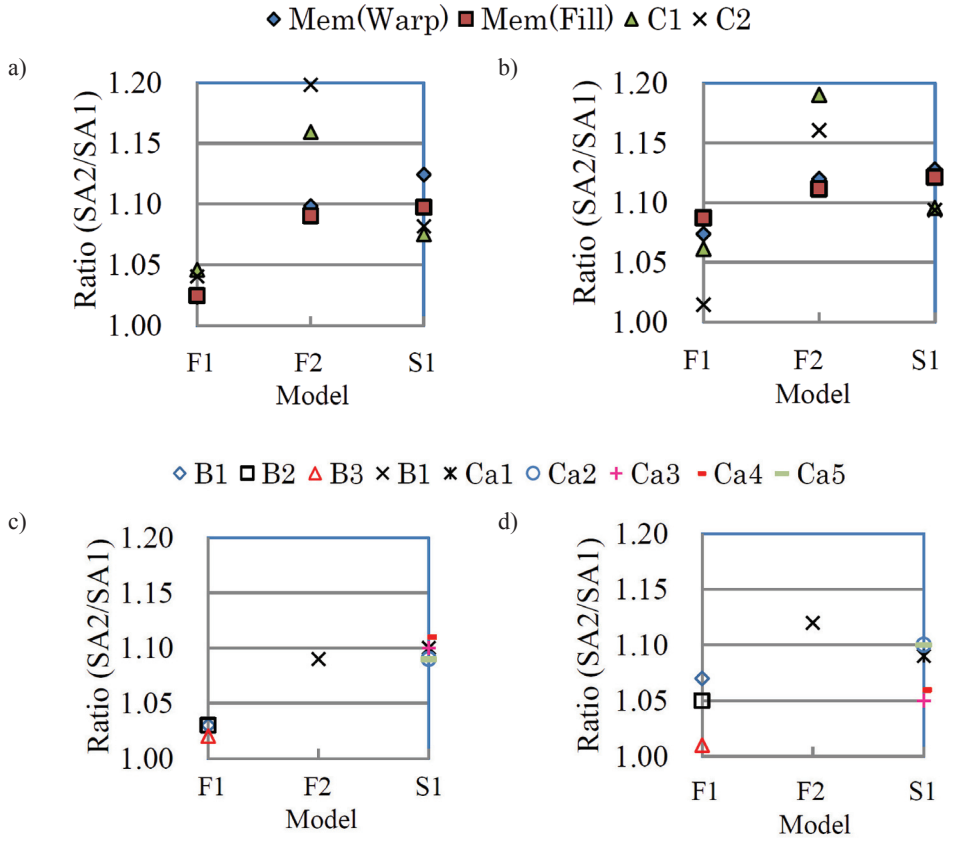

Fig. 24. Ratio of the maximum stress obtained from SA-2 to that obtained from SA-1 for the mono-sloped models, a) wind direction θ = 0°, b) wind direction θ = 180°, c) wind direction θ = 0°, d) wind direction θ = 180°

6. Design wind force coefficients for membrane-free roofs

The results in Chapters 4 and 5 suggest that the design wind force coefficients proposed based on the results of wind tunnel experiments with rigid models should be improved by considering the effect of the roof-supporting systems and roof deformation on the membrane structure load. The simplest formula of the wind force coefficients may be given by the following equations:

$$C_{NW}^{*} = \frac{\gamma\mu C_{NW0}}{G_f} \qquad C_{NL}^{*} = \frac{\gamma\mu C_{NL0}}{G_f} \tag{20) (21}$$

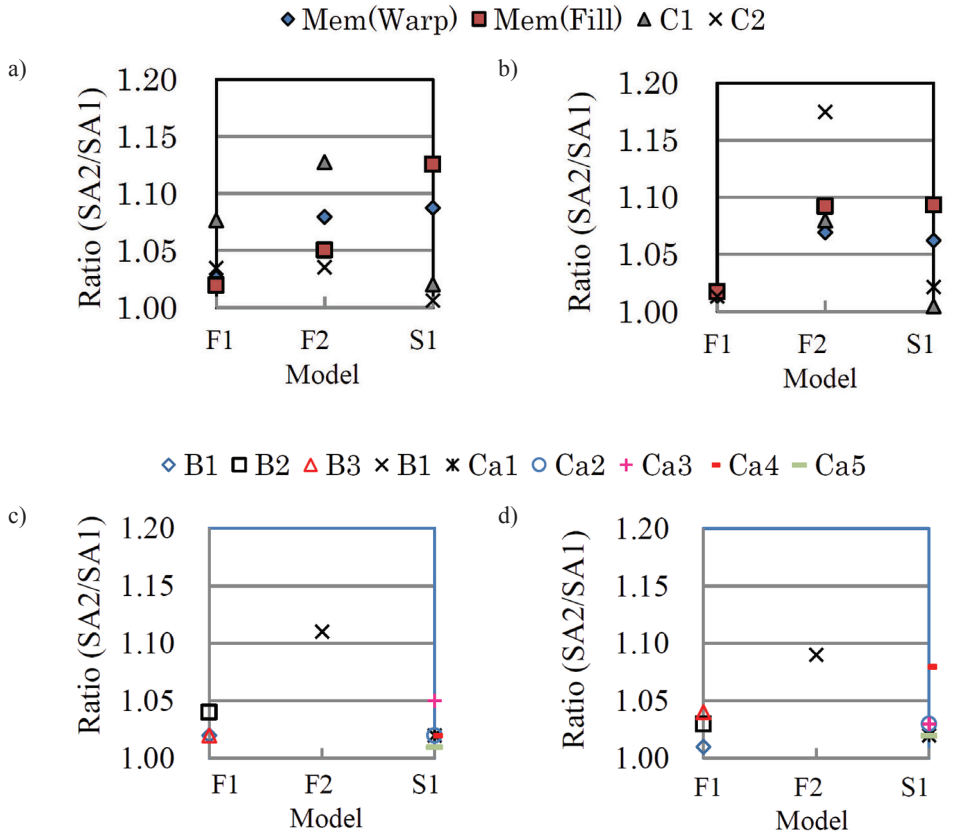

Fig. 25. Ratio of the maximum stress obtained from SA-2 to that obtained from SA-1 for the HP-shaped models, a) wind direction θ = 0°, b) wind direction θ = 90°, c) wind direction θ = 0°, d) wind direction θ = 90°

where μ represents a correction factor for membrane roofs and may be given by

$$\mu = \mu_s \times \mu_d \tag{22}$$

where μ_s and μ_d represent correction factors for the roof-supporting system and roof deformation, respectively.

An appropriate value of μ_s may be determined from the results of the structural analysis investigating the effect of the roof-supporting systems on the load effects (Chapter 4). The stress ratios for the mono-sloped and HP-shaped roofs are summarized in Tables 6 and 7, respectively. In most cases, the ratio is nearly equal to or less than 1.1. Therefore, an appropriate value of μ_s may be 1.1. Actually, the maximum value of the stress ratio is 1.32 for the B3 member of the F1 model (see Table 7). The B3 member is located along the boundary of the leeward and windward halves (Fig. 26). The design wind force coefficient changes discontinuously along the boundary line, whereas the actual wind force coefficient changes

smoothly. The discontinuous change in the wind force coefficient along the B3 member may induce a large unbalanced force on the member, resulting in a large stress ratio that may be unrealistic.

Regarding the μ_d value, based on the results of the CFD and structural analysis on the effect of roof deformation (Chapter 5), an appropriate value of μ_d may be approximately 1.2, which was obtained from the results in Figs. 24 and 25. Using the above-mentioned μ_s and μ_d values, the correction factor μ for membrane roofs is ~1.3 within the limits of the present study.

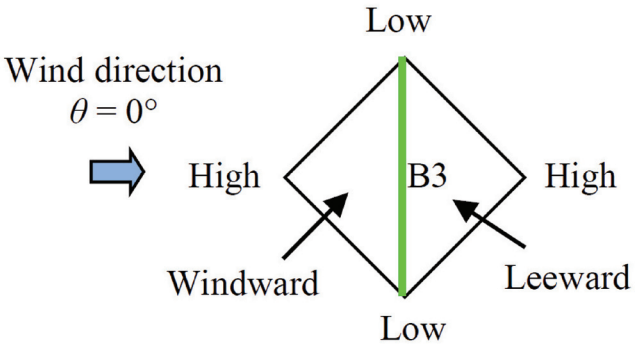

Fig. 26. B3 member of the F1 model for the HP-shaped roof

7. Concluding remarks

The present study has presented wind force coefficients for designing free-standing canopy roofs of membrane structures. The membrane roofs are so lightweight and flexible that the roof easily deforms under wind loading. In addition, there are various roof-supporting systems for membrane structures. In a previous study, we proposed the design wind force coefficients based on the results of wind tunnel experiments with rigid roof models. The proposed wind force coefficients was obtained assuming that four corner columns supported the roof and the roof deformation could be neglected. The axial forces induced in the columns were considered as the most important load effect. In this study, however, we show that the previously proposed design wind force coefficients are inappropriate for designing flexible membrane roofs and should be improved. It is also shown that load effects such as the bending moment should be considered when discussing the design wind force coefficients. Among the many roof configurations, we focused on mono-sloped and hyperbolic paraboloid (HP)-shaped roofs. The effects of roof deformation and roof-supporting systems of those roofs on the wind force coefficients were investigated. Based on the results of the investigation, we have introduced a correction factor (μ) in the previously proposed wind force coefficients. The μ is given by $\mu = \mu_s \times \mu_d$. The μ_s and μ_d represent correction factors for the roof-supporting system and roof deformation, respectively. The correction factor μ is ~1.3 within the limits of the present study.

References

[1] Michalski A., Britto D., Gelenne Ph., Haug E., *Fluid structure interaction simulation of wide-span membrane structures,* Extended Abstracts of the 6th International Symposium on Computational Wind Engineering Hamburg, Germany 8-12 June 2014.

[2] Michalski A., Kermel P.D., Haug E., Lohner R., Wuchner R., Bletzinger K.-U., *Validation of the computational fluid-structure interaction simulation at real-scale tests of a flexible 29 m umbrella in natural wind flow,* Journal of Wind Engineering and Industrial Aerodynamics, Vol. 99, 2011, 400-413.

[3] Nagai Y., Okada A., Kanda M., Miyasato N. and Saitoh M., *Study on wind response on horn-shaped membrane structure,* Journal of Structural and Construction Engineering, AIJ, Vol. 77(672), 2012, 211-219.

[4] OpenFOAM, http://www.openfoam.com, 2008.

[5] Pun P.K.F., Letchford C.W., *Analysis of a tension membrane hypar roof subjected to fluctuating wind loads,* Proc 3rd Asia-Pacific Symposium on Wind Engineering, Hong Kong, 13-15 December 1993.

[6] Takeda F., Yoshino T., Uematsu Y., *Design wind force coefficients for hyperbolic paraboloid free roofs,* Journal of Physical Science and Application 4(1), 2014, 1-19.

[7] Takeda F., Yoshino T., Uematsu Y., *Discussion of design wind force coefficients for hyperbolic paraboloid free roofs*, Proc. 7th International Colloquium on Bluff Body Aerodynamics and Applications, Shanghai, China 2012.

[8] Takeda F., Yoshino T., Uematsu Y., *Discussion of design wind force coefficients on mono-sloped free roofs*, Proc. of the International Association for Shell and Spatial Structures (IASS) Symposium, Seoul, Korea, 2012.

[9] Uematsu Y., Arakatsu F., Matsumoto S., Takeda F., *Wind force coefficients for the design of a hyperbolic on wind engineering*, Taipei, Taiwan 2009.

[10] Uematsu Y., Iizumi E., Stathopoulos T., *Wind loads on free-standing canopy roofs: Part 2 overall wind forces,* Journal of Wind Engineering and Industrial Aerodynamics, Vol. 96 (6-7), 2008, 1029-1042.

TECHNICAL TRANSACTIONS | CZASOPISMO TECHNICZNE
CIVIL ENGINEERING | BUDOWNICTWO
2-B/2015

YASUSHI UEMATSU[*], YOSHIKI SHIMIZU[**],
YOSHIMASA MIYAKE[***], YUSUKE KANEGAE[***]

WIND-INDUCED SCATTERING OF PERMEABLE UNIT FLOORING DECKS LOOSELY LAID ON ROOFTOPS AND BALCONIES OF HIGH-RISE BUILDINGS

PODRYWANIE PRZEZ WIATR NIEZAMOCOWANYCH PODESTÓW TARASOWYCH UKŁADANYCH NA BALKONACH I DACHACH BUDYNKÓW WYSOKICH

Abstract

The present paper discusses the mechanism of the wind-induced scattering of permeable unit flooring decks loosely laid on the rooftops and balconies of high-rise buildings. Firstly, the scattering mechanism of decks was investigated, based on a blowing test using a blower and actual decks. Subsequently, a simulation model was constructed for estimating the internal pressures under the decks (pressures acting on the bottom surface of decks) obtained from a wind tunnel experiment – this is based upon the unsteady Bernoulli equation and the time history of external pressures on the rooftop and balconies. Combining the simulated internal pressures and the experimentally obtained external pressures, the time history of net wind pressures acting on the decks were computed. Finally, the threshold wind speed of scattering (scattering wind speed) was obtained by applying the scattering mechanism to the simulated time history of the net wind pressures.

Keywords: scattering, permeable deck, numerical simulation, wind tunnel experiment, high-rise building, rooftop, balcony

Streszczenie

W niniejszej pracy omówiono mechanizm rozwiewania przez wiatr przepuszczalnych podestów tarasowych luźno ułożonych na dachach i balkonach wieżowców. W pierwszym etapie przeanalizowano mechanizm rozwiewania podestów przy użyciu dmuchawy i rzeczywistych podestów. Następnie zbudowano model symulacyjny do szacowania ciśnienia wewnętrznego na podesty (ciśnienie działające na dolną powierzchnię podestów). Model oparto na nieustalonym równaniu Bernoulliego i przebiegach czasowych ciśnienia zewnętrznego działającego na dach i balkony, które zostały otrzymane w ramach eksperymentu przeprowadzonego w tunelu aerodynamicznym. Na podstawie symulowanych ciśnień wewnętrznych i uzyskanych doświadczalnie ciśnień zewnętrznych, obliczono przebieg czasowy całkowitych ciśnień działających na podesty. W ostatnim etapie obliczono progową prędkość wiatru podczas rozwiewania (prędkość rozwiewania) przez zastosowanie mechanizmu rozwiewania do symulowanych przebiegów czasowych ciśnienia wiatru.

Słowa kluczowe: rozwiewanie, podesty przepuszczające wiatr, symulacje numeryczne, badania w tunelu aerodynamicznym, budynki wysokie, dach, balkon.

DOI: 10.4467/2353737XCT.15.132.4169

[*] Department of Architecture and Building Science, Tohoku University, Japan.
[**] Design Division, Shimizu Corporation, Japan.
[***] Technology Department, Tokyo Plant, Sekisui Chemical Co., Ltd, Japan.

1. Introduction

Permeable unit flooring decks, as shown in Fig. 1a, are often laid on the rooftops and balconies of high-rise buildings (see Fig. 1b). Because such decks are usually just put on (not fixed to) the floors, they are easily blown off by strong winds; this may cause damage to other buildings and people. Because the decks have holes or slits, the internal pressures underneath the decks (i.e. pressures acting on the bottom surface of the decks) depend on their permeability as well as on the external pressures. It is quite difficult to measure the internal pressures directly in a wind tunnel experiment with reduced scale models, because the length L and gap g between the deck and the floor is very small, such as $L \approx 300$ mm and $g \approx 15$ mm, for example. By comparison, it is relatively easy to measure the external pressures on the rooftops and balconies in a wind tunnel experiment. The results can be used for evaluating the internal pressures by using a numerical simulation.

a) b)

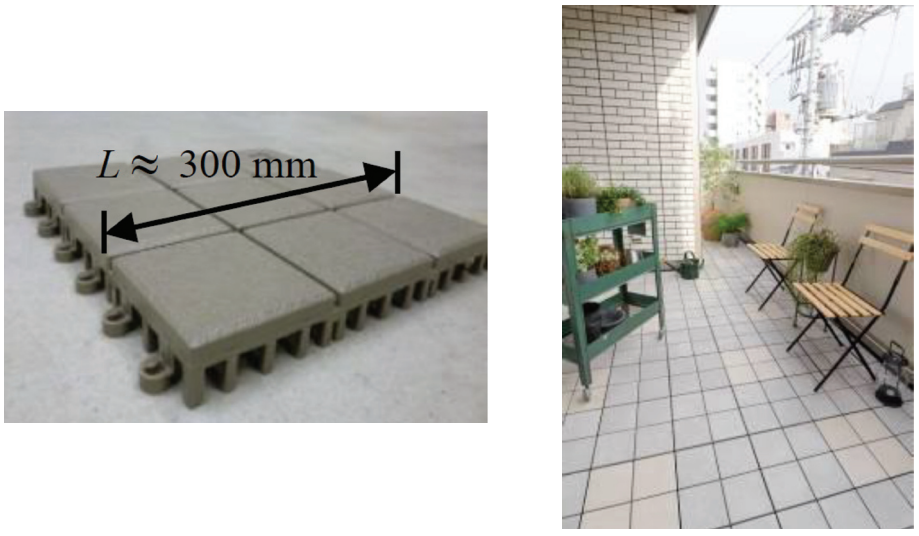

Fig. 1. Permeable unit flooring decks, a) sample, b) unit flooring decks loosely laid on balcony floor (example)

Wind loads on permeable materials placed on the external surfaces of buildings have been studied by many researchers. For example, Cheung and Melbourne [5] measured the net wind pressures acting on porous roofs with a number of small circular holes uniformly distributed over the roof area in a wind tunnel – this showed a significant reduction of the wind forces due to pressure equalization. The effects of porosity and internal volume on the wind load reduction were qualified for a wind direction normal to a wall of the building. A similar problem was numerically studied by Trung et al. [17]. Loose-laid concrete blocks are often used for roof-insulation systems on flat-roofed buildings. Because the blocks

are held in place by gravity, they may be blown off by strong winds. Kind and Wardlaw [9] investigated the mechanism responsible for wind damage to loose-laid roof-insulation systems in a large wind tunnel. They focused on the uplift produced by the differences in static pressure between the exterior and under-surfaces of the block. In the wind resistant design of such decks, it is important to predict the net wind pressures acting upon them. The pressure in the cavity underneath the deck depends on many factors, such as external pressures at the openings and wind permeability and resistance at the gaps. Bienkiewicz and Sun [3, 4] discussed the wind loading on and wind resistance of loose-laid roof paver systems on a low-rise flat-roofed building based on a wind tunnel experiment. They focused on a cornering wind of 45^{o} that causes high levels of suctions near the windward corner. An analytical model for predicting the cavity pressures was proposed by Amano et al. [1], which was an extension of the analytical model proposed by Liu and Saathoff [12]. They used the unsteady discharge equation for flows in the cavity between the layers, perceiving the cavity flow as the orifice flow. The analytical model was validated by a comparison with a wind tunnel experiment. Oh and Kopp [15] developed an analytical model to simulate time-varying pressure distributions in the cavity of air-permeable, double-layer roof systems. The simulated results were found to strongly agree with the wind tunnel results for a low-rise flat-roofed building. Mooneghi et al. [13] made a large scale testing on the wind uplift of roof pavers, in which both wind blow-off tests and pressure measurements were carried out on a square portion of a flat roof for the critical wind direction that generates conical vortices. Most of the previous studies, including the above-mentioned studies, focused on loose-laid roof paver systems placed on the rooftops of low-rise flat-roofed buildings. The blocks are usually made of concrete, and are consequently relatively heavy. Okada et al [16] developed an analytical method for predicting the wind pressures under roof tiles laid on a gable roof, based on the model proposed by Oh et al. [14]. They carried out full-scale measurements, the results of which agreed relatively well with the predicted results.

Besides the roofing systems, wind loads on permeable materials, such as facades, rainscreen walls and siding, have been studied by many researchers [6, 7, 11].

The objective of the present study is to propose a procedure for predicting the threshold wind speed that causes the scattering of permeable unit flooring decks loosely laid on the rooftops and balconies of high-rise buildings. The unit flooring decks under consideration are generally small and light compared with the roof pavers that were investigated in the previous studies. Therefore, they may be blown off by strong winds more easily. Furthermore, the decks are often laid on the balconies of high-rise apartment buildings (see Fig. 1b). To the authors' best knowledge, no study has been conducted on the scattering of unit flooring decks from the balconies of high-rise buildings.

The present paper is divided into three main parts. Firstly, a wind blow-off test using a blower and actual flooring decks is conducted to investigate the scattering mechanism. The distribution of net wind pressure (pressure difference) on the decks is also measured. A discussion is made of the condition that causes the scattering of decks based on a balance of moments caused by the deadweight of and the wind force on the deck. In this test, the flow around decks under practical conditions is not necessarily simulated. The main purpose of this experiment is not to predict the scattering wind speeds under practical conditions but to understand the fundamental mechanism that causes the scattering of decks. Secondly, a numerical simulation model for evaluating the internal pressures underneath the decks is constructed based on the unsteady Bernoulli equations and the time history of external

pressures obtained from a wind tunnel test. The simulation model is based on those proposed by Oh et al. [14] and Okada et al.[16]. A tuning of the parameters involved in the model is carried out by using the wind tunnel data with a porous roof model. Finally, a wind tunnel experiment is conducted with scale models of high-rise buildings to measure the external pressures simultaneously at many points on the rooftop or balconies. The internal pressures underneath the decks laid on the rooftop or balconies are computed from the external pressures and the numerical simulation model constructed at the second step. The critical wind speed causing the scattering of decks is predicted, based on the time history of net wind pressures, provided by the difference between the external and internal pressures, and the scattering mechanism obtained in the first step.

2. Wind blow-off test on actual unit flooring decks

2.1. Experimental method and procedure

As mentioned above, the main purpose of this experiment was to discuss the mechanism underlying the scattering of permeable unit flooring decks. For this purpose, a blow-off test with full-scale decks was carried out. Regarding the decks laid on the rooftop of a flat-roofed building, the most critical condition may occur near the windward corner in a cornering wind; this is where large suctions are induced by conical vortices. Such large suctions may be suppressed by parapets (see [2, 10], for example). Since the flooring decks under consideration in the present study are usually used for flat-roofed buildings with 1.1 – 1.2 m high parapets, the above-mentioned cornering winds are not encountered in practice. Therefore, the experiment was carried out for a wind direction normal to the wall. Furthermore, the flow did not simulate the practical condition around the decks.

In the evaluation of scattering wind speeds in Chapter 5, cornering winds are also considered for comparative purposes; the external pressure distributions are measured in Chapter 4. In such a flow condition, the net wind pressure acting on the deck changes both in two directions parallel and perpendicular to the windward wall. However, because the width of the decks was as small as 300 mm (see Fig. 1a), it was assumed that the variation in the direction parallel to the wall could be neglected when predicting the wind speeds which result in scattering. That is, the mechanism for the scattering of decks obtained in this chapter can be used for such a case as tested in Chapter 5.

Fig. 2a shows the experimental set up. Nine actual decks were laid on a testing floor and subjected to strong winds (uniform flow) generated by a blower. The outlet of the blower was 1.0 m wide and 0.9 m high. Two kinds of unit flooring decks, named P3 and P5, were tested. The weight and porosity were respectively 4.53 N and 3.3% for P3 and 4.01 N and 10% for P5. The decks had double cross-shaped slits (see Fig. 1a) and were connected to each other by joints at two points along each perimeter. Therefore, there were slits between two adjacent decks.

The leading edge of the testing floor is schematically illustrated in Fig. 2b. A plate was installed at the leading edge of the testing floor, which acted like a parapet. The height h_p above the testing floor was 0 or 30 mm (equal to the deck height). The distance d between the plate and the leading edge of the first deck was changed from 0 to 300 mm. When $h_p = 0$ mm, the

wind blows into the gap between the decks and the floor; this may generate positive internal pressures, as shown in Fig. 3a. When h_p = 30 mm, on the other hand, the flow separates at the top of the plate, as shown in Fig. 3b. In this case, the decks located near the leading edge were immersed in a separation bubble. Therefore, the flow around the decks and the resultant wind forces acting on the decks were quite different from those for h_p = 0 mm.

It should be mentioned that the purpose of this experiment was not to simulate the practical condition of the flow around the decks but to generate various conditions for discussing the scattering mechanism of the decks. That is, we measured the wind pressures acting on the decks and the critical wind speed that caused the scattering of decks under various conditions. Based on these results, discussion is made of the scattering mechanism.

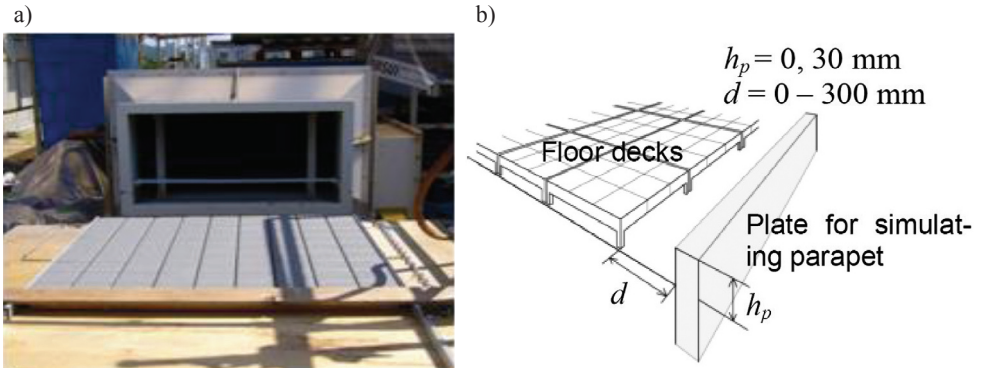

Fig. 2. Experimental setup, a) general view, b) leading edge condition

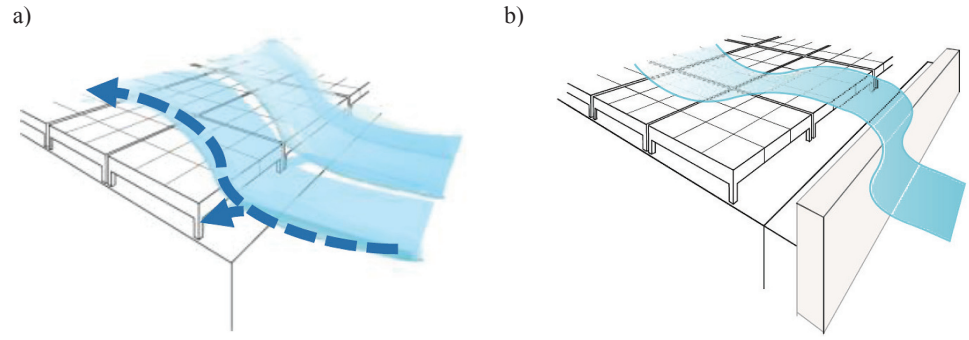

Fig. 3. Flow pattern around flooring decks, a) h_p = 0 mm, b) h_p = 30 mm

Pressure taps of 0.5 mm diameter were installed along the centerline of the deck models and the testing floor. The pressure taps on the testing floor were located just under those on the deck to calculate the net wind pressures acting on the deck, assuming that the pressure on the testing floor was equal to that on the bottom surface of the deck. The pressure taps were connected to pressure transducers in parallel via 100 cm lengths of flexible vinyl tubing with a 1 mm internal diameter. The wind pressures at all taps were sampled simultaneously

at a rate of 200 Hz for 1 min. The compensation for the frequency response of the pneumatic tubing system was carried out in the frequency domain by using the frequency response function of the pressure measuring system. In this experiment, the decks were fixed to the floor so as not to be blown off. Using the time history of the net wind pressures along the centerline, the lift and overturning moment about the leeward edge of the first deck were computed, as shown in Section 2.2.

Next, the critical wind speed U_{cr} (hereafter referred to as 'scattering wind speed') causing the scatter of decks was measured. In this experiment, the decks were loosely laid on the floor. In order to understand the behaviour of decks before scattering, the displacement of the first deck was measured by a laser displacement meter at a point 50 mm downstream from the leading edge.

2.2. Discussion of the scattering mechanism

Figs. 4a and 4b respectively show the time history of displacement of deck (P5) for $h_p = 0$ and 30 mm, as the wind speed U was increased gradually (almost linearly with time); the increasing rate of wind speed was 2 to 3 m/s per minute depending on U_{cr}. The scattering wind speed U_{cr} is presented in the figure. When $h_p = 0$ mm, the decks are raised by the uplift generated by negative external pressure and positive internal pressure (Fig. 4a). At a relatively low wind speed, the decks are blown off almost instantaneously. When $h_p = 30$ mm, on the other hand, the decks start to move up and down (vibrate in the vertical direction) at some wind speed. As the wind speed is increased further, the vibration amplitude increases and finally the decks are blown off at the scattering wind speed U_{cr}. The behaviour of decks is quite different from that for $h_p = 0$ mm. The vibration before scattering may be related to a slower response of the decks to fluctuating wind forces. When $h_p = 0$ mm, once the decks are raised by the uplift, the positive internal pressure is increased by winds blowing into the gap between the decks and the testing floor, generating further increase in the uplift, which in turn raises the decks further. As a result, the decks are blown off almost instantaneously. This behaviour is similar to a divergence. When $h_p = 30$ mm, the decks are immersed in the separation bubble (see Fig. 3b). Therefore, the internal pressure does not change so much even if the decks are raised by the uplift. The decks move up and down according to the fluctuations of wind forces acting on the decks. Such a movement of decks does not affect the flow pattern and the resultant wind forces acting on the decks significantly.

Fig. 5 shows a schematic illustration of the forces acting on the first deck. In the figure, Mg represents the weight of the deck acting on the center of the deck (center of gravity); $C_{p\mathrm{net}}$ represents the net wind pressure coefficient (or pressure difference coefficient), which is a function of the distance x from the leading edge and time t; and L = length of deck (= 300 mm in the present case). The scattering wind speed U_{cr} can be evaluated based on the balance of moments induced by the weight of the deck (counterclockwise) and by the net wind pressure acting on the deck (clockwise) about the trailing edge ($x = 300$ mm) of the first deck. When the moment $m(t)$ induced by the net wind pressure exceeds that by the weight of the deck, the deck will be blown off. Therefore, the scattering wind speed U_{cr} may be given by the following equation:

$$Mg \times \frac{L}{2} = \frac{1}{2}\rho U_{cr}{}^2 \hat{C}_m L^3 \tag{1}$$

where ρ = air density; and $\hat{C}_m$ represents the maximum peak value of the moment coefficient $C_m(t)$ given by the following equation:

$$C_m(t) = \frac{1}{L^2}\int_0^L C_{p\text{net}}(x,t)\cdot\varphi(x)\cdot(L-x)dx \tag{2}$$

where φ(x) is a function representing the effect of a slit on the net wind pressure on the deck; i.e. φ(x) = 0 at the location of slit, while φ(x) = 1 at the other locations. Note that Eq. (2) can be used for square decks with sides L and slits. Kind and Wardlaw [9] proposed a scattering mechanism on the basis of the balance of the lift force and the weight of the deck. Because the application point of the lift is generally different from that of the weight, the scattering mechanism based on the balance of moments seems more reasonable than that based on the balance of vertical forces.

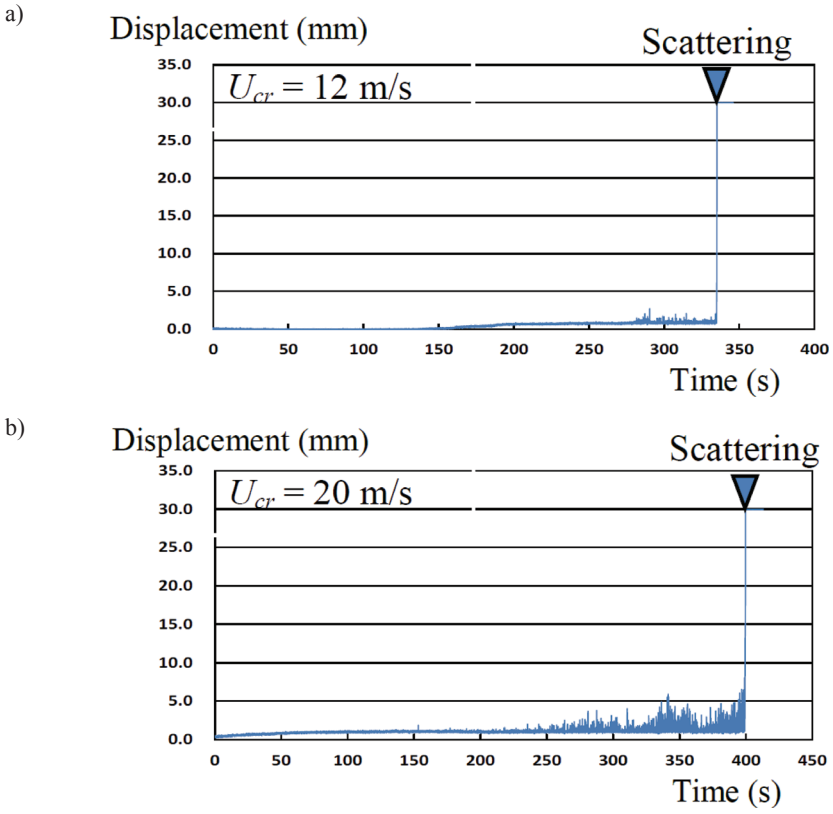

Fig. 4. Time history of displacement of the deck (P5), a) h_p = 0 mm, b) h_p = 30 mm

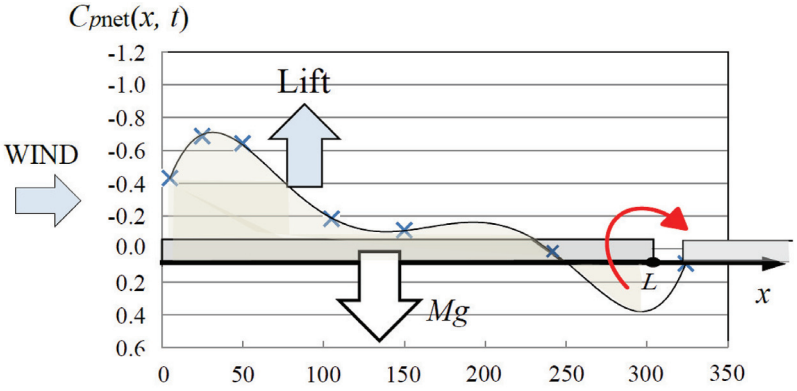

Fig. 5. Deck subjected to wind and gravity forces

The scattering wind speed U_{cr} can be obtained by using the time history of $C_{pnet}(x,t)$. In the calculation, we should consider the difference of the deck's behaviour before scattering, as shown in Fig. 4. This feature may be related to the response of flooring decks to the change in the flow pattern and the resultant wind force acting on the deck, as mentioned above. When $h_p = 0$ mm, the decks are blown off at the moment when Eq. (1) is satisfied. On the other hand, when $h_p = 30$ mm, this is not the case because of the effects of acceleration and damping forces. Such a slow response of the decks to fluctuating wind forces can be considered by applying a moving average to the time history of $C_m(t)$ when evaluating $\hat{C}_m$. Comparing the experimental results on U_{cr} with those predicted by Eq. (1), we found that an averaging time of 1 sec was the most appropriate when $h_p \geq 30$ mm.

Fig. 6 shows a comparison between experimental results and prediction for U_{cr}. A good agreement can be seen in the figure; this implies that the proposed scattering mechanism is reasonable.

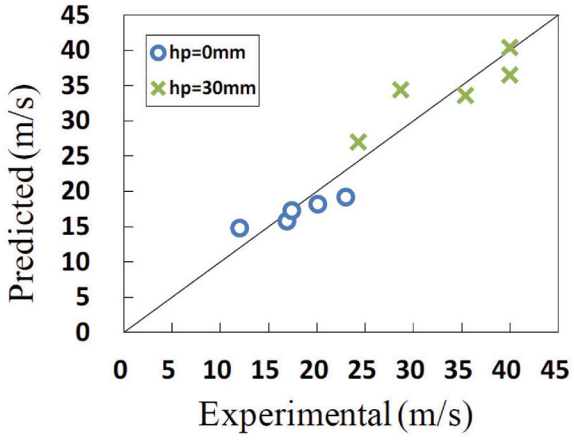

Fig. 6. Comparison between experiment and prediction for scattering wind speed U_{cr}

3. Numerical simulation of internal pressures

3.1. Analytical model of simulation

The internal pressures underneath the decks depend on many factors, such as the external pressures, the gap between adjacent decks and flow resistance underneath the decks. This is identical to the problem of building internal pressure, when the space underneath the deck is regarded as a room in a building [1]. The air flows through the slits or gaps in a vertical direction as well as through the gaps between the adjacent 'rooms' in horizontal directions. The internal pressure is determined from the balance of mass of air flowing into and out of the space underneath each deck. The governing equation of the flow through the gap and/or slit in the deck in the vertical direction (see Figure 7) may be represented by the unsteady Bernoulli equations. The equation for the flow passing through an opening in the vertical direction may be given by the following equations:

$$\rho l_e \frac{dU_e}{dt} = p_e - p_i - \Delta p_1 - \Delta p_2 \tag{3}$$

$$\Delta p_1 = \frac{1}{2} C_{Le} \rho U_e |U_e| \tag{4}$$

$$\Delta p_2 = \lambda \frac{l_e}{d_e} \frac{\rho}{2} U_e |U_e| \tag{5}$$

where l_e = effective depth of the opening; U_e = flow speed in the opening; p_e and p_i represent the external pressure at the opening and the internal pressure, respectively; C_{Le} = pressure loss coefficient of the opening; and λ represents a friction coefficient, which is approximately given by the following equation assuming that the flow through the slit is Hagen-Poiseuille flow:

$$\lambda = 6 \frac{\nu}{U_e d_e} \tag{6}$$

where ν represents the coefficient of kinematic viscosity of the flow. The effective depth l_e may be given by the following equation [18]:

$$l_e = l_0 + 0.89\sqrt{A_e} \tag{7}$$

where l_0 and A_e represent the actual depth and area of the opening, respectively.

Similarly, the governing equation for the flow through the gap between two adjacent 'rooms' in the x direction (see Fig. 7) may be given by the following equation:

$$\rho l_{i,j} \frac{dU_{i+1,j}}{dt} = p_{i,j} - p_{i+1,j} - \frac{1}{2} C_L \rho U_{i+1,j} \left| U_{i+1,j} \right| - \Delta p_{1,x} \tag{8}$$

$$\Delta p_{1,x} = \lambda \frac{L}{d} \frac{\rho}{2} U_{i+1,j} \left| U_{i+1,j} \right| \tag{9}$$

where (i, j) represents the location of the 'room' with i and j being the numbers of the 'room' in the x and y directions, respectively; $l_{i,j}$ = distance from the center of one 'room' to the center of another ; $U_{i+1,j}$ = wind speed in the x direction from 'room' (i, j) to 'room' $(i+1, j)$; $p_{i,j}$ and $p_{i+1,j}$ represent the internal pressures of 'rooms' (i, j) and $(i+1, j)$; and d = height of the 'room'. Similar equations can be obtained for the internal flow in the y direction.

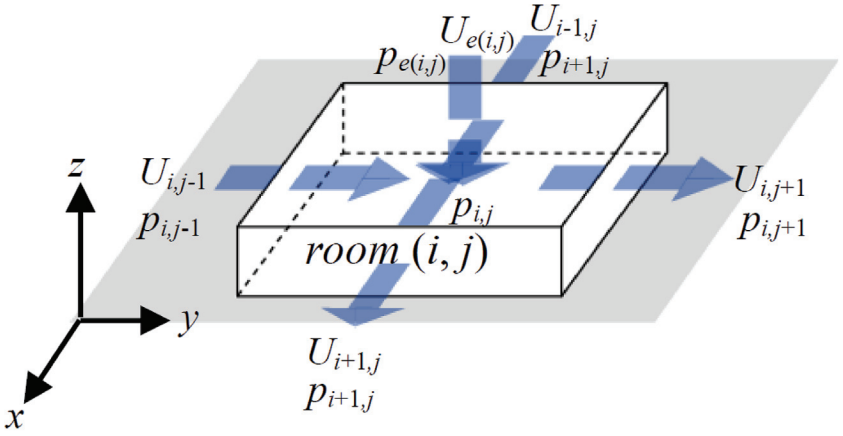

Fig. 7. Schematic illustration of the flow through the slit and gaps

An assumption of weak compressibility of the air and adiabatic condition yields a differential equation that relates the internal pressure to the flow speed through the slits and/or gaps as follows:

$$\frac{dp}{dt} = \frac{\gamma P_0}{V_0} \sum kAU_e \tag{10}$$

where γ = specific heat ratio; P_0 = atmospheric pressure; V_0 = volume of the virtual internal space underneath the deck; k = discharge coefficient; and A = area of the opening.

The non-linear simultaneous equations thus obtained can be solved numerically by using a well-known Runge-Kutta method of the fourth order together with the time history of external pressures obtained from a wind tunnel experiment. The values of parameters involved in the analytical model are calibrated so that the numerical simulation provides results similar to the experimental results, as described in the following section.

3.2. Calibration of the simulation model

The experiments are carried out in a boundary layer wind tunnel with a working section 1.4 m wide, 1.0 m high and 6.5 m long at the Department of Architecture and Building Science, Tohoku University. A turbulent boundary layer with a power law exponent of $\alpha = 0.21$ for the mean wind speed profile is generated on the wind tunnel floor (see Fig. 8). A flat roof model of 360 mm square in cross-section and 60 mm in height is installed in the wind tunnel flow. A 2.5 mm thick plate with many square openings and 36 pressure taps is placed above the roof with a gap of 4 mm, as shown in Fig. 9a. The space underneath the top plate is assumed to be divided into 36 sub-spaces. The area of the openings corresponds to that of the slits and gaps of typical permeable decks. The roof has pressure taps right under the location of the taps on the top plate. The pressure at each tap on the rooftop may represent the internal pressure in each sub-space. The model has parapets along the perimeter, the height (h_p) of which is 6.5 mm or 30 mm. When h_p = 6.5 mm, the top of parapet coincides with the upper level of the 2.5 mm thick permeable plate. The mean wind speed at the roof height H is approximately 10 m/s. The wind direction θ is varied from 0° (normal to a wall) to 45° (parallel to a diagonal). The pressures at 72 taps are low-pass filtered at 300 Hz and then sampled simultaneously at a rate of 400 Hz for a period of 160 sec, from which 16 sets of 10 min data in full scale are obtained.

It should be mentioned that this model is not a scale model of a flat-roofed building on which permeable decks are laid but a virtual model to construct an analytical model for predicting the internal pressures by using the time history of external pressures obtained from a wind tunnel experiment. The statistics of wind pressure coefficients are obtained by applying ensemble average to the results of these 16 consecutive runs.

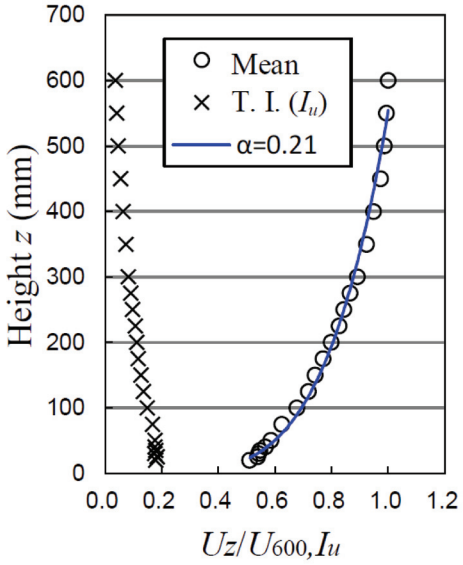

Fig. 8. Profiles of mean wind speed and turbulence intensity

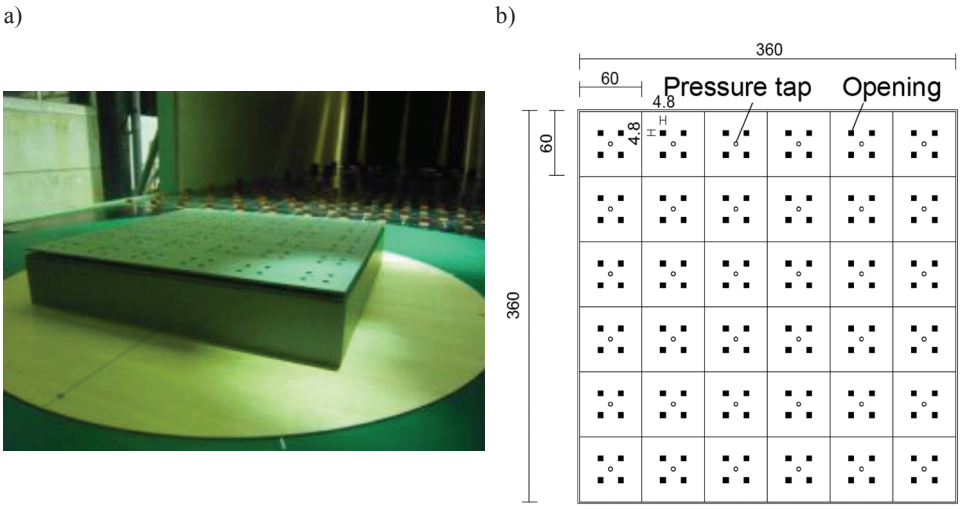

Fig. 9. A flat roof model for the calibration of the analytical model predicting the internal pressures underneath the decks, a) wind tunnel model, b) openings and pressure taps

Because the time step Δt for the pressure measurements is so large for the Runge-Kutta method, a spline function of the 3rd order is applied to the experimental data in order to obtain time history with Δt = 1/4000 s for stable and accurate computations. Furthermore, optimum values of the parameters in the governing equations are determined so that they provide results similar to the experimental results together with theoretical considerations and the results of previous studies. For example, appropriate values of k and C_L are found to be 0.002 and 18.0, respectively.

Figs. 10 to 12 show comparisons between experimental and simulation results for the mean, rms and minimum peak values of internal pressure coefficients, respectively. A relatively good agreement is observed. Similar results were obtained for the other wind directions and for h_p = 30 mm. Therefore, the analytical model will be applied to the decks laid on the rooftop and balconies of buildings in the next chapter.

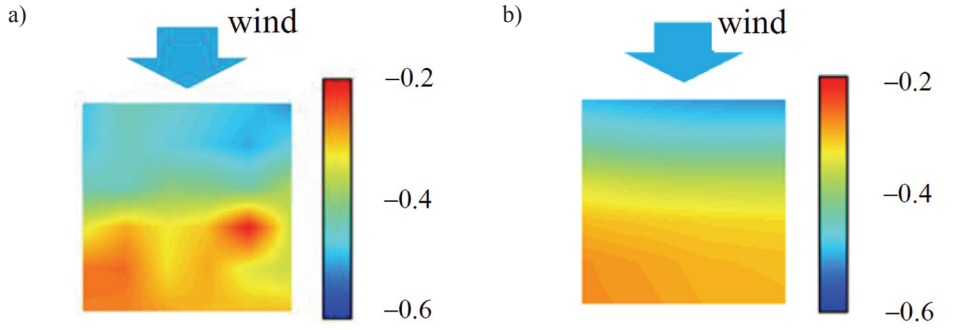

Fig. 10. Comparison between experiment and simulation for the mean internal pressure coefficients (h_p = 6.5 mm, θ = 0°), a) experiment, b) simulation

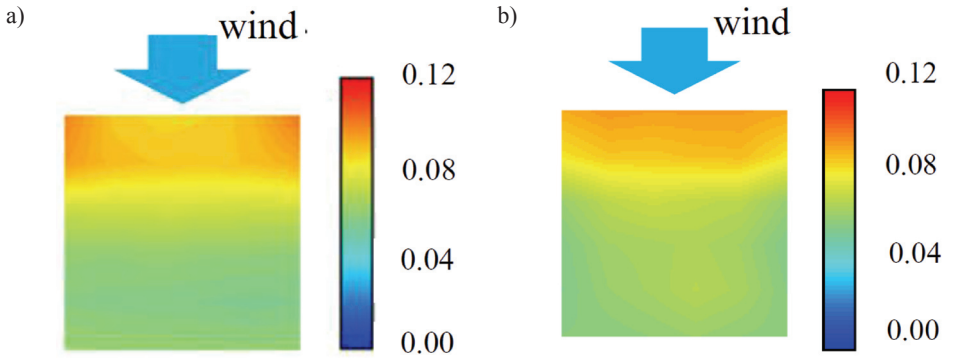

Fig. 11. Comparison between experiment and simulation for the rms internal pressure coefficients (h_p = 6.5 mm, θ = 0°), a) experiment, b) simulation

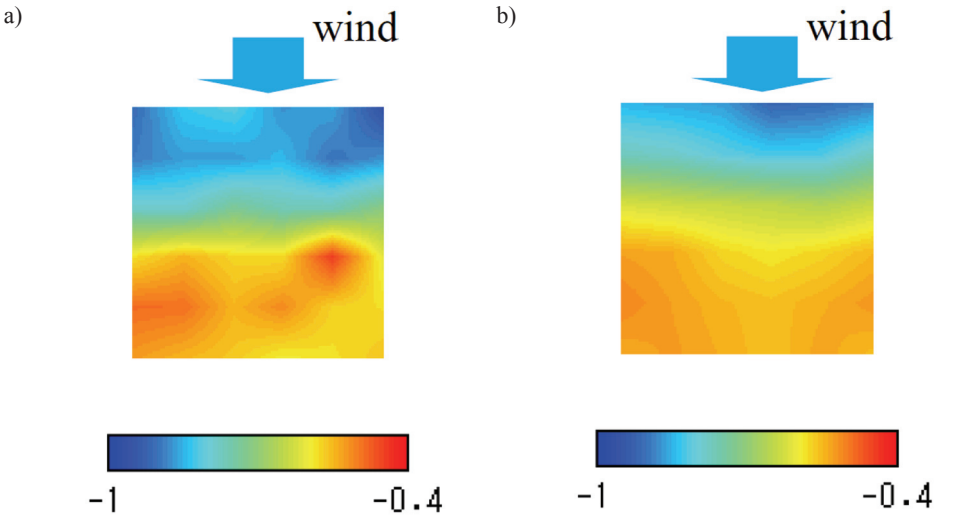

Fig. 12. Comparison between experiment and simulation for the minimum peak internal pressure coefficients (h_p = 6.5 mm, θ = 0°), a) experiment, b) simulation

4. Wind tunnel experiments for measuring external pressures on the rooftops and balconies of buildings

4.1. Experimental procedures

The experiments were carried out in the same wind tunnel flow as that used in Section 3.2. Two models with a geometric scale of λ_L = 1/200 were used; these were called Models A and B, respectively. Model A was a flat roof model with a 10 cm by 10 cm square cross-

section to measure the pressures on the rooftop (Fig. 13a). The aspect ratio H/D of the model was changed from 0.5 to 3.0. Note that not only high-rise but also low-rise and middle-rise buildings were tested in the experiment. The parapet height h_p was changed from 0 to 6 mm (0 to 1.2 m at full scale). As mentioned above, in the case of a flat-roofed building where people can go on the rooftop, the roof generally has parapets 1.1 – 1.2 m high. Even in cases where the balustrade is installed on the parapet (although it is not popular for high-rise buildings), the parapet height is higher than about 0.3 m at full scale. Therefore, lower parapets with $h_p < 0.3$ m are not practical. Many researchers have shown that the parapet affects the negative peak pressure coefficients on the roof significantly. This feature indicates that the parapet affects the scattering wind speed of decks significantly. Therefore, lower parapets were also investigated here for comparative purposes.

Fig. 13b shows the layout of pressure taps on the roof; sixty four taps were drilled on the one quarter area of the roof. The wind direction θ was changed from 0° to 45° at increments of 15°. Model B is a model of 20-story building with balconies (Fig. 14a). Seventy eight pressure taps were drilled on one half of the balcony at the floor, as shown in Fig. 14b. The model consisted of an instrumented part and several dummy parts. Combining these parts in various ways, we measured external pressures on the balconies at the 5th, 10th, 15th and 20th floors. Three kinds of balcony configuration, as shown in Fig. 15, were tested. Note that the *balustrade* type had no walls in the wind tunnel model. The wind direction θ was changed from 0° to 187.5°; i.e. from 0° to 180° at increments of 15° and 187.5°. The pressures at all taps were low-pass filtered at 300 Hz and then sampled simultaneously at a rate of 400 Hz for a period of 160 sec, from which we obtained 16 sets of full-scale 10 min time histories. The statistics of wind pressure coefficients were obtained by applying ensemble average to the results of these 16 consecutive runs in the same manner as that used in Section 3.1.

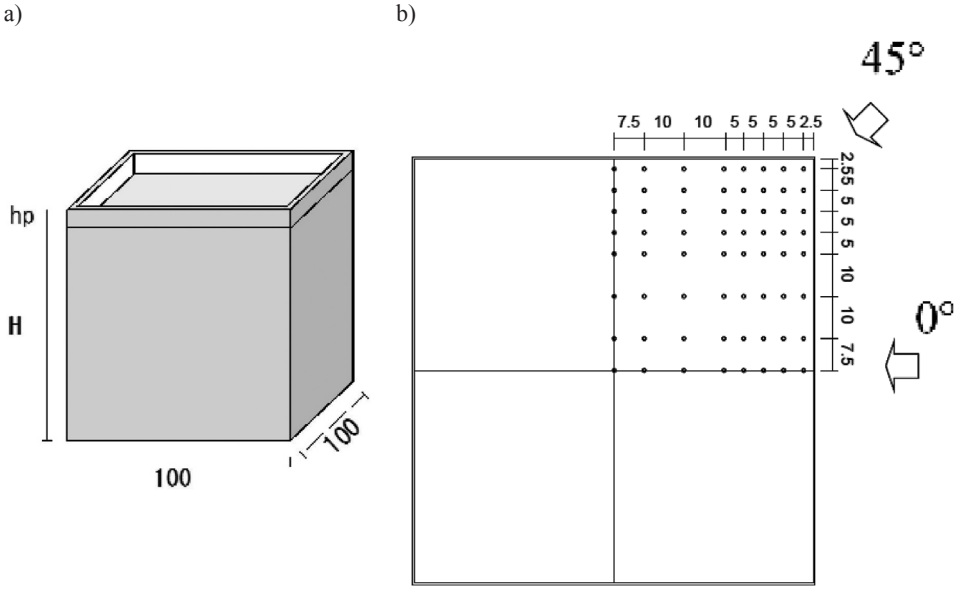

Fig. 13. Flat roof model (Model A), a) general shape, b) layout of pressure taps

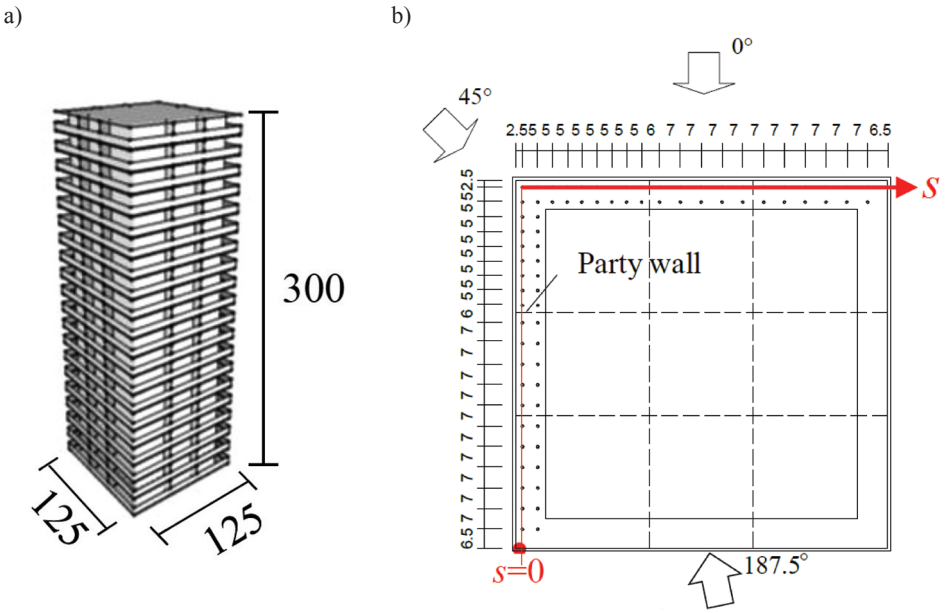

Fig. 14. Model of high-rise building with balconies (Model B), a) general shape, b) layout of pressure taps

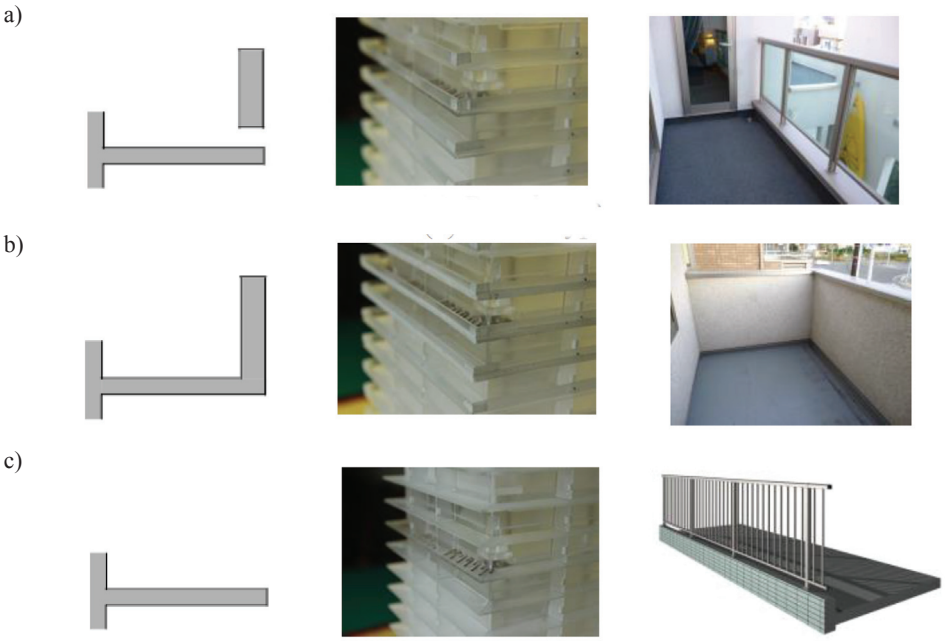

Fig. 15. Balcony configurations tested (Model B), a) *panel* type, b) *spandrel wall* type, c) *balustrade* type

4.2. Experimental results on external pressure coefficients

4.2.1. Pressure distribution on the rooftop of Model A

Fig. 16 shows the effect of h_p on the distribution of the minimum peak pressure coefficients C_{pe_min} on the rooftop of Model A with H = 50 mm. Note that the distribution only in the instrumented area is represented in the figure. As many previous papers (e.g. [8]) have indicated, high peak suctions are induced near the windward corner of the roof without parapets due to the generation of conical vortices in oblique winds (i.e. θ = 30° and 45°). It is interesting to note that the magnitude of negative peak suctions near the corner for h_p = 1 mm is somewhat larger than that for h_p = 0 mm (without parapets). As the parapet height h_p increases further, the magnitude generally decreases, probably due to a longer distance of vortices from the roof surface. The results for h_p = 2 mm, not shown in the present paper to save space, indicate that the negative peak suctions are smaller in magnitude than those for h_p = 0 mm. Further increase in h_p reduces the magnitude of the negative peak suctions, and the distribution becomes more uniform.

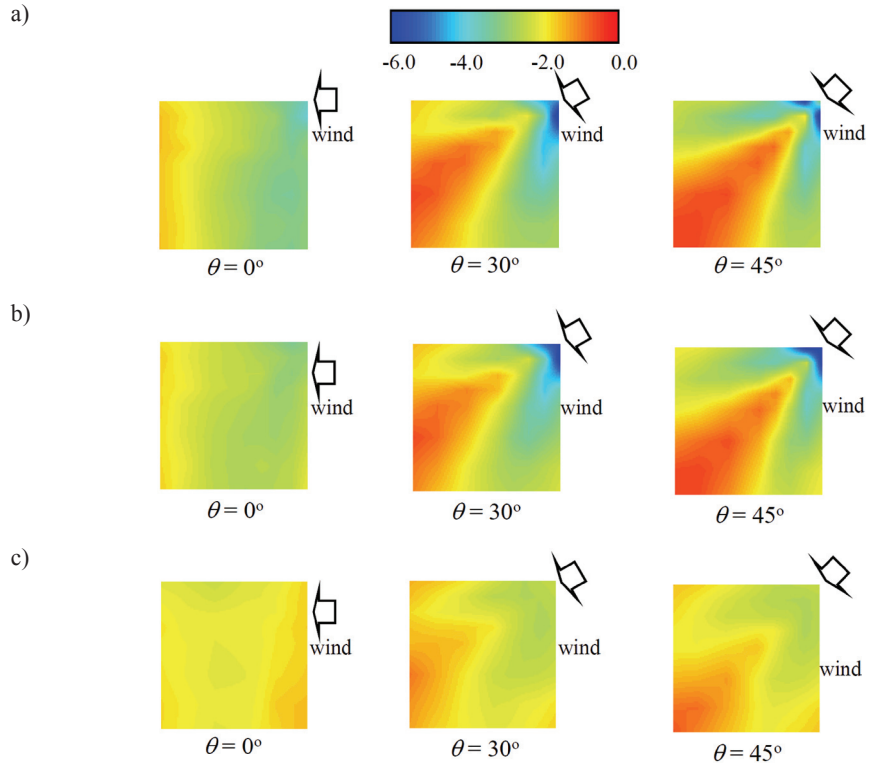

Fig. 16. Distribution of the minimum external peak pressure coefficients C_{pe_min} on the rooftop of Model A with H = 50 mm, a) h_p = 0 mm (0 m in full scale), b) h_p = 1 mm (0.2 m in full scale), c) h_p = 6 mm (1.2 m in full scale)

The results for $H = 300$ mm are shown in Fig. 17. They are qualitatively similar to those in Fig. 16, regarding the effects of h_p and H on the distribution of C_{pe_min}. However, the magnitude of C_{pe_min} is somewhat smaller than that for $H = 50$ mm. This feature may be related to smaller turbulence intensity of the approach flow at the level of the rooftop.

Regarding the effect of parapet height on the negative peak pressure coefficients on the rooftop of low-rise and high-rise buildings, similar features were observed in the previous studies (e.g. [2]). This implies that the present experiment is consistent with the previous ones and the time history of external pressures obtained here can be used for predicting the scattering wind speeds of flooring decks laid on the rooftop of flat-roofed buildings.

The above-mentioned results imply that parapets higher than approximately 30 cm at full scale are effective for preventing the scattering of flooring decks.

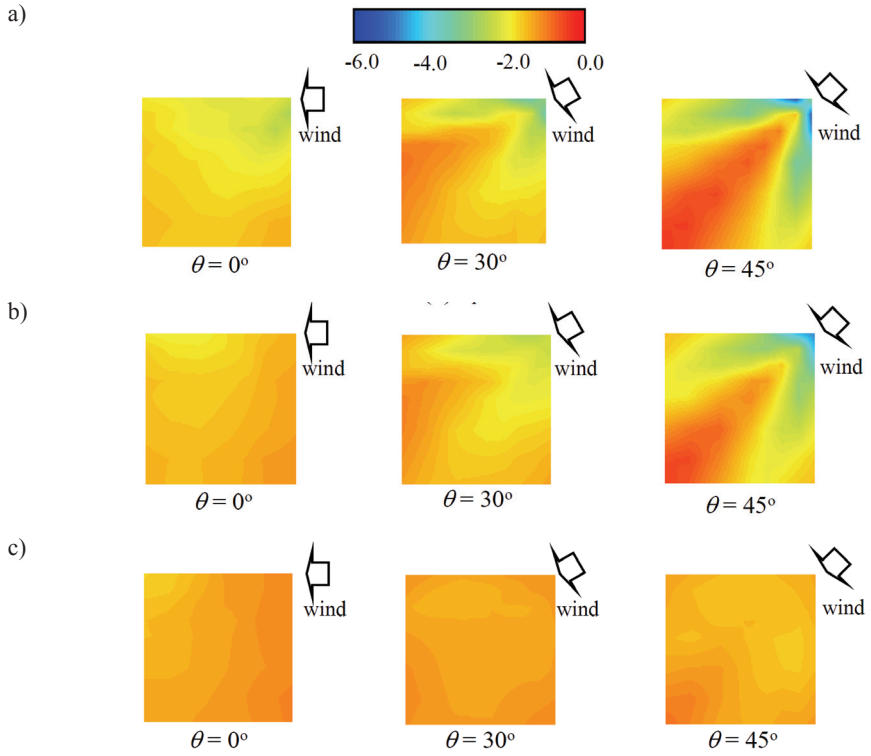

Fig. 17. Distribution of the minimum external peak pressure coefficients C_{pe_min} on the rooftop of Model A with $H = 300$ mm, a) $h_p = 0$ mm, b) $h_p = 1$ mm, c) $h_p = 6$ mm

4.2.2. Pressure distribution on balconies

Figs. 18a and 18b respectively show the distributions of C_{pe_min} along the line passing through the outer pressure taps on the balcony (see Fig. 14b) for *Panel* and *Balustrade*

types, when the wind direction is θ = 0°. In the figures the vertical dashed lines represent the locations of party walls. It is found that the magnitude of C_{pe_min} for the *balustrade* type is generally larger than that for the *panel* type. This feature implies that the *balustrade* type is affected by the separated flow more strongly. The results for the *spandrel wall* type is similar to those for the *panel* type, which means that the gap between the balcony floor and the panel (approximately 10 cm at full scale) minutely affects the external pressures on the balcony.

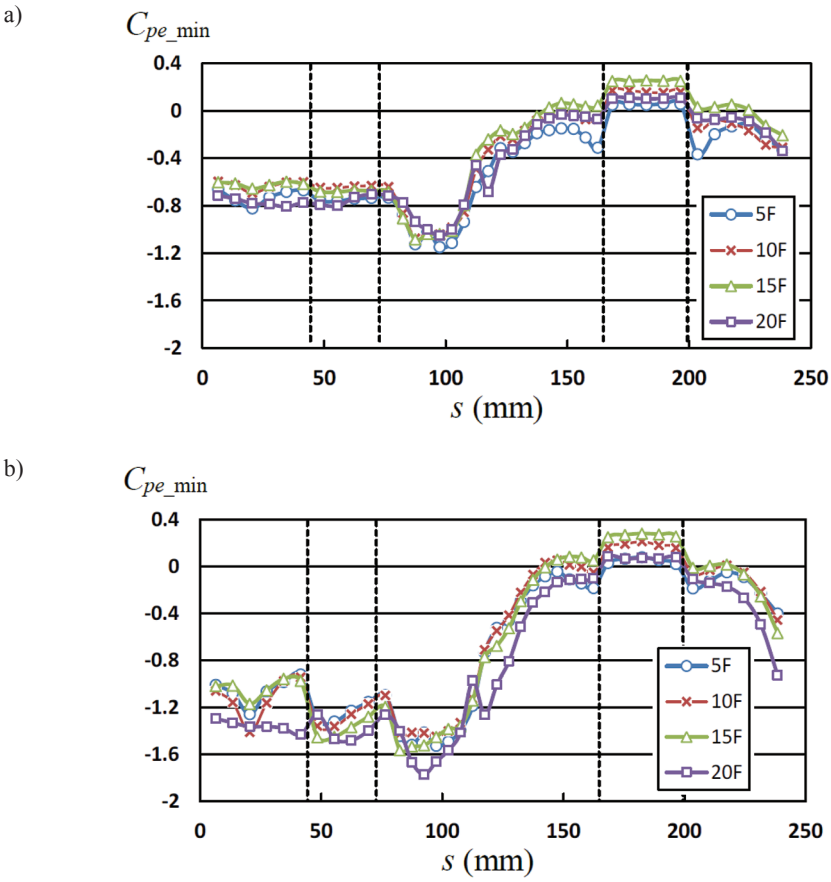

Fig. 18. Distribution of the minimum external peak pressure coefficients C_{pe_min} along the line passing through the outer pressure taps on the balcony of Model B (θ = 0°), a) *panel* type, b) *balustrade* type

The value of C_{pe_min} at each pressure tap changes with wind direction θ significantly. Figure 19 shows the most critical negative peak pressure coefficient at each pressure tap irrespective of wind direction for three balcony types; this may be very important when discussing the scattering of decks. In the figure, the results are represented by coloured circles; each colour represents a range of the pressure coefficient. In the *panel* and *spandrel wall* type cases, larger negative peak values occur near a party wall. The results are similar to

each other. On the other hand, much larger negative peak values are induced in wider areas in the *balustrade* type. Therefore, we should pay much more attention to the scattering of decks in the *balustrade* type.

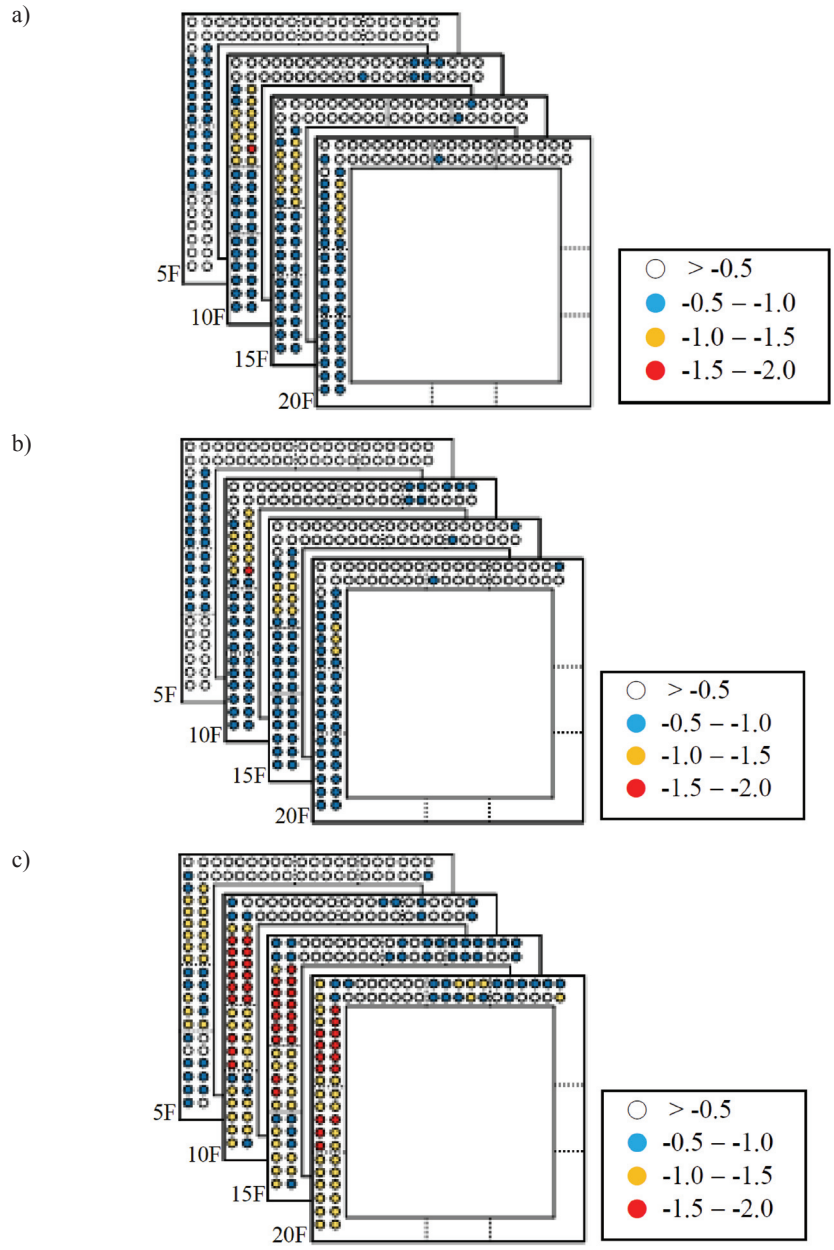

Fig. 19. Most critical negative peak pressure coefficient at each pressure tap irrespective of wind direction, a) *panel* type, b) *spandrel wall* type, c) *balustrade* type

5. Prediction of critical wind speed for the scattering of flooring decks

5.1. Simulated results of internal pressure coefficients

The internal pressures underneath the flooring decks laid on the rooftop or balcony are simulated by using the procedure described in Section 3.1. Fig. 20 shows the distribution of the minimum peak internal pressure coefficients C_{pi_min} on the rooftop of Model A with H = 50 mm when θ = 45°. The results for h_p = 0 and 6 mm are shown in the figure. The distribution of C_{pi_min} looks similar to that of C_{pe_min} (see Fig. 16). The values of C_{pi_min} are generally smaller in magnitude than those of C_{pe_min}, which may be related to the effect of pressure equalization caused by the slits and holes. Similar features are observed for C_{pi_min} on the balconies of high-rise buildings, as shown in Fig. 21. In the figure, the distributions of C_{pi_min} along the line passing through the outer pressure taps on the balcony (*balustrade* type) of Model B are plotted together with that of C_{pe_min}, when the wind direction is θ = 0°.

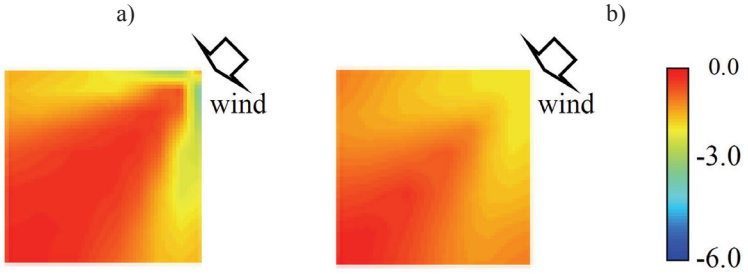

Fig. 20. Distribution of the minimum peak internal pressure coefficients on the rooftop of Model A (H = 50 mm, θ = 45°), a) h_p = 0 mm, b) h_p = 6 mm

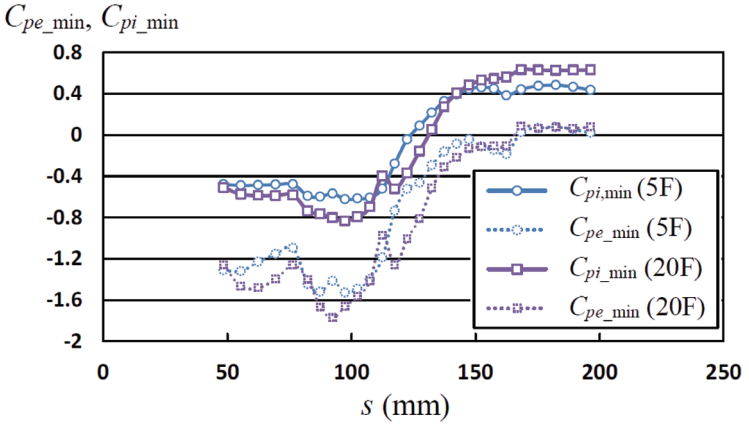

Fig. 21. Distribution of the minimum internal peak pressure coefficients C_{pi_min} along the line passing through the outer pressure taps on the balcony of Model B (θ = 0°)

5.2. Prediction of scattering wind speeds

The procedure for predicting the critical wind speed for the scattering of decks (scattering wind speeds) is as follows. Firstly, the internal pressure coefficients $C_{pi}(x, t)$ underneath the decks are simulated using the time history of external pressure coefficients $C_{pe}(x, t)$ obtained from a wind tunnel experiment. The net wind pressure coefficients $C_{p\text{net}}(x, t)$ on the decks are computed from the time history of $C_{pe}(x, t)$ and $C_{pi}(x, t)$, i.e. $C_{p\text{net}}(x, t) = C_{pe}(x, t) - C_{pi}(x, t)$. Then, the time history of moment coefficient $C_m(t)$ is computed by using Eq. (2). If parapets are installed on the roof or balcony, a moving average of 1 sec in full scale is applied to the time history of $C_m(t)$, from which the peak value $\hat{C}_m$ is obtained. Finally, the scattering wind speed U_{cr} at the level of rooftop H is obtained from Eq. (1) for a given mass M of decks. The value of U_{cr} is the lowest value for all decks and wind directions.

As an example, Table 1 summarizes the predicted values of U_{cr} for the flooring decks when $M = 0.4$ kg.

Table 1

Predicted values of scattering wind speeds U_{cr} for flooring decks (P3) with $M = 0.4$ kg loosely laid on the rooftop of flat-roof buildings and on the balconies of a 20 story building

(a) Rooftop

H (m)	h_p (m)	U_{cr} (m/s)
10	0.0	10.5
	0.2	22.2
	1.2	51.7
20	0.0	11.4
	0.2	26.3
	1.2	57.7
40	0.0	11.8
	0.2	24.1
	1.2	37.1
60	0.0	12.5
	0.2	26.1
	1.2	66.5

(b) Balcony

Type	Floor	U_{cr} (m/s)
Panel	5	35.9
	10	37.6
	15	35.5
	20	34.0
Spandrel wall	5	36.4
	10	36.9
	15	35.5
	20	35.2
Balustrade	5	30.6
	10	28.4
	15	27.0
	20	27.2

6. Concluding remarks

A discussion was made on a prediction model for the critical wind speed causing the scattering of permeable unit flooring decks loosely laid on the rooftop and balconies of high-

rise buildings. This was based on a blowing test, a wind tunnel experiment and a numerical simulation of the internal pressures underneath the decks. In the case of decks laid on the rooftop, the effects of the parapet were considered. Three different types of balcony, which are often used in practice, were considered. The results of a case study indicate that the parapet height significantly affects the scattering wind speeds of decks laid on the rooftop. As the parapet height increases, the scattering wind speed decreases significantly. The balcony type also affects the scattering wind speed of decks. However, the effect is less significant than the parapet height. In general, the *balustrade* type of balcony provides lower scattering wind speeds.

References

[1] Amano T., Fujii K., Tazaki S., *Wind loads on permeable roof-blocks in roof insulation systems*, Journal of Wind Engineering and Industrial Aerodynamics, Vol. 29, 1988, 39-48.

[2] Baskaran A., Stathopoulos T., *Roof corner wind loads and parapet configurations,* Journal of Wind Engineering and Industrial Aerodynamics, Vol. 29, 1988, 79-88.

[3] Bienkiewicz B., Sun Y., *Wind-tunnel study of wind loading on loose-laid roofing systems*, Journal of Wind Engineering and Industrial Aerodynamics, Vol. 41–44, 1992, 1817-1828.

[4] Bienkiewicz B., Sun Y., *Wind loading and resistance of loose-laid roof paver systems*, Journal of Wind Engineering and Industrial Aerodynamics, Vol. 77, 1997, 401-410.

[5] Cheung J.C.K., Melbourne W.H., *Wind loading on a porous roof*, Journal of Wind Engineering and Industrial Aerodynamics, Vol. 29, 1988, 19-28.

[6] Cope A.D., Crandell J.H., Liu Z., Stevig L.J., *Wind loads on fasteners used to attach flexible porous siding on multi-layer wall systems*, Journal of Wind Engineering and Industrial Aerodynamics, Vol. 133, 2014, 150-159.

[7] Gerhardt H.J., Janser F., *Wind loads on wind permeable facades*, Journal of Wind Engineering and Industrial Aerodynamics, Vol. 53, 1994, 37-48.

[8] Kawai H., Nishimura, G., *Characteristics of fluctuating suction and conical vortices on a flat roof in oblique flow*, Journal of Wind Engineering and Industrial Aerodynamics, Vol. 60, 1996, 211-225.

[9] Kind R.J., Wardlaw R.L., *Failure mechanisms of loose-laid roof-insulation systems*, Journal of Wind Engineering and Industrial Aerodynamics, Vol. 9, 1982, 325-341.

[10] Kopp G. A., Surry D., Mans C., *Wind effects of parapets on low buildings: Part 1. Basic aerodynamics and local loads,* Journal of Wind Engineering and Industrial Aerodynamics, Vol. 9, 2005, 817-841.

[11] Kumar, K.S., *Pressure equalization of rain screen walls: a critical review*, Building and Environment, Vol. 35, 2000, 161-179.

[12] Liu H., Saathoff P.J., *Building internal pressure: sudden change*, Journal of Engineering Mechanics Division, ASCE, Vol. 107, 1981, 309-321.

[13] Mooneghi M.A., Irwin P., Chowdhury A.G., *Large-scale testing on wind uplift of roof pavers*, Journal of Wind Engineering and Industrial Aerodynamics, Vol. 128, 2014, 22-36.

[14] Oh J.H., Kopp G.A., Inculet D.R., *The UWO contribution to the NIST aerodynamic database for wind loads on low buildings: Part 3. Internal pressures*, Journal of Wind Engineering and Industrial Aerodynamics, Vol. 95, 2007, 755-779.

[15] Oh J.H., Kopp G.A., *Modeling of spatially and temporally-varying cavity pressures in air-permeable, double-layer roof systems*, Building and Environment, Vol. 82, 2014, 135-150.

[16] Okada H., Ohkuma T., Katagiri J., *Study on estimation of wind pressure under roof tiles*, Journal of Structural and Construction Engineering, Architectural Institute of Japan, Vol. 73, 2008, 1943-1950 (in Japanese).

[17] Trung V., Tamura Y., Yoshida A., *Study on wind loading on porous roof cover sheets on a low-rise building: effects of parapet height and underneath volume*, Proc. 11th Americas Conference on Wind Engineering, San Juan, Puerto Rico 2009.

[18] Vickery B.J., *Gust-factors for internal pressures in low rise buildings*, Journal of Wind Engineering and Industrial Aerodynamics, Vol. 23, 1986, 259-271.

ENVIRONMENTAL EFFECTS ON BUILDING MATERIALS, STRUCTURES AND PEOPLE

WPŁYWY ŚRODOWISKOWE NA MATERIAŁY BUDOWLANE, KONSTRUKCJE I LUDZI

TECHNICAL TRANSACTIONS | CZASOPISMO TECHNICZNE
CIVIL ENGINEERING | BUDOWNICTWO
2-B/2015

JAN BENČAT*, BRANISLAV HADZIMA*

FULL-SCALE DYNAMIC TESTING OF THE CORROSION-DAMAGED, STEEL-TRUSS STRUCTURE OF OLD BRIDGE OVER THE DANUBE IN BRATISLAVA

BADANIA DYNAMICZNE W SKALI RZECZYWISTEJ USZKODZONEGO KOROZJĄ KRATOWEGO, STALOWEGO STAREGO MOSTU PRZEZ DUNAJ W BRATYSŁAWIE

Abstract

A large number of existing bridges need to be rehabilitated due to increasing traffic and/or loading requirements and also corrosion action. In this paper, a procedure is presented for estimating the ultimate capacity of a steel bridge over the Danube in Bratislava – Old Bridge (built in 1945). The development of a simplified Finite Element Model (FEM) and basic modal parameter calculations preceded the experimental investigations of the bridge via static and dynamic in-situ loading tests, so that the main assumptions adopted in the FEM were assessed through comparison between measured and predicted dynamic and modal parameters of the bridge structure. The bridge structure computational model was then optimized by structure variables (primarily, steel structure joints mass and corrosion grade) to achieve the minimum differences between the experimental and theoretical results. The calibrated FEM with the optimal combinations of the mentioned variable values were defined and finally used for structure calculations and for strengthening the design of the real bridge structure.

Keywords: *corrosion action, structural health monitoring, system identification, FEM, experimental tests in situ, spectral analysis*

Streszczenie

Wiele istniejących mostów musi zostać odnowionych w związku z rosnącym natężeniem ruchu i/lub z powodu wymagań obciążeniowych, a także w skutek działania korozji. W niniejszej pracy przedstawiono procedurę szacowania nośności granicznej stalowego mostu na Dunaju w Bratysławie - Old Bridge (zbudowanego w 1945 r.). Opracowanie uproszczonego modelu MES i podstawowe obliczenia parametrów modalnych poprzedzały badania statyczne i dynamiczne mostu w skali rzeczywistej. W związku z tym główne założenia modelowania MES zostały przyjęte na podstawie porównania między zmierzonymi i przewidywanymi dynamicznymi i modalnymi parametrami konstrukcji mostu. Model obliczeniowy konstrukcji mostu został następnie zoptymalizowany przez parametry konstrukcji (przede wszystkim przez uwzględnienie masy węzłów stalowych, stopnia korozji), aby osiągnąć minimalne różnice między wynikami badań doświadczalnych i teoretycznych. Skalibrowany model MES z optymalnymi kombinacjami wymienionych parametrów został zdefiniowany i wykorzystany do obliczeń i następnie wzmocnienia konstrukcji rzeczywistej mostu.

Słowa kluczowe: *działanie korozji, monitoring konstrukcji, identyfikacja systemu, MES, badania in situ, analiza widmowa*

DOI: 10.4467/2353737XCT.15.133.4170

* Research Centre UZ, University of Žilina, Slovakia.

1. Introduction

Riveted bridges account for the majority of steel bridges that were built in different parts of the world before the middle of the last century. A large number of these bridges are still in service today. However, some of these bridges are more than 100 years old. Therefore, it is clear that while many existing bridges are structurally adequate with respect to the maximum design axle loads, they may suffer from fatigue related to the cyclic application of modern freight equipment axle loads [1–8]. It should be noted that, generally, bridges designed within the past 50 years have considered fatigue effects, but that earlier bridge design did not include such considerations, even though, in some cases, the bridge may be found to be adequate for fatigue loads. The problems came up of how the resistance against repeated loads of the bridges is today. Usually, the authorities ask about two important issues, the first is that the bridge should be sufficiently safe for actual service conditions and if so, the second issue is, what is the expected residual life and what are the requirements for inspection and maintenance to ensure the expected residual life [6–9]. An essential part of the safety check of existing road bridges is the assessment of the static load-carrying capacity, and in some cases, a static or dynamic load test (even fatigue strength test) becomes necessary [9–12]. There are presently no regulations for the assessment of existing road bridges, expert opinions are normally used to obtain fatigue life estimates. It must be underlined; however, that fatigue is a far less relevant issue for road bridges than it is for railway bridges. As traffic density and traffic loads are constantly increasing, it is assumed that fatigue will be increasingly important for road bridges too. Because of the fatigue strength test time and financial implications, it is preferable to perform static or dynamic loading tests [13, 14] of the bridge structure as a part of the long-time monitoring to control its ultimate capacity [9, 12, 15].

2. Steel bridge case-study

The steel bridge over the Danube in Bratislava (Old Bridge) was built in 1945. The load-bearing structure of the bridge is created partly with continuous truss main beams over the river of 75.71 m, 91.50 m, 75.64 m (spans 2, 3, 4) and partly by single adjacent truss beams of 32.42 m and 75.82 m (spans 0, 1) and 75.18 m and 32.22 m (spans 5, 6), [3]. The bridge deck is composed of a steel grate system (cross and longitudinal beams) bearing the reinforced double T–prefabricated road panels, Figure 1. The soil conditions for foundations of the two massive abutments are very similar on both sides of the river and the resistant substratum (gravel and sandy gravel) is a depth of more than 22 m.

Foundations of the pylons are big reinforced concrete blocks on the same substratum as both of the massive abutments. The 91.5 m longest span (span 3) and two ≈ 75.0 m adjacent truss main beams (spans 2, 4) was chosen for the case study presented in this paper. These three truss continuous spans are the most representative and most failing part of the 461.07 m long bridge. Most of the cracked stringer to floor-beam connections were located in this part of the bridge. Figure 2 shows a bridge cross-section and bridge schematic view.

Fig. 1. View of the Old Bridge in Bratislava

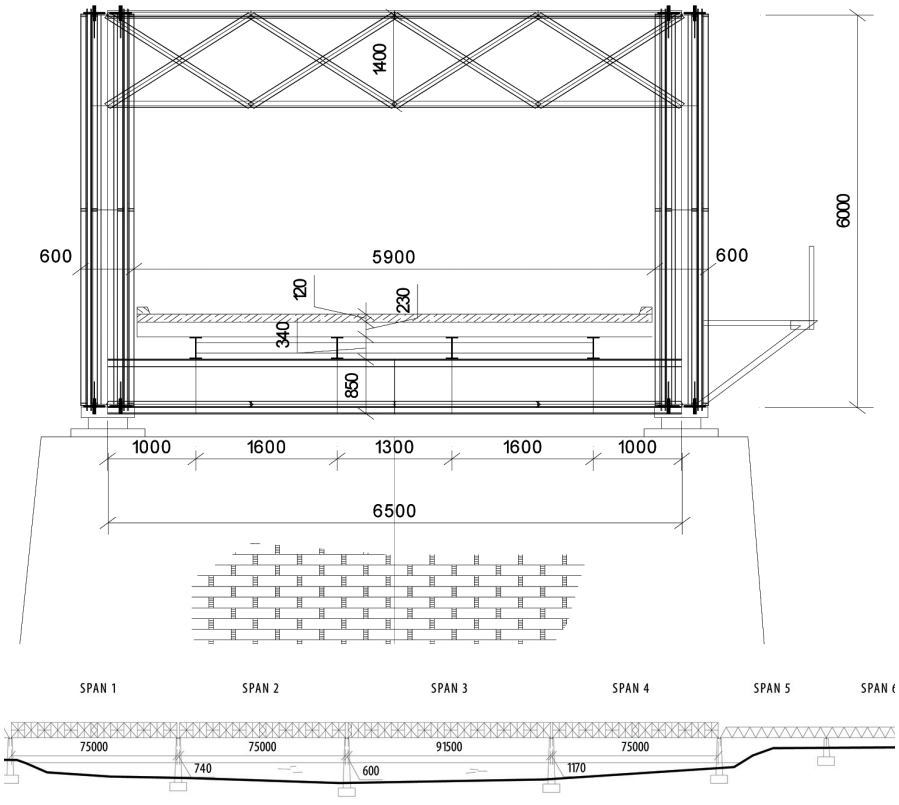

Fig. 2. Cross section and schematic view of the Old Bridge over the Danube in Bratislava

3. FEM analysis

Analysis of the bridge was performed using the IDA NEXIS software. The 3D global model incorporated all primary and secondary load-carrying members in the bridge was, however, excluded at this stage. Heavily gusseted connections, such as those between the main truss members and between wind-bracing elements and the main truss, were modelled as moment-stiff connections, while pin connections were adopted for secondary members, such as sway and cross-bracing elements. Eccentrically connected members, such as floor beams and wind–bracing elements, were coupled in the model. Longitudinal and transverse floor beams created as the built-up section from double angles with riveted steel plates were modelled using beam elements. The connections between longitudinal and transverse floor beams were made using multi-point constraints (MPC) and eccentric node-to-node gap elements were employed to simulate the contact condition between the double angles and the longitudinal floor beam web. All non-bearing elements of the truss girders and the bridge deck were included as a mass load of the structure. Four variations of the expected conditions were simulated: with and without corrosion effect; lower and higher joint mass estimation. The simplified FE model is created by 2758 joints and 5904 beam elements. A render of the computing model layout is presented in Fig. 3.

The first fifteen natural frequencies and modes of natural bridge vibration were calculated to compare with their experimental values from the DLT measurements. As an example, some of them are shown in Fig. 4. Variations of expected conditions and the comparison of results are explained in Figure 5. From comparison of these FEM natural frequency results it seems that the numerical natural frequency values are affected by the bridge steel structure joints mass, corrosion grade and FE–model degree of accuracy. Bridge deflection calculation for static and dynamic loading test: The maximum static vertical deflection values in the relevant points of the spans, positions of measured points, load positions and the effectiveness of the testing loads (SCANIA lorry of 15.7 ton mass) according to the Slovak standards [13, 14] for the static loading test (SLT) were taken into account and also calculated via IDA Nexis software package. Results from the calculations of static deflection were also used for dynamic loading test (DLT) load effectiveness.

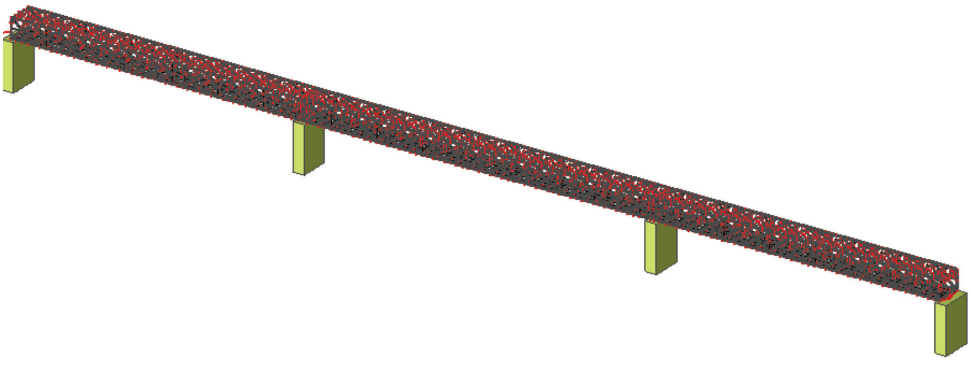

Fig. 3. Global FEM layout

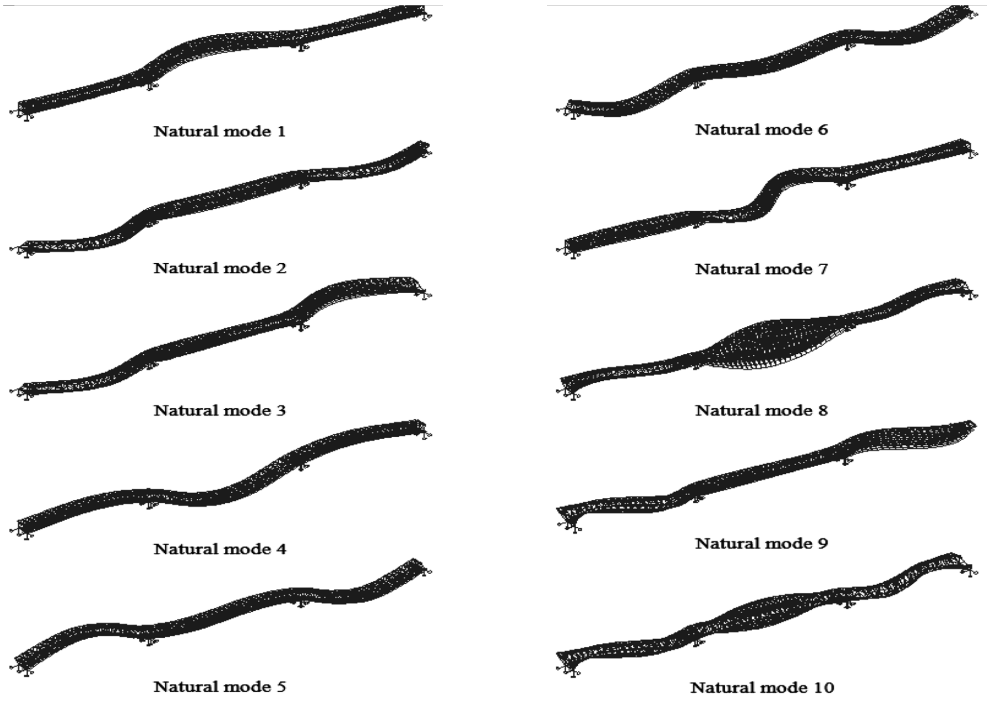

Fig. 4. Calculated modes of the bridge natural vibration

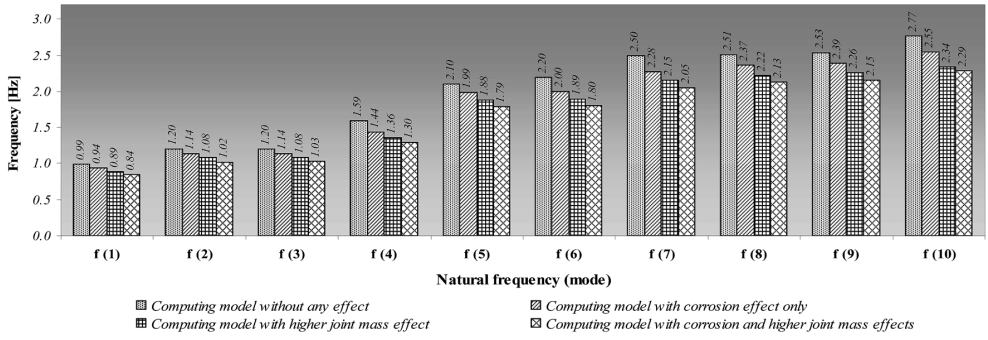

Fig. 5. Computational models natural frequencies results comparison

4. Dynamic loading test

Before the bridge dynamic loading test performance, the static loading test was carried out using the SCANIA load vehicle with mass of 15 700 kg. The deflection values in the relevant points of the tested spans (3, 4 and 5 spans) were measured using the precise geodesy levelling method with Leica equipment [9].

The dynamic response tested spans of the bridge was also induced by passing load vehicle SCANIA in the both directions with various speed. The sensor positions are shown in Fig. 6. The operating dynamic loading test started with a load speed of v = 5 km/h (crawling speed) which increased up to the maximum achievable speed v = 62 km/h.

A computer-based measurement system (CBMS) was used to record the dynamic response of the bridge excitations induced by the testing vehicle over the DLT period. The investigated vibration acceleration amplitudes were recorded at selected points with the maximum calculated deflection in each of the investigated four spans (Fig. 7). At the same points, the vibration amplitudes in both horizontal (longitudinal and perpendicular to bridge) directions were also recorded. Output signals from the accelerometers (Brüel–Kjaer, BK8306) were preamplified and recorded on two PC facilities with A/D converters and software packages NI and DISYS, The experimental analysis was carried out in the Laboratory of the University of Zilina. Natural frequencies were obtained using spectral analysis of the recorded bridge response dynamic components of the structure vibration, which are considered ergodic and stationary [15, 16, 17, 18]. The vibration ambient ability has been investigated by means of the correlation and spectral analysis in order to obtain cross-spectral densities $G_{xy}(f)$ and coherence function $\gamma_{xy2}(f)$, see also [9, 16]. The frequency response spectrum has also been obtained by using a two-channel, real-time analyzer BK–2032 in the frequency range 0–10 Hz. The output signal in the form of the Fourier frequency spectrum (power spectrum – $G_{xx}(f)$) was also recorded by computer and printed by laser printer and x-y plotter. Spectral analysis was performed via National Instruments software package NI LabVIE.

As an example, Figure 8 (a, b), shows a part of the spectral analysis procedure results PSD $G_{xx}(f)$ of the dynamic vertical components structure vibration from the bridge DLT. Figure 8 also shows corresponding cross-power spectral density $G_{xy}(f)$, Figure 8 (c), with its phase spectrum $\theta_{xy}(f) \rightarrow$ (d), coherence function $\gamma_{xy2}(f) \rightarrow$ (e) and transfer function $H_{13}(f) \rightarrow$ (f). In Table 1, values of the calculated and measured natural frequencies are introduced for comparison.

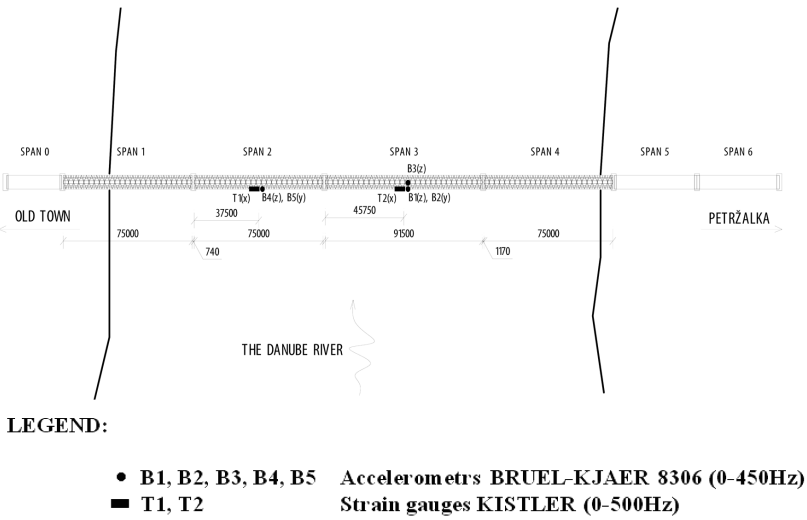

Fig. 6. Sensor positions layout

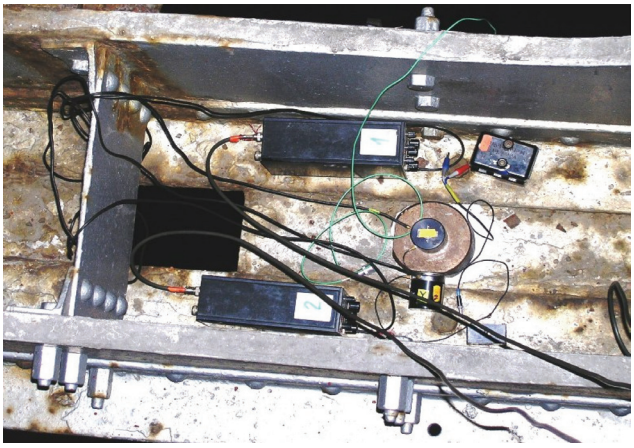

Fig. 7. Acceleration sensors with amplifiers

a)

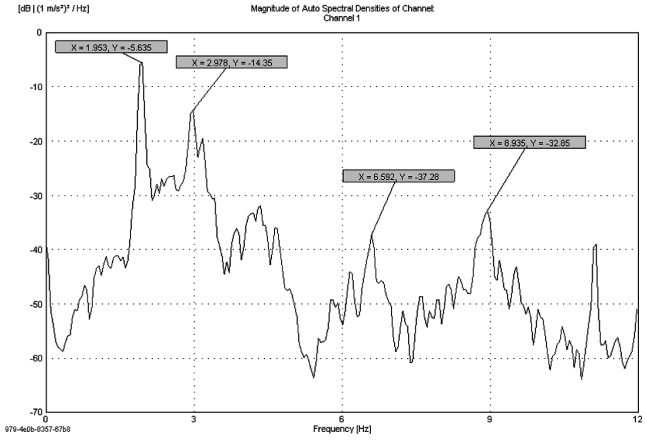

b)

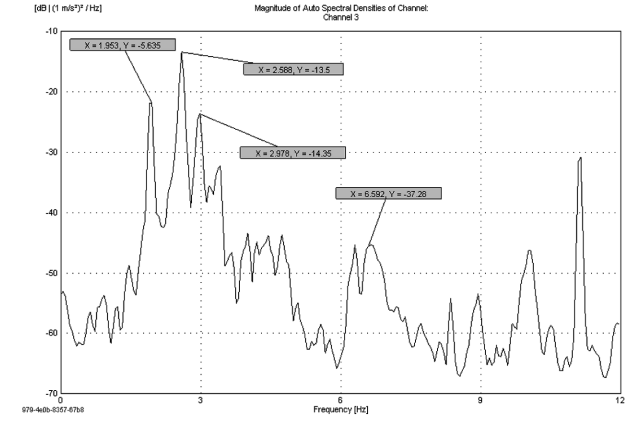

Fig. 8. Spectral analysis procedure

c)

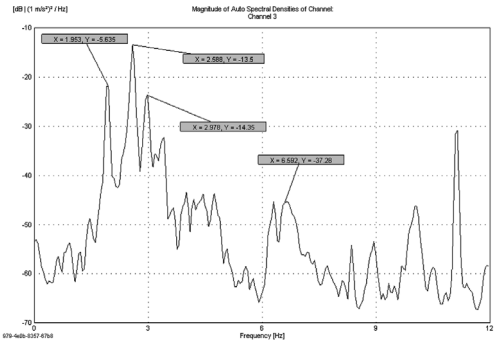

d)

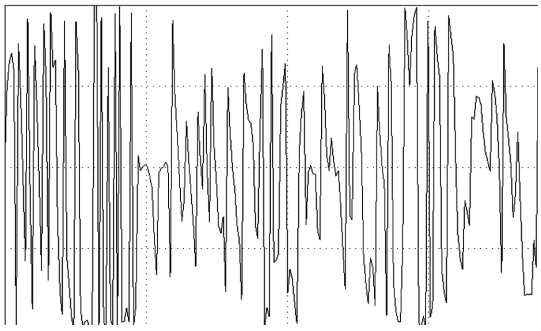

e)

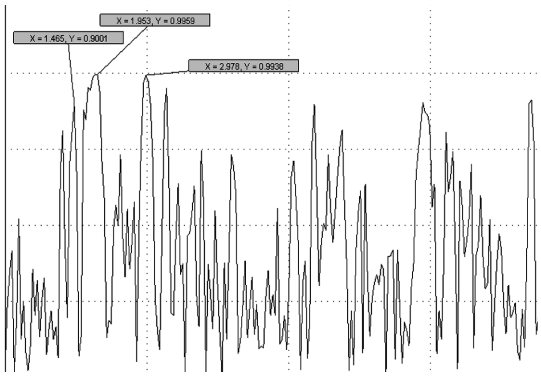

f)

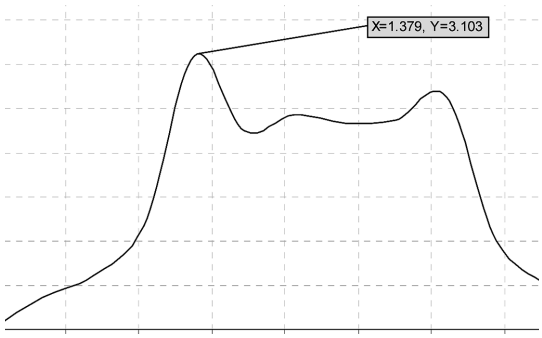

Fig. 8 (cont.). Spectral analysis procedure

Table 1

Calculated and measured natural frequencies

Natural frequencies ofthe bridge				
Natural mode	Numerical calculation *		Experimental analysis **	Vibration tendency
	Model 1	Model 2	2 – 3 span	
1	0.993	0.844	-	horizontal bending
2	1.200	1.024	-	horizontal bending
3	1.204	1.027	-	horizontal bending
4	1.589	1.298	-	vertical bending
5	2.104	1.788	1.53	horizontal bending
6	2.199	1.801	1.85 (1.82)	vertical bending
7	2.501	2.049	1.93 (1.95)	vertical bending
8	2.514	2.129	~ 1.78 (1.79)	horizontal bending
9	2.531	2.152	~ 1.78 (1.79)	horizontal bending
10	2.767	2.291	2.55 (2.58)	torsion
11	2.934	2.681	~ 2.95	torsion
12	2.937	2.693	~ 2.97	torsion
13	3.091	2.977	~ 3.00	axial
14	3.154	2.994	2.58	horizontal bending
15	3.754	3.551	2.97	horizontal bending
16	3.772	3.568	3.42 (3.44)	horizontal bending

* FE Model 1 – without corrosion and higher joint mass effects. FE Model 2 – with corrosion and higher joint mass effects.

** Natural frequencies from PSD with dominant peaks.

5. Conclusions

Theoretical and experimental investigation of the Old Bridge structure over the Danube in Bratislava is briefly described in the paper. The following conclusions can be drawn:

- The predicted dynamic behaviour of the bridge by a simplified FEM analysis calculation was compared to the measured one. Despite both the complex structural layout of the bridge and simplifying assumptions of the model, results showed strong agreement for all identified frequencies in the basic frequency range 0–5 Hz;
- The bridge dynamic loading test results are proof of the truss main beams continuousness which is in strong agreement with the adopted computational model and applied input bridge parameters;

- From comparison of the FEM natural frequency result, it follows that the numerical natural frequency values are mainly affected by the bridge steel structure mass with adding joints mass, corrosion grade and FE–model degree of accuracy (e.g. 2D, 3D, etc.). If such effects are neglected in the FEM analysis, the resulting theoretical and experimental dynamic properties can be different, mainly during modal identification procedures;
- Calculations of the natural frequencies with several combinations of the input parameters (with and without corrosion effect, lower and higher joint mass estimation, etc.) were performed in the numerical FEM analysis. The computational model with acceptation of the 96% cross-section area (4% corrosion loss) and also including the steel structure higher joints mass effect yield very close natural frequencies values in comparison with experimental ones;
- This computational model can be applied for the bridge fatigue and resistance analysis [5, 19, 20] before starting a decision making process regarding bridge strengthening or general reconstruction.

We kindly acknowledge the project: Research Centre of University of Zilina, ITMS 26220220183, supported by European regional development fund and Slovak state budget.

References

[1] Proulx J., Hebert D., Paultre P., *Evaluation of the dynamic properties of a steel arch bridge*, Proc. 10th Int. Modal Analysis Conference, USA, San Diego 1992, 2, 1025-1031.

[2] Inaudi D., Bolster M., Deblois R., French C., Phipps A.. Sebasky J., Western K., *Structural health monitoring system for the new I–35W St. Anthony Falls Bridge*, Proc. 4th International Conference on Structural Health Monitoring on Intelligent Infrastructure (SHMII–4), Switzerland, Zurich 2009.

[3] Adamson D., Kulak G., *Fatigue tests of riveted bridge girders*, Structural Engineering Report No. 210, University of Alberta, August 1995.

[4] Akesson B., *Fatigue life of riveted steel bridges*, CRC Press/Balkema, London 2010.

[5] JRC Scientific and Technical Reports. Assessment of existing steel structures: recommendations for estimation of remaining fatigue life, Report No. 43401, Joint Research Centre, European Commission, Luxembourg 2008.

[6] Wysokowski A., *Durability of steel bridges as function of fatigue and corrosion phenomena's*, IBDiM, Studies and Materials 53, CD–ROM, 2001 (in Polish).

[7] Bień J., *Failures and diagnostics of bridges*, WKŁ Press, Warszawa 2011 (in Polish).

[8] Zhou Y.E., Yen B.T., Fisher J.W., Sweeney R.A.P, *Examination of fatigue strength (S–N) curves for riveted bridge members*, Proc. 12th Annual Bridge Conference, Canada, Montreal 1995, 102-109.

[9] Bencat J., *Static and dynamic test results of the Old Bridge – over the Danube in Bratislava*, Technical Report: No. 6–3–21/SvF/09, ZU/Zilina, 2009.

[10] Bata M., Plachy V., Sykora J., Bily V., Polak M., *Static and dynamic tests of bridges*, Proc. of Czech – US Bridge Conference, Prague 1994.

[11] Williams C., *The effects of vibration on large structures and the determination of dynamic characteristics*, Proc. International Conference on Engineering Integrity through Testing, UK, Birmingham 1990, 441-452.
[12] Williams C., *Testing of large structures using vibration techniques, Structural integrity assessment*, Elsevier Applied Science, UK, London 1992.
[13] Slovak Standard STN 73 6209: Loading test of bridges, (in Slovak).
[14] Slovak Standard STN EN 1991 – 3: Traffic loads on Bridges, (in Slovak).
[15] Ren W. X., Zhao T., Harik I. E., *Experimental and analytical modal analysis of a steel arch bridge*, Journal of Structural Engineering, ASCE, Vol. 130(7), 2004, 1022-1031.
[16] Bendat J.S., Piersol A.G., *Engineering applications of correlation and spectral analysis*, (2nd edition), Wiley Interscience, New York 1993.
[17] National Cooperative Highway Research Program (USA). Dynamic Impact Factors for Bridges, NCHRP Synthesis 266; National Academy Press, DC, Washington 1998.
[18] SIA 269/3 – Existing Structures: Steel Structures, Swiss Society of Engineers and Architects (SIA), Switzerland, Zurich 2011.
[19] Eurocode 3. Design of Steel Structures,Part 1– 9: Fatigue; European Standard EN 1993–1–9, Brussels 1993.
[20] European Community: Guidline for Load and Resistance Assessment of Existing European Railway Bridges. European Commission (EC) Sixth Framework Programme, Sustainable Bridges, Sweden, Malmö 2007.

TECHNICAL TRANSACTIONS | CZASOPISMO TECHNICZNE
CIVIL ENGINEERING | BUDOWNICTWO
2-B/2015

TADEUSZ CHMIELEWSKI*, PIOTR GÓRSKI*

REVIEW OF SOME RESEARCH ON THE FULL-SCALE MONITORING OF CIVIL ENGINEERING STRUCTURES USING GPS

PRZEGLĄD WYBRANYCH BADAŃ DOTYCZĄCYCH MONITOROWANIA KONSTRUKCJI BUDOWLANYCH ZA POMOCĄ TECHNIKI GPS

Abstract

The static and dynamic deformation monitoring of engineering structures has been a matter of concern for engineers for many years. This paper provides a review of research and development activities from 1993 in the field of bridges, tall buildings, and tower health monitoring using GPS. Firstly, early pioneering applications of GPS to measure the structural vibrations of these structures and the assessment of the measurement accuracy of GPS are briefly described. The progress on monitoring the displacements and dynamic characteristics of bridges and tall structures, caused by traffic loads, wind, and the combined influence of solar radiation and daily air temperature variations, is then presented.

Keywords: *Global Positioning System (GPS), measurement accuracy, displacement monitoring, bridges, tall buildings and towers*

Streszczenie

Monitorowanie statycznych i dynamicznych przemieszczeń konstrukcji budowlanych jest przedmiotem zainteresowań inżynierów od wielu lat. W artykule przedstawiono przegląd badań i rozwój od 1993r. techniki GPS w monitorowaniu stanu technicznego konstrukcji mostowych, wysokich budowli i wież. Opisano pionierskie zastosowania systemu GPS do pomiarów drgań wymienionych konstrukcji budowlanych i badania dokładności tego systemu pomiarowego. Przedstawiono rozwój techniki GPS w monitorowaniu przemieszczeń i badaniu charakterystyk dynamicznych mostów i wysokich konstrukcji, poddanych działaniom wywołanym ruchem komunikacyjnym, wiatrem, nasłonecznieniem i dobową zmianą temperatury powietrza.

Słowa kluczowe: *Globalny System Pozycyjny (GPS), dokładność pomiaru, monitorowanie przemieszczeń, mosty, wysokie budynki i wieże*

DOI: 10.4467/2353737XCT.15.134.4171

* Department of Civil Engineering, Opole University of Technology, Poland.

1. Introduction

The static and dynamic deformation monitoring of engineering structures has been a matter of concern for engineers for many years. Examples of deformation behaviour in engineering structures are historical full-scale experiments on the Eiffel Tower, the Empire State Building, the Stuttgart TV Tower and several others. These measurements have not only provided important clues for theoretical calculations but also provided the verification needed before a theory could be announced as being successful.

This paper provides an overview of the applications of the Global Positioning System (GPS) in monitoring engineering structures during the last twenty years. These applications have become a useful tool for measuring and monitoring the static, quasi-static, and dynamic responses in civil engineering structures exposed to thermal expansions, the action of wind, earthquakes, traffic loads, or even people's excitation on footbridges.

2. Preliminary research

The first pioneering applications of GPS to measure the structural vibrations of tall structures and large cable-stayed bridges took place in the years 1993-1996. Lovse et al. [9] installed two GPS receivers on the Calgary Tower (completed in 1968). Two GPS receivers were used on the tower only to provide backup data in case one receiver would fail. These receivers on the tower were mounted on tripods near the base of the main communication antenna above the observation deck (Fig. 1). The reference receivers were located on a tripod on the roof of a low-rise (three-story) apartment building situated approximately 1 km north of the Tower. Data was collected at 10 Hz for about 15 min in the morning of 19 November 1993.

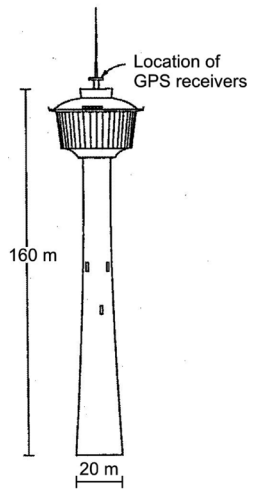

Fig. 1. The Calgary Tower and location of GPS receivers [9]

The analysis of the measured data gave the following results:

1) the Calgary Tower under wind loading vibrated with a natural frequency of about 0.3 Hz;
2) the N-S amplitude of displacement was approximately ±15 mm, and the E-W was ±5 mm.

The measured motion of the Calgary Tower using GPS receivers in both east-west and north-south directions is shown in Fig. 2 for a representative interval of 1 min.

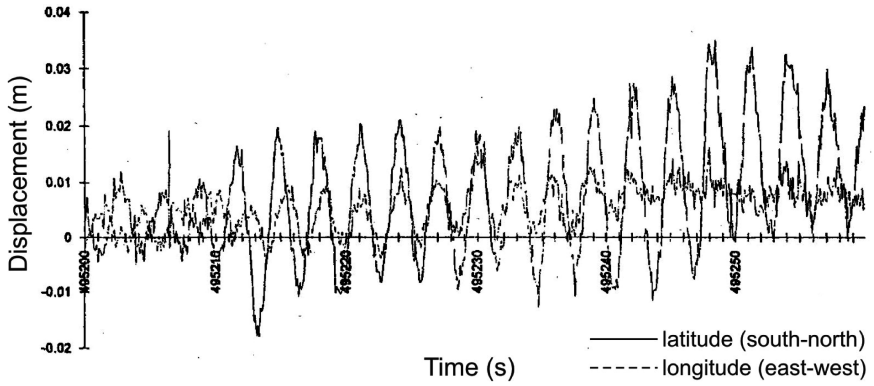

Fig. 2. Displacements of Calgary Tower [9]

Leach and Hyzak [8] reported their results as periodic movements on a large cable-stayed bridge, measured by GPS. Because the vertical movements, which had amplitudes in the order of ±30 mm, were caused by temperature changes rather than wind loading, a very slow sampling rate of one measurement every 10 s was sufficient to recover the movements.

Another example of preliminary research on the application of GPS in monitoring large-scale structures was conducted by Ashkenazi and Roberts [1]. Their paper describes the way in which the UK Humber Bridge was monitored using a 'kinematic GPS'. A rover receiver was placed on the west side rail of the bridge deck, at the mid span. The reference receiver was placed on the top of the bridge control tower. A measured test was carried out on two days – the first test on 7 March 1996, and the second on 7 May 1996. During the first test, the wind was fairly low and generally from the north-east along the length of the bridge. The authors have shown the results of the longitudinal, vertical, and lateral movements of the bridge deck, obtained from a selected period of time lasting 15 min. This was shown only for illustrative purposes. These tests were carried out only as a feasibility study of the kinematic GPS techniques for the in-situ monitoring of the movements of the bridge, and not as a full-scale experiment of a structural deflection analysis.

3. Assessment of measurement accuracy of GPS

After the first feasibility studies, GPS technology became an emerging tool for full-scale measuring and monitoring both static and dynamic responses to ambient loads of long-

standing structures. As a new method, GPS performance had to be thoroughly validated before its application as a full-scale test of structural displacement analysis. Many researchers [2, 4, 14, 18] carried out feasibility studies to investigate the following questions: (1) What is the accuracy of measurements of horizontal and vertical displacements? (2) What is the range and level of natural frequencies and mode shapes determined by GPS? (3) Does this accuracy depend on the frequency of recorded vibrations? (4) Can some of the first natural frequencies be detected from a single displacement record?

In order to answer these questions, many calibration tests were carried out by applying various kinds of equipment such as: an earthquake shake-simulator track; shaking platforms; slender structure simulating equipment; experimental apparatus consisting of one or three degree of freedom oscillators; rotating arm equipment.

The major outcome of these studies showed that GPS, advanced to record 10 samples per second (sps or Hz), could record vibrations with frequencies of 0.1 to 4 Hz with an accuracy ±0.5 cm horizontally and ±1 cm vertically.

The most recent paper which deals with the error properties of ultra-high-rate GPS data was published by Moschas and Stiros [12]. In this paper, the impact of the phase-locked loop (PLL) bandwidth on the noise and correlation of GPS measurements, sampled at 100 Hz, was investigated using short and long baselines, and stationary or moving GPS rovers recording vibrations with known characteristics relative to 'true' reference values. Data were collected under various satellite constellations using various values of PLL bandwidth, i.e. 25, 50, 100 Hz and were processed in differential mode using different software packages. The authors suggested that optimal results can be obtained using either a pre-set 50 Hz PLL bandwidth or a 100 Hz PLL bandwidth combined with a posteriori band-pass filtering of the coordinates. Such optimal results permitted an accurate recording with a standard deviation 4 mm horizontally and 7 mm vertically, and indicated that 100 Hz data are useful for monitoring high-frequency structural vibrations, and also strong earthquake and high-frequency movements from vehicles.

4. Monitoring vibrations in structures such as bridges, tall buildings and towers

Nakamura [13] described a field test using GPS conducted for about three weeks in March 1998 on a Japanese suspension bridge (with a main span of 720 m and two side spans of 330 m each) to measure the girder displacements induced by a strong wind. Two sets of GPS receivers were placed on the mid-span of the girder. The reference receiver was installed on a land office about 1 km away from the bridge's centre. The rover and reference receivers recorded displacements at a rate of 1 sample per second (sps = 1 Hz). Accelerometers were also set at the same position as the GPS rover receivers and acceleration data in three directions was collected at the same time. The main results of the described test are as follows: 1) the natural frequencies obtained by GPS data in the lateral (first), vertical (first), longitudinal (first and second) directions and those obtained by accelerometers matched very well. In addition, these values agreed well with the values obtained analytically by the FEM and in the forced vibration tests; 2) the vertical displacement measured by GPS showed 24-hour periodic movements because of the temperature changes in the cable; 3) it

may be concluded that GPS technology is reliable and useful in measuring the static and gust response behaviours of long span bridges.

Meng et al. [10] applied GPS array units and triaxial accelerometers in order to carry out a field test to record the response of the Wilford Bridge, a suspension footbridge over the River Trent in Nottingham. The footbridge response measurements to different excitations such as forced vibration excited by more than thirty people with a total mass of 2353 kg, as well as subsequent decayed free vibration and an ambient vibration caused by casual pedestrian traffic and a light wind loading were performed. Designing a proper digital filter for the extraction of structural dynamics parameters was an important aspect of the structural deformation analysis of this footbridge. Measurement time series in the format of coordinates or accelerations were filtered either to reduce the noise level or to split the measurements so that only the real signals to an allotted frequency band were the output for further analysis.

Tamura et al. [18] made two experiments to demonstrate the feasibility of real-time kinematic Global Positioning System (RTK-GPS) for measurements of the wind-induced response and its efficiency in measuring the displacement of a full-scale tower (108 m tall). In the first experiment, the accuracy of RTK-GPS in measurements of the sinusoidal displacements was examined using an electronic exciter. A GPS antenna was mounted on the measuring point of the exciter, and a wire displacement transducer was set to measure the actual displacement. Fig. 3 shows the set-up of the sinusoidal displacement tests. It was experimentally ascertained that when the vibration frequency was lower than 2 Hz and the vibration amplitude was larger than 2 cm, RTK-GPS results were very close to the actual displacement. The efficiency of RTK-GPS was then demonstrated in the full-scale measurement of the actual steel tower. The sketch of the steel tower and some results of the measurements are shown in Figs. 4, 5 and 6.

GPS offers great potential for the structural health monitoring (SHM) of tall buildings. Several tests have so far been conducted. Çelebi [3] made two preliminary tests to prove the technical feasibility of the application of GPS to monitoring tall buildings. The first test was performed with a standard stack steel bar to simulate a thirty to forty story flexible building. In the second test, they measured an ambient vibration (exposed to the wind and traffic noise) of a forty-four story building with a GPS unit temporarily deployed on its roof. The reference GPS unit was located within 500 m of the building. The signals were very noisy and the amplitudes very small (< 1 cm); therefore, the most common method to identify structural characteristics did not work. It was possible to identify the fundamental frequency of the building at 0.23 Hz.

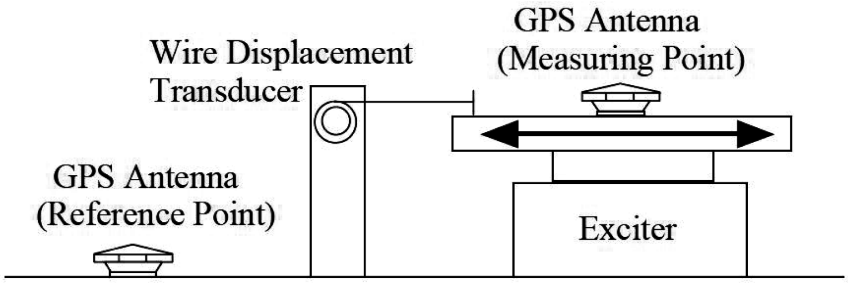

Fig. 3. Sketch of the experimental set-up of the sinusoidal vibration tests using an exciter [18]

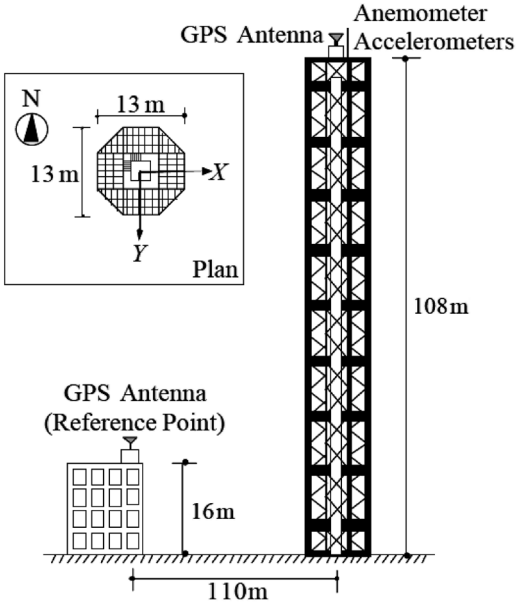

Fig. 4. A 108 m tall steel tower for full-scale measurements [18]

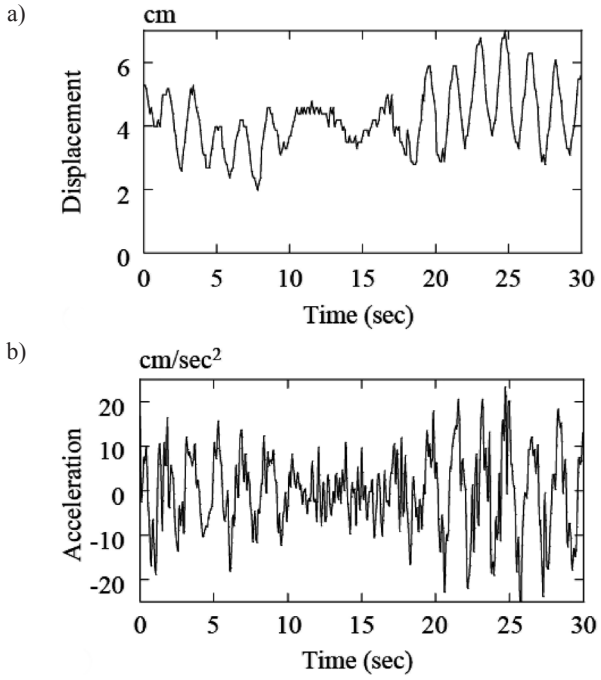

Fig. 5. Example of temporal variations of wind-induced responses of an actual steel tower during a typhoon: (a) RTK-GPS (Y-dir.) and (b) accelerometer (Y-dir.) [18]

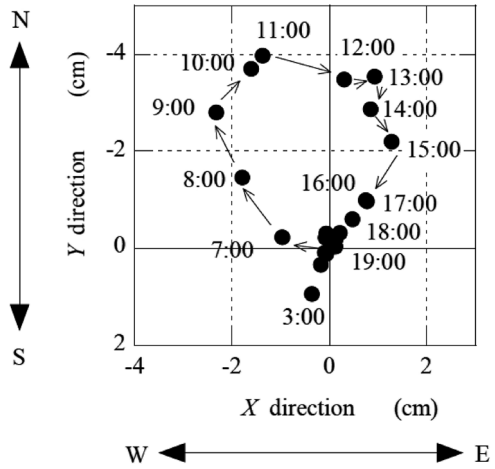

Fig. 6. Deformation of the tower caused by solar radiation and daily temperature variations [18]

Ogaja et al. [15] installed two Trimble 4700 units on the top of the Republic Plaza (280 m tall) in Singapore sampling at the rate of 1 Hz to measure the vibrations of the building due to the wind. Ogaja et al. [15, 16] used a pair of Leica GPS units installed on the Republic Plaza building again to generate a time series of the receiver positions. Chen et al. [5] conducted a field test employing two NovAtel Outrider DL RT2 dual frequency GPS units to measure the vibrations of the 384 m tall Di Wang building in Shenzen, China, under relatively strong wind conditions.

Kijewski-Correa et al. [6, 7] established a 'Chicago Full-Scale Monitoring Program' in 2001 to characterize the in-situ response of three tall buildings in order to verify design practices.

Breuer et al [2] examined field tests conducted on the Stuttgart TV tower to measure the displacements at the top of the tower caused by the wind and the combined influence of solar radiation and daily air temperature variations during different weather seasons and conditions. This paper presents the daily drift of the top of the Stuttgart TV Tower caused by solar radiation and daily air temperature variation during three GPS campaigns during different seasons. The daily elliptical path of the shift extends mainly in a west-east direction during summertime and in a northerly direction during winter. Fig. 7 shows the time-dependent records of the air temperature, the intensity of sun radiation and the air humidity during 4 days of measurements (4th–8th July 2006). The daily drift of the top of the Stuttgart TV Tower due to solar radiation and daily temperature variation, shown in Fig. 8, strongly depended on the meteorological conditions. The maximum displacement of the top towards the west appeared only during the first three days (4th–6th July), i.e. when solar radiation and daily air temperature variations were relatively high. During the final two days (7th–8th July), the positions of the top stabilized, indicating a reduced motion rate. This paper also presents the static and dynamic components (in the plane of the east-west and south-north directions) of the wind response during a thunderstorm (Fig. 9). For the wind response and for a sample rate equal to 2 sps, GPS was able to measure only the first natural frequency (0.191 Hz) of the Tower.

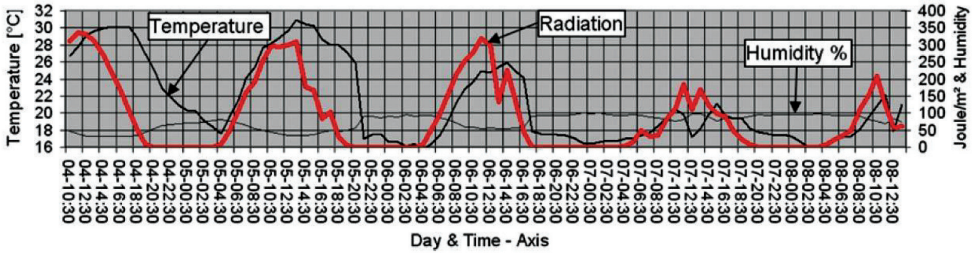

Fig. 7. The recorded temperature, the intensity of solar radiation and the humidity of the air during the GPS session (4th–8th July 2006) at the German Meteorological Station in Echterdingen, located 7 km from the Stuttgart TV Tower [2]

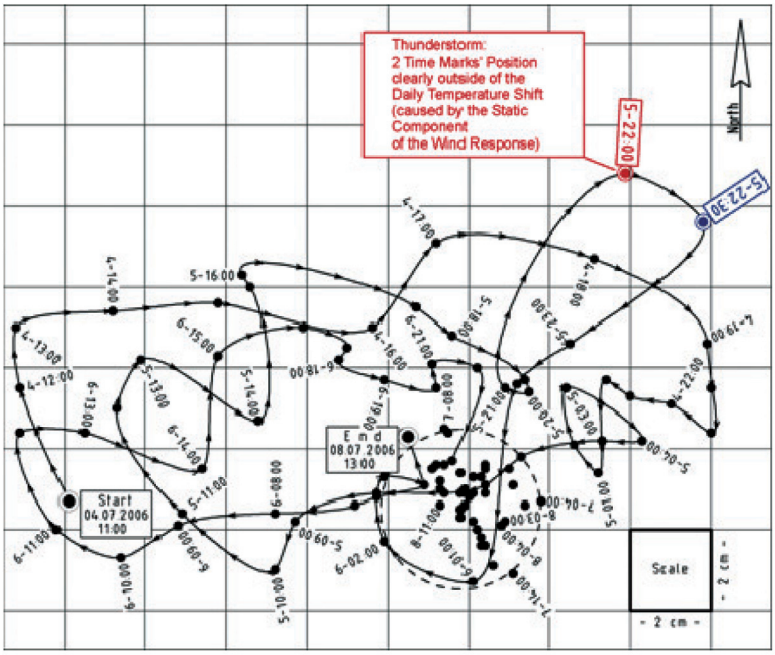

Fig. 8. The Stuttgart TV Tower, daily drift of the top due to solar radiation and daily temperature variation with hourly positions and time marks (4th–8th July 2006). In the north-east of the ground plan, two outliers are shown, caused by a thunderstorm with wind from the south-west at a peak velocity of about 17 m/s [2]

Moschas and Stiros [11] presented a new technique to reconstruct displacement records of relatively rigid structures (natural frequency: 1<f<5 Hz). This technique was based on the double digital filtering of high-frequency (10 Hz) GPS recordings of an oscillation, constrained and assessed by independent accelerometer data. This technique was applied to the processing of noisy GPS measurements of vibrations of a 40 m long steel footbridge excited by the coordinated jumps of a group of people.

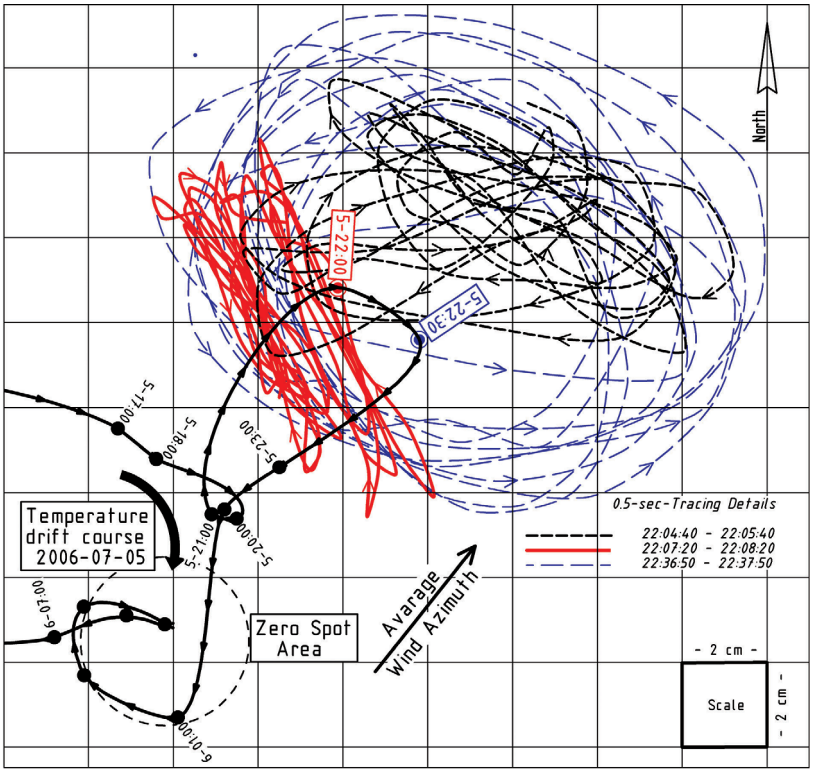

Fig. 9. The Stuttgart TV Tower, static and dynamic components of wind response during a thunderstorm producing an outline of the daily temperature drift (see Fig. 8). The wind from South-West with a peak velocity of about 17 m/s causes a north-east displacement (static component) of about 6 cm. The main direction of vibration is at a right angle to the wind direction with a displacement of 9–14 cm, 5th July 2006 [2]

5. Main characteristics in GPS monitoring technology

Although the GPS offers a useful tool for measuring static, quasi-static and dynamic responses of structures, it has its own limitations. The GPS satellite signals are susceptible to several kinds of error sources such as ionosphere and troposphere errors, receiver noise, multipath effects, satellite coverage and even GPS data sampling rates. During measurements, it is possible to eliminate or reduce (with mathematics and modelling) some of the troublesome GPS biases. However, two biases still remain that have not be eliminated, i.e. the geometric dilution of precision (GDOP) error, and the multipath effect (which occurs when duplicate satellite transmissions are received by the GPS receiver). The GDOP error is inherent in GPS technology and can be practically remedied through the addition of more satellites – this is now available by included more satellites from systems other than GPS, e.g. GNSS (Global Navigation Satellite System).

Regarding the application of GPS for the monitoring of structural vibrations, a sampling rate of 10 to 20 Hz only permits identifying the first natural frequency of common civil engineering structures, typically below 5 Hz. These sampling rates limit its capability for detecting higher mode signals of these structures.

The additional limitation is the price of GPS receivers which are high and hinder the application of GPS technology in practice.

In order to overcome the limitations mentioned above, it seems reasonable to apply an integrated sensor system consisting of GPS receivers combined with other sensors, i.e. accelerometers, laser scanners, displacement transducers, multi-waveform radars and fibre optic sensors. Such an integrated sensor system can increase the accuracy, reliability and effectiveness of the monitoring system.

6. Conclusions

1) In the last twenty years, the GPS with 10 Hz sampling rates has become a useful tool for measuring and monitoring static, quasi-static and dynamic responses in civil engineering structures exposed to settlement, gust-winds, earthquakes, thermal expansions traffic loads, and even some unforeseen events. These measurements allow the examination of both displacement levels and vibration characteristics such as natural frequencies, mode shapes, and damping ratios. These values are the key parameters when assessing the safety of flexible engineering structures. One should remember that the sampling rate of 10 Hz mostly permits us to identify the first natural frequency of the majority of civil engineering structures (below 5 Hz).
2) GPS can measure the total wind response, i.e. its dynamic fluctuating component and also a static component which is directly measured.
3) Ten years ago, a GPS sampling rate of 10 Hz was considered to be high. Recently, rates of 20, 50 or even 100 Hz have been used for some different kinematic applications. Further studies of the error properties of ultra-high-rate GPS data are needed in the near future.
4) In order to overcome the above limitations, it seems reasonable to apply an integrated sensor system consisting of the GPS receivers with other sensors, i.e. accelerometers, laser scanners, displacement transducers, multi-waveform radars and fibre optic sensors.

References

[1] Ashkenazi V., Roberts G.W., *Experimental monitoring of the Humber bridge using GPS*, Proceedings, Institution of Civil Engineers, Vol. 120, 1997, 177-182.

[2] Breuer P., Chmielewski T., Górski P., Konopka E., Tarczynski L., *The Stuttgart TV Tower − displacement of the top caused by the effects of sun and wind*, Engineering Structures, Vol. 30(10), 2008, 2771-2781.

[3] Çelebi M., *GPS in dynamic monitoring of long-period structures*, Soil Dynamics Earthquake Engineering, Vol. 20, 2000, 477-483.

[4] Chan W.S., Xu Y.L., Ding X.L., et al., *Assessment of dynamic measurement accuracy of GPS in three directions,* Journal of Surveying Engineering ASCE, Vol. 132(3), 2006, 108-117.

[5] Chen Y.Q., Huang D.F., Ding X.L., Xu Y.L., Ko J.M., *Measurement of vibrations of tall buildings with GPS: a case study,* Proc. of the International Symposium on NDE for Health Monitoring and Diagnostics, USA, California, Newport Beach 2001.

[6] Kijewski-Correa T., Kareem A., Kochly M., *Experimental verification and full-scale deployment of Global Positioning Systems to monitor the dynamic response of tall buildings,* Journal of Structural Engineering ASCE, Vol. 132(8), 2006, 1242-1253.

[7] Kijewski-Correa T., Pirnia J.D., *Dynamic behavior of tall buildings under wind: insights from full-scale monitoring,* The Structural Design of Tall and Special Buildings, Vol. 16(4), 2007, 471-486.

[8] Leach M.P., Hyzak M.D., *GPS structural monitoring as applied to a cable-stayed suspension bridge*, Proc. Int. Fed. of Surveyors (FIG) 20th Congr., Australia, Melbourne, 606.2/1-606.2/12, 1994.

[9] Lovse J., Teskey W., Lachapelle G., Cannon M., *Dynamic deformation monitoring of tall structure using GPS technology,* Journal of Surveying Engineering, Vol. 121(1), 1995, 35-40.

[10] Meng X., Dodson A.H., Roberts G.W., *Detecting bridge dynamics with GPS and triaxial accelerometers,* Engineering Structures, Vol. 29, 2007, 3178-3184.

[11] Moschas F., Stiros S., *Measurement of the dynamic displacements and of the modal frequencies of a short-span pedestrian bridge using GPS and an accelerometer*, Engineering Structures, Vol. 33(1), 2011, 10-17.

[12] Moschas F., Stiros S., *PLL bandwidth and noise in 100 Hz GPS measurements,* GPS Solutions, online: 7.05.2014.

[13] Nakamura S., *GPS measurement of wind-induced suspension bridge girder displacements*, Journal of Structural Engineering ASCE, Vol. 126(12), 2000, 1413-1419.

[14] Nickitopoulou A., Protopsalti K., Stiros S., *Monitoring dynamic and quasi-static deformations of large flexible engineering structures with GPS: Accuracy, limitations and promises*, Engineering Structures, Vol. 28(10), 2006, 1471-1482.

[15] Ogaja C., Rizos C., Han S.W., *Is GPS good enough for monitoring the dynamics of high-rise buildings*?, Proc. 2nd Trans Tasman Surveyors Congress, New Zealand, Queenstown 2000.

[16] Ogaja C., Rizos C., Wang J.L., Brownjohn J., *GPS and building monitoring case study: Republic Plaza Building, Singapore,* Proc. International Symposium on Kinematic Systems in Geodesy, Geomatics and Navigation, Canada, Banff 2001.

[17] Ogaja C., Wang J.J., Rizos C., *Detection of wind-induced response by wavelet transformed GPS solutions,* Journal of Surveying Engineering, Vol. 129(3), 2003, 99-104.

[18] Tamura Y., Matsui M., Pagnini L.-C., Ishibashi R., Yoshida A., *Measurement of wind-induced response of buildings using RTK-GPS*, Journal of Wind Engineering and Industrial Aerodynamics, Vol. 90, 2002, 1783-1793.

TECHNICAL TRANSACTIONS | CZASOPISMO TECHNICZNE
CIVIL ENGINEERING | BUDOWNICTWO
2-B/2015

ANDRZEJ FLAGA*

BASIC PRINCIPLES AND THEOREMS OF DIMENSIONAL ANALYSIS AND THE THEORY OF MODEL SIMILARITY OF PHYSICAL PHENOMENA

PODSTAWOWE ZASADY I TWIERDZENIA ANALIZY WYMIAROWEJ I TEORII PODOBIEŃSTWA MODELOWEGO ZJAWISK FIZYCZNYCH

Abstract

The paper concerns dimensional analysis and the theory of model similarity of physical phenomena. At the beginning of the considerations, basic notions, definitions, relationships and fundamental principles of the issues to be analysed has been presented. Next, Buckingham's Π-theorem of dimensional analysis and theory of similarity as well as authorial generalized theorems Π of this field of interest have been derived. A separate chapter has been devoted to the problem of the nature of physical phenomena occurring in the mechanics of continuous or discrete material mediums. At the end of the paper, an example of the determination of similarity numbers in the case of a system with one degree of freedom at mechanical and kinematic excitation have been given.

Keywords: dimensional analysis, model similarity, physical phenomena, principles and theorems

Streszczenie

Praca dotyczy analizy wymiarowej i teorii podobieństwa modelowego zjawisk fizycznych. Na wstępie przedstawiono podstawowe pojęcia, definicje, związki i fundamentalne zasady dotyczące rozpatrywanych problemów. Następnie wyprowadzono twierdzenie Π Buckinghama dotyczące analizy wymiarowej i teorii podobieństwa oraz autorskie uogólnienie twierdzenia Π. Oddzielny rozdział został poświęcony problemowi zjawisk fizycznych występujących w mechanice ośrodków ciągłych i dyskretnych. W części końcowej artykułu przedstawiono przykład określenia liczb podobieństwa w przypadku układu o jednym stopniu swobody przy wzbudzeniu mechanicznym i kinematycznym.

Słowa kluczowe: analiza wymiarowa, podobieństwo modelowe, zjawiska fizyczne, zasady i twierdzenia

DOI: 10.4467/2353737XCT.15.135.4172

* Wind Engineering Laboratory, Cracow University of Technology, Poland.

1. Introduction

Dimensional analysis offers a method for reducing complex physical problems to the simplest form prior to obtaining a quantitative answer.

The method is of great generality and mathematical simplicity. At the heart of dimensional analysis is the concept of similarity. In physical terms, similarity refers to some equivalence between two things, processes or phenomena that are actually different. Different with respect to nature or scale, processes or phenomena.

Mathematically, similarity refers to a transformation of variables that leads to a reduction in the number of independent variables that specify the problem. A problem that at first looks formidable may sometimes be solved with little effort after dimensional analysis.

In problems so well understood that one can write down in mathematical form all the governing laws and boundary conditions, and only the solution is lacking, similarity can also be inferred by normalizing all the equations and boundary conditions in terms of quantities that specify the problem and identifying the dimensionless groups that appear in the resulting dimensionless equations. This is an inspectional form of similarity analysis.

Dimensional analysis is, however, the only option in problems where the equations and boundary conditions are not completely articulated, and always useful because it is simple to apply and quick to give insight.

Some of the basic ideas of similarity and dimensional analysis had already presented in Fourier's work in the first quarter of the nineteenth century, but the subject received more methodical attention only toward the close of that century, notably in the works of Lord Rayleigh, Reynolds, Maxwell, and Froude in England, and Carvallo, Vaschy and a number of other scientists and engineers in France [22, 24]. By the 1920's Buckingham's now well-known Π-theorem had appeared [5] and Bridgman had published the monograph which still remains the classic in the field [4]. Since then, the literature has grown enormously. Applications now include different branches of knowledge and science. The procedure is the same in all applications, a great variety of which may be found in the references and in the scientific literature at large (see for example following books, handbooks and monographs: [2–3, 6, 8–21, 23, 25–34, 36–39].

2. Physical quantities and relationships

2.1. Physical properties

An object or event or phenomenon is described in terms of basic properties like length, mass, colour, shape, speed, and time. None of these properties can be defined in absolute terms. We can do no more than compare one thing with another.

A physical property first arises as a concept based on experience and is formalized by defining a comparison operation for determining whether two samples of it are equal ($A=B$) or unequal ($A\neq B$).

This operation, which is an entirely physical procedure, defines the property. Properties of the same kind are compared by means of the same comparison operation. Properties of different kinds cannot be compared. Asking whether a particular mass is physically equal to a particular length is meaningless: no procedure exists for making the comparison.

Properties like shape and colour are useful for describing things, but cannot play a role in any quantitative analysis.

2.2. Physical quantities and base quantities

Science begins with observation and description of things and phenomena. Its ultimate goal is to infer from those observations laws that express the phenomena of the physical world in the simplest and most general terms. The language of mathematics is ideally suited for expressing those laws. The allowed types of properties are called "physical quantities".

Physical quantities are of two types: base quantities and derived quantities. The base quantities form a complete set of derived quantities that may be introduced as necessary. The base and derived quantities together provide a rational basis for describing and analysing the physical world in quantitative terms.

A base quantity is defined by specifying two physical operations:

1. A comparison operation for determining whether two samples A and B of the property are equal ($A=B$) or unequal ($A\neq B$);
2. An addition operation that defines what is meant by the sum $C=A+B$ of two samples of the property.

Base quantities with the same comparison and addition operations are of the same kind. The addition operation $A+B$ defines a physical quantity C of the same kind as the quantities being added. All physical quantities are properties of physical things, events, processes, or phenomena.

The comparison and addition operations are physical, but they are required to have certain properties that mimic those of the corresponding mathematical operations for pure numbers [35]:

1. The comparison operation must obey the identity law (if $A=B$ and $B=C$, then $A=C$);
2. The addition operation must be commutative ($A+B=B+A$), associative [$A+(B+C)=(A+B)+C$], and unique (if $A+B=C$, there exists no finite D such that $A+B+D=C$).

The two operations together define, in entirely physical terms:

1. The concept of larger and smaller for like quantities (if there exists a finite B such that $A+B=C$, then $C>A$);
2. Subtraction of like quantities (if $A+B=C$, then $A\equiv C-B$);
3. Multiplication of a physical quantity by a pure number (if $B=A+A+A$, then $B\equiv 3A$);
4. Division of a physical quantity by a pure number (if $A=B+B+B$, then $B\equiv A/3$).

A base quantity is thus a property for which the following mathematical operations are defined in physical terms: comparison, addition, subtraction, multiplication by a pure number, and division by a pure number. Each of these operations is performed on physical properties of the same kind and yields a physical property of that kind, and each physical operation obeys the same rules as the corresponding mathematical operation for pure numbers.

It is important to note that mathematical operations other than the ones listed above are not defined in physical terms. Products, ratios, powers, and exponential and other functions such as trigonometric functions and logarithms are defined for numbers, but have no physical correspondence in operations involving actual physical quantities.

2.3. Measure unit, dimension and numerical value

The two operations that define a base quantity make it possible to express any such quantity as a multiple of a standard sample of its own kind, i.e. a unit of measure or simply – a unit. The standard sample – the unit – may be chosen arbitrarily.

The measuring process consists of physically adding replicas of the unit and fractions thereof until the sum equals the quantity being measured. A count of the number of whole and fractional units required yields the numerical value of the quantity being measured. If a is the unit chosen for quantities of type A, the process of measurement yields a numerical value $\breve{A}$ (a number) such that:

$$A = \breve{A}a \tag{2.1}$$

In further considerations the unit of measure a will be called the dimension of the quantity A and will be described as:

$$a = [A]; \qquad A = \breve{A}[A] \tag{2.2}$$

The numerical value of a base quantity depends on the choice of unit. A physical quantity exists independently of the choice of unit. A quantity A can be measured in terms of a unit a or in terms of another unit a', but the quantity itself remains physically the same, that is:

$$A = \breve{A}a = \breve{A}[A] = \breve{A}'a' = \breve{A}'[A'] \tag{2.3}$$

If the unit $[A']$ is times larger than $[A]$:

$$[A'] = \breve{N}[A], \tag{2.4}$$

it follows from equation (2.3) that:

$$\breve{A}' = \breve{N}^{-1}\breve{A}. \tag{2.5}$$

If the size of a base quantity's unit is changed by a factor $\breve{N}$, the quantity's numerical value changes by a factor $\breve{N}^{-1}$.

The ratio of the numerical values of any two base quantities of the same kind is independent of base unit size.

Note also that when base quantities of the same kind are added physically ($A+B=C$), the numerical values satisfy an equation of the same form as the physical quantity equation

($A+B=C$), regardless of the size of the chosen unit. In other words, the numerical value equation mimics the physical equation, and its form is independent of the unit's size.

2.4. Fundamental measure unit base

Set of k base quantities $\{A\}=\{A_1, \ldots, A_k\}$ which are one dimensionally independent, i.e. none of its members has a dimension that can be expressed in terms of the dimensions of the remaining members, and which are sufficient and complete to describe the dimensions all other quantities involving in describing a respective object, event or physical phenomenon, is called fundamental measure unit base or shortly fundamental unit base. For example in mechanics such a base contains three base quantities: L – length, M – mass, T – time. In thermomechanics problems another base quantity appears, i.e. τ – temperature.

2.5. Derived quantities, their dimensions and dimensionless quantities

Describing physical things, events or phenomena quantitatively, we refer to numerical values of base quantities and also introduce numbers derived by inserting these values into certain mathematical formulas, expressions, relationships, etc.

Derived quantities by definition are those quantities which satisfy the following rules:

1. An arbitrary derived quantity Q can be presented in a form:

$$Q = \breve{Q}[Q] \tag{2.6}$$

where $\breve{Q}$ is the numerical value of the Q and $[Q]$ is the dimension of the Q.

2. Numerical values of derived quantities are defined by respective mathematical formulas, expressions, relationships, etc. containing mathematical operators such as: algebraic operators, functional operators, derivative operators, integral operators, operators like: lim, $\sum$, etc., in which numerical values of base quantities appear.
3. Numerical values of derived quantities can be presented in a power-low form:

$$Q = \breve{q} A_1^{\alpha_{Q1}} \ldots A_k^{\alpha_{Qk}} \tag{2.7}$$

where $\breve{q}$ is a dimensionless quantity (number) and powers: $\alpha_{Q1}, \ldots, \alpha_{Qk}$ are real numbers, whose values distinguish one type of derived quantity from another. All monomial derived quantities have this power-law form; no other form represents a physical quantity.

4. The dimension $[Q]$ of the derived quantity Q mimics the mathematical formula for the numerical value of the quantity Q omitting the number $\breve{q}$, i.e.

$$[Q] = [A_1]^{\alpha_{Q1}} \ldots [A_k]^{\alpha_{Qk}} \tag{2.8}$$

5. The derived quantity Q is defined in terms of the numerical value Q which depends on the choice of base units.

Whether applied to a base or derived quantity, the dimension is simply a formulaic indication of how the quantity's numerical value transforms when the sizes of the base units are changed. A derived quantity's dimension follows from its defining equation. We simply substitute for each base quantity the symbol for its dimension, omit the numerical coefficient $\breve{q}$ and obtain the equation by algebra. Thus, a quantity's dimension depends on the choice of the system of units.

Base quantities have a transparently physical origin, which gives rise to the fact that the ratio of any two samples of a base quantity remains constant when the base unit size is changed. Bridgman [4] postulated that this is in fact a defining attribute of all physical quantities, both base and derived quantities. This is Bridgman's principle of absolute significance of relative magnitude: A number Q, obtained by inserting the numerical values of base quantities into a formula, is a physical quantity if the ratio of any two samples of it remains constant when base unit sizes are changed.

Bridgman went on to show [4] (see also the proof by Barenblatt [1] and others [32, 38]) that a monomial formula satisfies the principle of absolute significance of relative magnitude.

Some important points about derived quantities can be listed as follows [35]:

1. The dimension of any derived physical quantity is a product of powers of the base quantity dimensions.
2. Sums of derived quantities with the same dimension are derived quantities of the same dimension. Products and ratios of derived quantities are also derived quantities with dimensions which are usually different from the original quantities.
3. All derived quantities with the same dimension change their values by the same factor when the sizes of the base units are changed.
4. A derived quantity is dimensionless if its numerical value remains invariant when the base units are changed. An example is Vt/L, where $V = \mathrm{d}x/\mathrm{d}t$ is a velocity, t is a time and L is a length. The dimension of a dimensionless quantity is unity, the factor by which the quantity's numerical value changes when base unit sizes are changed.
5. Special functions (logarithmic, exponential, trigonometric, etc.) of dimensional derived quantities are in general not derived quantities because their values do not in general transform like derived quantities when base unit size changes. Only when the arguments of these functions are dimensionless are the values of the functions remain invariant when units changed. Special functions with dimensionless arguments are therefore derived quantities with dimension unity.

2.6. System of units

A system of units is defined by:

1. A complete set of base quantities with their defining comparison and addition operations;
2. The base units;
3. All relevant derived quantities, expressed in terms of their defining equations.

The set of derived quantities is open-ended; new ones may be introduced in some new problems and analyses.

Systems of units are said to be of the same type if they differ only in the magnitudes of the base units. In the SI system (Système International) there are six base quantities (Tab. 1): length, time, mass, temperature, current, number of elementary particles, and luminous intensity. The units of length, time and mass are the metre (m), the second (s) and the kilogram (kg), respectively. Force is considered a derived quantity by writing Newton's law as $F = ma$.

Also sometimes included among the base quantities are two dimensionless quantities, plane angle and solid angle, which are measured in radians and steradians, respectively. We consider them derived quantities because, though dimensionless, they are defined in terms of operations involving length, much like area is defined in terms of length operations. The SI system of units – derived quantities (incomplete set) is given in Tab. 2.

Table 1

The SI system of units – base quantities (complete set)

Quantity	SI name	SI Symbol
length, L	metre	M
time, t	second	S
mass, M	kilogram	kg
temperature, T	Kelvin	K
current, I	ampere	A
number of elementary particles	Mole	mol
luminous intensity	candela	cd

Table 2

The SI system of units – derived quantities (incomplete set)

Quantity	Defining equation/law	Dimension	Dimensional Symbol	Name
area	$A = \int dxdy$	L^2	m^2	---
volume	$V = \int dxdydz$	L^3	m^3	---
frequency	$f = 1/\tau$	t^{-1}	s^{-1}	hertz (Hz)
velocity	$v = dx/dt$	Lt^{-1}	ms^{-1}	---
acceleration	$a = d^2x/dt^2$	Lt^{-2}	ms^{-2}	---
density	$\rho = M/V$	ML^{-3}	kgm^{-3}	---
force	$F = Ma$	MLt^{-2}	$kgms^{-2}$	newton (N)
stress/pressure	$p = F/A$	$ML^{-1}t^{-2}$	$Nm^{-2}=kgm^{-1}s^{-2}$	pascal (Pa)
work/energy	$W = \int F dx$	ML^2t^{-2}	$Nm=kgm^2s^{-2}$	joule (J)
torque	$T = Fl$	ML^2t^{-2}	$Nm=kgm^2s^{-2}$	---
power	dW/dt	ML^2t^{-3}	$Js^{-1}=kgm^2s^{-3}$	watt (W)
charge	$Q = \int 1 dt$	It	As	coulomb (C)

It is important to point out that the dimension of a derived quantity depends on the choice of system of units, which is under the control of the observer and has nothing to do with the quantity's intrinsic nature. Indeed, quantities with quite different physical meaning, like work and torque, can have the same dimension.

2.7. Physical quantities dimensionally dependent and independent. Derived dimensional base

All physical quantities have dimensions which can be expressed as products of powers of the set of base dimensions. Alternatively, it is possible to express the dimension of one quantity as a product of powers of the dimensions of other quantities which are not necessarily base quantities.

Let us consider a set of physically independent dimensional variables $\{Q_1,\ldots,Q_i,\ldots,Q_n\}$; $i = 1,2,\ldots,n$. The variables Q_i are independent if the numerical value of each member can be adjusted arbitrarily without affecting the numerical value of any other member. This set is put in order in such a way that it is possible to pick out from the physically independent variables $Q_1,\ldots,Q_n$ a dimensionally independent and complete subset $\{Q_1,\ldots,Q_k\}$, i.e. one which satisfies the following features:

1. The dimensions of this subset contain dimensions of the fundamental units base $\{A_1,\ldots,A_k\}$.
2. The size (k) of the subset $\{Q_1,\ldots,Q_k\}$ is the same as the size of the fundamental base $\{A_1,\ldots,A_k\}$.
3. None of its members has a dimension that can be expressed as product of powers of dimensions of the remaining members.
4. Dimensions of all the remaining members i.e. $Q_{k+1},\ldots,Q_n$ can be expressed as product of powers of dimensions of the subset members i.e. $Q_1,\ldots,Q_k$. Such a subset $\{Q_1,\ldots,Q_k\}$ will be called the derived dimensional base of the set $\{Q_1,\ldots,Q_n\}$.

It can be proven that for the set $\{Q_1,\ldots,Q_n\}$ such a derived dimensional base exists and in general there is more than one derived dimensional base for the initial set $\{Q_1,\ldots,Q_n\}$.

2.8. Physical relationships. Dimensional homogeneity

Science is concerned only with expressing physical relationships between quantities characterizing different phenomena. In quantitative analysis of physical phenomena (objects, events, processes) one seeks mathematical relationships (expressions, functions, equations, inequalities) between the numerical values of the physical quantities that describe the phenomenon.

Nature is indifferent to the arbitrary choices of base units. So, we are interested only in numerical relationships that remain true independent of base unit size.

This puts certain constraints on the allowable form of physical relationships. In other words, a physical relationships must be dimensionally homogeneous. Dimensional homogeneity

imposes the following constraints on any mathematical representation of a relationship:

1. Both sides of the relationship must have the same dimension;
2. Wherever a sum of quantities appears in relationship, all the terms in the sum must have the same dimension;
3. All arguments of any exponential, logarithmic, trigonometric or other special functions that appear in functions must be dimensionless.

   For example, if physical equation is represented by:

$$A = Be^{-C} - \frac{(D_1 + D_2)}{E} + F\sin(\Omega t + \varphi) + G\log_{10}\left(\frac{H}{J}\right), \tag{2.9}$$

C must be dimensionless, D_1 and D_2 must have the same dimension, A, B, D/E, F and G must have the same dimension, $(\Omega t+\varphi)$ and H/J must be dimensionless.

An important consequence of dimensional homogeneity is that the forms of a physical relationships are independent of the size of the base units.

Every correct physical function, equation, inequality – that is, every relationship that expresses a physically significant dependence between numerical values of physical quantities – must be dimensionally homogeneous.

2.9. Recapitulation

The most important inferences, conclusions and statements of the considerations presented in p. 2 can be formulated as follows [35]:

1. A base quantity is a property that is defined in physical terms by two operations: a comparison operation, and an addition operation.
2. Base quantities are properties for which the following concepts are defined in terms of physical operations: equality, addition, subtraction, multiplication by a pure number, and division by a pure number. Not defined in terms of physical operations are: product, ratio, power, and logarithmic, exponential, trigonometric and other special functions of physical quantities.
3. A base quantity can be measured in terms of an arbitrarily chosen unit of its own kind and a numerical value.
4. A derived quantity is defined in terms of numerical value (which depends on base unit size) and dimension. Both are defined by power-law formula (2.7) and (2.8).
5. The same quantity (e.g. force) may have different dimensions in different systems of units, and quantities that are clearly physically different (e.g. work and torque) may have the same dimension.
6. Relationships between physical quantities may be represented by mathematical relationships between their numerical values. A mathematical expression, function, equation, inequality etc. that correctly describes a physical relationship between quantities is dimensionally homogeneous.
7. A system of units is defined by (a) the base quantities, (b) their units, and (c) the derived quantities. Both the type and the number of base quantities are open to choice.

3. Fundamental principles of dimensional analysis and model similarity of physical phenomena

These fundamental principles are listed below:

1. Real or postulated physical laws which are used in descriptions of physical phenomena should be objective, i.e. independent of the system of units adopted. It must be possible to transform a dimensional set of physical dependencies and then mathematical relationships (functions, formulas, expressions, equations, inequalities, etc.) which describe any physical phenomenon (more precisely – physical model and then mathematical model of that phenomenon) into a dimensionless form, in which the form does not depend on the system of units. Among all dimensional quantities characterizing some physical phenomenon it must be possible to create dimensionless quantities which appear in such relationships. This also concerns all mathematical operators which appear in these relationships. Moreover, dimensionless relationships describing some physical phenomenon must satisfy the principle of dimensional homogeneity too – as was pointed out previously.
2. Two physical phenomena are similar if:

- The structure of the relationships and mathematical operators used that describe these phenomena are similar;
- Dimensionless form of relationships describing these phenomena is similar.

3. Two types of similarity phenomena are distinguished:

- Similarity of analogy type similarity, where two phenomena have different physical natures (e.g. mechanical and electrical oscillations one degree of freedom systems presented in Fig. 1.)
- Similarity of model type similarity, where two physical phenomena have a similar physical nature but they are different with respect to the scale of this phenomenon (e.g. phenomenon in the natural scale and a phenomenon model in a smaller scale, but scales of particular physical quantities characterizing this phenomena can be different). In further considerations the second case will be considered, i.e. model similarity.

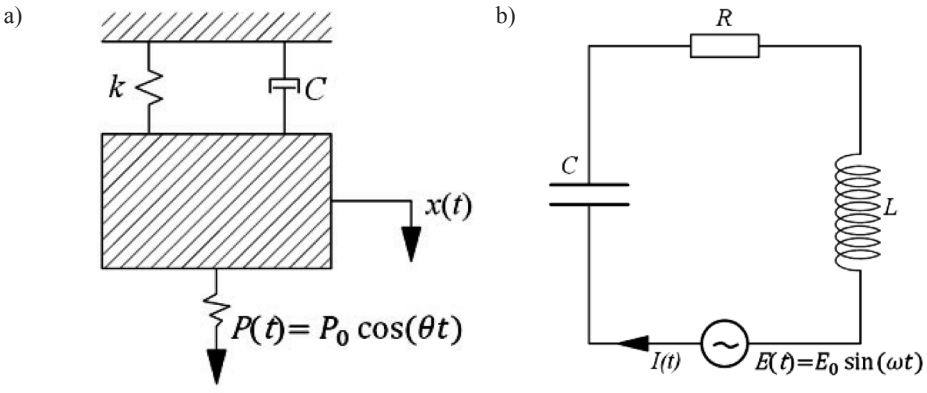

Fig. 1. One degree of freedom mechanical system (a) and its electrical analogy (b)

4. In dimensionless form relationships describing a given physical phenomenon at the natural scale (N) and the model scale (smaller) (M) appear dimensionless numbers dependent on the particular physical quantities characterizing that phenomenon and its scale. In general, the values of these numbers at the natural scale and the model scale are different. To make the phenomena similar, these numbers at the natural and model scales should be equal to each other. These are the model similarity criteria of both phenomena. The numbers are called similarity numbers. Their quotient – respectively at the natural and model scales should be equal to one. Hence, similarity criteria (or relationships) can be determined for the scales of different physical quantities characterizing a given physical phenomenon.
5. There is usually a cause and effect nature of physical phenomena. In this case, among all the dimensional and dimensionless physical quantities, characterizing a given cause and effect physical phenomenon, it is always possible to separate physical quantities connected with input – IN (action on system), system – O (material object), and output – OU (response of system, reaction of system). Then, physical phenomena can be described and analysed using terminology, notions, concepts and block diagrams of systems analysis treating physical phenomena as input/output physical systems. In the case of compound systems, there are in general several inputs, objects and outputs.

The essence of model investigations is to determine from the measurements dimensionless quantities of output (OU) at given quantities of input (IN) and system (O) and with criteria satisfying total or partial similarity. The numerical values of dimensionless output quantities obtained can then be transferred to the real system (natural scale) as the resulting similarity criteria numbers.

4. Buckingham's Π-theorem of dimensional analysis and theory of similarity

4.1. The steps of dimensional analysis and Buckingham's Π-theorem

The form of any physically significant function, equation, or inequality must be such that the relationship between the actual physical quantities remains valid independent of the magnitudes of the base units. Dimensional analysis derives the logical consequences of this premise. Buckingham's Π-theorem, which follows from dimensional analysis, can be performed using the four steps of dimensional analysis presented below [35].

Suppose we are interested in some particular physical quantity Q_0 that is a "dependent variable" in a well-defined physical process or event. By this we mean that, once all the quantities that define the particular process or event are specified, the value of Q_0 follows uniquely.

Step 1: The independent variables

The first and most important step in dimensional analysis is to identify a complete set of independent quantities $Q_1 ... Q_n$ that determine the value of Q_0:

$$Q_0 = f\left(Q_1, Q_2, \ldots, Q_n\right) \tag{4.1}$$

Starting with the correct set $Q_1 \ldots Q_n$ is as important in dimensional analysis as it is in mathematical physics to start with the correct fundamental equations and boundary conditions.

The relationship expressed symbolically in equation (4.1) is the result of the physical laws that govern the phenomenon of interest.

Step 2: Dimensional considerations

Next we list the dimensions of the dependent variable Q_0 and the independent variables $Q_1 \ldots Q_n$. We must specify at least the type of the system of units before we do this. For example, in a purely mechanical problem, all quantities have dimensions of the form:

$$[Q_i] = [L]^{l_i} [M]^{m_i} [T]^{t_i} ; \; i = 0,1,2,\ldots,n, \tag{4.2}$$

where the exponents l_i, m_i and t_i are dimensionless numbers that follow from each quantity's definition.

We now pick from the complete set of physically independent variables $Q_1 \ldots Q_n$ a complete, dimensionally independent subset $Q_1 \ldots Q_k$ ($k \leq n$), and express the dimension of each of the remaining independent variables $Q_{k+1} \ldots Q_n$ and the dependent variable Q_0 as a product of the powers of $Q_1 \ldots Q_k$.

Since equation (4.1) is dimensionally homogeneous, the dimension of the dependent variable Q_0 is also expressible in terms of the dimensions of $Q_1 \ldots Q_k$.

The dimensionally independent subset $Q_1 \ldots Q_k$ may be selected in different ways, but the number k of dimensionally independent quantities in the full set $Q_1 \ldots Q_n$ is unique to the set and cannot exceed the number of base dimensions which appear in the dimensions of the quantities in that set. For example, if the dimensions of $Q_1 \ldots Q_n$ involve only length, mass, and time, then $k \leq 3$.

Having chosen a complete, dimensionally independent subset $Q_1 \ldots Q_k$, we express the dimensions of Q_0 and the remaining quantities $Q_{k+1} \ldots Q_n$ in terms of the dimensions of $Q_1 \ldots Q_k$. These will have the form:

$$[Q_j] = [Q_1]^{\alpha_{j1}} [Q_2]^{\alpha_{j2}} \cdots [Q_k]^{\alpha_{jk}} \tag{4.3}$$

if $j > k$ or $j = 0$. The exponents are dimensionless real numbers and $l = 1,2,\ldots,k$.

Let us take Q_1, Q_2, and Q_3 as the complete dimensionally independent subset. Equating the dimension given by equation (4.2) with that of equation (4.3), we obtain three equations:

$$l_j = \sum_{l=1}^{3} \alpha_{jl} l_l \quad m_j = \sum_{l=1}^{3} \alpha_{jl} m_l \quad t_j = \sum_{l=1}^{3} \alpha_{jl} t_l \tag{4.4}$$

which can be solved for the three unknowns α_{j1}, α_{j2}, and α_{j3}.

Step 3: Dimensionless variables

We now define dimensionless forms of the n-k remaining independent variables by dividing each one with the product of the powers of $Q_1 \ldots Q_k$ which has the same dimension:

$$\breve{\Pi}_j = \frac{Q_j}{Q_1^{\alpha_{j1}} + Q_2^{\alpha_{j2}} \ldots Q_k^{\alpha_{jk}}} \tag{4.5}$$

where $j = k+1,\ldots,n$, and a dimensionless form of the dependent variable Q_0:

$$\breve{\Pi}_0 = \frac{Q_0}{Q_1^{\alpha_{01}} + Q_2^{\alpha_{02}} \ldots Q_k^{\alpha_{0k}}} \tag{4.6}$$

Step 4: The end game and Buckingham's Π–theorem

An alternative form of equation (4.1) is:

$$\breve{\Pi}_0 = f^* \left(Q_1, Q_2, \ldots, Q_k; \breve{\Pi}_{k+1}, \breve{\Pi}_{k+2}, \ldots, \breve{\Pi}_n\right) \tag{4.7}$$

in which all quantities are dimensionless except $Q_1 \ldots Q_k$. The values of the dimensionless quantities are independent of the sizes of the base units. The values of $Q_1 \ldots Q_k$, on the other hand, do depend on base unit size. They cannot be put in dimensionless form since they are (by definition) dimensionally independent of each other. From the principle that any physically meaningful relationships (i.e. the function in the case analysed) must be dimensionally homogeneous, that is, valid independent of the sizes of the base units, it follows that $Q_1 \ldots Q_k$ must in fact be absent from equation (4.7), that is:

$$\breve{\Pi}_0 = \breve{f}\left(1,1,\ldots,1;\breve{\Pi}_{k+1},\breve{\Pi}_{k+2},\ldots,\breve{\Pi}_n\right) = \breve{f}\left(\breve{\Pi}_{k+1},\breve{\Pi}_{k+2},\ldots,\breve{\Pi}_n\right) \tag{4.8}$$

This equation is the final result of the dimensional analysis, and is the base of Buckingham's *Π*-theorem*:*

When a complete relationship between dimensional physical quantities is expressed in dimensionless form, the number of independent quantities that appear in it is reduced from the original n to n-k, where k is the number of the dimensional base size, which reduces the number of independent quantities in the problem by k and simplifies the problem enormously.

The Π-theorem itself merely tells us the number of dimensionless quantities that affect the value of a particular dimensionless dependent variable. It does not tell us the forms of the dimensionless variables. That form has to be discovered by experimentation or by solving the problem theoretically knowing the mathematical model of the problem.

Dimensionless numbers $\breve{\Pi}_j$; j=k+1, k+2,…,n are independent of the system of units and constitute specified similarity criteria (similarity criteria numbers) of a given physical phenomenon with other similar to its physical phenomenon. In the case of two phenomena *I* and *II* of different physical nature but similar in terms of analogy type similarity: $\breve{\Pi}_j^I = \breve{\Pi}_j^{II}$. In the case of two physical phenomena of the same physical nature but of two scales: real (*N*) and model (*M*), similar in terms of model similarity: $\breve{\Pi}_j^N = \breve{\Pi}_j^M$.

In the case when an initial functional relationship is performed in a form of implicit function, i.e.:

$$F(Q_0, Q_1, ..., Q_n) = 0 \tag{4.9}$$

where respective dimension quantities $Q_0, Q_1, \ldots, Q_N$ are quantities dependent or independent of each other, the successive steps of dimensional analysis leading to the theorem Π are similar as before and final result is as follows:

$$\breve{F}\left(\breve{\Pi}_0, \breve{\Pi}_1, \ldots \breve{\Pi}_{n-k}\right) = 0 \tag{4.10}$$

4.2. The second method of reaching Buckingham's Π-theorem

There are n dimensional physical quantities: $Q_1, Q_2, \ldots, Q_n$; some of these may be dependent on others. Furthermore, there is a functional relationship between these quantities:

$$F(Q_1, Q_2,...,Q_n) = 0 \tag{4.11}$$

Moreover, one may consider the basic dimensional base of the physical phenomenon described by relationship (4.11) i.e. $\{A_1,A_2,\ldots,A_k\}$. Dimension of any dimensional quantity Q_i; $i = 1,2,\ldots,n$ can be performed as a product of the powers of base quantities A_l, $l = 1,2,\ldots,k$ as:

$$\begin{aligned}
[Q_1] &= [A_1]^{\alpha_{11}} [A_2]^{\alpha_{21}} \ldots [A_k]^{\alpha_{k1}} \\
[Q_2] &= [A_1]^{\alpha_{12}} [A_2]^{\alpha_{22}} \ldots [A_k]^{\alpha_{k2}} \\
&\ldots \\
[Q_n] &= [A_1]^{\alpha_{1n}} [A_2]^{\alpha_{2n}} \ldots [A_k]^{\alpha_{kn}}
\end{aligned} \tag{4.12}$$

The basic issue can be formulated as follows: are there any dimensionless expressions in the form:

$$\breve{\Pi} = Q_1^{q_1} Q_2^{q_2} \ldots Q_k^{q_k}, \tag{4.13}$$

where $q_1, q_2, \ldots, q_k$ – real numbers, and how many such numbers $\breve{\Pi}$ are there in the particular case? Since:

$$\left[\breve{\Pi}\right] = [A_1]^0 [A_2]^0 \ldots [A_k]^0 == \left([A_1]^{\alpha_{11}} [A_2]^{\alpha_{21}} \ldots [A_k]^{\alpha_{k1}}\right)^{q_1} \ldots \left([A_1]^{\alpha_{1n}} [A_2]^{\alpha_{2n}} \ldots [A_k]^{\alpha_{kn}}\right)^{q_n} \tag{4.14}$$

hence, by comparing the exponents of base quantities, it can be obtained:

$$\begin{aligned}
&\alpha_{11}q_1 + \alpha_{12}q_2 + \ldots + \alpha_{1n}q_n = 0 \\
&\alpha_{21}q_2 + \alpha_{22}q_2 + \ldots + \alpha_{2n}q_n = 0 \\
&\ldots \\
&\alpha_{k1}q_1 + \alpha_{k2}q_2 + \ldots + \alpha_{kn}q_n = 0
\end{aligned} \tag{4.15}$$

This is a homogeneous system of linear equations consisting of k equations of n unknowns.

The question of the system's solvability comes down thereby to the question of rank of the following dimensional matrix:

	Q_1	Q_2	…	Q_n
A_1	α_{11}	α_{12}	…	α_{1n}
A_2	α_{21}	α_{22}	…	α_{2n}
…	…	…	…	…
A_k	α_{k1}	α_{k2}	…	α_{kn}

As we know, the rank of a matrix is expressed as r if it consists of one determinant different from zero of the rank r at least, while the other determinants of higher order are zeros. So, it is correct to use the theorem from linear algebra to the relationships (4.15): homogeneous, linear set of equations with n unknowns, whose matrix has coefficient of rank r, have exactly n-r independent solutions. With respect to our basic problem of dimensional analysis it looks as follows (Buckingham's Π-theorem): There are n quantities Q_1, Q_2, …, Q_n and a dependence (4.11) between them. Thus, there exist exactly n-r dimensionless quantities $\breve{\Pi}$, wherein the rank of dimensional matrix is $r \le m \le n$. Dependence: $\breve{F}\left(\breve{\Pi}_1, \breve{\Pi}_2, \ldots, \breve{\Pi}_{n-r}\right) = 0$ is the solution of this issue.

4.3. The third (original) method of reaching Buckingham's Π-theorem

For dependent and independent dimensional quantities $Q_1, Q_2, \ldots Q_n$ appearing in the functional relationship $F(Q_1, Q_2, \ldots Q_n) = 0$ it dimensionless quantities $Q_{ref,1}$, $Q_{ref,2}, \ldots, Q_{ref,n}$ can be created, assuming for each of these quantities Q_i, $i = 1,2 \ldots n$ some reference quantities $Q_{ref,i}$ in the following way:

$$\breve{Q}_{ref,i} = \frac{Q_i}{Q_{ref,i}} \tag{4.16}$$

And then the starting functional relationship can be performed in such a form:

$$F\left(\breve{Q}_{ref,1} Q_{ref,1}, \breve{Q}_{ref,2} Q_{ref,2}, \ldots, \breve{Q}_{ref,n} Q_{ref,n}\right) = 0 \tag{4.17}$$

where $\breve{Q}_{ref,i} Q_{ref,i}$ quantities are ordered in such a way that among the first few k quantities $Q_{ref,l}$, l=1,2,…,k it is possible to create the complete dimensional base of the problem. Thus, the dimensions of the other quantities $Q_{rej,j}$, j=k+1, k+2, ..., n (there is number n-k of them) can be performed in such a form:

$$\left[Q_{ref,j}\right] = \left[Q_{ref,1}\right]^{\alpha_{ref,1j}} \left[Q_{ref,2}\right]^{\alpha_{ref,2j}} \ldots \left[Q_{ref,k}\right]^{\alpha_{ref,kj}} \tag{4.18}$$

Hence, the following dimensionless quantities (numbers) $\breve{\Pi}^*_{Q_{ref,j}}$ and $\breve{\Pi}_{Q_{ref,j}}$ can be defined:

$$\breve{\Pi}^*_{Q_{ref,j}} = \frac{Q_{ref,j}}{Q_{ref,1}^{\alpha_{ref,1j}} Q_{ref,2}^{\alpha_{ref,2j}} \ldots Q_{ref,k}^{\alpha_{ref,kj}}} \tag{4.19}$$

$$\breve{\Pi}_{Q_{ref,j}} = \breve{Q}_{ref,l} \breve{\Pi}^*_{Q_{ref,j}} \tag{4.20}$$

Then function (4.17) can also be written in another form, namely:

$$F^*\left(\left\{\ldots, \breve{Q}_{ref,l}, \ldots\right\}; \left\{\ldots, Q_{ref,l}, \ldots\right\}; \left\{\ldots, \Pi_{Qref,j}, \ldots\right\}\right) = 0$$

$$l = 1,2,\ldots,k; j = k+1,\ldots,n \tag{4.21}$$

Since the physical laws and all the other relationships connected with them should be objective, they must be able to be written in dimensionless form in which dimensional quantities $Q_{ref,l}$ do not exist as they are dependent on a choice of measure unit system. This form is presented below:

$$\breve{F}\left(\left\{\ldots,\breve{Q}_{ref,l},\ldots\right\};\left\{\ldots,1_{ref,l},\ldots\right\};\left\{\ldots,\breve{\Pi}_{Qref,j},\ldots\right\}\right)=0 \tag{4.22}$$

If we change the scale of quantities: Q_i, i.e.:

$$\frac{Q_i^M}{Q_i^N}=\breve{k}_{Qi}=\frac{Q_{ref,i}^M}{Q_{ref,i}^N}=\frac{\breve{Q}_{ref,i}^M Q_{ref,i}^M}{\breve{Q}_{ref,i}^N Q_{ref,i}^N} \tag{4.23}$$

dimensionless quantities $\breve{Q}_{ref,i}$ do not change (i.e. $\breve{Q}_{ref,i}^M=\breve{Q}_{ref,i}^N$). Dimensionless quantities $\breve{\Pi}_{Qref,j}$ are or may be changed. And actually they represent model similarity criteria of two phenomena of similar nature but in two different scales.

Relationship (4.22) can be written shorter:

$$\breve{F}\left(\left\{\ldots,\breve{Q}_{ref,l},\ldots\right\};\left\{\ldots,\breve{\Pi}_{Qref,j},\ldots\right\}\right)=0 \tag{4.24}$$

Numbers $\breve{Q}_{ref,l}$ are in a specific case known numbers (constants) whereas variable dimensionless quantities (dependent or independent) of a specific case (physical phenomenon, process) are dimensionless numbers $\breve{\Pi}_{Qref,j}$.

In some special case, when $Q_{ref,l}=Q_l$, $\breve{Q}_{ref,l}=1$, the form of the relationship (4.24) takes an analogous form as in first case of deriving the theorem Π.

5. Model similarity scales of physical phenomena

From dimensional analysis one can also derived certain general relationships, which can be compiled in the case of scales of physical quantities characterizing some physical phenomenon. Therefore, if a set of these physical quantities is denoted as (Q_p, Q_q, Q_r; Q_1,Q_2,…,Q_n), where (Q_p,Q_q,Q_r) form dimensional base of phenomenon, i.e. dimensionally independent quantities, which contain dimensions of basic base M, $L$and T (e.g. in mechanical problems), the following relationships can be written:

$$[Q_1]=[Q_p]^{\alpha_1}[Q_q]^{\beta_1}[Q_r]^{\gamma_1} \qquad [Q_n]=[Q_p]^{\alpha_n}[Q_q]^{\beta_n}[Q_r]^{\gamma_n} \tag{5.1}$$

$$\left(\frac{Q_1}{Q_p^{\alpha_1}Q_q^{\beta_1}Q_r^{\gamma_1}}\right)_M=\breve{\Pi}_{1M}=\breve{\Pi}_{1N}=\left(\frac{Q_1}{Q_p^{\alpha_n}Q_q^{\beta_n}Q_r^{\gamma_n}}\right)_N$$

$$\left(\frac{Q_n}{Q_p^{\alpha_n}Q_q^{\beta_n}Q_r^{\gamma_n}}\right)_M=\breve{\Pi}_{nM}=\breve{\Pi}_{nN}=\left(\frac{Q_n}{Q_p^{\alpha_n}Q_q^{\beta_n}Q_r^{\gamma_n}}\right)_N \tag{5.2}$$

or

$$\frac{Q_{1M}}{Q_{1N}} = \breve{k}_{Q_1} = \frac{\left(Q_p^{\alpha_1} Q_q^{\beta_1} Q_r^{\gamma_1}\right)_M}{\left(Q_p^{\alpha_1} Q_q^{\beta_1} Q_r^{\gamma_1}\right)_N} = \breve{k}_{Q_p}^{\alpha_1} \breve{k}_{Q_q}^{\beta_1} \breve{k}_{Q_r}^{\gamma_1} \qquad \frac{Q_{nM}}{Q_{nN}} = \breve{k}_{Q_n} = \frac{\left(Q_p^{\alpha_n} Q_q^{\beta_n} Q_r^{\gamma_n}\right)_M}{\left(Q_p^{\alpha_n} Q_q^{\beta_n} Q_r^{\gamma_n}\right)_N} = \breve{k}_{Q_p}^{\alpha_n} \breve{k}_{Q_q}^{\beta_n} \breve{k}_{Q_r}^{\gamma_n} \tag{5.3}$$

where: $\breve{k}_{Qp}, \breve{k}_{Qq}, \breve{k}_{Qr}$ - scales of dimensional base quantities; $\breve{k}_{Q1}, \ldots \breve{k}_{Qn}$ – scales of the other dimensional dependent quantities.

Therefore, it is assumed that the dimensional base of some issue represent the following quantities: velocity v, length L and density ρ (or also reference quantities v_o, L_o, ρ_o), then, transferring the results of measurements obtained from the model to the object in the natural scale, the following relations between scales of dimensional base $\breve{k}_v$, $\breve{k}_L$, $\breve{k}_\rho$ and the scales of the other physical quantities characterizing that phenomenon should be used:

- the scale of actions $\breve{k}_p$:

$$[P]=[v]^2[L]^2[\rho]^1;\ \breve{k}_p = \breve{k}_v^2 \breve{k}_L^2 \breve{k}_\rho \tag{5.4}$$

- the scale of pressures (stresses) $\breve{k}_p$:

$$[p]=[P]^1[L]^{-2};\ \breve{k}_p = \breve{k}_v^2 \breve{k}_\rho \tag{5.5}$$

- the scale of time $\breve{k}_t$:

$$[t]=[v]^{-1}[L]^1;\ \breve{k}_t = \breve{k}_v^{-1} \breve{k}_L \tag{5.6}$$

- the scale of frequency $\breve{k}_f$:

$$[f]=[v]^1[L]^{-1};\ \breve{k}_f = 1/\breve{k}_t = \breve{k}_v \breve{k}_L^{-1} \tag{5.7}$$

- the scale of mass density per unit length of element $\breve{k}_m$:

$$[m]=[L]^2[\rho]^1;\ \breve{k}_m = \breve{k}_L^2 \breve{k}_\rho \tag{5.8}$$

- the scale of moment of mass inertia density per unit length of element $\breve{k}_{mb}$:

$$[m_b]=[L]^4[\rho]^1;\ \breve{k}_{mb} = \breve{k}_L^4 \breve{k}_\rho \tag{5.9}$$

- the scale of longitudinal rigidity $\breve{k}_{EA}$, flexural rigidity $\breve{k}_{EI}$ and torsional rigidity $\breve{k}_{GIs}$:

$$[EA]=[v]^2[L]^2[\rho];\ \breve{k}_{EA} = \breve{k}_v^2 \breve{k}_L^2 \breve{k}_\rho \tag{5.10}$$

$$[EI]=[v]^2[L]^4[\rho];\ \breve{k}_{EI} = \breve{k}_v^2 \breve{k}_L^4 \breve{k}_\rho \tag{5.11}$$

$$[GI_s]=[v]^2[L]^4[\rho];\ \breve{k}_{GIs} = \breve{k}_v^2 \breve{k}_L^4 \breve{k}_\rho = \breve{k}_{EI} \tag{5.12}$$

6. Original generalized theorems Π of dimensional analysis and model similarity of physical phenomena

Let a given physical phenomenon (process, event) describe different physical/ mathematical relationships, and these relationships contain the following set of all physical quantities characteristic of this phenomenon:

$$\{S\} = \left\{\{\ldots, Q_i, \ldots\}; \{\ldots, \breve{\Pi}_{Q,\alpha}, \ldots\}; \{\ldots, C_\beta, \ldots\}; \{\ldots, \breve{C}_\gamma, \ldots\}\right\} \tag{6.1}$$

where the subscripts: $i = 1,2,\ldots n$; $\alpha = 1,2,\ldots,N_\alpha$; $\beta = 1,2,\ldots N_\beta$; $\gamma = 1,2,\ldots N_\gamma$

The set {S} contains the following subsets:

- $\{\ldots, Q_i, \ldots\}$ – subset of dimensional quantities, which can be independent variables, dependent variables or parameters;
- $\{\ldots, \Pi_{Q,\alpha}, \ldots\}$ – subset of dimensionless quantities, which can also be independent variables, dependent variables or parameters;
- $\{\ldots, C_\beta, \ldots\}$ – subset of constant dimensional quantities;
- $\{\ldots \breve{C}_\gamma, \ldots\}$, – subset of constant dimensionless quantities (i.e. subset containing constant numbers).

Quantities Q_i, $\breve{\Pi}_{Q,\alpha}$ and C_β depend on the physical phenomenon scale (may take different values at the natural scale and at the model scale).

For all of dimensional quantities Q_i and C_β of the problem analysed some reference quantities are assumed:

$$Q_i = \breve{Q}_{ref,i} Q_{ref,i} \qquad C_\beta = \breve{C}_{ref,\beta} C_{ref,\beta} \tag{6.2}$$

Further we may assume that $C_\beta = C_{ref,\beta}$, so $\breve{C}_{ref,\beta} = 1$. Let the physical/mathematical model of the physical phenomenon analysed describe a set of relationships comprising the functional operators $F(\ldots)$, equation operators $E(\ldots)$ and inequality operators $I(\ldots)$ of the form:

$$F_p\left(\{\ldots, Q_i, \ldots\}_p; \{\ldots, \breve{\Pi}_{Q,\alpha}, \ldots\}_p; \{\ldots, C_\beta, \ldots\}_p; \{\ldots, \breve{C}_\gamma, \ldots\}_p\right) = O_p;\ p = 1,2,\ldots N_p \tag{6.3}$$

$$E_q\left(\{\ldots, Q_i, \ldots\}_q; \{\ldots, \breve{\Pi}_{Q,\alpha}, \ldots\}_q; \{\ldots, C_\beta, \ldots\}_q; \{\ldots, \breve{C}_\gamma, \ldots\}_q\right) = O_q;\ q = 1,2,\ldots N_q \tag{6.4}$$

$$I_r\left(\{\ldots, Q_i, \ldots\}_r; \{\ldots, \breve{\Pi}_{Q,\alpha}, \ldots\}_r; \{\ldots, C_\beta, \ldots\}_r; \{\ldots, \breve{C}_\gamma, \ldots\}_r\right) \leq O_r \text{ or } \geq O_r;\ r = 1,2,\ldots N_r \tag{6.5}$$

where $\{S\}_p$, $\{S\}_q$,$\{S\}_r$ denote respective p, q, r subsets of the initial set $\{S\}$.

Assuming for dimensional quantities Q_i and C_β a dimensional base $\{Q_{ref,1}, Q_{ref,2}, \ldots, Q_{ref,k}\} = \{\ldots, Q_{ref,l}, \ldots\}$; $l = 1,2,\ldots,k$ which is made from chosen dimensional quantities $Q_{ref,i}$ of the set $\{\ldots, Q_{ref,i}, \ldots\}$, the following dimensionless quantities can be defined (com. p. 4.3):

$$\breve{\Pi}_{Qref,j} = \breve{Q}_{ref,j} \frac{Q_{ref,j}}{Q_{ref,1}^{\alpha ref,1j} Q_{ref,2}^{\alpha ref,2j} \ldots Q_{ref,k}^{\alpha ref,kj}}; \tag{6.6}$$

$$j = k+1, k+2, \ldots, n; n = k + j$$

$$\breve{\Pi}_{Cref,\beta} = \frac{C_\beta}{Q_{ref,1}^{\alpha ref,1\beta} Q_{ref,2}^{\alpha ref,2\beta} \cdots Q_{ref,k}^{\alpha ref,k\beta}} \tag{6.7}$$

Taking into account the basic principles of dimensional analysis and theory of similarity of physical phenomena presented previously (i.e. the principle of dimensional homogeneity and the objectivity of physical phenomena, that is, independence from mathematical relationships describing these phenomena in the unit system), the dimensional dependences (6.3), (6.4) and (6.5) constituting the physical/mathematical model of the given physical phenomenon, can be brought into the following dimensionless form:

$$\breve{F}_p\left(\left\{\ldots,\breve{Q}_{ref,l},\ldots\right\}_p;\left\{\ldots,\breve{\Pi}_{Qref,j},\ldots\right\}_p;\left\{\ldots,\breve{\Pi}_{Q,\alpha},\ldots\right\}_p;\left\{\ldots,\breve{\Pi}_{Cref,\beta},\ldots\right\}_p;\left\{\ldots,\breve{C}_\gamma,\ldots\right\}_p\right)=0_p \tag{6.8}$$

$$\breve{E}_q\left(\left\{\ldots,\breve{Q}_{ref,l},\ldots\right\}_q;\left\{\ldots,\breve{\Pi}_{Qref,j},\ldots\right\}_q;\left\{\ldots,\breve{\Pi}_{Q,\alpha},\ldots\right\}_q;\left\{\ldots,\breve{\Pi}_{Cref,\beta},\ldots\right\}_q;\left\{\ldots,\breve{C}_\gamma,\ldots\right\}_q\right)=0_q \tag{6.9}$$

$$\breve{I}_r\left(\left\{\ldots,\breve{Q}_{ref,l},\ldots\right\}_r;\left\{\ldots,\breve{\Pi}_{Qref,j},\ldots\right\}_r;\left\{\ldots,\breve{\Pi}_{Q,\alpha},\ldots\right\}_r;\left\{\ldots,\breve{\Pi}_{Cref,\beta},\ldots\right\}_r;\left\{\ldots,\breve{C}_\gamma,\ldots\right\}_r\right)=0_i \tag{6.10}$$

Changing the scale of the physical phenomenon, the values of numerical quantities $\breve{Q}_{ref,l}$ and $\breve{C}_\gamma$ do not change. All the other dimensionless quantities Π, i.e. $\breve{\Pi}_{Qref,j}$, $\breve{\Pi}_{Q,\alpha}$ and $\breve{\Pi}_{Cref,\beta}$ depend on the scale of the given physical phenomenon.

Taking into account the above considerations, generalized Π-theorems of dimensional analysis and physical phenomena model similarity can be formulated as follows:

1. A physical/mathematical model of some physical phenomenon can be described by a system of independent mathematical relationships in dimensionless form containing dimensionless mathematical operators of functions: $\breve{F}_p(\ldots)$, equations $\breve{E}_q(\ldots)$, inequalities $\breve{I}_r(\ldots)$and dimensionless quantities characterizing this phenomenon: $\breve{Q}_{ref,l}$, $\breve{\Pi}_{Qref,j}$, $\breve{\Pi}_{Q,\alpha}$, $\breve{\Pi}_{Cref,\beta}$, $\breve{C}_\gamma$: l = 1,2,…,k; j = k+1, k+2,…n; α = 1,2,…,N_α; β = 1,2,…,N_β; γ = 1,2,…,N_γ. Dimensionless quantities $\breve{Q}_{ref,l}$, $\breve{C}_\gamma$ are numbers independent on a scale of some physical phenomenon, whereas dimensionless quantities $\breve{\Pi}_{Qref,j}$, $\breve{\Pi}_{Q,\alpha}$, $\breve{\Pi}_{Cref,\beta}$ are numbers dependent on the scale of this phenomenon. The dimensionless quantities $\breve{\Pi}_{Qref,j}$ and $\breve{\Pi}_{Cref,\beta}$ connected with the dimensional quantities of physical phenomenon Q_j and C_β are k less than all the dimensional quantities Q_i and C_β, where k is the number of elements of the dimensional base of the physical phenomenon.
2. Two phenomena with similar physical nature performed on different scales (e.g. natural scale N and model scale M) are similar if the set of relationships describing the physical/mathematical model of this phenomenon in dimensionless form (6.8), (6.9), (6.10) is the same. The numbers $\breve{\Pi}_{Qref,j}$, $\breve{\Pi}_{Q,}$, $\breve{\Pi}_{Cref,\beta}$ dependent on the scale of the phenomenon are similarity numbers (criteria) of the model similarity of this phenomenon. These numbers, for phenomena executed on two scales, should be equal. At partial model similarity, this satisfies only the equality of the most important criterial numbers, which have the greatest impact on the results of the studied phenomenon. This case is the most common in practice.
3. In the case of cause end effect phenomena, among all dimensionless quantities occurring in relationships (6.8), (6.9), (6.10),we can distinguish quantities connected with input

IN, system (object) O and output OU (or several inputs, subsystems and outputs). The essence of model investigations is to measure in model tests the values of output OU of dimensionless quantities at fulfilment equalities of the greatest number as possible of the other criterial numbers, and at assuming that the physical nature of the phenomenon executed in two scales is similar. Dimensionless quantities of output can be transferred from the model scale to the natural scale (or other) since they represent similarity criteria of the investigated physical phenomenon.

7. The nature of physical phenomena occurring in mechanics of continuous or discrete material mediums

7.1. Concept of an input/output physical system and its physical/mathematical model. Block diagram of a system

Material mediums in mechanics usually are divided into solid body (stiff or deformable) and fluids (liquids and gases). Physical phenomena in mechanics have a cause and effect character.

If for the processes or phenomena related to some material system (object) there is a cause and effect relationship (or relationships), then the block of data related to the cause is called the input (IN), the block of data related to the material system (object), which is the subject of input influence is called the system, characteristic object, or simply object (O), and the third block of data related to the effect of that influence is called the output (OU). In mechanics of material mediums is often called the input action, load or force acting on the system; the system (object) may be called the system, structure, construction, etc. and the output is called response or reaction of the system. Every set of these three blocks of data with one input, one object and one output we will call a simple system (comp. Fig. 2)

If several inputs IN act on the system O and there are also several outputs OU, we call such a system a complex system with several inputs and several outputs. Likewise, each of the series connections, parallel connections, or series-parallel connections of the simple systems create complex series, parallel or series-parallel systems. It is also possible to make complex mixed systems (e.g. a series system including subsystems with a large number of inputs and outputs). Issues of mechanics of material mediums can be classified just as input/output complex mixed systems.

Input and output quantities are sometimes dependent on each other. When system output quantities can influence system input quantities, then that system is called a system with feedback. The aerodynamic feedback which occurs between building vibrations and wind actions on a building is an example of such feedback. Building vibrations change the character of the air flow around the building, and thereby change the distribution of wind pressures on the walls of the building.

Examples of different complex input/output systems are shown schematically in Fig. 3.

For example, the system shown in Fig. 3c can be interpreted as follows: subset O1 is the domain of ground foundations adjacent to building foundations; input IN1 represents vibrations of ground foundations on the part of the outer surface of this domain from the

vibration source direction, which can be seismic or para-seismic excitations; output OU1 represents accelerations (displacements, velocities) of building foundations, which in turn represent cinematic excitation of the building itself, i.e. object O; input IN2 is for example the wind velocity field in front of the building, in the part of the outer surface of the air domain which is adjacent to the building, so subset O2; output OU2 represents the wind pressure field on the walls of the building, which in turn is wind action on the building itself.

The description of the relationships occurring in subsystems of the whole input/output system in mathematical formal "language" we call the mathematical model of that system.

The presentation of a system, actions (loads) on this system, and relationships occurring between them, using a set of some conventional graphic symbols in structural mechanics is called the static scheme of the system (if time is not significant) or the dynamic scheme of the system (if time is significant). If in consideration it is possible to omit the feature of the system called inertia, the dynamic scheme of the system is called the rheology scheme.

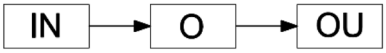

Fig. 2. Block diagram of a simple system (with one input and one output)

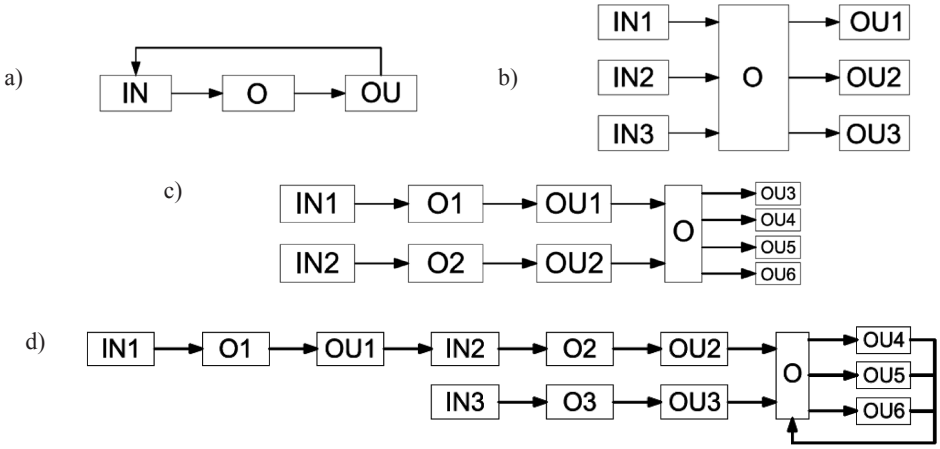

Fig. 3. Examples of block diagrams of complex input/output systems: a) simple system with feedback, b) system with several inputs and outputs, c) parallel system with several inputs and outputs, d) series-parallel system with feedback and several inputs and outputs

7.2. Initial and temporary (final) state of the system. Space-time variables used to describe the object's movement

The position of particular points of an object in the initial state (t_o) and a temporary state (t) is described by coordinates of radius vectors of these points: $\mathbf{r}_{\mathbf{oi}}(t_o)$ and $\mathbf{r}_{\mathbf{i}}(t)$, i.e.

$\{\ldots, x_{oi}, \ldots\}$ and $\{\ldots, x_i(t), \ldots\}$, where i – is the subscript which identifies any i-th point of the system. These coordinates can be defined in the global coordinate system for the whole system $OXYZ$ and/or in local coordinate systems $O_e x_e y_e z_e$ of the various parts of the system, where e – the subscript which identify any e-th element of the system. All of the geometrical quantities characterizing the transition from the system's initial state to a temporary state (displacements, deformations, velocities, accelerations, etc.) can be determined as a function of the initial coordinates $\{\ldots, x_{oi}, \ldots\}$ or of temporary coordinates $\{\ldots, x_i(t), \ldots\}$ and time t. In the first case we talk about a material description (Lagrange's substantial description) of the system movement, and in the second case we talk about a spatial description (Euler's description). It is similar with the other variables or parameters of particular inputs IN_α of objects O_β and outputs OU_γ, where α, β, γ – subscripts identifying particular inputs, objects and outputs of the whole system.

7.3. Types of relationships describing some mechanical phenomenon

In descriptions of some mechanical phenomenon we can distinguish the following groups of geometrical and physical relationships, which we express as mathematical relationships:

- Geometrical relationships describing initial geometry (configuration) of a single system or particular subsystems of the whole system (e.g. boundary surface equations of solid body, axle geometry equations of particular bars of bar system);
- Relationships for quantities related to the restrictions imposed on the system/subsystems, which result from the existence of different type of external/internal constraints of the system/subsystems, which restrain their movement/deformations. These can be kinematic constraints, mechanical constraints or out of mechanical constraints;
- Relationships resulting from initial conditions with respect to excitations (actions) kinematic, mechanical, out of mechanical acting on the system/subsystems;
- Relationships arising from geometry and mechanical laws, connecting quantities which describe the transition of system/subsystems from the initial state (initial configuration) to a temporary/final state (temporary/final configuration);
- Relationships related to imposing different types of restrictions on the system/subsystems connected with their serviceability (serviceability conditions) and safety (limit conditions).

These groups of relationships are associated with specific groups of geometrical and physical quantities (dimensional or dimensionless variables/parameters) dependent on the scale of the phenomenon, dimensional or dimensionless constants independent of the scale of the phenomenon), which in turn represent different subsets $\{S\}_s$ of the initial set $\{S\}$ of all the quantities characterizing this mechanical phenomenon.

The essence of model investigations of mechanical phenomena consists of performing respective investigations (tests) of that phenomenon at a smaller scale, on the fulfilment of model similarity criteria of that phenomenon, and on measurement of dimensionless output quantities of particular subsystems or the system as the whole and the transition of the same values of these quantities to the mechanical phenomenon at the natural scale (or another scale).

8. Example – vibration of a system with one degree of freedom with mechanical and kinematic excitation

The scheme of the system is shown in the Fig. 4.

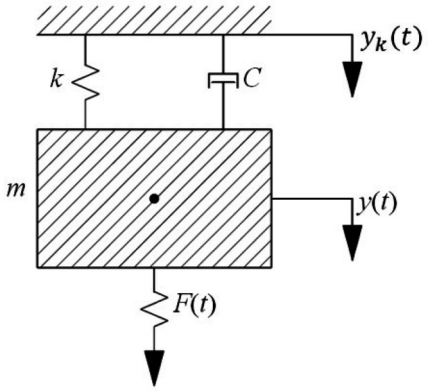

Fig. 4. Scheme of a system with one degree of freedom with kinematic $y_k(t)$ and mechanical excitation F(t)

8.1. Basic denotations and relationships

- The system parameters: m – mass; c - damping, k– rigidity
- Kinematic excitation:

$$y_k(t) = f_{yk}\left(t; Y_k, \sigma_{yk}\right) \tag{8.1}$$

Kinematic excitation is a stochastic process of parameters: Y_k (amplitude of excitation) and σ_{yk} (standard deviation or root-mean-square value of excitation).

- Mechanical excitation (action):

$$F(t) = mg + P_0 \sin(\theta t + \varphi) \tag{8.2}$$

where: mg –gravity force (g – acceleration of gravity); P_0 – amplitude of harmonic excitation; $\theta = 2\pi f = \frac{2\pi}{T}$ – circular frequency of excitation (f – frequency of excitation, T – period of excitation);φ – shift angle in radians.

- Static displacement of the system:

$$y_{st} = \frac{mg}{k} = \frac{g}{\omega^2} = \frac{gT_0^2}{4\pi^2} \tag{8.3}$$

- Absolute displacement $y(t)$, dynamic displacement $y_{dyn}(t)$ and relative displacement $y_{rel}(t)$ of the system:

$$y(t) = y_{st} + y_{dyn} \tag{8.4}$$

$$y_{rel}(t) = y_{dyn}(t) - y_k(t) \tag{8.5}$$

$$y(t) = y_{st} + y_{rel}(t) + y_k(t) \tag{8.6}$$

- System movement equation resulting from the laws of mechanics:

$$m\frac{\mathrm{d}^2 y(t)}{\mathrm{d}t^2} + \left(\frac{\mathrm{d}y(t)}{\mathrm{d}t} - \frac{\mathrm{d}y_k(t)}{\mathrm{d}t}\right) + k\left(y(t) - y_k(t)\right) = mg + P_o \sin\left(\theta t + \varphi\right) \tag{8.7}$$

- Additional denotations:

1. Circular frequency of free vibration ω (f_o – frequency of free vibration, T_o – period of free vibration)

$$\omega = \sqrt{\frac{k}{m}} = 2\pi f_o = \frac{2\pi}{T_o} \tag{8.8}$$

2. Dimensionless parameter of damping (damping ratio) γ:

$$\frac{c}{m} = 2\gamma\omega = 2\gamma\sqrt{\frac{k}{m}}; \quad \gamma = \frac{1}{2}\frac{c}{\sqrt{mk}} \tag{8.9}$$

- Different form of system motion equation:

$$\frac{\mathrm{d}^2 y_{rel}(t)}{\mathrm{d}t^2} + 2\gamma\omega\frac{\mathrm{d}y_{rel}(t)}{\mathrm{d}t} + \omega^2 y_{rel}(t) = -\frac{\mathrm{d}^2 y_k(t)}{\mathrm{d}t^2} + g + \frac{P_o}{m}\sin\left(\theta t + \varphi\right) \tag{8.10}$$

- Initial conditions in time instant t_o=0

$$y_{rel}(0) = y_o; \left.\frac{\mathrm{d}y_{rel}}{\mathrm{d}t}\right|_{t_o=0} = \frac{\mathrm{d}y_{rel}(0)}{\mathrm{d}t} = v_o \tag{8.11}$$

- Limits imposed on the system arising from serviceability and safety conditions:

$$y_{st} = \frac{gT_o^2}{4\pi^2} \le y_{st,lim} \tag{8.12}$$

$$Y_{dyn} = y_{dyn,max} \le y_{dyn,lim} \tag{8.13}$$

$$R(t) = 2\gamma\omega\frac{\mathrm{d}y_{rel}(t)}{\mathrm{d}t} + \omega^2 y_{rel}(t) \le R_{lim} \tag{8.14}$$

8.2. Main set and subsets of dimensional and dimensionless quantities characterizing the problem analysed

- Primary set:

$$\{S\}=\left\{y_{rel},t,2,\gamma,\omega=\frac{2\pi}{T_o},y_k,Y_k,\sigma_{yk},g,P_o,m,\theta=\frac{2\pi}{T},\varphi,y_o,v_o,y_{st,lim},Y_{dyn},y_{dyn,lim},R_{lim}\right\} \quad (8.15)$$

- Subset of variables (dependent and independent) and the dimensional parameters dependent on a phenomenon scale:

$$\{S\}_1=\left\{y_{rel},t,\omega=\frac{2\pi}{T_o},y_k,Y_k,\sigma_{yk},P_o,m,\theta=\frac{2\pi}{T},y_o,v_o,y_{st,lim},Y_{dyn},y_{dyn,lim},R_{lim}\right\} \quad (8.16)$$

- Subset of dimensionless parameters dependent on a phenomenon scale:

$$\{S\}_2=\{\gamma=\breve{\gamma}\} \quad (8.17)$$

- Subset of dimensionless parameters independent on a phenomenon scale

$$\{S\}_3=\{\varphi=\breve{\varphi}\} \quad (8.18)$$

- Subset of constant dimensional quantities:

$$\{S\}_4=\{g\} \quad (8.19)$$

- Subset of dimensionless (numerical) constants:

$$\{S\}_5=\{2\} \text{ or } \{S\}_5=\{2,2\pi,4\pi^2\} \quad (8.20)$$

dependent on the type of parameters that are used: ω and θ or T_o and T.

8.3. Dimensional analysis of the issue and the dimensionless forms of the relationships describing the physical/mathematical model of this issue

8.3.1. The basic reference base

Let the reference base of this issue represent the set of the following dimensional reference quantities:

$$\{B_{ref}\}=\{Y_{rel,ref};T_{ref};M_{ref}\} \quad (8.21)$$

where: $Y_{rel,ref},T_{ref},M_{ref}$ – reference quantities connected with length, time and mass.

The dimensionless reference quantities and mathematical operators (functional, differential) corresponding to this base are as follows:

$$y_{rel} = \breve{y}_{rel,ref} Y_{rel,ref} \tag{8.22}$$

$$t = \breve{t}_{ref} T_{ref} \tag{8.23}$$

$$y_{rel}\left(t\right) = Y_{rel,ref} \frac{y_{rel}\left(\breve{t}_{ref} T_{ref}\right)}{Y_{rel,ref}} = Y_{rel,ref} \breve{y}_{rel,ref}\left(\breve{t}_{ref}\right) \tag{8.24}$$

$$\mathrm{d}\left(y_{rel}\left(t\right)\right) = \mathrm{d}\left(Y_{rel,ref} \breve{y}_{rel,ref}\left(\breve{t}_{ref}\right)\right) = Y_{rel,ref} \mathrm{d}\left(\breve{y}_{rel,ref}\left(\breve{t}_{ref}\right)\right) \tag{8.25}$$

$$\mathrm{d}t = \mathrm{d}\left(\breve{t}_{ref} T_{ref}\right) = T_{ref} \mathrm{d}\breve{t}_{ref} \tag{8.26}$$

$$\frac{\mathrm{d}\left(y_{rel}\left(t\right)\right)}{\mathrm{d}t} = \frac{Y_{rel,ref}}{T_{ref}} \frac{\mathrm{d}\left(\breve{y}_{rel,ref}\left(\breve{t}_{ref}\right)\right)}{\mathrm{d}\breve{t}_{ref}} \tag{8.27}$$

$$\frac{\mathrm{d}^2\left(y_{rel}\left(t\right)\right)}{\mathrm{d}t^2} = \frac{\mathrm{d}}{\mathrm{d}t}\left(\frac{\mathrm{d}\left(y_{rel}\left(t\right)\right)}{\mathrm{d}t}\right) = \frac{Y_{rel,ref}}{T_{ref}^2} \frac{\mathrm{d}^2\left(\breve{y}_{rel,ref}\left(\breve{t}_{ref}\right)\right)}{\mathrm{d}\breve{t}_{ref}^2} \tag{8.28}$$

$$\omega = \frac{2\pi}{T_o} = \frac{2\pi}{\breve{T}_{o,ref} T_{ref}} \tag{8.29}$$

$$y_k\left(t; Y_k, \sigma_{yk}\right) = Y_{rel,ref} \frac{y_k(\breve{t}_{ref} T_{ref}; \breve{Y}_{k,ref} Y_{rel,ref}; \breve{\sigma}_{yk,ref} Y_{rel,ref}}{Y_{rel,ref}} = Y_{rel,ref} \breve{y}_{k,ref}\left(\breve{t}_{ref}; \breve{Y}_{k,ref}; \breve{\sigma}_{yk,ref}\right) \tag{8.30}$$

$$\frac{\mathrm{d}^2\left(y_k\left(t\right); Y_k, \sigma_{yk}\right)}{\mathrm{d}t^2} = \frac{Y_{rel,ref}}{T_{ref}^2} \frac{\mathrm{d}^2(\breve{y}_{k,ref}\left(\breve{t}_{ref}; \breve{Y}_{k,ref}; \breve{\sigma}_{ykref}\right)}{\mathrm{d}t_{ref}^2} \tag{8.31}$$

$$g = \breve{g}_{ref} \frac{Y_{rel,ref}}{T_{ref}^2} \tag{8.32}$$

$$P_o = \breve{P}_{o,ref} \frac{Y_{rel,ref} M_{ref}}{T_{ref}^2} \tag{8.33}$$

$$m = \breve{m}_{ref} M_{ref} \tag{8.34}$$

$$\theta = \frac{2\pi}{T} = \frac{2\pi}{\breve{T}_{ref} T_{ref}} \tag{8.35}$$

$$y_o = y_{rel}\left(0\right) = \breve{y}_{rel,ref}\left(0\right) Y_{rel,ref} \tag{8.36}$$

$$v_o = \frac{\mathrm{d}y_{rel}\left(0\right)}{\mathrm{d}t} = \frac{Y_{rel,ref}}{T_{ref}} \frac{\mathrm{d}\breve{y}_{rel,ref}\left(0\right)}{\mathrm{d}\breve{t}_{ref}} \tag{8.37}$$

$$y_{st,lim} = \breve{y}_{st,lim,ref} Y_{rel,ref} \tag{8.38}$$

$$Y_{dyn} = \breve{Y}_{dyn,ref} Y_{rel,ref} \tag{8.39}$$

$$y_{dyn,lim} = \breve{y}_{dyn,lim,ref} Y_{ref,ref} \qquad (8.40) \qquad R_{lim} = R_{lim,ref} \frac{Y_{rel,ref}}{T_{ref}^2} \qquad (8.41)$$

The relationships which describe the physical/mathematical model of the mechanical phenomenon analysed are written in dimensionless form as follows:

$$\frac{Y_{ref}}{T_{ref}^2} \frac{d^2 \breve{y}_{rel,ref}\left(\breve{t}_{ref}\right)}{d\breve{t}_{ref}^2} + 2\breve{\gamma} \frac{2\pi}{\breve{T}_{o,ref} T_{ref}} \frac{Y_{ref}}{T_{ref}} \frac{d\breve{y}_{rel,ref}}{d\breve{t}_{ref}} + \frac{4\pi^2}{\left(\breve{T}_{o,ref} T_{ref}\right)^2} Y_{ref} \breve{y}_{rel,ref}\left(\breve{t}_{ref}\right) =$$

$$= -\frac{Y_{ref}}{T_{ref}^2} \frac{d^2 \breve{y}_{k,ref}\left(t_{ref}; \breve{Y}_{k,ref}, \breve{\sigma}_{yk,ref}\right)}{d\breve{t}_{ref}^2} + \breve{g}_{ref} \frac{Y_{ref}}{T_{ref}^2} + \frac{\breve{P}_{o,ref}}{\breve{m}_{ref}} \frac{\frac{M_{ref} Y_{ref}}{T_{ref}^2}}{M_{ref}} \sin\left(\frac{2\pi}{\breve{T}_{ref} T_{ref}} \breve{t}_{ref} T_{ref} + \breve{\varphi}\right) \qquad (8.42)$$

or after dividing the equation by $\frac{Y_{ref}}{T_{ref}^2}$:

$$\frac{d^2 \breve{y}_{rel,ref}(\breve{t}_{ref})}{d\breve{t}_{ref}^2} + 2\breve{\gamma} \frac{2\pi}{\breve{T}_{o,ref}} \frac{d\breve{y}_{rel,ref}\left(\breve{t}_{ref}\right)}{d\breve{t}_{ref}} + \frac{4\pi^2}{\breve{T}_{o,ref}^2} \breve{y}_{rel,ref}\left(\breve{t}_{ref}\right) =$$

$$= -\frac{d^2 \breve{y}_{k,ref}\left(\breve{t}_{ref}; \breve{Y}_{k,ref}; \breve{\sigma}_{yk,ref}\right)}{d\breve{t}_{ref}^2} + \breve{g}_{ref} + \frac{\breve{P}_{o,ref}}{\breve{m}_{ref}} \sin\left(\frac{2\pi}{\breve{T}_{ref}} \breve{t}_{ref} + \breve{\varphi}\right) \qquad (8.43)$$

$$\breve{y}_{rel,ref}(0) = \frac{y_o}{Y_{ref}} \qquad (8.44) \qquad \frac{d\breve{y}_{ref,ref}(0)}{d\breve{t}_{ref}} = \frac{v_o T_{ref}}{Y_{ref}} \qquad (8.45)$$

$$\breve{g}_{ref} \frac{Y_{ref}}{T_{ref}^2} \frac{\breve{T}_{o,ref}^2 T_{ref}^2}{4\pi^2} \le \breve{y}_{st,\lim,ref} Y_{ref} \qquad (8.46) \quad \text{or:} \qquad \breve{g}_{ref} \frac{\breve{T}_{o,ref}^2}{4\pi^2} \le \breve{y}_{st,\lim,ref} \qquad (8.47)$$

$$\breve{Y}_{dyn,ref} Y_{ref} \le \breve{y}_{dyn,\lim,ref} Y_{ref} \qquad (8.48) \quad \text{or:} \qquad \breve{Y}_{dyn,ref} \le \breve{y}_{dyn,\lim,ref} \qquad (8.49)$$

$$2\breve{\gamma} \frac{2\pi}{\breve{T}_{o,ref} T_{ref}} \frac{Y_{ref}}{T_{ref}} \frac{d\breve{y}_{rel,ref}\left(\breve{t}_{ref}\right)}{d\breve{t}_{ref}} + \frac{4\pi^2}{T_{o,ref}^2 T_{ref}^2} Y_{ref} \breve{y}_{rel,ref}\left(\breve{t}_{ref}\right) \le \frac{Y_{ref}}{T_{ref}^2} \breve{R}_{\lim,ref} \qquad (8.50)$$

or

$$2\breve{\gamma} \frac{2\pi}{\breve{T}_{o,ref}} \frac{d\breve{y}_{rel,ref}\left(\breve{t}_{ref}\right)}{d\breve{t}_{ref}} + \frac{4\pi^2}{\breve{T}_{o,ref}} \breve{y}_{rel,ref}\left(\breve{t}_{ref}\right) \le \breve{R}_{\lim,ref} \qquad (8.51)$$

When the scale of the mechanical phenomenon is changed, i.e. when the corresponding scales are:

$$\breve{k}_{yrel} = \breve{k}_{Yrel,ref}; \breve{k}_t = \breve{k}_{Tref}; \breve{k}_m = \breve{k}_{Mref} \tag{8.52}$$

dimensionless quantities: $\breve{y}_{rel,ref}, \breve{t}_{ref}, \breve{m}_{ref}$ are the same at the natural scale (N) as well as at the model scale (M), so that they are not dependent on the scale of the phenomenon.

Moreover, in the above relationships the following dimensionless quantities $\breve{\Pi}_{ref,j}$, $j = 1,2,\ldots,15$ occur dependent on the scale of the mechanical phenomenon, which constitute the model similarity criteria (conditions, numbers) of that phenomenon:

$$\breve{\gamma} = \frac{c}{2\sqrt{km}} = \breve{\Pi}_{ref,1} \tag{8.53}$$

$$T_{o,ref} = \frac{2\pi}{\sqrt{\frac{k}{m}}T_{ref}} = \breve{\Pi}_{ref,2} \tag{8.54}$$

$$\breve{y}_{k,ref} = \frac{y_k}{Y_{rel,ref}} = \breve{\Pi}_{ref,3} \tag{8.55}$$

$$\breve{Y}_k = \frac{Y_k}{Y_{rel,ref}} = \breve{\Pi}_{ref,4} \tag{8.56}$$

$$\breve{\sigma}_{yk,ref} = \frac{\sigma_{yk}}{Y_{rel,ref}} = \breve{\Pi}_{ref,5} \tag{8.57}$$

$$\breve{g}_{ref} = \frac{gT_{ref}^2}{Y_{rel,ref}} = \breve{\Pi}_{ref,6} \tag{8.58}$$

$$\breve{P}_{o,ref} = \frac{P_o T_{ref}^2}{M_{ref} Y_{ref,ref}} = \breve{\Pi}_{ref,7} \tag{8.59}$$

$$\breve{T}_{ref} = \frac{2\pi}{\theta_{T_{ref}}} = \breve{\Pi}_{ref,8} \tag{8.60}$$

$$\breve{\varphi} = \breve{\Pi}_{ref,9} \tag{8.61}$$

$$\breve{y}_{rel,ref}(0) = \frac{y_o}{Y_{rel,ref}} = \breve{\Pi}_{ref,10} \tag{8.62}$$

$$\frac{\mathrm{d}\breve{y}_{rel,ref}(0)}{\mathrm{d}t_{ref}} = \frac{v_o T_{ref}}{T_{rel,ref}} = \breve{\Pi}_{ref,11} \tag{8.63}$$

$$\breve{y}_{st,lim,ref} = \frac{y_{st,lim}}{Y_{rel,ref}} = \breve{\Pi}_{ref,12} \tag{8.64}$$

$$\breve{Y}_{dyn,ref} = \frac{Y_{dyn}}{Y_{rel,ref}} = \breve{\Pi}_{ref,13} \tag{8.65}$$

$$\breve{y}_{dyn,lim,ref} = \frac{y_{dyn,lim}}{Y_{rel,ref}} = \breve{\Pi}_{ref,14} \tag{8.66}$$

$$\breve{R}_{lim,ref} = \frac{R_{dop} T_{ref}^2}{Y_{rel,ref}} = \breve{\Pi}_{ref,15} \tag{8.67}$$

Thus, there are fifteen dimensionless numbers in total.

Moreover, in relationships describing the mechanical issue analysed, constant numbers appear, e.g. 2, 2Π, $4\Pi^2$.

Generally, with the exception of constant numbers, the number of dimensional and dimensionless output quantities characterizing the mechanical phenomenon is eighteen, so three more than numbers $\breve{\Pi}_{ref,j}$, i.e. about as much as the size of the dimensional base of this issue.

8.3.2. Other reference base

One may consider now the case of another reference base of the issue which consists of the following three dimensional reference parameters:

$$\left\{B^{*}_{ref}\right\}=\left\{B\right\}=\left\{\omega, g, m\right\} \tag{8.68}$$

The respective relationships in this case are as follows:

$$y_{rel}=\breve{y}_{rel}\frac{g}{\omega^2} \tag{8.69}$$

$$t=\breve{t}\,\frac{1}{\omega} \tag{8.70}$$

$$\frac{dy_{rel}\left(t\right)}{dt}=\frac{g}{\omega}\frac{d\breve{y}_{rel}\left(\breve{t}\right)}{d\breve{t}} \tag{8.71}$$

$$\frac{d^2y_{rel}\left(t\right)}{dt^2}=g\frac{d^2\breve{y}_{rel}\left(\breve{t}\right)}{d\breve{t}^{\,2}} \tag{8.72}$$

$$\gamma=\breve{\gamma} \tag{8.73}$$

$$y_k\left(t;Y_k,\sigma_{yk}\right)=\frac{g}{\omega^2}\breve{y}_k\left(\breve{t};\breve{Y}_k,\breve{\sigma}_{yk}\right) \tag{8.74}$$

$$Y_k=\breve{Y}_k\frac{g}{\omega^2} \tag{8.75}$$

$$\sigma_{yk}=\breve{\sigma}_{yk}\frac{g}{\omega^2} \tag{8.76}$$

$$\frac{d^2y_k\left(t;Y_k,\sigma_{yk}\right)}{dt^2}=g\frac{d^2\breve{y}_k\left(\breve{t};\breve{Y}_k,\breve{\sigma}_{yk}\right)}{d\breve{t}^{\,2}} \tag{8.77}$$

$$P_o=\breve{P}_o mg \tag{8.78}$$

$$\theta=\breve{\theta}\omega \tag{8.79}$$

$$\varphi=\breve{\varphi} \tag{8.80}$$

$$y_o=\breve{y}_o\frac{g}{\omega^2} \tag{8.81}$$

$$v_o=\breve{v}_o\frac{g}{\omega} \tag{8.82}$$

$$y_{st,lim}=\breve{y}_{st,lim}\frac{g}{\omega^2} \tag{8.83}$$

$$Y_{dyn}=\breve{Y}_{dyn}\frac{g}{\omega^2} \tag{8.84}$$

$$y_{dyn,lim}=\breve{y}_{dyn,lim}\frac{g}{\omega^2} \tag{8.85}$$

$$R_{lim}=\breve{R}_{lim}g \tag{8.86}$$

$$\begin{aligned} &g\frac{d^2\breve{y}_{rel}\left(\breve{t}\right)}{d\breve{t}^{\,2}}+2\breve{\gamma}\omega\frac{g}{\omega}\frac{d\breve{y}_{rel}\left(\breve{t}\right)}{d\breve{t}}+\omega^2\frac{g}{\omega^2}\breve{y}_{rel}\left(\breve{t}\right)= \\ &=-g\frac{d^2\breve{y}_k\left(\breve{t},\breve{Y}_k,\breve{\sigma}_{yk}\right)}{d\breve{t}^{\,2}}+g+\frac{\breve{P}_o mg}{m}\sin\left(\breve{\theta}\omega\frac{1}{\omega}\breve{t}+\breve{\varphi}\right) \end{aligned} \tag{8.87}$$

or after dividing equation by g:

$$\frac{d^2\breve{y}_{rel}(\breve{t})}{d\breve{t}^2}+2\breve{\gamma}\frac{d\breve{y}_{rel}(\breve{t})}{d\breve{t}}+y_{rel}(\breve{t})=-\frac{d^2\breve{y}_k(\breve{t},\breve{Y}_k,\breve{\sigma}_{yk})}{d\breve{t}^2}+1+\breve{P}_o\sin(\breve{\theta}\breve{t}+\breve{\varphi}) \tag{8.88}$$

$$\breve{y}_o=\frac{y_o\omega^2}{g} \tag{8.89}$$

$$\breve{v}_o=\frac{v_o\omega}{g} \tag{8.90}$$

$$1\le\breve{y}_{st,lim}=\frac{y_{st,lim}\omega^2}{g} \tag{8.91}$$

$$\breve{Y}_{dyn}=\frac{Y_{dyn}\omega^2}{g}\le\breve{y}_{dyn,lim}=\frac{y_{dyn,lim}\omega^2}{g} \tag{8.92}$$

$$2\breve{\gamma}\frac{d\breve{y}_{rel}(\breve{t})}{d\breve{t}}+\breve{y}_{rel}(\breve{t})\le\breve{R}_{lim}=\frac{R_{lim}}{g} \tag{8.93}$$

In relationships (8.88) and (8.93) $j = 15$ occurs following the dimensionless numbers $\breve{\Pi}_j$, which constitute the similarity criteria of the case analysed at another dimensional base:

$$\breve{y}_{rel}=\frac{y_{rel}\omega^2}{g}=\breve{\Pi}_1 \tag{8.94}$$

$$\breve{t}=\omega t=\breve{\Pi}_2 \tag{8.95}$$

$$\breve{\gamma}=\frac{c}{2\sqrt{km}}=\breve{\Pi}_{ref,1}=\breve{\Pi}_3 \tag{8.96}$$

$$\breve{y}_k=\frac{y_k\omega^2}{g}=\breve{\Pi}_4 \tag{8.97}$$

$$\breve{Y}_k=\frac{Y_k\omega^2}{g}=\breve{\Pi}_5 \tag{8.98}$$

$$\breve{\sigma}_{yk}=\frac{\sigma_{yk}\omega^2}{g}=\breve{\Pi}_6 \tag{8.99}$$

$$\breve{P}_o=\frac{P_o}{mg}=\breve{\Pi}_7 \tag{8.100}$$

$$\breve{\theta}=\frac{\theta}{\omega}=\breve{\Pi}_8 \tag{8.101}$$

$$\breve{\varphi}=\varphi=\Pi_{ref,9}=\breve{\Pi}_9 \tag{8.102}$$

$$\breve{y}_o=\frac{y_o\omega^2}{g}=\breve{\Pi}_{10} \tag{8.103}$$

$$\breve{v}_o=\frac{v_o\omega}{g}=\breve{\Pi}_{11} \tag{8.104}$$

$$\breve{y}_{st,lim}=\frac{y_{st,lim}\omega^2}{g}=\breve{\Pi}_{12} \tag{8.105}$$

$$\breve{Y}_{dyn}=\frac{Y_{dyn}\omega^2}{g}=\breve{\Pi}_{13} \tag{8.106}$$

$$\breve{y}_{dyn,lim}=\frac{y_{dyn,lim}\omega^2}{g}=\breve{\Pi}_{14} \tag{8.107}$$

$$\breve{R}_{lim} = \frac{R_{lim}}{g} = \breve{\Pi}_{15} \tag{8.108}$$

They are, as can be seen, similarity criteria numbers different from the ones in the first case. Moreover, in the dimensionless relationships of the physical/mathematical model of that issue another set of numerical constants {2,1} appear. The form of these relationships is simpler in the second case.

9. Conclusions

The basic principles and theorems of dimensional analysis and theory of model similarity of physical phenomena presented in this paper can be used in different branches of knowledge and science. The procedure is the same in all applications. These principles and theorems can be applied both in the case when all the equations and boundary conditions of the problem are known and in the case when only the general functional relationships of the problem are known or postulated. Similarity criteria numbers can be derived in general from the original generalized theorems Π of dimensional analysis and model similarity of physical phenomena.

References

[1] Barenblatt G.I., *Scaling, self-similarity, and intermediate asymptotics*, Cambridge University Press, Cambridge, UK 1996.

[2] Baker W.E., Westine P.S., Dodge F. T., *Similarity methods in engineering dynamics*, Hayden, Rochelle Park, NY 1973.

[3] Birkhoff G., *Hydrodynamics,* Princeton University, 1950.

[4] Bridgman P.W., *Dimensional analysis,* 2nd edition (the first edition appeared in 1922), Yale University Press, New Haven, 1931.

[5] Buckingham E., *On physically similar systems, Illustrations of the use of dimensional analysis*, Physical Review, 4,1914, 345-376.

[6] David F.W. Nolle H., *Experimental modelling in engineering,* Butterworths, London 1982.

[7] de Jong F.J., *Dimensional analysis for economists*, Nort Holland, Amsterdam 1967.

[8] Duncan W.J., *Physical similarity and dimensional analysis,* Arnold, London 1955.

[9] Flaga A., *Wind vortex-induced excitation and vibration of slender structures – single structure of circular cross-section normal to flow*, Monograph No. 202, Cracow University of Technology, Cracow 1996.

[10] Flaga A., *Inżynieria wiatrowa, Podstawy i zastosowania*, Arkady, Warszawa 2008.

[11] Flaga A., *Siłownie wiatrowe, Wydawnictwo Politechniki Krakowskiej*, Kraków 2012.

[12] Focken C.M., *Dimensional methods and their applications*, Arnold, London 1953.

[13] Gryboś R., *Podstawy mechaniki płynów*, PWN, Warszawa 1998.

[14] Huntley H. E., *Dimensional analysis,* MacDonald & Co., London 1952.

[15] Ipsen D. C., *Units, dimensions and dimensional number*s, McGraw Hill, New York 1960.
[16] Isaacson E. de St.Q. Isaacson M. de St.Q., *Dimensional methods in engineering and physics: Reference sets and the possibility of their extension,* Wiley, New York 1975.
[17] Kline S.J., *Similitude and approximation theory,* McGraw-Hill, New York 1965.
[18] Kolouek V., Pirner M., Fischer O., Naprstek J., *Wind effects on civil engineering structures*, Academia, Praha 1983.
[19] Kurth R., *Dimensional analysis and group theory in astrophysics*, Pergamon Press, Oxford 1972.
[20] Langhaar H.L., *Dimensional analysis and theory of models,* Wiley, New York 1951.
[21] Lokarnik M., *Dimensional analysis and scale-up in chemical engineering*, Springer Verlag, Berlin 1991.
[22] Macagno E.O., *Historico-critical review of dimensional analysis*, Journal of the Franklin Institute, 292, 1971,391-402.
[23] Martynow A.K., *Eksprиminetalnaja aerodinamika*, Moskwa 1958.
[24] Maxwell J.C., *A treatise on electricity and magnetism*, 3rd Edition, Clarendon Press, Cambridge 1891, republished by Dover, New York, 1954.
[25] McMahon T.A. and Bonner J.T., *On size and life.* Scientific American Library, New York 1983.
[26] Murphy G., *Similitude in engineering,* Ronald Press, New York 1950.
[27] Mller L., *Zastosowania analizy wymiarowej w badaniach modelowych*, PWN, Warszawa 1983.
[28] Palacios J., *Dimensional analysis*, MacMillan, London 1964.
[29] Pankhurst R.D., *Dimensional analysis and scale factors*, Reinhold, New York 1964.
[30] Sachs P., *Wind forces in engineering*, Pergamon Press, 1972.
[31] Schuring D.J., *Scale models in engineering: Bases and applications,* Pergamon, New York 1977.
[32] Siedov L.I., *Similarity and dimensional analysis in mechanics*, Academic Press, New York 1959.
[33] Simiu E. Scanlan R., *Wind effects on structures, An introduction to wind engineering, Fundamentals and applications to the design,* Third edition, John Wiley & Sons, New York 1996.
[34] Skoglund V.J., *Similitude: Theory and applications*, International Textbook Co. Scranton, 1967.
[35] Sonin A.A., *The physical basis of dimensional analysis,* Department of Mechanical Engineering MIT, Cambridge 2001.
[36] Szucs E., *Similitude and modeling*, Elsevier, Amsterdam 1980.
[37] Taylor E.S., *Dimensional Analysis for Engineers,* Clarendon Press, Oxford 1974.
[38] Zierep J., *Similarity and Modeling*, Marcel Dekker, New York 1971.
[39] Zierep J., *Kryteria podobieństwa i zasady modelowania w mechanice płynów*, PWN, Warszawa 1978.

TECHNICAL TRANSACTIONS | CZASOPISMO TECHNICZNE
CIVIL ENGINEERING | BUDOWNICTWO
2-B/2015

RENATA GNATOWSKA*

AN ANALYSIS OF INCOMING WIND PULSATION ON THE WIND EROSION PROCESSES ON A HILL

ANALIZA PODMUCHÓW WIATROWYCH W PROCESIE EROZJI GRUNTU NA POWIERZCHNI WZGÓRZA

Abstract

The present analysis undertakes the problem of surface wind over topography. The main focus is placed upon the effect of oncoming wind oscillations on the velocity field structure around a single sinusoidal shaped 2D hill. Additional effort has been undertaken to recognize the inflow gust influence on the surface shear stress related to the mechanism of wind induced erosion. Numerical simulations have been performed through the use of the phase-averaged form of RNG version of k-ε turbulence model. Experimental verification of numerical data has been done in wind tunnels equipped with devices generating unsteady wind boundary layers. The main findings of the simulations reveal: a strong dependence between the characteristics of inflow periodicity and the structure of vortices of the separation region; the mean position of the reattachment point; the phase averaged velocity field; skin friction variability downstream from the hill. The results have significant implications for the prediction of sand transport in unsteady winds.

Keywords: unsteady winds, surface friction over the bump, numerical modelling, wind erosion

Streszczenie

Niniejsza analiza podejmuje problem przepływu wiatru nad powierzchnią terenu o złożonej topografii. Główny nacisk położono na wpływ oscylacyjnych podmuchów wiatru na strukturę pola prędkości wokół pojedynczego sinusoidalnego 2D wzgórza. Dodatkowy wysiłek podjęto w celu rozpoznania wpływu podmuchów wiatru na powierzchniowe naprężenia ścinające związane z mechanizmem erozji wietrznej. Numeryczne symulacje przeprowadzano z zastosowaniem uśrednionego fazowo modelu turbulencji k-ε w wersji RNG. Weryfikacja danych numerycznych została wykonana w oparciu o wyniki badań eksperymentalnych zrealizowanych w tunelu aerodynamicznym wyposażonym w generator podmuchów wiatru w modelowej warstwie przyziemnej. Główne wnioski z przeprowadzonych symulacji wykazują silną zależność między okresowym charakterem napływu a strukturą wirów w obszarze separacji, średnim położeniem ponownego przylgnięcia; uśrednionym fazowo polem prędkości oraz zmiennością tarcia powierzchniowego za wzgórzem. Wyniki te mają istotne znaczenie dla prognozowania transportu piasku w nieustalonym polu wiatrowym.

Słowa kluczowe: niestacjonarne pole wiatrowe, tarcie powierzchniowe nad wzgórzem, modelowanie numeryczne, erozja wiatrowa

DOI: 10.4467/2353737XCT.15.136.4173

* Faculty of Mechanical Engineering and Computer Science, Czestochowa University of Technology, Poland.

1. Introduction

The experimental and numerical simulation of wind flow over hilly terrain has attracted considerable scientific interest during recent decades, [4, 5], because of the important implications of the problem in many fields (fire propagation, soil erosion, pollutant dispersion). Many factors have to be taken into account in order to accurately predict surface winds over complex terrain. In the predominant number of studies, the structure of the wind approaching the element of topography (hill or other object) is assumed to be steady and represented by a typical boundary layer profile (exponential or logarithmic) over the surface of different aerodynamic roughness. Considerably less effort has been made to take into account the unsteady features of incident wind associated with gust phenomena or large scale periodical pulsations generated in object environment. Wind gusts, which hardly affect the average wind speed and yet have a very strong effect on erosion are especially important in this context. Butterfield [1] indicated the role of sinusoidal velocity variations on sand transport. The present analysis undertakes the problem of the surface wind over topography. The main attention is placed on the effect of oncoming wind oscillations on wind erosion processes.

2. The methods of analysis

To recognize the effect of oscillating incident conditions on the wind flow around the hill, numerical as well as experimental simulations have been performed in the present study for different parameters of inflow periodicity. The hill considered was nominally 2D, symmetric with aspect ratio defined as slope of the hill $H/L = 0.6$ (Fig. 1a). The modelled hill has been placed in the boundary layer formed over the terrain of moderate roughness under the wind conditions characterised by oscillating component superimposed on mean velocity profile. The mean velocity profile can be described by the power law:

$$\bar{U}_0(z) = \bar{U}_\infty \cdot \left(\frac{z}{\delta}\right)^{\alpha} \tag{1}$$

where δ is the depth of boundary layer, and $\alpha = 0.16$ is the power law exponent, which corresponds to the velocity profile for open terrain with low vegetation (Fig. 1b).

Different values of flow frequency f_0 and amplitude A have been introduced into the simulations, described in equation:

$$U_0(t) = \bar{U}_\infty \cdot (1 + A \cdot \sin(2 \cdot \pi \cdot f_0 \cdot t)) \tag{2}$$

The numerical modelling was performed using commercial CFD code ANSYS FLUENT with phase averaged form of RNG version of k-ε turbulence model. Pressure-velocity coupling was performed with the SIMPLEC algorithm. The time step was based on an experimental estimation of the period of flow oscillations. The time step in non-dimensional unit ($\Delta t \cdot U_0/H$)

a)

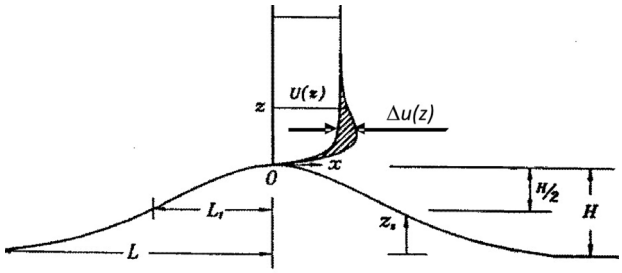

b)

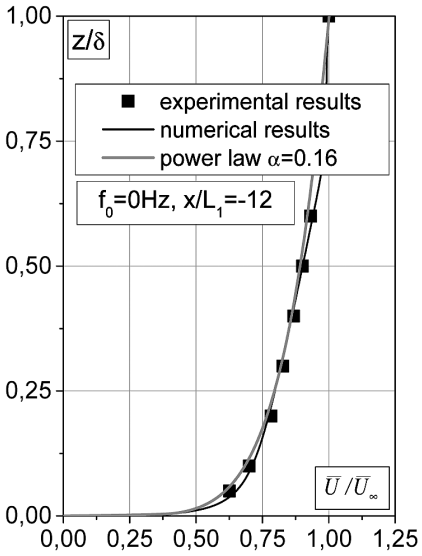

Fig. 1. Scheme of analysed hill (a) and mean velocity profile (b)

was about 0.14 in the present analysis. About 50 time steps per period were necessary to obtain converged pressure and velocity (both averaged) and rms values. A quadrilateral mesh with 15000 cells was generated in the computational domain according to [2, 3]. The hill was located 3 m from the entrance to the working section, perpendicular to the free-stream direction. Properly setting up the boundary conditions at the inlet and outlet of the model allowed for the achievement of an effect of real conditions. The following boundary conditions are used in calculations: at the inlet VELOCITY INLET; at the outlet PRESSURE OUTLET; for the upper and lower walls and the cylinder surface (WALL condition).

Experimental verification of numerical data was done in wind tunnels equipped with devices generating an unsteady wind boundary layer. Wind tunnel experiments comprised the modelling of unsteady wind conditions in the flow approaching the model of the hill, measurements of velocity distributions around the hill and surface wall shear stress. The velocity profiles around the model were measured by X hot wire anemometer. The wall shear stress was measured on the characteristic positions of the hill with the hot film sensor. Spectral analysis of the time records of velocity and wall shear stress were taken by means of a fast-scanning acquisition system.

3. The results

For the understanding of the shear flow in the region next to the ground surface, knowledge of characteristics of instantaneous velocity field is very important in the context of wind erosion processes. The following figures present the main findings of the numerical simulations, resulting on the basis of time sequences of velocity fields around the hill for different parameters of incident wind periodicity. Both frequency f_0 and amplitude A influence the extent of the recirculation zone as well as introduce some additional fluid flow actions in comparison to the steady case. The differences concerns mainly regular vortex street produced in the case of high frequency oscillations influx. The increase in the recirculation region is also observed, especially for higher values of amplitude.

Fig. 2 presents the experimental and numerical data performed for the velocity distributions at the top of the hill. Comparison between the mean velocity fields obtained through numerical methods and experimental methods shows strong correlation. A small disagreement has been noted for the vertical velocity component. Nevertheless, it should be emphasized here that the accuracy of the experimental determination of the cross velocity component by the use of an X hot-wire probe is about 15%. Phase averaging of the hot wire signal made it also possible to compare the experimental and numerical time records of the velocity at the points located at two distances above the hill top.

a)

b)

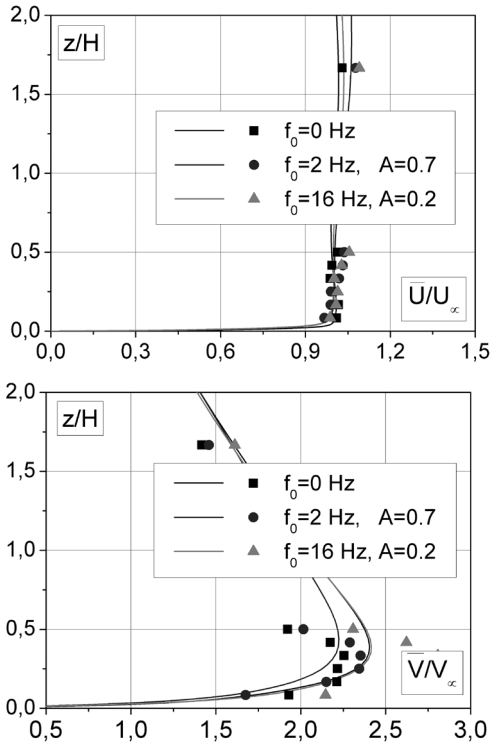

Fig. 2. Comparison of experimental (points) and numerical (curves) mean velocity profiles at the hill top for a) horizontal, and b) vertical component

The distribution of the averaged skin friction coefficient obtained as a result of numerical simulation and presented in Fig. 3 revealed a well-know behavior in the attached region. From the measurement of the skin friction, information about the position of separation points, recirculation zones or reattachment points can be derived. The skin friction starts from zero at the hill foot, peaks before the hill crest, drops from then on and achieves its negative values in the separation region. The separation is indicated by the vanishing of the skin friction. The influence of frequency of incident flow oscillation is strongly marked in the downwind area only for the case of higher value of amplitude of external gusts. Experimental verification of computational results has been done at the two points localized both on upwind (x/L_1 = -0.3) and downwind (x/L_1 = 0.3) sections of the hill surface.

a)

b)

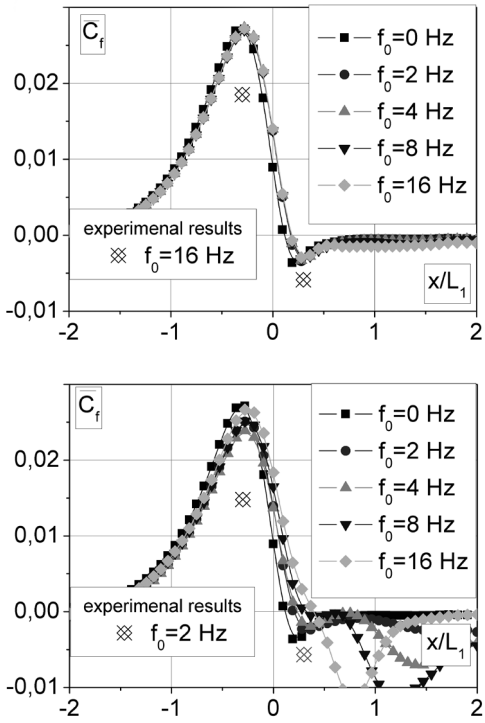

Fig. 3. Distribution of mean wall shear stress coefficient around the hill surface for a) low (A = 0.2) and b) high (A = 0.7) amplitude of inflow oscillations

Fig. 4 shows the time dependence of instantaneous values of friction coefficient $c_f(t) = \overline{c}_f + \tilde{c}_f(t)$, obtained on the basis of numerical simulations for sample inflow frequencies and amplitudes A = 0.2 and 0.7. The periodicity of the friction coefficient traces is clearly visible. At the point before the hill top (x/L_1 = -0.3), the influence of external gusts amplitude A dominates over effect of inflow frequency level. The time distributions recorded in the vicinity of boundary layer separation on downwind slope (x/L_1 = 0.3) are strongly related to frequency f_0, especially for A = 0.7 case. The periodicity of surface friction distribution loses its mono-harmonic character in this region.

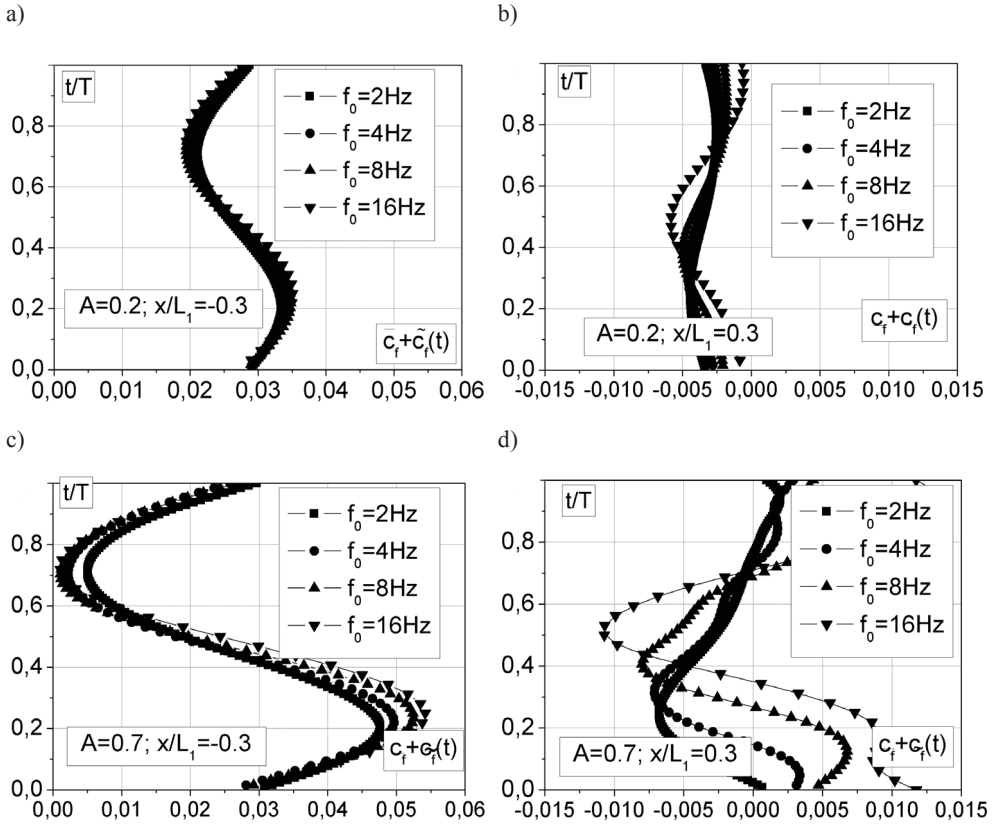

Fig. 4. Time dependent distributions of the wall shear stress coefficient obtained from numerical simulation for inflow amplitude $A = 0.2$ (a, b) and $A = 0.7$ (c, d) at upwind $x/L_1 = -0.3$ (a, c) and downwind $x/L_1 = 0.3$ (b, d) positions

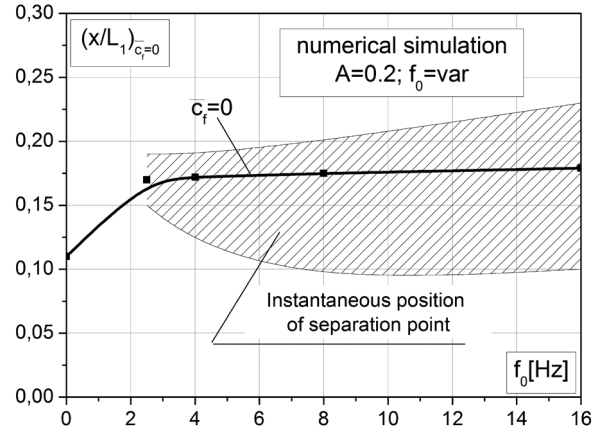

Fig. 5. The position of the separation point for low amplitude inflow conditions

The pictures observed as the results of numerical simulation of the instantaneous skin friction distributions over the hill surface given in the form of time-space distribution made it possible to analyse that problem for the modelling of the erosion process, [6]. One may see that the location of separation is changeable in time and space, undergoing oscillations around the position indicated by the zero value of mean skin friction coefficient. The results presented in Fig. 5 obtained on the basis of time-space distributions of the wall shear stress coefficient, indicate the band of possible instantaneous positions for which a zero value of skin friction may occur.

4. Concluding remarks

The conducted analysis of the experimental/numerical pattern allows the presentation of the influence of oscillating winds with changing frequency and amplitude on the shaping of the flow around a singular, waving hill. Analysis includes the wind surrounding a streamlined object, therein apex and recirculation zone in the track behind the hill. The main attention was focused on areas that were characterized by increased ground erosion during flow around the hill, localized in the section of oscillating wind field.

The instantaneous pictures of the flow field around the hill revealed the different features resulting from the inflow frequency and amplitude change. One can note the significant importance of large scale periodical pulsations of incident wind on the dynamics of separation zone behind the hill. Both frequency f0 and amplitude A influence the extent of the recirculation zone as well as introduce some additional fluid flow events in comparison with the steady inflow case.

The differences deal mainly with the regular vortex street generated in the case of high frequency inflow oscillations. Amplification of the downwind recirculation is also observed especially for the higher values of amplitude A. Periodic inflow disturbances bring about intensive oscillations of the wall shear stress. the location of separation is changeable in time and space, undergoing oscillations around the position indicated by the zero value of the mean skin friction coefficient.

This work was partially supported by the Statutory Research, No BS/PB-1-103-3010/11/P.

References

[1] Butterfield G.R., *Transitional behaviour of salation: wind tunnel observation of unsteady winds*, Journal of Arid Environments, Vol. 39, 1998, 377-394.

[2] Gnatowska R., Sikora S., *Numerical analysis of wind flow and erosion in flow around the bump terrain*, AIP Conference Proc. 1648, 850124, 2015.

[3] Jarża A., Ciechanowski J., *Dynamics of separation zone behind the 2D hill in oscillating incident wind*, Proc. XXI International Congress of Theoretical and Applied Mechanics, Poland, Warsaw 2004.

[4] Kim H.G., Lee Ch.M., Lim H.C., Kyong N.H., *An experimental and numerical study on the flow over two-dimensional hills*, Journal of Wind Engineering and Industrial Aerodynamics, Vol. 66, 1997, 17-33.

[5] Lee S.J., Lim H.-Ch., *A numerical study on flow around a triangular prism located behind a porous fence*, Fluid Dynamics Research, Vol. 28(3), 2001, 209-221.

[6] Zhang J., Cui E., Fu G., *Investigation of the flow field and the starting conditions of wind-induced erosion of the railway embankment*, Journal of Wind Engineering and Industrial Aerodynamics, Vol. 54/55, 1995, 573-581.

TECHNICAL TRANSACTIONS | CZASOPISMO TECHNICZNE
CIVIL ENGINEERING | BUDOWNICTWO
2-B/2015

PAWEŁ KISIEL*, ZBIGNIEW MIKULSKI*, ARKADIUSZ KWIECIEŃ*, PIOTR FIELEK*

REDUCTION OF DISPLACEMENT IN CONCRETE TRAM TRACKS UNDER ENVIRONMENTAL EFFECTS USING POLYMER FLEXIBLE JOINT TECHNOLOGY

REDUKCJA PRZEMIESZCZEŃ BETONOWEJ NAWIERZCHNI TRAMWAJOWEJ WYWOŁANYCH WPŁYWAMI ŚRODOWISKOWYMI ZA POMOCĄ POLIMEROWEGO ZŁĄCZA PODATNEGO

Abstract

Large displacements caused by temperature loads are a significant problem in the design and operation of concrete tram surfaces. There is frequently observed damage to expansion joints between slabs induced by high displacements as well as aging processes. As a result, water penetrates through cracked expansion joints causing structural degradation. Tests performed in situ indicate that polymer flexible joints may be used as concrete slab connections in concrete tram surfaces. Besides sealing, this technology allows transferring loads within large deformation states, additionally, rotation angles of slab edges are decreased, reducing the risk of damage to connections. This work analyzes the structural behaviour of a section of a tram surface connected by polymer flexible joint technology. A FEM numerical model in was constructed in Abaqus 6.12 with the analysis of thermal loads. This paper presents the analysis of deformation and stress distribution in structural elements, in cases of different constructional variants; the results are presented and conclusions are drawn.

Keywords: concrete slab, polymer flexible joint, temperature load, tram surface

Streszczenie

Duże przemieszczenia wywołane obciążeniami termicznymi stanowią znaczny problem przy projektowaniu i realizacji nawierzchni betonowych. W konstrukcjach tych często obserwuje się występowanie uszkodzeń dylatacji wywołanych dużymi przemieszczeniami i starzeniem się materiałów. W wyniku utraty szczelności połączenia może dojść do negatywnych skutków wywołanych penetracją wody pod konstrukcję. Pierwsze próbne aplikacje *in situ* Polimerowego Złącza Podatnego wykazały, że może być ono stosowane jako dylatacja w nawierzchniach betonowych. Dzięki swoim właściwościom złącze nie tylko efektywnie uszczelnia nawierzchnie betonowe, ale również przenosi obciążenia przy dużych przemieszczeniach. W rezultacie następuje redukcja kąta obrotu obrzeży płyt, co znacznie zmniejsza ryzyko uszkodzenia połączenia. Artykuł zawiera analizę pracy mechanicznej typowego torowiska tramwajowego, w którym zastosowano Polimerowe Złącze Podatne. Wykonano model numeryczny z obciążeniem termicznym w programie Abaqus 6.12. W pracy zaprezentowano szereg wyników analiz wykonanych w różnych wariantach konstrukcyjnych oraz zaprezentowano wnioski.

Słowa kluczowe: nawierzchnia betonowa, obciążenie termiczne, polimerowe złącze podatne, nawierzchnia tramwajowa

DOI: 10.4467/2353737XCT.15.137.4174

* Institute of Structural Mechanics, Cracow University of Technology, Poland.

1. Introduction

Polymer flexible joint (PFJ) technology is an innovative approach for structural connections. One of the most important features of the technology is the ability to transfer loads in large deformation states. Large deformations in concrete pavements are an inevitable problem due to high level of loads caused by temperature. Traditionally made expansion joints often encounter damage due to environmental and mechanical effects. Large dislocations may force the filling (bitumes) to squeeze outside the expansion joint. Unfortunately, due to the filling's low adhesion to concrete, detachment of the filling material can be observed (Fig. 1). Environmental cycles can lead to the filling leaking; as a result, water penetration into expansion joint and next under concrete structures can be commonly observed, this causes further destruction through a hydrodynamic effect [1, 2].

Fig. 1. Damaged expansion gap filled with bitumen

In-situ tests show that PFJ can be used in concrete slab connections. The joint has been used in surface repair since 2007 and it has been working properly for 7 years, until reconstruction of the concrete pavement. It has been shown that joints' hyper-elastic behaviour causes displacement reduction, due to its ability to transfer loads [1, 3]. Consequently, the rotation angle of the slab's edges is reduced, this decreases the amount of filling (bitumes) being squeezed out of the expansion joint. PZP usage can also positively influence stresses coming from loads from vehicle passes due to dislocation reduction in the middle of the slabs.

This work is the numerical analysis of a typical concrete precast tram surface. The aim of this paper is to examine the influence of PFJ application on displacement reduction and stress distribution change in a section of tram track support under temperature loads.

2. Research methodology

2.1. Analyzed structure's description

A set of numerical analyses were performed in Abaqus 6.12 using the finite element method. In this investigation, a section of tram surface with a typical construction and consisting of 7 precast slabs is analyzed. The analyzed construction variant was applied in Krakow with expansion gaps filled with bitumen – this was damaged after a couple of years of operation. In this research, 6 constructional and load variants are analyzed, as shown in Tab. 1.

Table 1

List of analyzed numerical variants

	Type of construction	PFJ width	Temperature difference
Variant 1	without PFJ	-	55°C
Variant 2	with PFJ	2 cm	55°C
Variant 3	with PFJ	1 cm	55°C
Variant 4	with PFJ	3 cm	55°C
Variant 5	with PFJ	2 cm	40°C
Variant 6	with PFJ	2 cm	20°C

Variant 1 represents a construction with a typical expansion gap filled with bitumen. Variant 2 uses very similar parameters to Variant 1, but has constructed PFJ in expansion joint. Comparison of results obtained for these two variants would indicate the influence of PFJ usage in place of traditional expansion joints.

The next analyzed series is represented by variants 2, 3 and 4. Analysis of these examples show the influence of PFJ thickness change on dislocations and stress distribution. In present in-situ experiments, it is most common to apply a PFJ thickness of 2 cm, but the optimal thickness has not been proven for various applications.

The influence of temperature load level on construction behaviour was analyzed in variants 2, 5 and 6. These cases show how displacement changes the load level in a mid-span of the slabs at different temperatures.

This work is an analysis of a typical tram track support in urban areas that allows car movement. Fig. 2 presents the visualization and cross-section of the analyzed structure. It consists of four slabs transferring tram loads and three slabs between them.

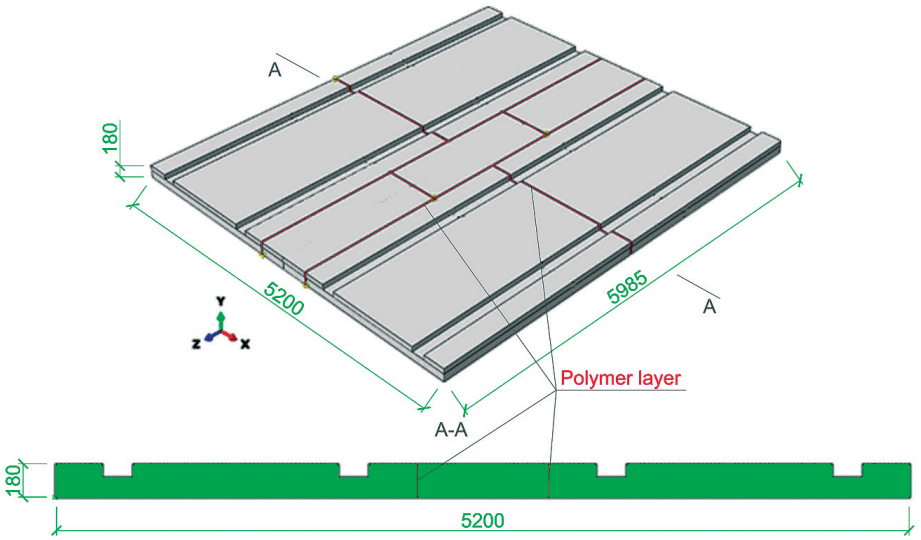

Fig. 2. Visualization of the structure and it's A-A cross-section, dimensions in [mm]

2.2. Numerical model description

Numerical analysis uses the finite element method analysis made in Abaqus 6.12. Three-dimensional elements are used to model concrete (type C3D8R) and polymer (C3D8H). Geometrical nonlinearity was considered due to large deformations in polymer material filling expansion joints. The elements mesh was dense in the joint zone. Contact with friction was set up as foundation for the slabs. With this solution, the slab can detach from its base during deformation. Material parameters for the concrete were assumed according to the Eurocode rules [4]. Numerical model visualization is presented in Fig. 3.

Boundary conditions set in Variant 1 allow the slabs to be freely lifted and rotated on a contact surface during deformation. The analysis was performed in two steps. Firstly, a heat flow analysis was made. A temperature of 60°C was applied at the upper surface of the construction, and 5°C at the bottom, based on measurements from previous research [1]. As a result, temperature distribution in each node has been obtained. Secondly, a static analysis was performed with the thermal load. A coefficient of thermal expansion for concrete of $1.2 \cdot 10^{-5}$ 1/°C [4] was assumed.

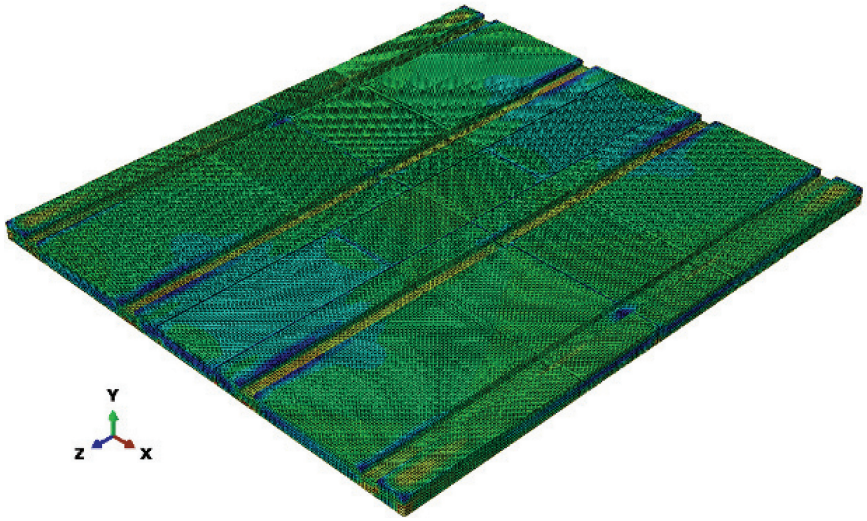

Fig. 3. Numerical model visualization

2.3. Material model of polymer

This analysis based on hyper-elastic Mooney-Rivlin model of polymer, according to the relationship:

$$U = C_{10}\left(\overline{I}_1 - 3\right) + C_{01}\left(\overline{I}_2 - 3\right) + \frac{1}{D_1}\left(J^{el} - 1\right)^2 \tag{1}$$

where U is the strain energy per unit of reference volume; C_{01} and D_1 are temperature-dependent material parameters; $\overline{I}_1$ and $\overline{I}_2$ are the first and second deviatoric strain invariants [5].

The material model uses a set of simplifications. Parameters: C_{10}, C_{01} were obtained in laboratory tests performed at room temperature, different from presented in the analyzed case. Additionally, the coefficient of thermal expansion for polymer was set as $1.56 \cdot 10^{-4}$ 1/°C after [6,7].

3. Results and discussion

A series of stress and displacement maps was obtained as a result of FEM calculations. In order to facilitate visual comparison, maps are shown at the same scale. It should be noted that deformation images are not at a 1:1 scale – they were resized 100 times in order to show the type of deformation of each slab.

3.1. PFJ application

Fig. 4 presents displacement maps for Variants 1 and 2. It can be noticed that for the variant with applied PFJ, the maximum displacement reduction is approximately 20%. The comparison of the two maps also shows a lower value of the angle of rotation of the slabs' edges (this can be noticed by smaller dislocations increments). This can by caused by mechanical properties of the PFJ. Fig. 5 presents a stress map comparison. It is clearly shown that in variant 1, the middle slab does not transfer any load in the analyzed cross-section. Continuing, the stress map for Variant 2 indicates mechanical cooperation of the middle slab. It visibly shows that the PFJ application positively influences stress distribution in the whole structure.

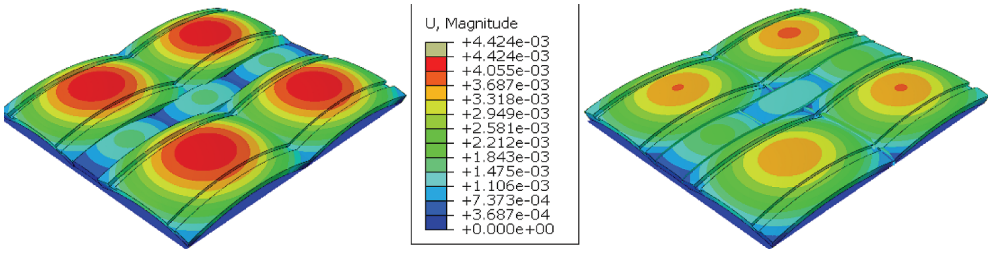

Fig. 4. Displacement maps for Variants 1 (on the left) and 2 (on the right) are at the same scale in [m]

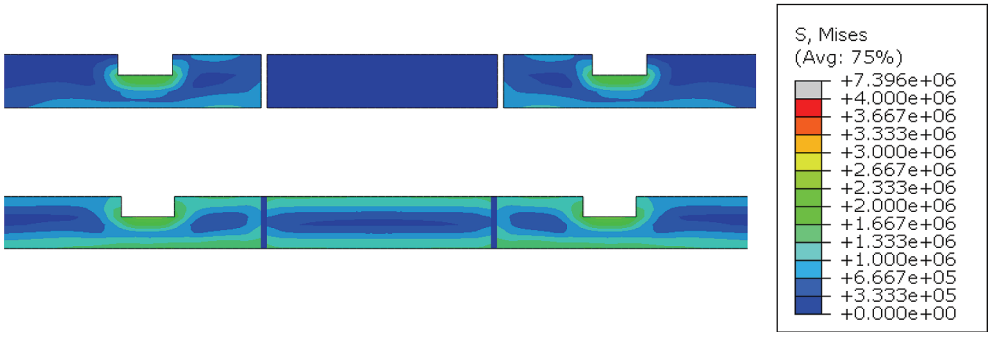

Fig. 5. Stress maps for Variants 1 (at the top) and 2 (at the bottom) at the same scale in [Pa] for middle section of A-A cross-sections

3.2. Thickness of PFJ

Displacement maps calculated for Variants 2, 3 and 4 are presented in Fig. 6. It can be noticed that the smallest values of displacement were obtained for variant 2. One can conclude that for particular design parameters (geometrical variant, temperature loads and stiffness of elements), a PFJ thickness of 2 cm is optimal. For variant 3 (thinnest PFJ of 1 cm),

all the slabs react as a stiffly connected continuous structure – this can be observed in Fig. 6. Additionally, displacements calculated for variant 4 are larger than for variant 2. This can be caused by too low stiffness of the connection due to its large width. However, one can also notice that the maximum displacement calculated for this variant is 8% smaller than for Variant 1 which represents the structure with the expansion gap filled with bitumen.

Analysis of stress maps from Fig. 7 lead to the conclusion that stress levels in analyzed cross-section increase with a decrease of the thickness of the connection. In all variants, stresses are redistributed over all slabs.

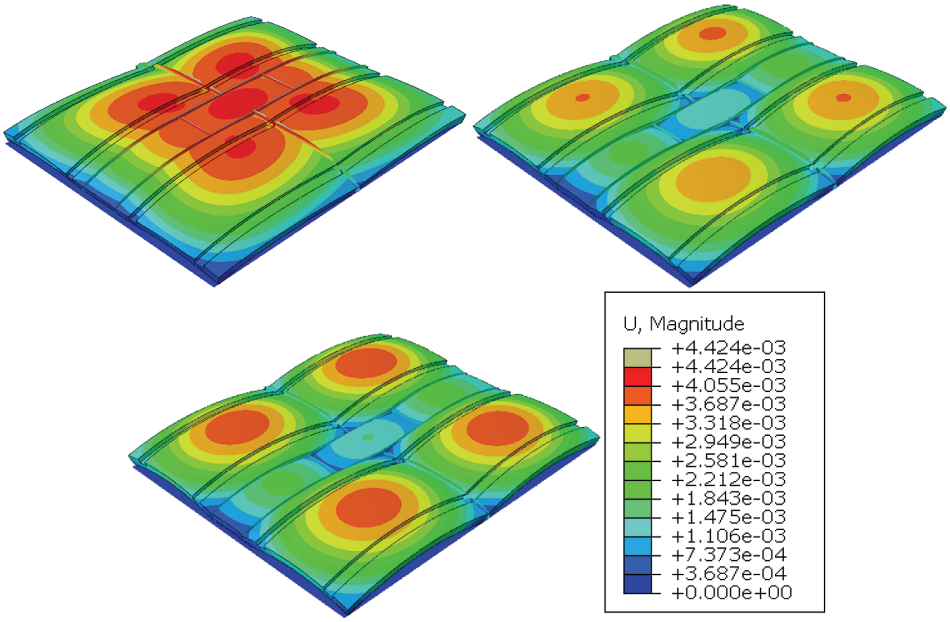

Fig. 6. Displacement maps for Variants 3 (in the upper left), 2 (in the upper right) and 4 (at the bottom) at the same scale in [m]

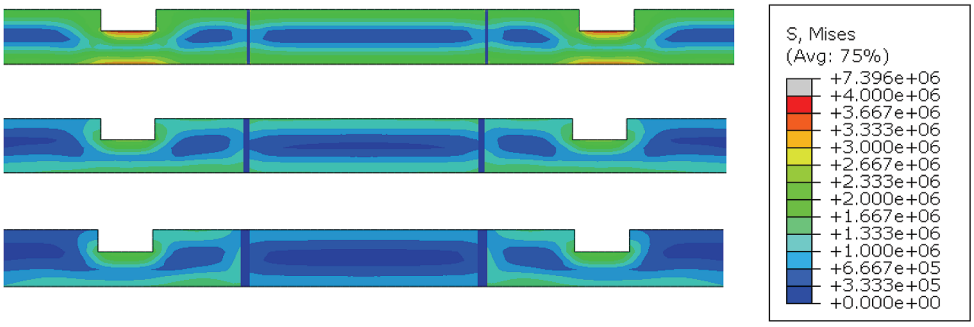

Fig. 7. Stress maps for variants 3 (at the top), 2 (in the middle) and 4 (at the bottom) in the same scale in [Pa] for the middle section of A-A cross-sections.

3.3. Level of temperature load

Fig. 8 presents dislocation maps calculated for variants 2, 5 and 6. The level of deformation decreases proportionally to the reduction in the temperature difference as expected. Changes of maximum displacement with the temperature difference are shown using a graph presented in Fig. 9. Stress maps for analyzed variants are shown in Fig. 10. Comparison leads to the conclusion that stress distributions in the analyzed cross-section are similar for various levels of thermal load and differ only in the stress value.

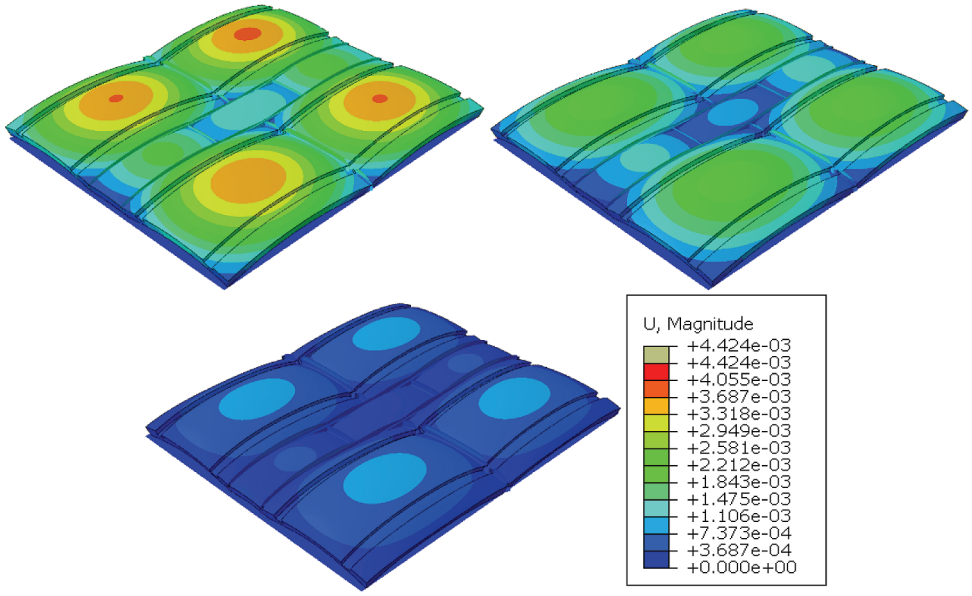

Fig. 8. Displacement maps for Variants 2 (in the upper left), 5 (in the upper right) and 6 (at the bottom) at the same scale in [m]

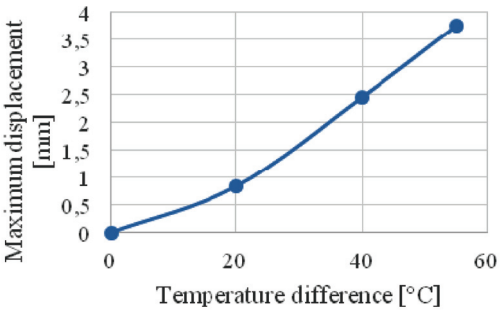

Fig. 9. Changes of maximum vertical displacement with the temperature difference of slabs with PFJ (for Variants 2, 5 and 6) in point M as indicated in Fig. 8

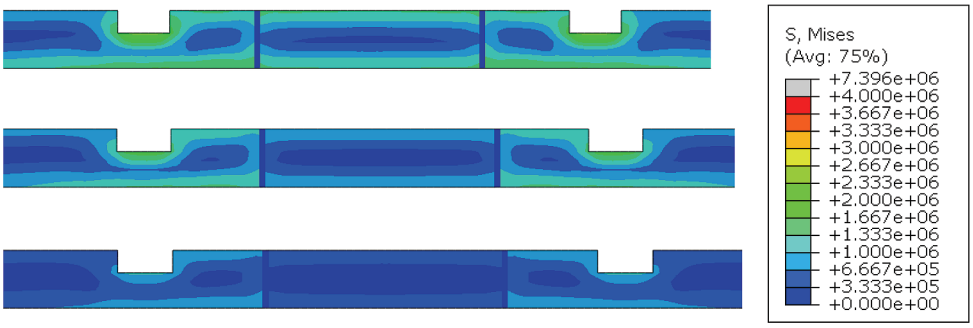

Fig. 10. Stress maps for Variants 2 (at the top), 5 (in the middle) and 6 (at the bottom) in the same scale in [Pa] for the middle section of A-A cross sections

4. Conclusions

Analysis of the presented results may lead to the following conclusions:

- PFJ application significantly reduces displacements in concrete tram track support made of precast slabs (19% in analyzed example);
- PFJ application introduces stresses in expansion joint zones, allowing for the transfer of loads;
- The thickness of PFJ has a significant influence on the behaviour of the system and its efficiency. For the analyzed example, the connection thickness of 2 cm provides a much better structural behaviour than a thickness of 1 cm or 3 cm;
- The dependence of the displacement reduction is approximately linearly proportional to the thermal load level;
- Due to the compression transfer, PFJ may protect slabs' edges from chipping resulting from large deformations.

This research will be continued by taking further load cases into account. Next, FEM models will be supplemented by loads coming from tram and car passes as well as from temperature uniform loads.

References

[1] Kwiecień A., *Uszkodzenia beotnowych nawierzchni lotniskowych*, XXVI Konferencja Naukowo-Techniczna „Awarie Budowlane", Szczecin-Międzyzdroje 2009.

[2] Zając B., *Aspekt termiczny wypełniania szczelin i ubytków przy naprawie nawierzchni betonowych*, XXV Konferencja Naukowa „Metody Komputerowe w Projektowaniu i analizie Konstrukcji Hydrotechnicznych", Korbielów 2013.

[3] Kwiecień A., Gruszczyński M., Zając B., *Tests of flexible polymer joints repairing of concrete pavements and of polymer modified concretes influenced by high deformations*, Key Engineering Materials, Vol. 466, 2011, 225-239.

[4] Ajdukiewicz A., *EUROKOD 2. Podręczny skrót dla projektantów konstrukcji żelbetowych*, Stowarzyszenie Producentów Cementu, Kraków 2009.

[5] Kwiecień A., Kuboń P., Zając B., *Experimental verification of hyperelastic model of polymer on a case study of the flexible polymer joint*, Zeszyty Naukowe Politechniki Rzeszowskiej, Rzeszów 2011.

[6] Zając B., *Potentials of using PU in structural joints in civil engineering considering aspect of thermal work,* Polyurethanes, Ustroń 2013.

[7] Tedeschi C., Kwiecień A., Valluzzi M.R., Binda L., Zając B., *Effect of thermal ageing and salt decay on bond between FRP and masonry*, Materials and Structures, Vol. 47, 2014, 2051-2065.

TECHNICAL TRANSACTIONS | CZASOPISMO TECHNICZNE
CIVIL ENGINEERING | BUDOWNICTWO
2-B/2015

KLEMM KATARZYNA*

THE ASSESSMENT OF MICROCLIMATIC CONDITIONS IN A WELL-SPACED URBAN STRUCTURE

OCENA WARUNKÓW MIKROKLIMATYCZNYCH W DOBRZE ROZMIESZCZONEJ STRUKTURZE MIEJSKIEJ

Abstract

A proposed assessment method for microclimatic conditions in urban structures is presented in the paper. The assessment model defines the quantitative and qualitative features of the study area. The three main elements of the urban environment – local climate, urban development, and the type of the area surfaces – are all evaluated. The proposed method constitutes an approximation. Parameters such as the location, shadow fall, or heat loss by the external surfaces of the building were not included.

Keywords: microclimate, human comfort, CFD

Streszczenie

W pracy przedstawiono metodę szacowania warunków mikroklimatu w strukturze miejskiej. Model szacowania definiuje jakościowe i ilościowe cechy rozpatrywanego obszaru. Oceniane są trzy główne elementy środowiska miejskiego – klimat lokalny, rozwój zabudowy oraz rodzaj powierzchni obszaru. Proponowana metoda stanowi przybliżenie. Nie zostały uwzględnione parametry takie jak położenie, zacienienie, czy utrata ciepła przez zewnętrzne powierzchnie budynku.

Słowa kluczowe: mikroklimat, komfort ludzki, CFD

DOI: 10.4467/2353737XCT.15.138.4175

* Department of Geodesy, Environmental Cartography and Descriptive Geometry, Technical University of Lodz, Poland.

1. Introduction

The external environment, determined by natural conditions such as climate or topography, and also by anthropogenic factors, that is; urban development, the density of urban structures or the size of green areas, have a major impact on living conditions. Dense urban structures in city areas affect unique microclimatic conditions that greatly influence residents' comfort. In some situations, local problems connected with excessive air flow in the vicinity of the buildings or the formation of strong turbulences, may arise. At the same time, tall, concentrated buildings sometimes cause a significant decrease in urban ventilation. This may lead to a deterioration in hygienic conditions and encourage local accumulations of snow or pollution. The ventilation degree of urban areas also depends on the climatic conditions of individual residential districts, as these may enhance or counteract the influence of urban development.

Analysis of the human body's heat balance shows that in order to create comfortable wind conditions it is essential to take into account thermal factors. This is especially important when the temperature is below -5°C and wind speed is greater than 1 m/s, and also in cases when the temperature is greater than +25°C but wind speed is less then 3 m/s. In the above circumstances, discomfort is caused by a deficiency of heat exceeding 40 W/m^2 and in the case of temperature above zero by a heat surplus above 40 W/m^2, [8].

Knowledge of environmental conditions and an appropriate application of assessment results greatly contribute to increasing residents' living comfort.

2. The assessment of microclimatic conditions in urban areas

2.1. Criteria and general model of microclimatic conditions assessment

The assessment of environmental impacts on human presence is a complex issue, as the consideration of the great number of variables that characterise individual occurrences is necessary. The descriptive method and the model method are the most frequently used for these purposes. In the latter, a model that comprehensively characterises environmental functions is constructed. It constitutes a certain physical or mathematical pattern that incorporates the greatest number of variables affecting individual occurrences.

The quantitative and qualitative structure of the external environment should be considered in the assessment of microclimatic conditions. For this purpose two models: an exponential function model and a model analogous to Ohm's law can be used. In the exponential function model, the function base characterises quantitative features of the environment $y = x^z$, while the index exponent – its qualitative features. The value of the function y ranges between 0 and 1. No favourable features of the environment occur for $y = 0$, and the ideal state is recorded for $y = 1$. Values x fall within the range of variable between 0 and 1 whereas z may range between 0 and $+\infty$. For the most favourable qualitative features $z = 0$ the function y equals 1, [9]. The second model can be described by:

$$y_i = \frac{P_i}{R_i} \tag{1}$$

where: y_i – value of a given parameter, P_i – potential, treated as favourable features of the environment, R_i – resistance, treated as the conditions that make long-term human occupation difficult or impossible.

Finally, the proposed model is a combination of two above mentioned models and has the following form:

$$y = \left(\frac{P_x}{R_x} \right)^{\frac{R_z}{P_z}} \tag{2}$$

where: P_x, R_x – potential and resistance of quantitative features, P_z, R_z – potential and resistance of qualitative features.

2.2. Human comfort criteria

The comfort sensation is associated with changes in body temperature caused by an increase or decrease in ambient temperature, the cooling effect of wind, and the convective and the radiative heat loss from the body. There are a number of factors which affect the heat exchange between man and the external environment. The most important physical parameters include: air temperature, wind speed, solar radiation, relative humidity and radiation temperature. Equally important are the parameters related to the individual person, such as the activity, exposure time, clothing thermal insulation and finally the psychological factors associated with the level of adaptation, expectations or previous experiences [11, 12].

Human comfort studies carried out over many years have resulted in the development of about 100 indices which assess the influence of the atmospheric environment on a human being. Most of the indices are not strongly correlated with physiological reaction in human. They are based on single or composite meteorological parameters, such as wet – bulb or equivalent temperature. Since the 1970s the psychological relevant indices derived from the human energy balance have become more popular. The MEMI model (Munich energy balance for the individual) and the derived thermal assessment index PET (physiologically equivalent temperature) proposed by Höppe [7] were commonly used. Other models are the predicted mean vote (PMV) Fanger [5], Klima-Michel Model and PT index (Perceived Temperature) by Jendritzky (1990), standard effective temperature (SET*) Gagge et al. [6] and MENEX_2005 by Błażejczyk [2] with PST (Physiological Subjective Temperature) and PS (Physiological Strain) indexes. Recent years have brought a new generation of models – multi node models that consider all mechanisms of thermoregulation. Among them the most popular is the UTCI (Universal Thermal Climate Index) derived from the Fiala multi-node model of human heat balance. The UTCI is defined as the air temperature of the reference condition causing the same model response as actual conditions. The UTCI was developed in 2009 by international experts within the COST Action 730 Błażejczyk et al. [3]. All of the models presented require detailed input information both meteorological and physiological

which in practice are sometimes difficult to obtain, like mean radiant temperature or skin temperature. As a result there is a need for a more simplified method of determining the individual components of the heat balance equation.

$$M + R + Q_C + Q_E + Q_K + Q_L + Q_R = \Delta Q \tag{3}$$

where: M – metabolic rate, R – absorbed solar radiation, Q_c – heat transfer by convection, Q_E – heat transfer by evaporation, Q_K – heat transfer by conduction, Q_L – heat transfer by long wave radiation, Q_R – heat loss by respiration.

In the light of extensive research carried out in many countries, described by Błażejczyk [1], it can be demonstrated that there is a correlation between the intensity of heat fluxes with air temperature and wind speed, which allows approximations to be applied.

In the author's proposed method comfort criteria were based on the heat balance equation and the aforementioned findings. In order to specify the individual components some assumptions have been made based on standard values for a typical human and long term meteorological data of the analysed location (solar radiation):

- Metabolism M – 70 W/m^2
- Thermal insulation of the cloths 1 clo
- Solar radiations absorption R – 30 W/m^2
- Heat exchange through evaporation Q_E – 8 W/m^2 for $T_a < +5^oC$, 20 W/m^2 for $T_a \geq +5^oC$
- Heat exchange through conduction Q_K is not taken into account
- Heat loss caused by respiration Q_R – 8 W/m^2

Both human body parameters and solar radiation absorption can take different values depending on local conditions.

The remaining components of the heat balance equation i.e. heat transfer by convection and long wave radiation were determined analytically using Błażejczyk's [1] observation.

Furthermore heat transfer by convection and long wave radiation, based on temperature and wind speed, are specified thus:

For weather conditions where wind speed $U \leq 4$ m/s and temperature $T_a \geq +5^oC$

$$Q_C + Q_L = 3,4T_a + 0,2\overline{U} - 118,8 \tag{4}$$

Where the wind speed $U \leq 4$ m/s and temperature $T_a < +5^oC$

$$Q_C + Q_L = 1,7T_a + 6,0\overline{U} - 101,4 \tag{5}$$

Where the wind speed $U > 4$ m/s and temperature $T_a \geq +5^oC$

$$Q_C + Q_L = 3,3T_a + 0,2\overline{U} - 127,8 \tag{6}$$

Where the wind speed $U > 4$ m/s and temperature $T_a < +5^oC$

$$Q_C + Q_L = -1,5T_a + 0,3\overline{U} - 126 \tag{7}$$

By applying the above equations (4–7) and assumptions to the heat balance equation, thermal loads on the body were derived for specified ranges of temperature and wind speed [4]. The parameter can be used for the relative comparison of different environmental conditions.

In weather conditions where wind speed $U \leq 4$ m/s and temperature $T_a \geq +5^{o}$C

$$\Delta Q = 2,8T_a - 4,8\overline{U} - 29,8 \tag{8}$$

Where the wind speed $U \leq 4$ m/s and temperature $T_a < +5^{o}$C

$$\Delta Q = 1,7T_a - 6,0\overline{U} - 23,0 \tag{9}$$

Where the wind speed $U > 4$ m/s and temperature $T_a \geq +5^{o}$C

$$\Delta Q = 2,3T_a - 3,5\overline{U} - 35,4 \tag{10}$$

Where the wind speed $U > 4$ m/s and temperature $T_a < +5^{o}$C

$$\Delta Q = 1,5T_a - 3,0\overline{U} - 34,0 \tag{11}$$

Taking into account the efficiency ranges of the thermoregulatory systems, which are applied in thermophysiology, it is assumed that $|\Delta Q| < 20$ W/m^2 does not trigger system loads. However, where there is deficiency and excess heat ΔQ equal to 20–40 W/m^2 then unfavourable loads will affect the body. Strong heat load can be observed when ΔQ is between 40–80 W/m^2. Higher values than the threshold value 90 W/m^2 can trigger disturbances in the proper function of the thermoregulatory system, which consequently can lead to dangerous overheating or conversely hypothermia.

Finally the criteria for thermal comfort were established based on the following thresholds for heat loads on the body ΔQ.

- $|\Delta Q| < 20$ W/m^2 – comfortable condition,
- $|\Delta Q|$ in ranges 20 – 40 W/m^2 – unfavourable loads on the body,
- $|\Delta Q|$ in ranges 40 – 80 W/m^2 – strong unfavourable loads on the body,
- $|\Delta Q| > 80$ W/m^2 – dangerous loads on the body.

The proposed criteria were the basis for weather typology used in the assessment of weather conditions of the urban structure analysed.

Fig. 1. presents the relationship between ΔQ and air temperature T_a and wind speed as well as body heat load thresholds.

The detailed analysis of body heat loads with the corresponding ranges in temperature and wind speed are presented in Klemm [9].

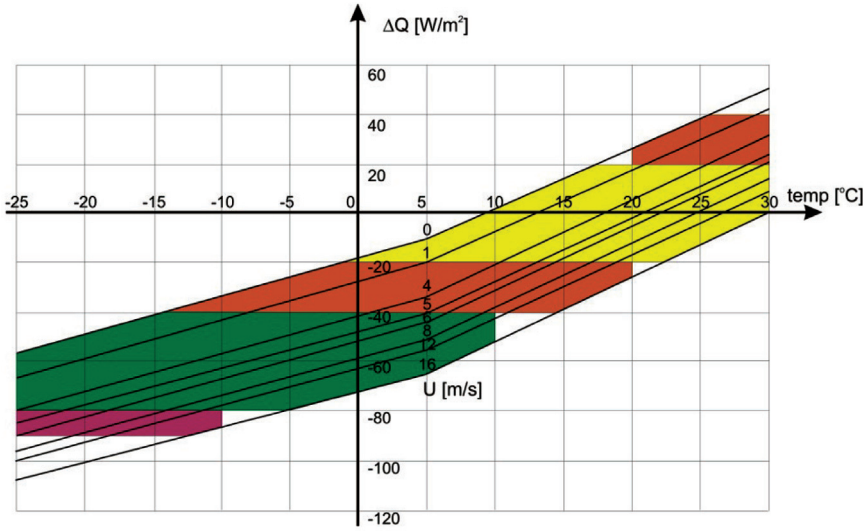

Fig.1. Threshold values of the thermal loads on the body

2.3. Assessment of weather conditions

For the purpose of the study, a weather typology was proposed. As the basic feature of the weather type, human thermal sensation caused by the reaction of the thermoregulatory system to atmospheric stimuli (air temperature, wind speed) were used. Three types of weather conditions and twenty groups were determined.

Type A includes weather situations in which wind conditions allow a human to spend a long period of time outdoors. Wind speed is lower than 8 m/s, and the thermal conditions are perceived as comfortable $\Delta Q \leq 20$ W/m^2.

Type B includes weather situations not conducive to relaxation, walks or cycling, but allowing work in the open air. Thermal conditions are perceived as causing adverse thermal load on the body. The physical influences of the wind are crucial, wind speed exceeds the threshold of 5m/s. Type B also includes the situation where wind speed is less than 5 m/s and a thermal effect is pronounced due to very unfavourable thermal conditions of the body, loss or excess heat at 20–40 W/m^2.

Type C includes situations of definitely unfavourable windy weather. Thermal influences are clear, a strong thermal load on the body, heat loss from 40 to 80 W/m^2 and over 80 W/m^2. The detailed typology of weather conditions including body heat loads with the corresponding ranges in temperature and wind speed are presented in Klemm [9].

In the assessment of weather conditions, quantitative features are represented by the occurrence of favourable and unfavourable weather types from a human comfort point of view. Qualitative features of weather conditions may be described by the parameters of the intensity of wind speed, wind direction and air temperature changes. Intensity changes were defined as the relation of a standard deviation to mean value.

$$K_w = \left[\frac{cA_1 + cA_2 + cA_3 + cA_4 + cA_5}{1 + \left(cC_1 + cC_2 + cC_3 + ...cC_8\right)} \right]^{\left[\frac{\left(1+I_U^C\right)\left(1+I_k^C\right)\left(1+I_T^C\right)}{\left(1+I_U^A\right)\left(1+I_k^A\right)\left(1+I_T^A\right)} \right]} \tag{12}$$

where: cA_1, cA_2, cA_3, cA_4, cA_5 – occurrence frequency of favourable weather conditions, defined by groups A_1, A_2, A_3, A_4, A_5, cC_1, cC_2, ...cC_8 – occurrence frequency of unfavourable weather conditions, defined by groups C_1, C_2, ...C_8, I_U^A, I_U^C – intensity of wind speed changes in *A* and *C* weather groups, I_k^A, I_k^C – intensity of wind direction changes in *A* and *C* weather groups, I_T^A, I_T^C – intensity of air temperature changes in *A* and *C* weather groups.

2.4. Assessment of urban development

The second important element with an effect on the final assessment of microclimatic conditions is the structure of the urban area i.e. participation of various urban structures, tall vegetation, and open area in the total surface, as well as zones with wind comfort and discomfort. The above estimation is carried out using numerical simulations, assuming wind speed 4 m/s and by simultaneously taking into account frequencies of wind flow occurring from 8 or 12 directions and also its related temperature.

The participation of the open area Z_w in the total surface was considered to be the potential of quantitative features of the land development coefficient Z_t and the participation of various urban structures and green areas in relation to the study area was considered to be their resistance (Z_m).

$$Z_m = \frac{S_m}{S_o}, \quad Z_w = 1 - Z_m,$$

where: S_m – surface area of buildings and tall vegetation [m^2], S_o – study area [m^2].

Then quantitative features may be described by:

$$x = \frac{Z_w}{1 + Z_m} \tag{13}$$

The qualitative features z may be described by:

$$z = \left[\frac{1 + Z_1^C}{1 + Z_1^A} \cdot \frac{1 + Z_2^C}{1 + Z_2^A} ..... \frac{1 + Z_8^C}{1 + Z_8^A} \right] \tag{14}$$

From the human sensation point of view, uncomfortable conditions are influenced by wind flow and air temperature. Weak air flow in built-up areas leads to deterioration of hygienic conditions and encourages local accumulation of pollution, whereas increased speeds can trigger dynamic loads. Simultaneously even at moderate wind conditions local discomfort may appear due to low or high temperatures. High temperatures especially can cause serious

problems in big cities. Nowadays heat islands and poor ventilation as a result of inappropriate urban planning become the most serious factors which influence human health and comfort. This fact was considered in the qualitative features proposed.

The resistance of qualitative features was determined from the equation

$$Z_k^C = Z_k^{C(U)} + Z_k^{C(T)} \tag{15}$$

The first element in the equation describes situations in which, due to low wind speed, ventilation of the area is problematic ($U < 1$ m/s) and situations in which high wind speed can cause discomfort ($U > 4$ m/s). In order to assess wind flow conditions around buildings and determine the sizes of zones in which wind speed reaches values lower than 1 m/s and over 4 m/s numerical simulations can be used.

$$Z_k^{C(U)} = \left[\frac{S_k^{U<1}}{S_{Lg}} + \frac{S_k^{U>4}}{S_{Lg}} \right] \cdot f_k^{U=4} \tag{16}$$

where: $\frac{S_k^{U<1}}{S_{Lg}}$ and $\frac{S_k^{U>4}}{S_{Lg}}$ – ratios of the areas of zones in which wind speed $U < 1$ m/s and $U > 4$ m/s to the surface S_{Lg}, which is characterised by clear fluctuations in wind speed caused by buildings.

Surface size S_{Lg} is determined on the basis of the principle proposed by Bottema [4]. The length L_g is specified using the formula

$$L_g / H = \frac{W/H}{1 + 0,5 W/H} \tag{17}$$

where: L_g – geometrical influence scale [m], W – building width [m], H – building height [m].

Since the wind speed $U_{ref} = 4$ m/s (wind speed measured at the meteorological station at a height of 10m) assumed in the numerical simulation as the inflow wind speed occurs with different probabilities in different directions, it was necessary to introduce a weighting coefficient $f_k^{U=4}$, resulting from meteorological data analysis.

The second element in eq. 15 refers to conditions when, despite comfortable wind speed, thermal loads of human body exceeded 40 W/m^2.

$$Z_k^{C(T)} = \left(\frac{S_k^{1 \le U \le 4}}{S_{Lg}} \right) \cdot f_k^{U=4} f_k^{U=4, \Delta Q>40} \tag{18}$$

where: $f_k^{U=4, \Delta Q>40}$ – weighting coefficient taking into account the thermal conditions in the direction of k, when the heat loss of the body exceeds 40 W/m^2, and the inflow wind speed is at the level of 4 m/s.

The potential of qualitative features Z_k^A describes situations in which human comfort is achieved through moderate wind speed ($1 \le U \le 4$) and temperature which guarantee thermal loads $\Delta Q \le 20$ W/m^2.

$$Z_k^A = \left(\frac{S_k^{1\le U\le 4}}{S_{Lg}} \right) f_k^{U=4} f_k^{U=4,\Delta Q\le 20} \tag{19}$$

where: $f_k^{U=4,\Delta Q\le 20}$ – weighting coefficient taking into account the thermal conditions considered as comfortable in the direction of k, when the thermal loads $\Delta Q \le 20$ W/m^2 and the inflow wind speed is at the level of 4 m/s.

The above mentioned qualitative features were determined using numerical simulations of wind flow around buildings and analysis of meteorological data.

The urban development coefficient was finally described by:

$$Z_t = \left(\frac{Z_w}{1+Z_m} \right)^{\left[\frac{1+Z_1^C}{1+Z_1^A} \cdots \frac{1+Z_2^C}{1+Z_2^A} \cdots \frac{1+Z_8^C}{1+Z_8^A} \right]} \tag{20}$$

2.5. Assessment of surface

An equally important element in the analysis of microclimatic conditions is assessment of the surface in the vicinity of the urban area being examined. Special attention was paid to the size and thermal characteristics of the surface and also to the impact of direct solar radiation, air temperature and wind speed. Taking into account the aforementioned elements has allowed the partial inclusion of thermal turbulence, caused by solar radiation in the above analysis.

The great participation of artificial areas in urban environment, characterised by low albedo contributes to an increase in the thermal turbulence and the air temperature. This phenomenon has a major impact on heat island formation and worsening human comfort.

In order to create a comfortable environment, conditions increasing the participation of natural areas (low vegetation, water areas) characterized by maximum albedo are recommended.

The quantitative features of the surface coefficient were determined taking into account participation of surfaces with different albedo in the general area.

$$x = \frac{Z_{A_l>0,25}}{1+Z_{A_l<0,25}} \tag{21}$$

The qualitative features may be described using the refractive index structure coefficient, one of the main parameters describing turbulent fluctuations caused by sensible heat fluxes:

$$z = \left[\frac{1+Z_{0<R\le 30}^{A_l<0,25}}{1+Z_{0<R\le 30}^{A_l>0,25}} \cdot \frac{1+Z_{30<R\le 60}^{A_l<0,25}}{1+Z_{30<R\le 60}^{A_l>0,25}} \cdot \frac{1+Z_{60<R\le 90}^{A_l<0,25}}{1+Z_{60<R\le 90}^{A_l>0,25}} \cdot \frac{1+Z_{R>90}^{A_l<0,25}}{1+Z_{R>90}^{A_l>0,25}} \right] \tag{22}$$

$Z_R^{A_l<0,25}$ and $Z_R^{A_l>0,25}$ where determined for four ranges of direct solar radiation $0 < R \le 30$, $30 < R \le 60$, $60 < R \le 90$ and $R > 90$ W/m^2 using equations:

$$Z_R^{A_l<0,25} = C_n^* \cdot f_R \quad \text{and} \quad Z_R^{A_l>0,25} = C_n^* \cdot f_R \tag{23}$$

where: C_n^* – normalized value of refractive index structure coefficient dependent on albedo and direct solar radiation for analysed for ranges $0 < R \leq 30$, $30 < R \leq 60$, $60 < R \leq 90$ and $R > 90$ W/m^2, f_R – weighting coefficient of direct solar radiation incidence for four ranges $0 < R \leq 30$, $30 < R \leq 60$, $60 < R \leq 90$ and $R > 90$ W/m^2 (determined on the basis of the typical meteorological tear), C_n – refractive index structure coefficient which characterise fluctuation of turbulent air flow

Refractive index structure coefficient can be determined based on wind tunnel measurement by the use of narrow laser beam. The optical properties of the air on the path of the laser beam are subject to constant changes caused by turbulent air flow. In the method described it is possible to gain 1000 to 2000 records in a short period of time (10^{-9} s). This allows for accurate analyses of turbulence phenomena. Detailed information on this method is presented in Klemm [9]. It is also possible to define the refractive index structure coefficient in an analytical way using Monin Obuchov theory, the aerodynamic characteristic, and wind profile of analysed location Klemm [10].

2.6. Overall assessment of microclimatic conditions

The overall assessment of environmental conditions may be described by the coefficient B_k, expressed by:

$$B_k = \left[0,2K_w + 0,5Z_t + 0,3Z_n\right] \tag{24}$$

The highest coefficient weight was attributed to urban development due to the fact that the layout of the buildings can be controlled to a greater extent in comparison with macroclimatic conditions. The lower value of the surface coefficient results from taking into account only horizontal surfaces. In real conditions vertical elements can play a major role the in radiation and heat balance of complex urban structures. This problem will be developed in future research.

3. Conclusions

The paper presents a proposal for an assessment method for microclimatic conditions in the urban environment. An assessment model defines quantitative and qualitative features of the study area from the human comfort aspect. Three main elements of the urban environment – local climate, urban development, and surface characteristic – are evaluated. Apart from local scale analyses it also takes into account long term climatic characteristics.

In the case of weather condition assessment a typical meteorological year can be used as the base for weather typology.

The second important element having an effect on the final assessment of microclimatic conditions is the structure of the urban area, i.e. the participation of various urban structures, tall vegetation and open area in the total surface, as well as zones with wind comfort and discomfort. The above estimation is carried out using numerical simulations, assuming wind speed 4 m/s (mean value for analysed location) and by simultaneously taking into account frequencies of wind flow occurring from 8 or 12 directions and also its related temperature. The combined consideration of temperature and wind speed is very important in the case of human comfort. Taking into account the above elements allows for estimation of the impact of the urban structure, especially building geometry, their location in relation to each other, and to compass directions on wind comfort. The above assessment answers the question of whether the assumed urban development can be treated as comfortable or not from the wind conditions point of view.

An equally important element in the analysis of microclimatic conditions is assessment of the surface in the vicinity of the examined urban area. Special attention was paid to the size and thermal characteristics of the surface and also to the impact of direct solar radiation, air temperature, and wind speed. Taking into account these elements has allowed the partially inclusion of thermal turbulence caused by solar radiation into the above analysis.

The proposed method constitutes a certain approximation due to many parameters not included, such as the lay of the land, shadow fall, or heat lost by the external surfaces of the building. The construction of the model also allows other elements to be taken into account. Preliminary verification of the model regarding urban development and surface assessment conducted by the use of numerical simulation and wind tunnel tests shows consistent results. However, more detailed analysis are still under way.

References

[1] Błażejczyk K., *Heat exchange between man and his surroundings in different kinds of geographical environment*, Institute of Geography and Spatial Organization, Polish Academy of Sciences, Geographical Studies, 159, 1993 [in polish].

[2] Błażejczyk K., *Bioklimatyczne uwarunkowania rekreacji i turystyki w Polsce*, Prace Geograficzne, IGiPZ PAN, 192, 2004 [in polish].

[3] Błażejczyk K., Jendritzky G., Bröde P., Fiala D., Havenith G., Epstein Y., Psikuta A., Kampmann B., *An introduction to the Universal Thermal Climate Index (UTCI)*, Geographia Polonica, Vol. 86(1), 2013, 5-10.

[4] Bottema M., *Wind climate and urban geometry*, Ph.D. Thesis, FAGO, Technical University of Eindhoven, 1993.

[5] Fanger P.O. *Thermal comfort*. McGraw-Hill, New York, 1972.

[6] Gagge A.P., Fobelets A.P., Berglund L.G. *A standard predictive index of human response to the thermal environment*, ASHRAE Trans, Vol. 92, 1986, 709-731.

[7] Höppe P., *The physiological equivalent temperature in a universal index for the biometeorological assessment of the thermal environment*, International Journal of Biometeorology, Vol. 43, 1999 71-75.

[8] Klemm K., *Kryterium komfortu człowieka w terenach zabudowanych*, Budownictwo i Architektura, Vol.12 (2), 2013, 127-133 [in polish].
[9] Klemm K., *The complex assessment of microclimatic conditions in well-spaced and dense urban structures*, Studia z Zakresu Inżynierii PAN, Warszawa 2011 [in polish].
[10] Klemm K., *Wykorzystanie badań modelowych w przybliżonej ocenie strumienia ciepła jawnego z powierzchni zabudowanej*, Fizyka Budowli w Teorii i Praktyce, Łódź 2015 (accepted for publication) [in polish].
[11] Koss H., Sahlmen J.*, Method in pedestrian wind comfort assessment; Theoretical and practical comparisons,* Proc. of COST Action C14 Workshop, Nantes 2002.
[12] Nikolopoulou M., Steemers K., *Thermal comfort and psychological adaptation as a guide for designing urban spaces*, Energy and Building, Vol. 35, 2003, 95-101.

TECHNICAL TRANSACTIONS | CZASOPISMO TECHNICZNE
CIVIL ENGINEERING | BUDOWNICTWO
2-B/2015

SERGEY KUZNETSOV*, STANISLAV POSPÍŠIL*, RADOMIL KRÁL*

CLIMATIC WIND TUNNEL FOR WIND ENGINEERING TASKS

WYKORZYSTANIE TUNELU KLIMATYCZNEGO DO ZAGADNIEŃ INŻYNIERII WIATROWEJ

Abstract

This paper introduces a new climatic wind tunnel laboratory, which is one of the laboratories of the Institute of Theoretical and Applied Mechanics (ITAM) of the Academy of Science of the Czech Republic. The tunnel is used for fundamental research in civil engineering, architecture, and heritage care and in other fields where wind effects appear along with other factors. The paper includes essential information about the interior layout of the tunnel, descriptions of the principal parts of the tunnel which were designed taking into account both the optimal flow characteristics together with the description of some facilities serving for the simulation of a strong wind, rain, freeze and heat radiation, and the modelling of the atmospheric boundary layer. A design for a rectangular contraction nozzle, based on a parabolic profile and extending the capacity of the wind tunnel is presented.

Keywords: *climatic tunnel, wind tunnel, atmospheric boundary layer, flow resistance, wind tunnel contraction*

Streszczenie

Artykuł opisuje nowy tunel klimatyczny, który stanowi jedno z laboratoriów Instytutu Mechaniki Teoretycznej i Stosowanej (ITAM) Akademii Nauk Republiki Czeskiej. Tunel jest wykorzystywany do badań podstawowych z zakresu inżynierii lądowej, architektury i ochrony zabytków oraz w innych dziedzinach, w których pojawia się oddziaływanie wiatru wraz z innymi czynnikami zewnętrznymi. Artykuł zawiera kluczowe informacje o układzie wnętrza tunelu, opis jego głównych części, które zaprojektowano z uwzględnieniem optymalnej charakterystyki przepływu i z uwzględnieniem atmosferycznej warstwy przyściennej oraz opis urządzeń służących do symulacji silnego wiatru, deszczu, zamarzania i promieniowania ciepła jak . Zaprezentowano opis konstrukcji konfuzora, utworzonego w oparciu o profil paraboliczny, który zwiększa możliwości tunelu.

Słowa kluczowe: *tunel klimatyczny, tunel aerodynamiczny, atmosferyczna warstwa przyścienna, opór przepływu, konfuzor*

DOI: 10.4467/2353737XCT.15.139.4176

* Climatic Wind Engineering Laboratory CET, ITAM, Czech Republic.

1. Introduction

The Centre of Excellence Telč (CET) [13, 14] for research on materials and structures (particularly historic materials and structures) is equipped with a unique infrastructure designed and manufactured to enhance fundamental knowledge and to verify the application and innovation potential of newly developed technologies in the domain of diagnostics, life cycle extension, preventative protection and conservation. The CET consists of many laboratories, one of which is a climatic wind tunnel that has an environmentally and economically optimized size. The laboratory has both on-site developed and commercial measuring equipment for the industrial aerodynamics as well as for the flow visualization.

The scientific objective of climatic wind tunnel CET (CWT CET) is to create models of the interactions between solid bodies and the surrounding environment, utilizing the findings about wind load on structures, including monuments, and taking into account the influence of other weather factors, e.g. cyclic changes in temperature and exposure to rain. A further objective is to obtain new findings and knowledge by means of long-term sustainable monitoring and modelling of the behaviour of real structures exposed to long-term weather effects and susceptible to vibrations and to damage caused by high-cycle fatigue. Using appropriate models, the research leads to proposals for measures to provide a more comfortable environment in housing estates and in the neighbourhood of transport structures.

2. Description of CET wind tunnel

The wind tunnel is designed as a closed circuit with controlled wind velocity and temperature conditions. It consists of climatic and aerodynamic sections see Fig. 1. While the aerodynamic section provides well-fitted conditions to study wind effects on scaled models of prototypes, a piece of equipment of the climatic section is suited for investigations on the influences of weather including the wind, temperature, rain and heat radiation. Using the cooling/heating exchanger, cyclic temperature changing of the airflow is available in the whole tunnel within the range of –10 to +40°C in a relatively short time period. The integral part of the tunnel equipment consists of instruments for airflow diagnostics, data acquisition system, direct pressure surface measurements, precise thermometry and many other types of handy accessories for instant use. It is a unique wind laboratory at this size, while there is one such climatic laboratory in Europe, though much larger, residing in the CSTB research facility in Nantes, France see Barlow et al. [1].

The aerodynamic section consists of a converting nozzle with a honeycomb and the working part with a turning table. The working part is in a rectangular cross-section area of 1.9 × 1.8 m, the total length of the working part is 11.0 m. High quality airflow with low turbulence of about 1% is achieved in the free aerodynamic section without turbulence generators. The converting nozzle placed upwind compresses the incoming flow at ratio of 2.85. It increases wind speed at approximately the same rate and forms the airflow uniformity over the rectangular cross-section with the maximal wind speed exceeding 30 m/s.

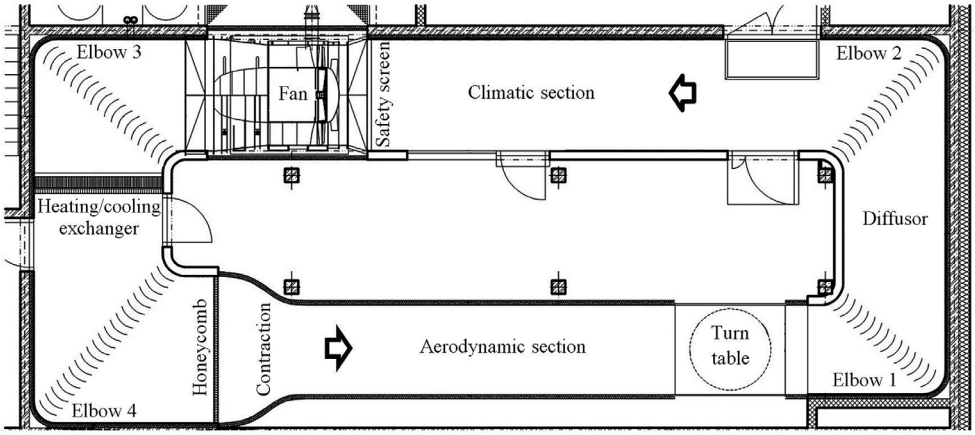

Fig. 1. Ground plan of the wind tunnel, designed in a near-oval closed shape adapted for aerodynamic and climatic testing, respectively. Arrows point in the wind direction

Using the diffusion passage and the pair of elbows, the cross-section expands twice towards the climatic chamber. To make the climatic section versatile for various types of experiments as much as possible, the ceilings with a sprinkler system and infrared lamps are continuously adjustable in height independently and over a wide range, see Fig. 2. The transition zone between the fixed tunnel roof and the sliding ceiling with the sprinklers is ensured with a rotationally adjustable flap. This chamber is in a rectangular cross-section of 2.5 × 3.9 m with a length of 9.0 m. The wind speed ranges are regulated by the position of the vertically moveable ceiling and flow nozzle from 0.8 to 30 m/s. The rain intensity together with the size of drops is regulated to simulate effects corresponding to drizzle or heavy rain. The radiation system with four infrared lamps with a total power of 8 kW, and maximal incidence of 60° to the floor, is available. The power is regulated to a large full extent and, if needed, just one lamp can be in operation.

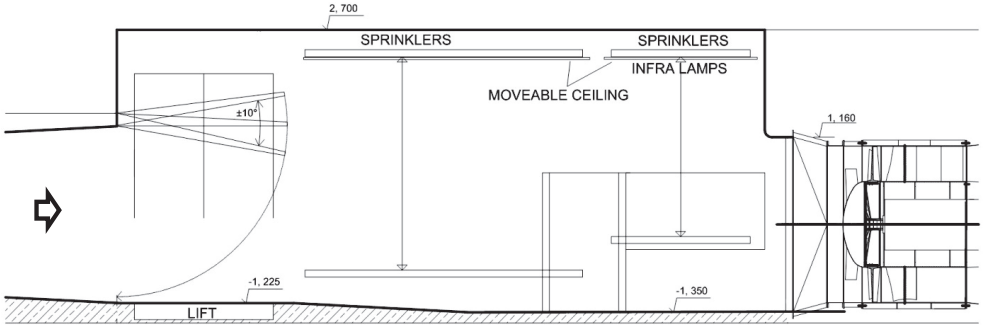

Fig. 2. Side view of the climatic section. The wind approaching from left can be adjusted by the nozzle and the moveable ceilings provide the flat plane towards the fan

Further downwind, the ventilator, an exchanger unit for air cooling/heating is integrated into the entire cross-section in a place with relatively low wind velocity (see Fig. 3). It consists of very thin aluminium ribs put next to each other on a distribution pipe with a small gap. The exchanger also functions as a screen considerably reducing the non-uniformity turbulence of flow generated by the ventilator. This arrangement shortens the disturbed zone behind the propeller by equalizing the wind speed distribution over the cross-section and prepares favourable airflow conditions for the aerodynamic section.

Fig. 3. Downwind view on aerodynamic section with historic tower model (left); View on the climatic chamber with 200 kW fan (right)

The airflow temperature is one of the main parameters of the climatic tunnel, it is measured and controlled from the control system of the wind tunnel. The design of the cooling capacity of the liquid-air heat exchanger takes into account three basic forms of heat gain: dissipative heat generated by air flow friction; accumulated heat in the tunnel structure and internal air; heat transfer due to the temperature gradient between the tunnel and surroundings. In order to minimize the energy consumption of the cooling unit, aluminium-wool or polystyrene insulation material was used on the outer walls.

The air humidity parameter is not controlled and its value is only monitored. In certain unfavourable cases at temperatures below zero, repeated condensing of the air moisture on the cooling exchanger can be used to decrease the humidity. This procedure serves for the reduction of ice accretion causing a potential decrease in the cooling efficiency and rise of pressure losses in the heat exchanger.

The wind tunnel is equipped with a sprinkler system. The rain intensity together with the size of drops is regulated to simulate effects corresponding to drizzle or heavy rain. Up to eighteen spray heads mounted on a moveable frame generate water drops using aerosol drifted with the air current towards the specimen. Afterwards, water is collected at several floor drains located at suitable places. The researchers can also use the infrared lamps for simulation of the temperature and solar radiation. The humidity generated with the sprinkler system brings increased demands on materials used both for the tunnel core itself and for the principal equipment. The material surface protection or non-corrosive materials have been used.

The majority of the tunnel devices are fully controlled by a central computer. This brings the possibility to schedule a test plan in advance using a common spreadsheet document and after importing, automatically execute the given tasks in chronological order. Because of remote access via internet and two cameras installed in both test sections, the tunnel can be controlled from a remote computer, tablet or smartphone with live video streaming.

3. Determination of the pressure losses

Two methods of determination were used. The first follows on from the experimental work by Fried and Idelchik [2] that provides a solution of fundamental cases appearing in internal fluid engineering problems. While the straight portions with a constant cross-sectional profile did not exhibit any significant issue, increased attention was paid to the tunnel components with complex shapes such as the contraction duct, elbows and screens. Starting from the basic arrangement as introduced in [2], step-by-step modelling consisting of slight changes in geometry was applied in order to achieved an optimal geometry from both the flow characteristic and flow resistance point of view. The numerical solution using direct Numerical Simulation in COMSOL was carried out to determine the pressure losses at the corners and to compare with empirical knowledge. In Fig. 4, velocity field distributed over the elbow area is presented. The picture on the left hand side shows the elbow behind the aerodynamic test section.

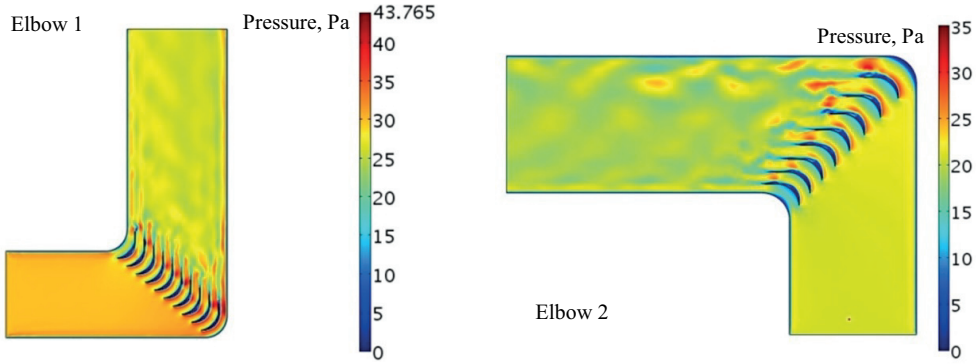

Fig. 4. Velocity field formed through the tunnel elbows: fine distribution of vanes is used for the elbow placed downwind from the aerodynamic section (left); for the remaining elbows, coarser spacing is employed (right)

Table 1 gives values of the pressure drop at certain points in the wind tunnel. Results according to Idelchik's guide are tabulated in the second column, while the last one expresses the contribution to overall pressure losses. Finally, values in the middle represent numerical results. Good results agreement was achieved although only a two-dimensional numerical model of CFD was employed. In Fig. 5, the results are processed in graphical form.

Table 1

Pressure losses of tunnel components by empirically and numerically determined values for maximal designed wind velocity

Flow passage	Empirical method [Pa]	Numerical method [Pa]	Total [%]
aerodynamic section	38		5
elbow 1	150	135	20
diffusor	3		0.4
elbow 2	70	57	
tube	1.8		0.25
climatic section	3.4		0.45
safety screen	37		4.9
fan	–	–	–
elbow 3	33	25	4.3
tube	0.6	–	0.1
heating/cooling exchanger	345	–	46
elbow 4	15	10	3.5
honeycomb	15	–	2
contraction duct	26	25	3.4

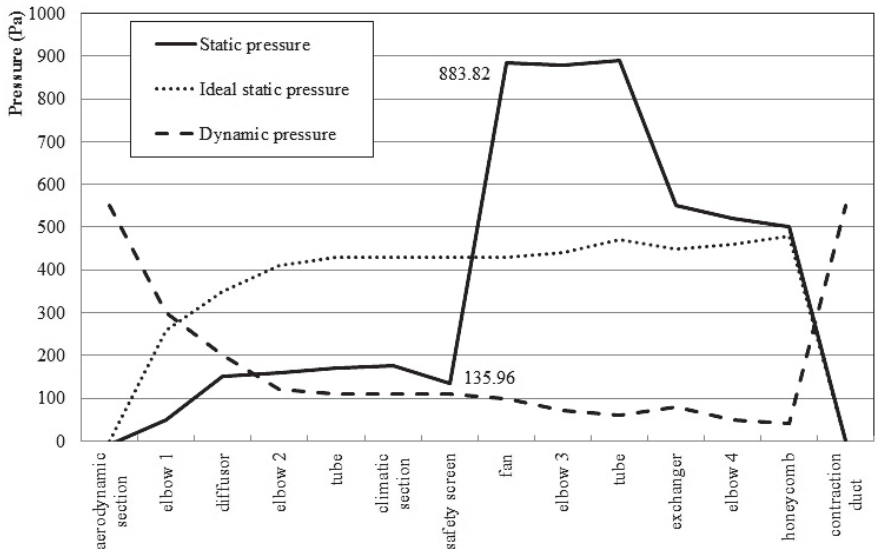

Fig. 5. Pressure development along the longitudinal centreline. The thick line represents an estimation of static pressure including flow resistance of tunnel elements

The dotted line represents the ideal static pressure determined regardless of the pressure losses. Provided that the losses are respected, a strong discontinuity appears being represented by the thick line. This jump clearly shows the required pressure gain of the fan to overcome the losses emerging when the maximal wind speed requirement is met. A 20% pressure reserve was used for the final design.

4. Atmospheric boundary layer modelling in CWT CET

The modelling of atmospheric boundary layers (ABL) is based upon well-established procedures as described by, among others, Cook [3] and Cermak [4]. The fundamental principles were originally suggested by Jensen [5]. Due to the long working part of the aerodynamic section of the tunnel, a satisfactory representation of the ABL can be obtained by the methods described below. The simulation of the ABL with demanded characteristics is based upon turbulent elements, such as spires, grids, and barrier and floor roughness (see Fig. 6). The influence of secondary recirculation in the working part is removed by means of barrier devices just after the contraction. Before these were installed, the flow near the floor at the downstream end of the test part was far from being horizontally homogeneous. Boundary-layer thickness can be increased without significant loss of similarity with the ABL by introduction of augmentation devices at the test-section entrance provided that the test-section is sufficiently long for the flow structure to reach statistical equilibrium.

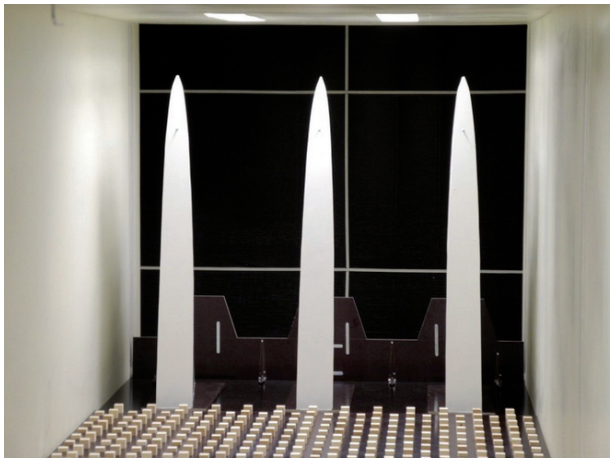

Fig. 6. Atmospheric boundary layer modelling by vortex generator array, roughness elements and the barrier

An acceptable simulation of several category terrains for various scales (basically for 1:100) was obtained in the CWT CET.

The asymptotic matching of the similarity laws applicable to boundary layers which are governed by two characteristic length scales provides formal derivation of the 'logarithmic' velocity profile, while coupling the flow in the outer layer with the flow in the inner layer. A convenient empirical formulation often used for boundary layers in general is the 'power law' given by the following equation:

$$\frac{V(z)}{V(z_r)} = \left(\frac{z}{z_r}\right)^{1/\alpha} \tag{1}$$

where $V(z)$ is mean flow speed at height z, z_r is a reference height, $1/\alpha$ is exponent in power law approximation boundary layer. Vertical profiles for the four terrain categories according to Eurocode [6] and the testing campaign using vortex generators, spires and roughness elements (full ABL for the terrain category IV) are presented on the Figure 7. Spires in

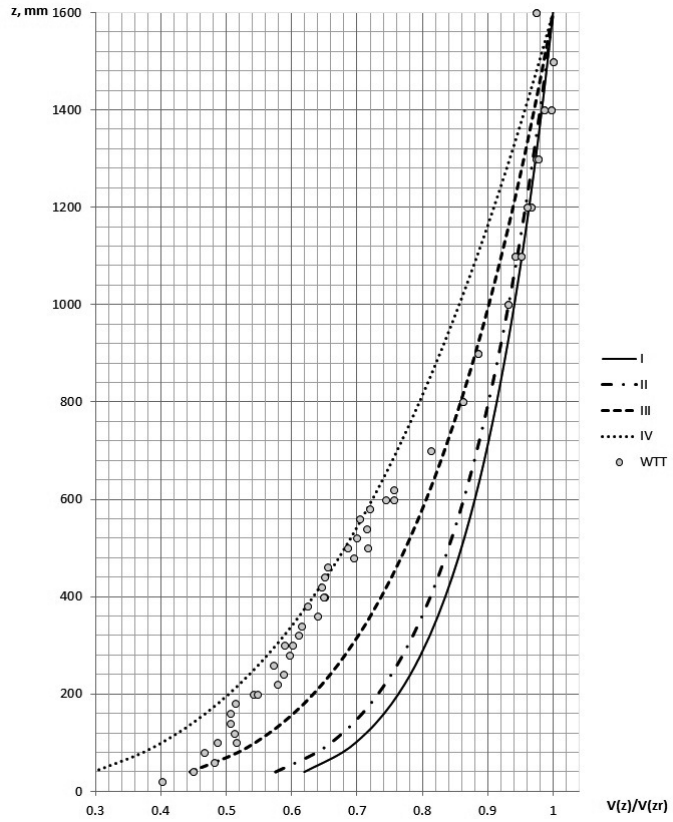

Fig. 7. Vertical profiles of mean velocity in the wind tunnel tests (WTT) compared with empirical calculation for terrain categories according to Eurocode [6] (I is rough, open sea, lakes and smooth flat country without obstacles; II is farmland with boundary hedges, occasional small farm structures, houses or trees; III is suburban or industrial areas and permanent forests; IV is urban areas in which at least 15% of the surface is covered by buildings with an average height exceeding 15 m)

the flow-processing section were combined with a block evenly distributed in the working section. The turbulent length scale of the boundary-layer flow was thereby much improved. Urban boundary layers formed over rough surfaces and approached equilibrium more rapidly through enhanced diffusion than those formed over relatively smooth surfaces.

Turbulent flow velocities vary randomly in both time and space and can be expressed either in terms of their spectral characteristics or in brief, by auto or cross-power spectral densities S_{ivv}. Statistics of primary interest for wind engineering applications are variances and standard deviations σ_i, the integral length scales ${}^{j}L_i$ for the i-th velocity component and j-th coordinate direction. Knowing the dispersion, turbulence intensity is given by the following formula:

$$I_u(z) = \frac{\sigma_j(z)}{V(z)} \tag{2}$$

The measured turbulence intensity profiles are presented in Figure 8. In the lower part of the ABL, near to the ground, is an intensity of around 27% when using the equipment as shown in Fig. 6.

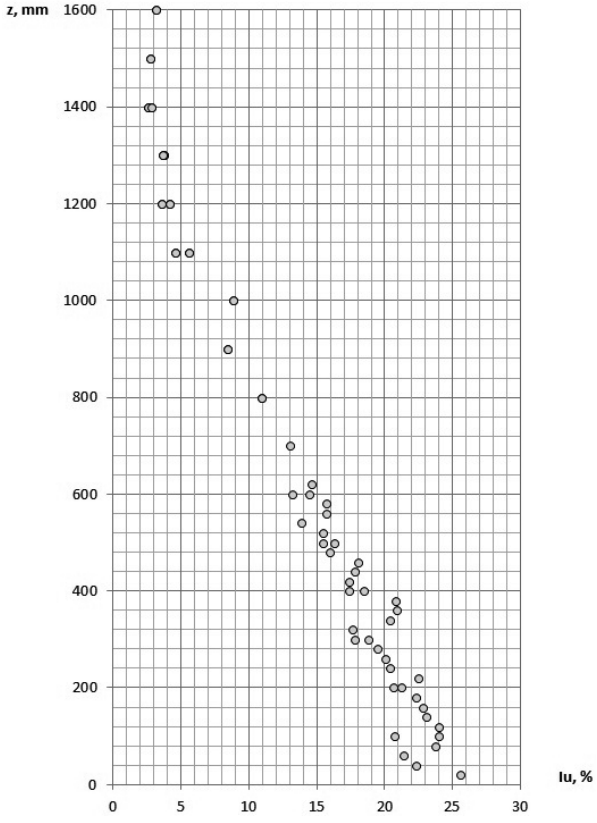

Fig. 8. Vertical profile of longitudinal turbulence intensity obtained from the wind tunnel tests

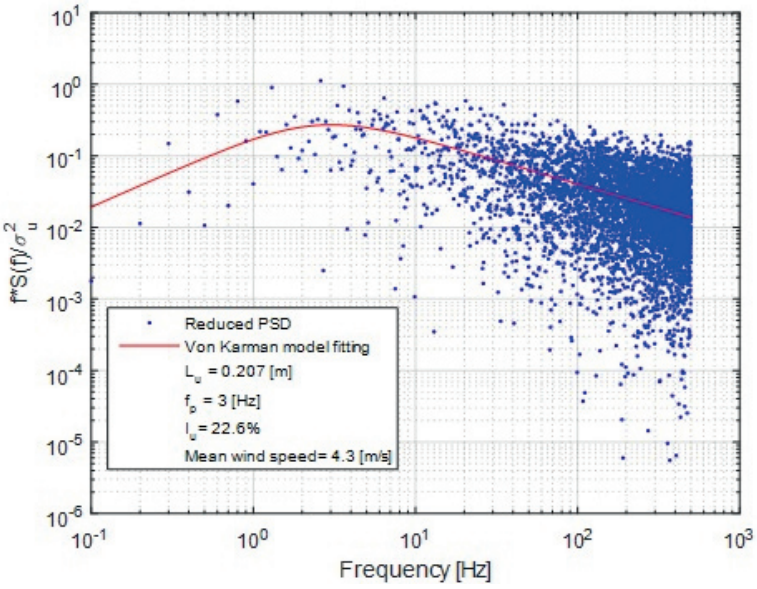

Fig. 9. Longitudinal turbulence spectra in the wind tunnel. Best fitting curve is given by the von Karman spectrum

Figure 9 shows an example of wind speed power spectral density for some point in the lower part of the ABL. Low-frequency side of a velocity spectrum corresponds to the large scale turbulence (which corresponds to large eddies in the flow and hence defines the integral length scale). The high frequency part of the spectrum, however, corresponds to small eddies in the flow (small-scale turbulence).

5. Inbuilt high speed nozzle

An important characteristic of a wind tunnel is the flow quality inside the test chamber and the overall performance. The three main criteria that are commonly used to define them are: maximum achievable speed; flow uniformity; turbulence level-intensity. Therefore, in general, the aim of contraction design is to get a better controlled flow in the test chamber, achieving the necessary flow performance and quality parameters.

Besides the stationary elements for the atmospheric flow simulation, the authors have designed a rectangular contraction nozzle, based on a parabolic profile for the significant enhancement of the aerodynamic measurements in a climatically wind tunnel – this provides a better controlled flow in the test chamber, achieving the necessary flow performance and quality parameters [7, 8]. To describe and characterize its performance, intensive experimental measurements have been conducted using pressure transducers and hot-wire anemometry.

The design of a contraction of a given area ratio and cross-section centres on the production of a uniform and steady stream at its outlet and requires the avoidance of flow separation within it. Another desirable flow quality is a minimum boundary layer thickness (in a laminar state) at the contraction exit [9–12]. This suggests that the contraction length should be minimized in order to minimize the boundary layer growth. Shorter contractions are also, of course, desirable for saving in the aerodynamic section space. However, the risk of boundary layer separation increases as the contraction length is reduced.

A long contraction produces better results for the fulfilment of these requirements. However, very long contraction leads to an increase of the boundary layer along walls and also the aerodynamic section of CET climatic wind tunnel cannot be fully used for this. The length of the contraction should be thus in the range from 1.5 to 2.5 of the outlet diameters (according to our experiences). Cylindrical section is located between the contraction and the working part to ensure a smooth transition and radius of cylinders should be 0.1–0.2 outlet diameter of the contraction.

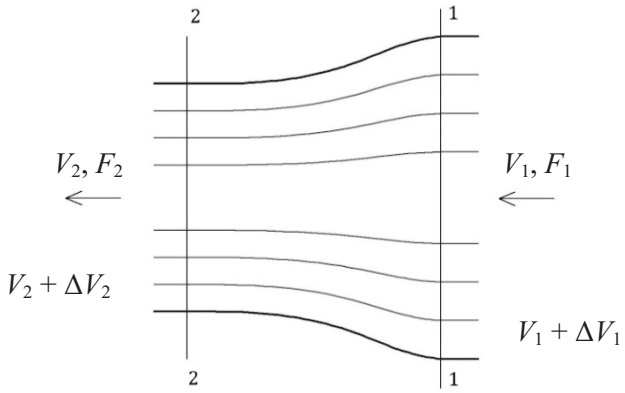

Fig. 10. Flow streamlines of the contraction

The aligning action of the contraction can be determined from the following description: in the cross-section F_1 No. 1 (inlet of the contraction, see Fig. 10); one of a streamline has velocity is V_1 and another is $V_1 + \Delta V_1$ wherein a cross-section pressure is constant, similarly for the cross-section F_2 No. 2 where V_2 and $V_2 + \Delta V_2$ (outlet of the contraction, see Fig. 10). Bernoulli equation has been formulations for both sides and obtained the following:

$$V_1 \Delta V_1 = V_2 \Delta V_2 \quad \text{or} \quad \Delta V_1 = \Delta V_2 \frac{V_2}{V_1} \tag{3}$$

The uniformity of flow velocity can be used as follows:

$$a_1 = \frac{\Delta V_1}{V_1} \quad \text{and} \quad a_2 = \frac{\Delta V_2}{V_2} \tag{4}$$

$$a_1 = \Delta V_2 \frac{V_2}{V_1^2} = \Delta V_2 \frac{V_2}{\left(\frac{V_2}{n}\right)^2} = n^2 a_2 \tag{5}$$

where n is contraction ratio and $n = V_2/V_1 = F_1/F_2$. Thus, the uniformity of outlet flow velocity n^2 times less than the uniformity of inlet flow velocity of a contraction. After some optimization steps, the shape of the contraction was determined according to the formula:

$$y = \frac{r_2}{\sqrt{1-\left[1-\left(\frac{r_2}{r_1}\right)^2\right]\frac{\left(1-3x^2/\left(4r_2\right)^2\right)^2}{\left(1+3x^2/\left(4r_2\right)^2\right)^3}}} \tag{6}$$

where x is along stream direction coordinate, r_1 is radius of inlet cross-section, r_2 is radius of outlet cross-section.

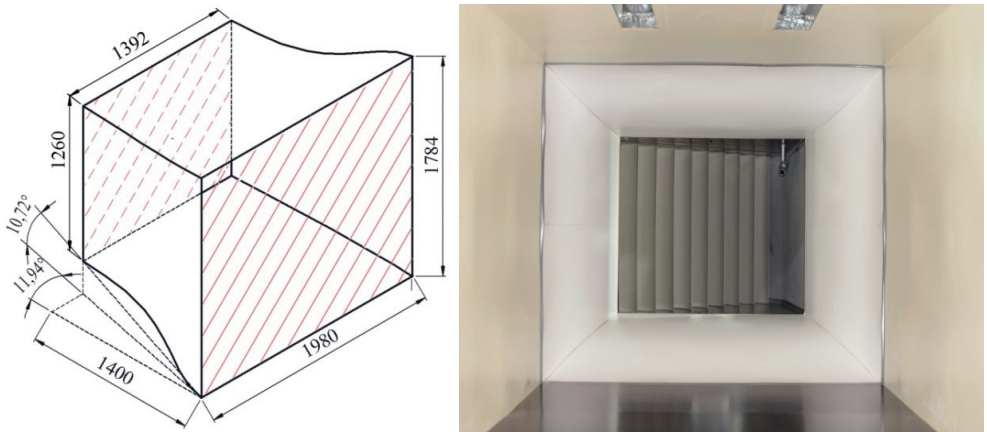

Fig. 11. The high speed chamber: geometrical parameters of the contraction (left), the downstream view (right)

The contraction resulted in the increase of speed up to 55 m/s. Turbulence intensities below 0.3% were obtained for the whole range of velocities. Constant uniform flow was obtained for all the cross-sections along the nozzle. These indicators show that the special contraction nozzle is an excellent enhancement improving wind tunnel performance.

The quality of the flow has changed due to the compression of air stream and reducing of the contraction outlet cross-section area. The uniformity velocity distribution was 0.7 % in accordance with the experimental results (see Fig. 12).

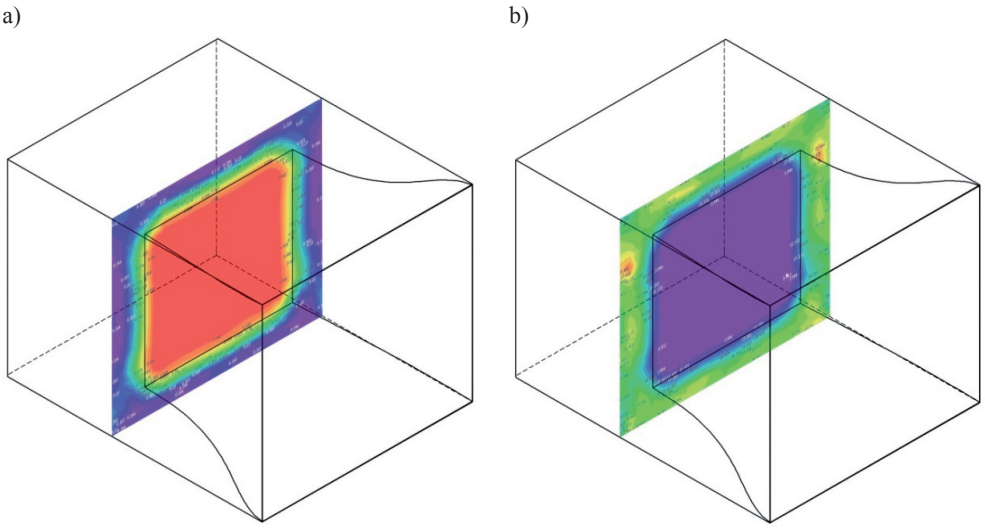

Fig. 12. Flow characteristics of the working section: a) velocity; b) turbulence

6. Conclusions

This paper presents a description of the newly-built wind tunnel developed for fundamental research of engineering problems related to the study of wind and climatic effects on structures. The paper describes the pressure loss determination and other important design issues. The unique wind climatic tunnel uses a combination of two working sections. This arrangement is advantageous due to its wide universality and adaptability to experimental demands. Besides the interior layout tunnel description, the full paper focuses on the description of the flow resistance of essential tunnel parts, the modelling of atmospheric boundary layers and the design of a rectangular contraction nozzle.

This work was supported by the European Regional Development Fund of the project CZ.1.05/1.1.00/02.0060, the project GAČR 14-12892S, the Ministry of Education, Youth and Sports, and the Academy Sciences of the Czech Republic

References

[1] Barlow J., Rae W.H., Pope A., *Low-speed wind tunnel testing*, John Wiley & Sons, USA, 1999.

[2] Fried E., Idelchik I.E., *Flow resistance: A design guide for engineers*, Taylor & Francis, London 1998.

[3] Cook N.J., *The designer's guide to wind loading of building structures*, Part 1, Butterworths, London 1985.

[4] Cermak J.E., *Development of wind tunnels for physical modeling of the atmospheric boundary layer*, [In:] *A State of the Art in Wind Engineering*, Davenport Sixtieth Birth Anniversary Volume, Wiley Eastern Limited, USA, 1995, 1-25.

[5] Jensen M., *The model law for phenomena on natural wind*, Ingeniøren, Int'l Edition, 2, 1958, 121-128.

[6] Eurocode 1: Actions on structures − Part 1–4: General actions − Wind actions.

[7] Fang F., *A design method for contractions with square end sections*, Journal of Fluids Engineering, Vol. 119, 1997, 454-458.

[8] Mehta R., *The aerodynamic design of blower tunnels with wide-angle diffusers*, Progress in Aerospace Sciences, Vol. 18, 1979, 59-120.

[9] Fang F., Chen J., Hong Y., *Experimental and analytical evaluation of flow in a square-to-square wind tunnel contraction*, Journal of Wind Engineering and Industrial Aerodynamics, Vol. 89, 2001, 247-262.

[10] Song C.C.S., Yuan M., *A weakly compressible flow model and rapid convergence methods*, Journal of Fluids Engineering, Vol. 110, 1988, 441-455.

[11] Wolf T., *Design of a variable contraction for a full-scale automotive wind tunnel*, Journal of Wind Engineering and Industrial Aerodynamics, Vol. 56, 1995, 1-21.

[12] Michalcová V., Kuznetsov S., Brožovský J., Pospíšil S., *Numerical and experimental investigations of air flow turbulence characteristics in the wind tunnel contraction*, Applied Mechanics and Materials, Vol. 617, 2014, 275-279.

[13] http://www.itam.cas.cz

[14] http://cet.arcchip.cz

TECHNICAL TRANSACTIONS | CZASOPISMO TECHNICZNE
CIVIL ENGINEERING | BUDOWNICTWO
2-B/2015

RYOJI SASAKI*, AKINORI AKAHOSHI*, YASUSHI UEMATSU**

RELATIONSHIP BETWEEN SURFACE ROUGHNESS AND TURBULENCE OF NATURAL WINDS NEAR THE GROUND SURFACE

ZWIĄZEK MIĘDZY CHROPOWATOŚCIĄ I TURBULENCJĄ NATURALNYCH WIATRÓW W WARSTWIE PRZYZIEMNEJ

Abstract

The design of low-rise buildings such that they can handle wind loads makes it necessary to accurately evaluate those wind loads, both on the structural framework and on the cladding/components. To this end, it is necessary to fully understand the characteristics of the wind near the ground around a building. This study sets out to develop a quantitative means of estimating the turbulence of the wind near the surface of the ground, based on field measurements obtained at different points across Japan. The surface roughness is evaluated based on several factors taken from a building information database. The relationship between these factors and the turbulence of the wind is discussed. The effect of the observation height, relative to the surface of the ground, on the turbulence is also investigated.

Keywords: *gust factor, surface roughness, building information database, field measurement, observation height*

Streszczenie

Projektowanie niskich budynków w taki sposób, aby opierały się one działaniu wiatru, wymaga dokładnej oceny obciążenia wiatrem zarówno konstrukcji, jak i elementów pokrycia. W tym celu konieczne jest pełne zrozumienie charakterystyk wiatru w warstwie przyziemnej w pobliżu budynku. W niniejszej pracy podjęto próbę oszacowania wielkości turbulencji wiatru w pobliżu powierzchni w oparciu o pomiary w terenie w różnych punktach na obszarze Japonii. Chropowatość powierzchni została wyznaczona na podstawie kilku parametrów przyjętych na podstawie baz danych informacji o budynkach. Omówiony został związek między tymi czynnikami i turbulencją. Analizowano także wpływ wysokości nad powierzchnią podłoża, na której prowadzona jest obserwacja na turbulencję.

Słowa kluczowe: *współczynnik działania porywów wiatru, chropowatość powierzchni, bazy danych informacji o budynkach, pomiary terenowe, wysokość obserwacyjna*

DOI: 10.4467/2353737XCT.15.140.4177

* Wind Engineering Institute Co., Ltd., Japan.
** Department of Architecture and Building Science, Tohoku University, Japan.

1. Introduction

The wind-resistant design of low-rise buildings makes it necessary to understand the characteristics of the wind near the surface of the ground around those buildings, e.g., the mean wind-speed profiles, the turbulence intensity, and the gust factor. In the AIJ Recommendations for Loads on Buildings [2] and the Building Standard Law of Japan, the mean wind speed profile is specified as being constant up to a specific height Z_b, corresponding to the surface roughness category, beyond which it is expressed by a power function of height Z above the ground. The turbulence intensity profile is also specified, much like the mean wind speed in the AIJ Recommendations [2]. Such vertical profiles may significantly overestimate the wind loads on low-rise buildings, both on the structural framework and on the cladding/components. To evaluate the design wind loads, the characteristics of the wind near the surface of the ground should be fully understood.

The goal of this study was to develop a quantitative means of estimation for assessing the turbulence of the wind near the surface of the ground, based on field measurements made at many locations across Japan. The relationship between the characteristics of the surface roughness and the turbulence of wind is discussed. Special attention is paid to the gust factor in this paper.

2. Characteristics of surface roughness

2.1. Measured data

In the AIJ Recommendations [2], surface roughness is divided into five categories, I to V. The profile of the turbulence intensity I_Z is specified as follows:

$$I_Z = \begin{cases} 0.1\left(\dfrac{Z}{Z_G}\right)^{-\alpha-0.05} & Z_b < Z \le Z_G \\ 0.1\left(\dfrac{Z_b}{Z_G}\right)^{-\alpha-0.05} & Z \le Z_b \end{cases} \tag{1}$$

where Z represents the height above the ground [m]; α, Z_G, and Z_b are the parameters defining the profile, the values of which are listed in Table 1.

Fig. 1 shows the turbulence intensity profiles for the five surface roughness categories. The value of I_z is specified as being constant up to a height Z_b, according to the category.

Full-scale measurements of the wind speed near the surface of the ground were carried out at various sites with different terrains; in most cases, the measurement height was less than Z_b. Similar measurements were performed at many Japan Meteorological Agency (JMA) meteorological observatories and Automated Meteorological Data Acquisition System (AMeDAS) sites. Wind data from as many as 243 observation sites across Japan were used

for this study. The observation height ranged from 5 m to about 70 m, as shown in Fig. 2. In most cases, the observation height was less than 15 m. The data were used to analyze the characteristics of the wind near the surface of the ground, e.g., the intensity and scale of the turbulence, the power spectrum, and the peak factor. The dependence of these factors on the observation height as well as on the surface roughness of the upwind area is discussed.

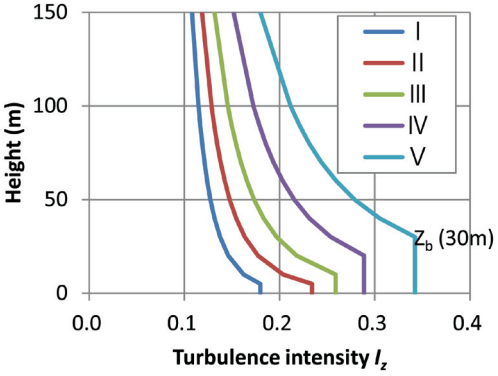

Fig. 1. Turbulence intensity profiles

Table 1

Parameters for defining turbulence intensity profile

Category	I	II	III	IV	V
α	0.10	0.15	0.20	0.27	0.35
Z_G [m]	250	350	450	550	650
Z_b [m]	5	5	10	20	30

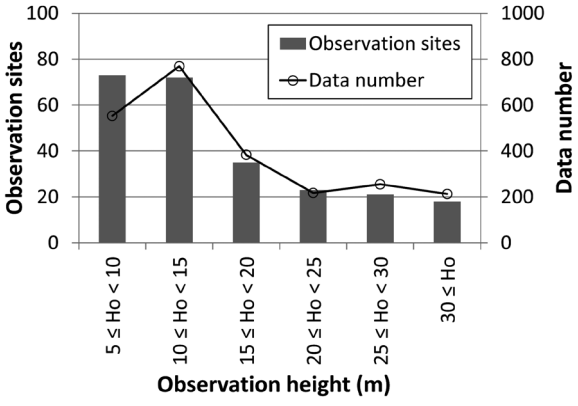

Fig. 2. Histograms of numbers of observation sites and data used in the present study

For this study, data collected over the course of one year at each point were used. The wind speed and direction were sampled at a rate of 4 Hz, and a moving average of 3 s was applied to the data. Data for which the 10-min mean wind speed is higher than a predetermined value (3 to 5 m/s) corresponding to the observation height (H_O) were used.

Approximately 75% of the data was obtained from the JMA and AMeDAS sites. For these databases, only statistical values have been published, e.g., the 10-min average wind speed and the 3-s average wind speed. Therefore, as the first step, the gust factor (G_F), defined as the ratio between the 3-s average wind speed and the 10-min average wind speed, is investigated.

2.2. Analysis area

The characteristics of the surface roughness near the observation sites significantly affect the characteristics of the wind speed and direction. For this analysis, we focused on the 16 upwind trapezoidal areas defined as shown in Fig. 3. The length of the area is 200 m, and the width changes from 50 m to 110 m in the upwind direction. Our previous study [1] indicates that this area is appropriate for discussing the relationship between the surface roughness and the turbulence of the wind near the ground.

Up to 2390 sets of data were used in this study, as illustrated in Fig. 2. The gust factor was calculated from these data.

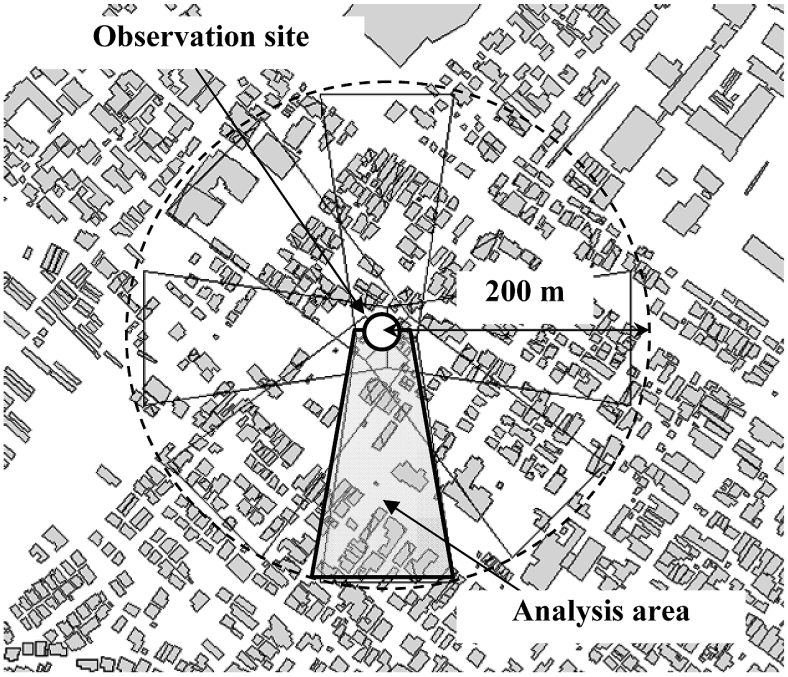

Fig. 3. Analysis area

2.3. Definition of surface roughness factors

Surface roughness is characterized by many factors, including the building coverage ratio, the average height of the building, and the building volume. The eight major surface roughness factors are defined in Table 2 and by Eqs. (2) to (9). The details of these factors are presented in [1, 3]. In this study, a "high building" refers to a building with more than four stories. The values of these factors are evaluated by using a building information database.

Table 2

Surface roughness factors

Average height of building [m]	$\overline{h} = \left(\sum_{i=1}^{n} h_i \right) / n$	(2)
Average area of building [m^2]	$\overline{a_{bi}} = \left(\sum_{i=1}^{n} a_{bi} \right) / n$	(3)
Average volume of building [m^3]	$\overline{V_{bi}} = \left(\sum_{i=1}^{n} a_{bi} h_i \right) / n$	(4)
Building coverage ratio [–]	$R_b = \left(\sum_{i=1}^{n} a_{bi} \right) / A$	(5)
Building volume ratio [m]	$V_b = \left(\sum_{i=1}^{n} a_{bi} h_i \right) / A$	(6)
Density of building volume [–]	$V_D = \left(\sum_{i=1}^{n} a_{bi} h_i \right) / A\overline{h}$	(7)
Ratio of high buildings [–]	$H_4 = \left(\sum_{i=1}^{n} n_{\geq 4} \right) / n$	(8)
Ratio of high building area [–]	$\overline{h_4} = \left(\sum_{i=1}^{n} a_{\geq 4} \right) / A$	(9)

where h_i represents the height of each building (m); a_{bi} is the area of each building (m^2); $a_{\geq 4}$ is the area of a high building (m^2); A is the analysis area (m^2); n is the number of buildings (–); $n_{\geq 4}$ is the number of high buildings (–) in the area under consideration.

The correlation coefficients between pairs of factors among these eight factors are listed in Table 3. It can be seen that the correlations between R_b and V_b, $\overline{h}$ and H_4, V_b and V_D, and V_b and $\overline{h_4}$ can be as high as 0.89, 0.81, 0.80, and 0.80, respectively. On the other hand, the correlations between $\overline{a_{bi}}$ and the other factors are generally low. Therefore, in this study, focus is on R_b, V_b, $\overline{h}$, and $\overline{h_4}$.

Table 3

Correlation coefficient of eight factors

	$\overline{h}$	$\overline{a_{bi}}$	$\overline{V_{bi}}$	R_b	V_b	V_D	H_4	$\overline{h_4}$
$\overline{h}$	–	0.32	0.66	0.31	0.58	0.37	0.81	0.52
$\overline{a_{bi}}$	0.32	–	0.58	0.25	0.28	0.23	0.28	0.21
$\overline{V_{bi}}$	0.66	0.58	–	0.19	0.69	0.32	0.55	0.46
R_b	0.31	0.25	0.19	–	0.59	0.89	0.22	0.45
V_b	0.58	0.28	0.69	0.59	–	0.80	0.56	0.80
V_D	0.37	0.23	0.32	0.89	0.80	–	0.32	0.66
H_4	0.81	0.28	0.55	0.22	0.56	0.32	–	0.72
$\overline{h_4}$	0.52	0.21	0.46	0.45	0.80	0.66	0.72	–

Fig. 4 represents the relative frequency distributions of R_b, V_b, $\overline{h}$, and $\overline{h_4}$ for all of the observation sites. It was found that the distribution pattern of the relative frequency is highly dependent on these factors. As illustrated in Figs. 4(a) and 4(b), the values of R_b and V_b are distributed almost uniformly within the range of 0 to 0.4. Therefore, these two factors seem to be closely related to the turbulence of the wind. In the Tokyo Metropolitan area, the value of R_b varies from 0.1 to 0.5, while approximately 90% of the data ranges from 0.15 to 0.40 [3]. In this study, data obtained at many locations in both suburban and rural areas is included. By comparison, the range of $\overline{h}$ and $\overline{h_4}$ is relatively narrow, as shown in Figs. 4(c) and 4(d). These values change relatively little. Because the building height is not included in the building information database that was used for this study, the height of a story was assumed to be 3 m for every building. There are many 2-story buildings, such as residential houses, in most areas. Therefore, the relative frequency of 6 m is fairly high for $\overline{h}$. Fig. 4(d) indicates that the number of high buildings is relatively small.

Fig. 5 represents four areas (shaded areas) with different R_b values from 0.1 to 0.4, in which 16 areas, each corresponding to a different direction, are also shown. The terrain categories defined by AIJ and the values of several surface roughness factors from A to D are shown in Table 4. It was found that these factors generally increase with an increase in R_b. However, sites where there are only a few large buildings, and the values of $\overline{h}$ and $\overline{h_4}$ are large despite the value of R_b being small should be considered.

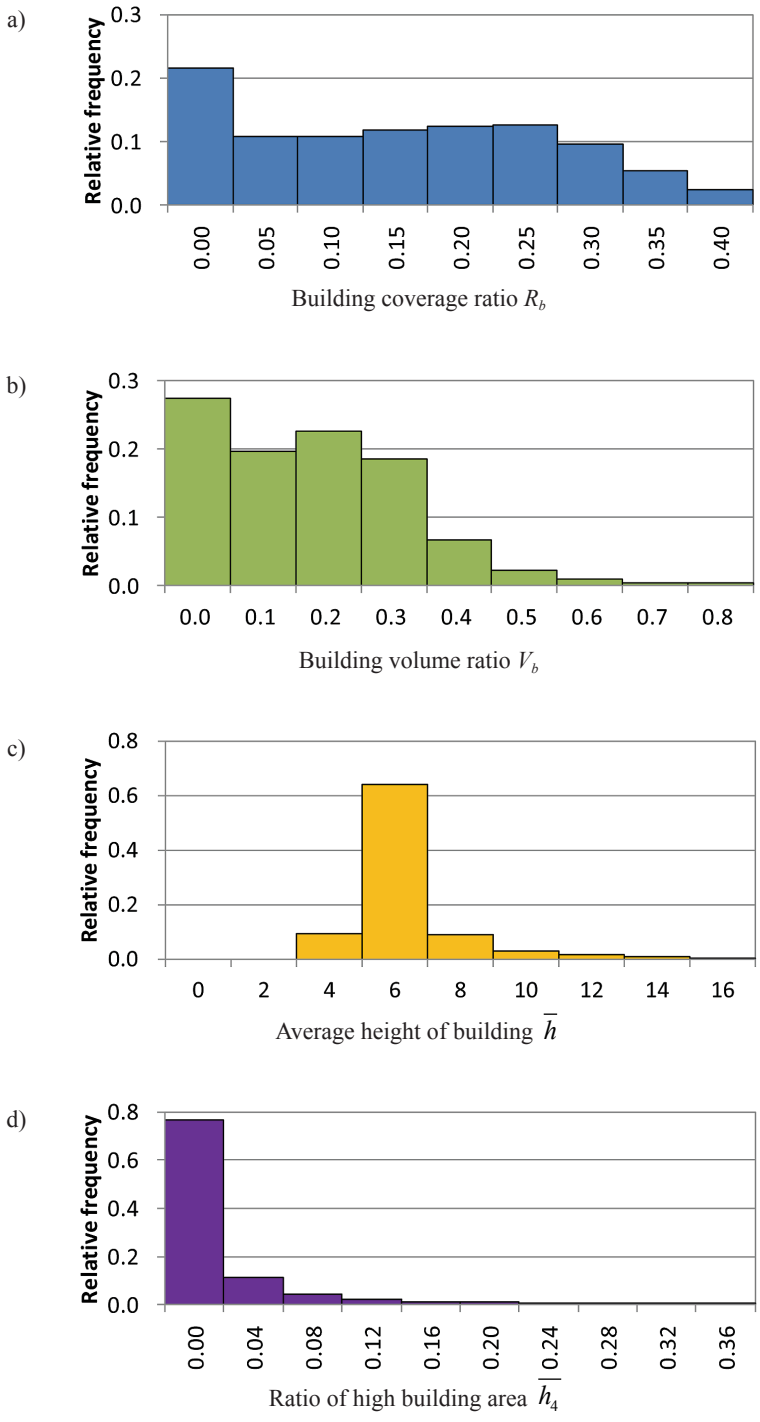

Fig. 4. Relative frequency distributions of R_b, V_b, $\overline{h}$, and $\overline{h_4}$

(a) Site A, $R_b = 0.1$ (b) Site B, $R_b = 0.2$

(c) Site C, $R_b = 0.3$ (d) Site D, $R_b = 0.4$

Fig. 5. Arrangement of buildings in four areas with different R_b values

Table 4

Values of surface roughness for the four sites

Site	A	B	C	D
Category (AIJ)	II	II	III	III
Wind direction	N	WNW	W	SW
$\overline{h}$ (m)	6.0	6.0	6.2	6.8
$\overline{a_{bi}}$ (m^2)	72	84	78	90
$\overline{V_{bi}}$ (m^3)	433	504	501	615
R_b	0.10	0.20	0.30	0.40
V_D	0.10	0.20	0.31	0.40
$\overline{h_4}$	0.00	0.00	0.01	0.03

3. Gust factor

3.1. Relationship between surface roughness and gust factor

The relationship between G_F and surface roughness was investigated based on the above mentioned analysis. Figs. 6(a) and 6(b) show the dependence of G_F on R_b and V_b, respectively, for all the data. Although the data exhibit scattering, a trend whereby the value of G_F first increases slightly and then reaches an upper limit as the values of R_b and V_b increase can be identified. A similar trend was observed for the relationship between G_F and the other factors, e.g., $\overline{h}$ and $\overline{h}_4$ [4]. Note that the data for a wide range of H_O values, from 5 m to about 95 m, are plotted in Fig. 6.

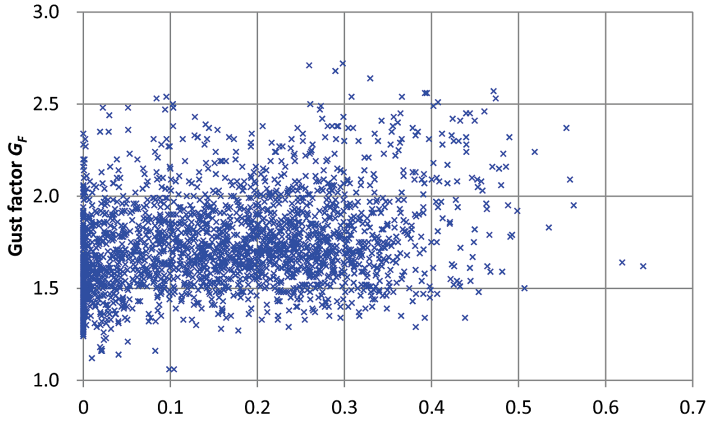

(a) Building coverage ratio R_b

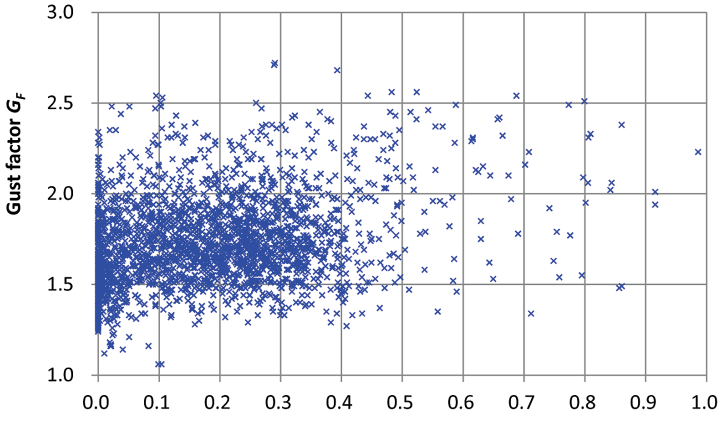

(b) Building volume ratio V_b

Fig. 6. Relationship between G_F and surface roughness

3.2. Influence of observation height on gust factor

The turbulence of the wind is also dependent on the observation height H_O. In this analysis, we classified the data into several heights, with a spread of 5 m. Fig. 7 shows the dependence of G_F on R_b, V_b, $\overline{h}$, and $\overline{h_4}$ for each height class. Although the results exhibit scattering, the value of G_F generally increases as the value of H_O decreases. The value of G_F seems to increase with R_b and V_b (see Figs. 7(a) and 7(b)). For $\overline{h}$ and $\overline{h_4}$, on the other hand, no dependence of G_F on these factors was observed. This may be due to the fact that the range of these factors that could be used for this study is rather limited.

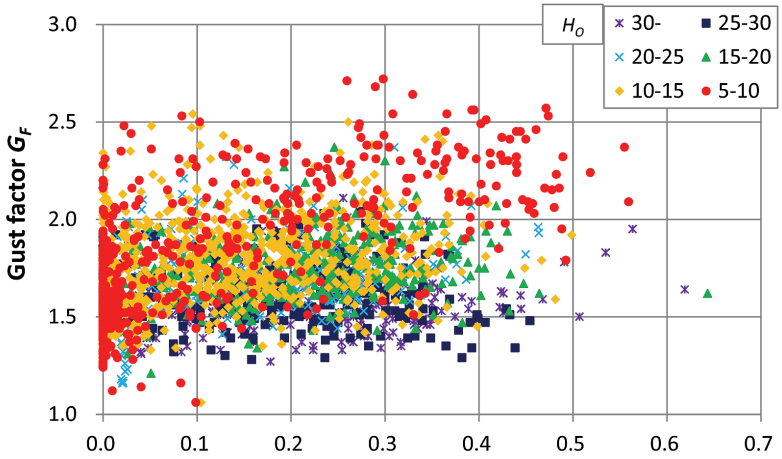

(a) Building coverage ratio R_b

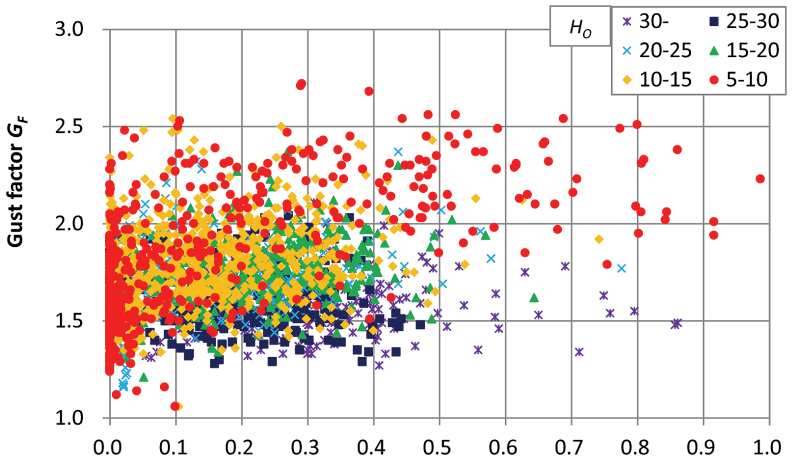

(b) Building volume ratio V_b

Fig. 7. Relationship between G_F and surface roughness classified into several height classes

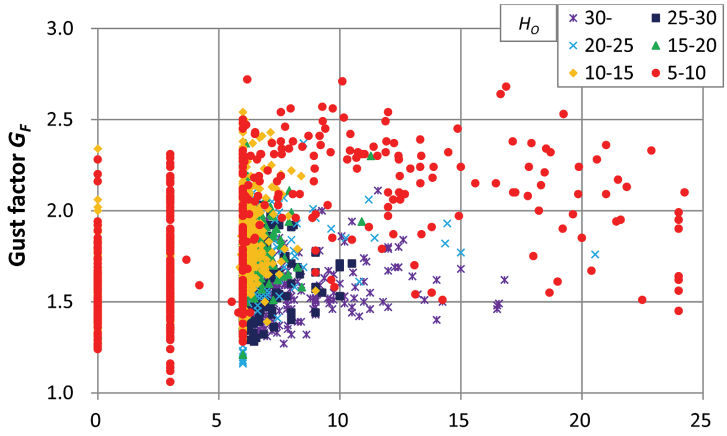

(c) Average height of buildings $\overline{h}$

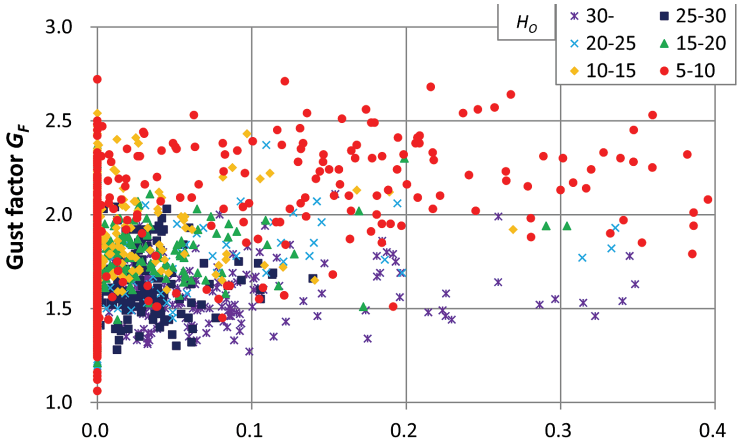

(d) Ratio of high building area $\overline{h_4}$

Fig. 7 (cont). Relationship between G_F and surface roughness classified into several height classes

To investigate the influence of H_O on G_F in more detail, the average value of G_F for each class of height was plotted against each factor of surface roughness, as shown in Fig. 8. As shown in Fig. 8(a), when H_O is less than about 20 m, the value of G_F first increases and then reaches a constant value as R_b increases. The constant value of G_F depends on H_O. For example, when H_O is within the range from 5 m to 10 m, the value of G_F is approximately 2.2 to 2.3. This constant value decreases as H_O increases. When H_O is greater than about 25 m, the value of G_F is only very slightly affected by R_b. A similar effect can be seen for the other factors, particularly for R_b and V_b, the values of which vary over a wide range. The value of G_F is approximately 1.5 to 1.6 regardless of the value of H_O, as the value of each factor approaches zero. It was found that both the observation height and the surface roughness factors significantly affect the characteristics of G_F.

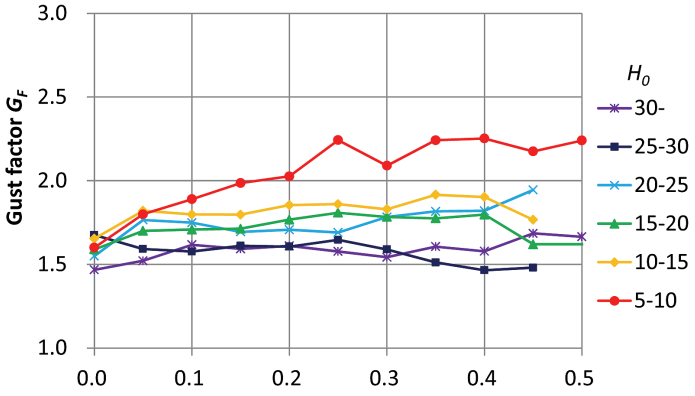

(a) Building coverage ratio R_b

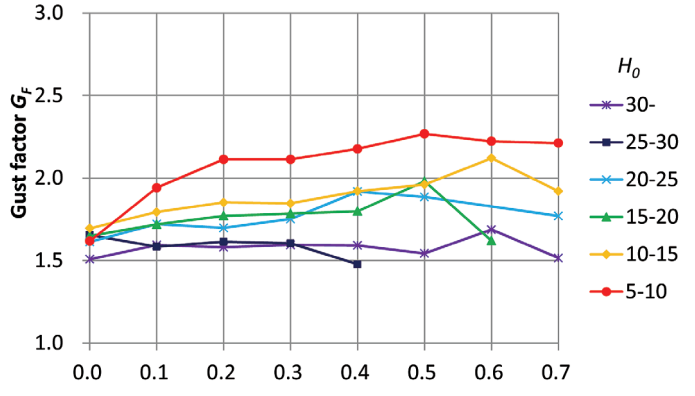

(b) Building volume ratio V_b

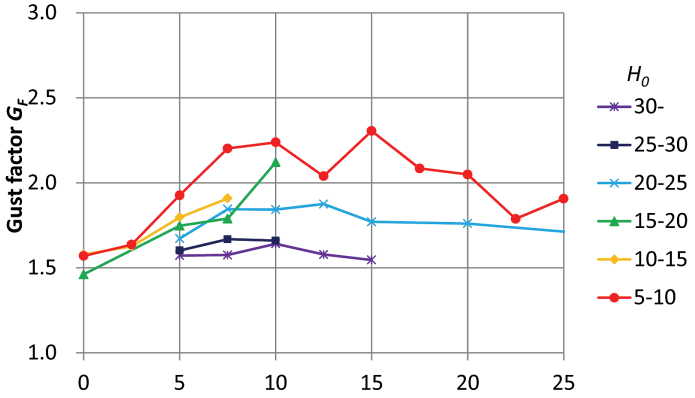

(c) Average height of buildings $\overline{h}$

Fig. 8. Average value of G_F for each class of height against each factor of surface roughness

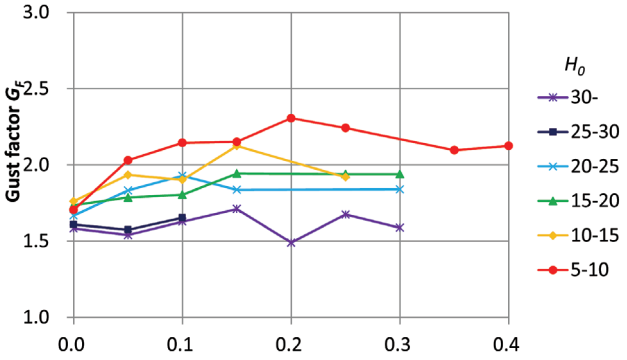

(d) Ratio of high buildings area $\overline{h_4}$

Fig. 8 (cont.). Average value of G_F for each class of height against each factor of surface roughness

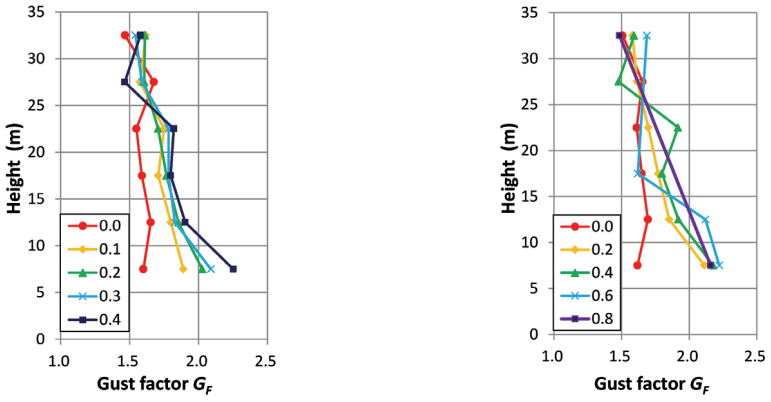

(a) R_b (b) V_b

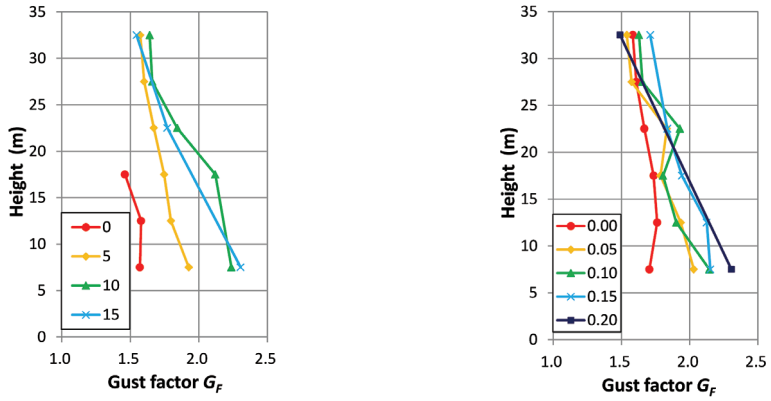

(c) $\overline{h}$ (d) $\overline{h_4}$

Fig. 9. Relationship between H_O and G_F for each factor

Fig. 9 illustrates the relationship between H_O and G_F for each factor. In this figure, the values of each factor are divided into several classes and the average values are plotted. It was found that the variation of G_F with H_O becomes more significant as the value of each factor increases. Furthermore, G_F is greatly affected by the surface roughness when H_O is low. With this increase in H_O, G_F becomes less sensitive to the surface roughness factors.

Therefore, the authors suggest that G_F can be defined by the values of the surface roughness parameters such as R_b and the height.

4. Conclusions

The relationship between the surface roughness characteristics and the gust factor has been discussed based on data obtained from measurements taken in the field and a building information database. It was found that some surface roughness factors, such as the building coverage ratio, are closely related to the gust factor when $H_O < 15$ m. Furthermore, the observation height also has a significant effect on the gust factor. The gust factor can be given by a function of these factors and the height above the ground.

In future work, to investigate this relationship in more detail, statistical analysis, such as multivariate analysis, will be applied to the data. Variation in the turbulence will be taken into consideration. Furthermore, it is intended to investigate the relationship between the gust factor and the turbulence of the wind like turbulence intensity based on measurements and wind tunnel tests using a variety of surface roughnesses.

References

[1] Akahoshi A., Sasaki R., Miyashita K., Nakamura O., Uematsu Y., *Comparison of characteristics of terrain roughness and ground surface wind - Part 1 Parameters related to the terrain*, Summaries of Technical Papers of Annual Meeting, Architectural Institute of Japan, 2012, 119-120 (in Japanese).

[2] Architectural Institute of Japan, Recommendations for Loads on Buildings, 2004 (in Japanese).

[3] Nakamura O., Miyashita K., Uematsu Y., Yamada M., *Actual conditions of terrain roughness evaluated from numerical data of structural dimensions in Tokyo*, Journal of Wind Engineering, JAWE. No. 84, 2000, 59-69 (in Japanese).

[4] Sasaki R., Akahoshi A., Miyashita K., Nakamura O., Uematsu Y., *Comparison of characteristics of terrain roughness and ground surface wind - Part 2 Effects on the characteristics of fluctuating wind speeds*, Summaries of Technical Papers of Annual Meeting, Architectural Institute of Japan, 2012, 120-121 (in Japanese).

TECHNICAL TRANSACTIONS | CZASOPISMO TECHNICZNE
CIVIL ENGINEERING | BUDOWNICTWO
2-B/2015

ELIZA SZCZEPAŃSKA-ROSIAK*, DARIUSZ HEIM*

THE EFFECT OF WALL THICKNESS AND WINDOW POSITION ON EFFICIENT DAYLIGHT UTILISATION IN BUILDING INTERIORS

WPŁYW GRUBOŚCI ŚCIANY I POŁOŻENIA OKNA NA WYDAJNE WYKORZYSTANIE ŚWIATŁA DZIENNEGO WE WNĘTRZACH BUDYNKU

Abstract

This paper presents a numerical analysis of the daylighting of exemplary office interiors. Simulation results were obtained using a radiance model. The following indexes: UDI, DF, DA, DSP were calculated and analysed for different solutions of building façade. The construction differs in the total thickness of the wall. Two cases were considered: 25 cm and 50 cm opaque sections. Additionally, window magnitude changes from 0.36 m^2 to 1.44 m^2, with different shapes and locations relative to the centre of the wall. The idea of the work was to find out the architectural solution of the transparent element (geometry and magnitude) taking into account two criteria: decreasing solar heat gains; increasing the daylight utilisation factor. The results are presented in the form of a diagram of daylight distribution as well as average values of visual comfort indexes. The highest values of each indicator (DF, DA and DSP) were obtained for a centrally placed window 1.44 m^2. However, the results of useful daylight index UDI depend on the assumed range and it is not easy to identify a relationship between window size and daylight efficiency.

*Keywords***:** *daylighting, façade, solar, efficiency, office*

Streszczenie

W pracy przedstawiono analizę numeryczną dziennego naświetlenia wnętrza pomieszczenia biurowego. Wyniki uzyskano za pomocą modelu radiacyjnego. Dla różnych rozwiązań fasady budynku obliczono i analizowano następujące wskaźniki UDI, DF, DA, DSP. Założone konstrukcje różnią się całkowitą grubością ściany. Rozważono dwa przypadki: 25 cm i 50 cm nieprzezroczystych przekrojów. Wielkość okna zmienia się od 0.36 m^2 do 1.44 m^2. Okno ma różne kształty i położenie względem środka ściany. Ideą pracy było wskazanie rozwiązania architektonicznego elementu przezroczystego (wielkości i geometrii), przy przyjęciu dwóch kryteriów: zmniejszenie słonecznego gromadzenia ciepła, zwiększenie czynnika wykorzystania nasłonecznienia dziennego. Wyniki przedstawiono w formie rozkładów światła dziennego i średnich wartości wskaźników komfortu wizualnego. Największe wartości wszystkich wskaźników (DF, DA and DSP) otrzymano w przypadku centralnego położenia okna 1.44 m^2. Jednakże, wyniki dotyczące wskaźnika UDI zależą od założonego zakresu i nie łatwo jest wskazać zależność między rozmiarami okna i sprawnością światła dziennego.

Słowa kluczowe: oświetlenie dzienne, elewacja, słoneczność, sprawność, biuro

DOI: 10.4467/2353737XCT.15.141.4178

* Department of Environmental Engineering, Lodz University of Technology, Poland.

1. Introduction

Daylight utilisation in the design of healthy buildings is a crucial point, not only with regard to indoor environment quality but also from an energy efficiency point of view. In selected types of non-residential buildings, e.g. offices, people spend a majority of time during the day. Therefore, it is necessary to provide high indoor comfort parameters including the lighting quality.

Daylight distribution and directionality of light determine the main parameters of visual comfort and comfort indexes. The main visual comfort indexes are based on two parameters: luminance and illuminance. Horizontal illuminance at work plane should be well adapted to the needs of the occupants e.g. the type of activity performed in the workplace. Additionally, daylight illuminance inside the building is changeable and depends on external parameters like weather, time of day, season and urban development. Similarly, the amount of light inside the building strongly depends on architectural design, geometry, size of windows and surface properties (transmission and reflection characteristics).

Nowadays, the starting point for daylight design is a collection simple guidelines – this initial guidance is imprecise and provides only an approximation. This approximation is based on the percentage of glazing, the ratio of glazed area to floor area or the maximum depth of the room that should not be exceeded. This is relatively easy but fails to be precise enough.

2. Visual comfort

The use of daylight for lighting building interiors is a prerequisite to ensure a comfortable and healthy working environment, Heim et al. (2007). Daylight colour temperature is recognized by the human eye as comfortable, because its spectrum is continuous; therefore, this kind of light is the healthiest for humans. Lighting conditions have an impact on speed, accuracy and effort associated with activity, it has also a great influence on health, well-being and quality of life. Therefore, it is important to create a visually comfortable interior by providing suitable qualitative and quantitative characteristic of lighting. It should be emphasized that comfort depends on many parameters, it is also very subjective in nature.

According to [1, 6] ensuring an appropriate internal daylight environment providing visual comfort and visual effectiveness as well as security, is mainly associated with the following values: lighting intensity, luminance distribution, glare. Providing an adequate level of illuminance with sufficient spatial distribution affects how quickly and easily visual tasks can be executed. Insufficient lighting causes tiredness, sleepiness and worsening moods of workers and may additionally be the cause of accidents. The required illuminance average in the field of work and on the immediate surroundings of the workspace are given in standard EN 12464-1 Light and Lighting, Lighting Jobs, Part I, Indoor Work Places. In most cases, the illuminance on the work area should be in the range of 20 lux (noticeable human traits) to 2000 lux. In the immediate surroundings of the workspace, the illuminance value might be slightly lower. Another important parameter is the uniformity of illumination. For

continuous operations, it is assumed that the uniformity of illuminance on the work plane (ratio of the smallest measured illuminance on a given surface to the average illuminance on the plane) should be at least 0.7 and 0.5 on the immediate surroundings. A lack of uniformity of illumination causes ocular muscle fatigue, this is related to the need to adapt to changing light intensity.

Moreover, certain visual comfort indexes exist which are useful in creation of an appropriate lighting environment. In the following paper, only few of these are consider. The most popular that represents the amount of illumination available indoors relative to the illumination present outdoors at the same time under overcast skies is called the daylight factor (DF). This is a metric used to quantify the amount of diffused daylight in a space. The mean daylight factor, according to literature CISBE, should be in the range of between 2% and 5%. This ensures a well lit space requiring little or no additional lighting during the daytime. Early versions of the USGBC, LEED rating system originally required a DF ≥ 2 for at least 75% of the critical visual task zones [4].

New climatically and temporally sensitive metrics, categorized as dynamic daylight metrics, have been developed to cope with ever-increasing demands for daylight design. The most significant of these are daylight autonomy, useful daylight illuminance, and the daylight saturation percentage.

Daylight autonomy (DA) is represented as a percentage of annual daytime hours that a given point in a space is above a specified illumination level. Its modification conceived by Mardaljevic and Nabil in 2005 is useful daylight illuminance (UDI). This metric bins hourly time values based upon three illumination ranges, 0-100 lux, 100-2000 lux (the so-called useful range), and over 2000 lux (unwanted due to potential glare or overheating). There is significant debate regarding the selection of 2000 lux as an upper limit of useful range; therefore, in 2006, the Lighting and Daylighting Committee for the Collaborative for High Performance Schools program developed the daylight saturation percentage (DSP). This is a modification of useful daylight illuminance that increases the lower limit to 150 lux and decreases the upper to 1500 lux.

3. Case study

In this paper, visual comfort, taking into account DF, DA, UDI, DSP indexes and the illuminance level for the combination of size and geometry of vertical windows was analysed. The calculated values include luminance distribution along a room, mean values and spatial distributions of all comfort indexes. The numerical calculation has been done using Daysim software program RADIANCE – the calculation methodology originating from the well-known 'Backward Ray Tracing Method', Larson and Shakespeare (1998), taking into consideration the geometry, materials, time, date and sky conditions.

The building under study was located in central Europe climatic conditions (longitude, latitude, meridian 52.25N, 21.0E, –15.0 respectively). The external boundary condition was assumed as a typical meteorological year (TMY). The test cell analysed here was 2.4 m high, 2.4 m wide and 6 m deep. The transparent part of the external wall was orientated to the west. The transparent element was defined in software as a glass pane with a thickness of 4 mm

and visual transmittance of τ_{vis} = 0.75 (defined using RGB values of visual transmissivity and specularity equal 0). Simulations were done for different cases of geometry and area of window – these are presented in table 1. Additionally, different thickness of external wall (25 cm and 50 cm) for each case of window geometry were analysed. The working plane with an area equal to the surface floor was located 85 cm high.

The analysed room was defined as a typical office room occupied from 8:00 to 16:00. A minimum illuminance level of 300 lux for the whole working area was assumed.

Table 1

Geometry and size of window

Size of window [m^2]	Percentage of window area [%]	Scheme of window geometry
		Case1
0.36	6.25	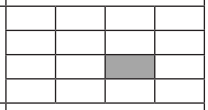
		Case 2a / Case 2b
0.72	12.50	
		Case 3a / Case 3b
1.08	18.75	
		Case 4a / Case 4b
1.44	25.00	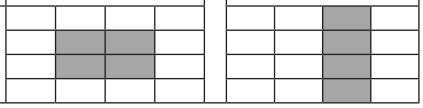

4. Results analysis

The results were presented in 2D distribution at the level of the working plane as well as averaged value of visual comfort indexes (Tab. 2). An effect of wall thickness is clearly noticeable for the daylight factor (DF). For daylight autonomy (DA) and daylight saturation percentage (DSP) the differences are much smaller, while for UDI they are almost noticeable. A similar effect can be recognized on the graph (Fig. 1–6). The values of UDI (100 lux-2000 lux) show that it's not only the biggest windows that can provide a proper indoor environment because in some configurations, the indexes are equals (cases 3b and 4b).

Taking into account the effective working area (Figs. 1 and 2), the effect of wall thickness is important in cases 3a and 4a (the cases with window centrally placed). The differences

in results of DF and DSP are not significant for 25 cm and 50 cm of wall thickness. This means that use of these parameters is not justified in the presented case. However, a different configuration of window (cases 2a and 2b) give a totally different set of results with regard to UDI distribution (Figs. 1 and 2).

Table 2

Average value of visual comfort indexes

Wall thickness	Window geometry	UDI			DF	DF > 2%	DA	DSP
		>100	100–2000	>2000				
		[%]	[%]	[%]	[%]	[%]	[%]	[%]
50 cm	Case 1	89.8	10.1	0.1	0.1	0.8	2.2	1.1
	Case 2a	66.9	32.6	0.5	0.4	2.8	9.6	4.5
	Case 2b	59.8	39.3	1.0	0.6	4.7	14.4	6.9
	Case 3a	44.9	53.3	1.7	0.9	7.5	23.7	12.7
	Case 3b	39.5	58.4	2.1	1.0	10.8	27.2	14.6
	Case 4a	27.4	69.3	4.4	1.5	22.5	39.0	24.6
	Case 4b	31.2	66.3	2.4	1.2	13.6	32.7	18.1
25 cm	Case 1	89.4	9.9	0.4	0.2	1.7	3.3	2.0
	Case 2a	76.7	22.1	1.2	0.4	4.4	8.8	5.1
	Case 2b	60.0	38.3	1.8	0.8	7.8	17.3	9.7
	Case 3a	53.4	43.8	2.8	1.0	11.4	22.9	13.8
	Case 3b	39.2	57.6	3.3	1.3	17.2	31.0	19.0
	Case 4a	36.2	58.4	5.4	1.7	23.3	34.6	22.6
	Case 4b	39.5	57.2	3.3	1.3	17.2	30.9	19.0

When considering the best position of workers seats and desks in an office space, only UDI index can give us reasonable results. Based on results presented in Figure 2, it can be concluded that for all analysed cases, the requirements are fulfilled at the same level but the highest values of UDI occurs in a different places (distance from windows). For case 1 and 2 it is in 1/3 depth of the room, while in case 3 and 4 the local maximum is in 1/2 of depth. What is more only DA index shows similar effect. However, based on this indicator it is not possible to estimate the effect of over-lighting.

The above remarks can be confirmed with the results of illuminance distribution presented in figures 7–10. During a sunny day, 21st of June, when direct solar beam radiation penetrates the indoor space, the illuminace level achieves 40 klux at a distance of 1 m from the window and above 10 klux at a distance of 2 m. This means that in the direct vicinity of the window, the illuminance level is above the acceptable level and the work place should be moved inside the room. For cloudy sky conditions (22nd of December), while the DF is estimated, the calculated illuminance does not exceed 1 klux (December) and 2 klux (June) at a distance of 1 m from the window.

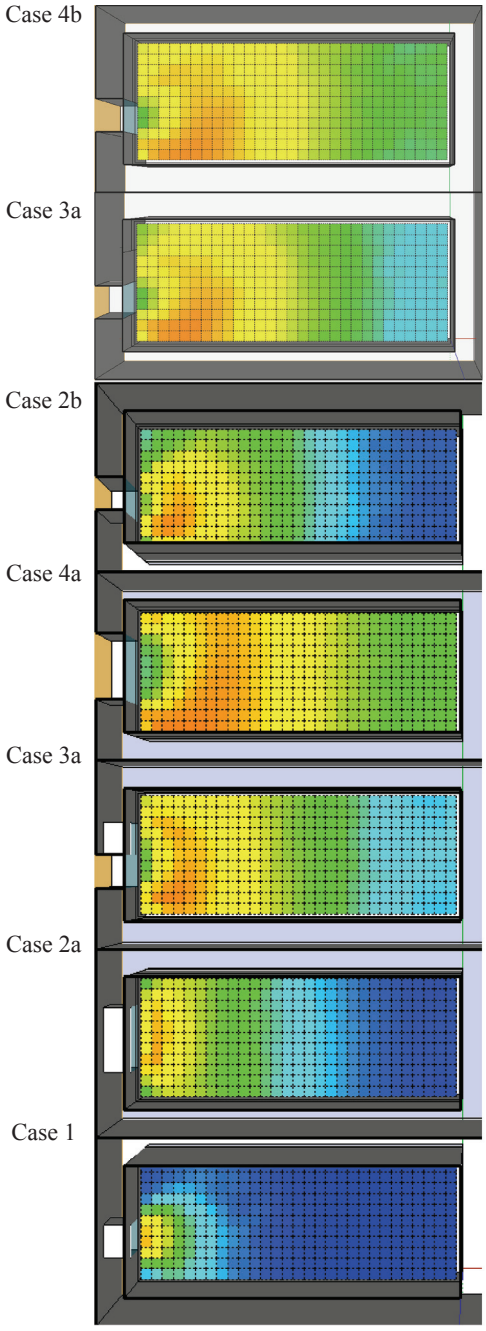

Fig. 1. Spatial distribution of UDI (100-2000 lux) in room for different window geometry for 50 cm wall

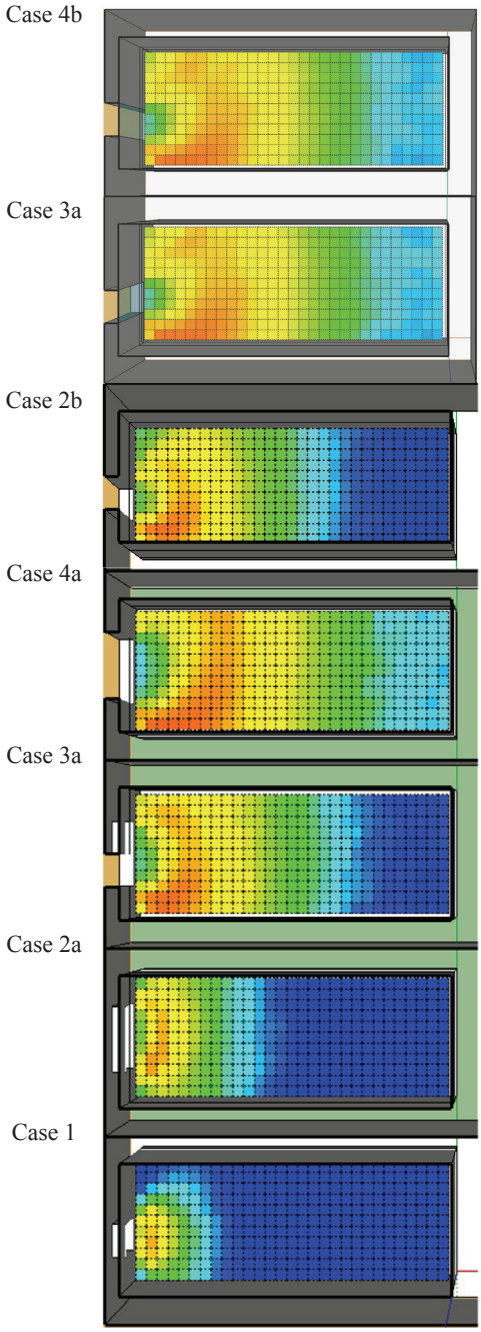

Fig. 2. Spatial distribution of UDI (100-2000 lux) in room for different window geometry for 25 cm wall

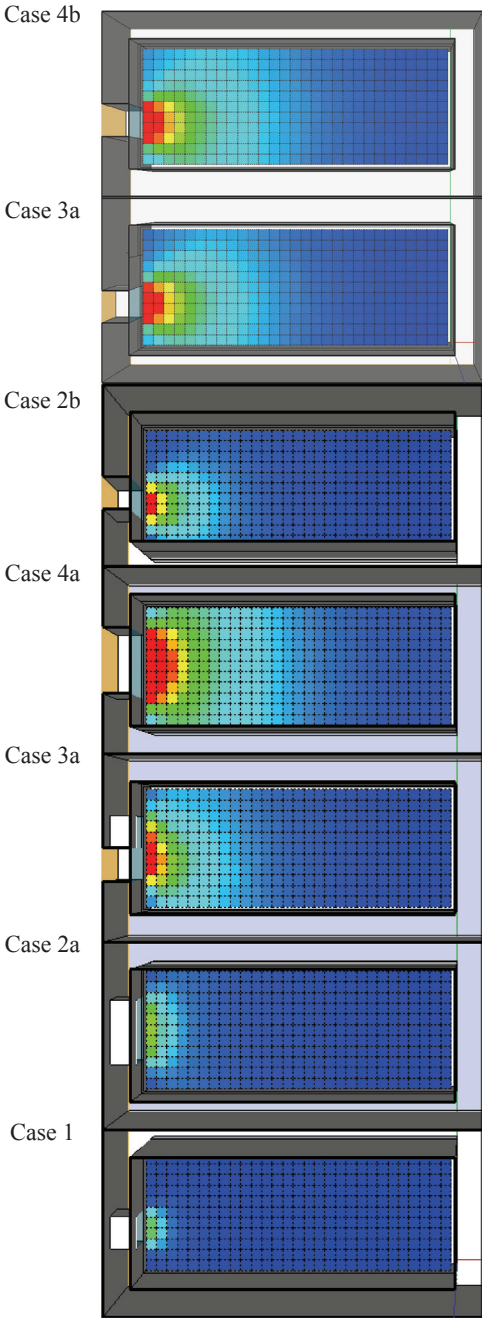

Fig. 3. Spatial distribution of DF in room for different window geometry for 50 cm wall

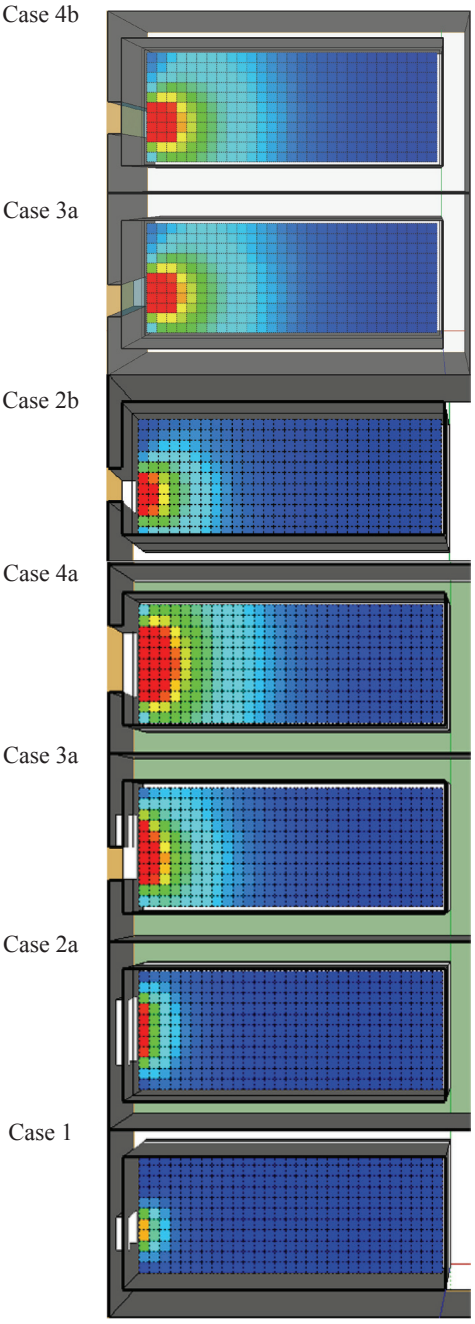

Fig. 4. Spatial distribution of DF in room for different window geometry for 25 cm wall

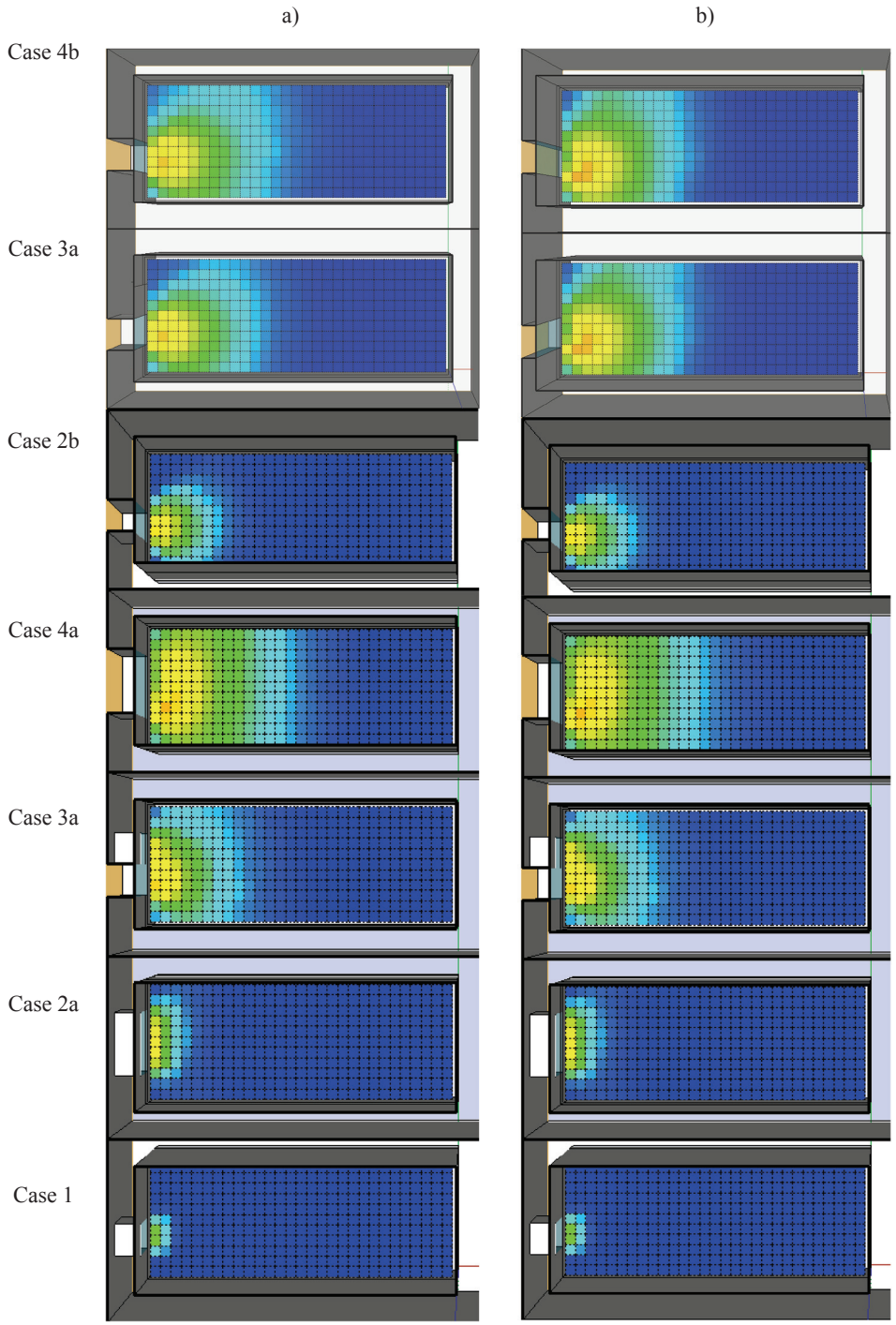

Fig. 5. Spatial distribution of DSP in room for different window geometry a) 50 cm wall, b) 25 cm wall

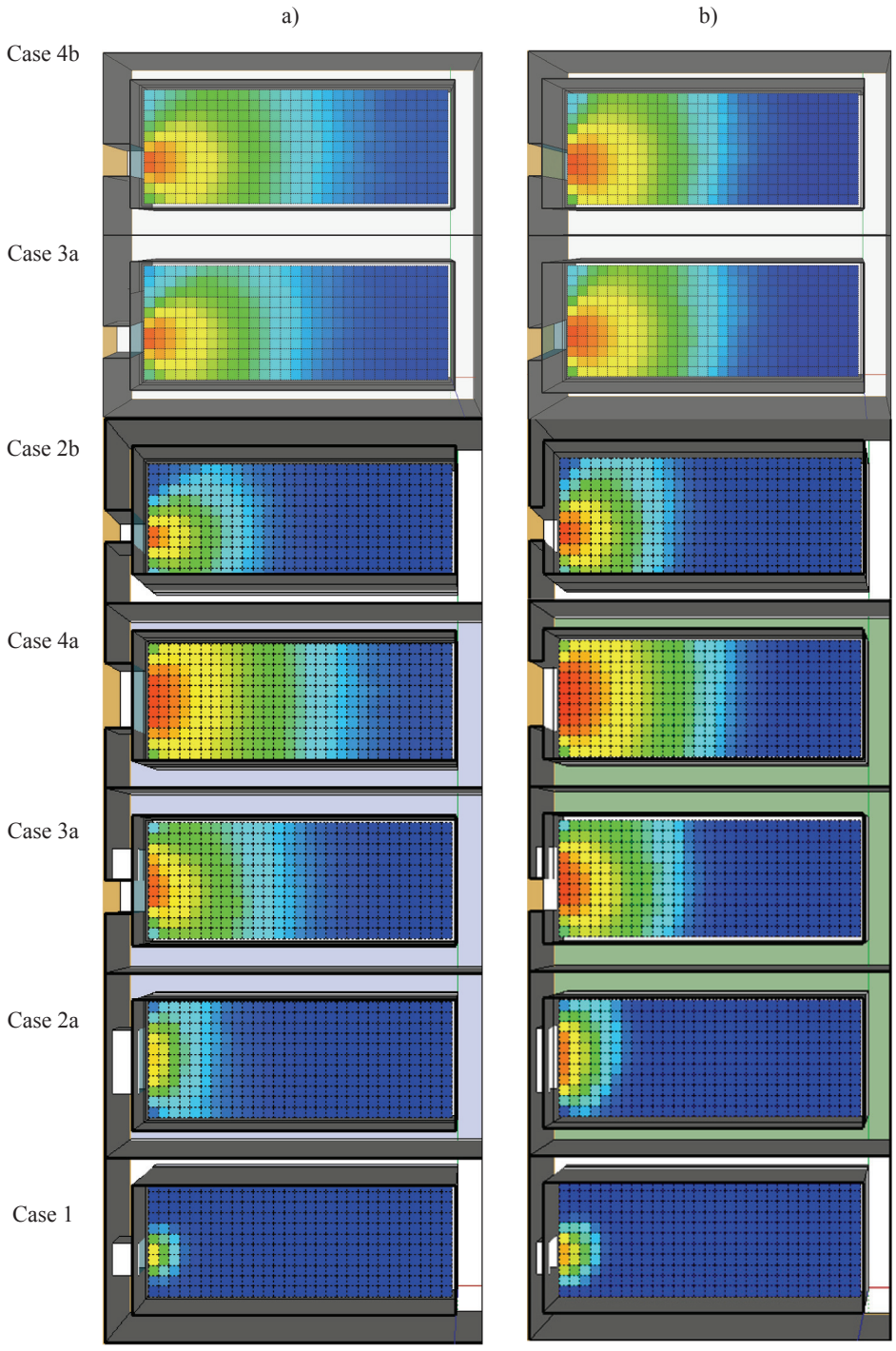

Fig. 6. Spatial distribution of DA in room for different window geometry a) 50 cm wall, b) 25 cm wall

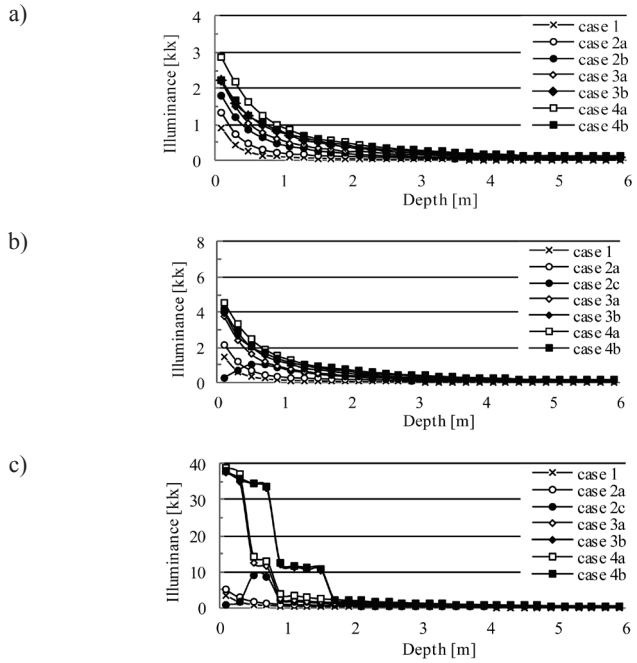

Fig. 7. Illuminance distribution for 21st of June for 50 cm wall thickness a) 09:00, b) 12:00, c) 15:00

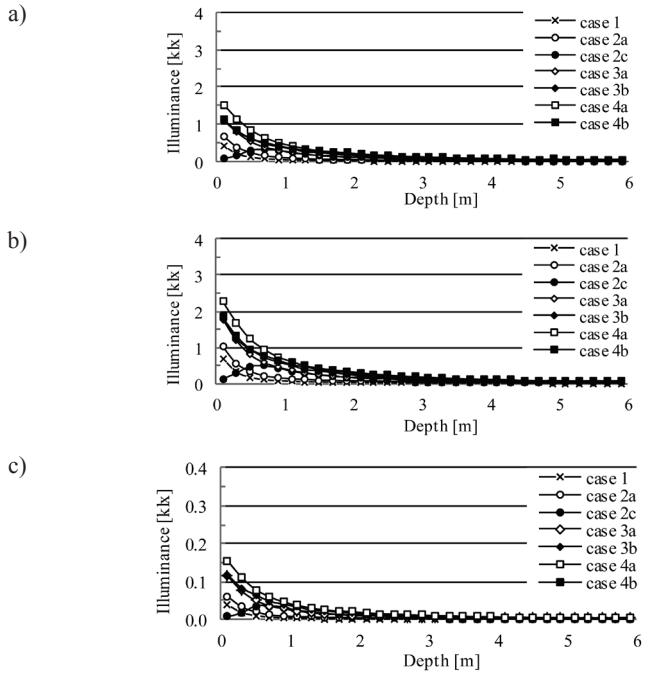

Fig. 8. Illuminance distribution for 22nd of December for thickness 50 cm a) 09:00, b) 12:00, c) 15:00

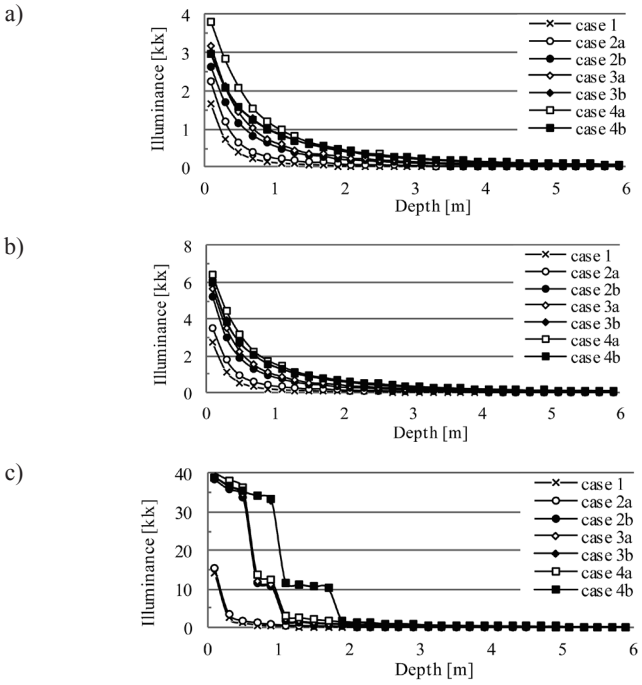

Fig. 9. Illuminance distribution for 21st of June for 25 cm wall thickness a) 09:00, b) 12:00, c) 15:00

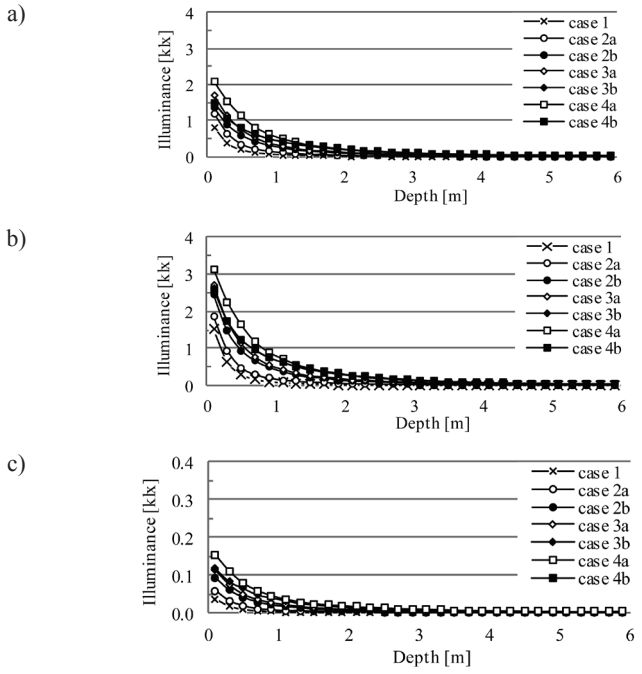

Fig. 10. Illuminance distribution for 22nd of December for thickness 25 cm a) 09:00, b) 12:00, c) 15:00

5. Conclusions

The main goal of the presented analysis was a comparison between different daylighting indexes and its effect on final decisions. The general remark concerns the choosing of the most useful indicator for daylight analysis in typical office space. Considering the upper and lower limit of illuminance at the working plane, the most useful parameter is the UDI index for the required range of illuminance.

Taking into account the UDI index, it could be concluded that the effect of wall thickness is noticeable, while different configurations can give considerably different results.

The proper analysis of UDI can also be effective in the better positioning of workers desk in an office area. This means that for different window sizes and geometries, a different section of the floor area should be recommended as the best position to work.

This work was funded by The National Centre for Research and Development as part of the project entitled: 'Promoting Sustainable Approaches Towards Energy Efficiency in Buildings as Tools Towards Climate Protection in German and Polish Cities: developing facade technology for zero-emission buildings' (acronym: GPEE).

References

[1] Bąk J., Pabjańczyk W., *Podstawy techniki świetlnej,* Wydawnictwo Politechniki Łódzkiej, Łódź 1994.

[2] Heim D., Klemm P., Narowski P., Szczepańska E., *Komputerowa analiza oświetlenia dziennego i ocena parametrów komfortu wizualnego w pomieszczeniach*, red. D. Heim, Katedra Fizyki Budowli i Materiałów Budowlanych, Politechnika Łódzka, Łódź. 2007.

[3] Larson G.W., Shakespeare R., *Rendering with radiance – the art and science of lighting visualization,* Morgan Kaufman Publishers Inc., California, San Francisco 1998.

[4] Reinhard C., *Daylighting handbook I, Fundamentals and designing with the sun*, 2014.

[5] The British Standards Institution, BS 8206 part 2 CIBSE.

[6] Tragenza P., Loe D., *The design of lighting*, 2nd edition, Routledge 2014.

TECHNICAL TRANSACTIONS | CZASOPISMO TECHNICZNE
CIVIL ENGINEERING | BUDOWNICTWO
2-B/2015

AGATA SZELĄG*, ANDRZEJ FLAGA*

AN ACOUSTIC STUDY OF THE AUDITORIUM HALL TO BE LOCATED IN THE PROPOSED BUILDING OF THE APPLIED ACOUSTICS LABORATORY OF CRACOW UNIVERSITY OF TECHNOLOGY

STUDIUM AKUSTYKI SALI AUDYTORYJNEJ ZNAJDUJĄCEJ SIĘ W PROJEKTOWANYM BUDYNKU LABORATORIUM AKUSTYKI STOSOWANEJ POLITECHNIKI KRAKOWSKIEJ

Abstract

This paper presents an acoustic study of the auditorium hall located in the proposed building of the Applied Acoustics Laboratory of Cracow University of Technology. The study shows a comparative analysis of two solutions to the acoustic adaptation of this room. The aim of this study was to demonstrate that with a given room shape and finishing materials, it is possible to optimize the sound quality of the interior through changes to some architectural details, for example, by the adequate formation and arrangement of finishing elements.

Keywords: building and architectural acoustics, room acoustic parameters

Streszczenie

W niniejszej pracy przedstawiono studium obejmujące adaptację akustyczną sali audytoryjnej znajdującej się w projektowanym budynku Laboratorium Akustyki Stosowanej Wydziału Inżynierii Lądowej Politechniki Krakowskiej. W opracowaniu zaprezentowano i dokonano analizy porównawczej dwóch wariantów adaptacji akustycznej analizowanego pomieszczenia. Celem pracy było wykazanie, że przy zadanej bryle pomieszczenia i zestawie materiałów wykończeniowych sposobem optymalizowania jakości akustycznej wnętrza są działania w zakresie detalu architektonicznego, np. odpowiednie rozmieszczenie i formowanie elementów wykończenia wnętrza.

Słowa kluczowe: akustyka budowlana i architektoniczna, parametry akustyczne wnętrz

DOI: 10.4467/2353737XCT.15.142.4179

* Institute of Structural Mechanics, Cracow University of Technology, Poland.

1. Introduction

Since ancient times, room acoustics have been an important consideration in the design of buildings. Initially, this was perceived subjectively, so some impressions connected with speech intelligibility, sound volume or sound clarity were particularly important. However, mathematical apparatus was not sufficient to describe such acoustic parameters until the twentieth century, hence their prediction and measurement. The progress of understanding some acoustic phenomena and the ability to describe them had a beneficial effect upon the development of room acoustics. Due to this, it has become possible to confirm the subjective feelings by objective values. The objective criteria has an advantage over the subjective criteria due to their replicability, their measurable outcome and the possibility of applying them during the design stage. In the literature, a number of objective parameters for determining the acoustic quality of a given room are defined. In the case of auditoria, the most important predictors describing the sound field are reverberation time T_{60}, speech transmission index *STI* defining the level of speech intelligibility and sound strength *G*.

Reverberation time T_{60} is a commonly used parameter and the earliest defined in room acoustics. This indicates the time required to reduce the sound pressure level of 60 dB [1]. The length of reverberation determines the suitability of the analysed room for specific purposes, however, it does not provide information regarding the sound quality. The speech transmission index *STI* is a particularly important parameter in auditoria. It provides values from 0 to 1, wherein a value of 1 means excellent speech intelligibility while a value of 0 defines the lowest quality. In order to determine the *STI* parameter, there are some techniques used based on the modulation of noise with a bandwidth similar to the human voice band by frequencies similar to those found in natural speech. Changes to the modulation depth of the output of the system are then analysed. The next mentioned parameter, sound strength *G*, is the difference of volume at which the source is heard in the room compared with the volume in free field at a distance of 10 m from the same source [2].

The values of the described acoustic parameters highly depend on the room's shape and facing materials used. The suitability (from an acoustic perspective) of the designed room's shape and the arrangement of sound absorbing and reflecting materials might be verified using one of the three basic methods: wave; geometric; statistical [3]. Each of these methods enables studying a different set of acoustic field parameters, therefore, the combined use of all methods allows the acoustic properties of the room to be determined to a high degree of precision. The analyses presented in this paper are mainly based on geometric and statistical methods due to the application of CATT-Acoustics software during numerical analysis.

2. The subject of study

The analysed auditorium is one of the rooms of a proposed building that has been designed for the Applied Acoustics Laboratory of the Faculty of Civil Engineering at Tadeusz Kościuszko Cracow University of Technology [4]. This building would be located on the campus on the Avenue of John Paul II on Czyżyny (Fig. 1). It is simple in form, on the plan

of a regular rectangle with dimensions of 35.75 m x 22.70 m (Fig. 2). It has two ground floors where there are located laboratory rooms, offices, sanitary facilities, as well as the designed auditorium and an underground floor with exhibition rooms, storage rooms and technical rooms.

The discussed auditorium (Figs. 3, 4) was designed for an audience of 220 people. The room dimensions in plan are 20.9 m × 9.8 m and its volume is approximately 1025 m^3. The lectern is located at -1.2 m, while the audience rises upward at an angle of 9° (the front portion of the audience) and 10° (the rear portion of the audience). In the auditorium there are three doors – two at a level of -1.2 m and one at 0.0 m. Six windows on one side-wall extend from the floor up to the false ceiling. Additionally, there are some technical rooms located behind the back wall of the auditorium.

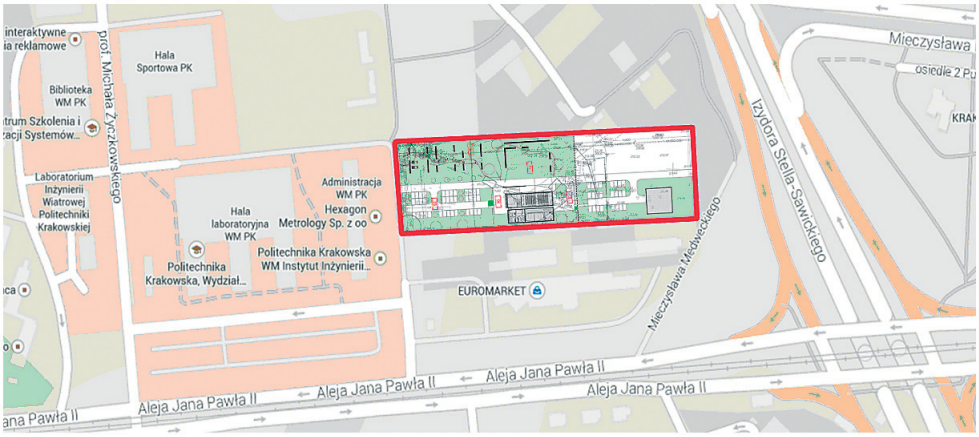

Fig. 1. The location of the Applied Acoustics Laboratory on the campus at the Avenue of John Paul II on Czyżyny [5]

Fig. 2. The visualization of the building of the Applied Acoustics Laboratory [4]

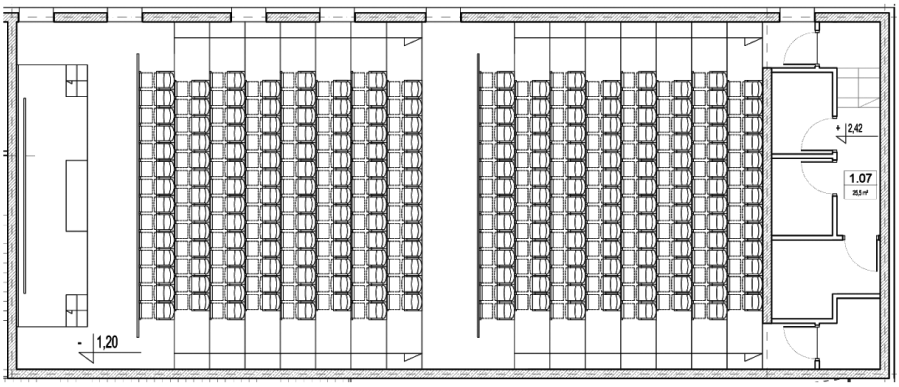

Fig. 3. The plan of the first floor in the designed auditorium located in Applied Acoustics Laboratory [4]

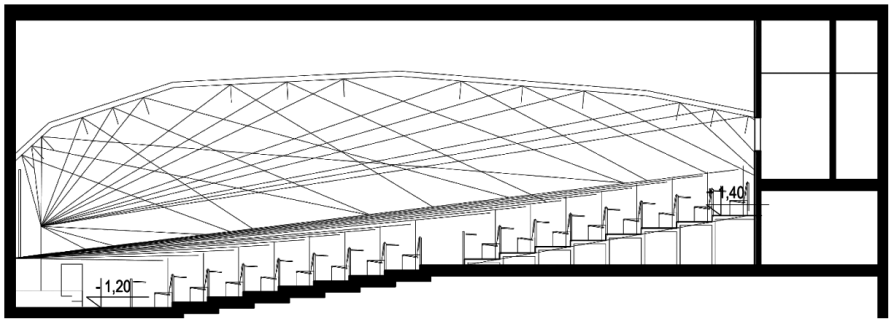

Fig. 4. The cross-section of the designed auditorium located in Applied Acoustics Laboratory [4]

3. Guidelines for acoustic adaptation

The model of the designed auditorium was made in CATT-Acoustics v9.0c software which allows the determination of the acoustic field in a room. The aim of the simulation was to obtain and assess the values of the following parameters, i.e. the reverberation time T_{60}, the speech transmission index *STI*, and the sound strength *G*.

In the literature, there are several formulas for determining the recommended reverberation time for auditoria depending on their volumes. The presented study was based on two empirical formulas:

$$T_{60}(V) = 0.20 \log V + 0.21 \quad [6] \tag{1}$$

$$T_{60}(V) = 0.30 \log V - 0.20 \quad [1] \tag{2}$$

where V is the volume of the room [m^3]. According to the above formulas, the recommended reverberation time for the octave band with a center frequency of 1000 Hz is equal to 0.81 s by equation (1) or 0.70 s by equation (2). Due to the fact that the room will be also equipped with an additional electroacoustic sound system, the required reverberation time is assumed to be 0.70 s. The guidelines for reverberation time include its frequency range, which is from 125 to 4000 Hz. This parameter should be approximately equal over the entire range, however, a higher value is allowed for low sound frequencies due to the wave nature of the acoustic field in this frequency range and a lower value for higher frequencies due to the medium damping. The recommended reverberation time dependence for the designed auditorium hall as a function of frequency is given in Fig. 5 with a tolerance range of ±20% [7].

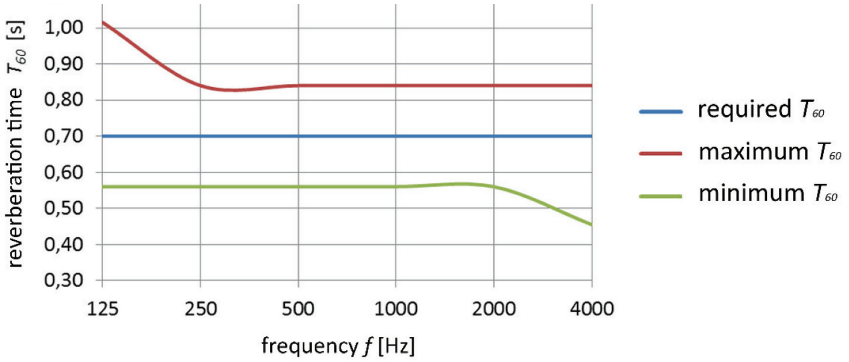

Fig. 5. The recommended reverberation time dependence for the designed auditorium as a function of frequency with a tolerance range of ±20% [7, 8]

Furthermore, it is assumed that the parameter *STI* should exceed the limit value of 0.6 at each point in the audience [8]. The sound strength G should not decrease more than 5 dB in the last row of seats in relation to the seats at the front of the room, which are close to the sound source [9].

4. The acoustic adaptation of the auditorium in two variants

The paper presents an analysis of two variants of an acoustic adaptation designed for the discussed auditorium. The first variant assumes that the shapes of the inner surfaces of the room are the same as are shown in the conceptual project. The required values of acoustic parameters were obtained by selecting appropriate finishing materials for walls, ceiling and floor. Sound absorbing and reflective materials were placed in accordance with the principle that reflective materials are situated close to the sound source, while sound absorbing materials are located in the back of the room, in particular, on the rear wall. Moreover, it was significant to choose seats with an appropriate absorption coefficient. Figs 6 and 7 show the model of the auditorium in the first variant.

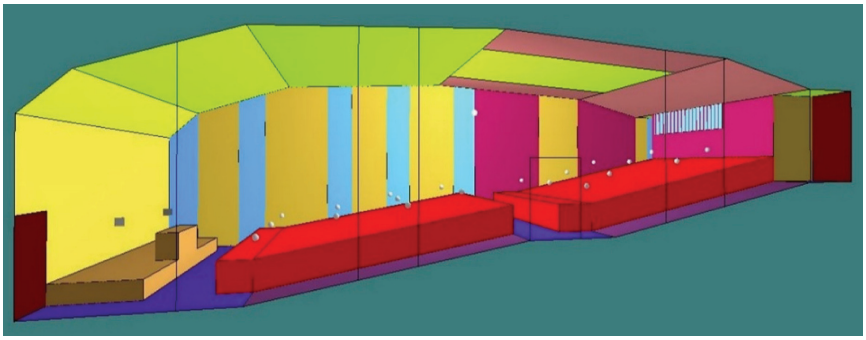

Fig. 6. The 3D model in variant I: an axonometric view (on the wall with windows) of the designed auditorium

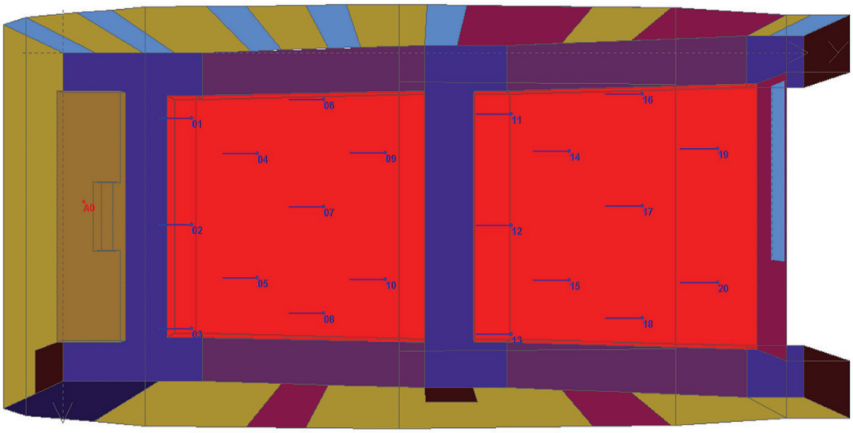

Fig. 7. The model in variant I: a z-direction view of the designed auditorium

The second variant of the auditorium's acoustic adaptation allows changing the shape of the inner surfaces to provide the best visual and auditory contact between a speaker and the audience. The conceptual project assumes the room on a rectangular plan with dimensions of 20.9 m x 9.8 m. Due to the fact that the room is quite long relative to its width, it is important to direct as much of the acoustic energy in the auditorium's rear regions in order to compensate for the sound level over the entire audience. Therefore, it was proposed that the room model should have appropriately shaped side walls. The depth of the cavities is in the range of 15 to 25 cm. Both side walls in the auditorium were uniformly shaped. Such designed reflective and absorbing surfaces do not only affect the uniformity of the sound field in the room, they also reduce some basic acoustic defects, i.e. sound focusing, sound creeping or flutter echo. In comparison with the model in the first variant, some changes in the arrangement of the materials used to cover the walls and ceiling were also made due to the need to ensure the required values of the basic acoustic parameters, e.g. the reverberation time. Figs 8 and 9 show the model of the auditorium in the second variant.

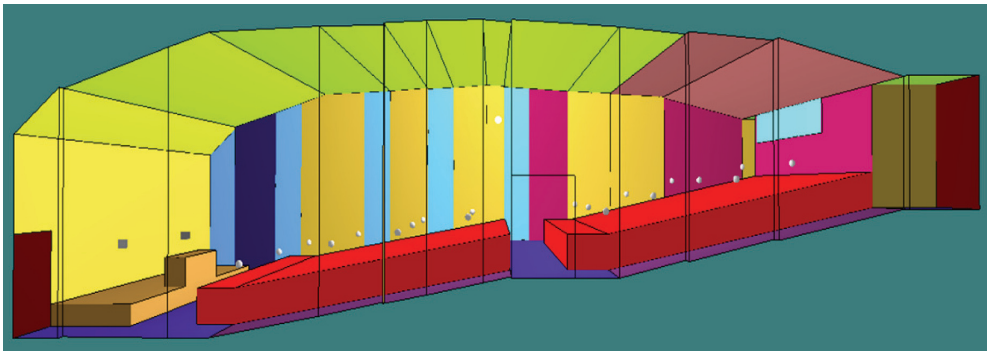

Fig. 8. The 3D model in variant II: an axonometric view (on the wall with windows) of the designed auditorium

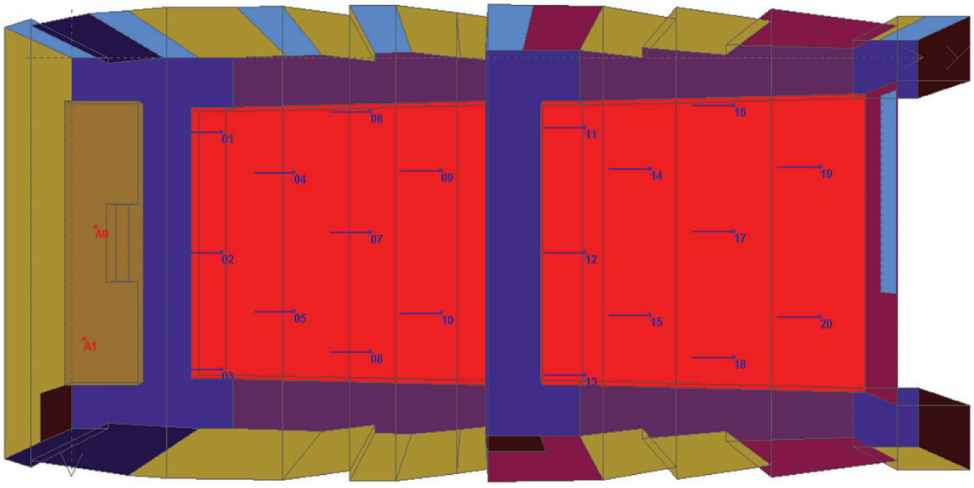

Fig. 9. The model in variant II: a z-direction view of the designed auditorium

Both proposed solutions to the auditorium's acoustic adaptation required the use of the same finishing materials, however, their placement was varied. To cover the walls, panels from Gustafs Panel System combined with mineral wool were used with an air-gap width of 30 mm. The side walls and the front wall, marked on the drawings in a brown-orange colour, were covered with plain panels characterized by a low sound absorption coefficient (Fig. 10). On the rear wall and some parts of the side walls, perforated panels PG5 were used, these have a moderate absorption coefficient (Fig. 11). In the drawings, these panels are marked in purple. At the front of the room, on the walls next to the lectern (the wall marked in dark blue), Gustafs RS8-C40 panels were placed – these have a linear perforation, characterized by a high sound absorption coefficient (Fig. 12). Strong sound absorption in the high frequency band might reduce the unfavourable flutter echo phenomenon that could occur in the region of this room where the sound source is located.

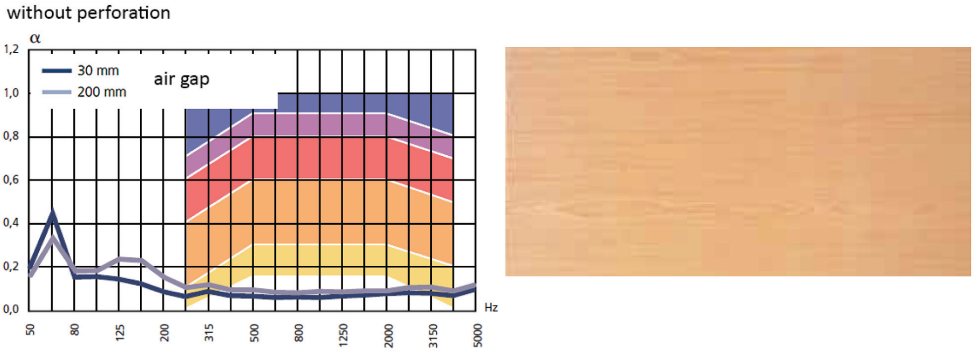

Fig. 10. The plain Gustafs panels (on the right) and their sound absorption characteristic as a function of frequency (on the left) (according to the the product catalog)

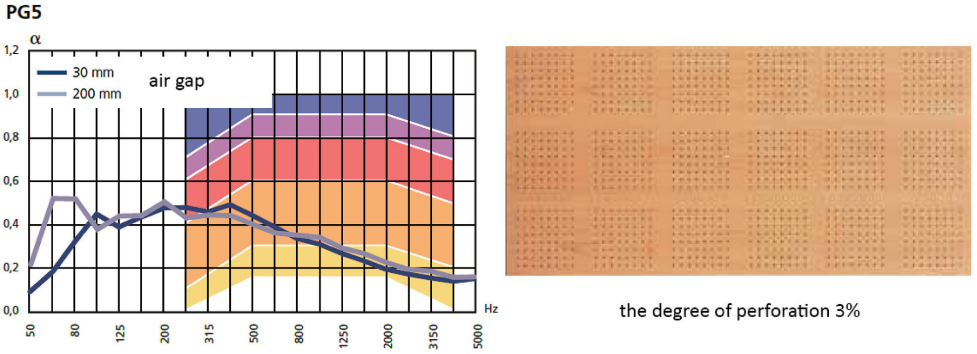

Fig. 11. The perforated PG5 Gustafs panels (right) and their sound absorption characteristic as a function of frequency (left) (source: product catalogue)

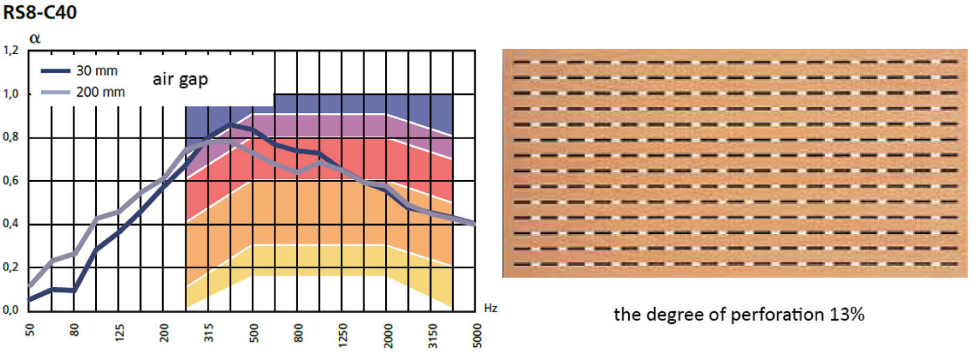

Fig. 12. The perforated RS8-C40 Gustafs panels (right) and their sound absorption characteristic as a function of frequency (left) (source: product catalogue)

The suspended ceiling is designed with two different technologies. The greater part of the surface is covered with a plain plasterboard on the system mounting with mineral wool filling having a thickness of 5 cm (the surface marked in green). Such a constructed ceiling provides the sound reflections towards the audience. Moreover, the ceiling also reduces the time when first reflections reach the listeners and ensures uniform sound distribution in the entire room [10, 11]. At the back of the auditorium, the ceiling was made with plasterboards with slotted perforations (surfaces marked in violet). Rigips panels were used (Gyptone Line 4) at a distance of 200 mm, additionally covered by the acoustic fabric. These panels have a high average sound absorption coefficient $\alpha_w = 0.65$ and the arrangement and size of the holes provide the uniform sound absorption throughout the frequency range (Fig. 13). Owing to such a characteristic, the panels used had a positive effect on reducing the reverberation time in the designed auditorium and they minimised sound reflection from the rear wall.

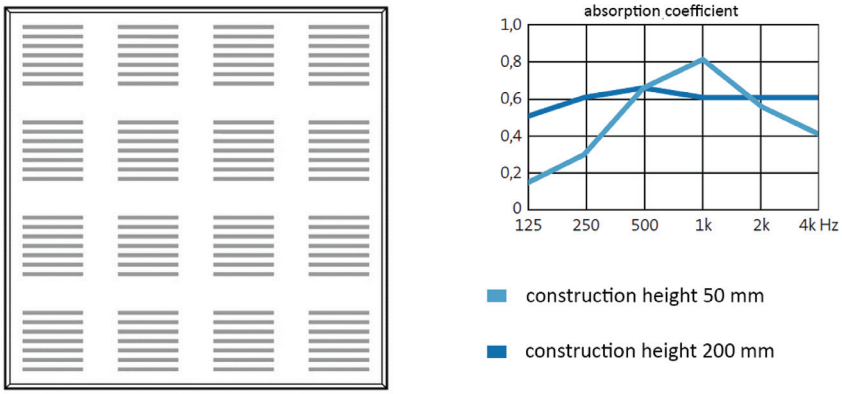

Fig. 13. The perforated Rigips panels – Gyptone Line 4 (left) and their sound absorption characteristic as a function of frequency (right) (source: product catalogue)

The floor is the next modelled surface. It was covered with a flocked lining which is durable and easy to clean and has an aesthetic appearance. Moreover, such a covering has a positive influence on reducing impact noise thereby improving the acoustic comfort in used rooms. Furthermore, the lectern and the doors were modelled as solid wood, the windows have double glazing and the seats for the audience were assumed as slightly upholstered.

5. The comparison of results of the auditorium sound field simulation in two variants

The prepared model of the discussed auditorium was used to carry out a computer simulation of sound propagation in this interior with the use of the aforementioned software CATT-Acoustics. Figs. 7 and 9 show the locations of the sound source and twenty receivers in the analysed model. It was decided to model two positions of the sound source which represent the typical orientations of the speakers. The virtual omnidirectional sound source

generated a white noise signal of 94 dB for the octave band with a center frequency of 1 kHz. Furthermore, twenty receivers were placed uniformly over the entire surface of the audience at a height of 1.30 m.

The first step in the analysis was to check the inclination angles and positions of the ceiling's reflective surfaces. For the purposes of this study, the spatial geometry method was applied. The analysis was performed for the sound source position A0, i.e. for the source located near the lectern. Such a position refers to the typical location of the speaker and also to the point of the apparent sound source for wall-mounted loudspeakers spaced symmetrically on both sides of the audience. Based on these results, it can be concluded that the proposed shape of the ceiling provides proper sound distribution in the room (Fig. 14). Moreover, it is confirmed that there exists a need for using some sound absorbing panels in the rear areas of the auditorium due to the large amount of acoustic energy reflected from these planes towards the rear wall (Fig. 15).

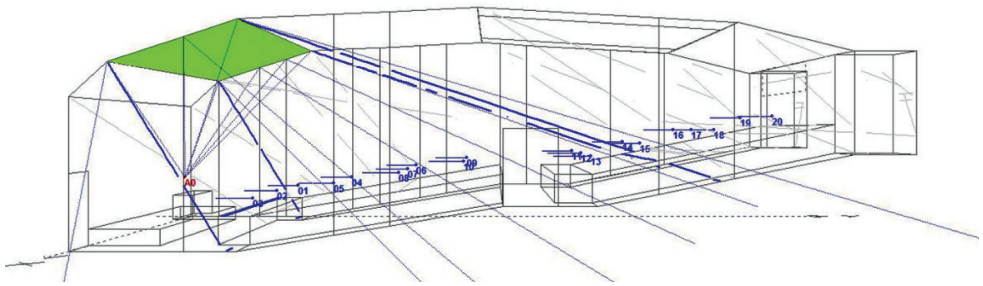

Fig. 14. An analysis of the first sound reflections from the sample ceiling's surface – the front surface (reflective) – variant I

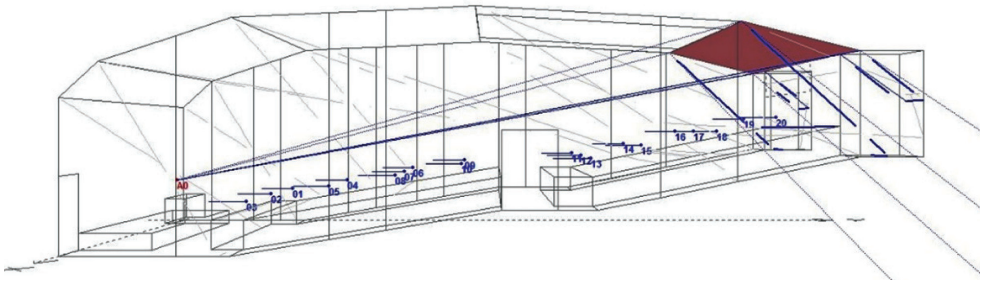

Fig. 15. An analysis of the first sound reflections from the sample ceiling's surface – the back surface (absorbing) – variant I

Calculations of the selected room acoustic parameters were performed for a full room. Sound masking effect was also included by introducing external noise at a level of 35.8 dB (28 NCB curve) to the model. The accuracy of numerical calculations was verified by Schroeder's decay curves. If some disturbances in the decay curve occurred, the number of rays increased until a smooth characteristic was obtained.

Reverberation time T_{60} is the first analysed room acoustic parameter. Fig. 16 shows the average reverberation time in the designed auditorium after adaptations in two variants against the assumptions given in the third chapter. On the basis of the presented results, it can be concluded that the reverberation time obtained from the simulation of both models meets the previously defined requirements, i.e. it has a flat characteristic in the whole analysed frequency band and its values are in accordance with the guidelines. In order to compare two of the proposed auditorium's acoustic adaptations, the convergence of obtained reverberation times for both solutions with the required values were determined. The comparative criterion was a minimum root mean square distance. In the first case, it was 0.0069, while for the second variant, it was equal to 0.0031. Therefore, it may be stated that the acoustic adaptation in the second variant provides a reverberation time closer to requirements. Moreover, the values of the reverberation time are slightly lower for the second model which can be considered as favourable due to the function of the room.

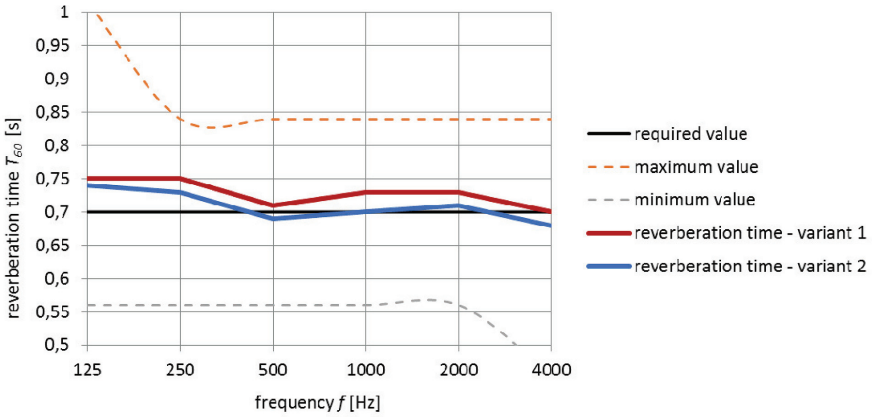

Fig. 16. The average reverberation time in the designed auditorium after adaptations in two variants against the assumptions

The speech transmission index *STI* is the next analysed acoustic parameter of the designed auditorium. Figs. 17 (variant I) and 19 (variant II) show the sample distribution of the values of this parameter in the audience for the A0 sound source location. In relation to these maps, Figs. 18 and 20 present the areas in the audience with the best speech intelligibility (E – 'excellent', G – 'good'). Based on the results obtained from the simulation, it can be concluded that both proposed acoustic adaptations of the auditorium meet the requirements for high speech intelligibility. Nevertheless, the average value of *STI*, calculated for twenty receivers' points, is slightly higher for the model in the second variant. In the first variant, it is equal to 0.74 and the minimum and maximum values of *STI* are 0.72 and 0.77 respectively. On the other hand, the average value of *STI* in the second variant is 0.76 and the minimum and maximum values are equal to 0.71 and 0.78 respectively. Furthermore, the differences between both models are even more visible on the adequate maps (e.g. Figs. 18 and 19). It is clear that in the case of the second variant, a larger area of the audience has 'excellent' values of the *STI* parameter.

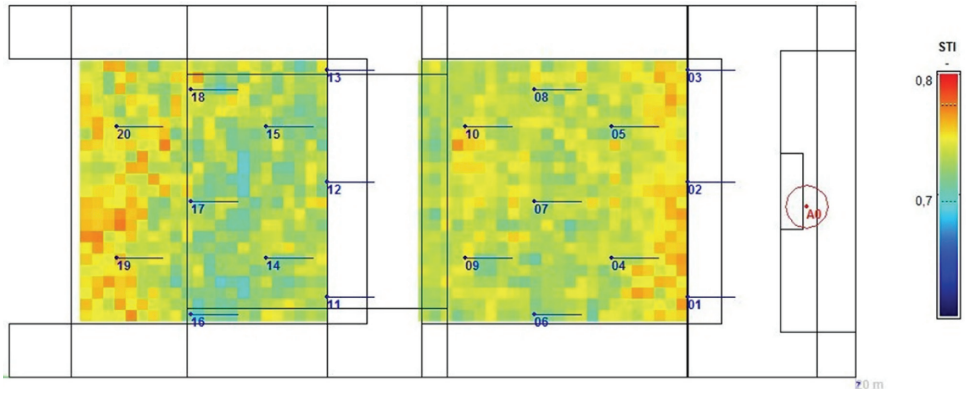

Fig. 17. Map showing the distribution of the speech transmission index *STI* values in the audience and for the A0 sound source location – Variant I

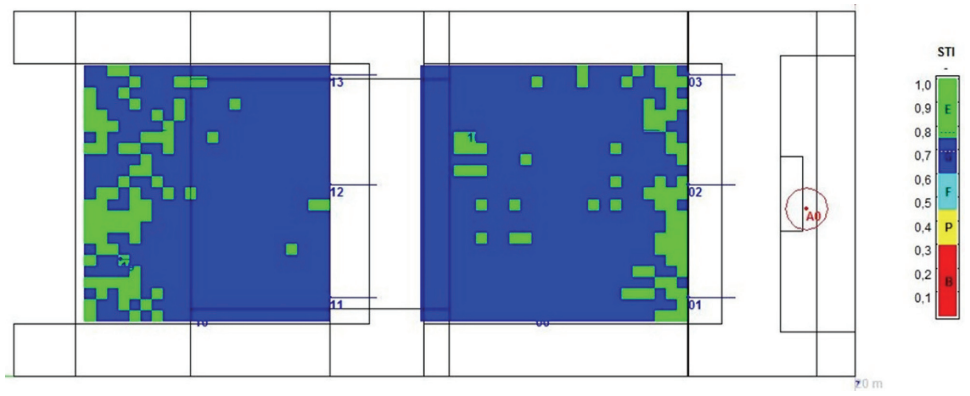

Fig. 18. Map showing the areas in the audience with the best speech intelligibility – the A0 sound source location – Variant I

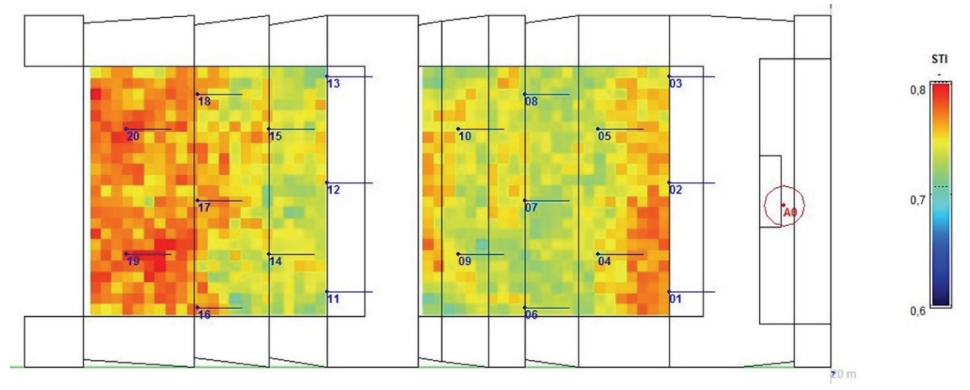

Fig. 19. The map showing the distribution of the speech transmission index *STI* values in the audience and for the A0 sound source location – Variant II

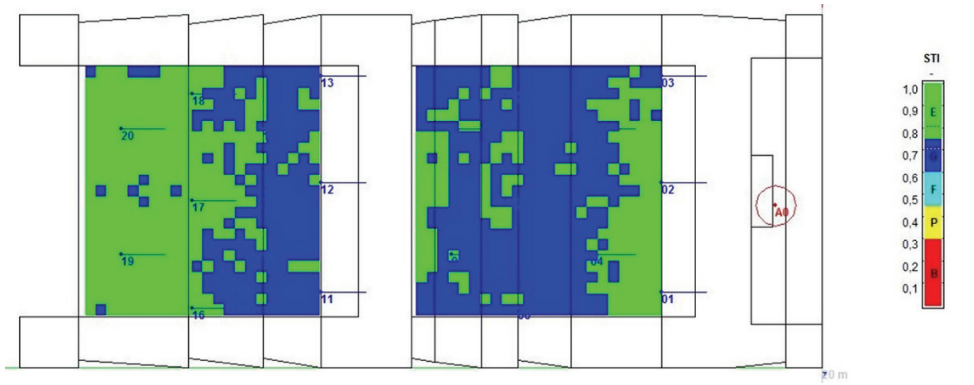

Fig. 20. The map showing the areas in the audience with the best speech intelligibility – the A0 sound source location – Variant II

The sound strength *G* is the last analysed room acoustic parameter. Figs. 21 (variant I) and 23 (variant II) show a sample distribution of its values in the audience for the A0 sound source location and an octave band with a center frequency of 1 kHz. Moreover, in Figs 22 (variant I) and 24 (variant I), the appropriate percentage shares of specific values of the sound strength *G* in relation to all data were also presented. Naturally, the final analysis was based on all the results obtained in the simulation. On the basis of the results, it was found that the assumed room's acoustic adaptations provide a basic sound dispersion throughout the room space with a uniform distribution of the sound field. The differences in the values of the sound strength for both models do not exceed the assumed 5 dB between the seats situated near the sound source and the seats located far from it. Moreover, the sound reaching the audience is properly amplified by the reflections. The analysis of the sound strength parameter confirmed the uniform distribution of sound throughout the audience for both variants and showed no significant difference between these two acoustic adaptations.

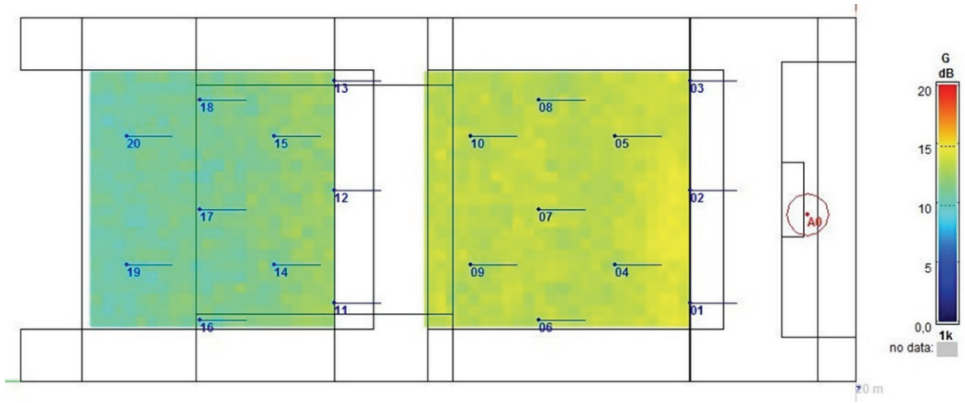

Fig. 21. Map showing the distribution of the sound strength *G* values in the audience for the A0 sound source location and the octave band with a center frequency of 1 kHz – Variant I

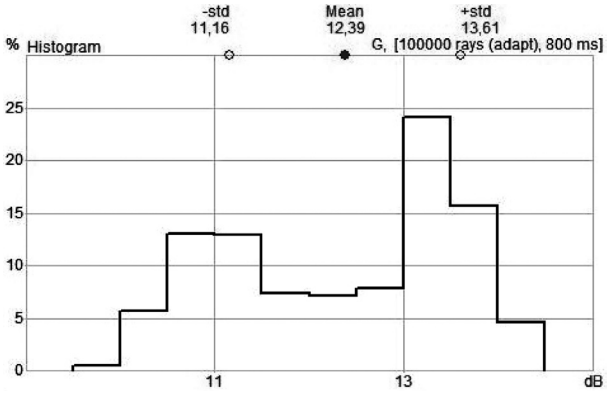

Fig. 22. The percentage share of specific values of the sound strength *G* in relation to all data for the A0 sound source location and the octave band with a center frequency of 1 kHz – Variant I

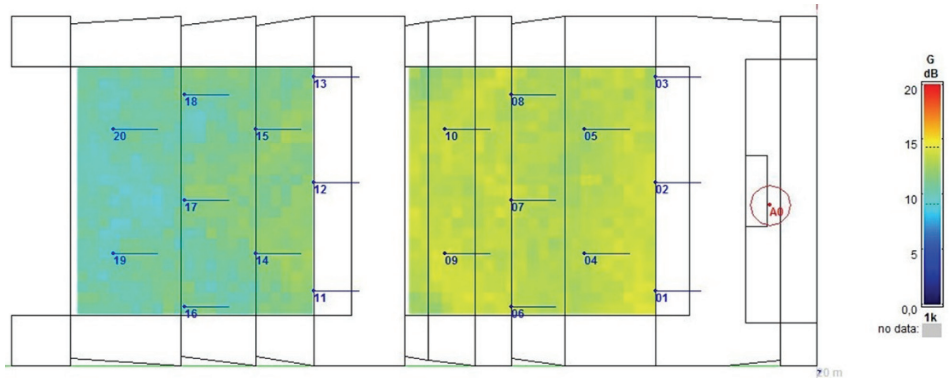

Fig. 23. Map showing the distribution of the sound strength *G* values in the audience for the A0 sound source location and the octave band with a center frequency of 1 kHz – Variant II

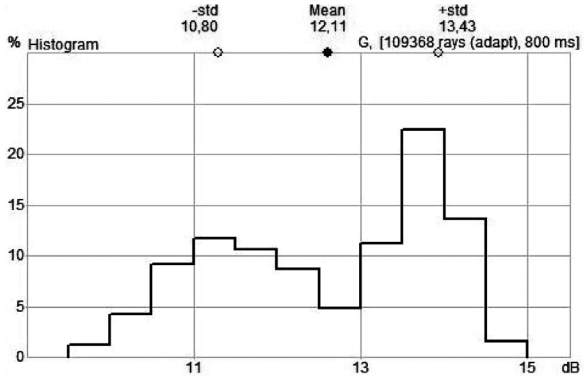

Fig. 24. The percentage share of specific values of the sound strength *G* in relation to all data for the A0 sound source location and the octave band with a center frequency of 1 kHz – Variant II

6. Conclusions

This paper presents an acoustic study of the auditorium hall located in the designed building of the Applied Acoustics Laboratory of Cracow University of Technology. The aim of this study was to demonstrate that having a given room shape and finishing materials, it is possible to optimize the sound quality in the interior through changes of some architectural details, for example, by the appropriate arrangement or formation of finishing elements. The study shows a comparative analysis of two solutions to the acoustic adaptation of the analysed auditorium. The first variant assumes that the shape of the room's inner surfaces is the same as shown in the conceptual project. The second variant allows changing the shape of the inner surfaces. Hence, it was proposed the room model having appropriately shaped side walls. After an appropriate analysis, it was found that although both solutions satisfy the previously defined guidelines for some acoustic parameters, i.e. the reverberation time, speech intelligibility and sound strength, the adaptation in the first variant gave worse results for the room's acoustic field simulation than the adaptation in the second variant. First of all, the values of *STI* parameter are more favourable in the latter model; additionally, the reverberation time in the whole band is closer to the recommended value. Moreover, an adaptation in the second variant is more interesting architecturally. For example, there is the possibility of non-standard illumination of walls by hiding the luminaires in the folds.

References

[1] Kulowski A., *Akustyka sal. Zalecenia projektowe dla architektów*, Wydawnictwo Politechniki Gdańskiej, Gdańsk 2011.

[2] Wróblewska D., Kulowski A., *Czynniki akustyki w architektonicznym projektowaniu kościołów*, Wydawnictwo Politechniki Gdańskiej, Gdańsk 2007.

[3] Engel Z., Engel J., Kosała K., Sadowski J., *Podstawy akustyki obiektów sakralnych*, Wydawnictwo Instytutu Technologii Eksploatacji PIB, Kraków-Radom 2007.

[4] Majczak M., Bugajska K., *Projekt koncepcyjny. Budowa Budynku Laboratorium Akustyki Stosowanej Wydziału Inżynierii Lądowej na terenie kampusu PK wraz z urządzeniami budowlanymi i infrastrukturą techniczną,* cooperation: Flaga Ł., consultation: Flaga A., Kraków 2012.

[5] www.google.pl/maps, access: 01.06.2014.

[6] Rettinger M., *Acoustic design and noise control*, Chemical Publishing Co., Vol.1, New York 1997.

[7] Fasold W., Winkler H., *Bauphysikalische Entwurfslehre*, Veb Verlag für Bauwesen, Berlin 1976.

[8] Abdou A., Guy R., *Spatial information of sound fields for room-acoustics evaluation and diagnosis*, Journal of Acoustical Society of America, Vol. 100(5), 1996.

[9] Beranek L., *Music, Acoustics and architecture*, J. Wiley and Sons, New York 1962.

[10] Kamisiński T., Szeląg A., Rubacha J., *Sound reflection from overhead stage canopies depending on ceiling modification*, Archive of Acoustics, Vol. 37(2), 2012, 213-218.

[11] Szeląg A., Rubacha J., Kamisiński T., *Narrow sound frequency range problem of reflector arrays*, Acta Physica Polonica, Vol. 123(6), 2013, 1059-1063.

TECHNICAL TRANSACTIONS | CZASOPISMO TECHNICZNE
CIVIL ENGINEERING | BUDOWNICTWO
2-B/2015

THOMAS THIIS*, ALMERINDO D. FERREIRA**, MARKUS MOLNAR*,
ARNOLD V. ERICHSEN*,

CHARACTERIZATION OF SHEAR STRESS DISTRIBUTION ON A FLAT ROOF WITH SOLAR COLLECTORS

CHARAKTERYSTYKA ROZKŁADU NAPRĘŻEŃ STYCZNYCH NA PŁASKIM DACHU Z KOLEKTORAMI SŁONECZNYMI

Abstract

In the search for new renewable energy sources, photovoltaic systems and solar thermal collectors have become more common in buildings. With increased efficiency and demand for energy, solar power has also become exploitable at higher latitudes where snow is a major load on buildings. For flat roofs, one usually expects approximately 80% of the snow to be eroded off the roof surface. Installing solar panels would change this since the flow pattern and wind conditions on the roof are affected by their presence. This study shows the erosion of sand particles from underneath solar panels of various configurations associated with different wind velocities. The pattern of erosion is used to determine the relative friction velocity, $u_{*\mathrm{REL}}$, of the wind on the roof. This value is the friction velocity on the roof relative to the friction velocity on a flat roof without solar panels. The experiments, conducted in a wind tunnel, show that the area where $u_{*\mathrm{REL}}$ is 0 and where it is expected that sand and snow will accumulate in case of an upwind particle source and decrease with increasing distances between roof and solar panel. It is also shown that a larger gap between the solar panel and roof surface creates larger erosion zones, where $u_{*\mathrm{REL}} > 1$ for both wind directions. Since the erosion is closely linked to the air flow under the solar panels, and that higher air velocity increases the erosion, it is likely that a larger solar panel, extending higher into the free air flow would be desirable to avoid snow accumulation on a flat roof with solar panels. If the solar panel has large enough dimensions, the solar panels can be used as a deflector to decrease snow accumulation on flat roofs. With solar panels of the size in the current experiments, a building with a length smaller than the equivalent of $x/L = 0.3$ would have $u_{*\mathrm{REL}} > 1$ on most of the roof surface and would thus likely have a lower snow load than an equivalent float roof without solar panels.

Keywords: wind engineering, wind tunnel, snow load, environmental actions, wind erosion

Streszczenie

Wraz ze zwiększoną efektywnością i zapotrzebowaniem na energię, energia słoneczna stała się możliwa do wykorzystywania w większych szerokościach geograficznych, gdzie śnieg jest głównym obciążeniem budynków. W przypadku płaskich dachów, można się spodziewać, że 80% śniegu jest zwiewane z jego powierzchni. Po zainstalowaniu paneli słonecznych, sytuacja ulega zmianie, gdyż przepływ powietrza i warunki wiatrowe na dachu zmieniają się. Praca przedstawia erozję ziaren piasku spod paneli słonecznych, w różnych układach, przy różnych prędkościach wiatru. Forma erozji jest wykorzystywana do wyznaczania względnej prędkości tarciowej, $u_{*\mathrm{REL}}$, wiatru na dachu, względem dachu bez paneli. Doświadczenia w tunelu aerodynamicznym wskazują obszar, gdzie $u_{*\mathrm{REL}} = 0$ i gdzie piasek i śnieg będą się zbierać w przypadku źródła ziaren w napływie i zmniejszać się wraz ze wzrostem odległości między dachem i panelem słonecznym. Większy odstęp między panelem i dachem przyczynia się do zwiększenia obszarów erozji, gdzie $u_{*\mathrm{REL}} > 1$, dla obu kierunków wiatru. Ponieważ erozja jest silnie związana z przepływem pod panelami, a większa prędkość powietrza powoduje wzrost erozji, prawdopodobne jest, że większy panel słoneczny, sięgający wyżej w przepływie powietrza, jest pożądany, aby uniknąć gromadzenia się śniegu na powierzchni dachu. Jeśli panel ma wystarczająco duże wymiary, może zostać wykorzystany do zmniejszenia gromadzenia się śniegu na dachu. W przypadku paneli słonecznych w rozmiarach użytych w badaniach, budynek o długości mniejszej niż $x/L = 0{,}3$ ma $u_{*\mathrm{REL}} > 1$ na większości powierzchni dachu i będzie charakteryzować się mniejszym obciążeniem śniegiem, niż na odpowiednim dachu bez paneli słonecznych.

Słowa kluczowe: inżynieria wiatrowa, tunel aerodynamiczny, obciążenie śniegiem, oddziaływania środowiskowe, erozja eoliczna

DOI: 10.4467/2353737XCT.15.143.4180

* Department of Mathematical Science and Technology, Norwegian University of Life Sciences, Norway.
** ADAI-LAETA, Department of Mechanical Engineering, University of Coimbra, Portugal.

1. Introduction

Solar radiation is a form of power that is being increasingly utilized. The increased popularity is connected to the improved efficiency of photovoltaic systems and the decrease in production costs. In the search for new renewable energy sources, the solar thermal collector has also become more frequent in buildings. Common for these two principles are that they need large areas facing the sun to have adequate effect. Since these systems are generally light weight, this has led to installations on top of flat roofs. This brings the systems out of the public space and uses areas that otherwise would have been unused. One drawback of placing solar panels on roofs is that they become exposed to higher wind speeds than if placed on the ground. This has been investigated thoroughly and there are now several guidelines on wind loads on solar panels, e.g: NVN 7250 [10] and BRE Digest 489 [2].

With increased efficiency and demand for energy, solar power has also become exploitable in higher latitudes where snow is a major load on buildings. Snow load on roofs is usually a combination of a drift load and a balanced load [7]. Usually, the drift load consists of the snow that is accumulated in sheltered areas of the roof and the balanced load that is calculated as the fraction of the ground snow load which is not eroded by wind. For flat roofs with no drift load, this fraction ranges from 70% for a wind exposed roof, 84% on a normally exposed roof to 96% for a sheltered roof. The corresponding fractions in the Eurocode are 64% for an exposed roof, 80% for a normal roof and 96% on a sheltered roof.

When placing obstructions to the wind flow on a flat roof, such as solar panels, there will also be sheltered zones were snow can accumulate in snow drifts. The snow load standards describe how to calculate snow loads around such obstructions if they are continuous all the way down to the roof. This usually constitutes a considerable extra snow load. However, if the solar panels could be mounted with an air gap between the roof and the obstruction, this is likely to create a speed increase under the panel. This will prevent snow drift accumulation, thus reducing the snow load. This effect was studied by Tabler [13] in connection with snow fences, which have the function of collecting snow to avoid problems on roads and infrastructure. However, solar collectors are located close together and the aerodynamic effects of the closely grouped solar collectors are different than in the case of snow fences. Tabler [12] also describes so-called deflectors the purpose of which is to deflect wind to avoid snow accumulation. Additionally, Thiis et al. [14] investigated the use of deflectors on buildings to reduce problems with snow accumulation.

Being a granular material, the physics of snow transport has several similarities to the physics of sand particles. One important physical feature of snow erosion is the threshold friction velocity. This is the friction velocity, exerted by the wind on the snow surface, below which snow transport ceases [11]. Viegas and Borges [15], and also Ferreira [4], have used the erosion technique to determine the relative wind exposure of an area. Such technique consists of a thin layer of sieved and calibrated sand that is exposed to gradually larger wind speeds. The eroded contours are recorded using a digital video camera, for later image treatment. Using such an experimental technique, areas of larger exposure, i.e., of higher friction velocity, can be quickly identified.

Sand has been used as granular material for determining snow accumulation. Zhou et al. [16] has analyzed three different materials and concludes that silica sand of diameter 0.2 mm gives good results in reproducing full scale accumulation patterns of snow drifts on a multilevel roof in a wind tunnel using a model with a height of 240 mm.

This study aims to analyze the wind exposure of a flat roof surface equipped with several configurations of solar collectors. Both the distance between the roof and the solar collector and the spacing between the collectors are investigated. Since the erosion is an important mechanism in determining the snow load on roofs, this might be a support in developing future provisions for snow load codes. The equipment and method used is similar to what was used in Ferreira [4].

2. Method

The experimental tests were conducted on the wind-tunnel installed in the Industrial Aerodynamics Laboratory – University of Coimbra. The test chamber of the wind-tunnel is 5m long, no roughness elements were used to control the boundary layer thickness and shape due to its relatively short length. The approaching wind and turbulence profiles, measured upstream, have the shapes shown in Fig. 1. The wind profile can be fitted by a power law ($u/U_0=(z/\delta)^{\alpha}$), where $\alpha = 0.11$ and $\delta = 0.4$ m [6], U_0 is the undisturbed wind speed, and δ the boundary layer thickness. The turbulent intensity (i) can be assumed as being close to 15%.

The tests were conducted using the sand-erosion technique [15], for which a 1 mm layer of sieved and calibrated sand is exposed to gradually larger wind speeds. The sand used has a prevailing grain diameter equal to 0.5 mm, to which correspond a threshold shear velocity, u_{*t0}, of approximately 0.33 m/s [5]. Each wind speed was maintained for 120 seconds, which was the observed time interval necessary to define the eroded contour. The contours were recorded continuously using a digital video camera for later image treatment. Although the video was recorded continuously, just the contour images, each one of them defined after 120 s of constant wind speed, are shown in section 3. Using such an experimental technique, the areas of larger exposure were quickly identified.

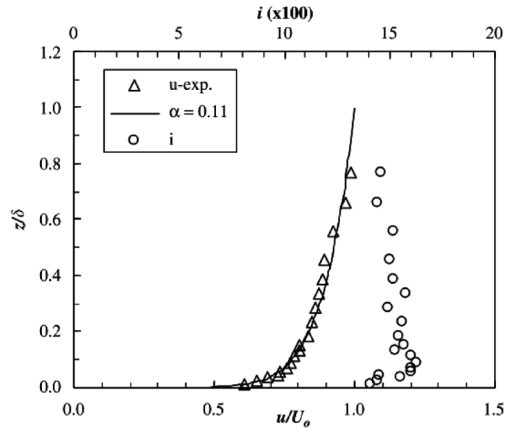

Fig. 1. Streamwise mean velocity component (u) and turbulence intensity (i) profiles, measured at the center of the wind tunnel test chamber (z – vertical coordinate; U_0 – undisturbed wind speed; δ – boundary layer thickness) [6]

The building model used in this study represents a typical three-story building with solar collectors installed on its roof. It is made at 1:25 scale with dimensions H x W x L = 30 cm x 120 cm x 60 cm, as shown in Fig. 2. The model solar collector has a height of 75 mm and a thickness equal to 8 mm. This represents a solar collector of approximately 2 meters in height and a thickness of 20 cm.

The distances between the roof and the solar collectors varied from 8 mm to 16 mm and 24 mm, corresponding to approximately 20 cm, 40 cm and 60 cm in full scale. The angle of the solar collectors, relatively to the horizontal, was set at 70°, assuming a relatively high latitude. In this study, the undisturbed wind direction was set as perpendicular to the longest side of the model and thus, also to the solar panels. Both a positive inclination (solar panel leaning against the wind) and a negative inclination were tried. The combinations of 2, 3 and 5 rows of solar panels were tested. In the case of 2 rows of panels, panels no. I and V were used. The case of 3 rows used panels no. I, III and V, whereas the last case included all the rows of solar panels. A total of 19 different experiments were accomplished including the reference case without panels.

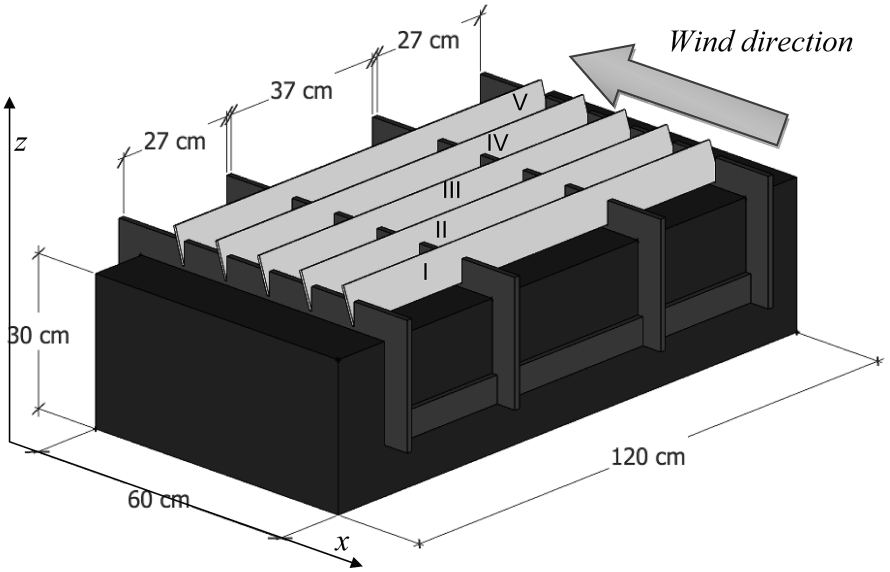

Fig. 2. Model with five rows of solar panels and negative inclination

In the post processing of the data, the erosion on the building model without solar panels was used as a reference to normalize the data. Since friction velocity is directly proportional to velocity following the logarithmic wind profile close to the boundary, it is possible to determine the relative friction velocity at which sand erodes, $u_{*\mathrm{REL}}$, as given by Eq. (1):

$$u_{*\mathrm{REL}} = \frac{u_{e0}}{u_{e\mathrm{PANEL}}} \tag{1}$$

where u_{e0} is the undisturbed velocity in the wind tunnel, upwind the model at roof height without solar panels at which sand erodes on a specific part of the roof and u_{ePANEL} is the velocity at the same spot with solar panels mounted.

3. Results and discussions

The post processing of the pictures taken during the wind tunnel erosion experiment involved combining various pictures of erosion contours, each one corresponding to a different undisturbed wind velocity, into one picture for each configuration. The area from which sand was eroded was colored with a different color for every wind velocity. Fig. 3a shows the erosion pattern on the reference case without any solar panels mounted and Fig. 3b shows one example of the erosion pattern for the configuration of five rows of solar panels with an 8 mm gap between the solar panel and the roof and a negative inclination towards the wind. As mentioned in section 2, silica sand (ρ_p = 2650 kg/m^3), with a prevailing grain diameter equal to 0.5 mm, was used in these experiments as a modelling particle. The corresponding threshold friction velocity (u_{*t}), as given by Eq. (2), where ρ is air density, and A = 0.1 [1], is approximately equal to 0.33 m/s.

$$u_{*t} = A\sqrt{\frac{(\rho_p - \rho)}{\rho} gd} \tag{2}$$

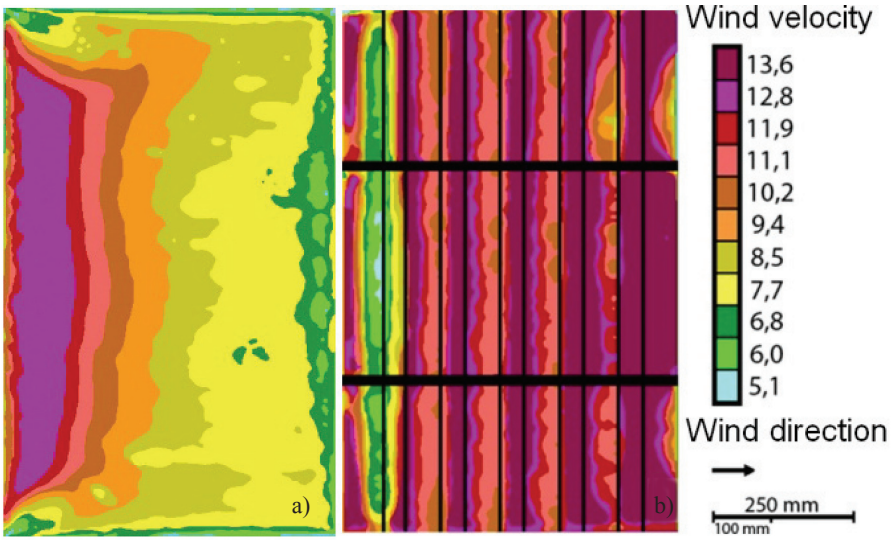

Fig. 3. Erosion pattern at different velocities, a) reference case without solar panels, b) 5 rows of solar panels, 8 mm gap, negative inclination towards the wind (wind from left to right)

Such a threshold velocity ensures that, according to Kind [9], the flow field in the tests is fully rough, as:

$$\left(\frac{u_{*t}^3}{2g\nu}\right) \approx 120 \geq 30 \tag{3}$$

The use of such sand particles makes certain that saltation of these high density particles ($\rho_p / \rho \geq 600$), is dynamically similar to those of real snow in air, even though this implies abandoning the Froude-number similarity requirement, as discussed by Kind and Murray [8]. For a thorough discussion on the similarity requirements, the references of Kind [9] and Zhou et al. [16], e.g., are recommended.

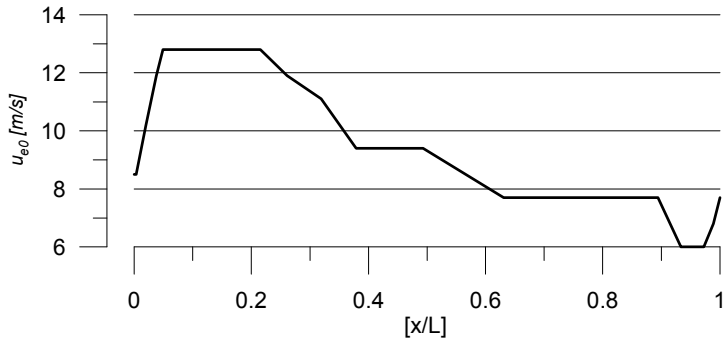

Fig. 4. u_{e0} distribution on the flat roof model without solar panels, along the symmetry plane parallel to the wind direction

Fig. 4 shows u_{e0}, the undisturbed velocity in the wind tunnel upwind the model at roof height at which sand erodes on a specific part of the flat roof without panels, along the longitudinal symmetry plane. (The Fig. 4 is the result of multiple wind tunnel runs with different wind velocities and is in fact the wind velocity along the symmetry plan in Fig. 3a).

The relative friction velocity was calculated along the symmetry plane, parallel to the wind direction. A value of $u_{*\mathrm{REL}} = 1$ indicates the same friction velocity on the roof surface as is the case of the roof without solar panels. A value of $u_{*\mathrm{REL}}$ larger than unity represents a higher friction velocity on the roof with panels (for the same undisturbed wind speed); therefore, a larger potential for erosion of sand/snow. Conversely, $u_{*\mathrm{REL}} < 1$ reveal areas where the potential for erosion is lower than in the case of no solar panels. Values of 0 indicate areas where no sand is eroded even at the highest wind velocity tested (equal to 13.6 m/s). Therefore, areas of $u_{*\mathrm{REL}} = 0$ correspond to locations where it is likely that snow will accumulate in the course of snowfall coinciding with wind. The solar panels will then cause snow drifts on top of the roof which might be larger than in the case of the roof with no solar panels. Fig. 5 shows $u_{*\mathrm{REL}}$ distributions for the 9 experimental cases with negative inclination and Fig. 6 shows $u_{*\mathrm{REL}}$ for the other 9 corresponding cases with positive inclination. A low value of $[x/L]$ indicates an upwind position.

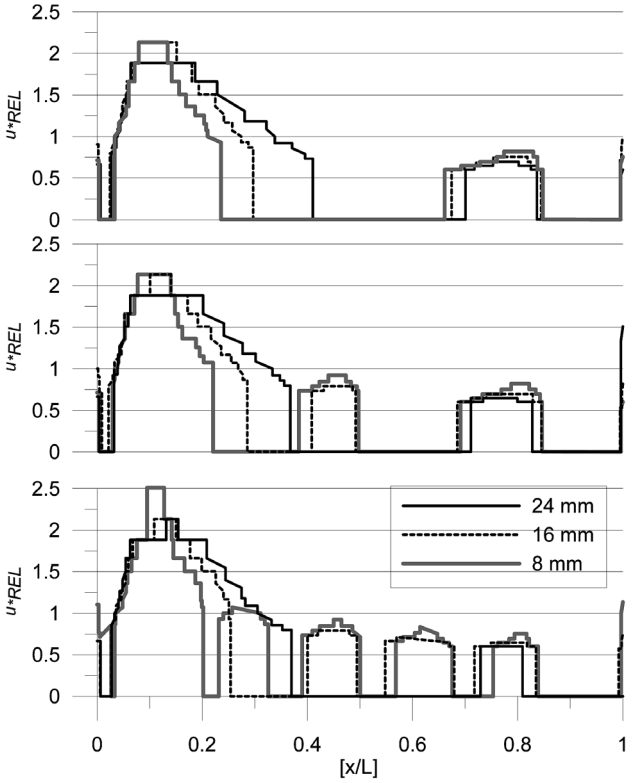

Fig. 5. Relative friction velocity for the experiments with solar panels with negative inclination: a) 2 panels; b) 3 panels; c) 5 panels

Generally, it can be seen from those two figures that the solar panels induce areas of increased relative friction velocity, but also some sheltered spaces where $u_{*\mathrm{REL}}$ is 0. From Fig. 5a it can be seen that an increased distance between the roof and the solar panel has two main effects. The most visible effect is that the area of erosion increases close to the most upwind panel; conversely, the eroded region is slightly decreasing around the downwind panel. The other effect is that $u_{*\mathrm{REL}}$ is slightly reduced in the case of the largest gap between roof and solar panels. The first is due to the Venturi effect creating the velocity speed-up below the solar panel. As the panel is moved vertically, more air is forced to flow between the roof and the solar panel – this promotes erosion and increases the size of the eroded zone. The most upwind solar panel is creating a zone with $u_{*\mathrm{REL}}$ larger than unity for a distance of approximately 0.3 [x/L] downwind from the solar panel when the gap is at its largest distance from the roof. As the zone increases, $u_{*\mathrm{REL}}$ decreases slightly. However, the zone where there is no erosion and accumulation is expected to be relatively large. Comparing Fig. 5a to Fig. 6a (where the inclination of the solar panels is positive, i.e., the solar panel is leaning towards the wind), it is possible to see that a positive inclination creates a higher $u_{*\mathrm{REL}}$ and that the zone with $u_{*\mathrm{REL}}$ larger than unity extends up to 0.6 [x/L] when the gap is at its highest. This is likely because the positive inclination is funneling air under the panels.

At the maximum distance between the panel and the roof, it also seems that the flow pattern around the downwind panel is different from the case with a gap distance of 16 mm. When the gap is at its largest, no erosion was observed experimentally underneath the downwind panel. However, it should be highlighted that erosion occurs under that panel at a 16 mm panel to roof distance and increases at an 8 mm distance. A similar tendency is visible in Fig. 5b which illustrates three rows of solar panels and negative inclination; there is no erosion underneath the center solar panel when the distance between the panel and the roof is at its maximum and erosion occurs at the smaller distances. Except for the erosion underneath the center panel, these measurements are quite similar to the case with two rows of solar panels. In Fig. 6b, the positive inclination causes the erosion zone to extend beyond the center row of solar panels in the cases of distances equal to 16 and 24 mm. However, the area where $u_{*\mathrm{REL}} > 1$ is quite similar to the case with two rows of panels. This is also the case when five rows of solar panels are used; the area of relative friction velocity higher than unity is approximately equal for all experiments of same wind direction when the gap is 24 mm, Fig. 6c. In such cases, the sand is eroded from most of the roof. This is in contrast to cases with a negative inclination and a 24 mm gap, shown in Fig. 5c, where the five rows of solar panels gives approximately the same erosion pattern as in the case of tree and two rows. With smaller distances, there is local erosion underneath the solar panels.

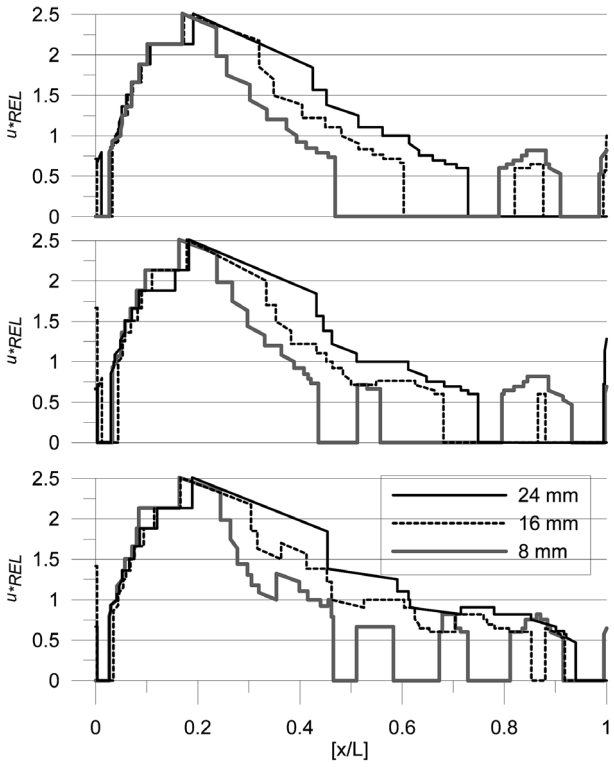

Fig. 6. Relative friction velocity for the experiments with solar panels with positive inclination: a) 2 panels; b) 3 panels; c) 5 panels

The areas where the relative friction velocity is 0 most likely correspond to locations where sand or snow would accumulate if there was an upwind particle source present. If these areas are too large, it might facilitate accumulation of significant snow loads in real cases. It is therefore desirable to avoid having such zones on a roof. Based on the present experiments, it can be assumed that a larger gap between the solar panel and roof surface promotes larger erosion zones where $u_{*\mathrm{REL}} > 1$ for both wind directions.

However, snow particle are different from sand in the sense that snow particles make interparticular bonding within hours to days after a snow fall. This means that if snow falls in calm conditions and is then subjected to such metamorphosis, the snow surface will not erode easily. This might block the gap between the solar panel and the roof surface thus reducing the erosion of the snow surface.

The measurements indicate that elevating the panels increases particle erosion. Specifically, Fig. 5c shows that the elevated solar panel configuration creates airflow that also erodes the sand around panel number II. It is likely that this effect, partly caused by extending the solar panel into a height with a higher wind velocity, causes more air to pass underneath the panel. One way of increasing this effect further would be to make larger panels which would increase the air flow under the solar panel. It is likely that, if local accumulation of snow drifts is a problem, it would be preferable to have one large solar panel instead of several smaller ones.

Assuming that there is little change in the general wind pattern if the length L of the building is reduced, one might assume that if the length L had been smaller than the equivalent of $x/L = 0.3$, the whole roof would be more exposed to wind than the reference case; thus, they would have a lower snow load than a roof without solar panels. Above this length, $u_{*\mathrm{REL}}$ is larger than unity for both wind directions. The experiments concern only two wind directions. It is shown that negative inclination gives relative friction velocity lower than unity under all but the most upwind solar panel indicating that this is unfavorable compared to a roof without solar panels. Other wind directions might give even more unfavorable snow loading conditions – this has to be considered.

3. Conclusions

This study shows the erosion of sand particles placed underneath solar panels of various configurations associated with different wind velocities. The pattern of erosion is related to the relative friction velocity, $u_{*\mathrm{REL}}$, of the wind on the roof. Locations where sand was not eroded were set to $u_{*\mathrm{REL}} = 0$ and those are areas where it is likely for sand or snow to accumulate if there is an upwind particle source present.

The experiments show that the area where $u_{*\mathrm{REL}} = 0$ decreases with an increasing distance between the roof and the solar panel. It is also shown that a larger gap between the solar panel and roof surface leads to larger erosion zones where $u_{*\mathrm{REL}} > 1$ for both wind directions.

Since the erosion is closely linked to the air flow underneath the solar panels, and that higher air velocity increases the erosion, it is likely that a larger solar panel extending higher into the free air flow would be desirable to avoid snow accumulation on a flat roof with solar panels.

If the solar panel has large enough dimensions, the solar panels can be used as a deflector to decrease snow accumulation on flat roofs. With solar panels of the size used in the current experiments, a building with a length smaller than the equivalent of $x/L = 0.3$ would have $u_{*\mathrm{REL}} > 1$ on most of the roof surface and thus, would most likely have a lower snow load than on an equivalent float roof without solar panels.

References

[1] Bagnold R.A., *The Physics of Blown Sand and Desert Dunes*, Methuen, London 1941.

[2] Blackmore P., *Wind loads on roof-based photovoltaic systems*, BRE Digest 489, 2004.

[3] European Committee for Standardization, CEN, EN 1991-1-3, Eurocode 1, Actions on structures – Part 1-3: General actions – Snow Loads, 2003.

[4] Ferreira A.D., *Structural design of a natural windbreak using computational and experimental modelling*, Environmental Fluid Mechanics, Vol. 11, 2011, 517-530.

[5] Ferreira A.D., Lambert R.J., *Numerical and wind tunnel modeling on the windbreak effectiveness to control the aeolian erosion of conical stockpiles*, Environmental Fluid Mechanics, Vol. 11, 2011 61-76.

[6] Ferreira A.D., Oliveira A.R., *Wind erosion of sand placed inside a rectangular box*, Journal of Wind Engineering and Industrial Aerodynamics, Vol. 97, 2009, 1-10.

[7] International Organization for Standardization ISO- ISO 4355 Bases for design of structures, Determination of snow loads on roofs, 2013.

[8] Kind R.J., Murray S. B., *Saltation flow measurements relating to modeling of snow drifting*, Journal of Wind Engineering and Industrial Aerodynamics, Vol. 10, 1982, 89-102.

[9] Kind R.J., *A critical examination of the requirements for model simulation of wind-induced erosion/deposition phenomena such as snow drifting*, Atmospheric Environment, Vol. 10(3), 1976, 219-227.

[10] NEN, NVN 7250, Solar energy systems, Integration in roofs and facades, Building aspects, 2007.

[11] Pomeroy J.W., Gray D. M., *Saltation of snow*, Water Resources Research, Vol. 26(7), 1990, 1583-1594.

[12] Tabler R.D., *Controlling blowing and drifting snow with snow fences and road design*, Final report, NCHRP Project 20-7 (147), 2003.

[13] Tabler R.D., *Design guidelines for the control of blowing and drifting snow*, SHRP H-381, US National Research Council, 1994.

[14] Thiis T., Delpech P., DeVirel M., *The use of deflectors to remove snowdrifts around buildings*, Proc. 5th Conference on Snow Engineering, Davos, Balkema, 2004.

[15] Viegas D.X, Borges A.R., *An erosion technique for the measurement of the shear stress field on a flat plate*, Journal of Physics E: Scientific Instruments, Vol. 19, 1986, 625-630.

[16] Zhou X, Hu J. Gu M., *Wind tunnel test of snow loads on a stepped flat roof using different granular materials*, Natural Hazards, Vol. 74(3), 2014, 1629-1648.

TECHNICAL TRANSACTIONS | CZASOPISMO TECHNICZNE
CIVIL ENGINEERING | BUDOWNICTWO
2-B/2015

ADAM ZABORSKI*

SIMULATION OF CONCRETE CORROSION AND INTERACTION SURFACES USING CELLULAR AUTOMATA

SYMULACJA KOROZJI BETONU I POWIERZCHNI INTERAKCJI AUTOMATAMI KOMÓRKOWYMI

Abstract

This paper presents a new approach to determining the synergetic effects of environmental conditions and mechanical loading on the load bearing capacity of structural members. Cellular automata are used to estimate the residual strength of a RC section subjected to concrete corrosion. The evolution of interaction surfaces resulting from bending moments and axial force caused by a continuous degradation process is presented.

Keywords: *concrete corrosion, cellular automata, continuum damage mechanics, cross-section bearing capacity*

Streszczenie

W artykule przedstawiono próbę oszacowania skutków oddziaływania środowiska i mechanicznego obciążenia na nośność elementów konstrukcji. Postępy korozji betonu i rezydualną wytrzymałość przekroju żelbetowego określono automatami komórkowymi. Przedstawiono ewolucję powierzchni interakcji momentów gnących i siły osiowej spowodowaną postępującymi procesami degradacji.

Słowa kluczowe: *korozja betonu, automaty komórkowe, kontynualna mechanika uszkodzeń, nośność przekroju*

DOI: 10.4467/2353737XCT.15.144.4181

* Institute of Structural Mechanics, Cracow University of Technology, Poland.

1. Introduction

The deterioration of concrete under combined environmental actions and mechanical loading involves different mechanisms acting on different scales, from the nanometer to the meter level, [11]. The governing equations used to describe the processes at the molecular level are usually averaged statistically at the mesoscale. Due to the limited possibilities of laboratory testing, the process parameters are determined at the macro scale. As a result, the understanding of the process mechanisms is blurred and the parameters are averaged over a representative volume. The use of averaged values leads to a phenomenological description where the bulk behaviour of the body can be explained statistically and applied to macroscopic state variables.

This paper deals with a phenomenological model of stress-assisted concrete corrosion. It presents constitutive equations for the viscoelastic continuum and multicomponent transport through porous material. The deterioration of material is described by a scalar parameter split into chemical and mechanical parts. For each part, a proper evolution equation is adopted. Compound chemical and mechanical deterioration allows the prediction of the stress state in the material. To transpose these results onto the real scale of structural members, the stress is integrated over a cross-section. The bearing capacity of the partially damaged cross-section is simulated numerically. The ultimate limit state, prescribed by Eurocode 2, provides the interaction surfaces of the cross-sectional forces. Evolution of these surfaces over time exemplifies the change of the cross-section bearing capacity. Almost all numerical simulations are carried out by a novel method of cellular automata. In this method, the space is divided into identical cells. The simulation relies on a series of actualization of cell states on the basis of an automation rule – this is identical for all the cells and uses the state of neighboring cells. For more information about cellular automata, please see [12].

In the paper, the main characteristics of the proposed model are reported succinctly, while more attention is paid to the construction of interaction curves.

2. Constitutive equations

2.1. Concrete matrix

Concrete is considered to be a viscoelastic material with fading memory. The creep of the material in response to loading can be described by the hereditary theory in the form of Volterra integral equation of the second type [1]:

$$\varepsilon(t) = \frac{\sigma(t)}{E(t)} - \int_{\tau_o}^{t} J(t,\tau)\sigma(\tau)d\tau \tag{1}$$

where σ is the effective stress, and the compliance function J can be expanded in a Dirichlet series:

$$J(t,\tau)=\sum_{i=1}^{k} f_i(t)g_i(\tau) \tag{2}$$

which leads to a generalized Kelvin chain with a series arrangement. This is equivalent to the second order differential equation but is in contradistinction to the generalized Maxwell chain where each element sustains the same stress value. This achieves two goals. Firstly, the constitutive laws for a viscoelastic material can be written in terms of a limited number of internal variables. Secondly, a recurrent definition of internal variables can be introduced, [1, 13]:

$$Y_0^{(k)}=0\,,\quad Y_i^{(k)}=Y_{i-1}^{(k)}+\int_{t_i}^{t_{i+1}}\sigma(\tau)g_k(\tau)d\tau \tag{3}$$

and limited to two elements of the chain:

$$\begin{aligned}\varepsilon(t_{i+1})=\varepsilon(t_i)+\frac{\sigma(t_{i+1})}{E(t_{i+1})}-\frac{\sigma(t_i)}{E(t_i)}+\\ +[e^{-\gamma t_{i+1}}-e^{-\gamma t_i}]\mathbf{Y}_{i-1}+\int_{t_i}^{t_{i+1}}\sigma(\tau)[g_1(\tau)+e^{-\gamma t_{i+1}}g_2(\tau)]d\tau\end{aligned} \tag{4}$$

and only one internal variable in each calculation point takes into account the history of the process. This reduces the number of numerical operations and demands on computer memory. Therefore, a remark in Cervera et al. [2] about the integral approach being unsuitable for numerical computation does not seem to be justified in a general sense.

The material behaviour is not dependent on ongoing diffusion processes. The effects of liquid and gas pressure are not included.

2.2. Transport equations

The mixture theory describes the behaviour of simultaneous multicomponent flows that occur inside the material. The mass balance equations for each constituent concentration c_i result in a set of Fick's second law equations:

$$\begin{aligned}\rho\frac{\partial c_i}{\partial t}=\underbrace{-\rho\mathbf{w}\cdot\mathbf{grad}c_i}_{\text{convection}}+\underbrace{\operatorname{div}\sum_{\mathrm{k}=1}^{\mathrm{m}}\overline{\mathrm{D}}_{ik}\mathbf{grad}\sigma_k}_{\text{pressure diffusion}}+\underbrace{\operatorname{div}\sum_{k=1}^{n-1}D_{ik}\mathbf{grad}c_k}_{\text{conc.diffusion}}-\\ \underbrace{-\operatorname{div}\sum_{\mathrm{k}=1}^{\mathrm{n\text{-}1}}L_{ik}\left(\mathbf{F}_k-\mathbf{F}_n\right)}_{\text{ext.forces}}+\underbrace{r_i}_{\text{sources}}\end{aligned} \tag{5}$$

where some terms can be neglected. The terms of pressure diffusion and external forces are irrelevant for free inflow of aggressive species, and when the Peclet number is much smaller than one, the transport processes are diffusion driven and the convection term can be omitted, [5, 9]. The actual form of diffusion equations:

$$\rho \frac{\partial c_i}{\partial t} = \mathrm{div} \sum_{k=1}^{n-1} D_{ik} \mathbf{grad} c_k + r_i \tag{6}$$

serves as the basis for the determination of components concentration. The above formulae describe conjugated as well as coupled flows. Using the concept of cellular automata, [14], equations (6) can be written as:

$$\begin{aligned} c_{m,n}^{\alpha(1)} &= c_{m,n}^{\alpha(0)} \left(1 - a^{\alpha}\right) + \frac{a^{\alpha}}{4} \left(c_{m+1,n}^{\alpha(0)} + c_{m,n+1}^{\alpha(0)} + c_{m-1,n}^{\alpha(0)} + c_{m,n-1}^{\alpha(0)}\right) - \\ &- \sum_{\beta \neq \alpha} a^{\alpha\beta} c_{m,n}^{\beta} + \sum_{\beta \neq \alpha} \frac{a^{\alpha\beta}}{4} \left(c_{m+1,n}^{\beta(0)} + c_{m,n+1}^{\beta(0)} + c_{m-1,n}^{\beta(0)} + c_{m,n-1}^{\beta(0)}\right) \end{aligned} \tag{7}$$

$$a^{\alpha\beta} = \frac{4 D_{\alpha\beta} \Delta t}{h^2} \tag{8}$$

using the von Neumann automaton rule, and:

$$\begin{aligned} c_{m,n}^{\alpha(1)} &= c_{m,n}^{\alpha(0)} \left(1 - a^{\alpha}\right) + \frac{a^{\alpha}}{5} \left[\left(c_{m+1,n}^{\alpha(0)} + c_{m,n+1}^{\alpha(0)} + c_{m-1,n}^{\alpha(0)} + c_{m,n-1}^{\alpha(0)}\right) + \right. \\ &\left. + \frac{1}{4} \left(c_{m+1,n+1}^{\alpha(0)} + c_{m+1,n-1}^{\alpha(0)} + c_{m-1,n+1}^{\alpha(0)} + c_{m-1,n-1}^{\alpha(0)}\right) \right] - \sum_{\beta \neq \alpha} a^{\alpha\beta} c_{m,n}^{\beta} + \\ &+ \sum_{\beta \neq \alpha} \frac{a^{\alpha\beta}}{5} \left[\left(c_{m+1,n}^{\beta(0)} + c_{m,n+1}^{\beta(0)} + c_{m-1,n}^{\beta(0)} + c_{m,n-1}^{\beta(0)}\right) + \right. \\ &\left. + \frac{1}{4} \left(c_{m+1,n+1}^{\beta(0)} + c_{m+1,n-1}^{\beta(0)} + c_{m-1,n+1}^{\beta(0)} + c_{m-1,n-1}^{\beta(0)}\right) \right] \end{aligned} \tag{9}$$

$$a^{\alpha\beta} = \frac{20 D_{\alpha\beta} \Delta t}{h^2} \tag{10}$$

using the Moore automaton rule. The diffusion coefficients depend on the volumetric strain, [12].

The presented automata rules are a novel and alternative method to the simultaneous multicomponent flows that occur inside the material.

2.3. Evolution equations

Within a frame of continuous damage mechanics, the material deterioration can be entirely described by a scalar parameter composed of two parts – chemical and mechanical. The effective stress due to material degradation is, [4]:

$$\bar{\sigma} = \frac{\sigma}{(1-d_{ch})(1-d_m)} \tag{11}$$

2.3.1. Chemical part

The diffusion processes through the porous material are very slow when compared to the rate of chemical reactions. The calculation recounted in [9] for similar chemical processes gave the Damköhler number of order 800, so much greater than one. This means that the chemical reaction process is strongly diffusion controlled. This is called an encounter complex where the formation of products is almost instantaneous. The actual rate of chemical reaction is limited by the slowest step – diffusion.

Considering a first order reaction kinetics, a formula similar to that which was proposed in [3] can be used:

$$\frac{dK}{dt} = \chi \left\langle c_a - c_{a0} \right\rangle_+ \tag{12}$$

where two parameters play an important role: they limit the concentration c_{a0} of the onset of the corrosion process and the coefficient χ is of a stoichiometric nature.

A simple linear dependence of the chemical damage parameter and the chemical reaction extent can be assumed:

$$d_{ch} = \xi K, \quad \xi \in (\xi_0, 1) \tag{13}$$

where ξ_0 stands for maximum material damage or residual strength of the material due to its non-homogeneity. A similar idea has been presented in [8].

2.3.2. Mechanical part

The mechanical damage parameter is defined by the formula in terms of an equivalent tensile strain, [6]:

$$d_m = 1 - \frac{\eta_0}{\eta}\left[1 - \alpha_m\right] + \alpha_m \exp\left[\beta_m \left(\eta_0 - \eta\right)\right] \quad \eta(\varepsilon) = \sqrt{\frac{1}{E_0}\boldsymbol{\varepsilon} : \mathbf{C_0} : \boldsymbol{\varepsilon}} \tag{14}$$

The above formula is well suited for the modeling of concrete under compression as well as under tension and was compared with the Eurocode nonlinear elastic-plastic prescription, [14].

3. Numerical examples

A reinforced concrete cross-section exposed to 10% ammonium nitrate (V) solution and flexure stress is considered. Two cases of environmental action are considered: the first without protection; the second with one side protected, Fig. 1.

All required material and process data were adopted from the author's previous works, [12], or from numerical simulation of laboratory experiments on cementitious samples, [10]. The cement characteristics from [15] are recalculated here onto concrete characteristics.

3.1. Cross-section damage

The concentration contour lines were obtained as a solution of the transport equations with the use of the cellular automata. The reaction products are calcium nitrate and ammonia with a residual strength of the solid phase, this indicates the deterioration of the material.

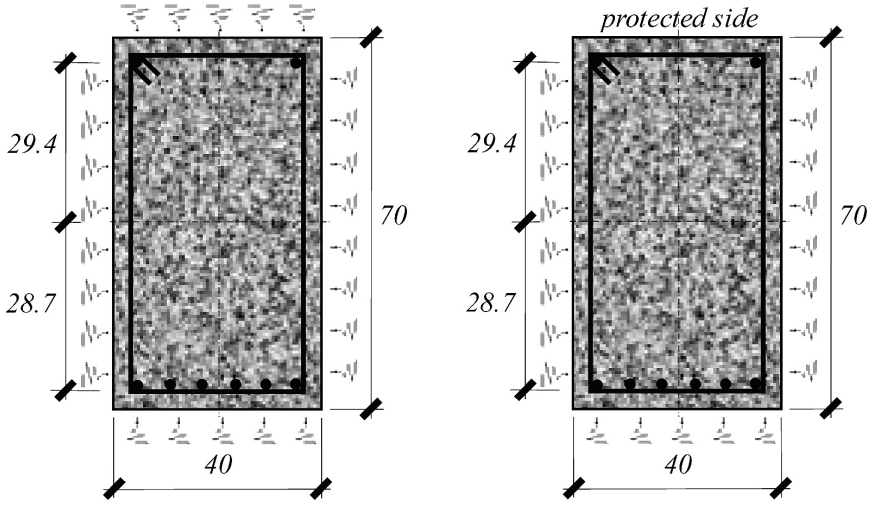

Fig. 1. A cross-section of RC beam: without protection (left); with one side protected (right)

The contour lines of the accumulative damage parameter are presented in Fig. 2. The solution for the case without protection demonstrates a lack of horizontal symmetry due to the mechanical load and different damage rate from the tensioned side in relation to the compressed side. The comparison of the solutions with different protections clearly shows the influence of boundary conditions on the actual form of cross-section damage. The bearing capacity of the RC cross-section comes from a combined action of the reinforcement and the compressed zone of concrete. Therefore, the damage processes in the compressed zone of the cross-section can considerably influence its bearing capacity.

3.2. Interaction surfaces

The cross-section bearing capacity decreases as a consequence of the material damage. The determination of cross-sectional forces in ultimate limit state is very important from the point of view of structural engineering. To assess limit values of the forces, the effective stress should be integrated over the cross-section area. The more general picture of limit values can be presented by interaction surfaces, or, due to poor visibility of 3D objects in 2D presentation, their sections commonly named the interaction curves.

However, the stress integration is not a standard procedure here for two reasons. Firstly, the effective stress state always depends on both space variables. In such cases, the ordinary integration procedures commonly employed in structural mechanics are useless. Secondly, due to stress softening, both in tension and compression, the ultimate values of cross-sectional forces are obtained for imminent but not exactly limit strains. The use of limit strains as prescribed by Eurocode for standard cases yields partially non-convex interaction curves. This is not an exact denouement to the problem, but such an erroneous solution can be found in several research papers ([7], for instance).

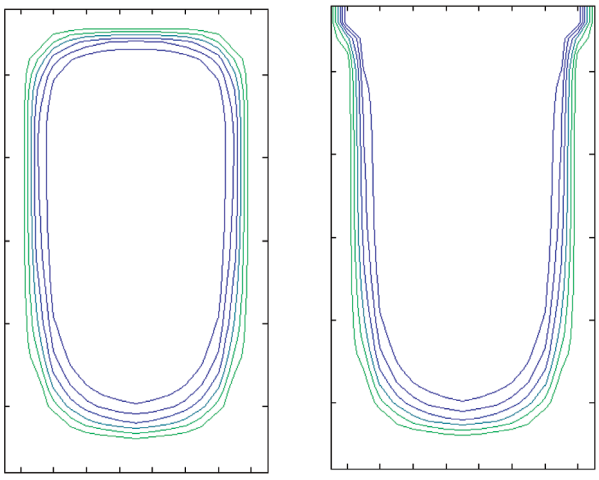

Fig. 2. Contour lines of damage parameter: without protection (left); with one side protected (right).

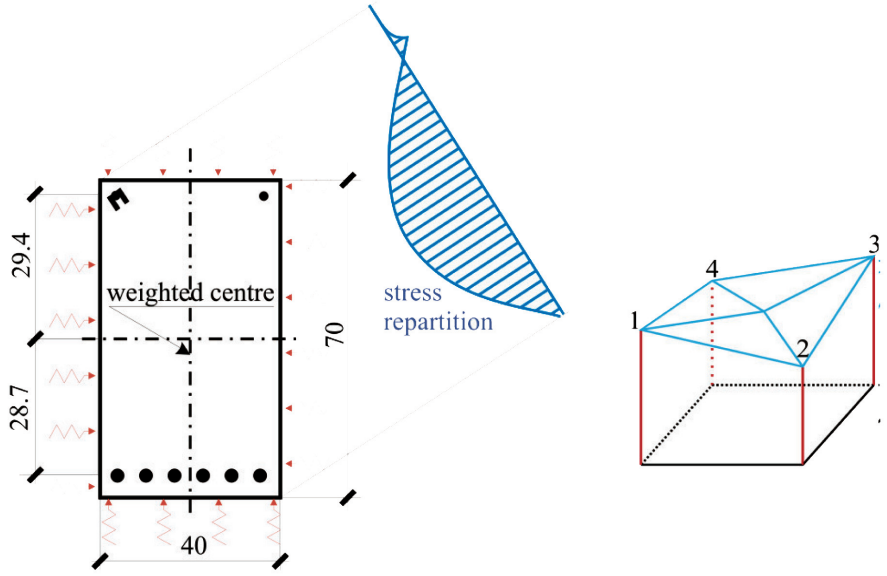

Fig. 3. A nominal stress repartition and stress integration method

A method of stress integration adopted here uses triangularisation based on the cellular automata discretization (Fig. 3). Using linear approximation, we get simple formulae for the finite difference resultant and its position:

$$\sigma_m = \sum_{i=1}^{4} \sigma_i, \quad S = \frac{1}{4}\Delta x^2 \sigma_m,$$
$$y_S = \frac{\Delta x}{24} \sum_{i=1}^{4} (-1)^i \frac{\sigma_i}{\sigma_m}, \quad z_S = \frac{\Delta x}{24} \sum_{i=1}^{4} (-1)^{(i+\mathrm{mod}(i,2))/2} \frac{\sigma_i}{\sigma_m} \tag{15}$$

The interaction curves are a solution of an inverse problem. For a given strain repartition, an appropriate stress repartition is calculated and integrated. In this way, a point in cross-sectional space is created. The interaction curves are simply a convex hull of all possible interaction points. To complete the task, a sufficiently dense, computer-generated set of possible strain repartition should be used.

The interaction curves of axial force and bending moment, (N–M_y), result from strain repartitions conserving symmetry, with the neutral axis perpendicular to the cross-section symmetry axis. The interaction curves of bending moments, (M_y–M_z), require an additional loop of iterations to fulfill the condition of zero axial force.

The interaction curves evolve over time. In Fig. 4, N–M_y and M_y–M_z curves are presented for the case without protection, and in Fig. 5, for the case with one side protected.

Due to ongoing material deterioration, the residual bearing capacity of the cross-section diminishes and the interaction curves shrink over time. Protection of one side of the cross-section results in smaller damage to the compression zone and a much greater bending moment capacity. The difference, however, is less visible on M_y–M_z curves.

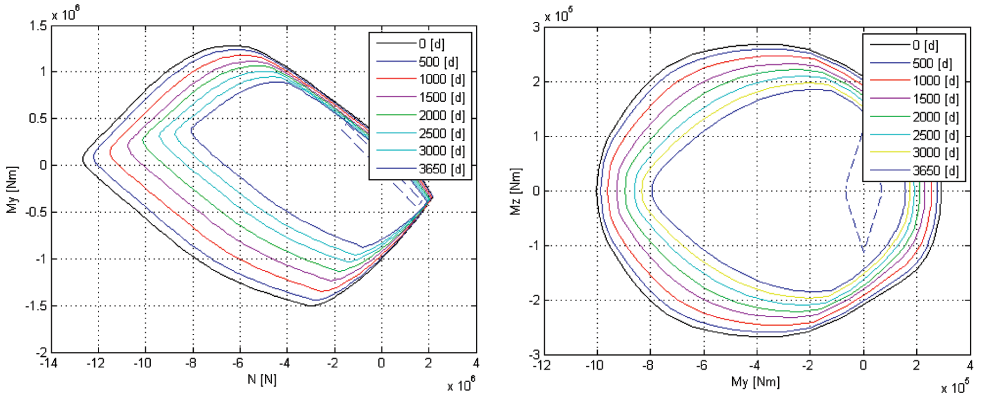

Fig. 4. Interaction curves N–M_y (left) and M_y–M_z (right), no protection

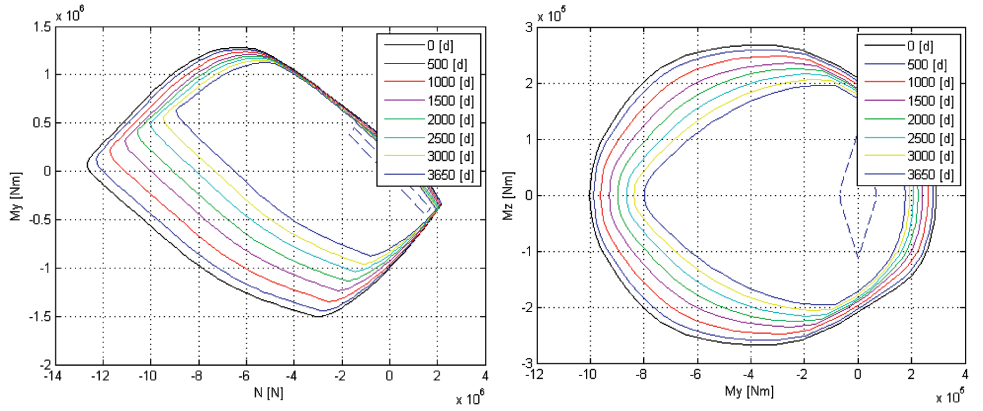

Fig. 5. Interaction curves N–M_y (left) and M_y–M_z (right), one side protected

4. Conclusions

Despite the many simplified assumptions adopted, the physical and chemical modelling of concrete corrosion presented here seems to be adequate to reproduce the characteristic material damage as well as the synergetic action of the environmental and mechanical load. The material and process parameters used in calculations were collected from various experimental works presented by other researchers so the results presented here have an informative character only.

Cellular automata are a robust tool for numerical analysis of the transport equations as well as stress integration. The existing 'classical' methods (Alternating Implicit Direction method, for instance) can be successfully replaced by this 60-year-old but novel method.

Most notably, to author's knowledge this is the first study to simulate the long-term effects of concrete corrosion for different boundary conditions on the load-bearing capacity of the structural member cross-section.

References

[1] Bažant Z.P., Hauggaard A.B., Baweja S., Ulm F.-J., *Microprestress-solidification theory for concrete creep. I: Aging and drying effects*, Journal of Engineering Mechanics, Vol. 123(11), 1997, 1188-1194.

[2] Cervera M., Oliver J., Prato T., *Thermo-chemo-mechanical model for concrete. II: Damage and creep*, Journal of Engineering Mechanics, Vol. 125(9), 1999, 1028-1039.

[3] Comi C., Kirchmayr B., Pignatelli R., *Two-phase damage modeling of concrete affected by alkali–silica reaction under variable temperature and humidity conditions*, International Journal of Solids and Structures, Vol. 49, 2012, 3367-3380.

[4] Kattan P.I., Voyiadjis G.Z., *Decomposition of damage tensor in continuum damage mechanics*, Journal of Engineering Mechanics, Vol. 129(9), 2001, 940-944.

[5] Kubik J., *Przepływy wilgoci w materiałach budowlanych*, Oficyna Wyd. Politechniki Opolskiej, Opole 2000.

[6] Kuhl D., Bangert F., Meschke G., *Coupled chemo-mechanical deterioration of cementitious materials. Part I: Modeling*, International Journal of Solids and Structures, Vol. 41, 2004, 15-40.

[7] Papanikolaou V.K., *Analysis of arbitrary composite sections in biaxial bending and axial load*, Computers and Structures, Vol. 98-99, 2012, 33-54.

[8] Saetta A.V., Scotta R., Vitaliani R., *Mechanical behavior of concrete under physical-chemical attacks*, Journal of Engineering Mechanics, Vol. 124(10), 1998, 1100-1109.

[9] Samson E., Marchand J., *Modeling the transport of ions in unsaturated cement-based materials*, Computers and Structures, Vol. 85, 2007, 1740-1756.

[10] Schneider U., Chen S.-W., *Deterioration of high-performance concrete subjected to attack by the combination of ammonium nitrate solution and flexure stress*, Cement and Concrete Research, Vol. 35, 2005, 1705-1713.

[11] Xi J., Willam K.J., Frangopol D.M., *Multiscale modeling of interactive diffusion processes in concrete*, Journal of Engineering Mechanics, Vol. 126(3), 2000, 258-265.

[12] Zaborski A., *Zastosowanie automatów komórkowych do numerycznej symulacji korozji betonu pod obciążeniem*, Technical Transactions, series Mechanics, Vol. 107(9), 2010, 147-158.

[13] Zaborski A., *Corrosion of reinforced concrete due to stress-assisted diffusion*, Archive of Civil Engineering, Vol. 41(3), 1995, 447-460.

[14] Zaborski A., *Symulacja numeryczna wpływu korozji chemicznej betonu na nośność elementów żelbetowych*, Ochrona przed Korozją, Vol. 6, 2012, 279-281.

[15] Zaborski A., *Zmiany nośności przekroju żelbetowego wynikające z postępującej degradacji chemiczno-mechanicznej betonu*, Przegląd Budowlany, Vol. 5, 2014, 73-75.

SNOW LOAD AND ICE LOAD

OBCIĄŻENIE ŚNIEGIEM I OBLODZENIEM

TECHNICAL TRANSACTIONS | CZASOPISMO TECHNICZNE
CIVIL ENGINEERING | BUDOWNICTWO
2-B/2015

PHILIPPE DELPECH*, THOMAS THIIS**

APPLICATIONS OF "SNOWIND" ENGINEERING – CLIMATIC WIND TUNNEL METHODS

ZASTOSOWANIA TECHNIKI „SNOWIND" – METODY BADAWCZE STOSOWANE W TUNELU KLIMATYCZNYM

A b s t r a c t

Transport and deviation of snow by wind induce many constraints on buildings, vehicles and industrial systems. A selection of questions from snow-wind engineering are presented in the paper. The experimental method that was undertaken to investigate these questions makes use of a large climatic wind tunnel, partly designed to address snow engineering problems at full scale: snow penetration in buildings, into ventilation systems of buildings and vehicles and snow or ice accretions on structures.

Keywords: snow engineering, atmospheric icing, environmental actions, wind tunnel

S t r e s z c z e n i e

Transport i przemieszczanie śniegu przez wiatr powodują wiele ograniczeń dotyczących budynków, pojazdów i systemów przemysłowych. W niniejszej pracy przedstawiono kilka problemów z zakresu inżynierii wiatrowo-śniegowej. W celu uzyskania na nie odpowiedzi użyto metod badawczych wykorzystujących duży tunel klimatyczny, zaprojektowany częściowo z przeznaczeniem do rozwiązywania zagadnień inżynierii śniegowej w skali naturalnej, np.: przedostawania się śniegu do budynków, systemów wentylacyjnych budynków i pojazdów oraz gromadzenia się śniegu lub lodu na konstrukcjach.

Słowa kluczowe: inżynieria śniegowa, oblodzenie atmosferyczne, oddziaływania środowiskowe, tunel aerodynamiczny

DOI: 10.4467/2353737XCT.15.145.4182

* Centre Scientifique et Technique du Bâtiment, Nantes, France.
** Department of Mathematical Sciences and Technology, Norwegian University of Life Sciences, Norway.

1. Introduction

Snow may interact in different ways with structures and can induce many problems in buildings and systems exposed to atmospheric conditions. Due to the multiform nature of snow, the deposition process and the mechanical and thermal properties of snow, it may induce many problems which, in some cases, may have tragic consequences.

The low density of snow flakes and the granular, solid form of the material (unlike rain) make it disposed for aeolian transport into open elements such as building ventilation openings. Depending on the system concerned, the consequences may be very detrimental to the proper use of the building and the safety of occupants; ventilation failure, damages to the insulation, local mechanical constraints, and potentially tragic if safety devices are affected.

Wet snowfall episodes produce localized snow accretions on all kind of surfaces (façade elements, inclined walls, solar shades, …). These snow accretions with high cohesive forces induce constraints on structures as well as many mechanical systems in fields as diverse as transport, buildings, infrastructures, energy production and transports.

Beyond local mechanical constraints, which these types of snow accretions induce at the time of creation, the accidental risk is increased if the accumulations occur on high rise structures or fast moving vehicles and suddenly fall off due to temperature rise, vibrations of support, or wind effects.

These situations may require an experimental approach that allows control of the main climatic parameters such as air temperature, wind velocity and concentration of snow/ice particles, to reproduce the interaction phenomena as they are observed in nature. This possibility is offered by a large climatic wind tunnel where it is possible to reproduce the phenomena at scale 1:1. The thermal circuit of the Jules Verne climatic wind tunnel (Fig. 1), with artificial snow making capabilities, can reproduce various kinds of snowstorm events. Wind velocity, ambient air temperature and air/water ratio in the snow guns are fully controllable to determine the snow properties (dry or wet snow). The large dimension of the test chamber, 25 m long, 10 m wide and 7 m high, enables simulation of mechanisms of snow/building interaction at a full- or moderately reduced scale.

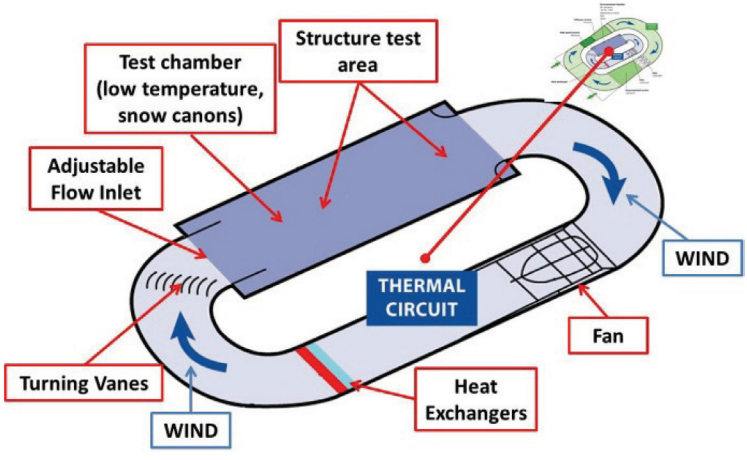

Fig. 1. The thermal circuit of the Jules Verne climatic wind tunnel

The appropriate thermodynamic conditions (air temperature and humidity) are controlled by two heat exchangers (cold and warm) across the section of the wind tunnel. Snow guns are fitted into the test section nozzle. They are used to generate a freezing water spray, which produces the snow cover. The typical grain flake diameters produced by the snow gun in the wind tunnel range from 0.150 to 0.450 mm.

The air temperature, and air/water ratio in the snow guns, can be set to control the liquid to solid ratio of the snow which determines the quality of the snow i.e. dry or wet snow.

2. Snow ingress in buildings and ventilation systems

2.1. Snow ingress in building components

Several kinds of questions are raised due to the ability of snow to enter openings in buildings located in snow drifting areas. One of the most important points concerns the ingress of snow in the ventilation system of a building.

In case of long exposure of building ventilation openings to wind and snow fall, a likely consequence is the partial or total obstruction of ventilation channels and filters by snow. Ventilation failure of the building causes an increase of the relative humidity inside the building which generates unhealthy indoor ambiances. When the ventilation system is able to recover due to the melting of the snow, it produces humidity absorption by filters which diffuse for a long time in the building. In turn, this induces mould growth and spread inside the building. According to studies, these kinds of problems are not rare in snowy regions of Europe since about 10% of building ventilation systems may be affected [2].

One mitigation strategy for this risk is to design a settling chamber upstream the ventilation opening which aims at reducing the air flow speed below the threshold suspension wind velocity. An air velocity of 1 to 2 m/s is usually agreed as the threshold settling velocity for snow. The main constraint of this strategy is to increase the building size with the settling volume.

An example of this kind of system from Greenland is shown in Fig. 2. The system includes a snow retention volume upstream the actual ventilation opening that behaves as a snow trap, collecting the snow to maintain the efficiency of the ventilation air flow.

A similar snow retention volume was studied with the use of full scale wind tunnel tests in parallel with field tests and numerical simulations. This allowed the comparative assessment of the efficiency of several configurations of the snow trapping volume [5]. To investigate the penetration of snow particles into the ventilation opening, a 2.5 metre cube was chosen to represent the building in which the ventilation opening was situated (Fig. 3).

The goal of the experiment was to find the amount of snow entering into the inlet when the opening was covered with different materials. The cubical shape was chosen for several reasons. The particle tracks of the snow particles are influenced by the air flow pattern around the building implying that the building shape is important for the amount of snow entering a ventilation inlet. Since a cube is a well-known shape with well-known and documented aerodynamics, this shape was found suitable for the experiments. The building should also be of a manageable size in the field experiments, a 2.5 metre cube is just about manageable

for manual work in the field. Even if the experimental site has a unidirectional wind direction, some adjustments of the direction of the opening was necessary just before the experiments started. For that reason, the building should be of a modest size and easily moveable. Fig. 4 shows the cube, its openings and internal baffles.

Fig. 2. Snow retention volume in building in Nuuk, Greenland

Fig. 3. Comparative testing of various air inlet snow traps in the wind tunnel

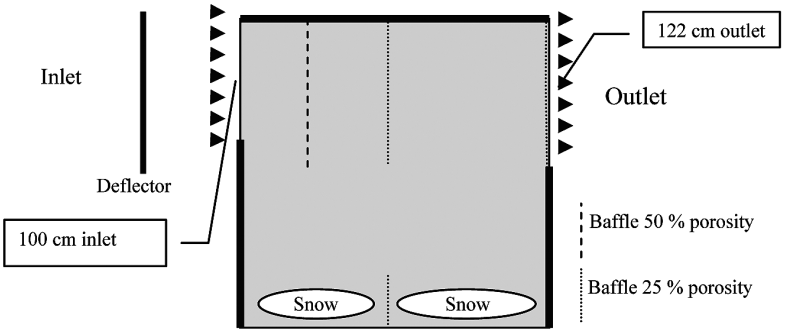

Fig. 4. Section of the cube - internal baffle arrangement

The openings of the cubes were equipped with inlets of different design to be able to study the snow penetration into the boxes during equal conditions. The differences consisted of different covering of the inlet. Three different inlets were tried; open inlet, inlet covered with insect netting of approximately 25 % porosity and a slotted wall with approximately 40 mm slots resulting in 30 % porosity.

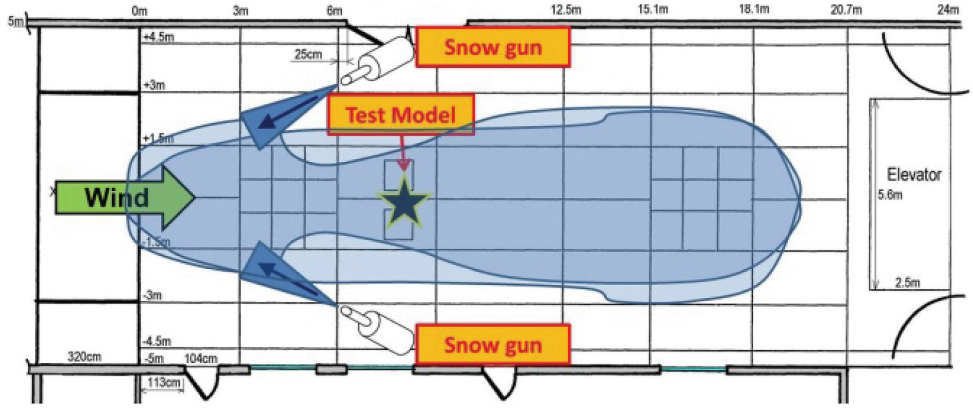

Fig. 5. Top view of the thermal unit test section, experimental setup for the snow ingress tests

Due to the experimental set-up and location of snow production systems, the snow flux obtained during the wind tunnel experiments can be locally much higher than in the field during a snow storm (60 g/m²s versus 1 – 1.6 g/m²s). Moreover, the snow flux in the field is highly dependent on the height above ground. Therefore, the ratio of snow flux upwind the cube to the snow flux in to the cube is a relevant parameter to compare wind tunnel to field experiments. The snow flux into the cube is found by dividing the sum of the accumulated snow mass inside the cube and the snow escaping from the outlet with the area of the inlet and the exposure time, thus the unit [g/m²s].

The good agreement between the experimental methods allows to present the results from all inlet designs together in Fig. 6. This Fig. also presents the average air velocity in the inlet for the experiments in the wind tunnel. The average air velocity is lower in the case of an inlet with insect netting than in the case of slotted wall. However, the snow penetration ratio is lower for the insect netting than for the slotted wall. This indicates that the snow concentration in the air entering the cube is higher in the case of slotted wall compared to insect netting.

Visual observations of the snow particle paths show that the slotted wall produces local jets in the slots that entrain snow particles. Particles impinging on the blocked part of the inlet are deflected towards the slots and entrained into the cube. In the case of the inlet covered with insect netting, there were no local jets and more particles were deflected away from the inlet, resulting in a lower snow concentration in the air.

It is worth noticing that if an insect screen seems a good configuration for dry snow, the case of precipitation as wet snow completely blocked the inlet with insect netting after a short period of time. These snow particles are large and sticks to the surface they land on.

Ingress of snow directly into the building's roof, through the tiles, may cause serious damage in the building's attics, as humidity stagnation and reduction of insulation properties of materials will appear. This may be the case in most snowy regions of Europe. Although the use of roof underlays has been generalized in new buildings, it may still be necessary to reduce snow ingress between tiles by using dedicated tightness sealing. Comparative testing of several products can greatly accelerate the development of a particular design.

For such particular driving snow tests, the wind tunnel is operated in a way which enables the assessment of the tiles snow tightness in severe conditions. Since the making of snow is carried out while the wind is blowing at the appropriate test velocity, the location of the snow gun on the leeward side of the test models allow the freezing particles to go all along the wind tunnel circuit before reaching the roof models. This trajectory is long enough to freeze the water droplets producing dry snow (Fig. 7).

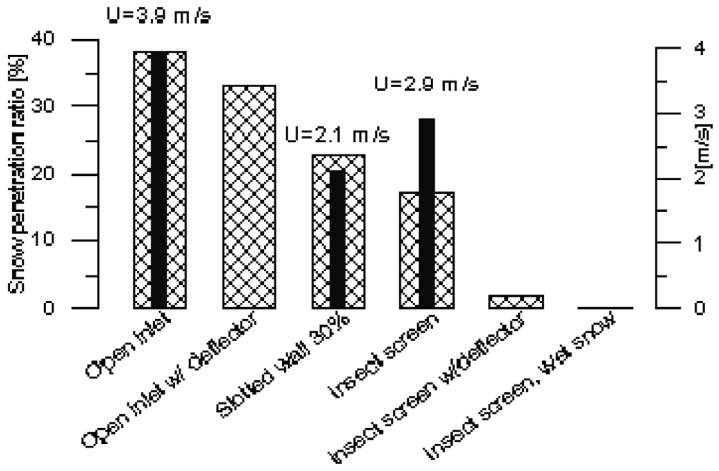

Fig. 6. Snow ingress ratio for all configurations

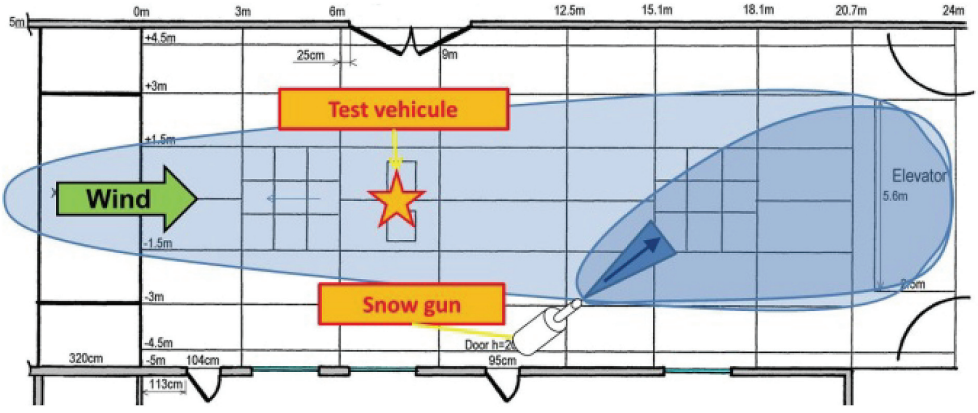

Fig. 7. Top view of the thermal unit test section, experimental setup for dry snow tests

The roof slope, the wind velocity and incidence are the test parameters to be varied in the experiment. The shape of the model itself influences the penetration of snow into the roof. As is the case in real roofs, the under pressure in the attic, which drives the snow ingress, can be adjusted naturally by using a duo pitched roof with similar tiles on both sides or by drilling holes on the leeward side which equilibrate the pressure of the inside roof with the wake zone.

A typical wind tunnel experiment may consider roof models with 2 different realistic roof slopes from 15° to 40°. The model can be made of closed boxes whose upper side reproduce a typical roof cover. The model should include a door to get inside the roof model and to evaluate the snow quantity collected.

In order to give order of magnitude of the collection phenomenon in the roof, it is interesting to mention that an event of 1 h may result in the collection of 1 to 2 kg of snow per square metre of model floor surface (Fig. 8).

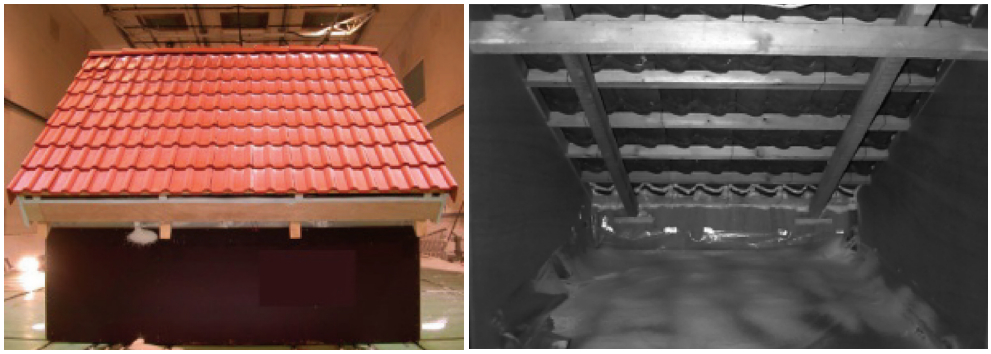

Fig. 8. Snow ingress between tiles in the model attic

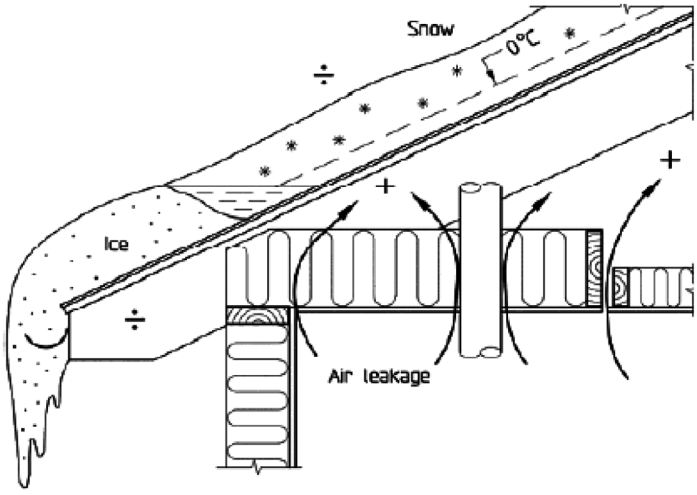

Fig. 9. Ice formation at the eave due to obstruction by snow of the ventilated cold roof

Ventilated cold roofs are commonly used in snowy regions of northern Europe. The objective is to make possible the ventilation of the under roof to maintain the temperature of the roof below freezing. Hence, the snow deposition on the roof is maintained in solid state during the winter and does not cause damages at the eave which would occur if the snow would partially melt due to unavoidable heat losses from the roof (Fig. 9). However, it is of paramount importance to protect the ventilation opening against snow ingress. The objective is to prevent the snow from entering the ventilated volume and avoid any obstruction that would cancel the benefit of ventilation.

One solution to avoiding snow penetration into the ventilated roof is to use a so-called eave cover. Several local variants of the eave cover have evolved in the Scandinavian countries. The solutions are based on reducing the air velocity in certain accumulation zones to make the snow particles settle before reaching the roof. Also different positions of the inlet have been tried, to avoid penetration of snow in the first place. Much experience and thought has been employed in the development of the local solutions.

A controlled comparative study is a valuable method to experiment and validate the design of the snowproof roof eaves. Such an approach has been undertaken in the wind tunnel [4]. To rate the performance of different eave covers, full scale tests have been performed in an environmental wind tunnel. The different eave covers were mounted on a building with duo pitched roof. The principle of ventilated, cold attic was applied in the experiments.

The measurements of the building were height = 279 cm, width = 300 cm, depth = 323 cm, and the angle of the roof was 24 ° (Fig. 10). The roof ridge was closed in the experiments, so no snow entered or escaped the attic through the ridge. To observe any possible end effects, the roof was divided in sections by width of 75 cm. One of the sections (sections b and B) was equipped with transparent roofing for observation of the snow penetration during the experiment. An overview of the different experiments (eave configurations on the windward side) is shown in Fig. 11 (right).

During the blowing phase, the wind velocity was set to 15 m/s in order to observe snow drifting. Wind tunnel data were obtained from several experiments of 60 and 120 minute periods depending on the snow penetration in the roof construction.

During the experiments, the snow transport in the wind tunnel was measured continuously to assure the same experimental conditions for every test. Mechanical snow traps with the shape of a tube with one end closed by netting were used for measuring the snow flux in the wind tunnel. The mean snow flux in the wind tunnel was 1.75×10-2 kg/m²s 135 cm above the floor, which corresponds well to the snow flux in a real snow storm of 15 m/s and no precipitation.

The snow concentration in the channel connecting the eave to the attic is defined as:

$$c = \frac{\text{Snow in attic / Test period}}{(\text{Area of channel}) \times (\text{Air velocity})} \quad [\text{kg/m}^3] \tag{1}$$

c is regarded as a measure of the effectiveness of the whole construction to withstand snow penetration. The construction with the lowest snow concentration in the inflowing air has the best ability to prohibit snow penetration into the roof.

The ratio of the snow concentration in the wind tunnel to the snow concentration in the channel connecting the eave to the attic provides a quantitative way to assess the effectiveness of the different constructions. Configuration 2 was considered as reference as the most commonly used construction in Norway.

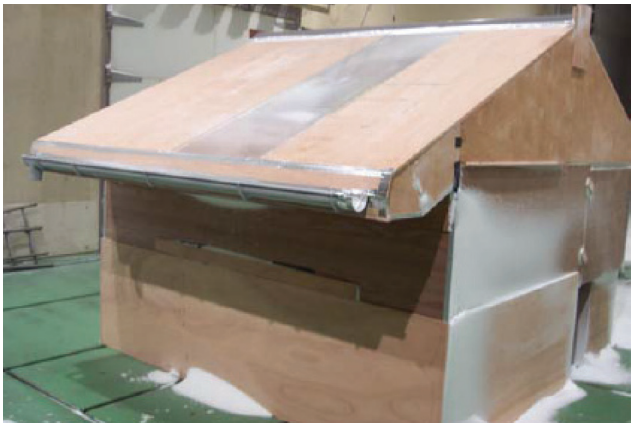

Fig. 10. Wind tunnel test of snow ingress through ventilated roof eaves

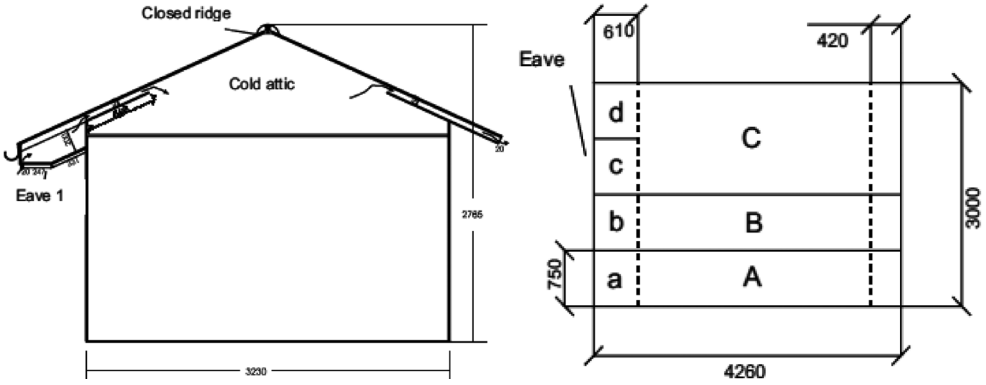

Fig. 11. Section and schematic top view of the windward roof pitch with division of the ventilated attic and eave construction

The experiments show that the design of the eave construction is important for the snow penetration into the roof. The design in experiment 5 gives the best result in avoiding snow penetration into the roof. However, this solution also introduces a flow resistance, which is higher than in experiment 2. The result of the increased flow resistance might be a reduced ability to remove moist air from the construction. Such a design is therefore favourable in a windy climate were the wind will produce an airflow in the channel for a longer period of the year. In areas of more moderate wind, and where the snow penetration problem also is smaller, the design in experiment 2 might be sufficient to avoid snow penetration and still maintain adequate ventilation of the roof.

Other interesting results were obtained, as the justification of the position of the ventilation opening should not be close to the wall, since this increases the quantity of snow transported into the attic. The reason for this is probably that large parts of the snow particles impinging on the windward are transported upwards along the wall, thus entering the ventilation opening. A deflector on the building wall will not improve this result significantly.

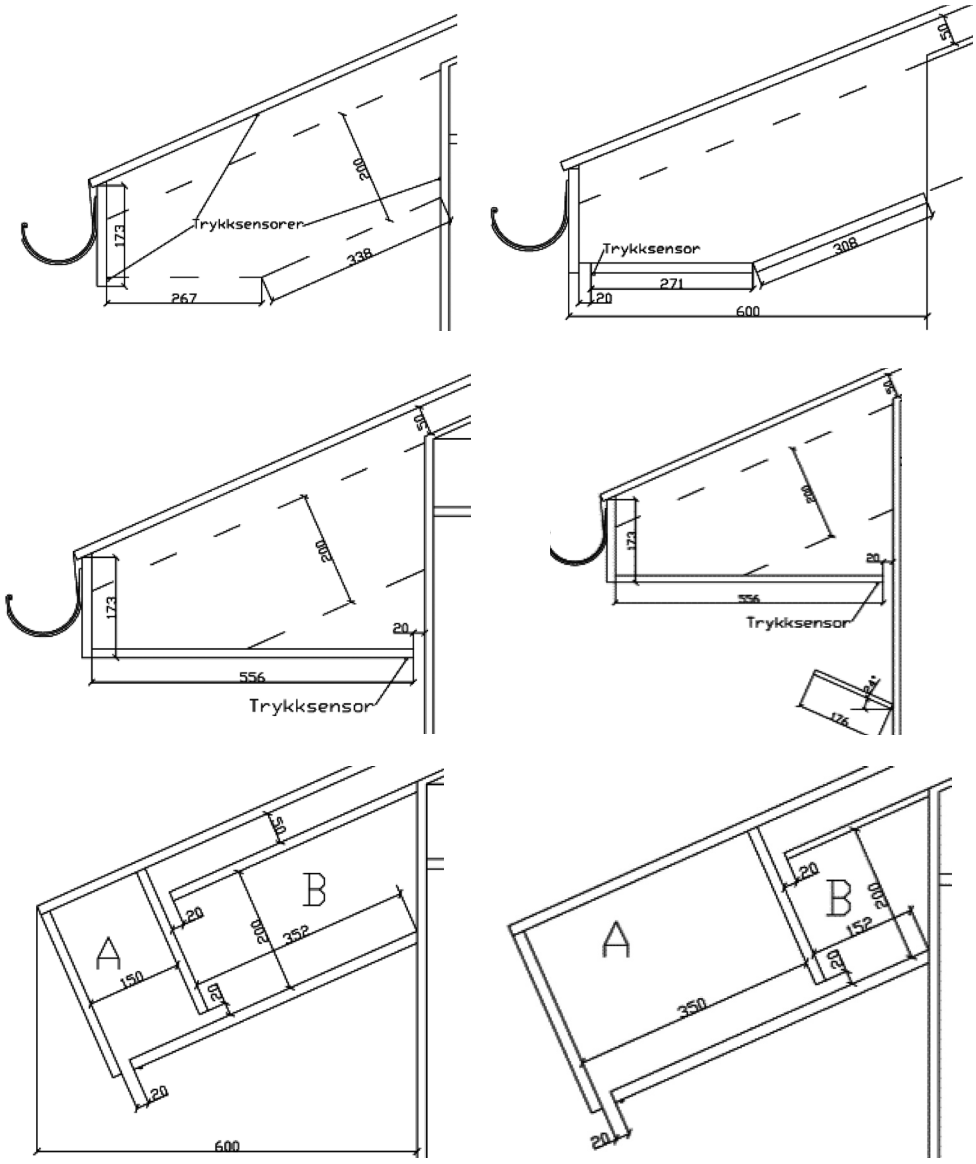

Fig. 12. Eave construction configuration included in the comparative test (construction 1 to 6)

For other alternative designs of ventilation openings in roofs or cladding, the position and design of the opening is probably the most important factor in reducing snow penetration. The opening must not face the impinging snow particles directly and it should be positioned away from surfaces or obstacles capable of funnelling blowing snow particles into the opening. Even with a small snow concentration entering the roof the amount of snow can be considerable. The air velocity of the entering air should therefore not be too high.

Snow ingress and accumulation into the air inlet of engines can cause severe damages to vehicles. Amongst the most critical conditions for road vehicles, let us mention the follow-up configuration where a vehicle follows one or several other vehicles. The snow falling is added to the snow picked-up by vehicles ahead made of fine particles. The ingress capacity of the fine particles is high and can impact several systems as engine air intake, Air conditioning system, wipers or brake systems.

Similar situations are experienced by helicopters that can be maintained in stationary flight over snow covered ground. In this case, it is important to locate and assess the quantity of snow that accumulates in the heated air intake channel of the turbine engines. The risk is to observe a local snow accumulation that could be released in large blocks and damage the turbine. The remedial strategy involves heating mats inside the air intake whose efficiency needs to be assessed according to standard procedures.

Test configurations commonly used during the design stage of new road vehicles deal with most of the aforementioned subjects. The experimental set-up enables the operation of the vehicle, engine on, fitted on a roller bench that simulates the resistant force due to drag. The test in snow storm conditions is carried on until the engine stops. Sensitivity to high snow concentration in the air is assessed by weighing the snow collected in the air filters.

Fig. 13. Operation of vehicles in snow conditions

Fig. 14. Snow test of vehicles in the wind tunnel

3. Snow jamming of mechanical systems

Another example of the interaction of snow with building equipment with potential severe consequences concerns the operation of smoke vents. The validating standard test method of smoke vents makes use of simulated loads with metallic plates or sand bags. Field tests of smoke vent under snow loads demonstrated that there are serious risks with certain types of smoke vents, made of multiples louvers, to observe jamming due to icing at the interfaces. In other cases, although the smoke vents would actually open, the snow cohesion induced compact blocks that remain attached to the louvers or even above the open louvers thus drastically reducing the free opening necessary for the efficient smoke exhaust in a fire situation.

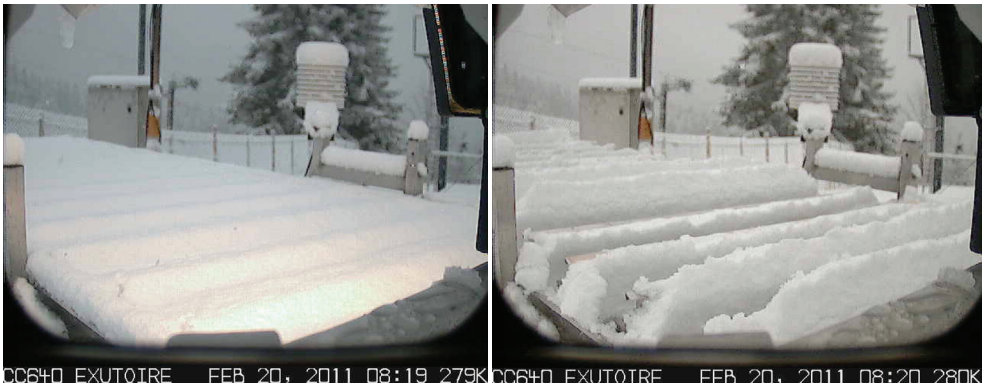

Fig. 15. Field test of smoke vent opening under snow loads

Climatic wind tunnel testing allowed simulating many opening situations of a smoke vent under controlled snow loads. The preliminary step to validate the wind tunnel approach was reproducing the natural conditions with the same test specimen used for the field tests.

For the snow load simulation in the climatic chamber, the tests were made by using two snow guns, located on each side of the test chamber at 9 m from the air nozzle. The snow guns were pointed against the wind (Fig. 5). In this configuration, the water sprays are re-oriented from their initial trajectory by the air stream of the wind tunnel. This enhanced both the freezing of the droplet and the uniformity of the snow fall in the test chamber. The air temperature was controlled at -10°C or -15°C, and the wind velocity was maintained at a few m/s.

It is noticeable that, as observed in the field, when the opening succeeded, the snow layer was broken by the louvers movement but remained attached to the louvers. In other cases, with the same load, the smoke vent did not open when the electric opening system was triggered. The vent remained in the closed position although the current absorbed was twice the current required for the unloaded configuration.

In some other case, when the vent opening was manually forced, the snow cover was not broken in pieces but remained solid above the louver edge in vertical position. In all cases, the aerodynamic free area was significantly reduced (Fig. 16).

Fig. 16. Smoke vent opening test with snow loads

This study showed that the standard test procedure of snow load of the smoke vent (load simulated by metallic plates) is not equivalent to snow load tests performed with real snow and thus inadequate for testing the functionality of smoke vents.

A single load, placed on the vent louvers does not produce the same constraints as a snow layer of equivalent mass. The cohesion forces of the snow are likely responsible for this and it is difficult to render in a simple manner the additional constraints that remain during the opening sequence of the vent. The wind tunnel test procedure demonstrated the capacity to realistically assess the capacity of smoke vent to operate in case of snow loads.

4. Wet snow accretions on building facades and high speed trains

4.1. The case of high rise buildings

Questions regarding snow accretions to building façades are more and more frequent. As far as high rise buildings are concerned, the questions deal with risk assessment in urban areas.

In these cases, the recommended approach requires a statistical snow fall study at the site of the construction, associated with an experimental modelling of snow icing of a full scale element of the skin façade. The experimental study provides quantitative and qualitative information regarding the snow accumulation process.

For a high rise building surrounded by a dense urban environment, it is sometimes necessary to assess the impact of more complex climatic scenarios. The heat generated by solar irradiation of the top parts of the building that melts the snow and ice is an example of this. The dripping water can potentially refreeze at the shaded bottom parts of the building. This is the case when the design ice or snow load can be far higher than the load due to direct exposure to precipitation as deduced from the climatology study (Fig. 18).

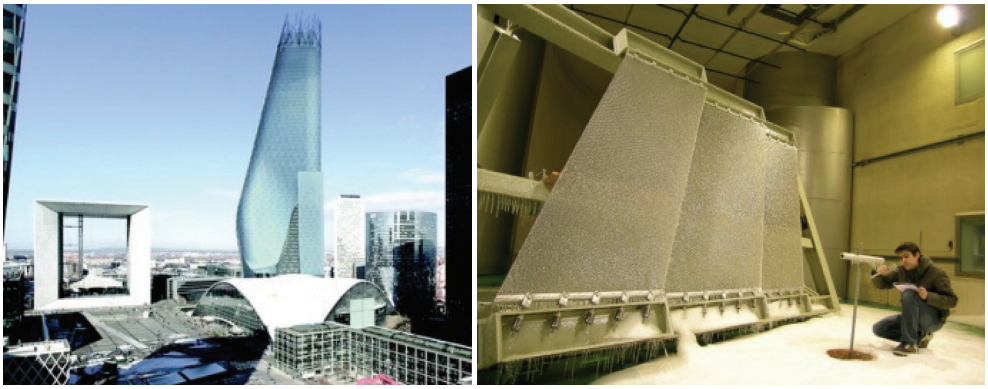

Fig. 17. Full scale icing test of double skin façade of high rise building

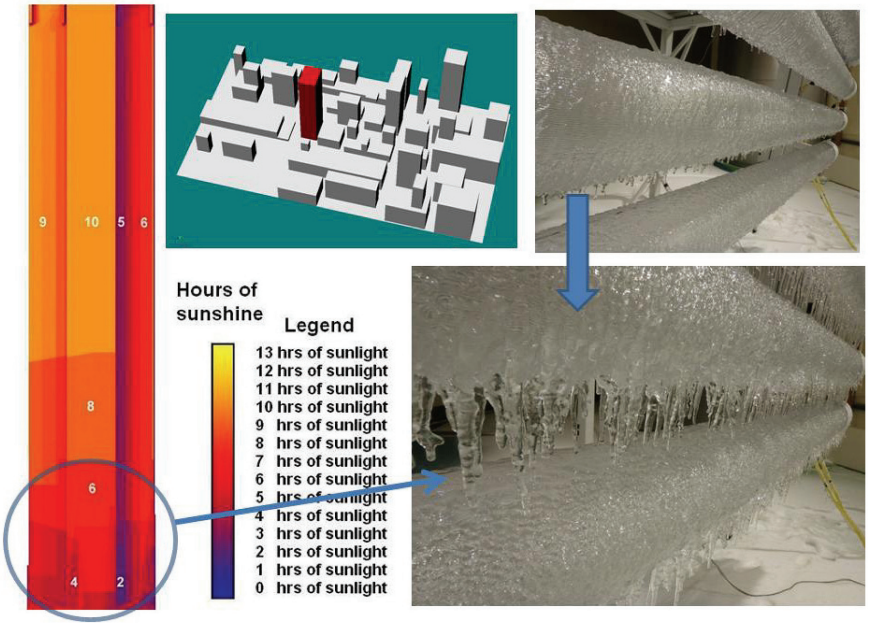

Fig. 18. Solar irradiation of high rise building in urban environment (melting of ice at the top of the building and re-icing at the bottom)

Apart from the additional load induced by snow that has to be taken into account for the dimensioning of the structure, the risk associated by falling pieces of ice during melting stage increases in the urban environment. The risk is highly dependent on the shape and porosity of the facade elements subjected to icing. Moreover, scenarios of successive melting and icing period determine the size and shapes of ice pieces that may fall. Once again, the experimental modelling provides valuable information regarding the risk as well as the possibility to design and test systems to reduce that risk.

Wind tunnel simulation can also show unexpected situations as the one observed during a de-icing test of facade elements. Solar radiation and ambiance warming induced local melting between the ice and the material. Ice is actually a semi-transparent material and the visible solar radiation was absorbed by the elements of the support which generated a rise in local temperature above freezing point. The gap between the ice and the support made the pieces of ice sensitive to wind and prone to falling.

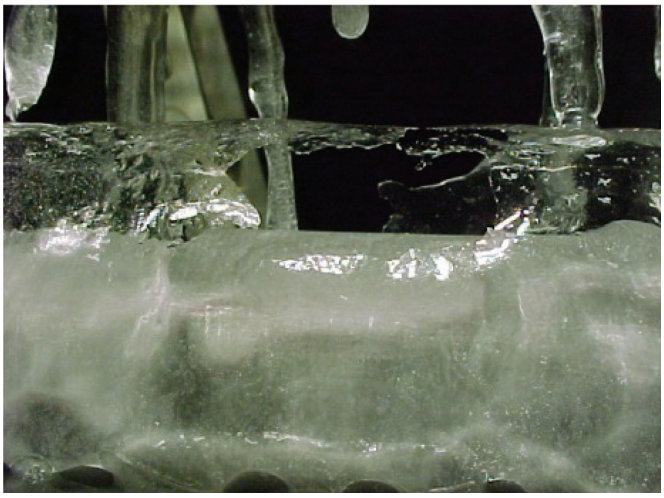

Fig. 19. Local melting of ice at the interface with structure material due to solar radiation

4.2. Railway vehicles

To maintain the development of high-speed train traffic, railway operators have to face extreme conditions, in particular during winters, with impacts on both infrastructure and rolling stock, and associated maintenance. Usual major consequences of snowfalls are both on traffic regulation with cruising speed reductions and on rolling stock with severe damage (underbody structure, windows) due to ice and snow accretions and shedding, leading for instance to ice-drop ballast projection.

In order to minimize the impact of extreme winter conditions on high-speed trains, wind tunnel experiments were undertaken as a part a research program conducted by the French railway company SNCF. The aim was to explore solutions to reduce the snow accumulation on trains. The first part of the study was dedicated to collecting data and identifying the mechanism of snow accumulation by performing tests in a climatic wind tunnel.

Most of the tests were performed with one snow cannon located on the central axis of the test section (Fig. 20). The snow cannon was set up in a counter-current configuration to enhance the spatial uniformity of particle concentration in the air flow. This configuration also ensures that particles are carried out to the test structure in equilibrium with the air flow.

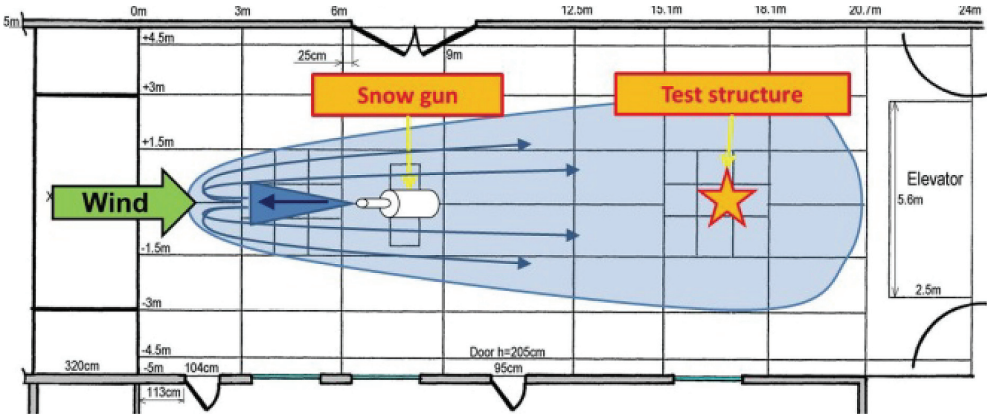

Fig. 20. Top view of the thermal unit test section, experimental setup for the snow tests

Generic simple-shaped prisms and a railway shape geometry at 1/2 reduced scale were used. The obtained results consist in snow and ice growths and localizations, with the influence of different parameters, with particular attention to the wind speed, air flow temperature, characteristics of snow particles (i.e. density, liquid water content and mass flow) and their behaviour on various angles of impact.

Two superimposed planes were used to support the prisms outside the boundary layer of the wind tunnel air flow. The prisms were located underneath the supporting planes to include the impact of the horizontal plane on the accretion phenomena to the vertical surfaces of the prisms in the simulation. This arrangement intended to mimic the volume locations under a TGV floor.

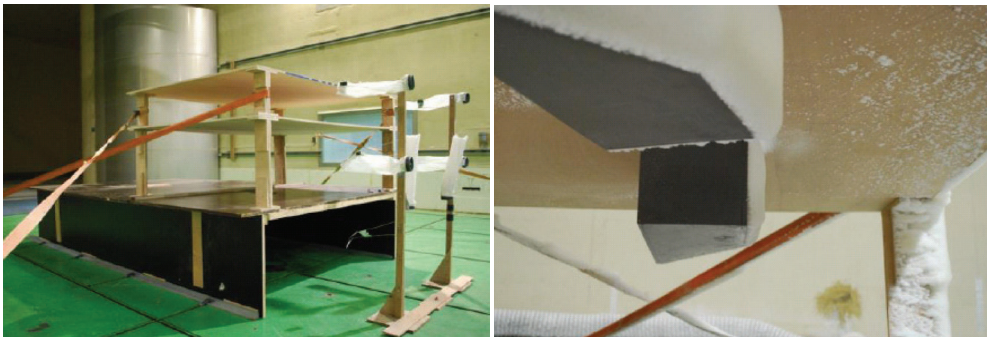

Fig. 21. Experimental set-up supporting the simple-shaped prisms in the wind tunnel test section (the wind comes from the right of the picture)

The snow concentration was derived from the collected snow mass regarding the collection area, the local wind velocity and the test duration. The average value of the snow concentration was 11 g/m^3.

The prisms have been designed to explore various inclination angles of the walls, two sizes, from 0° to 90°, with respect to the main flow. The measurement of the mass of snow captured by each face during a run, enabled us to get a table of mass flux expressed in kg/m²-s depending on the face area and the duration of the run.

To normalize the results, the snow mass fluxes have been divided by a 'reference mass flux'. This reference mass flux is measured on the face perpendicular to the flow, which gets the highest flux and is associated to a ratio of 1. To resolve uncertainty problems linked to the inhomogeneous aspect of the snow cloud (which presents higher density in its centre), several reference faces have been designated, according to their distance from the centre so that, in the end, the only parameter considered is the face slope angle versus main flow direction.

Some results were excluded when the inclination angle was altered by a large quantity of snow, inducing a deformation of the shape, and modifying the inclination angle of impacting particles.

The second part consisted in reproducing these mechanisms using numerical simulations whose methodology has been validated by comparing computational results to measurements on both the prisms and the railway mock-up [1].

In order to supplement the prism measurements with results on a more realistic under floor train geometry, a railway vehicle model at 1/2 reduced scale was designed. The model simulates two parts of a TGV body including the connection between two railroad cars (Fig. 22). The overall train model was 8m long. A bluff body shape upstream the bogie was designed in order to model the aerodynamic influence of the front part of the train.

An entire bogie was reproduced. The bogie model was simplified compared to a real one, but the main elements which may collect snow were reproduced, including the brake system (Fig. 23).

In order to reproduce the air flow underneath the train body, the model was suspended. An additional floor simulating the track was fitted 70 cm above the wind tunnel floor. The height of the floor was intended to maintain the area of interest outside the boundary layer of the wind tunnel. The rotation of the wheels was simulated by a belt drive system and an electric engine.

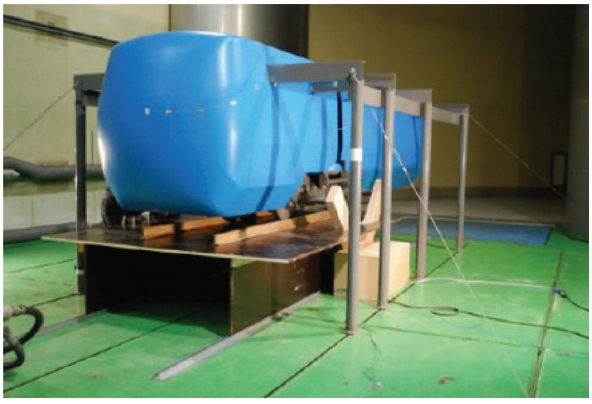

Fig. 22. TGV model set-up in the climatic wind tunnel

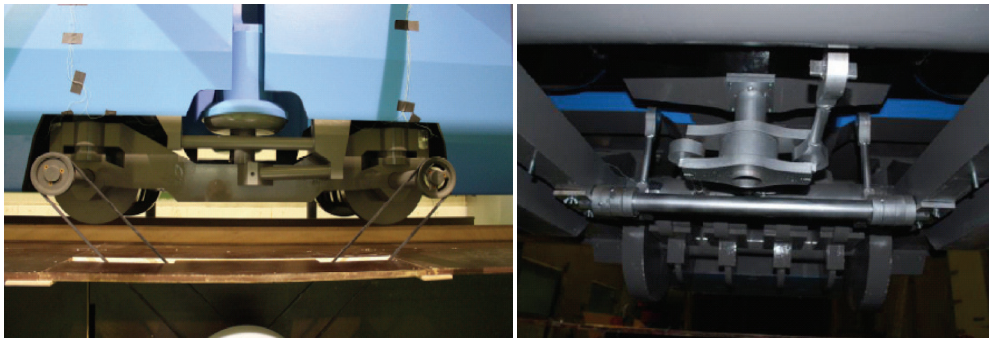

Fig. 23. TGV bogie model including anti-roll bar and the bogie-car drive system

Fig. 24. Snow accumulation in the bogie cavity (wind tunnel model and real TGV train)

At the end of each test period, the measurements of accumulated snow were made and photographs were taken at predefined locations and angles of view (Fig. 24). The snow accumulated on specific spots was collected and weighed.

A CFD methodology has been developed concurrently with the wind tunnel experiments. The measurements made on the prismatic bodies with various sizes and shapes allowed fast and precise tuning with the exploration of a large panel of parameters. The resulting simulation chain has been deployed on the more complex geometry, reproducing the TGV car details, and the workflow has been enriched with the mesh growing, in respect with the snow accretion rate obtained, and the associated volume of snow calculated.

4.3. Experimental and numerical modelling of snow accretion

The availability of realistic models that enable to predict the risks of snow and ice accretion on building or vehicle elements requires a better knowledge of the climatic constraint. In particular, the possibility to assess the sticking capacity of the snow particles at time of impact is important.

Such a modelling is possible if one can assess the liquid water content of the snow at the impact time. Recent PhD these have shown the primary effect of the liquid water content of snow on the snow accretion mass and volume [6]. The experimental approach was based on the assessment of wet snow accretion formation on simple geometric shapes. Cylinders were placed in the snow particle flow produced in the climatic wind tunnel. If all other parameters were kept constant, the ambient temperature setting (from -10°C to -2°C) enables the thermodynamic state of the snow particle at time of impact to be modified. It is then possible to assess the effect of the liquid water ratio on the accretions and perform a parametric study.

A numerical model for two-phase flows simulation has also been developed in parallel. The study conducted has been set up mainly to identify the most important parameters that drive the accretion phenomenon.

The results obtained with -10°C and -2°C experimental tests provided the limiting cases of the study as being the conditions were the accretion was either very thin and could not be weighted or too humid and could no longer be considered as actual snow.

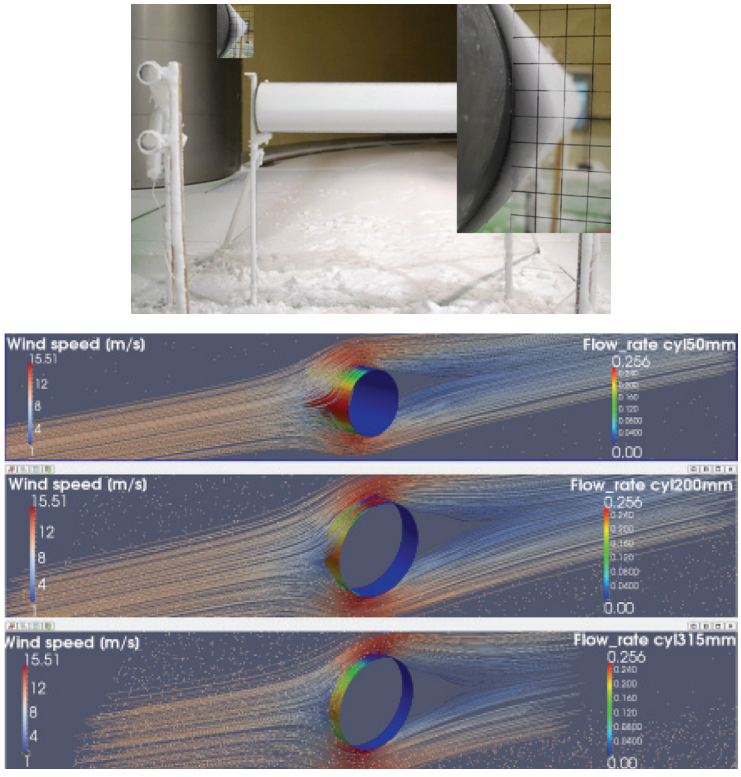

Fig. 25. Experimental and numerical modelling of wet snow accretion on a cylinder

With the three intermediate ambient temperatures, 6°C, -5°C, -4°C, one can observe the evolution of the accretion sizes to the structures (Fig. 26).

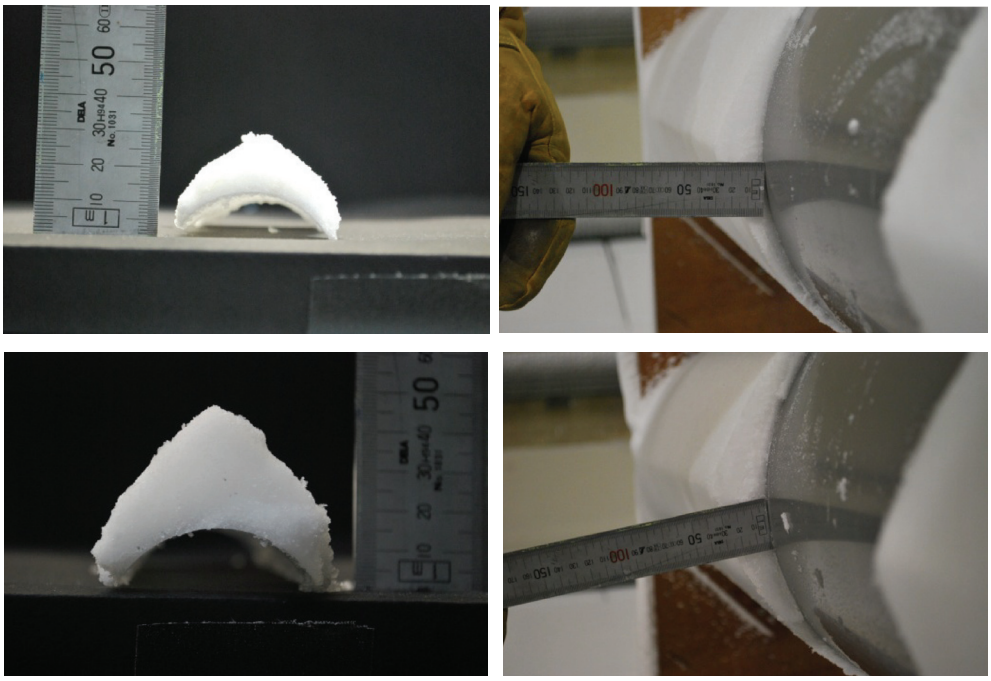

Fig. 26. Examples of wet-snow accretion (ambient temperature -6°C top and -4°C bottom)

To better describe the accretion on the test structure a parameter β has been defined as the ratio of the normalized mass of snow accreted to the cylinder ψ_a to the incident flux of snow φ_s, $\beta = \psi_a/\varphi_s$.

With the three intermediate ambient temperatures, 6°*C*, -5°*C*, -4°*C*, one can observe the evolution of the normalized collection parameter $\beta^* = \beta_t/\beta_{-6°}$ which shows how the mass of accretion grows for both cylinders (Fig. 27). Qualitatively, one can observe how the augmentation of temperature induces accretions more humid and dense on the cylinders.

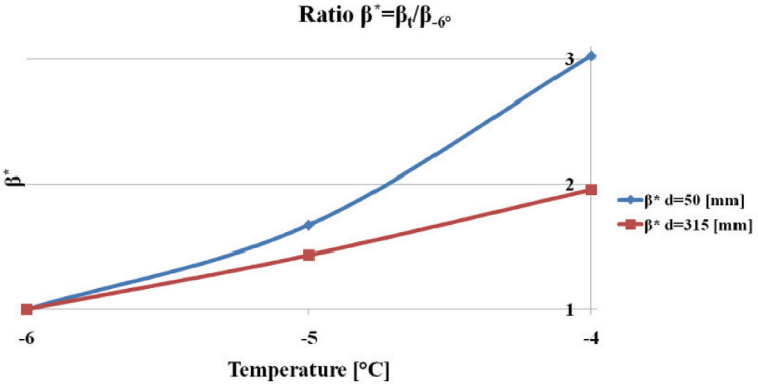

Fig. 27. The β* coefficient as a function of ambient temperature

The comprehension of these parameters, which govern wet snow accretion, leads to the possibility to undertake a numerical study to characterize the different accretions by using a so called "stick-function" for wet snow particles. The study will also aim at producing an experimental database of climatic wind tunnel icing simulations for comparisons with outdoor real-scale phenomena.

The criterion implemented in the numerical modelling of accretion takes into account the angle between the particle path at the impact with the surface and the normal to the surface, i.e. if this angle α_{imp} is lower than a threshold angle α_t the particle sticks to the surface. The approach has simulated accretion shapes showing fair similarities with the experimental. However, it fails to predict accretion on the upper and lower part of the cylinder. This might lead to a more comprehensive model to take into account the particle energy, the liquid water ratio and the angle of impact that have been identified as the crucial aspects involved in the wet snow accretion process.

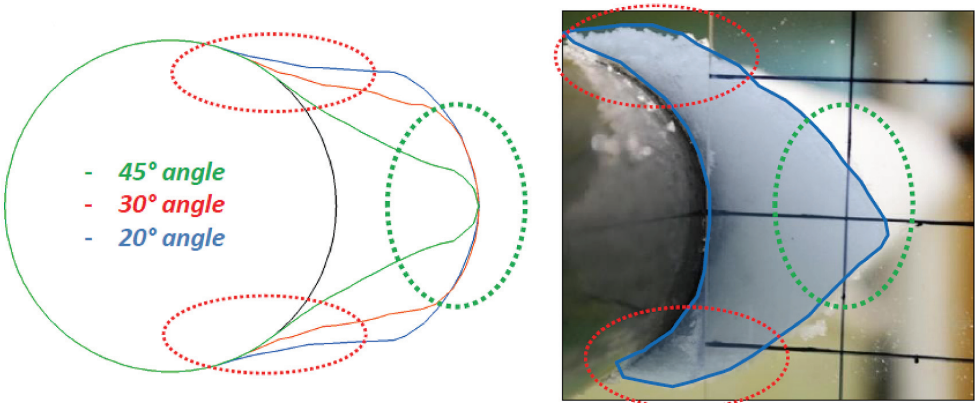

Fig. 28. Comparison of accretion shapes obtained by numerical modelling with experimental results, analysis of the upper and lower part of a cylinder d_{cyl} = 50 mm: (a) numerical simulation α_t = 20°, 30° and 45° (b) experimental result

5. Discussion and perspectives

To reduce the risks induced by associated wind and snow events, proper design of structures and systems that takes into account the actual climatic conditions is a priority.

Due to the diversity of situations, i.e. snow ingress or accretion and accumulation in buildings and vehicles, there is no single approach to investigating these situations and assessing solutions to alleviate the risks. But in all cases the use of experimental facilities that provide controlled ambiances and snow making capacities is valuable.

The climatic wind tunnel provides the controlled ambient environment which allows the influencing variables to be isolated and the causes of a phenomenon to be analysed. Nevertheless, the wind tunnel remains a simulating situation of the natural environment. From

this point of view the use of experimental field tests are useful to validate lab simulations. Although there is a wide range of potentialities in climatic wind tunnels, many conditions remain absent from the material and financial possibilities. In some cases, numerical modelling can supplement the experiments in wind tunnels. A parallel approach, experimental and experimental field tests, seems the most productive way since it enables the pitfalls of each method to be avoided. It seems this should be the favoured method in the future.

Common to all of the examples given in this paper is that no absolute solution has been proposed. The presented results provided the basis of analysis for future developments. The main benefit of the experimental work, and this seems crucial, is the ability to predict the severity of the observed phenomena. This is the essential first step, whatever the corrective action further considered, design improvement, or maintenance action is.

With regard to the ingress of snow in ventilation systems, optimization of air inlets is certainly possible. Similarly, reducing the risk of snow accretion on structures and vehicles may be due to a better design for a de-icing system and shape optimization. But in any case, it is not certain that this eliminates the problem permanently. However, an intervention strategy will result from the a priori assessment of the real risks.

Analytic experimental means to characterize the risk of snow and ice accretion are still missing. This would enable the theoretical and experimental modelling of the phenomena to be developed. Such a modelling seems possible provided one can measure the liquid ratio content of the snow. Early tests achieved with a dedicated probe derived from a measurement device used in aeronautics to assess icing conditions are promising.

This is a derivative of a probe used in air born cloud physics studies. The so called "Nevzorov" probe combines a heated convex and concave shape system. The two-phase flow behaviour around these elements enables the solid and liquid particles to be differentiated. The convex element only receives the liquid fraction of the particles, since the solid part rebound and is carried away by wind, while the concave element captures all the particles. The surface temperature of the probes is kept high to allow complete melting of the particles that impact. The detailed heat balance of the probes makes it possible to deduce the amount of liquid and solid water in suspension in the air flow.

An interesting protecting strategy is provided by icephobic coatings. If these kinds of coating do not yet fully prevent ice and snow deposition, they greatly reduce the adhesion. Hence, the mechanical movements of the iced structure enable the fall of the accretion. Similarly, during the melting phase, the protective coatings enable the icing cover to be reduced more quickly.

The authors acknowledge the European Commission and SNCF for the financial support of studies presented in this paper.

References

[1] Allain E., Paradot N., Ribourg m. Delpech P., Bouchet JP., De la Casa X., Pauline J., *Experimental and numerical study of snow accumulation on high speed trains*. Proc. 49th International Symposium on Applied Aerodynamics, France, Lille 2014.

[2] Asikainen, V., Pasanen, P., *The prevention of snow entrance to the HVAC-system*, Proceedings of Clima 2007 WellBeing Indoors.
[3] Delpech P., Dufresne de Virel M., Tétard Y., *Snow loads testing of smoke vents*, Proc. 7th International Conference on Snow Engineering, Japan, Fukui 2012.
[4] Thiis T., Barfoed P., Delpech P., Gustavsen A., Hofseth V., Uvslokk V., Dufresne de Virel M., *Penetration of snow into roof construction – wind tunnel testing of different eave cover designs*, Journal of Wind Engineering and Industrial Aerodynamics, Vol. 95(9), 2007, 1476–1485.
[5] Thiis T., Delpech P., *Measurements of snow penetration in to ventilation openings in buildings*. Proc. 6th International Conference on Snow Engineering, Canada, Whistler 2008.
[6] Vigano A., *Experimental and Numerical modelling of wet snow accretion on structures*, PhD thesis, France 2012.

TECHNICAL TRANSACTIONS | CZASOPISMO TECHNICZNE
CIVIL ENGINEERING | BUDOWNICTWO
2-B/2015

SVEIN M. FIKKE*, BJØRN EGIL K. NYGAARD**

ASSESSING ENVIRONMENTAL ACTIONS FROM MODERN METEOROLOGY

OCENA ODDZIAŁYWAŃ ŚRODOWISKOWYCH W OPARCIU O NOWOCZESNĄ METEOROLOGIĘ

Abstract

This paper gives an overview of current achievements where modern weather forecasting techniques are implemented for the assessment of especially ice and wind loadings on electrical overhead lines, TV towers, masts and similar infrastructure. Modern numerical weather prediction models (NWP) incorporate far more details on e.g. cloud physics and dynamics than those generally necessary for regular weather forecasts. Such models describe in principle all physical and dynamical processes in the atmosphere in 3-D. In combination with detailed data on the physical properties of land and water surfaces, it is now possible to obtain realistic values of weather parameters related to wind, turbulence, precipitation and atmospheric icing down to a horizontal scale of a few hundred meters. Such models are therefore powerful tools for the planning and final design for various infrastructures in remote terrain where little or no weather data can provide sufficient bases for the establishment of extreme weather loads necessary for their design.

Keywords: *wind engineering, atmospheric icing, wet snow load, environmental actions, numerical weather prediction models*

Streszczenie

W artykule przedstawiono przegląd aktualnych osiągnięć w zakresie szacowania oddziaływań środowiskowych w oparciu o nowoczesne techniki prognozowania pogody. Szczególną uwagę zwrócono na oblodzenie i oddziaływanie wiatru w odniesieniu do napowietrznych linii energetycznych, wież telewizyjnych, masztów telewizyjnych, itp. Nowoczesne modele prognozowania (NWP) wykorzystują dużo więcej szczegółowych danych, np. odnośnie fizyki i dynamiki chmur, niż te, które są zazwyczaj potrzebne do zwykłego prognozowania pogody. Takie modele opisują zasady rządzące wszystkimi fizycznymi i dynamicznymi procesami atmosferycznymi w przestrzeni trójwymiarowej. W połączeniu ze szczegółowymi danymi odnośnie właściwości fizycznych powierzchni lądowych i wodnych, możliwe jest obecnie otrzymanie rzeczywistych wartości parametrów pogodowych związanych z wiatrem, turbulencją, opadami i oblodzeniem w skali poziomej sięgającej kilkuset metrów. Modele te są więc potężnym narzędziem pozwalającym na planowanie i końcowe projektowanie różnych elementów infrastruktury w odległych zakątkach, gdzie jest zbyt mało lub w ogóle brak jest danych pogodowych, niezbędnych do ustalenia ekstremalnych wartości obciążeń, które są potrzebne podczas projektowania.

Słowa kluczowe: *inżynieria wiatrowa, oblodzenie atmosferyczne, obciążenie mokrym śniegiem, oddziaływania środowiskowe, numeryczne modele prognozowania pogody*

DOI: 10.4467/2353737XCT.15.146.4183

* Meteorological consultant, Lørenskog, Norway.
** Kjeller Vindteknikk, Kjeller, Norway.

1. Introduction

To meet the constantly increasing demands from developing societies, as well as from industrialised countries, for the supply of electric power and telecommunication, the necessary infrastructure is more and more often forced to expand into new land and mountain areas. In such locations there is typically limited or no knowledge about the frequency or magnitude of adverse weather phenomena that need to be considered in the design of the new overhead lines or telecom towers. Likewise, in order to assess the operational reliability, as well as in the contingency planning, it is necessary also to consider the operational regularity and alternatives for maintenance under extreme weather, and the access conditions and reliability for their maintenance and repair under harsh weather conditions.

Local weather conditions in mountain areas having a complex topography are critical for planning, design and operation of overhead electric power lines, radio and TV towers, ski-lifts and other types of infrastructure in such areas. The evaluation of the design loads attributable to wind and ice, the operating characteristics such as conductor galloping and fatigue experienced by overhead line conductors, or signal reductions for microwave antennas, are dependent on both historical and actual local weather conditions. However, it has been almost impossible, by conventional methods, to obtain the necessary information from regular weather observation station data, with a spatial resolution adequate for the route of a transmission line or for a mountain top with a microwave antenna.

Over the last decades there has been a tremendous development in global weather observations and computer capacities, and so has also the knowledge of the physical and dynamical processes in the atmosphere similarly progressed. These developments have in turn led to significant improvements in the quality and reliability of modern regular weather forecasts in general. Following the same developments, the potential is similarly huge also for point studies of many weather parameters in any type of terrain, with a spatial resolution relevant for the span lengths of a transmission line or a singular tower on a mountain top, independent of the location or earlier measurements of meteorological data.

A particular numerical weather prediction model (NWP) is applied in this article for such type of local weather studies. This model is called the "WRF model" (WRF: Weather Research and Forecasting model), and is developed and maintained by universities mostly in the US. In principle this is a standard weather forecasting model, but instead of the regular coding limitation such models normally require in order to meet the time limitations for delivering the weather forecast in due time for media presentations, the WRF model is allowed to keep all physics, equations and expressions "undisturbed" and only deliver its output when all necessary calculations are done. In this case the WRF model is practical for special studies and research of particular weather phenomena.

As input to the WRF model is used 6-hourly gridded weather data for the whole atmosphere, available from a few regional weather data bases in the world. This weather data base contains assimilated and interpolated sets of all relevant weather parameters from regular weather stations, automatic stations, ocean buoys, weather radars, satellites, etc., and gives therefore a complete 3-D description of the state of the lower atmosphere (troposphere) globally at 6 hours intervals (Fig. 1). Combined with high resolution data for the characteristics of the surface of the Earth, such data therefore give a more comprehensive description of the weather at one location than a standard set of data from a regular weather station could provide.

The first approach along these lines was presented in [2]. Later, this method was implemented in order to study rime icing conditions for a Norwegian transmission line project in [5, 6] (Fig. 2). During the European COST collaboration under COST Action 727 "Atmospheric icing of structures" the method was successfully tested and applied on several locations in Europe, including in the Alps [7].

In addition to in-cloud icing (rime ice) electrical overhead lines are also exposed to accretions of wet snow. The accretion model for wet snow is also improved and tested on numerous field cases.

As a result of these developments it is now possible to perform case studies of historical severe weather events and study both rime icing and wet snow conditions along remote transmission line routes. Furthermore, it became possible to create new maps of ice loadings for design purposes for Great Britain and Ireland with grid size 500 m x 500 m.

It is also now proposed to combine the interests of CENELEC and CEN to develop homogeneous and coherent icing maps for Europe by using this technology to accomplish the needs for both the electric overhead line industry and the tower and mast sector.

This paper deals mainly with atmospheric icing. However, modern NWPs can be applied similarly for any other weather parameter emerging from these models, like for instance temperature, wind speed, wind direction, wind turbulence, precipitation, snow depth, snow drift, etc. as long as a good topographic model with appropriate resolution is available.

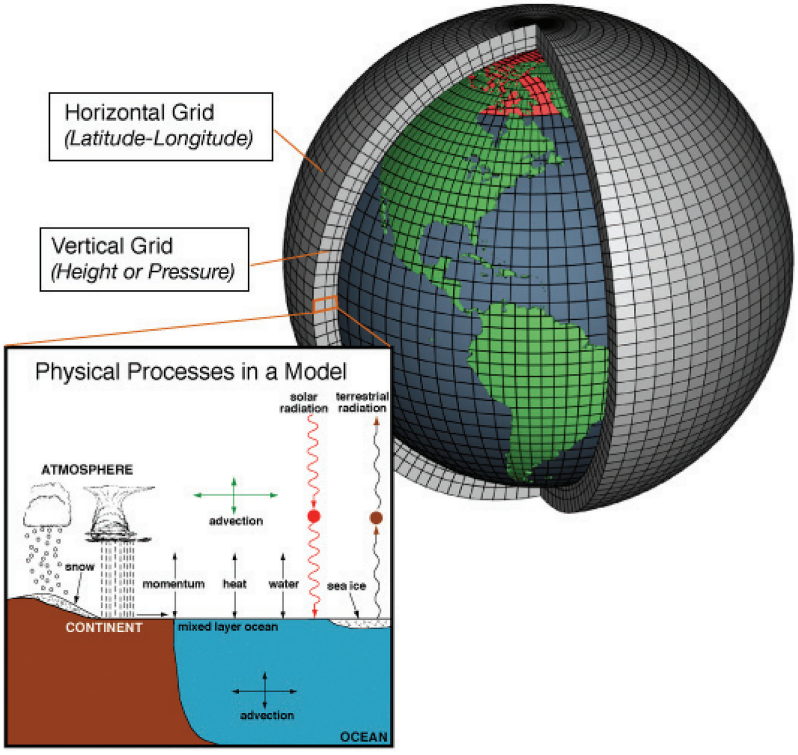

Fig. 1. Illustration of a global NWP modelling system

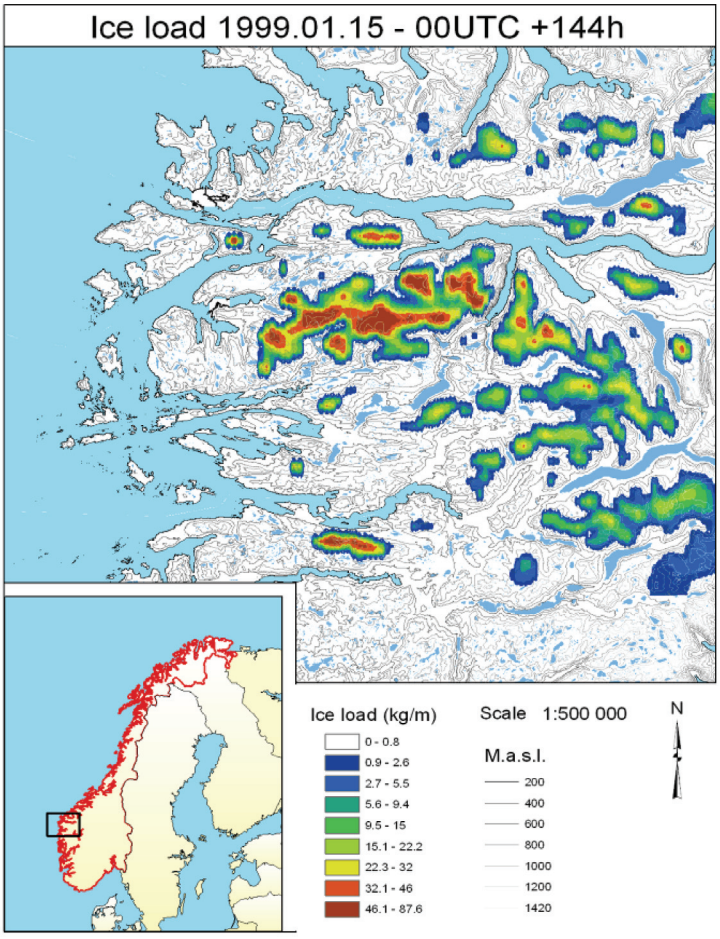

Fig. 2. Example of a local icing map produced from WRF model simulations (from [6]).

2. The WRF model

The Weather Research and Forecast (WRF) model is a state-of-the-art meso-scale (10 – 10 000 km horizontal resolution) numerical weather prediction system, used both in operational forecasting and in atmospheric research (http://www.wrfmodel.org/ and http://www.wrfuserspage.com). WRF solves coupled equations for all important physical processes (such as winds, temperatures, stability, clouds, radiation etc.) in the atmosphere based on both initial fields and lateral boundary values derived from global analysis data. Historic model runs can be initiated with three dimensional analysis of the state of the atmosphere obtained from the ECMWF (European Centre for Medium-range Weather Forecasting) data archive which goes several decades back.

Because atmospheric icing often occurs as a very local phenomenon, and icing intensity is varying greatly in space, especially in complex terrain, it is necessary to run the model at high horizontal resolution to produce useful icing maps. In order to obtain a good representation of the local terrain in the model, data sets at about 90 m horizontal resolution can be implemented.

The model is set up with nested domains, which means that the model goes stepwise from the global scale to local scale with a grid resolution in the range of 0.4 – 0.8 km in the finest resolution domain. This resolution is considered as extremely high for meso-scale models.

A second important factor for simulation of atmospheric icing is how the model computes or parameterises the cloud microphysics. A variety of so-called cloud microphysics parameterization schemes are available in current NWP models. There is however one particular scheme [10] which is considered to provide the best representation of the physical transformations of all water phases in clouds and precipitation, important for prediction of atmospheric icing, also at ground level [4, 8].

The icing simulations are carried out in a two step manner:

1. Meteorological data is produced at high spatial and temporal resolution using the WRF model. In addition to standard variables like wind speed, temperature and humidity, the WRF model also output data like mass concentration of supercooled cloud water, and also an estimate of the median volume cloud droplet size.
2. The data from WRF is processed through a time dependant accretion model for rime icing or wet snow, calculated using the standard ISO specification [6].

Accumulated ice load is calculated in all grid cells in the model domain, serving the basis for an icing map, which can also be used as an overlay in Google-Earth. The output files also contain information on predicted precipitation, wet snow and maximum wind speed. Meteograms showing the time evolution of icing together with weather parameters can be extracted from these files, as well as vertical profiles of the same parameters.

3. Application examples

This method has up to now been applied on several transmission line projects in Norway, Greenland, Chile, Newfoundland and the UK. In all these cases new overhead lines were planned in remote areas where very little or absolutely no relevant weather data was available, especially for the parts of these lines going through high level mountain terrain with varying exposure.

The first application of this approach was applied for a proposed route for a new 420 kV overhead transmission line in the western part of Norway, where a section of the line would be exposed to air coming directly in from the North Sea at an altitude of 1,100 m above mean sea level. Here the risk of extreme icing was expected to be very high. The model set-up included a control with 10 years of field measurements from a test site located roughly 150 km SSE of the line route, as well as with local measurements during one winter.

The calculated ice loads on a theoretical vertical cylinder of 30 mm in diameter resulted in a maximum ice load close to 50 kg/m for the test period of 10 years. The accumulated ice loads over the area for this particular extreme case is shown in Fig. 2. It is anticipated that the vertical cylinder represents a conservative assessment of the ice load on a horizontal conductor of the same size.

In December 1990 there was a major storm in England with significant amounts of wet snow in the Pennines (Fig. 3). Approximately 250 000 customers lost power from the failure of about 700 HV overhead line circuits and many low voltage networks in the area of one Distribution Network Operator (DNO). A WRF study of this event showed that the equivalent radial ice thickness (Req) could be about 30 mm. According to reports from the DNOs these results compared very well with their own observations and experiences from the event, in particular in terms of the areas mostly affected by this blizzard.

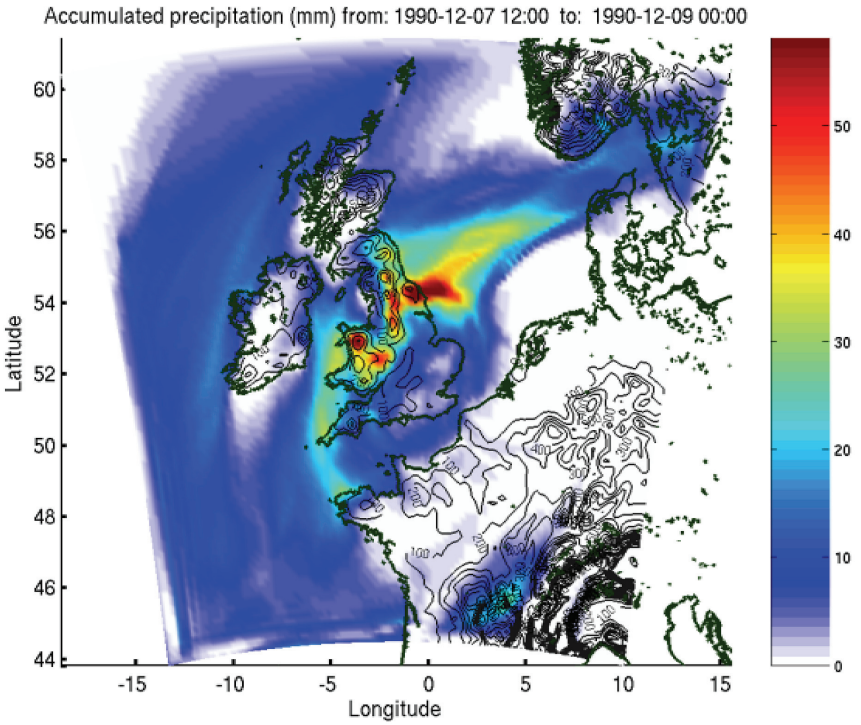

Fig. 3. Simulated accumulated surface precipitation for the 1990 wet snow event in the English Midlands

Another example from the British Isles is shown in Figure 4. Severe rime icing was observed on the EA Technology test site at Deadwater Fell (580 m amsl, near the English-Scottish border) during the period 11-14 January 2010. This icing case was tested with the WRF model and the model was also extended to cover the British Isles. The model confirmed rime ice loads in excess of 3 kg/m compared with measured loads of 3,5 kg/m at the Deadwater Fell site in this period. This confirms the successful prediction of rime icing levels that occurred over all high areas across the British Isles The highest loads in mountains being recorded in Scotland, Northern Pennines, Wales and Ireland. It was later confirmed by the Eire Supply Board (ESB) that severe outages and failures in distribution networks occurred as well in the Wicklow hills in the Eastern parts of Ireland during this event.

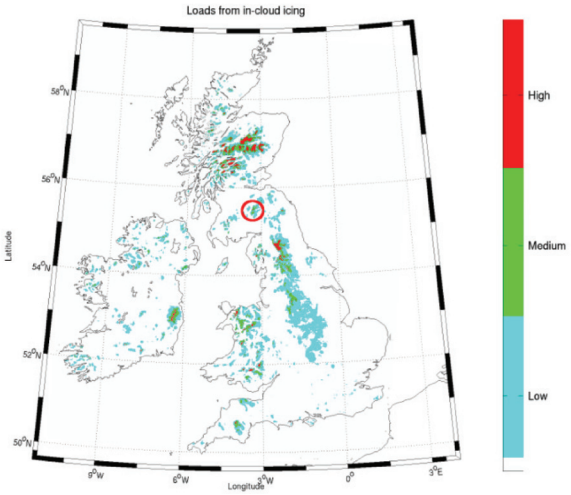

Fig. 4. Simulated rime icing during the period 11-14 January 2010. Based on WRF simulation with at horizontal grid spacing of 1.5 km

The output from the WRF model can also be embedded into Google Earth files, as shown in Figure 5. This provides a very useful tool for visualization, and makes it possible to move in and out of the landscape and see the local terrain in combination with the 3-D ice load outputs from any viewpoint of interest in each case. The value of this enhanced application was used in the assessment of ice loads for an exposed 420 kV line in the western Norway. The line suffered severe damage due to high rime ice loads accumulating during December 2013. The simulated ice loads corresponded very well with the measurements and the experiences collected at the site. The method is currently being applied to assess the local icing conditions for all new transmission line projects in Norway.

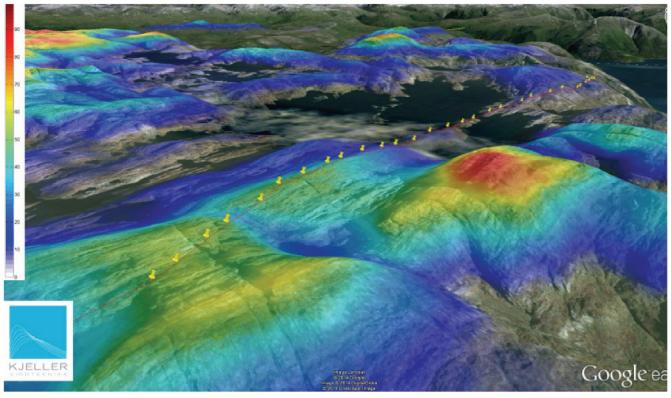

Fig. 5. Simulated rime ice loads in the terrain surrounding a 420 kV line in Norway. Based on a WRF simulation with 500 m x 500 m resolution

The WRF model based approach was also used to assess the icing conditions for a new HVDC line crossing the Long Range Mountains in Newfoundland, Canada. The planned line is crossing the mountain range at altitudes of about 600 m amsl, where again very little data are available on adequate weather conditions and potential ice loadings. This project is also supported by field measurements of temperature, wind speed, wind direction and accumulated ice load on 80 m long test spans. So far these measurements confirm the model output of the same parameters reasonably well.

The WRF model output includes values for identical parameters not only for the lowest layer closest to the earth surface, or in the range of 25–30 m above ground (depending of the grid size and inherent smoothing of the terrain), but also for higher levels. Figure 6 shows an example from the Long Range Mountains where the ice loads are calculated for the three lowest model levels (25 m, 90 m and 175 m above model ground, respectively) for five locations along the proposed line route and for three different case studies.

Case 1 gave the highest ice loadings relevant for the conductor levels above ground for all the five selected locations, especially locations 4 and 5. In this case the prevailing wind was easterly, and it is seen that the ice loads increase significantly at higher levels above ground, and most dramatically for locations 1, 2 and 3. This is because the selected line route in this case is reasonably well sheltered for this wind direction for all locations, but at locations 1-3 this shelter is very shallow. For locations 4 and 5 the ice loads increase by a factor of two from 25 m to 90 m, but no further increase to higher altitudes.

This event emphasizes then the importance and limitation of such a shelter. For the further planning of the line any displacement of the route into slightly higher altitude areas, or areas where there are some openings of the terrain towards the eastern sector, should for this reason be carefully avoided. Another point to make is that a double circuit line in vertical configuration, where the upper phase conductors and earth wires may reach more than 50 m above ground, may be at significantly higher risk concerning ice loads and high winds than a double circuit with a horizontal configuration.

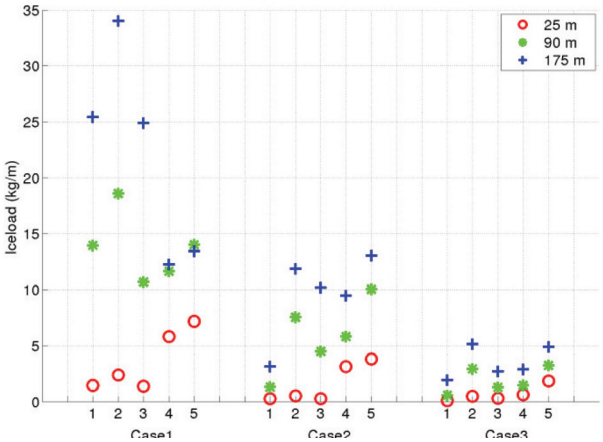

Fig. 6. Simulated ice loads at five locations along the transmission line route. At each location the icing is calculated at three height levels for three different icing cases. Based on WRF simulations with 400 m x 400 m resolution, covering central parts of Long Range Mountains, Newfoundland

Although less pronounced, similar effects can be seen in Case 2 when westerly winds prevailed during the ice accretion. Here there is also an increment in ice loads from 90 m to 175 m at locations 4 and 5, but very light icing above location 1. Case 3 had the lowest ice loads of all three cases, and the height increments are very small. In this case the icing was connected to northerly to north-easterly winds.

Similar output is certainly also applicable to tall tower and masts in mountain terrain.

4. Icing map for Great Britain

Following the promising results of the WRF modelling system, UK utilities decided to initiate a project on revising the wind and ice loading maps for Great Britain [9]. In this project the processes of wet snow and rime icing were studied separately and combined into one icing map for Great Britain as shown in Fig. 7. The wet snow analyses were made from precipitation data from British weather stations, and smoothed out by regression analyses. The rime ice part was analysed by a WRF model.

Fig. 7. High resolution ice load map showing 50 years return values for the Great Britain

A similar map is also produced for Ireland and Northern Ireland.

The underlying data base for these maps for the British Isles are provided in a horizontal grid squares where each grid is 500 m x 500 m, and the maps will be introduced in the next revision of EN 50341-1 as National Normative Annexes (NNA) for the mechanical design of electrical overhead line systems in these countries.

A similar approach has recently been studied also for wet snow load assessments for overhead line design in France [1].

The models used to establish Figure 7 are validated with various wet snow and rime ice data from Iceland, Norway and UK. The wet snow model is also qualitatively checked against reports and experiences from UK utilities, such as the one presented in Figure 3. See also (Nygaard et al., 2014).

5. Proposal for an icing map for Europe

The ISO Standard 12494 "Atmospheric Icing" has been widely used internationally for design purposes of especially antenna towers and masts since its first publication in 2000. CEN TC 250/SC1 has decided to transform this standard as a new part of the series of Eurocodes on Actions (EN 1991), and established a new WG (CEN/TC250/SC1/WG2 "Atmospheric Icing) for this task. The member countries of WG2 have clearly expressed the need for a European icing map in order to take full benefit of this new Eurocode. However, it has also been emphasized very clearly that such icing data will have much in common with the needs for similar information from the electric overhead line industry, represented by CENELEC.

Based on this understanding, CEN/TC250/SC1/WG2 sent in August 2014 a letter to CENELEC TC11 "Overhead lines", and inviting CENELEC to discuss a common icing map for Europe applicable for both industries. How such maps should be produced and financed are not yet neither discussed nor decided.

The letter from CEN certainly acknowledges the existence of such icing maps in many European countries, like for instance Czech Republic, Germany, France, as well as Great Britain and Ireland (see above). However, it is also realised that many of these maps are developed on various sets of data and methods. Hence maps from two neighbouring countries do not necessarily match along the common border.

Mostly, these maps are also developed on the basis of the needs for either the building industry or the electric overhead line industry, and therefore one map for one purpose is not necessarily applicable for the other.

However, the letter from CEN indeed also recognizes the aggregated knowledge and expertise on local icing conditions within all those countries that have already developed such maps. If the proposal for developing a new and comprehensive icing map for Europe should be accepted, it is extremely important that all countries involved contributes with their own experiences and knowledge from their earlier work in a possible all-European collaboration in this field.

It shall also be emphasized that an icing map like the one developed for Great Britain (Fig. 7), where the underlying icing data are given in a 500 m x 500 m grid, also opens for other

meteorological information, such as extremes for wind speeds, temperature, precipitation, snow depths and combined ice and wind actions, as well as directional frequency distribution of wind speeds, turbulence parameters, or other information relevant for the industry, in a GIS format.

References

[1] Ducloux H., Nygaard, B.E.K., *50-year return-period wet-snow load estimation based on weather station data for overhead line design in France*, Natural Hazards and Earth System Science, Vol. 14, 2014, 3031-3041.

[2] Fikke S.M., *Modern meteorology and atmospheric icing*, Proc. IWAIS XI, Montreal, June 2005.

[3] International Standard Organization, 2000: ISO 12494 "Atmospheric Icing", ISO 2000.

[4] Liu C., Ikeda K., Thompson G., Rasmussen R., Dudhia J., *High-resolution simulations of wintertime precipitation in the Colorado headwaters region: sensitivity to physics parameterizations*, Monthly Weather Review, Vol. 139, 2011, 3533-3553.

[5] Nygaard B.E.K., Kristjánsson J.E., Berge E., Makkonen L., *Using NWP models to simulate in-cloud atmospheric icing episodes*, Proc. IWAIS XII, Yokohama, October 2007.

[6] Nygaard B.E.K., Fikke S.M., Elvertrø L., Harstveit K., *Modeling icing in exposed mountain terrain*, Proc. IWAIS XII, Yokohama, October 2007.

[7] Nygaard B.E.K, *Evaluation of icing simulations for the COST 727 icing test sites in Europe*, Proc. IWAIS XIII, Andermatt, Switzerland, September 2009.

[8] Nygaard B.E.K., Kristjánsson J.E., Makkonen L., *Prediction of in-cloud icing conditions at ground level using the WRF model*, Journal of Applied Meteorology and Climatology, Vol. 50, No. 12, 2011, 2445-2459.

[9] Nygaard B.E.K., Seierstad I. A., Veal A.T., A *new snow and ice load map for mechanical design of power lines in Great Britain*, Cold Regions Science and Technology, Vol. 108, 2014, 28-35.

[10] Thompson G., Field P.R., Rasmussen R.M., Hall W.D., *Explicit forecasts of winter precipitation using an improved bulk microphysics scheme. Part II: Implementation of a new snow parameterization*, Monthly Weather Review, Vol. 136(12), 2008, 5095-5115.

TECHNICAL TRANSACTIONS | CZASOPISMO TECHNICZNE
CIVIL ENGINEERING | BUDOWNICTWO
2-B/2015

PIOTR GÓRSKI*, MARCIN TATARA*, STANISLAV POSPIŠIL**,
SERGEJ KUZNETSOV**, ANTE MARUŠIĆ***

INVESTIGATIONS OF STROUHAL NUMBERS OF ICED CABLE MODELS OF CABLE-SUPPORTED BRIDGES WITH RESPECT TO ANGLE OF WIND ATTACK

BADANIA LICZB STROUHALA MODELI OBLODZONYCH CIĘGIEN MOSTÓW PODWIESZONYCH Z UWZGLĘDNIENIEM KĄTA NATARCIA WIATRU

Abstract

The influence of the ice accretion, angle of attack and *Reynolds* number on the flow field around iced cables of cable-supported bridges is not clearly understood. The Strouhal number is one of the most important parameters which is necessary for an analysis of the vortex excitation response of slender structures. This paper presents the method and results of wind tunnel investigations of the Strouhal number of stationary iced cable models of cable-supported bridges. The investigations were conducted in a climatic wind tunnel laboratory of the Czech Academy of Sciences in Telč. The methodology leading to the experimental icing of the inclined cable model in the climatic section of the laboratory was prepared. The shape of the ice on the cable was registered by photogrammetry and numerical evaluation. For the aerodynamic investigations, the iced cable model in a smaller scale was reproduced using a 3D printing procedure. The Strouhal number was determined within the range of the Reynolds number between $2.4 \cdot 10^4$ and $16.4 \cdot 10^4$, based on the dominant vortex shedding frequency measured in the flow behind the model. The model was orientated at three principal angles of wind attack for each of the Reynolds number values. In order to recognize the tunnel blockage effect, the Strouhal number of a smooth circular cylinder was tested. Strong agreement with the generally reported value in the subcritical Reynolds number range for a circular cylinder was obtained.

Keywords**:** *bridge cable, ice accretion, Strouhal number, angle of attack, vortex shedding frequency*

Streszczenie

Wpływ oblodzenia, kąta natarcia wiatru i liczby Reynoldsa na zjawisko opływu powietrza wokół oblodzonych cięgien mostów podwieszonych nie został dotychczas dobrze poznany. Liczba Strouhala jest jednym z ważniejszych parametrów, którego znajomość jest niezbędna na etapie analizy odpowiedzi smukłych konstrukcji na wzbudzenie wirowe. W artykule przedstawiono sposób i wyniki badań liczby Strouhala nieruchomych modeli oblodzonych cięgien mostów podwieszonych. Badania wykonano w tunelu aerodynamicznym z komorą klimatyczną Laboratorium Czeskiej Akademii Nauk w Telč. W komorze klimatycznej wykonano doświadczalne oblodzenie modelu cięgna o osi nachylonej pod kątem 30° do płaszczyzny poziomej. Kształt oblodzonej powierzchni zarejestrowano metodą fotogrametrii cyfrowej. Do badań w tunelu aerodynamicznym wykonano nowy model sekcyjny oblodzonego cięgna metodą druku 3D. Liczbę Strouhala wyznaczono w zakresie wartości liczby Reynoldsa od $2{,}4 \cdot 10^4$ do $16{,}4 \cdot 10^4$ na podstawie pomiaru częstości odrywania się wirów w śladzie aerodynamicznym za modelem. Badania wykonano przy trzech podstawowych kierunkach napływającego powietrza. W celu określenia wpływu zjawiska blokowania tunelu na wyniki pomiarów wykonano badanie liczby Strouhala gładkiego walca kołowego. Otrzymane wartości były zgodne z wartościami podanymi w literaturze przedmiotu w zakresie podkrytycznym liczby Reynoldsa.

Słowa kluczowe: cięgno, oblodzenie, liczba Strouhala, kąt natarcia, częstość wzbudzenia wirowego

DOI: 10.4467/2353737XCT.15.147.4184

* Department of Road and Bridges, Opole University of Technology, Poland.
** Institute of Theoretical and Applied Mechanics, Academy of Sciences of the Czech Republic, Czech Republic.
*** Faculty of Mechanical Engineering and Naval Architecture, University of Zagreb, Croatia.

1. Introduction

The excitation mechanism of cables on cable-supported bridges and associated boundary conditions are described in a paper by Flaga and Michałowski [5]. A complete analysis of the dynamic wind response of such structures requires that the along wind response, vortex excitation response and lateral turbulence component response should be evaluated. Such phenomena become more significant especially for cables longer than 100 m. Theoretical background and proposals of the mathematical description of wind excitation components are presented in the respective monographs Flaga [3, 4].

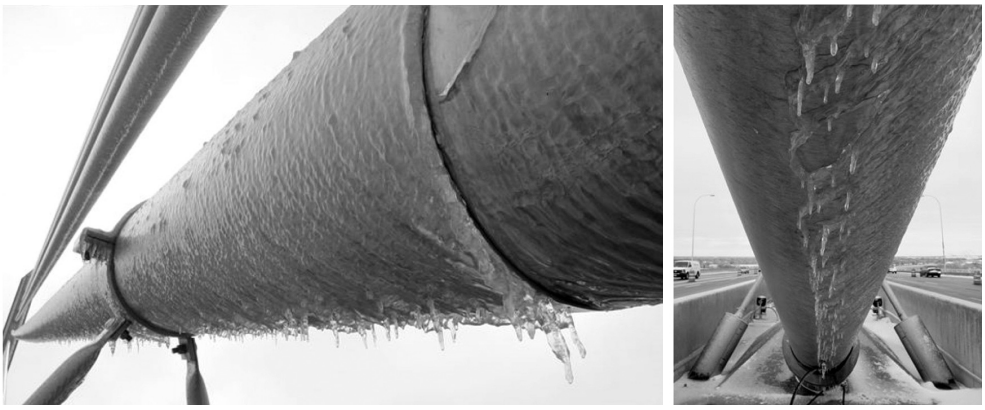

Fig. 1. Example of the iced cable of cable-supported Veteran's Glass City Skyway Bridge in Toledo, Ohio, USA [11]

The change of the cross-section of the cable due to ice accretion (see Fig. 1) has a significant influence on the flow field around the cables and its aerodynamics. In this case, an asymmetric airflow around the cable appears; thus, an asymmetric distribution of wind pressure exists on its surface. For this reason, three aerodynamic coefficients, i.e. drag, lift and moment coefficients, depending on the angle of the wind attack, should be taken into account. Moreover, in such conditions, an aeroelastic instability of the iced cable known as galloping instability may occur if the specific criteria proposed by Den Hartog [9] are met. It is well documented that the amplitude of the galloping of ice accreted cables or transmission lines can be very large [7, 8, 16].

Analysis of the vortex excitation response of the iced cables requires, among other things, knowledge of the Strouhal number – this characterizes the vortex shedding frequency. The value of Strouhal number depends on the icing shape accreted on the cable under specific conditions, structural motion and turbulence intensity, and in some cases, may depend on the Reynolds number determining the flow regimes for structures with a circular cross-section. Knowledge of the Strouhal number is necessary for the determination of critical wind velocity at which the largest amplitudes due to vortex excitation are observed.

Specific papers exist concerning modelling the icing of power lines [13], identification of amplitudes of wind induced vibrations [8] as well as investigations of the Strouhal number of iced electrical power cables [14] in scientific literature. However, because of the relative small outer diameter of electrical power cables (which do not exceeded several centimetres) as well as different shapes of the ice formations, the results are inappropriate for cables of cable-supported bridges due to their larger diameters, usually between 10 and several tenths of centimetres. Investigations of ice shaping and its influence on the aerodynamics of iced circular cylinders with diameters of 7.0 and 8.9 cm were presented in the papers by Gjelstrup et al. [7] and Koss et al. [12]; however, the Strouhal number was not investigated. Extensive studies of ice accretion processes and the final shapes of ice accreted on vertical and inclined cable models (cable diameter – 16.0 cm) were described in a paper by Demartino et al. [1]. In the paper, the aerodynamic force coefficients were also measured and it was found that they were significantly affected by the characteristics of the ice accretion.

This paper presents the method and results of wind tunnel investigations of the Strouhal number of a stationary iced cable model with respect to different angles of wind attack. The experiments were carried out in the climatic wind tunnel laboratory of the Czech Academy of Sciences in Telč (http://cet.arcchip.cz/wind-laboratory-en) using the rain sprinklers simulating the real situation during freezing rain conditions. The methodology leading to the experimental icing of the inclined cable model in the climatic section of the laboratory was prepared. The shape of the ice on the cable was registered by the photogrammetry method with the combination of numerical image analysis. For the aerodynamic investigations, the iced cable model was reproduced to a smaller scale with a 3D printing procedure. The Strouhal number was determined within the range of the Reynolds number between $2.4 \cdot 10^4$ and $16.4 \cdot 10^4$ based on the dominant vortex shedding frequency measured in the flow behind the model. The model was orientated at three principal angles of wind attack for selected values of the Reynolds number. To recognize the tunnel blockage effect, the Strouhal number of a circular smooth cylinder was tested. A good agreement with the generally reported value in the subcritical Reynolds number range for a circular cylinder was obtained.

2. The icing process of the cable model in the climatic section of the wind tunnel

The climatic section of the laboratory is combined as a closed circuit with the aerodynamic section. The climatic section has a rectangular cross-section which is 2.5 m in height, 3.9 m in width and 9.0 m in length. Using the cooling or heating system, the air temperature can be manipulated from -5°C to +30°C in a relatively short time period. In this section, the wind velocity ranges from 0.8 to 18 m/s (depending on the position of the vertically moveable ceiling and flow nozzle). The rain intensity together with the size of drops may be regulated to simulate effects corresponding to drizzle or heavy rain.

The experimental icing of the cable section model using a pipe with a 0.160 m diameter and 2.5 m length was conducted. The cable model was made of polyvinyl chloride (PVC), the outer surface structure of which was similar to the real surface of the cable cover made of high-density polyethylene (HDPE). The cable model was inclined at 30° and fixed to a special frame with the possibility of rotation relative to the airflow (Fig. 2).

Fig. 2. View of the support of the cable model on the special frame placed in the climatic section of the wind tunnel

Different types of ice can occur in different climatic conditions, i.e. with different combinations of temperature, wind velocity, angle of wind attack and droplets of the rain. For the purpose of this research, the most common natural conditions expected for a Central-European climate were selected, causing smooth evenly distributed ice accretion together with frozen rivulets on the cable for light rain, relatively low wind velocity (the droplets are able to attach the cooled cross-section) and a temperature slightly below 0°C. Another reason for this selection was to ensure an appropriate horizontal velocity component of the water droplets. Thus, the boundary conditions during the test were as follow: mean wind velocity 2.8 m/s; air temperature slightly below 0°C; diameter of the sprinkler heads – 2.8 mm. After several preliminary tests, a 40 min cooling exposure time period was selected as sufficient from the point of view of ice creation (no significant changes of ice shape occurred). During the experiment, the model was inclined on a horizontal plane to the airflow direction at an angle of 60°. The angle was found from several preliminary tests as the one at which the ice ribs on the underside of the model were much more distinctive. Before the test, several precooling procedures of the cable model were tested. Finally, the procedure using dry ice placed inside the tube was selected because this proved to be the most effective. In this case, the ice accreted on the cable was classified as a glaze dominant type of ice.

The final ice shape on the cable (see Fig. 3) was compared to Fig. 1 as the reference. The characteristic ice ribs (frozen rivulets on the underside of the model) were created and used for further examination. On the upper part of the model, the ice shape was similar to the circular shape. The cross-section of the cable with ice became strongly nonsymmetrical having dimensions of 0.192 m in height and 0.181 m in width.

It should be noticed that the cooling and icing procedure was carried out on a scale of 1:1; thus, no scaling factors were considered. Surface (roughness, material) effect on the flow around the cable during icing procedure is negligible because of low wind velocity, also, relatively large drops were simulated and the effect of the flow deflection near the surface of the cable on drop trajectory is negligible. The largest effect of the surface was with regard to water run-off – both the real surface and cable model surface behaved very similarly in this regard.

Fig. 3. Final icing effect of the cable model in climatic section (view from the bottom of the model)

3. Preparation of iced cable model for wind tunnel investigations

After the tests in the climatic section, the shape of the iced cable model was registered by a photogrammetry method with the combination of numerical image analysis. This method was realized by taking a series of 35 photographs at a distance of 1.2 m from the model. For taking the photographs, a Nikon D600 camera with a Nikon 50 mm f/1.4 AF-S lens was used for which the angular position was changed by about 9° around the model. The positions of the camera are shown in Fig. 4. In order to achieve the best results during the process of photogrammetry, the surface of the ice was painted white before taking photographs.

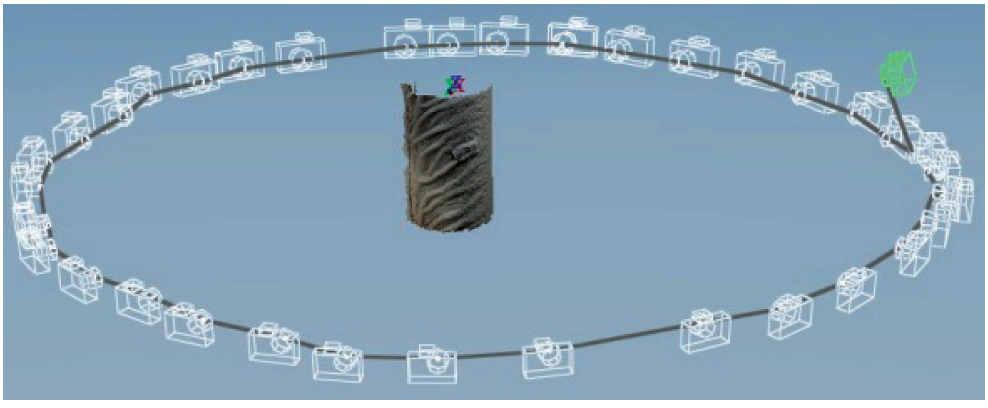

Fig. 4. Positions of the camera during a series of 35 photographs of the iced cable model

Based on the numerical image analysis of all photographs, a three-dimensional numerical model of the iced cable was obtained (Fig. 5a). For the wind tunnel investigations of the Strouhal number, the new iced cable model, shown in Fig. 5b, was made at a scale of 1:1.6 using a 3D printing procedure. The new model 0.43 m long and was constructed from polylactide plastic (PLA) – this is a standard material used for 3D printing. The dimensions of the cross-section of the new iced cable model were 0.120 m high and 0.113 m wide (see Fig. 7).

The roughness of the printed model (due to 3D printer resolution) can be neglected because the roughness caused by the ice shape (on the upper side by frozen drops, on the lower side by ice ridges) is of an order of magnitude bigger and is therefore dominant with respect to the flow characteristics. The 3D printed iced cable model has a rough shape with a surface roughness of 18% in the form of ice rivulets (covering about 150°) and 0.73% as small ice accretion on the rest of the surface of the cable model.

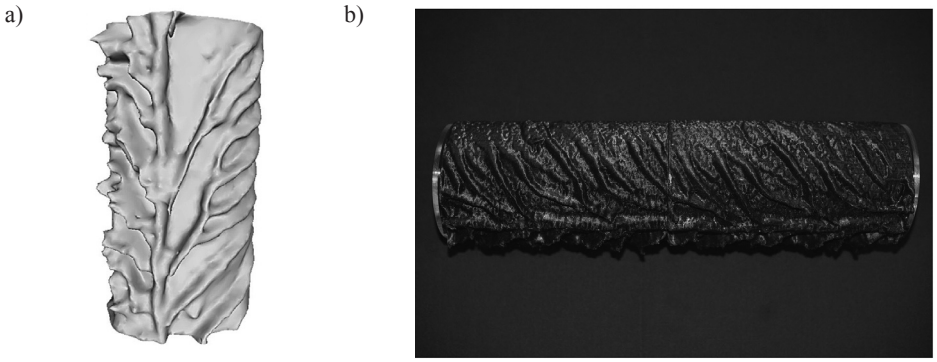

Fig. 5. a) Three-dimensional model of the iced cable; b) iced cable model for wind tunnel investigations made using 3D printing method

4. Strouhal number investigations in aerodynamic section

The Strouhal number investigations were carried out in the aerodynamic section of the wind tunnel. This section has a height of 1.8 m, and a width of 1.9 m. The flow development section is 11.0 m long to assure the appropriate simulation of the atmospheric boundary layer. The wind velocity ranges from 1.5 to 33 m/s.

During the tests, the flow was modelled as laminar with a turbulence intensity in the order of 3 %. The air temperature was in the range 24°C to 28°C. The tests were carried out at twelve sequential free stream velocities in the range 3.4 m/s to 22.9 m/s. This corresponded to the twelve Reynolds number regimes in the interval $Re = 2.4 \cdot 10^4$ to $16.4 \cdot 10^4$.

The cable with the ice model was fixed horizontally at a height of 76 cm above the floor of the aerodynamic section, perpendicular to the airflow within a special frame. Two sides of the frame were equipped with plexi-glass end-plates to ensure a two-dimensional flow around the model. The model connection to the special frame in the aerodynamic section is shown in Fig. 6.

The Strouhal effect was experimentally ascertained and analysed during three test series in which the iced cable model was orientated at three different angles of wind attack for each of the Reynolds number values. The principal model configurations and reference dimension *d* perpendicular to the wind direction are shown in Fig. 7.

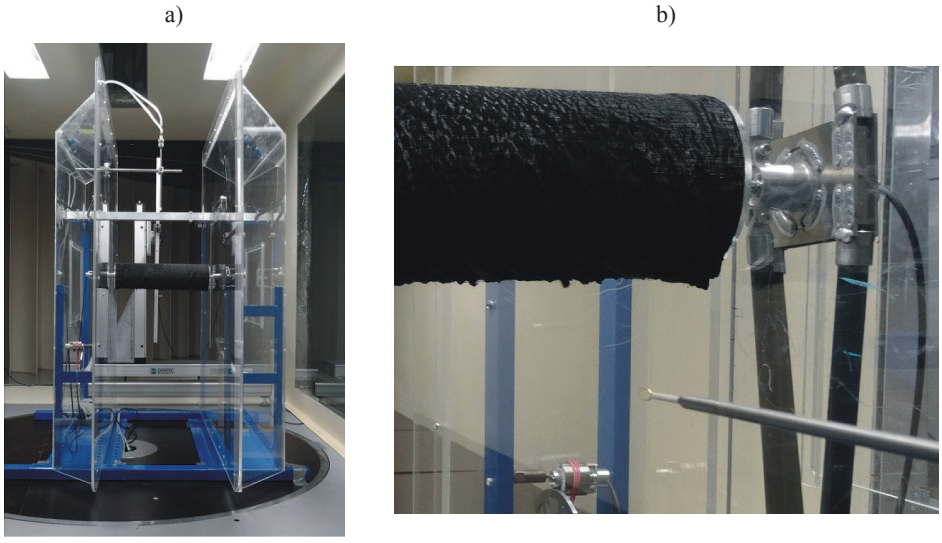

Fig. 6. a) View of the special frame with the iced cable model in aerodynamic section; b) view of the model connection to the frame and the hot-wire anemometer CTA behind the model

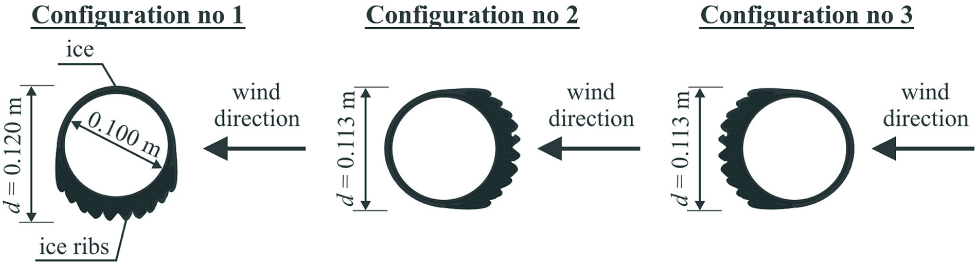

Fig. 7. Model configurations and their reference dimension *d* perpendicular to the wind direction considered for Strouhal number investigations

The Strouhal number was investigated according to the following procedure. At each step during the tests, the free stream velocity *u* in front of the model was measured by the Prandtl's tube. At the same time, the airflow velocity at a distance of about 1.5·*d* to 2.5·*d* (15 to 25 cm) behind the model was also measured by two hot-wire anemometers (CTA) during the 30 s interval with a sampling rate of 1000 Hz. Two CTA were fixed exactly 10 cm above and below the longitudinal axis of the model.

The Strouhal number was determined from the dominant vortex shedding frequency f_s that was evaluated on the basis of the power spectral density (PSD) of the airflow velocity behind the model.

The Strouhal number was calculated from the formula:

$$\mathrm{St} = \frac{f_s \cdot d}{\overline{u}} \tag{1}$$

where f_s is the vortex shedding frequency, d is the reference dimension of the iced model perpendicular to the wind direction (see Fig. 7) and $\overline{u}$ is the mean free stream velocity in front of the model.

The Reynolds number was evaluated according to the formula:

$$\mathrm{Re} = \frac{d \cdot \overline{u}}{\vartheta} \tag{2}$$

where $\vartheta = 1.64 \cdot 10^{-5}$ to $1.67 \cdot 10^{-5}$ m^2/s is the kinematic viscosity of the air.

In the wind tunnel investigations, the possibility of the tunnel blockage effect should be taken into account. In order to recognize if the blockage effect has any influence on the test results, the Strouhal number of the circular smooth cylinder was initially investigated. The diameter of the cylinder was 0.10 m and the mean free stream velocity during the test was $\overline{u}$ = 15.0 m/s. The cylinder model was fixed in the same manner as the iced model (Fig. 8a). Fig. 8b shows the PSD of the airflow velocity behind the circular cylinder model which corresponds to the mean free stream velocity of $\overline{u}$ = 15.0 m/s. The obtained Strouhal number value St = 0.18 equals that proposed in Eurocode [2]. Thus, no detrimental blockage effect of the tunnel was observed.

a)

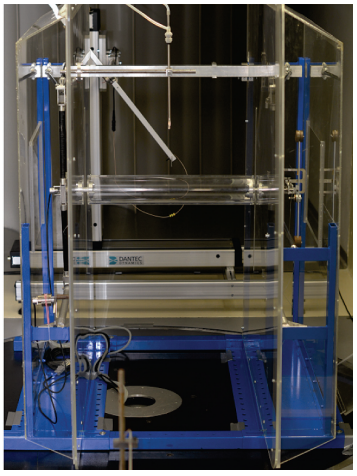

b)

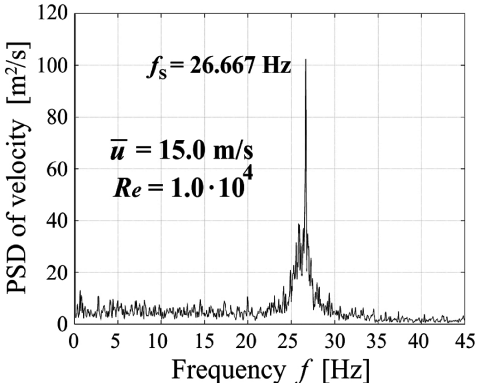

Fig. 8. a) View of the circular smooth cylinder in the special frame; b) the PSD of the airflow velocity behind the cylinder

5. Results of Strouhal number investigations for configuration no. 1

Fig. 9 depicts the selected PSDs of the airflow velocity behind the iced cable model for configuration no 1 (see Fig. 7), measured by CTA below the model at the mean free stream velocity from $\overline{u}$ = 3.5 m/s to $\overline{u}$ = 20.8 m/s. The differences between the dominant vortex shedding frequencies measured above and below the model did not exceed 5% – this is considered to be satisfactory.

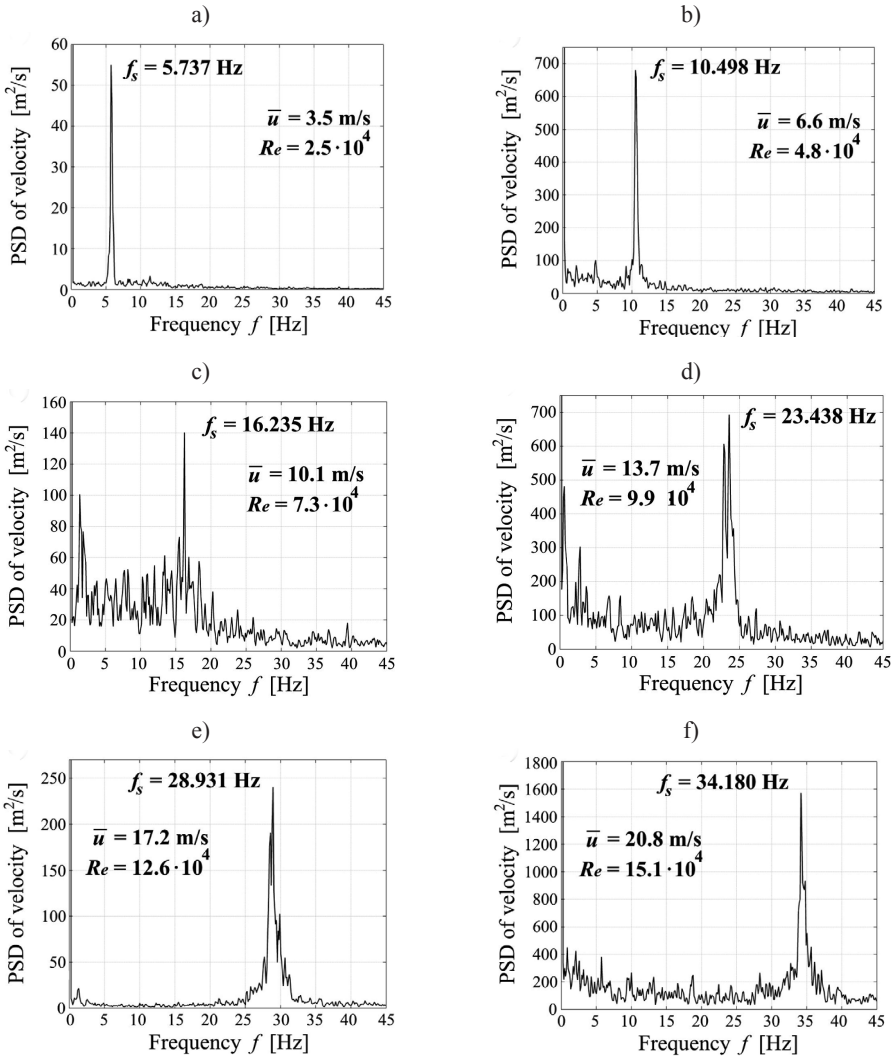

Fig. 9. Selected PSDs of the airflow velocity behind the iced cable model and dominant vortex shedding frequencies f_s for configuration no 1 correspond to the mean free stream velocities: a) $\overline{u}$ = 3.5 m/s, b) $\overline{u}$ = 6.6 m/s, c) $\overline{u}$ = 10.1 m/s, d) $\overline{u}$ = 13.7 m/s, e) $\overline{u}$ = 17.2 m/s, f) $\overline{u}$ = 20.8 m/s

Fig. 10 shows the variation of the vortex shedding frequency f_s with the mean free stream velocity $\overline{u}$. Fig. 11 depicts the variation of the Strouhal number with the Reynolds number values for configuration no. 1.

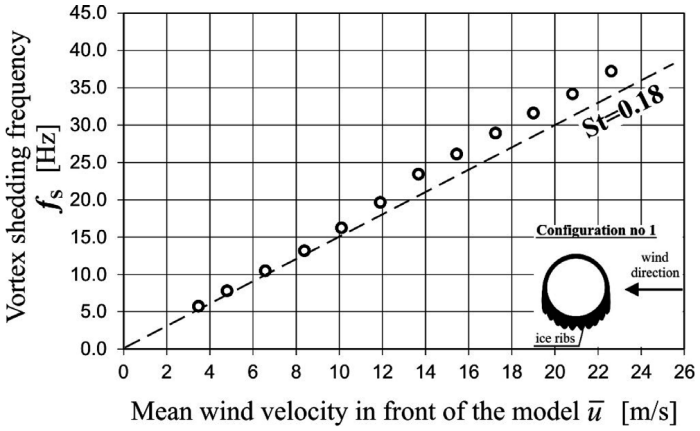

Fig. 10. Variation of the vortex shedding frequency f_s with the mean free stream velocity $\overline{u}$ in front of the model for configuration no. 1 with reference to St = 0.18 (dotted line)

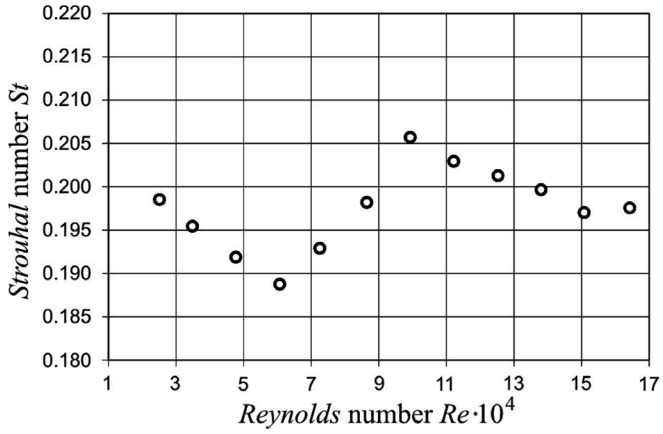

Fig. 11. Variation of the Strouhal number with the Reynolds number for configuration no 1

6. Results of Strouhal number investigations for configuration no. 2

Fig. 12 shows the selected PSDs of the airflow velocity behind the iced cable model for configuration no. 2, measured by CTA below the model at the mean free stream velocity from $\overline{u}$ = 3.4 m/s to $\overline{u}$ = 20.9 m/s. As in the previous case, the differences between the dominant

vortex shedding frequencies obtained from the measurements using CTA located above and below the model did not exceed 5%.

Fig. 13 shows the variation of the vortex shedding frequency f_s with the mean free stream velocity $\overline{u}$. Fig. 14 depicts the variation of the Strouhal number with the Reynolds number values for configuration no. 2.

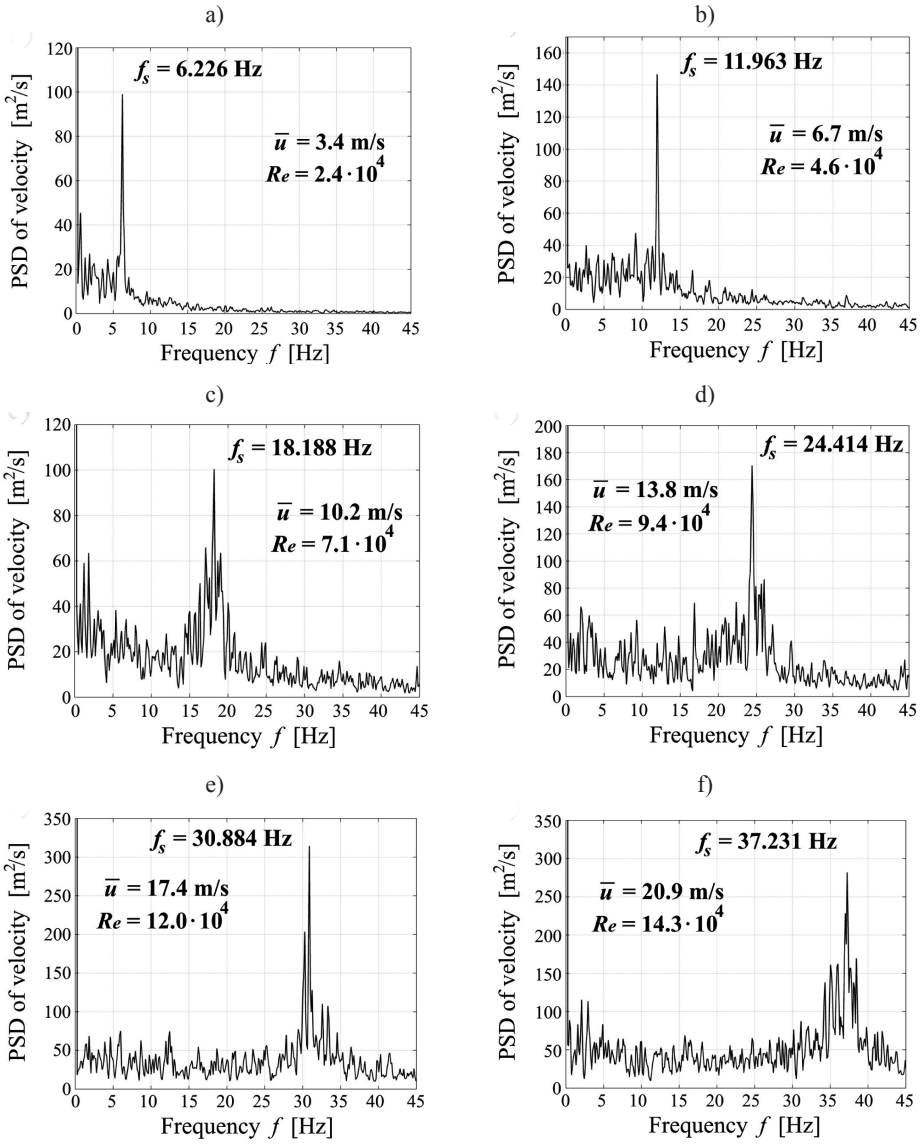

Fig. 12. Selected PSDs of the airflow velocity behind the iced cable model and dominant vortex shedding frequencies f_s for configuration no. 2 correspond to the mean free stream velocities: a) $\overline{u}$ = 3.4 m/s, b) $\overline{u}$ = 6.7 m/s, c) $\overline{u}$ = 10.2 m/s, d) $\overline{u}$ = 13.8 m/s, e) $\overline{u}$ = 17.4 m/s, f) $\overline{u}$ = 20.9 m/s

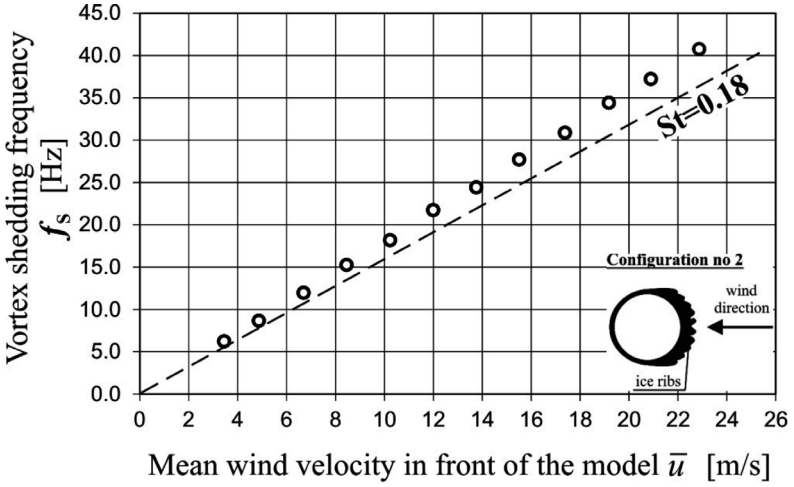

Fig. 13. Variation of the vortex shedding frequency f_s with the mean free stream velocity $\overline{u}$ in front of the model for configuration no. 2 with reference to St = 0.18 (dotted line)

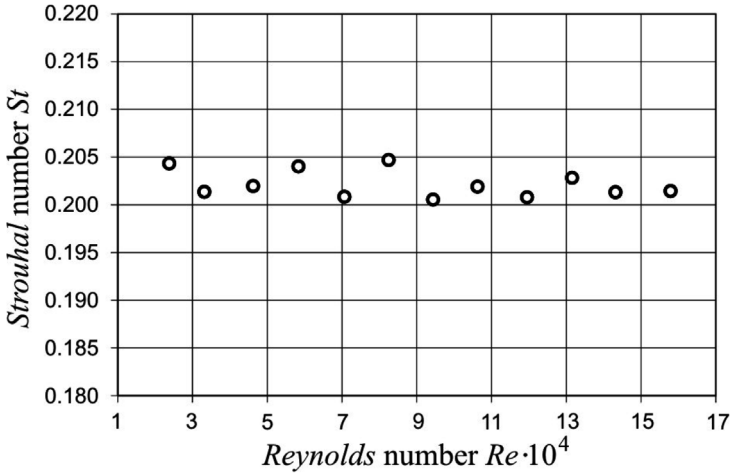

Fig. 14. Variation of the Strouhal number with the Reynolds number for configuration no. 2

7. Results of Strouhal number investigations for configuration no. 3

Fig. 15 shows the selected PSDs of the airflow velocity behind the iced cable model for configuration no 3 at the mean free stream velocity from $\overline{u}$ = 3.5 m/s to $\overline{u}$ = 21.0 m/s. The differences between the dominant vortex shedding frequencies obtained from the measurements using CTA located above and below the cylinder did not exceed 6%.

Fig. 16 shows the variation of the vortex shedding frequency f_s with the mean free stream velocity $\overline{u}$. Fig. 17 depicts the variation of the Strouhal number with the Reynolds number values for configuration no. 3.

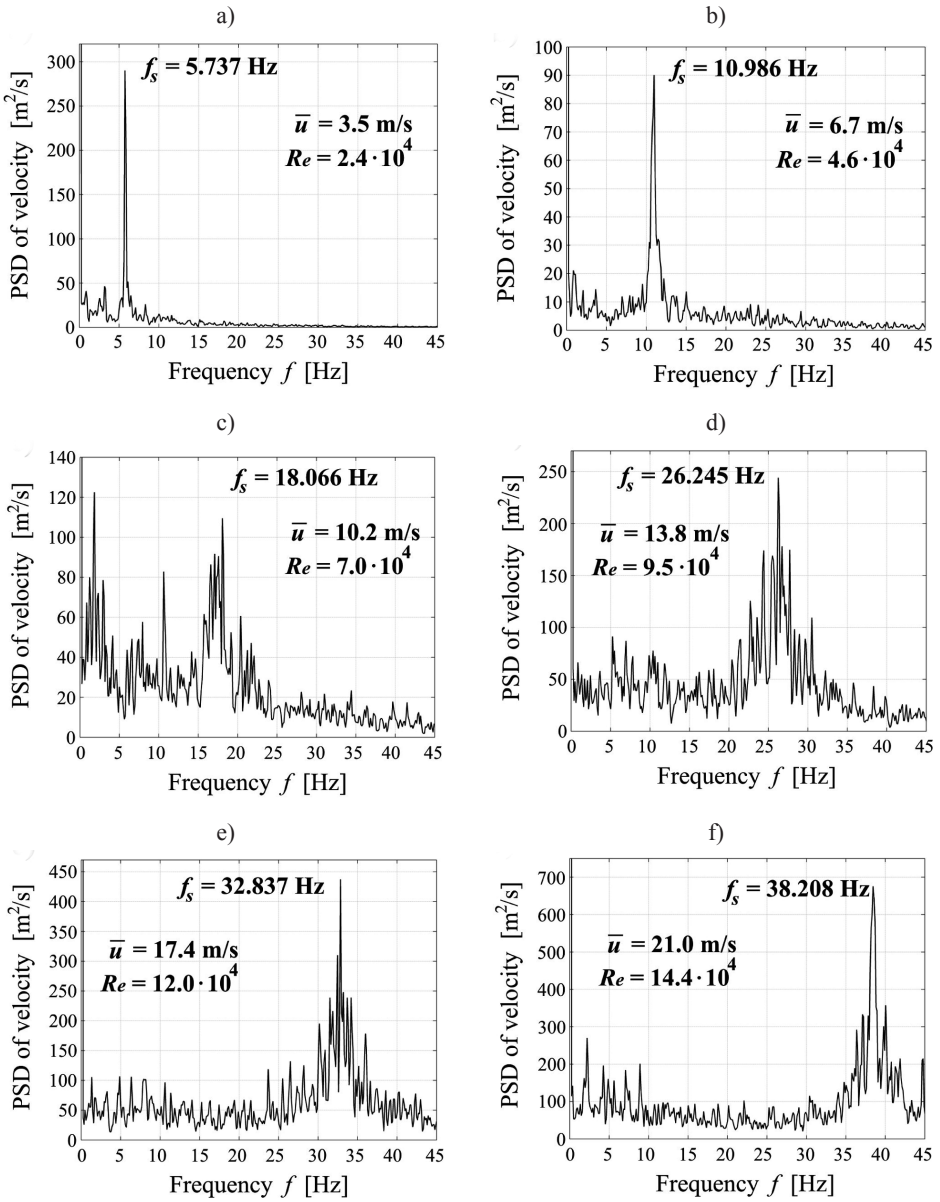

Fig. 15. Selected PSDs of the airflow velocity behind the iced cable model and dominant vortex shedding frequencies f_s for configuration no. 3 correspond to the mean free stream velocities: a) $\overline{u}$ = 3.5 m/s, b) $\overline{u}$ = 6.7 m/s, c) $\overline{u}$ = 10.2 m/s, d) $\overline{u}$ = 13.8 m/s, e) $\overline{u}$ = 17.4 m/s, f) $\overline{u}$ = 21.0 m/s

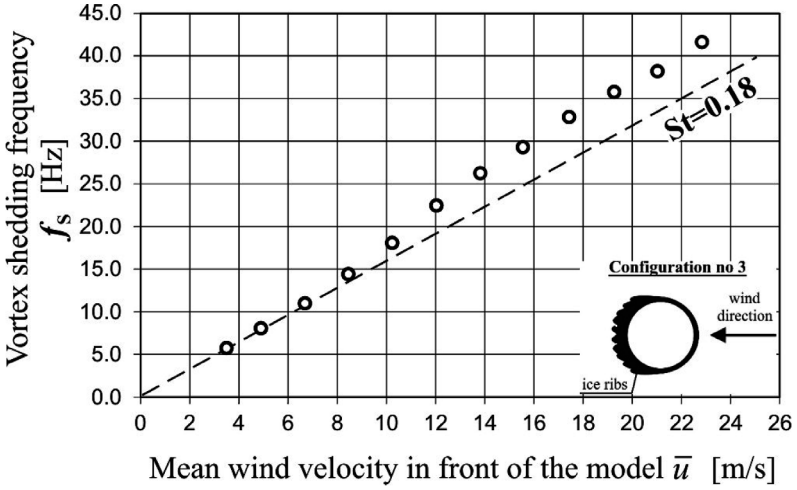

Fig. 16. Variation of the vortex shedding frequency f_s with the mean free stream velocity $\overline{u}$ in front of the model for configuration no 3 with reference to St = 0.18 (dotted line)

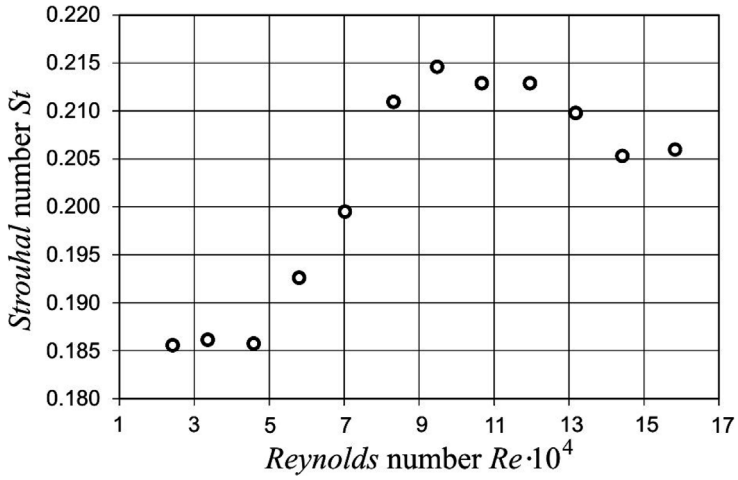

Fig. 17. Variation of the Strouhal number with the Reynolds number for configuration no. 3

8. Conclusions

The experimental creation of the ice on the inclined cable model of cable-supported bridges was carried out in the climatic chamber of the wind tunnel of CET ITAM. The Strouhal number was investigated for the stationary iced cable model with respect to three principal angles of wind attack within the range of the Reynolds number between $2.4 \cdot 10^4$ and $16.4 \cdot 10^4$.

The ice accretion process produced the asymmetrical and irregular iced cross-section of the cable model with rounded edges of ice ribs accreted on the underside of the model (with maximal surface roughness of 18%) and with the quasi-circular shape on its upper part (with minimal surface roughness of 0.73%).

The Strouhal number determined for configuration no. 1 depends on *Re* (Fig. 11). Initially, in the range of $Re = 2.5 \cdot 10^4 – 6.1 \cdot 10^4$, *St* values linear decrease from St = 0.199 to 0.189. In the range of $Re = 6.1 \cdot 10^4 – 9.9 \cdot 10^4$, *St* suddenly increased to St = 0.206 and for $Re > 9.9 \cdot 10^4$, St again decrease to St = 0.198.

The Strouhal number determined for configuration no 2 is changing in the range of St = 0.201 – 0.205 and seems to be independent of *Re* in the range that was studied (Fig. 14). All obtained *St* values are 12% to 14% higher than St = 0.18. The variability of the St values for configuration no. 2 can be incidental and caused by the randomness of the vortex excitation.

The Strouhal number determined for configuration no 3 strictly depends on Re (Fig. 17). St values were initially in the range of St = 0.186 – 0.187 for $Re = 2.4 \cdot 10^4 – 4.6 \cdot 10^4$. In the range of $Re = 4.6 \cdot 10^4 – 9.5 \cdot 10^4$, *St* suddenly increased to a maximum value St = 0.215. In the range of $Re = 9.5 \cdot 10^4 – 15.8 \cdot 10^4$, *St* is in the range of St = 0.205 – 0.215.

It is well known that in the case of the smooth circular cylinder, the studied Reynolds number range is in the subcritical range and the Strouhal number is approximately 0.18. However, previous wind tunnel studies (Zdravkovich, 1997) show that increased surface roughness of the cylinder induces transition to critical and transcritical range at lower Reynolds numbers. Thus, the change effect of the direction of wind acting on the iced cable model on variation of the Strouhal number with the Reynolds number corresponds to experimental data (Zdravkovich, 1997) obtained at different degrees of surface roughness of the cylinder.

This work was created with support from project no. LO1219 under the Ministry of Education, Youth and Sports National sustainability programme 1, and partially with the support from project No. FR-TI3/654 under the Ministry of Industry and Trade. Marcin Tatara is a scholar of a project 'PhD Scholarships - investment in the scientific staff Opole Voivodeship II' co-funded by the European Union within the European Social Fund.

References

[1] Demartino C., Koss H.H., Georgakis C.T., Ricciardelli F., *Effects of ice accretion on the aerodynamics of bridge cables*. Journal of Wind Engineering and Industrial Aerodynamics, Vol. 138, 2015, 98-119.

[2] Eurocode 1, Action on structures – part 1-4: General action – Wind action, 2009.

[3] Flaga A., *Inżynieria wiatrowa*. Arkady, Warszawa 2008.

[4] Flaga A., *Mosty dla pieszych*, WKŁ, Warszawa 2011.

[5] Flaga A., Michałowski T., *Zagadnienia aerodynamiki cięgien w mostach podwieszonych*, Inżynieria i Budownictwo, Vol. 6, 1997, 316-321.

[6] Gjelstrup H., Georgakis C.T., *A quasi-steady 3 degree-of-freedom model for the determination of the onset of bluff body galloping instability*, Journal of Fluids and Structures, Vol. 27, 2011, 1021-1034.

[7] Gjelstrup H., Georgakis C.T., Larsen A., *An evaluation of iced bridge hanger vibrations through wind tunnel testing and quasi-steady theory*, Wind and Structures, Vol. 15(5), 2012, 385-407.
[8] Gurung C.B., Yamaguchi H., Yukino T., *Identification of large amplitude wind-induced vibration of ice accreted transmission lines based on field observed data*. Engineering Structures, Vol. 24, 2002, 179-188.
[9] Hartog J.P.D., *Transmission-line vibration due to sleet*, Institute of Electrical Engineers, Vol. 51, 1932, 1074-1086.
[10] http://cet.arcchip.cz/wind-laboratory-en (online: 07.2014).
[11] http://www.toledoblade.com/gallery/Ice-closes-Skyway (online: 07.2014).
[12] Koss H., Gjelstrup H., Georgakis C.T., *Experimental study of ice accretion on circular cylinders at moderate low temperatures,* Journal of Wind Engineering and Industrial Aerodynamics, Vol. 104-106, 2012, 540-546.
[13] Makkonen L., *Modelling power line icing in freezing precipitation,* Atmospheric Research, Vol. 46, 1998, 131-142.
[14] Zdero R., Turan O.F., *The effect of surface strands, angle of attack, and ice accretion on the flow field around electrical power cables*, Journal of Wind Engineering and Industrial Aerodynamics, Vol. 98, 2010, 672-678.
[15] Zdravkovich M.M., *Flow around circular cylinders, Volume 1: Fundamentals,* Oxford University Press, USA, Oxford 1997.
[16] Zhitao Y., Zhengliang L., Eric S., William E.L., *Galloping of a single iced conductor based on curved-beam theory,* Journal of Wind Engineering and Industrial Aerodynamics, Vol. 123, 2013, 77-87.

TECHNICAL TRANSACTIONS | CZASOPISMO TECHNICZNE
CIVIL ENGINEERING | BUDOWNICTWO
2-B/2015

GRZEGORZ KIMBAR*

DYNAMICS OF SNOW MELTING ON TENTS DURING POSSIBLY THREATENING PRECIPITATION

PRZEBIEG TOPNIENIA ŚNIEGU NA DACHACH HAL NAMIOTOWYCH PODCZAS POTENCJALNIE NIEBEZPIECZNYCH OPADÓW

Abstract

Lightweight tent structures are allowed under European codes to be designed for reduced snow load if the interior of a tent is appropriately heated. The dependence of the resultant snow load on snowfall rate is considered in this paper for such cases. A simple thermodynamic model of the heat flux is derived. Numerical simulation reveals the occurrence of a precipitation rate threshold value above which safety measure provided by heating becomes ineffective.

Keywords: snow load, tents, safety

Streszczenie

Zgodnie z zapisami Eurokodów lekkie hale namiotowe mogą być projektowane na zmniejszone obciążenie śniegiem, jeżeli wnętrze hali jest odpowiednio ogrzewane. W artykule na podstawie prostego modelu termodynamicznego rozważana jest zależność wartości zgromadzonego obciążenia dachu od intensywności opadu śniegu. Obliczenia numeryczne ujawniają istnienie pewnej progowej wartości intensywności opadu śniegu powyżej której ogrzewanie hal staje się nieefektywne jako środek bezpieczeństwa.

Słowa kluczowe: obciążenie śniegiem, namioty, bezpieczeństwo

DOI: 10.4467/2353737XCT.15.148.4185

* Building Research Institute, Warsaw, Poland.

1. Introduction

Most regular roof structures are designed for a 50-year return period of snow loads. This strict regulation makes less sense in the case of light, temporary tent-like structures. Code EN 13782 [3] in section 6.4.3.2 allows applying only 0.2 a kNm^{-2} load (or 8 cm of snow cover) in its design, provided that the inside volume of the tent is heated by appropriate equipment 'in such a way, that the whole cladding has an outside temperature of more than +2°C' and that the heating begins prior to snowfall. This approach became quite common on the market, and the so-called 'not full-season' tent halls are being offered together with heating equipment and recommendations to clear away the snow in case of heavy precipitation. This last part remains problematic due to the fact that the very operation of snow clearance is in itself an additional load applied to the structure in situations when it could be close to the limit of its carrying capacity.

The melting of already deposited snow cover may require a significant amount of heat due to the relatively high latent heat of ice. However, in the above mentioned scenario, snowfall intensity would be a key factor shaping demand for heating power. According to ICAO [4], snowfall may be considered as 'light' if the precipitation rate does not exceed 1 kg $h^{-1}m^{-2}$. 'Moderate' snowfall conditions are those not exceeding 5 kg $h^{-1}m^{-2}$ (in some studies a 2.5 kg $h^{-1}m^{-2}$ is also given as a threshold value). Levels higher than those defined as 'moderate' snowfall precipitation are described as 'heavy'. These three categories of snowfall intensity are probably rooted in return period statistics similar to those applied to ground snow load, but unlike the latter, the spatial distribution of snowfall intensity is generally unknown.

2. Snow cover melting model

The problem of snow melt is well-covered in literature (for example [1, 2, 5]), and may be derived from the basic rules of thermodynamics. The heat flux generated by the provided equipment is distributed among heat conduction through the walls and ground, conduction through the roof (and the snow cover), increase of inside air enthalpy and increase of snow cover enthalpy which eventually causes melting. Estimation of these components in real applications may not be easy due to complicated phenomena such as convection, possible outside air infiltration, various inhomogeneities of the air, the roof structure and the snow itself. Therefore, the +2°C rule seems to be a reasonable condition at which large enough areas of the bottom layer of the snow cover melts and initiate liquid water flow or even snow slides (another two complicated phenomena).

A simple thermodynamic model is derived taking into account the heat balance in a light tent structure. The snow cover is treated as a one-dimensional domain with phase change, obeying the equation [7]:

$$\rho \frac{\partial h}{\partial t} = \nabla \left(\lambda \cdot \nabla T \right) \tag{1}$$

where: ρ − density, h − specific enthalpy, λ − specific thermal conductivity, T − temperature.

The temperature may be expressed as a function of enthalpy (13). Spatial derivative in a one-dimensional case may be replaced by a derivative over water content coordinate:

$$\nabla = \frac{\partial}{\partial y} = \rho \frac{\partial}{\partial w} \tag{2}$$

which further simplifies the governing equation to:

$$\frac{\partial h}{\partial t} = \frac{\partial}{\partial h}\left(\frac{\rho\lambda}{c}\right)\left(\frac{\partial h}{\partial w}\right)^2 + \left(\frac{\rho\lambda}{c}\right)\frac{\partial^2 h}{\partial w^2} \tag{3}$$

where y – vertical coordinate, w – water content coordinate ($w = 0$ for the bottom of the snow cover), c − specific heat of a substance (snow, water or mixture, depending on the value of the enthalpy).

The specific conductivity of snow may vary significantly [6] and even show anisotropic properties, but in approximation may be expressed as a function of density:

$$\lambda_s = 3\times10^{-6}\rho^2 - 1.06\times10^{-5}\rho + 0.024 \tag{4}$$

where both density and conductivity are expressed in standard SI units.

Total heat balance is given by (Fig. 1):

$$q_c + q_w + \partial_t H_c + \partial_t H_a = q_0 \tag{5}$$

It is assumed that no heat flux is present at equilibrium $T_i = T_e$ and beyond this point the heat flux is linear function of temperature difference (in other words: there is no persistent heat flux from the ground). Hence, the heat flux through walls and ground:

$$q_w = \Lambda_w \left(T_i - T_e\right) \tag{6}$$

rate of change of enthalpy of inside air:

$$\partial_t H_a = c_a \partial_t T_i \cdot V \tag{7}$$

total change of enthalpy of the snow cover:

$$\partial_t H_c = \partial_t \int_0^D h dy \tag{8}$$

where: H_c − total enthalpy of snow cover, H_a − total enthalpy of inside air, q_c − heat flux conducted by roof and snow cover, q_0 − heat source power, Λ_w − total conductivity of walls and ground, T_i − internal temperature, T_e − external temperature, c_a − specific heat of the air, V – inside volume of the tent, D – depth of the snow cover.

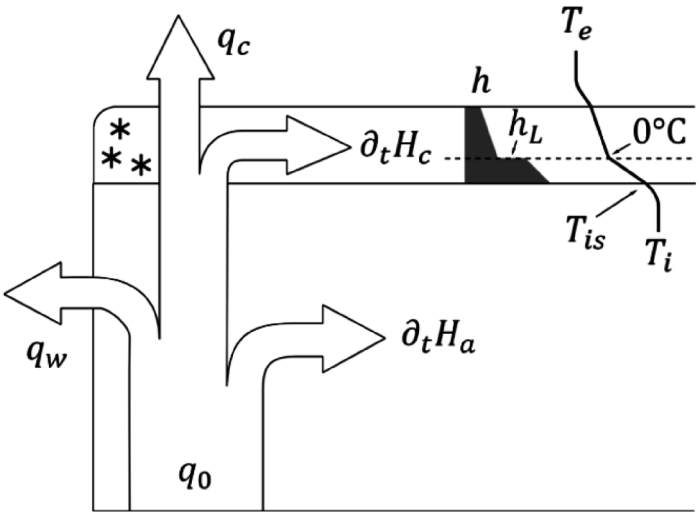

Fig. 1. Heat flow model in heated tent with snow cover

Air temperature inhomogeneity and cold air influx may be taken into account by appropriately modifying specific heat of the air to account for the loss of energy due to cold air mixing and gain in snow cover melting efficacy due to higher than average air temperature directly under the roof caused by convection.

The temperature at the top of the roof surface is expressed as:

$$T_{is} = T_i - \left(q_c + \partial_t H_c\right) \cdot \left(R_i + R_r\right) \tag{9}$$

where: R_i − thermal resistance of the heat interception, R_r − thermal resistance of the roof.

The thermal resistance of the roof in the case of tents covered with light fabric is negligible.

3. Calculation of snow melting during precipitation

The calculation involving phase change is susceptible to numerical instability due to stiffness of the governing equation in the transition region. To address this issue, known as the moving boundary problem, a dimensionless parameter (β) is used:

$$\beta = \frac{T_{is}}{w_t} \cdot \frac{w_t \kappa + R_e \rho_w \lambda_w}{\kappa T_{is} - T_e}, \quad \kappa = \frac{\rho_w \lambda_w}{\rho_s \lambda_s} \tag{10}$$

where: T_{is} − temperature on the internal surface, w_t − total water content in snow cover, $(\,)_w$ – water properties, $(\,)_s$ – snow properties.

The βw_t is a water content coordinate at which the phase transition occurs (shown as a "shelf" of h_L on Fig. 1). It is assumed that the curvature of the enthalpy function in snow and water layers is zero. This is a simplification, because the gain of the enthalpy in these regions can only occur by the second term of the RHS of (3). This approach may be called quasi-static – at each time point it is assumed that the enthalpy is at equilibrium and the change of system is accomplished only by a change of external conditions. In the case of this simulation, these external conditions are: the internal air temperature T_i, which changes due to the heating of the tent; the total water content of the snow layer w_t, which changes due to precipitation.

It is assumed that specific heat during melting is infinite, that is to say that the phase transition occurs at a constant temperature of 0°C, and the specific heats of the snow and water phases are constant.

With these assumptions, heat loss through the roof and snow layer may be expressed as:

$$q_c = \rho_w \lambda_w \frac{\kappa^\star T_{is} - T_e}{w_t \kappa + R_e \rho_w \lambda_w}, \quad \kappa^\star = \begin{cases} 1 \Leftarrow T_{is} \le 0 \\ \kappa \Leftarrow T_{is} > 0 \end{cases} \tag{11}$$

The snow enthalpy reference value is assumed to be 0 J kg^{-1} at the temperature of external air (T_e). This assumption simplifies the calculation of the heat budget during precipitation since falling snow does not add enthalpy to the system.

Total thermal energy contained in the snow layer may be expressed depending upon the location of phase change layer (β) as follows:

$$H_c = \begin{cases} \dfrac{h_e + h_i}{2} w_t & \Leftarrow \beta \le 0 \\ \dfrac{h_e - T_e c_s}{2}(1-\beta) w_t + \dfrac{h_L - T_e c_s + h_i}{2} \beta w_t & \Leftarrow \beta > 0 \end{cases} \tag{12}$$

where: h_e − specific enthalpy of the snow layer at external surface, h_i – specific enthalpy of the snow layer at internal surface, h_L – latent heat of ice melting, c_s – specific heat capacity of snow.

Temperature of the snow cover layer is a function of specific enthalpy:

$$T(h) = \begin{cases} \dfrac{h}{c_s} + T_e & \Leftarrow h < -c_s T_e \\ 0°\mathrm{C} & \Leftarrow -c_s T_e < h < h_L - c_s T_e \\ \dfrac{(h - h_L + c_s T_e)}{c_w} & \Leftarrow h > h_L - c_s T_e \end{cases} \tag{13}$$

where: c_w − specific heat capacity of water.

The problem in this form has two free variables: internal temperature of the roof surface T_{is}, and total water content of the snow layer w_t dependent on snow precipitation rate and time. Time derivatives of these variables may be calculated analytically.

4. Example

An example calculation is performed for a typical 20 m × 30 m × 8 m steel tent structure covered with a thin layer of PVC. The parameters of the simulation are gathered in Table 1.

Table 1

Simulation parameters

Simulation parameter			Snow	Water
Density	ρ	[kg m^{-3}]	200	1000
Conductivity · density	$\lambda\rho$	[kg m^{-2} s^{-3} K^{-1}]	≈ 28	580
Specific heat capacity	c	[J kg^{-1} K^{-1}]	2090	4190
Water/snow properties ratio (eq. 10)	κ	[1]	≈ 20.7	
Roof area		[m^2]	600	
Average tent height		[m]	8	
External temperature	T_e	[°C]	–4	
Latent heat of snow melting	h_L	[J kg^{-1}]	333 000	
Total heat conductivity of walls and ground	Λ_w	[W K^{-1}]	1500	
Thermal resistance of the inside surface of the roof	R_i	[K m^2 W^{-1}]	0.1	
Thermal resistance of the outside surface of the roof	R_e	[K m^2 W^{-1}]	0.04	

Initial condition of the simulation is $T_{is} = T_e$. It is a worst case scenario when the heating is being turned on only after precipitation starts. This condition violates the recommendation enclosed in EN 13782 [3] to heat the interior of the tent prior to the precipitation. The simulation of snow melting with initial temperature of the roof above 0°C becomes significantly more complex since in this case, snow-water mixture flow over sloped roofs must be taken into account. However, calculations show that the initial stage at which heating is mostly directed at increasing temperature of the internal air is relatively short compared to the time required to overcome the latent heat of precipitating snow. Moreover, this scenario is unfortunately quite probable in real-world situations.

Simulation is terminated when surface temperature exceeds +2°C which is (as assumed before) a time point when snow cover clearance occurs. The total amount of snow cover

accumulated to that point is shown in Fig. 2 in relation to heat source power q_0. The simulation was resolved by the RK4 algorithm with a time step of 3 seconds. The time step was adjusted at 0°C crossing due to numerical instability.

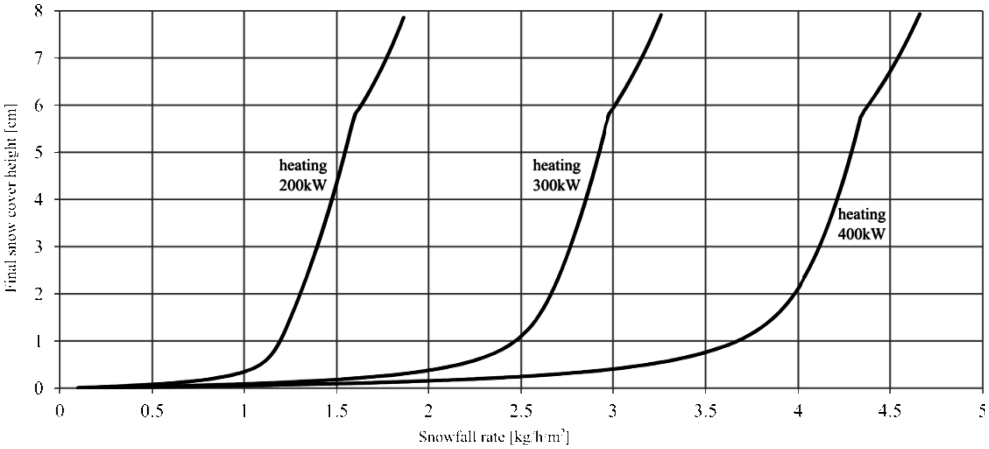

Fig. 2. Final (i.e. at T_{is} = ±2°C) snow cover height for different heating power

5. Conclusions

Although the snow melting phenomenon on a roof is a complex issue requiring many assumptions and simplifications, some general conclusions can be drawn regarding the reliability of safety measures obtained by heating of the interior of a tent. Despite the total heat power of heating devices, a threshold value of allowable snowfall intensity occurs in simulation. The final snow cover height (and roof load) is a step function for a relatively narrow range of snow precipitation rate, above which, weather conditions render the heating virtually ineffective as a means of preventing excessive snow loads.

Practical calculations aimed at assessing appropriate heating power must take into account many additional aspects of heat flux such as convection, outside air infiltration, snow permeability for melted snow, possibility of snow cover slide (roof fabric friction) etc. However, in any case, assumed snowfall intensity should remain as an important factor for such calculations.

The simulation shown in the paper shows that there is no safe level of heating power that can assure the safety of a large tent without relation to the expected snow-fall rate. Because the snow-fall rate is a random meteorological variable, the heating of a tent as a safety measure should be calculated with respect to the return period of this variable. An adequate value of this return period should be discussed among the engineering and scientific community.

References

[1] Anderson E.A., *Development and testing of snow pack energy balance equations*, Water Resources Research, Vol. 4(1), 1968, 19-37.

[2] Brun E., Martin E., Simon V., Gendre C., Coleou C., *An energy and mass model of snow cover suitable for operational avalanche forecasting*, Journal of Glaciology, Vol. 35(12), 1989, 1.

[3] EN 13782 Temporary structures − Tents – Safety.

[4] ICAO, Doc 9837 AN/454, *Manual on automatic meteorological observing systems at aerodromes*, International Civil Aviation Organization, 2011.

[5] Kondo J., Yamazaki T., *A Prediction model for snowmelt, snow surface temperature and freezing depth using a heat balance method*, Journal of Applied Meteorology, Vol. 29.5, 1990, 375-384.

[6] Riche F., Schneebeli M., *Thermal conductivity of snow measured by three independent methods and anisotropy considerations*, The Cryosphere, Vol. 7, 2013, 217-227.

[7] Zalba B., Marín J.M., Cabeza L.F., Mehling H., *Review on thermal energy storage with phase change: materials, heat transfer analysis and applications*, Applied Thermal Engineering, Vol. 23, 2003, 251-283.

TECHNICAL TRANSACTIONS | CZASOPISMO TECHNICZNE
CIVIL ENGINEERING | BUDOWNICTWO
2-B/2015

S. F. PICHUGIN*, YU.V. DRYZHYRUK**, N.M. POPOVICH***, I.V. CHERNETSKA****

THE FEATURES OF SNOW LOADS ON BUILDING ROOFS

WŁAŚCIWOŚCI OBCIĄŻENIA ŚNIEGIEM DACHÓW BUDYNKÓW

Abstract

In this paper the probabilistic model of the snow accumulation on the roofs with height discontinuity was worked out, the decreasing coefficient for the snow load weight was received and the ways of their application in the designing were elaborated. The probabilistic model for impulse stochastic process of snowfall sequence was developed. Data from meteorological stations in Ukraine allow determination of statistical characteristics: average annual snowfall amount and exponential distribution of values of one snowfall. The law of intensity distribution of snow melting has been determined experimentally. The territorial zoning map of Ukraine by characteristic values of the snow load on the roofs that emanate heat was developed.

Keywords: building roofs snow load, snow accumulation, snowfall, safety

Streszczenie

W pracy opracowano probablilistyczny model akumulacji śniegu przy zmianie wysokości dachu, otrzymano współczynnik zmniejszający dla obciążenia śniegiem oraz wypracowano sposoby jego wykorzystania w projektowaniu. Rozwinięto model probablistyczny dla impulsowego procesu stochastycznego dotyczącego opadu śniegu. Dane ze stacji meteorologicznych na Ukrainie pozwoliły określić charakterystyki statystyczne: średni roczny opad śniegu i wykładniczy rozkład wielkości w pojedynczym opadzie śniegu. Prawo rozkładu intensywności topnienia śniegu zostało określone eksperymentalnie. Rozwinięto mapę stref terytorialnych Ukrainy za pomocą charakterystycznych wielkości obciążenia śniegiem dachów wydzielających ciepło.

Słowa kluczowe: dachy budynków, obciążenie śniegiem, akumulacja śniegu, opad śniegu, bezpieczeństwo

DOI: 10.4467/2353737XCT.15.149.4186

* Department of Metal, Wooden and Plastic Structures, Poltava National Technical Yuri Kondratyuk University, Ukraine.
** Department of Engineering Management and Technology and Occupation Safety, Poltava National Technical Yuri Kondratyuk University, Ukraine.
*** Department of Structures, Products and Materials Engineering, Poltava National Technical Yuri Kondratyuk University, Ukraine.
**** Department of Hydraulics, Water Supply and Sewerage, Poltava National Technical Yuri Kondratyuk University, Ukraine.

1. Introduction

The Ukraine has practically adapted its atmospheric load codes to European ones with the help of new state Codes DBN B.1.2.-2:2006 'Loads and loading' [4]. It should be mentioned that there are still lots of issues concerning matching national Ukrainian codes with European ones. This problem is being complicated by the position of the state in the process of gradual transition to European codes as the national searching results should be taken into account. Modern probabilistic and numerical methods can help in solving the structure snow load comprehensive research. Climatic changes should be taken into consideration. The results of the scientific work have to be embodied into the national application of European Codes. These fully meet Ukraine climatic requirements and can be realized. These methods might be applied to the recommendation development for designers.

2. Review of the latest pieces of research and publications

Numerous scientific works of specialists of different countries were devoted to the description of snow falls as a natural phenomenon and a source of loading on buildings [1, 8, 11, 13]. Certain attention is spared to the questions of snow accumulation at points of different heights on buildings [9, 17, 18]. Advanced approaches to the study of snow loads are developed using methods of computational fluid dynamics which have been in applies in Japan, USA and Poland for some time. Verification of the obtained results is performed by comparing them with snow survey data and snow modelling in a wind tunnel [6, 7].

3. Separation of not solving parts of general problem

Significant drawbacks in the application of numerical methods and aerodynamic modelling are their high cost, the need for highly capable PC hardware and the considerable complexity of modelling such heterogeneous subject-matter as snow. Thus, until recently, the most informative way to obtain snow parameters (height, density, thawing and accumulation) was through snow surveys and natural snow investigation. Such approach allows solving the tasks such not decided fully, as a snow loading at points of different heights on buildings and code setting of the snow loading on cold roofs and roofs of heated buildings.

4. Target statement

The aim of the article is the development of engineering methods that allow taking into account an increased snow load on the covering of buildings of variable heights; this is in

order to estimate the processes of snow thawing on roofs of heated buildings and snow laying on cold roofs.

5. Principal material and results

In the limits of complex mode to the study of snow load, the snow crystals physical characteristics were analyzed, evolution of the national designing standards of snow loads was tracked, and factors that have an influence on the increased snow accumulation at points of different heights on buildings were determined (Fig. 1) [12, 15].

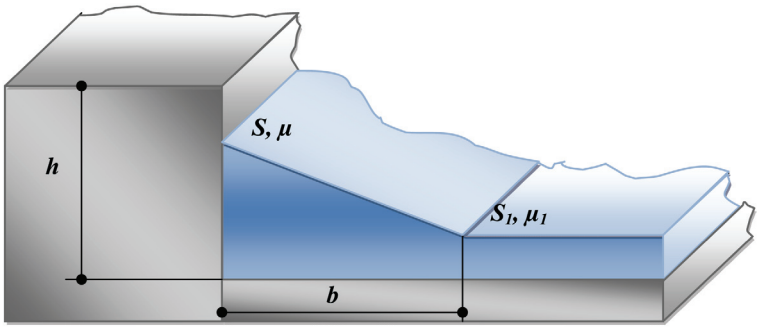

Fig. 1. Drifted snow load zone in the places of height discontinuity (according to codes of structural design)

Analysis of the results of the carried out investigations has shown that such variable factors as the physical characteristics of snow crystals, the solid atmospheric precipitation quantity, local wind patterns, thaw and pouring have a considerable influence on the formation of excess snow laying at points of different heights on buildings. However, this is not represented in the national and foreign design standards.

The snow cover experimental investigations (snow surveys) were the next stage in the studying of snow loads. They carried out in 2008–2010 with parallel information acquisition about physical and meteorological factors (wind speed and direction, external air temperature) that influence on the drifted snow load forming at points of different heights on buildings [12]. The statistical processing of the results was effectuated. It was ascertained that wind plays a main part in the increased snow accumulation at points of different heights on buildings. The comparison of the measurements on the ground surface and on the building roofs confirms this fact. It was proven that 20–25 % of snow from lower and upper roofs are blown away to the drifted snow load zone. The actual geometric parameters of the drifted snow load zone are in near total compliance with recommendations of DBN [4]. The main difference lies in the fact that current standards over-estimate the value of the increased snow accumulation at points of different heights and at the same time, clearly under-estimate (by 10–40%) the snow load in zone outside drifted snow load.

Special attention was paid to the comparative analysis of national standards [4] with Soviet standard, SNiP [16] and foreign analogues – American codes, ASCE [2] and European codes, Eurocode-1 [5]. It was established that there is no clear relationship between the drifted snow load calculated by SNiP and DBN for the same roofs. The drifted snow load may go up by 27–81% and decrease by 19% in the case of snow filling of the entire height difference with the increasing of the snow load on the ground at 48%. It was found that the drifted snow load calculated according to the DBN and Eurocode-1 standards varies by 15–30% on both smaller and larger sides, and European codes are distinguished by a too simplistic and generalized approach and a small amount of design schemes. Norms of the USA [2], in comparison with national standards, may significantly over-estimate (to 55%) the weight of excess snow laying at points of different heights in conditions up to 3m and under-estimate (to 58%) it for differences from 3m to 8m. The final stage of research was the creation of the probabilistic model of snow accumulation at points of different heights on buildings. Such important factors of drifted snow load forming as snow load on the ground, wind speed and direction, ambient air temperature and snow thawing were considered and evaluated. As a result of careful analysis of these influential factors, the most important of them, such as snow load on the ground and wind speed, were taken into consideration in an explicit probabilistic form. In addition, the frequency of winds with a speed greater than 4m/s was considered as a deterministic value. Other factors were not taken into account because they could lead to significant model complications, contributing only to the reduction of the snow quantity at points of different heights.

The obtained probability model of the snow accumulation at points of different heights on buildings allowed estimating the drifted snow load defined by the DBN [4]. The snow load combination coefficients for a number of roofs with lifetimes of 50 and 100 years [12] based on the developed method was determined. These coefficients allow the optimization of the drifted snow load at points of different heights. In order to implement them, engineering practice offers a special approach to adjusting design values of drifted snow loads, based on field studies (Fig. 2). This supposes redistributing the snow by moving some of it to the 'non-snow bag area'. This becomes possible when proportionally reducing the maximal value of coefficient μ to value μ_{sb}, along with the reduction of snowdrift run value from b to b_{sb}. Simultaneously, the coefficient μ_1 should be raised to μ_{1sb} value.

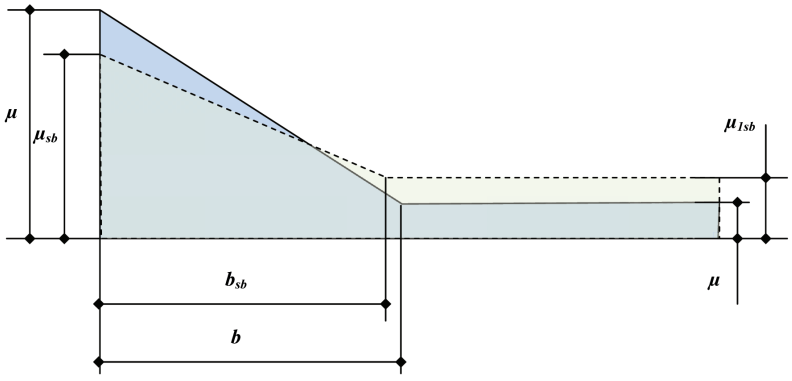

Fig. 2. Correction algorithm of design values of drifted snow load

According to the given rule, approximate correction relations have been found:

$$\mu_{sb} = \mu(\gamma_{sb} + 0.05)$$
$$\mu_{1sb} = \frac{\mu_1}{(\gamma_{sb} + 0.05)}$$
$$b_{sb} = b(0.2\gamma_{sb} + 0.77) \quad (1)$$

Standard deviation between theoretical values of reduced drifted snow load and those being calculated according to the above-given formulae (1) fluctuates in the range of 0.7 to about 8% adding to safety margin. That is, these formulae (1) can be successfully applied in engineering design.

These coefficients allow optimising the weight of snow deposits at points of different heights on buildings. The approach to the correction of the design parameters of drifted snow loads based on the field observations was proposed for use in engineering practice. Its essence lies in the redistribution of the part of snow from the drifted snow load area to other areas.

Thus, the probabilistic model of drifted snow load made it possible to get reasonable coefficients of the snow load at points of different heights on buildings. Their values for the Ukraine territory can be taken at first approximation on a level 0.8. This decision allows reducing the efforts in the truss elements by 6–16% and reducing the estimated load on structures.

At the same time with character of the snow distribution, snow blowing and snow moving on the roofs surfaces of various forms create the snow thawing on the roofs that also affects on the value of snow load. Moreover, thawing can have different intensities because of the different amounts of heat which depends on the thermal resistance of the roof surface. This process has not been studied enough, the existing standards DBN and SNiP [4, 16] take it into account through the use of reducing (thermal) coefficients of exploitation conditions C_e = 0.8 for the snow load value on non-insulated roof surfaces with increased heat loss while the roof slope is equal to more than 3% and proper drainage of meltwater is ensured. It is quite approximate that leads to the excessive materials consumption for some structures and the insufficient reliability of others. It remains unclear what roofs should be considered as non-insulated. Besides that, looking on the variety of using building materials and the wide limits of the possible thermal resistance structures, it would be reasonable to introduce a differentiated coefficient depending on the roof thermal resistance and climatic characteristics of the locality. All of these factors bring a necessity for studies of the process of snow thawing on roofs, the influence of thermal characteristics of the snow cover on the snow load size, and refinement coefficient of exploitation conditions of the roofs.

A number of field observations showed that some roofs have sufficient insulating properties and do not allow practically any heat loss and other roofs let pass significant heat flows, this can lead not only to the snow load decreasing, but full snow thawing. The decrease in the snow load on the roof was fixed at 30%.

The mathematical model and the calculation program of snow thawing on the roof on account of the heat proceed from the room [10] was developed on the basis of the information about the features of formation and physical properties of snow cover received from field

observations and analysis of the literature, as well as basic heat transfer laws. This program made it possible to predict the height and weight of the snow on the surface at any time from the beginning of melting. The comparison of calculation results with experimental data received in Poltava National Technical Yuri Kondratyuk University on real and simulated buildings showed good congruence of the total thawing time which affirms the adequacy of the proposed model.

The program of statistical snow load modelling based on the developed method of calculation of melting snow on roads was compiled. The snow-measuring data was collected over years 1980-2000 for 16 meteorological stations from different regions of the Ukraine and the processes of snow loads on the ground and on the roofs with different thermal resistances were modeled [10].

Coefficients of the roof exploitation conditions obtained for non-insulated roofs with low thermal resistance were found to be much lower than the current standards determine at a value of 0.8. With increasing of the roof thermal resistance, the thawing coefficient increases. At the same time, the return period of the designed snow load has virtually no influence on the result, it is therefore possible to be guided by T = 100 years in all cases, taking factor C_e in the range 0.6–1.0 in depend of the roof thermal resistance.

The selected meteostation network allowed covering all typical regions of the Ukraine. The territorial variability analysis of the obtained coefficients with their dependence on thermal resistance allows obtaining the analytical expression for the calculating of the coefficient of roof exploitation conditions

$$C_e = 1 - 0.00022 S_0 \cdot \exp\left(-0.6R\right) \tag{2}$$

where S_0 – characteristic snow load corresponding to DBN (Pa) [4], R– thermal resistance of roof ($m^2 \cdot ºC/Wt$).

As the coefficient of roof exploitation conditions decreases with increases in the snow load characteristic value, it can substantially reduce the snow load in areas with significant snow deposits that are accumulated during the winter. In areas where snow accumulation is practically unobserved, the snow thawing effect is minimal.

In order to estimate the economic effect of C_e coefficient using the calculation of real roof structures with consideration of suggested propositions and by the current DBN [4] was done. The maximum effect of using the specified coefficient of roof exploitation conditions was obtained in the conditions of snow region with the largest characteristic value of snow load. For heavy roofs, the snow load does not play a significant role thereafter the effect of its reduction was small. When calculating light roofs, the influence of the coefficient of roof exploitation conditions is the largest and using the specified C_e value saves the steel consumption by 5–30%.

Particular attention was paid to the investigation of the formation processes of snow load on the non-insulated (cold) roofs of industrial buildings with excessive heat emission [3] and to the development of scientifically based proposals for the snow load rationing on the roofs of metallurgical plants and agricultural industrial buildings (greenhouses and hotbeds) [3]. Thus, experimental studies of the formation process of snow cover on the roofs that emanate heat were conducted on a model that provided stable internal air temperature below

the glass roof and the ability to periodically determine the height and the average density of snow on the roof similar to the method of the snow survey. Observations after snow cover on the roof were carried out during the snowfall process and by the artificial creation of snow cover in order to determine its melting laws. Observations during two winters gave the possibility to find out the statistical characteristics of the random value of the snow melting speed on the roofs that emanate heat and also its dependence on a number of influencing factors. The theoretical model that allows determining the speed of snow melting on the emanating heat roofs was developed in consideration of the thermal snow properties, heat transfer from premise to the snow cover on the roof and heat consumption for the heating and melting of snow. Comparison of calculated data with experimental results has shown satisfactory coincidence. This fact allows using the developed theoretical model for the snow loads determining in consideration of snow melting on the non-insulated roofs of premise with heat excess emanating.

The calculated values of snow load on non-insulated roofs of buildings with excess heat emanating were determined on the basis of the developed probabilistic model of snowfall sequence after the results of snow surveys carried out over 20 years at 183 meteorological stations in the Ukraine. A relatively dense network of meteorological stations allowed obtaining representative statistical characteristics of snowfall sequences regarding average annual snowfall and the expectation value of single snowfall occurrences. Maps of the Ukraine showing territorial zoning that reflect the regularities of territorial variability of these characteristics were developed [14]. In consideration of the influence of the snowfall sequence random parameters, snowfall duration and snowmelt speed on the value of the snow load on the roof, the statistical modelling procedure by a specially developed program was used to calculate the design values. It was established that the value of snow load on the roof could be described by discrete-continuous exponential distribution – this takes into account both the value of snow load, and the possibility of its complete absence. Absence of enough closely relation with the characteristic value of full snow load on ordinary roofs given in the standards [4], stipulate the need of separate rate setting of the snow load on the roofs that emanate heat. For this purpose, through the generalization of the results of 132 plain meteorological stations, the map of the territorial districting of the Ukraine is worked out in correspondence with the characteristic values of the snow loading from one snow-fall S_0 that answer a return period of 10 years (Fig. 3).

The map identified 3 territorial regions with regional values of snow load equal to 250, 300 and 350 Pa. The averaged dependence of reliability coefficient is also determined for the snow loading from the return period of T (in years) :

$$\gamma_f^* = 0.1 + 0.9 \log T \tag{3}$$

The character of territorial variability of snow load on the roofs that emanate heat is significantly different from full snow load prescribed by standards [4]. Comparison of calculated values obtained by the developed recommendations with appropriate data of standards [4] showed an increase in the design values for the whole territory of the Ukraine. This fact will lead to increase of the materials consumption for roof framing, but provide social effect by increasing their reliability.

Fig. 3. The Ukraine territorial districting of the snow loading on cold roofs

6. Conclusions

The probabilistic model of the snow accumulation on the roofs with height discontinuity was worked out, the decreasing coefficient for the snow load weight was received and the methods of their application in the designing were elaborated. The proposed approach allows differentiating the coefficient of roof exploitation conditions C_e depending on the roof thermal resistance, and in some cases, significantly to reduce the design snow load values and to give a substantial saving of steel. The probabilistic model for impulse stochastic process of snowfall sequence has been developed. According to the data from 132 meteorological stations in the Ukraine, its statistical characteristics have been found – average annual snowfall amount and exponential distribution of values of one snowfall. The law of intensity distribution of snow melting has been determined experimentally. The territorial zoning map of the Ukraine by characteristic values of snow loads on roofs that emanate heat was developed.

References

[1] Allen D.E., *Snow load on buildings*, NRC, Canada, Ottawa 1959.
[2] ANSI/ASCE 7-05, Minimum Design Loads for Buildings and Other Structures, American Society of Civil Enginners, Reston, USA, 1996.
[3] DBN B.2.2-2-95, Buildings and Structures. Greenhouses and Hotbeds, Ukraine, Kyiv, 1995 (in Ukrainian).
[4] DBN B.1.2. 2-2006, Load and Loadings. Design Standards, Ukraine, Kyiv 2006 (in Ukrainian).

[5] EN 1991–1–3, Eurocode 1. Actions on Structures – Part 1–3: General Actions, Snow Loads. CEN, Belgium, Brussels 2003.
[6] Flaga A., Kimbar G., Matys P., *Wind-tunnel tests for snow load prediction on the roof of the Municipal Stadium in Poznań*, Proc. 6th International Conference on Snow Engineering, Canada, Whistler 2008.
[7] Joh O., Sakurai S., Abe O., *Wind tunnel investigation of snow accumulation on a single flat roof and a two-level flat roof using artificial snow,* Proc. 5th International Conference on Snow Engineering, Davos, Switzerland, 2004,169-175.
[8] Male D.H., Gray D.M., *Handbook of snow: principles, processes, management and use,* Pergamon Press, USA, 1981.
[9] Meloysund V., Hoiseth K.V., Leira B., Lis K., *Development of design snow loads on roofs in Norway,* Proc. 6th International Conference on Snow Engineering, Canada, Whistler 2008.
[10] Pashinskiy V.A., Molka I.V., Kutnyi B.A., *Statistical modeling of snow load on the roofs of heated buildings,* Collection of Scientific Papers "Resource-saving materials, structures and buildings" 22, Ukraine, Rivne 2011, 164-172 (in Ukrainian).
[11] Pichugin S.F., *Probabilistic description of ground snow loads for Ukraine*. Snow Engineering, Recent Advanced and Developments, A.A. Balkema, Rotterdam 2000, 251-256.
[12] Pichugin S., Dryzhyruk Y., *Snow load investigation for buildings of different heights,* Recent Advances in Research on Environmental Effects on Buildings and People (eds. Flaga A., Lipecki T.), PAWE, Poland, Cracow 2010, 279-286.
[13] Pichugin S.F., Mahinko A.V., *Snow and ice load on building structures,* ASMI, Poltava, Ukraine 2012 (in Russian).
[14] Pichugin S.F., Popovych N.M., *Esimation method for design values of snow loads on cold roofs,* Collection of Scientific Papers "Engineering Industry and Contsruction" 3 (22), Ukraine, Poltava 2012, 190-196 (in Ukrainian).
[15] Pichugin S., Dryzhyruk Y., *The features of snow load on building roofs,* Books of Keynote Lectures and Abstracts of 7th International Symposium on Environmental Effects on Buildings and People (EEBP7), eds. Flaga A., Lipecki T., PAWE, Poland, Lublin-Cracow 2014, 107-108.
[16] SNIP 2.01.07-85. Loads and loadings. Design standards, USSR, Moscow 1986 (in Russian).
[17] Taylor D.A*., Snow loads on multi-level flat roofs in Canada*, National Research Council of Canada, Canada, Vancouver 1987.
[18] Żurański J.A., Dufresne de Virel M., Suchecki A., *Field investigation of snow loads on a gable roof*, Proc. 5th International Conference on Snow Engineering, Switzerland, Davos 2004.

CONTENTS

SNOW LOAD AND ICE LOAD